Université de Montréal

Critical roles of Dendritic Cells and Macrophages in Cardiovascular Disease

par

Junseong Lee

Départment de microbiologie, infectiologie et immunologie

Facultè de Mèdecine

Thèse présentée à la Facultè de Mèdecine

en vue de l'obtention du grade de Philosophiae Doctor

en microbiologie and immunologie

October, 2019

Résumé

Les maladies cardiovasculaires représentent un risque majeur de mortalité dans le monde et la prévalence de ces pathologies ne cesse d'augmenter. Pour comprendre la réponse inflammatoire de ces maladies, nous avons fait d'énormes progrès dans la recherche moléculaire et cellulaire afin de démontrer clairement que les macrophages et les cellules dendritiques jouent un rôle central dans l'athérosclérose et l'infarctus du myocarde, deux maladies cardiovasculaires mortelles.

Nous avons trouvé que, à l'état normal, le cœur de souris abrite les deux types de cellules dendritiques classiques (cDC1 et cDC2). Conformément à ce qui est connue sur ces les cDC, nous avons constaté que les cDC1, qui expriment IRF8, dépendent du Flt3, un facteur de croissance important pour leur développement alors que les cDC2, qui expriment IRF4, sont Flt3 indépendantes. Nous avons trouvé que le nombre total leucocytes $CD45^+$ augment dans le cœur des souris ayant subi l'infarctus du myocarde. Ces leucocytes étaient majoritairement des macrophages, des neutrophiles et des cDCs. Parmi ces dernières, les cDC2 ont connu une plus forte augmentation.

Dans un premier projet, nous avons vérifié le rôle de ces cDCs dans cette pathologie. Pour ce faire, nous avons procédé à la déplétion de ces cellules en utilisant un modèle de souris exprimant le récepteur de la toxine diphtérique (DTR) au même temps que Zbtb46. L'expression spécifique de ce dernier dans les cDCs induit l'expression de la DRT et l'injection ultérieure de la toxine diphtérique provoque la déplétion des cDCs chez ces souris transgéniques. Nos travaux ont montré que la déplétion des cDCs diminue le recrutement des leucocytes et l'expression de la cytokine inflammatoire l'IL-1β dans le cœur des souris ayant subi l'infarctus du myocarde. Cela réduit considérablement l'ampleur de l'infarctus et améliore la fonction cardiaque, suggérant que les cDCs jouent un rôle important dans l'infiltration de cellules immunitaires après infarctus du myocarde.

Dans une autre étude, nous avons mis au point, pour la première fois, une méthode basée sur l'utilisation de sonde lipidique pour analyser les cellules spumeuses de l'aorte par cytométrie en flux. Cette méthode permet de cibler et isoler les macrophages spumeux et non-

spumeux afin d'analyser leur profile transcriptomique. En plus de caractériser ces cellules, cette technique permet d'évaluer la taille des plaques d'athérosclérose. Le séquençage des ARN (ARN-seq) a montré que les macrophages spumeux chargés de lipides dans les lésions athérosclérotiques expriment clairement différents transcrits par rapport aux macrophages non-spumeux. De manière surprenante, nous avons constaté que les macrophages non-spumeux présentaient une signature pro-inflammatoire reflétée par une régulation à la hausse de l'Il1β, le Tnf et Nlrp3. Par contre, les macrophages spumeux présentait un profile non inflammatoire caractérisé une augmentation de l'expression des gènes liés au transport et à l'absorption de lipides (cholestérol et acides gras). Contrairement à ce qui est connue jusqu'à maintenant sur le rôle pathogénique des macrophages spumeux, nos résultats montrent que ces cellules jouent un rôle plutôt protecteur dans l'athérosclérose.

Collectivement, nous avons spécifiquement identifié la fonction des cDC et des macrophages dans la pathogenèse des maladies cardiovasculaires. Comprendre le rôle précis de ces cellules aidera à développer une stratégie immunothérapeutique appropriée pour atténuer les maladies cardiovasculaires.

Mots clés : cellules dendritiques conventionnelles, macrophages, cellules spumeuses, athérosclérose, infarctus du myocarde, ARN-seq

Abstract

Cardiovascular disease is a major cause of mortality in the world, and is rapidly increasing. To understand the inflammatory response of various diseases, we have made tremendous advances in molecular and cellular research to show clear evidence that macrophages and dendritic cells play central roles in cardiovascular diseases, such as atherosclerosis and myocardial infarction.

We have identified the two conventional DCs subsets (cDC1 and cDC2) in heart of healthy mouse. As expected, we found that the IRF8-expressing cDC1, but not the IRF4-expressing cDC2, was dependent on Flt3 for its development. Myocardial infarction significantly increased the infiltration of $CD45^+$ leukocytes in the infarcted heart, including macrophages, neutrophils and DCs. Among cDC, the most significantly increased subset was the cDC2. The diphtheria toxin receptor (DTR) mediated depletion of Zbtb46-expressing DCs in myocardial infarcted mice led to a significant decrease of IL-1β expression together with an increased recruitment of leukocytes. This dramatically reduced the infarcted size and improved cardiac function, suggesting that cardiac DCs play an important role in immune cell infiltration following myocardial infarction.

In another study, we developed, for the first time, a lipid probe-based flow cytometry method to analyze foam cells in atherosclerotic aorta. Our method enables to isolate foamy and non-foamy macrophages in order to perform the transcriptomic analysis of these cells. In addition, this technique allows to assess the severity of atherosclerosis and the characteristics of foam cells. RNA-seq analysis showed that lipid-laden foamy macrophages in atherosclerotic lesions clearly expressed different transcripts compared to non-foamy macrophages. Surprisingly, we found that non-foamy macrophages showed a pro-inflammatory signature reflected by the up-regulation of cytokines, such as *Il1*β, *Tnf* and *Nlrp3*. However, foamy macrophages up-regulated genes related to the transport and uptake of lipids (cholesterol and fatty acid).

Collectively, we specifically identified the function of dendritic cells and macrophages in the pathogenesis of cardiovascular diseases. Understanding the precise role of these cells

will help to develop appropriate immune-therapeutic strategy to attenuate cardiovascular disease.

Keyworks : Conventional DCs, Macrophages, Foam Cells, Atherosclerosis, Myocardial Infarction, RNA-seq

Table of Contents

List of Tables

CHAPTER 1

CHAPTER 2

CHAPTER 3

CHAPTER 7

List of Figures

CHAPTER 1

CHAPTER 2

CHAPTER 3

CHAPTER 4

CHAPTER 5 (APPENDIX I)

CHAPTER 6 (APPENDIX II)

CHAPTER 7 (APPENDIX III)

CHAPTER 8 (APPENDIX IV)

CHAPTER 9 (APPENDIX V)

List of Abbreviations

ABCA1	ATP binding cassette subfamily A member 1
ABCG1	ATP binding cassette subfamily G member 1
APCs	Antigen presenting cells
ApoE	Apolipoprotein E
ARG1	Arginase 1
αSMA	Alpha smooth muscle actin
Batf3	Basic leucine zipper ATF-like transcription factor 3
BM	Bone marrow
BODIPY	4,4-difluoro-1,3,5,7,8-pentamethyl-4-bora-3a,4a-diaza-s-indacene
BPA	Bisphenol A
BPS	Bisphenol S
BrdU	5-bromodeoxyuridine
BSA	Body surface area
BST2	Bone marrow stromal cell antigen 2
CD	2-hydroxypropyl-β-cyclodextrin
cDC	Conventional dendritic cells
CHOW	Normal diet
CLP	Common lymphoid progenitor
CDP	Common dendritic cell progenitor
CMP	Common myeloid progenitor
COX2	Cyclooxygenase 2
cSMAC	Central supra-molecular activation complex
CTL	Cytotoxic T lymphocytes
CTL-P	Cytotoxic T lymphocyte-progenitor
CTMC	Continuous tme markov chain
CVD	Cardiovascular disease
hPCSK9	Human proprotein convertase subtilisin/kexin type 9
DALYs	Disability adjusted life-years
DAMP	Damage-associated molecular pattern

DCs	Dendritic cells
DEG	Differentially expressed gene
DN	Double-negative
DT	Diphtheria toxin
DTR	DT receptor
EC	Endothelial cells
ECG	Electrocardiography
ECM	Extracellular matrix
EMPs	Erythromyeloid progenitors
eNOS	Endothelial nitric oxide synthase
Erb	Estrogen receptor beta
ESAM	Endothelial cell-specific adhesion molecule
FAC	Fractional area change
FACS	fluorescence-activated cell sorting
Flt3	fms like tyrosine kinase3
Flt3L	Flt3 ligand
Foxp3	Forkhead box P3
FSC	Forward scatter
GBPs	Guanylate-binding proteins
GM-CSF	Granulocyte-macrophage colony-stimulating factor
GO	Gene ontology
GSEA	Gene set enrichment analysis
H&E	Hematoxylin and Eosin
HDL	High density lipoprotein
HDL	High density lipoprotein
HSCs	Human stem cells
HSPC	Hematopoietic stem and progenitor cells
Hu-mice	Humanized mice
IB	Immunoblotting
ICS	Intracellular staining
ID2	Inhibitor of DNA binding protein 2

IDL	Intermediate density lipoprotein
IDO-1	Indoleamine 2,3-dioxygenase 1
IFN	Interferon
IL	Interleukin
IRF	Interferon regulatory factor
LDL	Low density lipoprotein
LDL-C	Low density lipoprotein-cholesterol
LDLR	Low-density lipoprotein receptor
LFA-1	Lymphocyte function-associated antigen-1
LMICs	Low- and middle-income countries
LN	Lymph node
LPCAT3	Lysophos-phatidylcholine acyltransferase 3
LPS	Lipopoysacchride
LV	Left ventricle
LVID	Left ventricle internal diameter
LVM	LV mass
LXR	Liver X receptor
Ly6C	Lymphocyte antigen 6 complex
Lyve-1	Lymphatic vessel endothelial hyaluronan receptor-1
M-CSF	Macrophage colony-stimulating factor
MATL	Mucosa-associated lymphoid tissue
MCP-1	Monocyte chemotactic protein-1
MDP	Macrophage dendritic cell progenitor
MHC	Major histocompativility complex class
MI	Myocardial infarction
MMP	Metrix metalloproteinases
Mo-DCs	Monocyte-derived dendritic cells
MΦ	Macrophage
NDC	Non-communicable diseases
NF-κB	Nuclear factor κB
NO	Nitric Oxide

NOS	Nitric oxide synthase
OVA	Ovalbumin
P adj	Adjusted P value
P-dur	P-wave duration
PAMPs	Pathogen-associated molecular patterns
PCAM1	Platelet endothelial cell adhesion molecule
PDCA1	Plasmacytoid dendritic cell antigen-1
PDGF	Platelet derived growth factor
PHTPP	4-[2-Phenyl-5,7-bis(trifluoromethyl)pyrazolo[1,5-a] pyr-imidin-3-yl]phenol
PMSF	Phenylmethylsulfonyl fluoride
Poly I:C	Polyinosinic-polycydidylic acid
PPAR	Peroxisome proliferator-activated receptor
PR	P- to R-wave
Pre-cDCs	Pre-classical dendritic cells
PRRs	Pattern recognition receptors
PSGL-1	P-selectin glycoprotein ligand-1
pSMAC	Peripheral supra-molecular activation complex
qRT-PCR	Quantitative reverse transcription–polymerase chain reaction
RA	Right atrium
RNA-seq	RNA sequencing
ROS	Reactive oxygen species
scRNA-seq	Single-cell RNA sequencing
Seg	Segment
SIRPa	Signal regulatory protein alpha
SM22a	Smooth muscle protein 22 alpha
SMCs	Smooth muscle cells
sPLA2	cardiac secreted phospholipase A2
SR	Scavenger receptor
SREBP-2	Sterol regulatory binding protein 2
SSC	Side-scattered light

ssDNA	Single-strand DNA
ssRNA	Single-strand RNA
TAM	Tamoxifen
TCR	T cell receptor
TGF	Transforming growth factor
Ths	T helper cells
TLR	Toll-like receptor
TNF	Tumor necrosis factor
Treg	Regulatory T cells
TTC	Triphenyltetrazolium chloride
VCAM1	Vascular cell adhesion molecule 1
VLA-4	Very late antigen-4
VLDL	Very low density lipoprotein
VSMC	Vascular smooth muscle cells
WD	Western-type diet
WT	Wild type
YS	Yolk sac
Zbtb46	Zinc finger transcription factor Zbtb46

To remember Dr. Cheolho Cheong with his family forever

(1974 – 2016)

"The dream will come true.
If you always try to achieve your dream."

Acknowledgements

My doctoral course for 5 years was a series of really difficult circumstances. However, there were many people who helped me to overcome these difficulties and to finish my Ph.D course. I would like to appreciate them through this article.

First of all, I am grateful to Dr. Cheolho Cheong, like professor of my eternal professor and father, who might be now watching me from heaven. He led me to start my Ph.D with interest in immunology, and always cheered me on my side like a brother and father. I am able to grow a lot in his many teachings and know-how and have the honor of graduating doctoral course. I still miss times with professor so much with seeing him.

And I have one more father in Canada. He is Dr. Jacques Thibodeau. When I had the hardest time, he gave me so much courage and hope. Without your comments, teachings and love, I would not have been here now. The things he gave me could not change anything in this world. So, I would really appreciate and love him.

I would very appreciate the committee members for their generous advice in the process of reviewing my thesis: Dr. Ahmad Ali, Dr. Labrecque Nathalie, Dr. Divangahi Maziar and Dr. Gauchat Jean-Francois. In addition, I am grateful to the Fonds de Recherche du Québec - Nature et Technologies for my three-year scholarship funding in Canada. Finally, I would like to thank my parents, my sister, and my brother in law, who give me generous support whenever and wherever I need it.

CHAPTER 1

1 Introduction

1. 1 Cardiovascular Disease

Cardiovascular disease (CVD) is a major cause of global deaths and includes coronary artery disease, stroke, hypertension, and heart disease. The mortality of cardiovascular disease reaches 31% by 2016.[1] Over the 2000-2016 period, cardiovascular mortality rates in high-income countries, such as Canada, the United States, the United Kingdom, and the European Union, have declined by approximately 30 to 40 %. On the other hand, in developing countries, including those in Eastern Europe and Central Asia, the mortality rate is still high (80%).[2] **Figure 1.1** shows the loss of healthy years of life due to CVDs throughout the world. The decline was the highest in Eastern Europe and Central Asia. This trend is rapidly increasing due to changes in population aging and lifestyle.

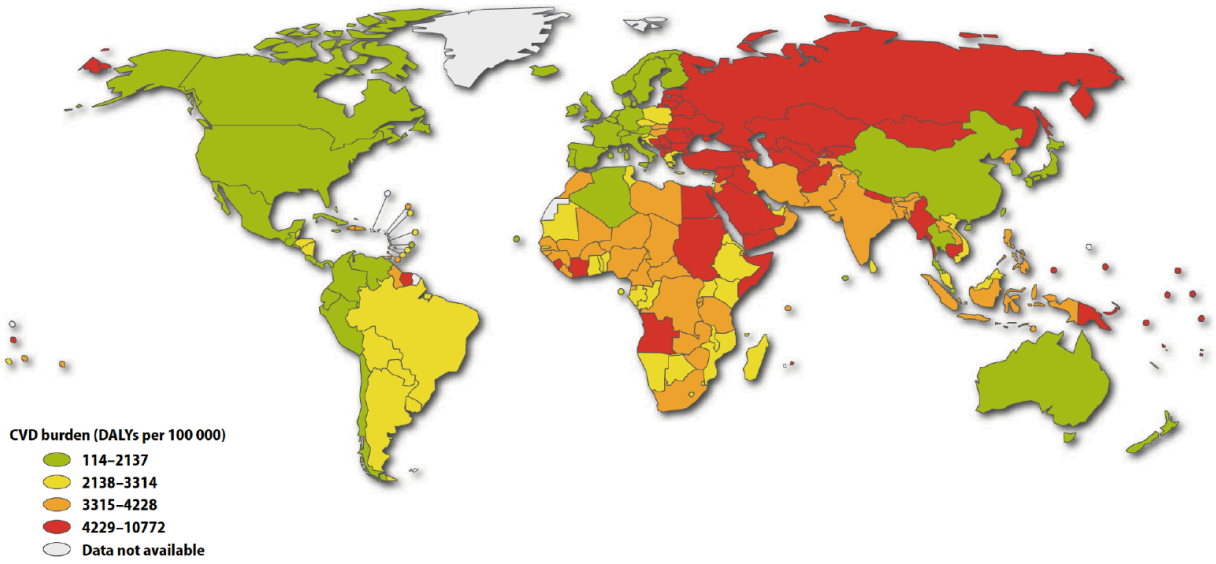

Figure 1.1. The comparison of disability adjusted life-years (DALYs) due to CVD in countries. Reproduced with permission from the World Health Organization.[3]

1. 1. 1 Causes of CVDs

As a typical complex disease, cardiovascular disease includes circulatory system-related diseases, such as ischemic heart disease (heart attack), stroke and hypertension. These influenced not only by blood biochemical indicators, such as cholesterol, but also by various risk factors, such as genetic factors inherited from parents or environmental factors, such as drinking and smoking. In addition, cardiovascular disease is strongly correlated with other diseases, such as diabetes and obesity. Stress can also indirectly effect on the onset of heart disease, but it is not yet clear whether it can have a direct influence.[4, 5, 6]

A prolonged exposure to these risk factors may lead to elevated blood pressure, increased blood sugar, resulting in blood lipid abnormality and obesity. In addition, it is related to non-communicable diseases (NCD), such as cancer, diabetes and chronic respiratory disease. In 2008, 60% of the global deaths were due to NCD, and 30% of these were caused by CVDs. Most CVD deaths occur in low- and middle-income countries (LMICs) and are the most frequent causes of death in most countries except in Africa.[7] In recent years, CVDs have rapidly increased on this continent, and it is expected that other diseases will be overtaken in the future as a cause of death. Coronary heart disease accounts for the largest portion of CVDs with 40%, followed by cerebrovascular disease (30%).[8, 9]

1. 1. 2 Types of CVDs

CVDs refer to diseases that occur in the heart or blood vessels. The cardiovascular system is a major organ that supplies oxygen and nutrition to the body, reacting promptly and precisely to various external stimuli. When these reactions become problematic, serious cardiovascular events, such as heart attack and stroke can be induced. As one of the major inflammatory diseases, atherosclerosis affects the whole of the cardiovascular system of the human body and results in the formation of plaques inside the arterial blood vessels.[10, 11] The most common risk factors are diabetes, smoking, hypertension and hyperlipidemia. It is influenced by family history, age, gender and lifestyle changes, obesity and stress.[12] Over time, the atherosclerotic plaque grows into the lumen of the blood vessels due to the accumulation of fat, cholesterol, calcium, and immune cells. This results in the narrowing of the vascular

passages, blocking the flow of blood to the organs and other parts of the body. If a sufficiently large plaque has fallen into the lumen of the vessel and the coronary vessels or blood vessels are blocked, a serious acute heart attack or stroke will occur.[10, 11] Cardiovascular disease can be divided into two broad categories according to the causes. The first group is CVDs caused by atherosclerosis and includes ischemic heart disease, coronary artery disease, cerebrovascular disease, hypertension, aortic and arterial disease or peripheral vascular disease. A second group includes congenital heart disease, rheumatic heart disease or cardiac arrhythmias.[13]

Over the past several years, the research on cardiovascular diseases, including arteriosclerosis and various cardiac diseases, has undergone tremendous growth through the epidemiological determination of risk factors with physiological exploration and the initiation of molecular and cellular studies. These developments have shown that cardiovascular diseases are involved in complex inflammatory responses characterized by the implication of some cellular and molecular player, which are known to drive inflammation, such DCs, T cells and some cytokines. This process also involves endothelial cells as well as vascular smooth muscle cells. It is important to study the immune system. Thus, we aimed to understand the biological mechanisms of cardiovascular immunity through the characterization of molecules and cell pathways, and further develop appropriate therapies.

1. 2 What is Atherosclerosis?

The innermost part of the blood vessel, which is a channel for transporting nutrients and oxygen throughout the body, is lined by the endothelium. The deposition of cholesterol in the endothelial cells (EC) results in the proliferation of endothelial cells and the formation of ‘atheroma’. This marks the beginning of atherosclerosis. The inside of the atheroma is thinned like porridge, and the surrounding area of atheroma is covered with a tightly hardened fibrous membrane. When the hardening fibrous membrane becomes unstable, the plaque ruptures and thrombosis occurs in the blood vessel. In addition, when bleeding into atheroma, the inside diameter of the blood vessel narrows rapidly or the blood vessel becomes completely blocked. As a result, the blood circulation to the peripheral tissues is obstructed.

In the past, atherosclerosis was recognized as a disease caused by deposits of lipids on the blood vessel wall. More recently, it has been shown that this disease results from the complex inflammatory action of blood vessel endothelial cells, immune cells and vascular smooth muscle cells (VSMC).[11] Atherosclerosis is the leading cause of ischemic heart disease and stroke in many countries, including Canada and the United States, accounting for more than 50% of the major causes of death[14, 15] and becoming the largest problem in the world.

1. 2. 1 The Role and Composition of Blood Vessels

Because the early stage embryo needs a means of delivery, the circulatory organ occurs first to develop and performs its function. Vessels circulate blood between the heart and the various tissues of the body, and providing oxygen and nutrients to all body or organs. The blood vessel walls consist of three layers, the tunica intima (intima), the tunica media (media), and the tunica adventitia (adventitia) **(Figure 1.2)**.

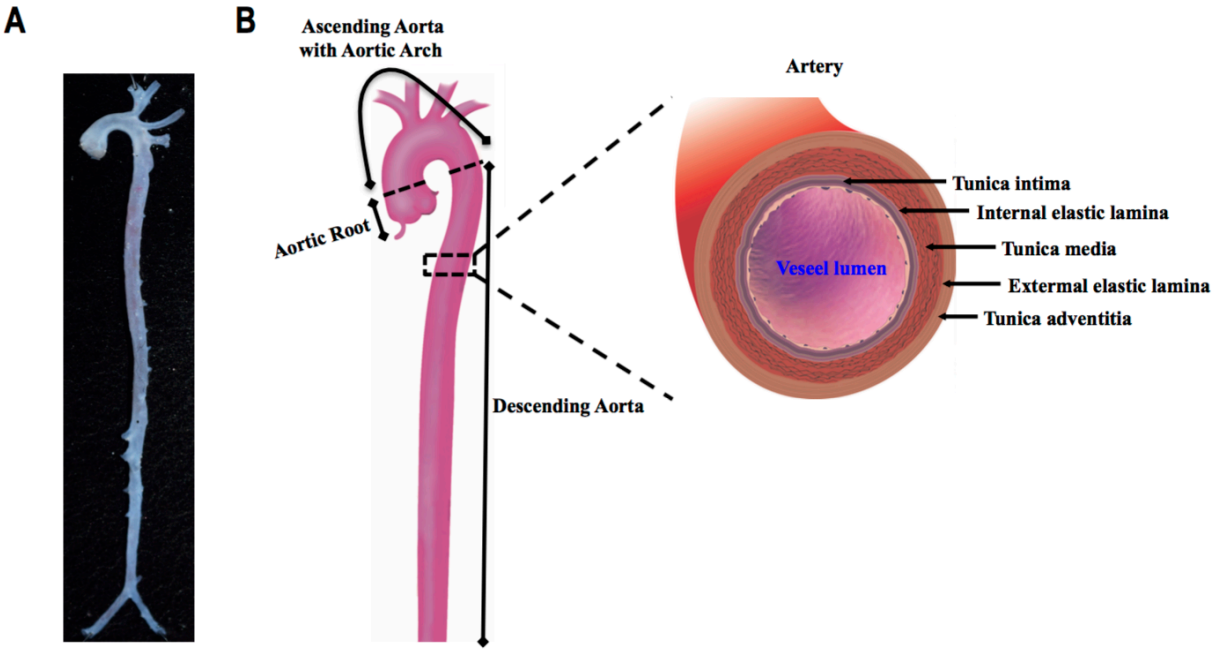

Figure 1.2. Three layers of arterial and venous wall. (A) A picture of aorta isolated from C57BL/6 mouse. **(B)** The aorta is composed of 3 parts, including the aortic root, ascending

aorta with aortic arch, and the descending aorta. The right panel shows a cross-section of the aorta, depicting the tunica intima, media, and adventitia.

The intima consists of a thin layer of endothelial cells in contact with the blood. This layer regulates the homeostasis and permeability of the blood vessel walls and is separated from the media by an internal elastic lamina (elastin layer). The media is the thickest layer and is composed of smooth muscle cells, elastic fibers and collagens. Among the three layers, the most robust adventitia is separated from the media by an external elastic lamina, consisting of connective tissue and elastic fibers, and preventing overexpansion of the blood vessels. They also have vasa vasorum (meaning the vessels of the vessels) supplying blood to the blood vessels themselves.

1. 2. 2 Is There A Specific Anatomical Site for The Initiation of An Atherosclerotic Lesion?

The atherosclerotic lesion usually begins at specific sites in the vascular system. These particular sites, such as branches, bifurcations, and curvature regions of the blood vessels, have features that include low shear stress and high turbulence, and correspond to changes in the blood flow.[16] These changes of blood vessels result in the functional impairment of vascular endothelial cells, which normally act as barriers between blood and tissues and affect selective permeability and gene expression of endothelial cells. The loss of cellular activity and the production of nitric oxide (NO) in endothelial cells is not only a major feature of endothelium dysfunction, is also closely related to the development of reactive oxygen species (ROS) **(Figure 1.3)**. In particular, low shear stress promotes the high production of superoxide and the absorption of low density lipoprotein (LDL) particles.[17] Accumulated or absorbed LDL on the blood vessel wall can be modified by interacting with various components, such as aggregation and matrix proteoglycans secreted by smooth muscle cells. These modified LDL increase the activation of endothelial cells to produce ROS. The production of ROS induces lipid oxidation, the activation of platelet and smooth muscle cell.[18, 19, 20] The activation of endothelial cells increases the expression of vescular cell adhesion molecules to recruit leukocytes, such as monocytes and macrophages. Eventually, these changes result in

functional impairment of endothelial cells and smooth muscle cells, contributing to the inflammatory response.[21, 22]

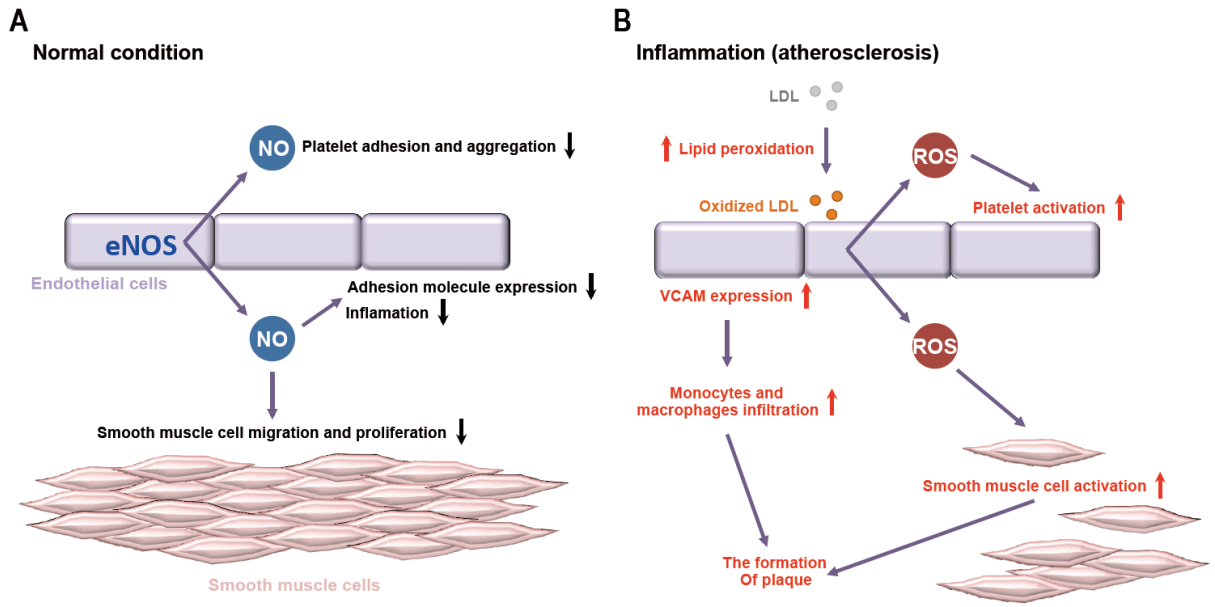

Figure 1.3. The function of vascular endothelial cells under steady state or under inflammation. Endothelial cells forming the intima layer maintain homeostasis of blood vessels by regulating the balance between vasodilatation and vasoconstriction. **(A)** These effects are regulated by NO produced by endothelial NO synthase (eNOS), and include inhibition of platelet activation, leukocytosis, VSMC proliferation and LDL oxidative changes. **(B)** Under inflammatory conditions, such as atherosclerosis, endothelial cells produce ROS. Then they show an activated phenotype and express various leukocyte chemo-attractants.

1. 2. 3 The Development of Atherosclerosis

The development of atherosclerosis passes through several steps. Atherosclerosis lesion can be observed in human fetus[9] and newborns. This lesion begins by the accumulation of foamy cells in blood vessels (Type I lesion).[23, 24] Then, a type II lesion develops with the formation of fatty streak together with foamy cells.[9] Fatty streak is not clinically important, but is characterized by the accumulation of smooth muscle cell that may initiate advanced lesions. Thereafter, the progress is rapid and passes through a pre-atheroma (type III lesion) stage where a small mass of lipid is scattered on the arterial wall. Atheroma, a type IV lesion, usually forms in the age of 20 to 30 **(Figure 1.4)**. In atheroma, the lipid mass is surrounded by

extracellular matrix and immune cells, including monocytes, macrophages, dendritic cells (DCs) and T cells. At this time, atherosclerotic symptoms begin to appear.[25]

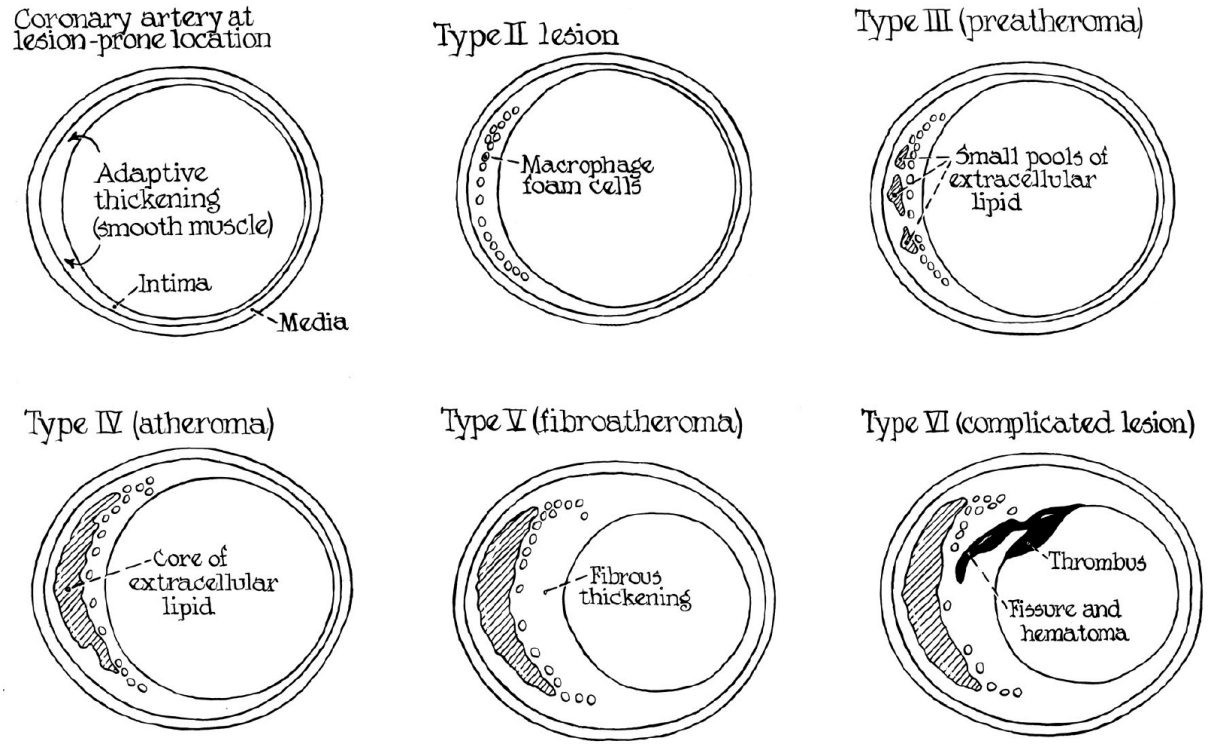

Figure 1.4. Development and characterization of atherosclerotic lesions. Fatty streak to pre-atheroma does not show atherosclerotic symptoms, but after type IV atheroma, symptoms may be caused by vascular stenosis or occlusion. Reproduced with permission from Circulation. (Stary, H. C., et al.)[26]

The progression to fibrosis, characterized by the accumulation of smooth muscle cells in the lipid center of atheroma, is called Fibro-atheroma and represents a type V lesion. There are two sub-subsets of this lesion: a Vb sub-type, which develops following coronary artery calcification or a Vc sub-type that can be caused by a decreased accumulation of lipids in fibro-atheroma compared to a type V lesion. Finally, complications, such as blood clot in type IV and V, are called a type VI lesion[26], which can lead to acute heart attack or stroke **(Figure 1.4)**.

1. 2. 3. 1 The Initiation of Atherosclerotic Lesions

The incidence of CVD has been increasing rapidly in recent years due to changes in lifestyle, westernized food habits, smoking, stress and lack of exercise. Among those, lipoprotein is known as the greatest risk factor for atherosclerosis. Lipoproteins, composed of lipids and apoproteins, absorb or store fats, such as cholesterol and triglycerides. They are then transferred to various tissues through the blood and used as energy. According to their density, these plasma lipoproteins can be classified as very low density lipoprotein (VLDL), LDL, intermediate density lipoprotein[27], and high density lipoprotein (HDL).[28] HDL, commonly known as healthy cholesterol, inhibits the oxidation of lipoproteins[29], while LDL is known as bad cholesterol.

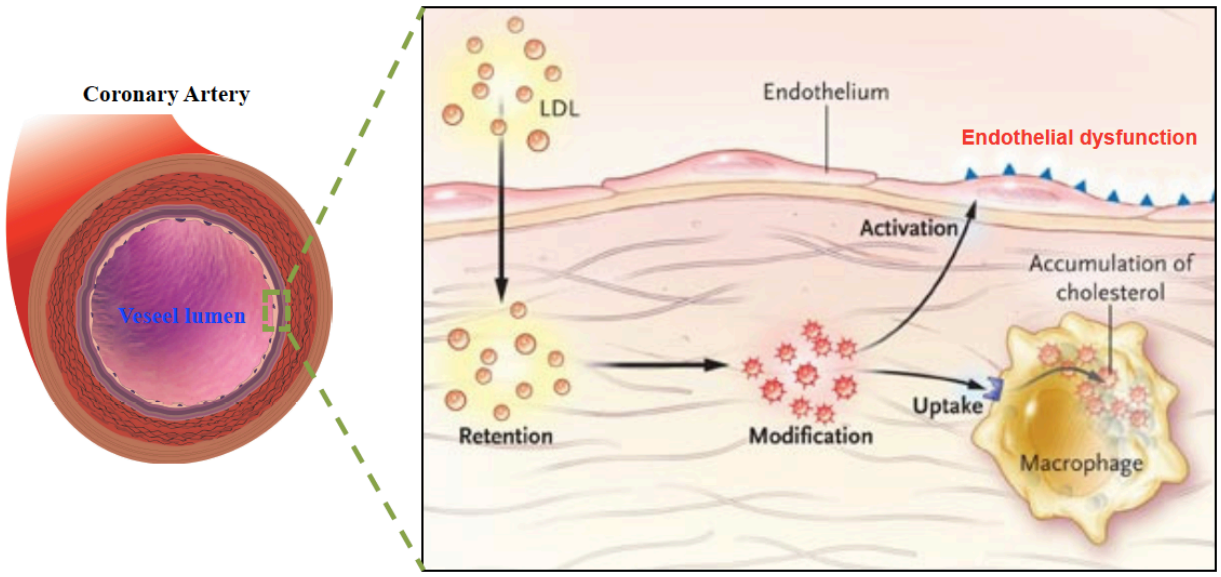

Figure 1.5. Endothelial dysfunction by modified LDL. LDL, one of the major risk factors for atherosclerosis, accumulates in the endocardium and becomes transformed. Modified LDLs cause endothelial cell damage leading to the expression of a variety of adhesion molecules and chemotactic proteins on their surface. Reproduced with permission from The New England Journal of Medicine, Copyright Massachusetts Medical Society. (Hansson, G. K.)[30]

The lesion of atherosclerosis begins with the accumulation of LDL in vascular endothelial cells or sub-endothelial matrix. At this time, if the concentration of low-density

lipoprotein cholesterol (LDL-C) in the blood is high or if vascular endothelial cells are damaged, the cholesterol accumulation worsens.[31] The accumulated LDL is transformed by oxidation, proteolysis and lipid degradation[18, 19], and the modified LDL leads to the activation of vascular endothelial cells that produce ROS, eventually resulting in an inflammatory response.[21, 22] The activation of endothelial cells promotes the expression of inflammatory genes or adhesion molecules on their cell surface **(Figure 1.5)**. Endothelial dysfunction is, therefore, the most important event in the early stages of arteriosclerosis.

1. 2. 3. 2 Endothelial Cell Dysfunction

Normal endothelial cells do not induce leukocyte adhesion. Conversely, endotherial cells activated by modified LDL increase the expression of adhesion molecules, such as VCAM1 (vascular cell adhesion molecule 1)[32], ICAM1 (intracellular adhesion molecule 1)[33], PECAM1 (platelet endothelial cell adhesion molecule)[34], P- and E-selectin[35] on their surface. They also produce MCP-1 (monocyte chemotactic protein-1/CCL2) and cytokines that regulate growth, such as M-CSF (macrophage colony-stimulating factor)[36] and GM-CSF (granulocyte-macrophage colony-stimulating factor)[37] **(Figure 1.6)**. Leukocytes, such as monocytes and macrophages, circulating in the blood vessels accumulate into arterial vascular lesions by following gradients of chemotactic molecules.

MCP-1 (CCL2) is the ligand for CCR2 on the cell surface of monocytes. A decrease in the number of these cells in atherosclerotic lesions was observed in the absence of MCP-1[38] or CCR2[39] in ApoE$^{-/-}$ mice. Similarly, lesions were significantly less severe in mice lacking the M-CSF gene.[40] The M-CSF gene and CCL2/CCR2 interaction play a critical role in the recruitment and the proliferation of monocytes[41], which ultimately leads to a local inflammatory response.

1. 2. 3. 3 Monocytes Influx into Atherosclerotic Lesions

Atherosclerotic lesions harbor various leukocyte sub-populations, including T cells, B cells and dendritic cells (DCs) as well as monocytes and macrophages.[41] Monocytes, which

are also found in the early fetal fatty streak **(Figure 1.4)**, are one of the most important cellular components in atherosclerotic lesions.[42] They are circulating in the blood to maintain homeostasis[43] and are transferred to lymphatic organs and tissues by infection or tissue damage signals.[44]

The migration of circulating monocytes into atherosclerotic lesions is regulated by a leukocyte adhesion cascade that depends on the up-regulation of cell adhesion molecules by activated endothelial cells.[45] This cascade of leukocyte extravasation can be described in four stages; (1) rolling mediated by selectins, (2) activation by chemokines, (3) arrest and adhesion by integrins, (4) endothelial transit. In the first step, leukocytes loosely adhere to the endothelium by low-affinity interations between PSGL-1 (P-selectin glycoprotein ligand-1)[46] and selectins[47]. This brief binding temporarily holds leukocytes to the endothelial cells, but leukocytes drop off the endothelium because of the fasting blood's shearing force. At that moment, another selectin in the adjacent endothelial cells captures leukocytes again. As this process is repeated, leukocytes roll along the endothelium. This type of binding is called rolling. Second step is activations by chemokines. The rolling process slows down the progression of leukocytes, allowing the interaction of between chemokines (such as MCP-1) on the endothelial cells and its receptors (such as CCR2) on leukocytes. Third step is arrest and adhesion by integrins, such as VLA-4 (very late antigen-4, $\alpha_4\beta1$-integrin, or CD49d/CD29) and LFA-1 (lymphocyte function-associated antigen-1, $\alpha L\beta_2$-integrin, or CD11a/CD18) on the surface of leukocytes, interacting with VCAM1 and ICAM on the surface of vascular endothelial cells.[48] Final step is endothelial transit. Homozygous interactions of PECAM1[49] on both leukocytes and endothelial cells allow leukocytes in the blood vessels to migrate in the wound sites, and monocytes that migrate into the subendothelial space differentiate into macrophages or inflammatory DCs **(Figure 1.6)**.[50]

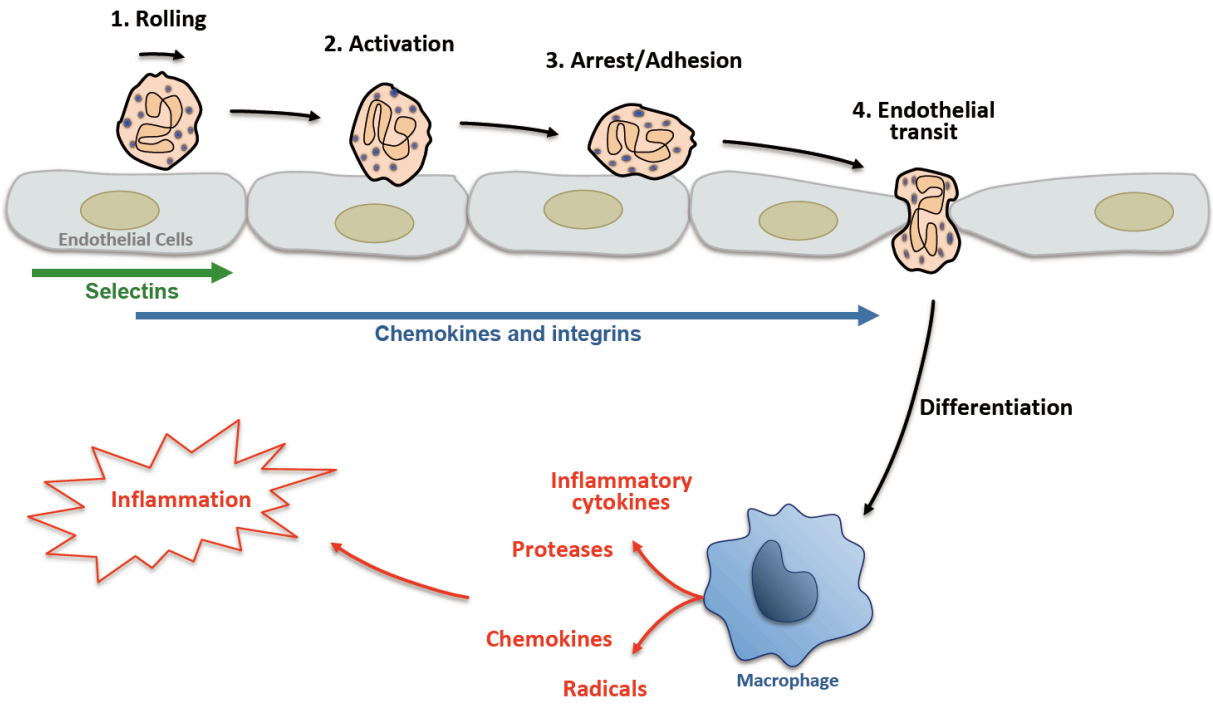

Figure 1.6. A four-step process of leukocyte extravasation. Capture and rolling occur when the selectin molecule binds to sialyated carbohydrate. Chemokines bind to its receptors belonging to the G porotein receptor of leukocytes and transmit activation signals. These signals together with blood shear forces induce conformational changes in integrin molecules. Leukocytes allow for more robust attachment through the Ig-superfamily molecules of endothelial cells. Finally, leukocytes migrate beneath the vascular endothelial cell layer. However, continuous inflow of monocytes leads to chronic inflammation.

1. 2. 3. 3. 1 Subpopulations of Monocytes

When hyperlipidemia or atherosclerosis occurs, the number of monocytes present in the blood vessels increases compared to steady state. The observation suggests that monocytes play an important role in the ensuing inflammatory response.[51, 52] Circulating monocytes can be divided into two subpopulations: classical monocytes or non-classical monocytes.

On one hand, classical monocytes have a $Ly6C^{high}$ phenotype. Their number considerably increases in inflammatory sites, and they account for most of the monocytes infiltrating lesions.[53] $Ly6C^{high}$ monocytes are characterized by the expression of specific chemokines, such as $CCR2^{+}$ and CX_3CR1^{low}, on their cell surface **(Figure 1.7)**.[54] Classical monocytes that enter the lesion are activated by GM-CSF and IFN-γ (interferon-γ) secreted

from vascular endothelial cells and type 1 T helper cells (Th1 cells). This allows their differentiation into classically activated macrophages (M1).[55] Activated Ml macrophages secrete pro-inflammatory cytokines, such as IL-1 (interleukin-1), IL-6, IL-8 and TNF-α (tumor necrosis factor-α) and increase their expression of the major histocompativility complex class II (MHCII) and co-stimulatory molecules (CD80/CD86) on their cell surface.[56]

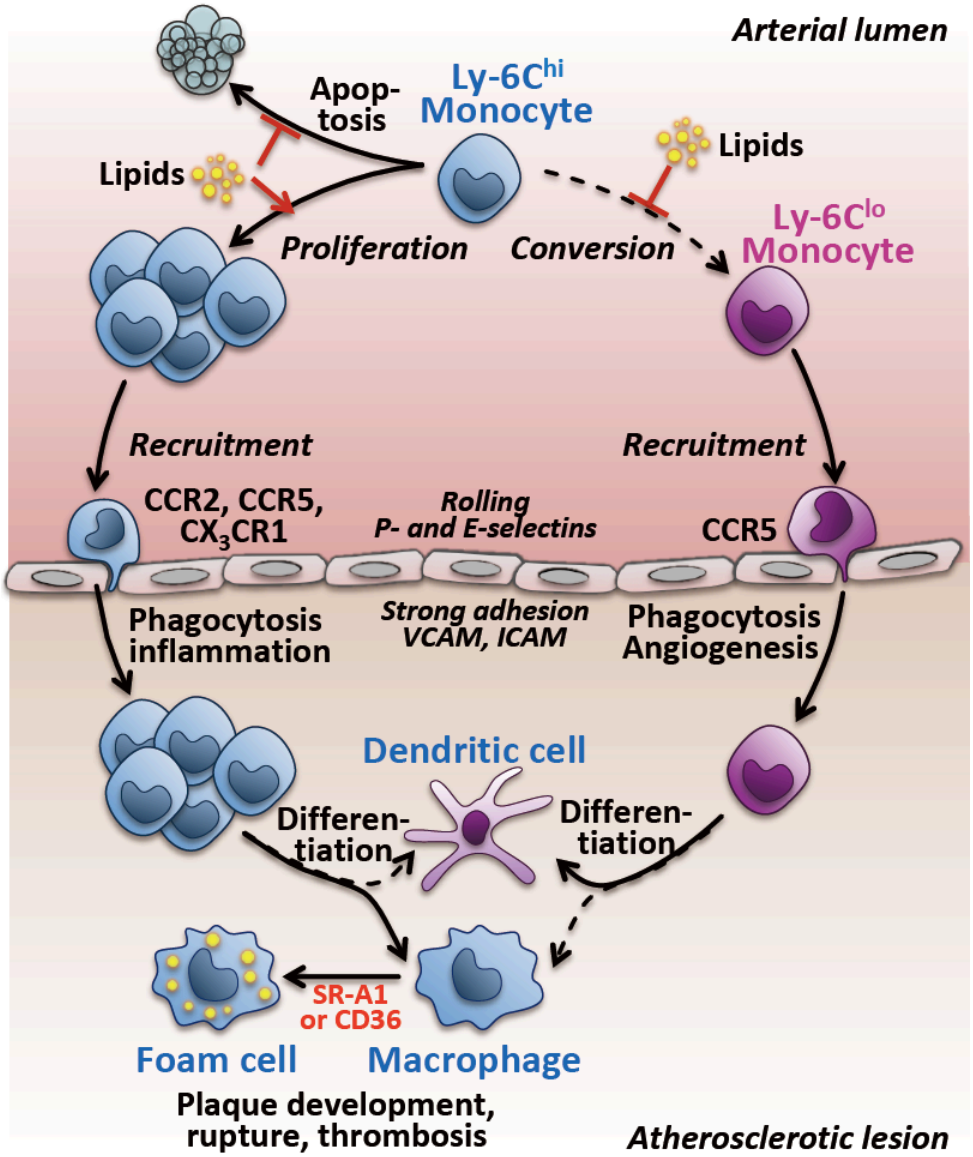

Figure 1.7. Important roles of chemokines secreted by activated endothelial cells for the recruitment of monocytes. Monocytes are distinguished into two distinct subpopulations

evident by chemokine receptors that are differentially expressed on their cell surface. Ly6C^{high} monocytes, predominant in lesions, are recruited on the wall of activated vascular endothelial cells by CCR1 and CCR5 and migrate into the endothelial cells by binding adhesion molecules (VLA-4/VCAM1, LFA-1/ICAM1 and PSGL-1/P- or E-selectins) and chemokines (CCL2/ CCR2, CCL5/CCR5 and CX_3CL1/CX_3CR1). Ly6C^{low} monocytes accumulate on the wall of vascular endothelial cells interacting with CCR5. After migration, monocytes differentiate into M1 and M2, and absorb the modified or oxidized LDL through their scavenger receptor type 1 (SR-A1) receptor and scavenger receptor class B member 3 (SCARB3 or CD36). They eventually form foam cells, which are the largest cell population in atherosclerotic lesions. Reproduced with permission from Arteriosclerosis, Thrombosis, and Vascular Biology. (Swirski, F.K., et al.)[57]

On the other hand, non-classical Ly6C^{low} monocytes are typically CCR2^{-} and CX_3CR1^{high},[54] and can be differentiated into alternatively activated macrophages (M2) by cytokines, such as M-CSF and IL-4,[58, 59, 60] secreted by endothelial cells and Type 2 T helper cells (Th2 cells).[55] Activated M2 macrophages increase the expression of mannose receptor 1 (CD206) on their cell surface and secrete anti-inflammatory cytokines, such as IL-1R antagonist, IL-10 and TGF-β (transforming growth factor β). Moreover, they are highly phagocytic.[56] Previous studies have shown that chemokine receptors, such as CCR2, CCR5[61], and CX_3CR1[62], are important for interacting with vascular endothelial cells and to move into wounded tissues or lesions. The absence of those chemokines inhibits the migration of monocytes and macrophages and also significantly reduces the magnitude of the disease.

1. 2. 3. 3. 2 Lesional Macrophages

Monocyte-derived macrophages are a major population of immune cells for atherosclerosis development.[63] The diversity and flexibility are the characteristics of these cells. Macrophage polarization in the atherosclerotic lesion give rise to M1 and M2 macrophages with a broad spectrum.[64, 65] M1 macrophages express high levels of pro-inflammatory cytokines, secrete reactive nitrogen and oxygen, and promote Th1 responses that play a major role in the defense of bacteria invading our bodies.[66, 67] Macrophages incubated with IFN-γ and LPS, a toll-like receptor 4 ligand, induce the differentiation into M1 macrophages in vitro.[68] On the other hand, M2 macrophages are involved in anti-inflammatory responses and tissue remodeling.[69, 70] Their phenotype can be induced in vitro by incubating

with IL-4 and IL-13, which suppress the differentiation of M1 macrophages and promote macrophages to produce cytokines (IL-10 and TGF-β) that are involved in tissue remodeling and repair. In particular, IL-4 is known to be a potent promoter or stimulant for the proliferation of macrophages.[71] However, in atherosclerotic lesions, macrophages are exposed to excessive stimuli, indicating a difference in the function and surface markers of macrophages.[72] Although both M1 and M2 macrophages are observed in atherosclerotic lesions, their phenotypes still require more understanding at each stage of atherosclerosis deverolpment.[73]

1. 2. 3. 3. 3 The Formation of Foam Cells

In the sub-endothelial space, there can be natural, modified or oxidized LDL, which are all absorbed and removed by macrophages. Natural LDL is normally absorbed through macrophage LDL receptors while cholesterol is modified by 27 hydroxylases and removed via transporters ABCA1 (ATP binding cassette subfamily A member 1) or ABCG1 (ATP binding cassette subfamily G member 1) present on the cell membrane.[74] Macrophage-secreted ApoE also increases the uptake of HDL into the lesions[75] and inhibits the oxidation of LDL.

Oxidized and modified LDL are mainly internalized through the SR-AI and SCARB3 receptors on the cell surface of macrophages.[76] The expression of these receptors is regulated by TNF-α or IFN-γ[34]. Macrophages accumulate oxidized and modified LDL in their cytoplasm, which lead to the formation of foam cells **(Figure 1.7)**.

The absence of scavenger receptors inhibits the formation of foam cells and decreases the size of atherosclerotic lesions.[77, 78] These findings demonstrate the importance of scavenger receptors in the formation of foam cells. In addition, the number of monocytes and macrophages expressing CX_3CR1 is increased in atherosclerotic lesions because CX_3CR1 signaling increases their lifespan.[79, 80] This leads to the accumulation of foam cells in the lesion and makes atherosclerotic lesions more severe.

1. 2. 3. 3. 3.1 What Do We Need to Analyze Foam Cells?

Macrophages form foam cells by accumulating modified or oxidized LDL into their cytoplasm. Foam cells are seen in the fatty streak in human as early as in the fetus, and they participate in the development of atherosclerotic lesions **(Figure 1.4)**.[24] It is believed that the formation or the activation of foam cells can contribute to lesion formation by controlling the microenvironment. Previous studies have shown that DCs[81] and smooth muscle cells (SMCs)[82], as well as monocytes and macrophages, are involved in foam cell formation. The formation of persistent foam cells leads to a plaque rupture that creates a large central necrotic area, which causes acute infarction or stroke.[83, 84]

Therefore, it is necessary to define the core cellular components of the lesions to better understand atherosclerosis. Classical staining methods[85], including Oil Red O and immunofluorescence, have been widely used to analyze atherosclerotic lesions but they have several disadvantages. The training for measuring lesions involves a number of labor-intensive procedures, and volumetric analysis of lesions is not possible as yet. Finally, the analysis of cellular components requires multiple cell marker assays, a task not possible by immuno-histochemistry. For example, cell markers, such as CD11c, are shared with other cells. Multi-parametric flow cytometry analysis overcome disadvantages of classical experimental methods by using various cell markers. However it has not yet been established because of the high autofluorescence of vascular tissue containing lipids.

1. 2. 3. 3. 4 Activation of Vascular Smooth Muscle Cells

Vascular smooth muscle cells of the intima layer[86] are the major producers of extracellular matrix (ECM), such as laminin, elastin, fibronectin, proteoglycans, and collagen, on the vessel wall.[87] One of the most important features of the progression of atherosclerotic lesions is the activation of vascular smooth muscle cells. These cells are activated by growth factors and pro-inflammatory cytokines secreted by activated immune cells, including monocytes, macrophages, dendritic cells, T cells and foam cells **(Figure 1.8)**.

In normal conditions, vascular smooth muscle cells are generally contracted and they are differentiated thorough the interaction with ECM.[27, 88] In inflammation, the activated

vascular smooth muscle cells begin to proliferate by dedifferentiation, and produce different type of extracellular matrix components, such as fibronectin, osteopontin, proteoglycans and type I and III collagens, other than normal conditions.[27, 89] They also express specific adhesion molecules that can interact with different types of extracellular matrix compoents[90, 91] and secrete pro-inflammatory cytokines, such as PDGF (platelet derived growth factor) and IFN-γ.[92] In addition, CD44 is known to be one of the most important receptors for the migration of vascular smooth muscle cells into the endothelium, which is promoted by the pro-inflammatory cytokine IL-1.[93] At steady state, vascular smooth muscle cells express low levels of CD44.[94]

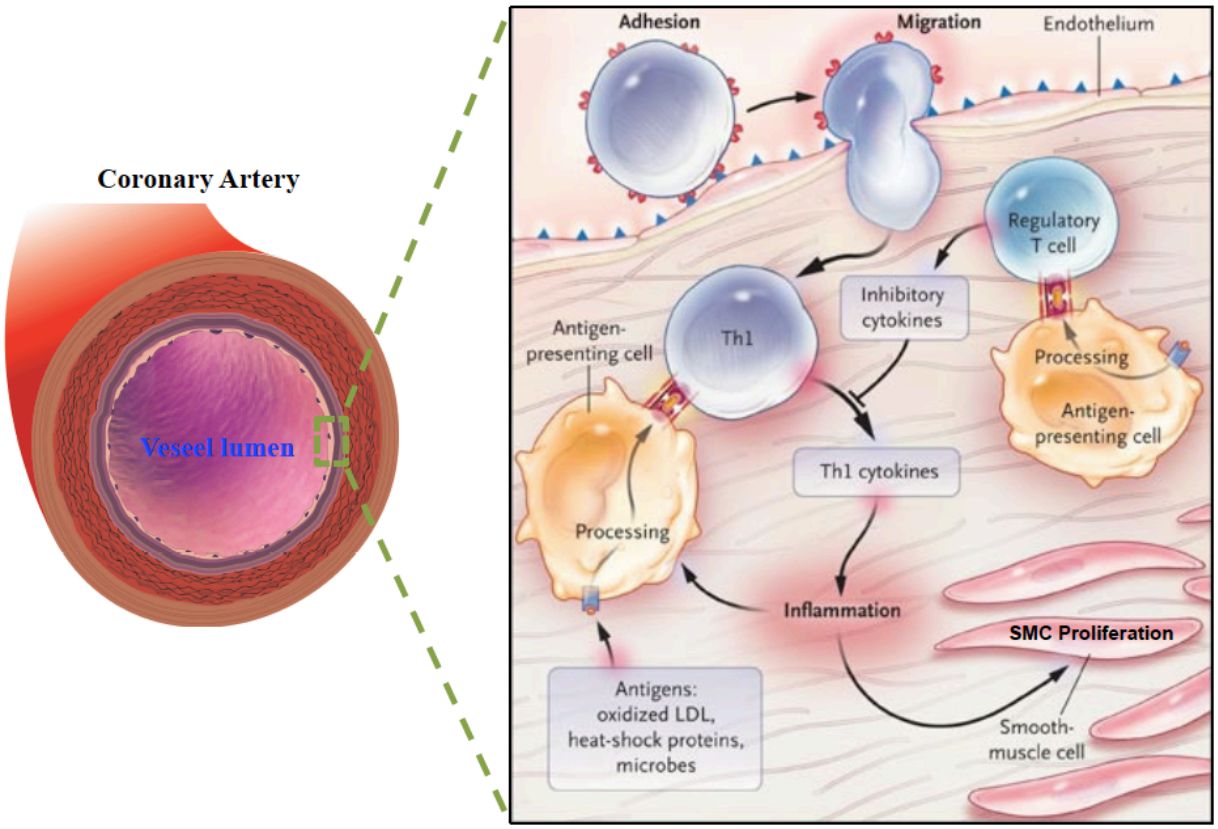

Figure 1.8. Interactions between immune cells in atherosclerotic lesions. Monocytes migrate into the lesion following cholesterol deposition on the vessel wall and differentiate into macrophages, which initiate the expression of MHC II molecules. Antigen-activated T cells, for example those specific for LDL presented through MHC II molecules by macrophages and DCs, are differentiated into T cell subtypes, such as Th1, that secrete their specific cytokines. The inflammatory condition that results from theses interactions activates

vascular smooth muscle cells that can migrate to the endothelium by changing their phenotype. The activation of vascular smooth muscle cells makes the local inflammatory reaction more severe. In contrast, Regulatory T (Treg) cells suppress local inflammatory responses by regulating the interactions between immune cells in the lesion. Reproduced with permission from The New England Journal of Medicine, Copyright Massachusetts Medical Society. (Hansson, G. K.)[30]

These series of changes make it possible to accumulate more modified and oxidized LDL at the site of inflammation and allow vascular smooth muscle cells to migrate to the endothelium.[95] Surprisingly, these vascular smooth muscle cells can form foam cells by accumulating modified LDL in their cytoplasm using their scavenger receptors[96] and continue to synthesize extracellular matrix to form a fibrous cap around the lesion.

1. 2. 4. Initiation of Adaptive Immune Responses by Activated APCs.

In general, naïve T cells differentiate into subsets of T helper cells in response to signals provided by antigen presenting cells (APCs). The Cytokines that are required for Th1 differentiation are IL-2, IL-18 and IFN-γ. To induce the Th1 polarization, these cytokines activate the expression of T-bet, a major transcription factor that controls the expression of Th1 cytokines, such as IFN-γ and TNF.[97, 98] IFN-γ as a potent cytokine activates macrophages to increase microbial destruction and induces MHC II expression and IL-12 production.[99] This cytokine also enhances phagocytosis and complement fixation reaction by inducing IgG class switching in B cells.[100, 101, 102] Finally, it allows $CD8^+$ T cells to differentiate into complete cytotoxic T lymphocytes.[103] Through these complex processes, Th1 cells are responsible for the defense mechanisms for parasitic microorganisms, such as viral infections. In contrast, the differentiation of Th2 cells is facilitated by the polarized cytokine IL-4 that increases the expression of a transcription factor GATA3. This transcription factor promotes the production of Th2 immune response specific cytokines, such as IL-4, IL-5 and IL-13.[104]

Under atherosclerosis, resting T cells will get activated by APCs, such as macrophages and DCs. Adaptive immunity initiated by the activation of T cells plays an important role in the formation of atherosclerotic lesions.[105] Among T cell subsets, $CD4^+$ T cells are predominant in atherosclerosis.[106, 107] $CD4^+$ T cells are activated following the binding of TCR

(T cell receptor) to MHCII molecules bearing modified LDLs on activated macrophages and DCs.[108] Activated T cells can function to promote or inhibit atherosclerosis **(Figure 1.8)**.

IL-12 and IL-18, secreted by activated APCs, induce the differentiation of IFN-γ-producing Th1 $CD4^+$ T cells.[109] IFN-γ inhibits not only formation of the extracellular matrix, but also the expression of scavenger receptors by macrophages.[110] However, another role of this cytokine is to induce the differentiation of monocytes into M1 macrophages expressing inflammatory cytokines, such as IL-1, IL-6, and TNF-α and to promote the expression of MHC II molecules on the surface of M1 macrophages. Ultimately, the signaling induced by IFN-γ has been shown to promote atherosclerosis.[111, 112]

Th2 $CD4^+$ T cells are induced by IL-4 secreted from vascular endothelial cells or by B cells, which secrete also IL-5 and IL-13.[113] IL-4 inhibits the expression of IFN-γ in macrophages and the differentiation into M1, interfereing with the differentiation of $CD4^+$ T cells into Th1 cells. However, it increases the expression of adhesion molecules and chemokines on the surface of vascular endothelial cells. Other cytokines secreted by Th2 cells, such as IL-5 and IL-13, act as anti-atherogenic by reducing modified LDL, inhibiting monocyte accumulation, and promoting TGF-β production from macrophages.[109] Although type 2 cytokines have been reported to be anti-atherogenic[107], many studies using mouse models seem to indicate a role in inducing inflammatory responses.[114, 115]

By promoting the expression of Foxp3 (a transcription factor, forkhead box P3), TGF-β plays a critical role in inhibiting the differentiation and proliferation of T cells into Th1 and Th2 cells and inducing their differentiation into Treg cells.[116] The cytokine IL-10 produced by cells differentiated into Tregs modulates the differentiation of Th1 and Th2 cells and reduces the activation of macrophages. This cytokine strongly inhibits the formation of atherosclerotic lesions.[117] Interestingly, the absence of IL-10 increases the cholesterol deposition in the blood vessel wall by almost three-fold. Accordingly, when overexpressed, atherosclerosis was dramatically decreased.[118]

1. 2. 5 Plaque Rupture and Thrombosis

The narrowing of the inner diameter of the blood vessel during progression of atherosclerosis causes the ischemic symptom. However, most acute infarctions, such as acute myocardial infarction or stroke, are caused by atherosclerotic plaque rupture and thrombosis. Plaque rupture occurs more often when the fibrous cap formed by vascular smooth muscle cells is thin, the number of foam cells in the lesion is high, or the central necrosis area is large.[83, 84]

The plaque size may be reduced slightly by natural cell death in lesions. However, matrix metalloproteinases (MMP) secreted by macrophages degrade the extracellular matrix produced by vascular smooth muscle cells, reducing plaque stability.[119] MMPs , including cell surface proteins and ECMs, are very diverse.[120] Their functions are related to the degradation of ECM. They also induce migration and proliferation of vascular smooth muscle cells[121] and the infiltration of immune cells to promote inflammatory responses.[122]

Due to plaque rupture, lipids and various tissue factors in the lesion become exposed to the circulation, which lead to blood clotting and platelet adhesion activation. This results in complications, such as acute coronary syndrome or myocardial infarction.[123]

1. 2. 6 Myocardial Infarction

The cardiac muscle is particularly powerful and allows blood to circulate throughout whole body. It is dependent on oxygen- and nutrient-rich blood, which is supplied through the coronary arteries on the surface of the heart. When the blood flow become blocked, cardiac muscle can be damaged and dangerous diseases, such as angina and myocardial infarction (MI) that are life-threatening, can occur. The main cause of these is arteriosclerosis of the coronary arteries, and due to plaque rupture, platelet activation and thrombogenesis occurs. This combination of events eventually leads to thrombotic occlusion and the death of cardiac muscle cells that are not receiving blood, which can contribute to cardiac dysfunction due to cardiac remodeling.[124]

Cardiomyocyte death induces the activation of peripheral inflammatory cells and endothelial cells, initiating the initial local inflammatory response. DAMP (damage-associated molecular patterns) signaling triggered by dead myocardial cells not only activates endothelial cells and neutrophils, but also acts as a chemoattractant to recruit neutrophils at the injured sites.[125]

Neutrophils can be also activated by TNF-α and histamine secreted from mast cells.[126] At the damaged site, neutrophils remove cell debris and begin to secrete IL-6, which attracts macrophages and more neutrophils.[127, 128] Subsequent inflammatory responses are mediated by B cells that produce CCL7 in the inflammed area. Monocytes promote their mobilization or expansion to the wound site by a CCL7-dependent manner.[129] $Ly6C^{low}$ monocytes, one of two subgroups of monocytes, move along damaged vascular wall to remove damaged cells[130, 131], while $Ly6^{high}$ monocytes enter damaged tissues and differentiate into macrophages that amplify the inflammatory response through the secretion of pro-inflammatory cytokines.

IL-23 has been reported to modulate the number of neutrophils under inflammation condition, including myocardial infarction.[132] It is expressed not only in macrophages but also in DCs.[133] Surprisingly, It has been also reported that DCs present in the endothelium under hyperlipemia accumulate lipids from blood, leading to the formation of foam cells.[81] These obsevastions strongly suggest that DCs play important roles during early inflammatory responses in cardiovascular disease, including myocardial infarction and atherosclerosis. These cells will be further described in the next sections.

1. 3 Dendritic Cells

In the 1970s, the term “dendritic cell” was used for the first time by Ralph M Steinman.[134, 135] They have morphologically distinctive dendrites and differ in function from macrophages.[134, 135] These cells are professional antigen presenting cells (APCs) and express all the necessary molecules for antigen processing and presentation to T cells.[136] As such, they play a crucial role in linking innate and adaptive immunity.

DCs come in different flavors. Four types of these cells exist; Langerhans cells, conventional DCs (cDCs), monocyte-derived DCs (Mo-DCs) and pDCs. Within these cells, cDCs are the most diversified. This diversification is dictated by the lymphoid and non-lymphoid in which these cDCs are found. However, based on their functions, these cells are classified in to two subsets. cDC1s ($CD103^{+}CD11b^{-}$ DCs) are professionalized in the priming of $CD8^{+}$ T cells, whereas cDC2 ($CD103^{-}CD11b^{+}$ DCs) are predominantly specialized in the activation of $DC4^{+}$ T cells. Lymphoid tissues contain a population of resident cDC that permanently lives in these tissues together with a migratory DC subset originating from non-lymphoid tissues. Migratory DCs are circulating between lymphoid and non-lymphoid tissues and constantly acquire circulating antigens. Once the antigen is recognized, they determine whether the immune system will induce an inflammatory response or tolerance. If necessary, they migrate to lymphoid tissues, deliver antigen to T cells, and play a key role in the activation and differentiation of T cells.

B cells and macrophages are also APC cells.[137] However, B cells focus on antibody secretion rather than T cell activation, and their capacity for antigen storage and antigen presentation to MHC I is very weak.[138, 139] Macrophages can increase their expression of MHC I, MHC II and co-stimulatory molecules through various types of antigen uptake, but their expression levels are relatively low compared to B cells or dendritic cells.[140, 141] Therefore, the phagocytosis by macrophages is more focused on protein degradation rather than antigen presentation.[142, 143]

1. 3. 1 Origin of Dendritic Cells

T cells and B cells originate from the common lymphoid progenitors (CLP), whereas the origin of dendritic cells begins with the common myeloid progenitors (CMP). CMP is capable of differentiating into dendritic cells, macrophages, monocytes, and red blood cells, and is characterized by a high expression of c-kit. CMP differentiates into the macrophage-dendritic cell progenitors (MDP) in the bone marrow (BM)[144] and begins to express a high level of fms like tyrosine kinase 3 (Flt3/CD135).[145] DC lineage precursors all express Flt3 that bind to its ligand (Flt3L) and control the development of cDCs.[146] Various tissues and

endothelial cells secrete Flt3L[147], which is also important for maintaining DC homeostasis in peripheral tissues.[145] In BM, MDP futher differentiates into the common dendritic cell progenitors (CDP). These cells produce pre-classical dendritic cells (Pre-cDCs) and plasmacytoid dendritic cells (pDCs). Pre-cDCs are precursors of DCs in lymphoid tissue and non-lymphoid tissue **(Figure 1.9)**.

1. 3. 2 Subpopulations of Dendritic Cells

Pre-cDCs leave the bone marrow and differentiate into DC sub-populations in lymphoid and non-lymphoid tissues.[148, 149] The differentiated DC sub-populations have a relatively short half-life. Therefore, in order for their proper number to be maintained in the tissues, they need to be constantly replaced by blood-derived precursors.[150, 151] Pre-cDCs express MHC II and a high level of CD11c, but are deficient in other cellular markers, such as T cells (CD3), monocytes (CD14), B cells (CD19) and NK cells (CD56). At this time, Zbtb46 (zinc finger transcription factor Zbtb46) begins to be expressed. Except for Pre-cDCs and DC sub-populations, it is not expressed in other immune cells, such as macrophages, monocytes and pDCs **(Figure 1.9)**.[152, 153] Although it is not important for the early growth of DCs, Zbtb46-deficiency alters DC sub-populations in spleen. The use of Zbtb46-DTR transgenic mice also allows the selective depletion of DCs by the administration of the diphtheria toxin (DT).[154]

1. 3. 2. 1 Non-lymphoid Tissue Dendritic Cells

Two DC sub-populations in non-lymphoid tissue can be clearly distinguished by the expression of CD103. Csf-2 (GM-CSF), which controls cell development and function in myeloid lineage, regulates the expression of CD103 on DCs.[155, 156] $CD103^+$ DCs are closely related to the origin and function of $CD8^+$ DCs in lymphoid tissues and have similar cell surface phenotypes.[157, 158] They strongly express XCR1, Langerin (CD207), CD205 (DEC 205), and Clec9A, whereas the expression of macrophage markers, such as CD11b, CX_3CR1, F4/80, CD115 (M-CSF) and CD172α (Signal regulatory protein alpha, SIRPα) can not be detected. In particular, these cells express a very high level of Flt3 and it has been shown that

in mice lacking Flt3, the number of $CD103^+$ and $CD8^+$ DCs were decreased in lymphoid tissue.[145] In addition, the deficiency of ID-2 (inhibitor of DNA binding protein 2)[159], IRF8 (interferon regulatory factor 8)[160] and Batf3 (basic leucine zipper ATF-like transcription factor 3)[161] cause the selective reduction of $CD103^+$ DCs and $CD8^+$ DCs both lymphoid tissue and non-lymphoid tissue.

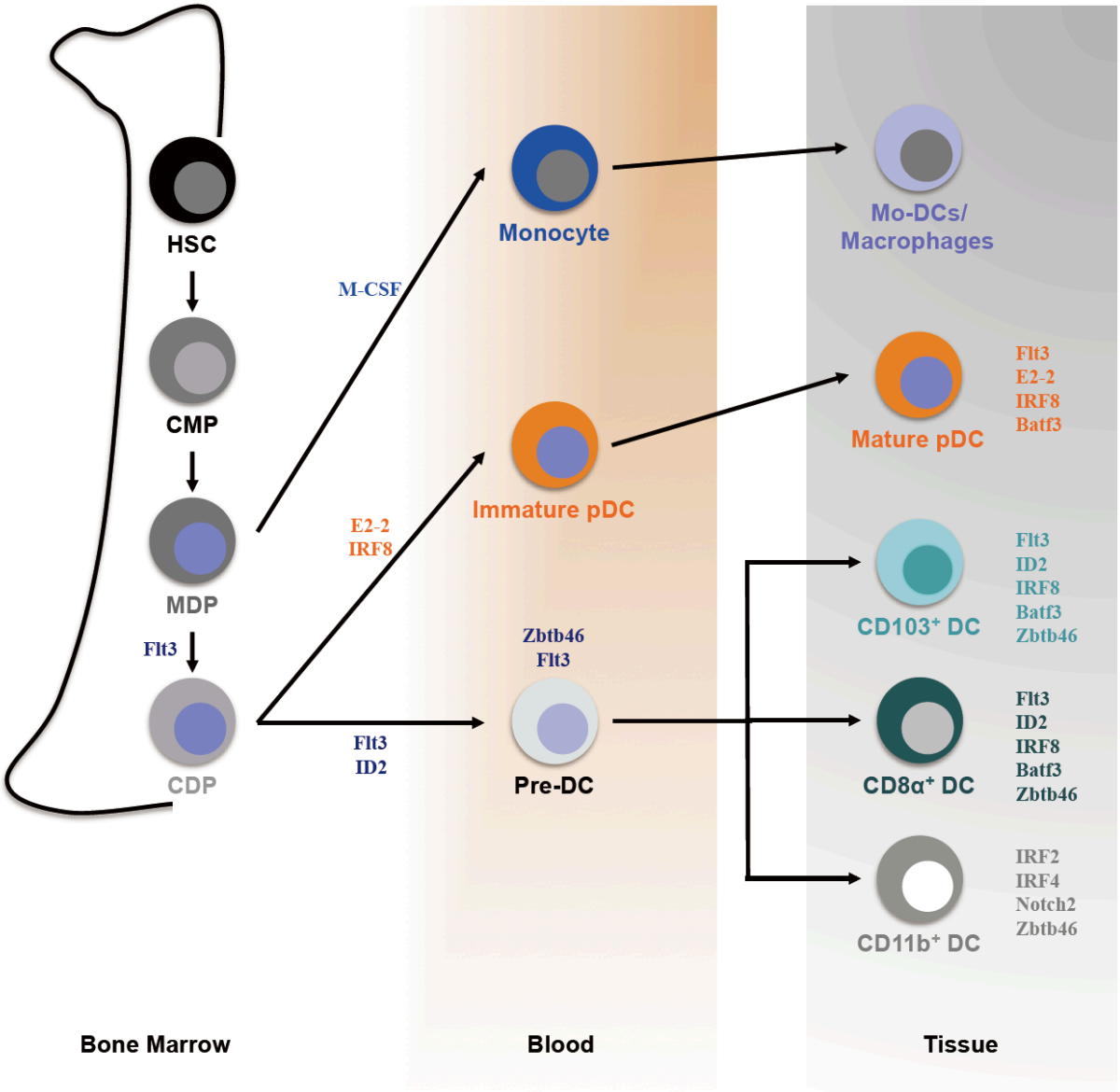

Figure 1.9. The development of cDCs and pDCs. DC lineage precursors are all highly dependent on Flt3/CD135. Transcription factors IRF8 and Batf3 are very important for their

growth and differentiation. Unlike these cells, the development of $CD11b^+$ DCs is regulated by IRF2 and IRF4. The differentiation fate of CDPs to cDCs or pDCs is determined by the expression pattern of transcription factor E2-2 or ID-2. All subsets can be maintained in lymphoid and non-lymphoid tissues by the constant entry of their precursors from the blood.

$CD11b^+$ DCs can be divided into two subsets according to their Pre-cDCs and monocytes origin. For example, the sub-populations of $CD11b^+$ DCs in lamina propria are classified by the CD103 expression. $CD103^+$ $CD11b^+$ DCs are derived from Pre-cDCs, whereas $CD103^-$ $CD11b^+$ DCs are originated from monocytes.[149, 162] However, it is not easy to classify the sub-populations in $CD11b^+$ DCs because the function and environment are different between non-lymphoid tissues. $CD11b^+$ DCs strongly express the macrophage-associated markers, such as CD11b, CX_3CR1, F4/80, CD115, and CD172α.[163] Even though similar to $CD103^+$ DCs, they show a slight increase with Flt3 signaling or the decrease in the absence of Flt3, the sensitivity of Flt3 signaling is poor compared to $CD103^+$ DCs **(Table 1.1 and 1.2)**.[145, 164]

Table 1.1. Phenotypes and locations of dendritic cells.

Location		Phenotypical markers
Lymphoid tissue	**$CD8^+$ DCs**	MHC II, CD11c, CD103 (subset), Langerin/CD207 (subset), CD24, XCR1, Clec9A, CD205
	$CD11b^+$ DCs	MHC II, CD11c, CD115/M-CSF, CD172α, CD209, F4/80
Non-lymphoid tissue	**$CD103^+$ DCs**	MHC II, CD11c, Langerin/CD207, CD24, XCR1, Clec9A, CD205
	$CD11b^+$ DCs	MHC II, CD11c, CD115/M-CSF, CD172α, CD209, F4/80, CX3CR1
	$CD103^+CD11b^+$ DCs (in lamina propria)	MHC II, CD11c, CD24, CD209/DC-SIGN
Langerhans cells		MHC II, CD11c, CD11b, Langerin/CD207

Interestingly, human $CD103^+$ DCs and $CD11b^+$ DCs similar to mouse DCs have also been found in non-lymphoid tissues. A sub-population expressing BDCA3 (CD141) is dependent on Flt3 signaling and shows high expression of Clec9A[165], XCR1[166] and transcription factors Clec9A and XCR1[167]. These characteristics are very similar to $CD103^+$ DCs and $CD8^+$ DCs in mice[168, 169]. Another sub-population expressing BDCA1 (CD1c) depends on IRF4 and shows similar features related as $CD11b^+$ DCs and $CD8^-$ DCs in mice **(Figure 1.9, Table 1.1 and Table 1.2)**.[163]

Table 1.2. Phenotypes and functions of CDs.

CD antigen	Functions
CD1a,b,c,d	MHC 1-like molecule, Specialized role in presentation of lipid antigens to NKT cells.
CD2	Adhesion molecule, Binding to CD58 (LFA-3) and CD48/BCM1 to activate T cells and mediate binding between T cells and other cells.
CD3	TCR signaling chain. key role in TCR signaling and TCR expression on cell surface.
CD4	Co-receptor for MHC II molecules. Binding to Lck on cytoplasmic face of membrain. Receptor for HIV-1 and HIV-2 gp120.
CD8	Co-receptor for MHC I molecules. Binding to Lck on cytoplasmic face of membrain.
CD11b	αM subunit of intgrin CR3 (associated with CD18). Binds to CD54, complement component iC3b, and exracelular matrix protein. It is involved in various adhesions between monocytes, macrophages and granulocytes.
CD11c	Complex with CD18 to form a αX subunit of integrin CR4. Adhesion molecule, a major form (CD11/CD18) of tissue macrophsges. Binding to fibrinogen.
CD14	Activation of innate immune system by binding to LPS binding protening (LBP) as a receptor for endotoxin (LPS). Delivering LPS/LBP complex to TLR4.
CD19	A important signaling molecule that binds to B cell receptor to regulate the development, activation and differentiation of B cells. Forms complex with CD21 (CR2) and CD81 (TAPA-1).
CD28	Activation of naïve T cells. Binding to CD80/86 to stimulate T lymphocyte proliferation and cytokine secretion.
CD56	Isoform of neural cell-adhesion molecule.
CD80/86	Interacting with co-stimulatory molecules of T lymphocytes, CD28 (activation) or CD152/CTLA-4 (inhibition).
CD103	Binding to E-cadherin and integrin β7.
CD115	Macrophage colony-stimulating factor (M-CSF) receptor to regulate the proliferation and differentiation of macrophages and monocytes.
CD123	IL-3 receptor α chain.
CD135	Growth factor receptor for early hematopoietic progenitor cells.
CD141	A essential molecule for C protein activation and inhibition of C protein anticoagulant pathway.
CD172α	Negative regulation of tyrosine kinase-associated signaling. Inhibition of phahocytosis by binding to CD47.
CD205	Endocytosis, putative antigen-uptake receptor on dendritic cells
CD207	Langerhans cell specific C-type lectin, an endocytosis receptor containing a functional C-type lectin domain with mannose specificity that promotes antigen recognition and uptake.
CD209	C-type lectin; binding to ICAM3 and HIV-1 envelope glycoprotein gp 120; Activating phagocytosis; involving in endtothelial cell adhesion.
CD303	Inhibition of IFNα/β production.
CD304	Co-receptor formation with plexin. Interaction with VEGF165 and semaphorin. Angiogenesis, cell growth, migration.

1. 3. 2. 1. 1 Dendritic Cells in the Skin

Skin DCs were be found both in the epidermis and the dermis. Langerhans cells constitute the epidermal layer and are characterized by a low level of MHC II and high level of Langerin (CD207). The development of these cells is dependent on M-CSF[170] since they are derived from fetal monocytes[171], not pre-cDCs. In homeostatic conditions, these cells are not replaced by precursors circulating the blood because they are maintained by self-renewal in situ after their differentiation in the early stages.[172] Conversely, inflammatory conditions allow

monocytes to migrate to the epidermis and to differentiate into Langerhans cells **(Table 1.1 and 1.2)**.[170]

DC sub-populations in the dermis include $CD103^+$ DCs and $CD103^-$ DCs that are heterogeneous in their origin. These subsets share the characteristics described above for the sub-populations in non-lymphoid tissues.

1. 3. 2. 2 Lymphoid Tissue Dendritic Cells

Spleen, lymph node and mucosa-associated lymphoid tissue[2] comprise two resident DC subpopulations. These subsets include $CD8^+$ DCs and $CD8^-$ DCs.[173] The $CD8^+$ DCs express cell markers similar to those $CD103^+$ DC described above in non-lymphoid tissue, and they do not express macrophage-specific markers. In contrast, the development of $CD8^-$ DCs depends on different transcription factors than those needed for $CD8^+$ DCs. These transcription factors include IRF2[174], IRF4[175] and RBP-J-mediated notch pathways[176]. The absence of these factors leads to a dramatic decrease of $CD8^-$ DCs. Interestingly, IRF2 may affect the growth of DCs through the down-regulation of IFNα/β. Notch2 signaling also regulates the development of $CD8^-CD11b^+$ DCs characterized by high expression of endothelial cell-specific adhesion molecule (ESAM) in spleen and $CD103^+CD11b^+$ DCs in lamina propria of small intestine.[177] $CD8^-$ DCs are also considered to be very heterogeneous in their origin. Changes in the expression of endothelial cell-specific adhesion molecule in this population have helped understanding their different origins. The $ESAM^{high}$ sub-population highly expresses Flt3, while $ESAM^{low}$ cells more strongly express CCR2. These observations suggest that the $ESAM^{low}$ cells may originate from monocytes **(Table 1.1 and 1.2)**.[177]

1. 3. 2. 2. 1 Migratory Dendritic Cells

Lymphoid tissues include resident DCs as well as DCs that migrate with captured tissue antigens to peripheral draining LN.[178] These cells are called migratory DCs. At steady state, similar to non-lymphoid tissue DCs, they exhibit higher level of MHC II and lower level of CD11c than resident DCs. During inflammation, DCs in tissues undergo maturation through

the up-regulation of MHC II and CD80/86 co-stimulatory molecules and chemokine CCR7 and migrate to T cell zones of draining LN in a CCR7-dependent manner.[179]

1. 3. 3 Monocyte-Derived Dendritic Cells

DCs expressing CD11b in lymphoid and non-lymphoid tissues are derived from monocytes or Pre-DCs in the blood. Monocyte-derived DCs (Mo-DCs, known as inflammatory DCs) increase in numbers during inflammatory response and promote inflammatory response. However, amounts of Mo-DCs induced by commensals are detectable in skin and peritoneum under normal condition.[180, 181] Mo-DCs were first found in skin draining LN but not in mesenteric lymph node or spleen.[182] The treatment of LPS increased the number of these cells and this increase requires the chemokine receptors CCR2 and CCR7. This finding indicates that these Mo-DCs rise in skin and migrate to skin draining LN. Consistent with this, another study from Samira groupe showed that Mo-DCs are present within the $CD11b^+$ cells in the dermis and can migrate to skin-draining lymph nodes at steady state.[183] However, monocytes can also be present in skin, lung and lymph nodes without differentiating to Mo-DCs or macrophages.[184]

Monocytes circulating in the blood vessels consist of classical $Ly6C^{high}$ and non-classical $Ly6C^{low}$ monocytes, but the direct precursor of Mo-DCs is thought to be $Ly6C^{high}$ monocytes **(Figure 1.7)**.[185, 186] The migration of monocytes from bone marrow to inflammatory sites is CCR2-dependent and the lack of CCR2 leads to a dramatic reduction of Mo-DCs.[187] Their Ly6C expression is decreased after migration to inflammatory site, and cells that differentiated into Mo-DCs begin to express macrophage markers, including CD209/DC-SIGN.[182] Surprisingly, they also express Zbtb46 and, accordingly, their numbers decline in the absence of Zbtb46.[153] Because these remarkable features of inflammatory DCs are very similar to those of lymphoid tissue $CD8^-CD11b^+$ DCs and non-lymphoid tissue $CD103^-CD11b^+$ DCs derived from Pre-cDCs, it is difficult to distinguish $CD11b^+$ DCs according to their origins **(Table 1.1 and 1.2)**.

1. 3. 4 Plasmacytoid Dendritic Cells

Plasmacytoid DCs and cDCs differentiate from CDP.[188, 189] The expression of transcription factor E2-2 in CDP induces the differentiation into pDC by the up-regulation directly of genes involved to pDC differentiation and the down-regulation of ID-2, which is needed for cDC differentiation.[190, 191] It suggests that the differentiation fate of CDPs can be regulated by the pattern of E2-2 or ID-2 exrpession **(Figure 1.9)**. pDCs, just as cDCs, are dependent on Flt3/Flt3L and, also, transcription factor IRF8 is essential for their development **(Figure 1.9)**.[192]

pDCs are characterized by the expression of Clec9A, Ly6C, PDCA-1, and CD135. They lack DC (Zbtb46, CD103, CD11c) and macrophage markers (CD11b and CX_3CR1).[193] They can be activated through TLR7[194] and TLR9[195], which are sensitive to viral single-strand RNA (ssRNA) and single-stranded DNA (ssDNA) viruses, and secrete large amounts of type 1 IFN.[196] Recently, it was demonstrated that pDCs, similar to pDCs in mice, are found in human blood and aorta. These cells express the high level of HLA-DR, BDCA2 (CD303), BDCA4 (CD304) and CD123 and secrete high IFN-α when treated with CpG oligodeoxynucleotide **(Table 1.2)**.[193]

1. 3. 5 Signaling of Dendritic Cells

Dendritic cells monitor the periphery and are specialized in antigen uptake. Dendritic cells recognize microbial "pathogen-associated molecular patterns" (PAMPs) through their "pattern recognition receptors" (PRRs), which lead to the activation of dendritic cells. Activated DCs increase the expression of an array of molecules, such as MHC I, MHC II and CD80/86, which are recognized by T cells. In order to activate those T cells, DCs transport the antigens to the secondary lymphoid organs through the lymphatic vessels in a CCR7-dependent manner.

Differentiation and proliferation of Naïve T cells proceed through three signals delivered by DCs. Dendritic cells present engulfed and processed antigens to $CD4^+$ T cells via MHC II, while internally generated peptides are presented to $CD8^+$ T cells through MHC I.

These are the first signaling. The secondary signal consists of the binding between CD80/86 on DCs and CD28 on T cells. This interaction provides the co-stimulatory signal and the increased affinity between the adhesion molecules (ICAM-1/LFA-1, LFA-3/CD2) further strengthens the connection between T cells and APCs. If this second reaction does not occur, it is said to be an anergy state. Finally, cytokines secreted by APCs induce the proliferation and differentiation of T cells **(Figure 1.10)**.[197]

1. 3. 5. 1 Differentiation of Th1 and Th2 Lymphocytes

In 1986, Time mosmann and Robert Coffman reported for the first time that $CD4^+$ T cells are divided into 2 groups in their phenotypes and functions.[198] The fate of activated T cells is determined by cytokines in addition to the TCR and costimulatory molecules essential for the activation of T cells. These cytokines, called signal 3, are produced by antigen-stimulated APCs. What cytokines are produced depends on the cells (dendritic cells, macrophages, B cells and NK cells), the maturation and activity of these cells, the type of pathogens, and tissues infected with pathogens. Thus, innate immune response plays a very important role in determining the pattern of adaptive immune response.

Dendritic cells produce IL-12 and IL-18 when their PRRs, such as TLR3 or TLR4, recognize PAMPs, such as gram-negative bacteria or viruses.[104, 199] IFN-γ produced by NK cells and activated T cells also promotes IL-12 production.[200] These cytokines induce transcription factor T-bet by stimulating naïve T cells via STAT1 signaling and the signaling by STAT3 and STAT4 increase the production of Th1-forming cytokines.[201] T-bet induces the differentiation into Th1 cells producing TNF and IFN-γ.[202] This cytokine increases the activation of macrophages and MHC II expression, promoting the proliferation of Th1 cells.[203]

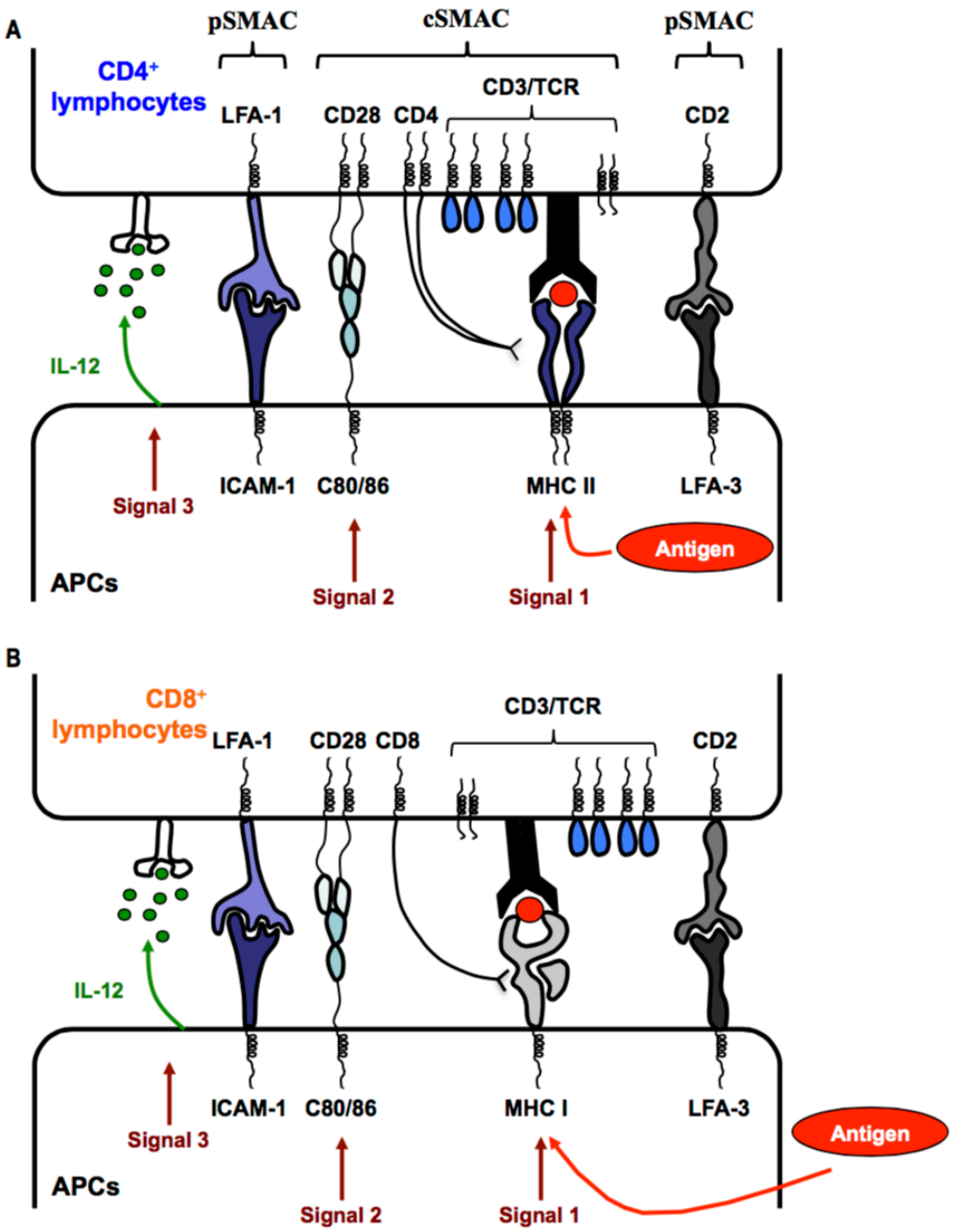

Figure 1.10. Surface interactions leading to activation of T lymphocytes. Schematic diagram showing $CD4^+$ T cells **(A)** and $CD8^+$ T cells **(B)** interacting with dendritic cells to form an immunological synapse. In particular, TCR/MHC-peptide and co-stimulatory molecules constitute the central supra-molecular activation complex (cSMAC) at the center of the synapse, and the periphery forms the peripheral supra-molecular activation complex (pSMAC). The binding between TCR/MHC-peptides is of low affinity, but the binding of other molecules increases total avidity.

The parasitic microorganisms differentiate naïve T cells into Th2 cells. Th2 polarization is caused by the cytokines IL-4, IL-6 and IL-10. IL-4 induces the production of STAT6 in naïve T cells and activates the expression of GATA-3.[204, 205] Also, GATA-3 increases the secretion of the Th2 immune response-specific cytokines IL-4, IL-5 and IL-13.[104, 206, 207] GATA-3 is expressed through the pathway of Th2 differentiation but is not detected in Th1 cells. Probably, it is dependent on the activity of IL-4/STAT6.[205, 208, 209] Interestingly, retroviral transduction of GATA-3 in Th1 cells led to a decrease in IL-12 and Th1 development.[205] These results suggest that GATA-3 plays a key role in determining the differentiation fates between Th1 and Th2. However, DCs do not secret IL-4. Mast cells, basophils and NKT cells produce IL-4 when they recognize the antigens.[210, 211] This cytokine plays a major role for the activation of B cell and eosinophil as well as the development of Th2 cells[203] and mediates IgE class switching in B cells.[212]

The major transcription factors expressed by Th1 and Th2 lymphocytes, T-bet and GATA-3, not only play a role in the immune response of T lymphocyte subsets, but also indirectly affect other T lymphocytes. First, they lead to the production of cytokines that induce the proliferation of bystander. Second, they suppress the differentiation and activation of their opposed subset. For example, an increase in T-bet inhibits the expression of GATA-3 and type 2 cytokines, such as IL-4 and IL-5, whereas the expression of GATA-3 leads to a decrease of T-bet and IFN-γ expression.[205] Therefore, the relative dominance between T-bet and GATA3 is a major key to determining the fate of Th1 vs Th2 cells.

1. 3. 5. 2 Differentiation of Th17 and Treg Lymphocytes

Tregs induce peripheral immune tolerance and inhibit autoimmune T lymphocyte activation by suppressing T lymphocyte responses. Naïve T cells differentiate into Tregs by increasing the expression of transcription factor Foxp3 by TGF-β.[213]

However, TGF-β in the presence of IL-6 secreted by DCs following fungi recognition induces naïve T cells to differentiation into Th17.[214] The STAT3 signaling-induced up-regulation of RORγt leads to an increase of IL-17.[215] This cytokine induces tissue inflammation with the recruitment of neutrophils to the infection site, and the expression of

IL-22 that promotes microbial elimination.[216] At the same time, the activation of IL-6 inhibits the production of Foxp3, which leads to the predominance of RORγt. Interestingly, individuals with acute inflammation show up-regulation of IL-6.

1. 3. 5. 3 Differentiation of Cytotoxic T Lymphocytes

Cytotoxic T lymphocytes (CTLs) originating from naïve $CD8^+$ T cells (known as cytotoxic T lymphocyte-progenitor, CTL-P) mainly recognize MHC I molecules. These cells have an important role in removing cells infected by intracellular pathogens, such as viruses or bacteria and cancer cells. Most nucleated cells express MHC I and can potentially be a target for CTLs. Uncontrolled destruction by CTLs is potentially very harmful to the host. Therefore, strict requirements are essential for their activity. To differentiate into CTLs, CTL-P require the help of both helper T cells (Th) and recognition of antigens presented by MHC I on activated DCs.[217]

1. 3. 5. 3. 1 Cross Presentation

Basically, MHC I-peptides come from endogenous of self- or non-self origin, such as viruses. MHC II peptides are derived from antigens supplied from outside the cells. However, if cells infected by viruses are not specialized antigen-presenting cells, they do not express the co-stimulatory molecules required for the activation of $CD8^+$ T cells. Also, if specialized antigen-presenting cells are not infected or infection does not occur in APCs, how does the immune system activate naïve $CD8^+$ T cells to remove intracellular microbes? and how do APCs present a virus-like pathogens surrounded by extracellular pathways that activate $CD8^+$ T cells to CTLs? The answer to this dilemma can be found in a process called cross-presentation. In some cases, APCs present extracellular antigens though MHC I rather than MHC II to $CD8^+$ T cells.[218] The efficiency of cross-presentation is initially up-regulated during DC maturation.[219] After a certain period of time (approximately 16~20 hours), this mechanism is down-regulated.[220] It is well known that $CD8^+$ DCs and $CD103^+$ DCs have excellent cross-presentation ability.[221]

1. 4 Role of DCs in Cardiovascular Disease

Atherosclerosis is the result of complex inflammatory responses of several immune cells, including vascular endothelial cells. Other immune cells, including macrophages and T cells, have been extensively studied and these cells are actually known to promote atherosclerosis. However, little is known about the function and role of antigen presenting cells, such as dendritic cells. Dendritic cells, the most potent antigen-presenting cells, regulate the immune tolerance under normal condition but promote the immune response under inflammation. Therefore, it is very important to understand the exact role of DCs in immune-related disease, such as atherosclerosis.

1. 4. 1 Dendritic Cell Subsets in Atherosclerosis

Recent studies have found DCs in healthy blood vessels[222] and in early atherosclerotic lesions.[223] The presence of these cells correlates with the accumulation of T cells.[224] Many studies using flow cytometry have been helpful in identifying DCs that express MHC II and CD11c in mice.[225] These DCs are distributed in specific blood vessel areas, including the aortic sinus, the lesser curvature of aortic arch and the arterial branch. Importantly, their numbers increase with the severity of atherosclerosis **(Figure 1.11)**.[226]

Initially, most DCs in the blood vessels were thought to originate from Mo-DCs, which also increase during atherosclerosis. These cells play a key role in promoting atherosclerosis and their numbers also show a tendency to increase with the size of the lesion.[41] The deficiency of CX_3CR1, which is highly expressed in Mo-DCs, dramatically reduces the size of atherosclerotic lesions.[227] Interestingly, the absence of GM-CSF to regulate the proliferation of DCs also led to a reduction of lesion size.[228]

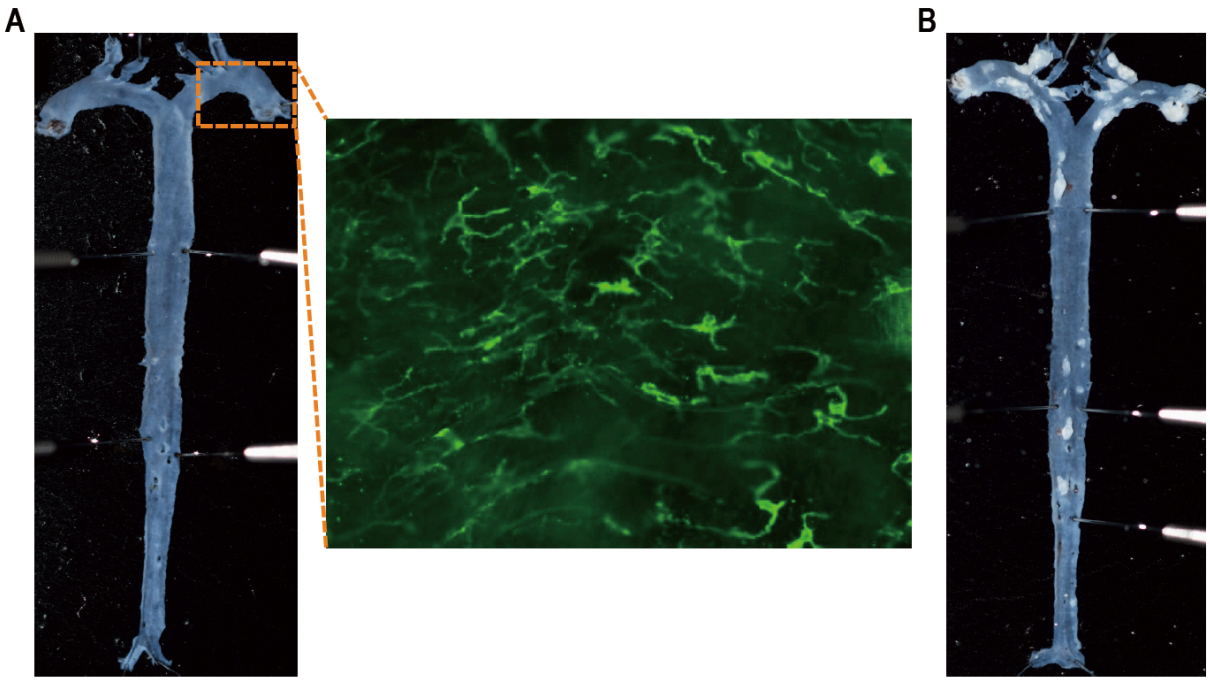

Figure 1.11. Visualization of location of aortic CD11c^{+} cells and atherosclerotic lesions. **(A)** The aorta from C57BL/6 mice was isolated, fixed, stained with a CD11c antibody coupled to Alexa 488. DCs were found in aortic sinus and ascending aorta, including the aortic arch. Right image taken on a LSM 710 confocal microscope (Zeiss). **(B)** This picture shows the distribution of the atherosclerotic lesions within aorta of ApoE$^{-/-}$ mice fed HFD for 10 weeks.

Recently, the presence of CD103^{+} DCs, which have a strong dependence on Flt3/Flt3L signaling, has also been shown in blood vessels. The deficiency of Flt3 or Flt3L leads to a decrease of CD103^{+} DCs and results in more severe lesions, with a decrease of Treg.[229] In addition, the co-stimulatory molecules CD80/86 on DCs are very important for Tregs generation and homeostasis. The deficiency of CD80/86 in Ldlr$^{-/-}$ mice results in defects in the generation and the homeostasis of Tregs. As a consequence, atherosclerosis was further promoted.[230] Therefore, CD103^{+} DCs seem to play an important role in maintaining the homeostasis of blood vessels and protecting against atherosclerosis by controlling Tregs.[229] Tregs inhibit the maturation of APCs by secreting anti-inflammatory cytokines, such as IL-10 and TGF-β. They also block the activation and the differentiation of T cells by expressing a significant amount of high affinity IL-2Rα.[231]

1. 4. 2 Foxp3$^+$ Tregs Are Regulated by IDO-1$^+$ Aortic Plasmacotoid DCs

Even though plasmacytoid DCs play an important role in the regulation of Treg differentiation, it has been suggested that they promote disease in atherosclerotic lesions.[232, 233] However, a recent study has found pDCs in normal mouse blood vessels. They are Flt3-dependent and are distributed in specific blood vessel areas where atherosclerosis occurs. pDCs are also found in atherosclerotic lesions and express IFN-α and CCR9.[234, 235] The extension of the atherosclerotic lesion leads to an increase in the number of these cells together with Treg. Interestingly, selective depletion of pDCs by the use of transgenic mice expressing diphtheria toxin receptor attenuates atherosclerosis and decreases Tregs.[230, 236] pDCs regulate the generation of Tregs by expressing indoleamine 2,3-dioxygenase 1 (IDO-1), which is important for the differentiation of Tregs. Surprisingly, Ldlr$^{-/-}$ IDO$^{-/-}$ mice showed aggravation of atherosclerosis with a decrease in Tregs. Indeed, it has been shown that there is an interaction between IDO$^+$ BDCA2$^+$ aortic pDCs and Foxp3$^+$ Tregs in human atherosclerotic lesions.[193] These results suggest that pDCs have a protective role in atherosclerosis.

1. 4. 3 The Role of Dendritic Cells in Myocardial Infarction

Angina and myocardial infarction are major life-threatening diseases. The majority of these diseases are caused by atherosclerosis. Although many studies have revealed the importance of DCs throughout the formation of atherosclerotic lesions[223, 224, 226, 229], their characteristics and function in Myocardial infarction are not been understood.

Recent studies in patients with myocardial infarction have shown that DCs are greatly increased in the lesions.[237, 238] In particular, the mature DCs infiltrated into the infarcted region show increased expression of CD209[239] and co-stimulatory molecule CD86[240]. These results suggest that DCs modulate immune responses in myocardial infarction. Therefore, a thorough characterization of the function of DCs in myocardial infarction is needed.

1. 5 Rationale

Cardiovascular disease is the leading cause of death worldwide, and its incidence is rapidly increasing. Tremendous advances have been made in molecular and cellular research to understand the inflammatory responses taking place in various diseases. There is now clear evidence that macrophages and dendritic cells play an important role in cardiovascular diseases. Therefore, in order to develop appropriate immune-therapeutic agents and vaccines, we need to understand the role of dendritic cells, macrophages and their sub-populations in cardiovascular disease through the characterization of molecules and cell pathways.

1. 5. 1 General Objective

The purpose of this study is to help develop new therapeutic concept by characterizing the function of dendritic cells and macrophages in cardiovascular diseases.

1. 5. 1. 1 Specific Objectives

Objective of chapter 2: To examine the effect of selective depletion of cDCs or pDCs on cardiac functions after myocardial infarction. The developmental and functional features of cardiac cDCs and pDCs were analyzed using flow cytometry and confocal microscopy. We also used the echocardiography to study heart function after infarction in BDCA2-DTR and Zbtb46-DTR mice.

Objective of chapter 3: To investigate the transcriptome of foamy and non-foamy macrophages isolated from atherosclerotic intima. We established for the first time a lipid probe (BODIPY493/503)-based flow cytometric method to investigate foamy macrophages in atherosclerosis. This method allows us to distinguish between foamy- and non-foamy macrophages in atherosclerosis and further analyze their gene expression pattern through transcriptome analysis.

CHAPTER 2

2 Conventional Dendritic Cells Impair Recovery after Myocardial Infarction

Jun Seong Lee[1,2,3], Se-Jin Jeong[4], Sinai Kim[4], Lorraine Chalifour[5], Tae Jin Yun[2,6], Mohammad Alam Miah[1,2], Bin Li[1,7], Abdelilah Majdoubi[1,3], Antoine Sabourin[1,3], Tibor Keler[8], Jean V Guimond[9], Elie Haddad[1,10], Eui-Young Choi[11], Slava Epelman[12,13,14], Jae Hoon Choi[15], Goo Taeg Oh[4], Jacques Thibodeau[1,3] and Cheolho Cheong[1,2,6,*]

[1]Département de microbiologie, infectiologie et immunologie, Université de Montréal, Montreal, Quebec H3T 1J4, Canada

[2]Institut de Recherches Cliniques de Montréal (IRCM), Montréal, Quebec H2W 1R7, Canada

[3]Laboratoire d'immunologie moléculaire, Université de Montréal, Quebec H3T 1J4, Canada

[4]Immune and Vascular Cell Network Research Center, National Creative Initiatives, Department of Life Sciences, Ewha Womans University, Seoul 120-750, South Korea

[5]Lady Davis Institute, Division of Experimental Medicine, McGill University, Montréal, Quebec H3T 1E2, Canada

[6]Division of Experimental medicine, Department of Medicine, McGill University, Montreal, Quebec H4A 3J1, Canada

[7]Département de Biologie Moléculaire, Université de Montréal, Quebec H3T 1J4,Canada

[8]Celldex Therapeutics, Hampton, NJ 08827, USA

[9]Centre de Santé et de Services Sociaux Jeanne-Mance, Montréal, Quebec H2T 2R9, Canada

[10]Centre Hospitalier Universitaire Sainte-Justine Research Center, Montréal, Quebec H3T 1C5, Canada

[11]Gangnam Severance Hospital, Yonsei University College of Medicine, Seoul 06273, South Korea

[12]Peter Munk Cardiac Center, Toronto, Ontario M5G 2N2, Canada

[13]Ted Rogers Centre for Heart Research, Toronto, Ontario M5G 1X8,Canada

[14]Toronto General Hospital Research Institute, University Health Network, Toronto Ontario M5G 2C4, Canada

[15]Department of Life Science, College of Natural Sciences, Research Institute for Natural Sciences, Hanyang University, Seoul 04763, South Korea
*Deceased.

Short Title: cDCs impair recovery after myocardial infarction

Corresponding authors

Jacques Thibodeau, Ph.D.
Laboratoire d'immunologie moléculaire, Département de microbiologie, infectiologie et immunologie, Université de Montréal, 2900, Boulevard Edouard Montpetit, Montréal, Québec. Canada H3T 1J4
Phone : +1-514-343-6279 Fax : +1-514-343-5701
E-mail : Jacques.thibodeau@umontreal.ca

Goo Taeg Oh, DVM.,Ph.D
Director, National Creative Research Center
for Immune and Vascular Cell Network,
Department of Life Sciences,
Ewha Womans University, Seodaemoon-gu, Seoul 120-750, Korea
Phone : +82-2-3277-4128, 4253 Fax : +82-2-3277-3760
E-mail : gootaeg@ewha.ac.kr

The Journal of Immunology. (2018). 201(6):1784-1798

2. 1 Abstract

Ischemic myocardial injury results in sterile cardiac inflammation that leads to tissue repair, two processes controlled by mononuclear phagocytes. Despite global burden of cardiovascular diseases, we do not understand the functional contribution to pathogenesis of specific cardiac mononuclear phagocyte lineages, in particular dendritic cells. To address this limitation, we used detailed lineage tracing and genetic studies to identify bona fide murine and human $CD103^+$ conventional dendritic cell (cDC)1s, $CD11b^+$ cDC2s, and plasmacytoid DCs (pDCs) in the heart of normal mice and immunocompromised NSG mice reconstituted with human $CD34^+$ cells, respectively. After myocardial infarction (MI), the specific depletion of cDCs, but not pDCs, improved cardiac function and prevented adverse cardiac remodeling. Our results showed that fractional shortening measured after MI was not influenced by the absence of pDCs. Interestingly, however, depletion of cDCs significantly improved reduction in fractional shortening. Moreover, fibrosis and cell areas were reduced in infarcted zones. This correlated with reduced numbers of cardiac macrophages, neutrophils, and T cells, indicating a blunted inflammatory response. Accordingly, mRNA levels of proinflammatory cytokines IL-1β and IFN-γ were reduced. Collectively, our results demonstrate the unequivocal pathological role of cDCs following MI.

2. 2 Introduction

Myocardial infarction (MI) caused by a thrombotic occlusion of a coronary artery is the most frequent cause of cardiac dysfunction and heart failure.[1] Ischemia results in oxygen and nutrient deprivation, leading to cardiomyocyte cell death in the nonperfused territory. This is accompanied by an intense sterile inflammatory response and a gradual collagen-driven scar formation that is required to replace the necrotic myocardium.[2] Ultimately, altered hemodynamic forces within the myocardium lead to adverse remodeling changes in the remote, uninfarcted myocardial segments.[3, 4, 5] Ischemic heart disease is the leading cause of death worldwide. Myocardial necrosis after MI triggers immuno-inflammatory reactions that are integral to the healing process but also contribute to left ventricular (LV) dysfunction.[6, 7] Such inflammation results from the activation of tissue-resident immune cells, which produce pro-inflammatory cytokines and chemokines capable of attracting leukocytes from the blood into the region of cardiac injury.[8] Various animal and human studies have provided evidence that the expansion and/or recruitment of inflammatory leukocytes such as mononuclear phagocytes, dendritic cells (DCs), monocytes, and macrophages (MΦs) either enhance or suppress the ability of the myocardium to recover after cardiac injury.[9] One key limitation has been the inability to distinguish the function of MΦs and DCs, which can express similar cell surface markers, such as MHC class II (MHC II), CD11c, and F4/80.[10] In this context, it is critical to precisely define the origin, developmental features, and functions of DCs in the heart.

DCs are professional APCs that bridge innate and adaptive immunity.[11] In mice, their ontogeny has been the subject of many important discoveries in recent years.[12] It is now established that common DC progenitors are heterogeneous and give rise to plasmacytoid DCs (pDCs) or precursor DCs, which all move from the bone marrow (BM) to the blood, the secondary lymphoid organs, and to nonhematopoietic tissues.[13] These cells express MHC II molecules and can act as Ag-presenting cells to power proatherogenic T cell immunity.[14] However, through the production of IDO, pDCs also promote tolerance by modulating regulatory T cell (Treg)-suppressive functions during autoimmunity and atherosclerosis.[15, 16]

BM and blood precursor cDCs (pre-cDCs) are heterogeneous and already committed to the conventional DC (cDC)1 and cDC2 lineages.[17] It is not clear, however, if pre-cDCs can be found in other tissues, such as the heart. In lymphoid organs, the resident cDC1s and cDC2s express CD8α and CD4, respectively. In nonlymphoid tissues such as the skin, cDC1s and cDC2s are rather characterized by the expression of CD103 and CD11b, respectively.[18] In addition to these phenotypic differences, cDCs are functionally distinguishable. cDC1s are dependent on the transcription factors IRF8, ID2, and BatF3. These $CD103^+$ cDCs are potent cross-presenting cells involved in Th1 polarization in response to pathogens. cDC2s, rather, rely on IRF4 and several additional transcriptional factors, such as RelB, RBP-J, and IRF2 for their development and promote activation of Th2 and Th17 cells.[19, 20, 21, 22, 23] As a whole, it is well established that DCs, although poorly phagocytic, are highly efficient in the capture, processing, and presentation of Ags to T cells.[24, 25]

In previous studies, the respective roles of cDCs and pDCs in a clinically relevant disease could not be established because of the lack of tools to separately track or deplete specific subsets. Although pDCs can be selectively depleted by diphtheria toxin (DT) in mice expressing the DT receptor (DTR) under the control of the human BDCA2 promoter, a similar approach to track cDCs has only been developed recently.[26] Indeed, *Zbtb46* is not shared by other hematopoietic cell types, and its expression marks the cDC lineage.[27, 28] In this study, we sought to characterize DC subsets in healthy and infarcted myocardium of C57BL/6 mice and humanized mice (hu-mice). Critically, using depletion strategies based on BDCA2 and *Zbtb46*, we addressed the functional impact of deleting individual DC subsets on ischemic cardiac injury.

2. 3 Results

2. 3. 1 Characterization of Cardiac Mouse DCs

Although heart MΦs at the steady state have been extensively studied[9], the nature of the resident DC populations remains to be fully characterized. To better define the cardiac DC subsets in C57BL/6 mice, single-cell suspensions from pooled healthy hearts were isolated and analyzed by flow cytometry (**Figure. 2.1**). First, granulocytes ($Ly6G^+$ $CD11b^+$), T ($CD3^+$), B ($CD19^+$), and NK ($CD49b^+$) cells were gated out from the $CD45^+$ leukocyte population, as these have been shown to be intravascular contaminants and not within cardiac tissue during steady state (**Figure. 2.1A**).[9] MΦs were specifically identified as $CD64^+$ $CD11b^+$. To identify pDCs, we analyzed the $Ly6G^-$ $CD64^-$ $CD3^-$ $CD19^-$ $CD49b^-$ MHC II^{lo} $CD11b^-$ $CD11c^{lo}$ subset and gated on $PDCA1^+$ $Ly6c^+$ cells, as described.[13] Putative cDCs ($CD11c^+$ MHC II^+) were further characterized using a combination of CD103 and CD11b out of the same exclusionary gate set. We observed that the expression of these markers was mutually exclusive, defining three subpopulations: $CD103^+$ $CD11b^-$ cDC1s, $CD103^-$ $CD11b^+$ cDC2s, and double-negative (DN) cDCs. To further characterize the putative cDC1s and cDC2s, total cDCs were gated on $CD11b^+$ or $CD103^+$ cells and analyzed for the expression of lineage and subset-specific markers (**Figure. 2.1B–E**). Their cDC origin was confirmed, as both subsets were *Zbtb46*$^+$ (**Figure. 2.1B and 2.1C**). In addition, cardiac cDC1s express Clec9a, Flt3/CD135, DEC205, CD24, and CD283, whereas cDC2s specifically expressed low levels of CD115/M-CSFR, F4/80, CX_3CR1, and Ly6C (**Figure. 2.1B–E**). cDCs did not express NK cells, B cells, T cells, granulocytes, or pDCs markers (**Supplemental figure. 2.1A and 2.1B**). Interestingly, we observed dichotomous expression of XCR1 and CD172α in mature cDC (**Figure. 2.1F**).[17] We also identified similar dichotomous expression in the DN cDC population, suggesting that these cells may represent a novel population of tissue pre-cDCs (**Figure. 2.1F**).

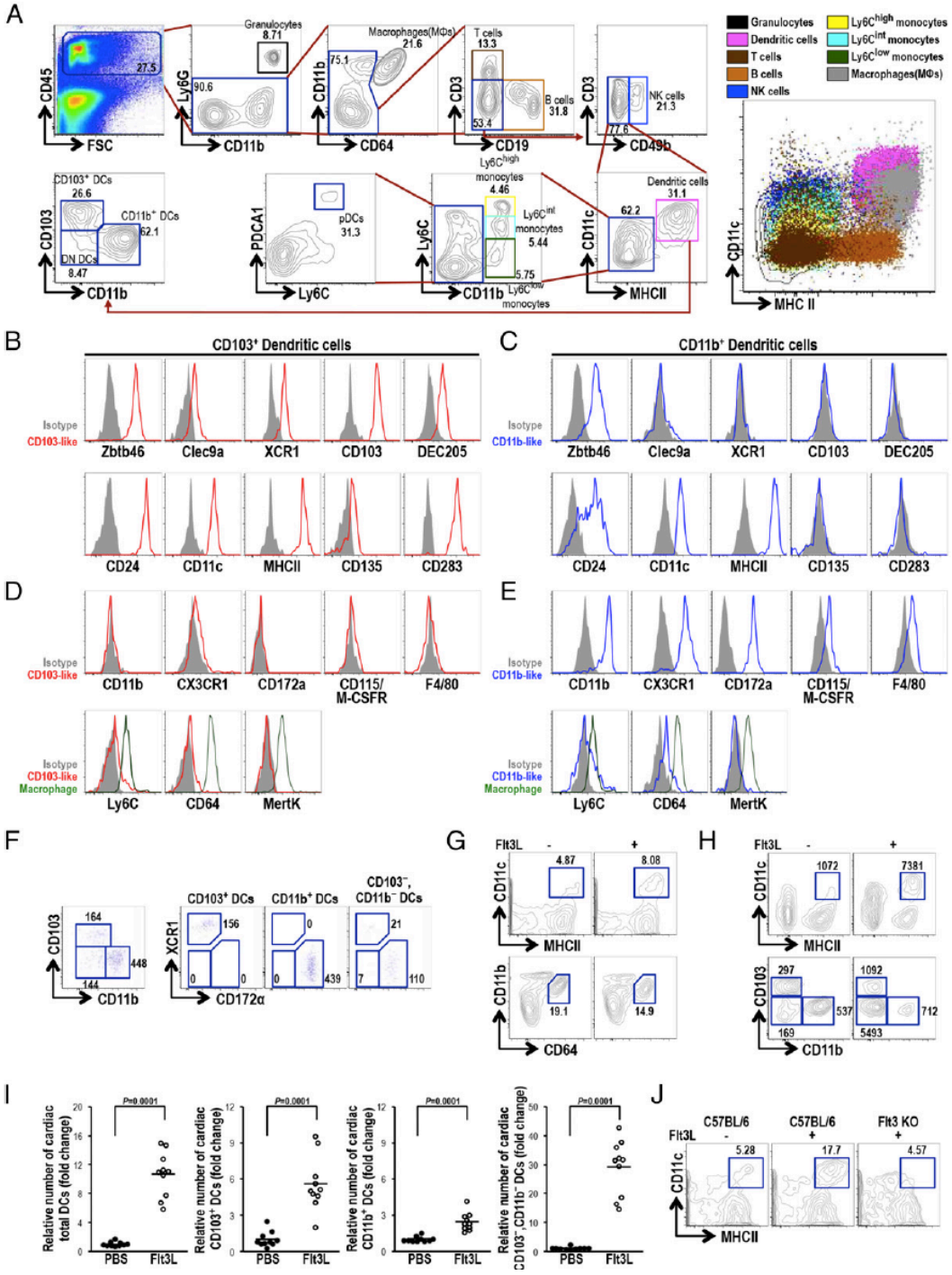

Figure 2.1. Identification of mouse cardiac DCs under steady state. (A) Cardiac single-cell suspensions were pooled from 3–5 hearts of WT C57BL/6 and analyzed by flow cytometry. SSC^{low} and FSC^{low} dead cells and doublets were excluded (data not shown). $CD45^{+}$ cells were further characterized, and the various subpopulations of cardiac leukocytes are visualized altogether on the dot blot (right panels) according to the expression of CD11c and MHC II. **(B–E)** Cardiac $CD103^{+}$ DCs (red line) and $CD11b^{+}$ DCs (blue line) were further characterized

phenotypically using a series of mAbs and their specific isotype controls (gray filled lines). All markers were surface stained except Clec9a, which was stained following permeabilization. *Zbtb46* (*Zbtb46*$^{+/+}$ [WT] and *Zbtb46*$^{gfp/+}$) and CX_3CR1 ($CX_3CR1^{+/+}$ [WT] and $CX_3CR1^{gfp/+}$) reporter mice were used for assessing the expression of these molecules. Cardiac MΦs were included as positive controls for the assessment of Ly6C, CD64, and MertK expression. **(F)** The expression of CD172α and XCR1 was analyzed in specific DC subsets. Absolute numbers are shown. **(G–J)** WT and Flt3/Flk2/CD135-deficient mice were injected i.p. with PBS (−) or with 2 μg of Flt3L (+) each day for nine consecutive days. Representative FACS plots from at least three experiments are shown. **(G)** Percentages of cardiac total DCs (top) and MΦs (bottom). **(H)** Absolute numbers of total cardiac DCs (top) and DC subsets (bottom). **(I)** Relative numbers of cardiac DC subsets in Flt3-treated mice normalized to the control PBS group. Graphs indicate the mean **6** SD; n = 10. **(J)** Percentages of cardiac total DCs from WT and Flt3 KO mice treated or not with Flt3L.

2. 3. 2 *Bona Fide* cDCs in The Heart

cDCs display a variety of distinctive developmental, functional, and phenotypic characteristics.[12] We performed in vivo and ex vivo experiments to monitor some of these parameters in the mouse heart, including the impact of depleting *Zbtb46*-expressing cells on the DC compartment. First, to definitely confirm the DC origin of the populations identified above, we examined whether Flt3L could affect cardiac cDC numbers. Flt3L is a DC growth factor, promoting survival and differentiation of progenitors.[29] Injection of Flt3 to mice was shown to dramatically increase the numbers of mature DC subpopulations.[30] Mice treated with Flt3L showed an increase in total DCs ($CD11c^+$ MHC II^+) in the heart (**Figure. 2.1G, top**) as well as in the spleen (**Supplemental figure. 2.1C**). In contrast, the proportion of $CD11b^+$ $CD64^+$ MΦs, in which development is dependent on CD115 rather than CD135 [12, 31], was decreased (**Figure. 2.1G, bottom**). Absolute numbers revealed that Flt3 increases predominantly the number of $CD103^+$ and DN DCs subsets (**Figure. 2.1H and 2.1I**). Cardiac $CD103^+$ DCs were particularly sensitive to the effect of Flt3L, showing a 5-fold increase (**Figure. 2.1I**). Interestingly, heart DN cDCs cells showed a dramatic expansion (～30-fold) in response to 9 days of Flt3 treatment, both in the heart ($CD103^-$ $CD11b^-$) and spleen ($CD8\alpha^-$ $CD11b^-$) (**Figure. 2.1H and 2.1I, Supplemental figure. 2.1D**). The effect of Flt3L was mediated through the FLT3 receptor (CD135), as the expansion of total cDC numbers was not observed in CD135-deficient (FLT3 KO) mice (**Figure. 2.1J**).

Next, to confirm the cDC nature of the cardiac cell subsets described above, we tested the impact of DT in lethally irradiated C57BL/6 mice reconstituted with Zbtb46-DTR BM. In these chimeric mice, DT selectively eliminated heart, spleen, and LN DCs ($CD11c^+$ MHC II^+) (**Figure. 2.2A, Supplemental figure. 2.1E**). All cardiac DC subsets were depleted, although some DN cells ($CD103^-$ $CD11b^-$) remained after DT treatment (**Figure. 2.2B**).

We also examined the levels of IRF4 and IRF8, as strong expression of these transcription factors delineates the two main cDC subsets.[32] Although IRF4 was more strongly expressed in $CD11b^+$ than in $CD103^+$ cDCs, we found more IRF8 in $CD103^+$ cDCs than in $CD11b^+$ cDCs (**Figure. 2.2C, bottom panels**). The $CD103^-$ $CD11b^-$ DN population appeared to be mostly $IRF4^{lo}$ and bimodal for the expression of IRF8. Interestingly, when mice were given Flt3L, cDC1 numbers greatly increased, whereas cDC2s were only marginally affected (**Figure. 2.2C, upper panels**). However, the $IRF8^{hi}$ subset of DN DCs strongly responded to the growth factor, and their numbers greatly increased in the heart (**Figure. 2.2C and 2.2D**). Thus, when total DCs were analyzed for IRF8 and IRF4 expression, the large increase in the proportions of $IRF8^{hi}$ cells is mostly caused by the response of $CD11b^-$ $CD103^-$ DN cells (**Figure. 2.2D**). Based on IRF4 and IRF8 expression, all DC subsets were affected by DT in the Zbtb46-DTR mice (**Figure. 2.2E**). These results suggest that the heart harbors $CD103^-$ $CD11b^-$ pre-cDCs, which are mostly committed to the $IRF8^+$ DC lineage.

Although DCs share some phenotypic properties with MΦs, they constitute a morphologically distinct and functionally specialized cellular subpopulation. Key characteristics that help distinguish these cell types are their morphology and phagocytic capability.[33] To further confirm the cDC nature of the $CD103^+$ $CD11b^-$ and $CD103^-$ $CD11b^+$ populations, we bathed cardiac cell suspensions in serum-containing RPMI medium with 1-μm fluorescent beads. Then, cells were stained based on the phenotypic markers described above, sorted by flow cytometry, and analyzed by fluorescence microscopy. **Figure. 2.2F** demonstrates the distinct morphology of MΦs and their high phagocytic activity as compared with $CD103^+$ DCs, $CD11b^+$ DCs, and the small resting B cells. The specific accumulation of large numbers of phagocytosed fluorescent beads in MΦs can be readily confirmed by flow cytometry (**Figure. 2.2G**).

As activated cDCs are highly migratory, we investigated the behavior of cardiac cDCs in mice treated with poly I:C. DC maturation induced by an inflammatory stimulus in nonlymphoid tissues triggers the migration toward lymphoid organs.[34] C57BL/6 mice received poly I:C i.v., and cardiac cDCs were analyzed by flow cytometry after 24, 48, and 72 h (**Figure. 2.2H**). Whereas neutrophils were increased in the heart by the inflammatory stimulus, total cDCs and all subsets rapidly decreased in numbers after poly I:C injection but gradually increased over time (**Figure. 2.2I**). Efficient systemic action of poly I:C was confirmed by CD86 upregulation on spleen DCs (**Figure. 2.2J**).

Next, we asked whether human cDCs could be identified in the heart of hu-mice.[15] Human myeloid DCs are classified on the basis of their expression of BDCA3 or BDCA1, and these subsets are related to mouse cDC1s and cDC2s, respectively.[10, 33] Irradiated mice reconstituted with human stem cells were injected i.p. with PBS or with 2 µg of Flt3L each day for nine consecutive days. Total DCs (HLA-DR$^+$ CD11c$^+$), including both BDCA1$^+$ and BDCA3$^+$ subsets, were detected in hu-mice heart (**Supplemental figure. 2.1F**), and this pool greatly expanded in response to Flt3L treatment (**Supplemental figure. 2.1G**). IRF8 was more expressed in BDCA3$^+$ DCs and, conversely, IRF4 expression was higher in BDCA1$^+$ DCs (**Supplemental figure. 2.1H**). Both IRF4- and IRF8-expressing cells responded to Flt3L (**Supplemental figure. 2.1I**). These results demonstrate the capacity of human DC subsets, functionally related to those found in mice, to colonize the heart. Altogether, our data provide evidence for the presence of bona fide cardiac cDC1s and cDC2s in mammals.

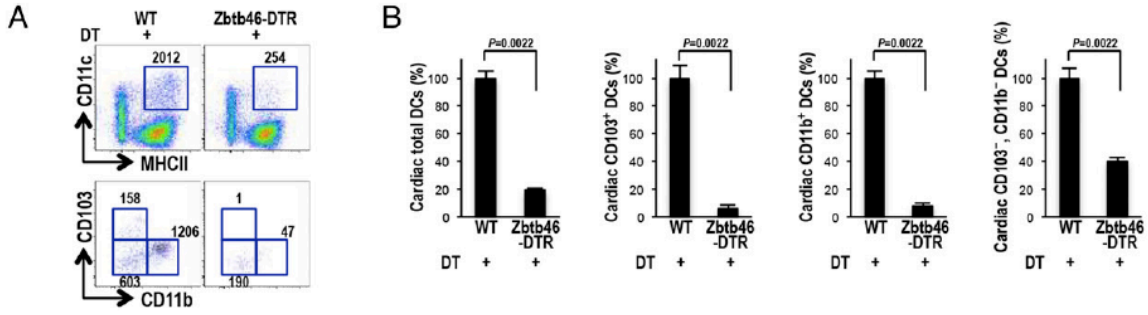

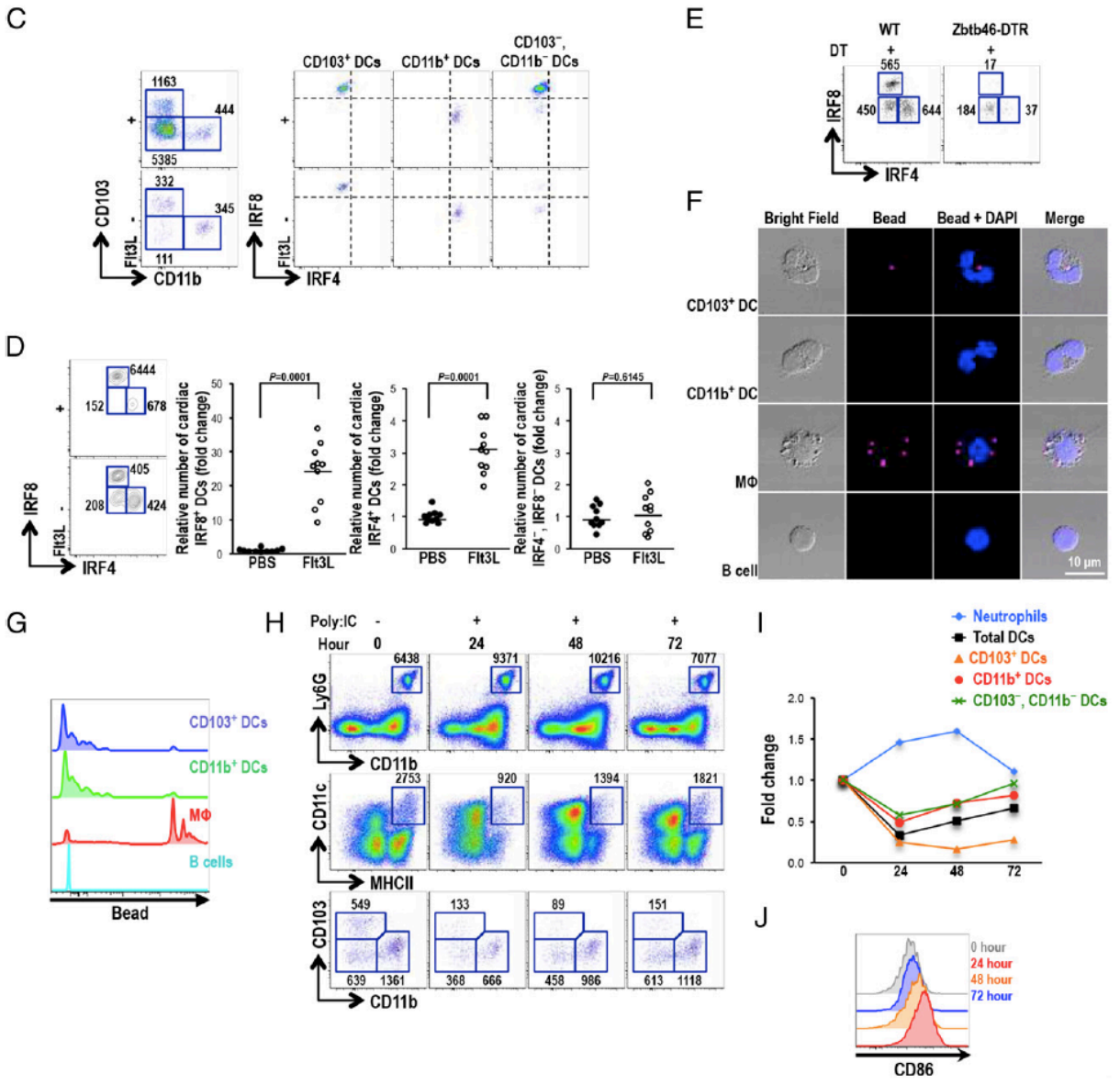

Figure 2.2. ***Bona fide*** **cDCs in the mouse heart.** Lethally irradiated C57BL6/J mice were reconstituted with BM from WT or Zbtb46-DTR mice. **(A)** Representative FACS plots showing the selective elimination of cardiac total DCs (top) and DCs subsets (bottom) in mice injected twice with DT at a 24 h interval. **(B)** Percentage (mean ± SD; n = 6 mice) of total DCs and DC subsets. **(C and D)** WT mice were injected intraperitoneally with PBS (−) or with 2 μg of Flt3L (+) each day for nine consecutive days. **(C)** The expression of IRF4 and IRF8 was analyzed in cardiac DC subsets of mice injected with with PBS (bottom) or with Flt3L (top). Representative FACS plots from at least three experiments. **(D)** Left: representative FACS plots of cardiac IRF4$^+$ DCs, IRF8$^+$ DCs and double negative cells. Right: Numbers of IRF4$^+$ DCs, IRF8$^+$ DCs and double negative cells normalized to the control PBS group. Graph indicates the mean ± SD; n = 10. **(E)** Representative FACS plots from at least three experiments showing the absolute numbers of cells expressing IRF4 and IRF8 in total CD11c$^+$

MHCII$^+$ cardiac DCs from WT and Zbtb-DTR chimeric mice treated with DT. **(F and G)** Morphology and phagocytic activity of cardiac CD103$^+$ DCs, CD11b$^+$ DCs, MΦs, and small resting B cells. Cardiac cells from 10 WT heart were pooled, incubated in serum-containing RPMI medium with 1 μm fluorescent yellow green microspheres for 1 h and stained with markers as in **Figure 2.1A**. Cells were sorted by flow cytometry based on cell type-specific markers, counterstained with DAPI (blue) and cytospined to assess morphology by fluorescence microscopy **(F)** and phagocytic activity by flow cytometry **(G)**. **(H)** WT mice were injected i.v. with 25 μg of poly I:C and heart cells were stained for granulocytes (top), total DCs (middle) and DC subsets (bottom). Absolute numbers of cells in each gate are shown. Data from three representative experiments were plotted in panel **(I)** to show the variations over time. **(J)** The biological activity of injected poly I:C was confirmed by CD86 up-regulation on spleen DCs.

2. 3. 3 Co-distribution of Macrophages and cDCs in The Heart

We have refined the anatomical distribution of cardiac MΦs and cDCs by surgically separating the heart into segment 1 (Seg1) with atria, segment 2 (Seg2), and segment 3 (Seg3). Seg1 with atria was further separated into right atrium (RA), left atrium, and Seg1 (**Supplemental figure. 2.2A**). Considering the small size of the atria (**Supplemental figure. 2.2B**), absolute numbers of hematopoietic cells in the different parts of the normal heart were determined, normalized by weight, and expressed for each subset as the percentage of these cells in a given section of the heart.

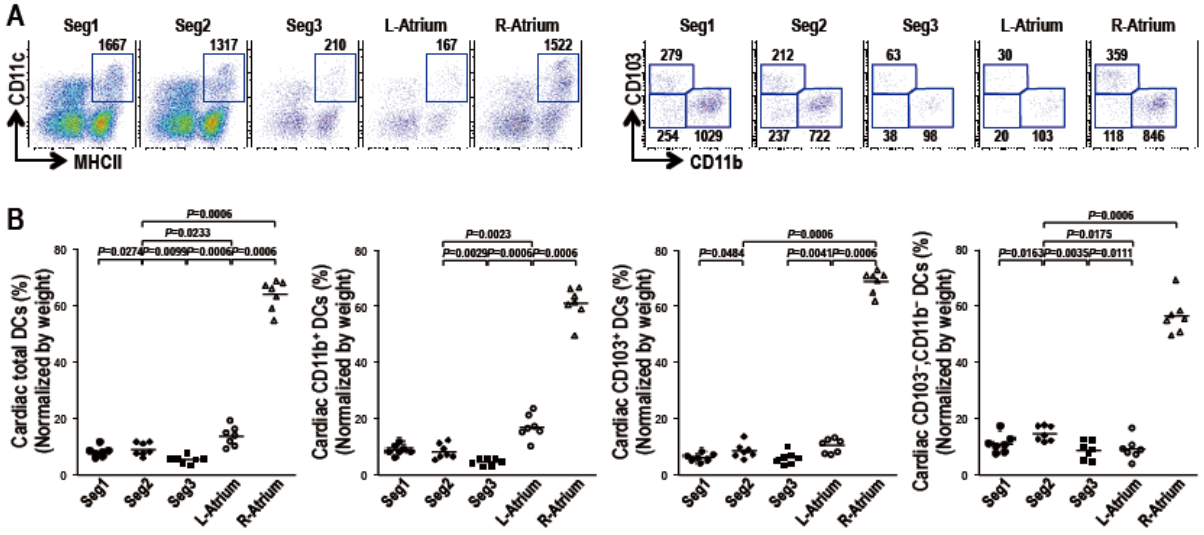

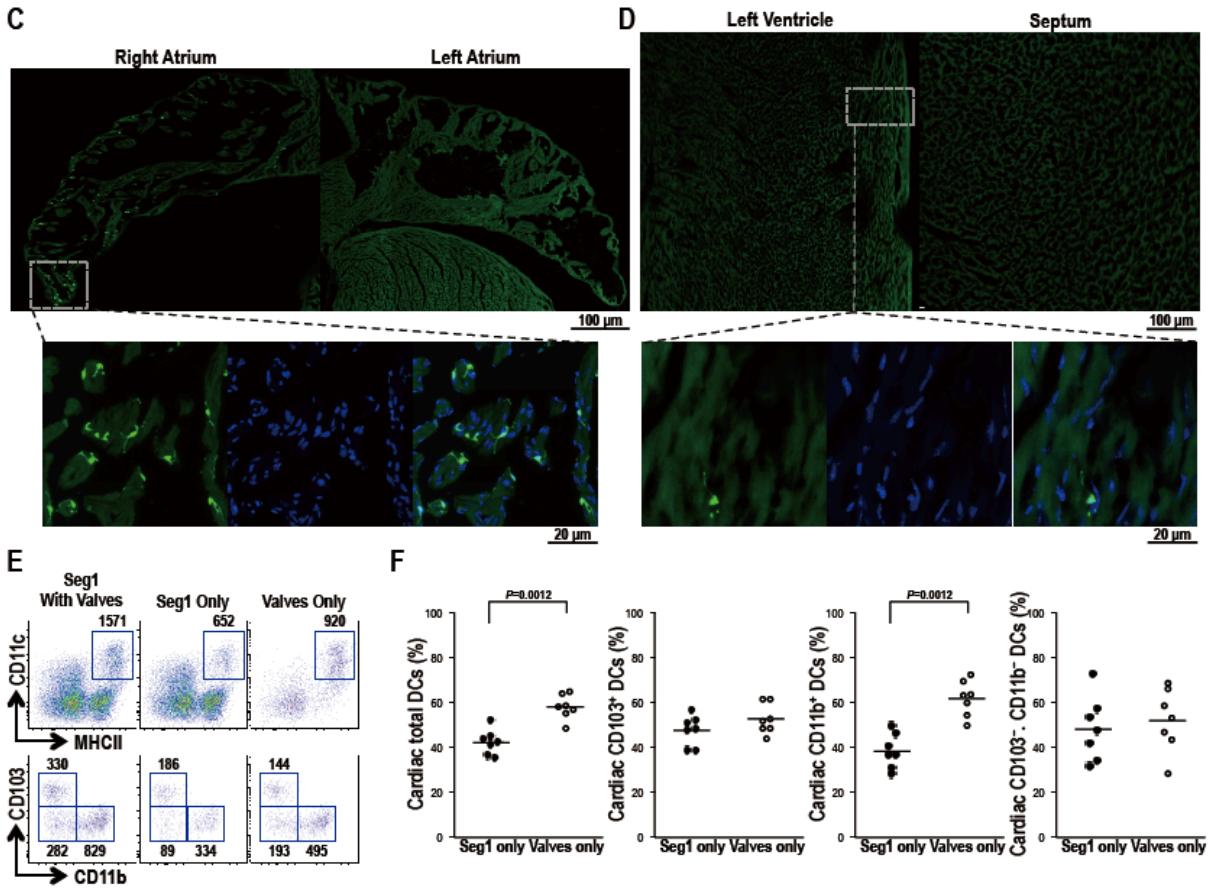

Figure 2.3. Anatomical location of DCs under steady-state conditions in mouse heart. (A) Cells from various mouse heart sections (**Supplemental figure 2.2A**) were analyzed by flow cytometry and the absolute numbers of total DCs (left panels) and DC subsets (right panels) are shown. **(B)** Absolute numbers were normalized relative to the weight (**Supplemental figure 2.2B**) of the different sections and these numbers were used to compare the percentage (mean ± SD; n = 7 mice) of a given cell population between heart sections. **(C and D)** Representative immunofluorescence sections (top, tile scan confocal images) of heart atria **(C)** and right and left ventricle **(D)** from CD11c-YFP$^{+/+}$ mice under steady state condition stained with anti-GFP antibody (green) and DAPI (blue). All experiments were performed on 12 µm frozen sections. **(E)** Valves were dissociated from Seg1 (**Supplemental figure 2.2E**) and cells were analyzed by flow cytometry. Absolute numbers for total DCs (upper panels) and DC subsets (bottom panels) are shown. **(F)** Percentages of total DCs and DC subsets in each section of the heart. Graphs indicate mean ± SD; n = 7.

Our flow cytometry analysis shows that CD45^{+} leukocytes, including MΦs, cDC1s, and cDC2s more densely populate the atria and principally the RA (**Figure. 2.3A and 2.3B, Supplemental figure. 2.2C and 2.2D**). Immunofluorescence microscopy confirmed the

strong presence of $CD11c^+$ cells in the RA of CD11c-YFP mice (**Figure. 2.3C and 2.3D**). We also examined whether DCs were present in the tricuspid and mitral valves included in Seg1. We surgically separated Seg1, including tricuspid and mitral valves, into Seg1 only or valves (**Supplemental figure. 2.2E**). Although $CD45^+$ leukocytes were reduced ~2-fold in valves compared with Seg1 only (**Supplemental figure. 2.2F**), MΦs as well as total DCs and the various subsets appear to be equally distributed between Seg1 and the valves (**Figure. 2.3E and 2.3F, Supplemental figure. 2.2F**). Notably, cardiac $CD11c^+$ cells in CD11c-YFP mice displayed DC morphology in the valve (**Supplemental figure. 2.2G**). Altogether, these results demonstrate that cardiac cDC subsets and MΦs show a similar distribution and localize more densely in the RA.

2. 3. 4 Increased Numbers of cDCs and Tregs in The Heart Following MI

We and others have shown that DC numbers increase under inflammatory conditions such as aging and atherosclerosis.[15, 35] Aging is a risk factor for all cardiovascular diseases, most likely related to the development of a panoply of conditions in the elderly, such as hypertension.[36] As we have recently shown in *Ldlr*$^{-/-}$ mice that atherosclerosis induced by a western-type diet correlated with an increase in the number of DCs in the aorta[15], we hypothesized that this inflammatory condition, as well as aging, could modulate cDC numbers in the heart. Interestingly, we found a positive correlation between age and the number of cardiac cDCs ($CD103^+$ and $CD11b^+$) (**Supplemental figure. 2.3A**). However, this was not the case for DN $CD103^-$ $CD11b^-$ DCs. Then, we investigated in *Ldlr*$^{-/-}$ mice the impact of a high fat diet on the number of heart DCs. After 10 wk, there was an increase in the number of $CD11b^+$ DCs (**Supplemental figure. 2.3B**). Interestingly, $CD103^+$ DC and DN $CD103^-$ $CD11b^-$ DC numbers remained unchanged in these conditions, suggesting a specific role for cDC2s in inflammation of the heart.

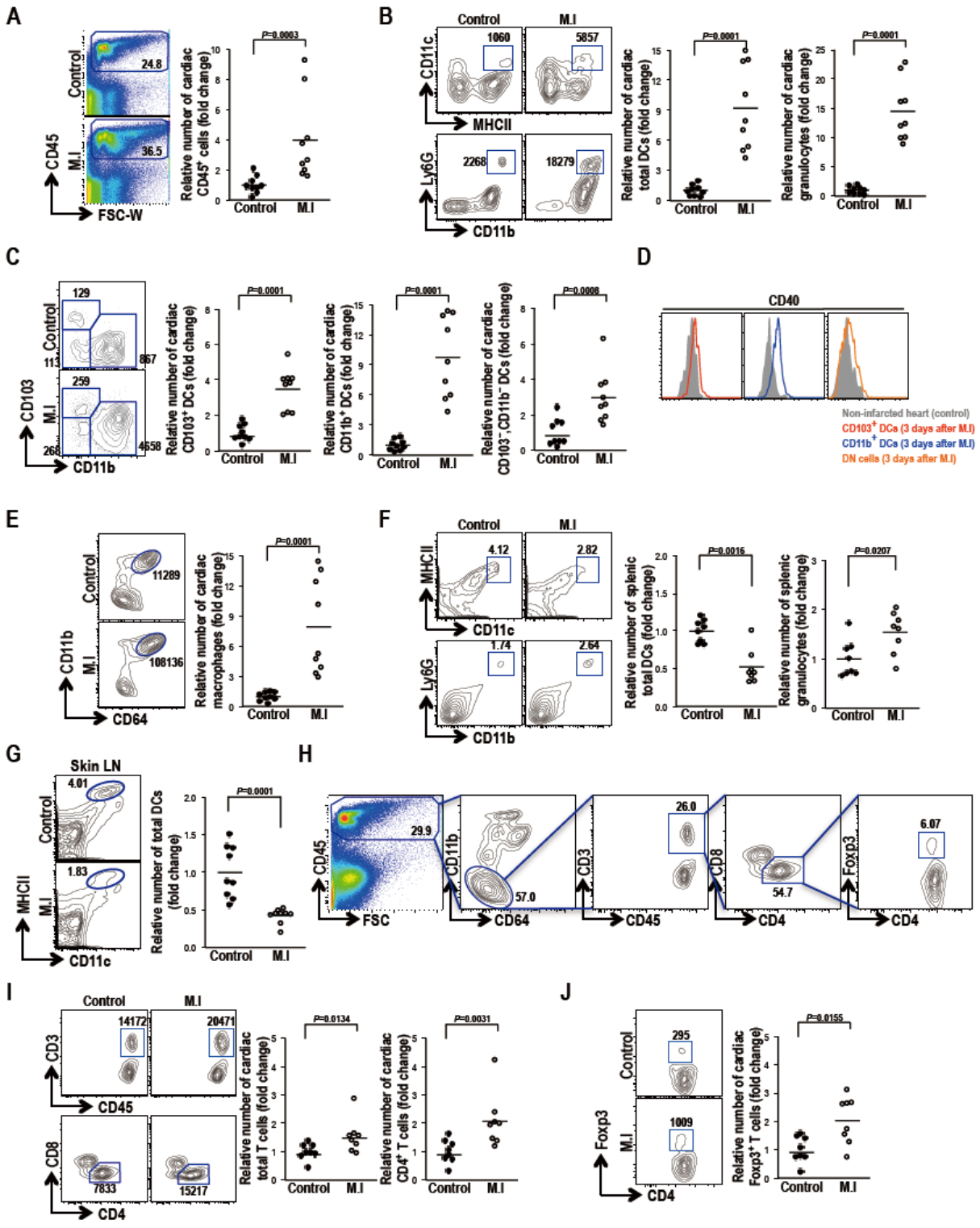

Figure 2.4. Cardiac immune cell numbers increase following MI. C57BL/6 mice underwent cardiac surgery to permanently block blood flow downstream of the left anterior

descending coronary artery. Cells from untreated (control) mice or mice 3 days after myocardial infarction (MI) were analyzed by flow cytometry. All relative cell numbers were normalized to the control group and graphs indicate mean ± SD; n = 9 mice. **(A)** Percentages and relative numbers of cardiac $CD45^+$ cells. **(B)** Absolute numbers of total cardiac DCs (upper left plots) and granulocytes (lower left plots). Relative numbers of cardiac total DCs and granulocytes (right panels). **(C)** Absolute numbers of cardiac DC subsets (left panels). Relative numbers are shown in the right panels. **(D)** The expression of CD40 was analyzed in cardiac DC subsets of mice with or without MI. Data from at least three experiments. **(E)** Absolute numbers and relative numbers of cardiac macrophages. **(F)** Percentages (left panels) and relative numbers (right panels) of splenic total DCs and granulocytes. n = 8 mice. **(G)** Percentages and relative numbers of total DCs in skin-draining LNs. **(H)** Gating strategy for total T cells, $CD4^+$ T cells and Tregs. CD4 and Foxp3 were detected following cell permeabilization. **(I)** Representative FACS plots and absolute numbers of gated cells (left panels) and relative numbers (right panels) of cardiac total T cells, $CD4^+$ T cells. n = 8 mice. **(J)** Representative FACS plots and absolute numbers of gated cells (left panels) and relative numbers (right panels) of cardiac Tregs**.** n = 8 mice.

Next, we investigated the impact of MI on immune cells numbers. We performed coronary artery ligation in wild type (WT) mice[37], and after 3 days, we analyzed by flow cytometry the immune cell composition within the myocardium. In response to ischemic injury, it is believed that the myocardium recruits a large number of leukocytes to protect injured or infected tissue.[38] Although the number of heart $CD45^+$ increased ∼4-fold, granulocytes and total DCs increased ∼15- and 10-fold, respectively (**Figure. 2.4A and 2.4B**). Of the DC subsets, $CD11b^+$ DCs appeared to be undergoing the most important change in terms of absolute numbers (**Figure. 2.4C**). Importantly, DCs display signs of activation following MI, as judged by the increase in CD40 expression (**Figure. 2.4D**). MΦs were also elevated in the heart 3 days after infarction (**Figure. 2.4E**). Interestingly, as opposed to granulocytes, DCs were reduced in spleen and skin-draining LNs (**Figure. 2.4F and 2.4G**). The importance of Tregs in MI and tissue recovery after injury has been addressed in human and rodent studies.[39] Recently, in atherosclerosis, an important interplay between Tregs and APCs has been revealed.[15] Our results show that the proportions of T cells and Tregs increase in the heart and spleen 3 days after MI (**Figure. 2.4H–J, Supplemental figure. 2.3C and D**).

2. 3. 5 Depletion of pDCs Does not Affect Muscular Contractility Following MI

We have recently shown that pDCs regulate inflammation in the aorta.[15] These cells may play a key role in the heart as well. In normal mice, cardiac pDCs were identified as PDCA1$^+$ Ly6C$^+$ CD11b$^-$ cells according to the gating strategy shown in **Figure. 2.1A**.[40, 41] They express Clec9a, Siglec H, PDCA-1/BST2/CD317, and low levels of CX_3CR1[42] but lack or express low levels of MΦ, monocyte, and DC markers (**Figure. 2.5A**). We previously reported that total pDCs in the aorta and spleen were expanded by Flt3L.[15] To confirm that the cardiac pDCs were genuine, we examined the impact of Flt3L on their numbers.[43] We show that Flt3L increased pDC numbers in both the heart and spleen of WT mice but not in Flt3/Flk2/CD135-deficient (Flt3 KO) mice (**Figure. 2.5B–D**). The anatomical distribution of heart pDCs is similar to the one described above for cDCs, except that pDCs were found to be equally concentrated in the two atria, and their relative proportions are lower in valves than in Seg1 (**Figure. 2.5E and F**). In addition, we could identify human pDCs in the heart of hu-mice (**Figure. 2.5G–I**). These CD123$^+$ BDCA2$^+$ human cardiac pDCs express IRF8 and were increased by Flt3L injections (**Figure. 2.5G and 2.5H**). The presence of pDCs in the heart of hu-mice was confirmed by immunohistochemistry using an anti-LAMP5 (Bad-LAMP) mAb, which is specific for pDCs (**Figure. 2.5I**).[44]

Then, we characterized the impact of MI on cardiac pDC numbers and the importance of these cells in muscular contractility during recovery. We ligated the left anterior descending coronary artery and analyzed pDCs after 3 days. These cells were increased ∼4-fold in the injured heart but significantly decreased in spleen (**Figure. 2.5J**). To assess the importance of pDCs in the pathophysiology of MI, we made use of the BDCA2-DTR mice. We tested the impact of DT on cardiac pDCs in lethally irradiated C57BL/6 mice reconstituted with WT or BDCA2-DTR BM. In the BDCA2-DTR chimeric mice, DT treatment resulted in the selective elimination of heart pDCs (**Figure. 2.5K**). Remarkably, mice without pDCs were not affected in left ventricle function as measured by fractional shortening for up to 3 wk after MI. (**Figure. 2.5L and 2.5M, Supplemental figure. 2.3E**). Altogether, the results suggest that in

response to ischemic myocardial injury, pDCs accumulate within the myocardium but did not have a major functional role in cardiac function after MI.

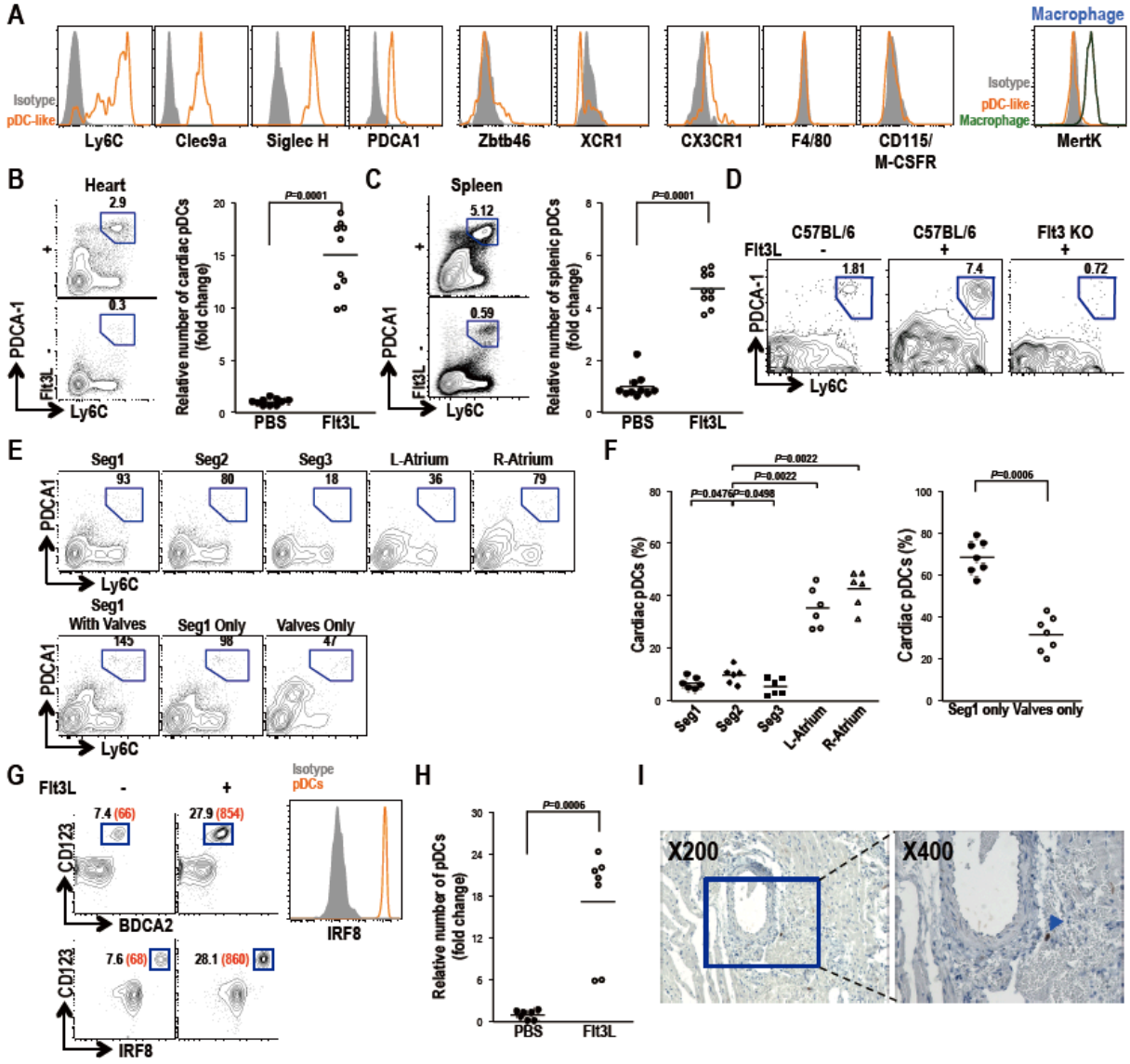

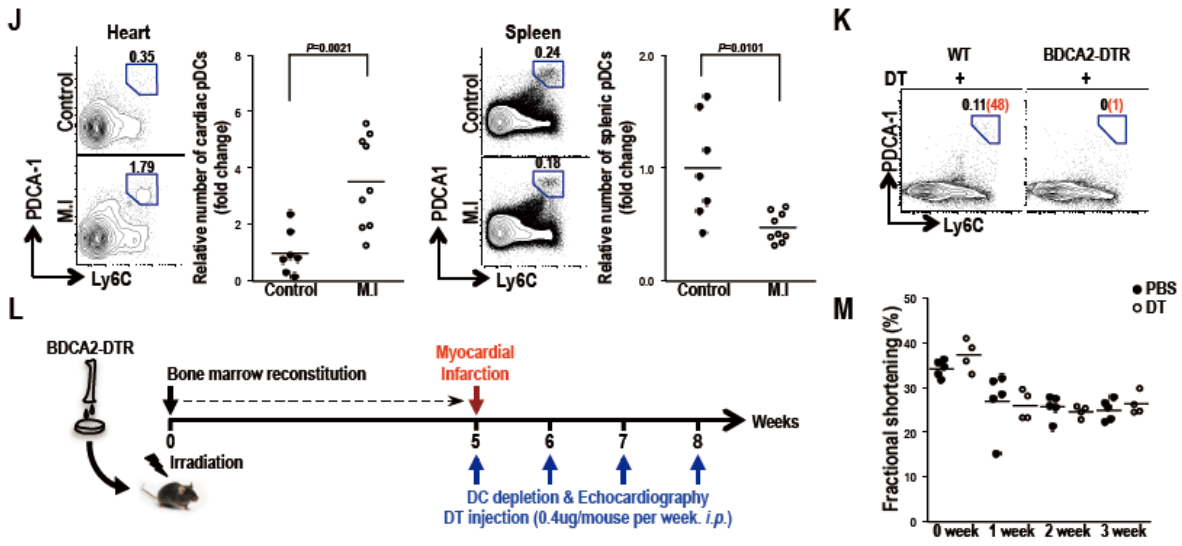

Figure 2.5. Depletion of pDCs does not modulate cardiac functions after MI. (A) Heart pDCs from WT mice (orange line) were further characterized phenotypically using a series of mAbs and their specific isotype controls (gray filled lines). pDCs were first gated according to the strategy depicted in **figure 2.1A**. *Zbtb46* (*Zbtb46*$^{+/+}$ [WT] and *Zbtb46*$^{gfp/+}$) and CX_3CR1 ($CX_3CR1^{+/+}$ [WT] and $CX_3CR1^{gfp/+}$) reporter mice were used for assessing the expression of these molecules. Other markers were surface stained except Clec9a, which was stained following permeabilization. Cardiac MΦs were included as positive controls (green) for the assessment of MertK expression. **(B-D)** WT and Flt3/Flk2/CD135-deficient mice were injected intraperitoneally with PBS (−) or with 2 µg of Flt3L (+) each day for nine consecutive days. Bar graphs indicate mean ± SD; n = 10. Cardiac pDC numbers were determined by flow cytometry. Representative FACS plots (left panels) and relative numbers normalized to the PBS groups (right panels) of cardiac pDCs in heart **(B)** and in spleen **(C)**. **(D)** Cardiac pDCs were quantified from WT and Flt3 KO mice. Representative FACS plots from at least three experiments. **(E and F)** Cells from the various mouse heart sections (**Supplemental figure 2.2A, 2.2E**) were analyzed by flow cytometry. **(E)** pDCs were analyzed in the different heart sections and absolute numbers are shown. **(F)** Absolute numbers were normalized relative to the weight of the different sections of the heart. Graphs indicate mean ± SD; n = 6 or 7. **(G-I)** Hu-mice were injected *i.p.* with 2 µg of Flt3L each day for nine consecutive days. **(G)** Left: representative FACS plots of cardiac pDCs (top) and $IRF8^+$ pDCs (bottom). Percentages are shown in black and cell numbers in red. Right: Expression of IRF8 in pDCs (orange) compared to isotype control (grey). **(H)** Relative number of cardiac pDCs normalized to the PBS group. Graph indicates mean ± SD; n = 7. **(I)** Paraffin sections of heart from Flt3L-injected hu-mice were stained for LAMP5 (brown) and counterstained with hematoxylin. Original magnification x200 **(J)** C57BL/6 mice underwent cardiac surgery to permanently block blood flow downstream of the left anterior descending coronary artery. Cells from normal (Control) mice or mice 3 days after myocardial infarction (MI.) were analyzed by flow cytometry. Representative FACS plots with percentages of gated cells and relative numbers of cardiac (left panels) and splenic (right panels) pDCs. Graphs indicate mean ± SD; Control n = 7, MI n = 9. **(K)** Selective elimination of cardiac pDCs from WT and BDCA2-DTR chimeric

mice injected with DT twice at a 24 h interval. Percentages (black) and absolute numbers (red) of pDCs are shown. **(L)** Schematic representation of the protocol used to assess heart damage following infarction. Five weeks after the transplantation of BDCA2-DTR BM into irradiated WT mice, MI surgery was performed and mice were injected with PBS or DT for 3 weeks. **(M)** Left ventricular systolic function quantified by fractional shortening (FS) in the left ventricle of BDCA2-DTR chimeric mice for 3 weeks after MI. PBS n = 5, DT n = 4.

2. 3. 6 Depletion of cDCs Imparoves Cardiac Function Following MI

We next evaluated the effect of *Zbtb46*$^{+}$ DCs depletion on the outcome of MI. Five weeks after reconstitution, Zbtb46-DTR chimeric mice underwent MI surgery and DT, or control PBS was administered (**Supplemental figure. 2.4A**). We verified the efficient depletion of DCs by DT following MI (**Supplemental figure. 2.4B**). Total DCs and all subsets were already reduced 3 d postinfarction after a single DT injection, whereas MΦ, neutrophils, and monocyte numbers were not affected by DT (**Supplemental figure. 2.4B–E**). Mice received two additional weekly (weeks 6 and 7) injections of DT or PBS, and echocardiography was performed at each time point according to the protocol depicted in **Figure. 2.6A**.

Interestingly, depletion of cDCs by DT led to a significant improvement of LV fractional shortening after 2 wk (**Figure. 2.6B and 2.6C, Supplemental figure. 2.4F, Supplemental videos 2.1–4**). This result prompted further characterization of the heart. We found that the absence of cDCs reduced infarct size (**Figure. 2.6D**). Moreover, the area of the border zone cardiomyocytes was significantly decreased in mice that received DT, indicating adverse cardiomyocyte hypertrophy was improved with cDC depletion (**Figure. 2.6E**).

The fact that cDCs impaired cardiac functions and remodeling after MI suggested a role for these cells in the establishment of a proinflammatory local environment. We analyzed the cardiac hematopoietic cell compartment in the heart of Zbtb46-DTR–reconstituted mice injected with PBS or DT for 7 days after MI. Interestingly, in the subacute phase after MI (day 7) (**Figure. 2.7A and 2.7B**), the depletion of DCs led to a reduction in the number of total leukocytes (CD45^{-} cells) and MΦs (**Figure. 2.7C**). These results show that cDCs are required for maintaining the innate leukocyte infiltrate. Then, we assessed if cDCs were required for infiltration of T cells into the myocardium. Notably, DT significantly decreased total T cells as

well as Tregs in the myocardium of Zbtb46-DTR chimeric mice 7 days after MI. (**Figure. 2.7D and 2.7E**).

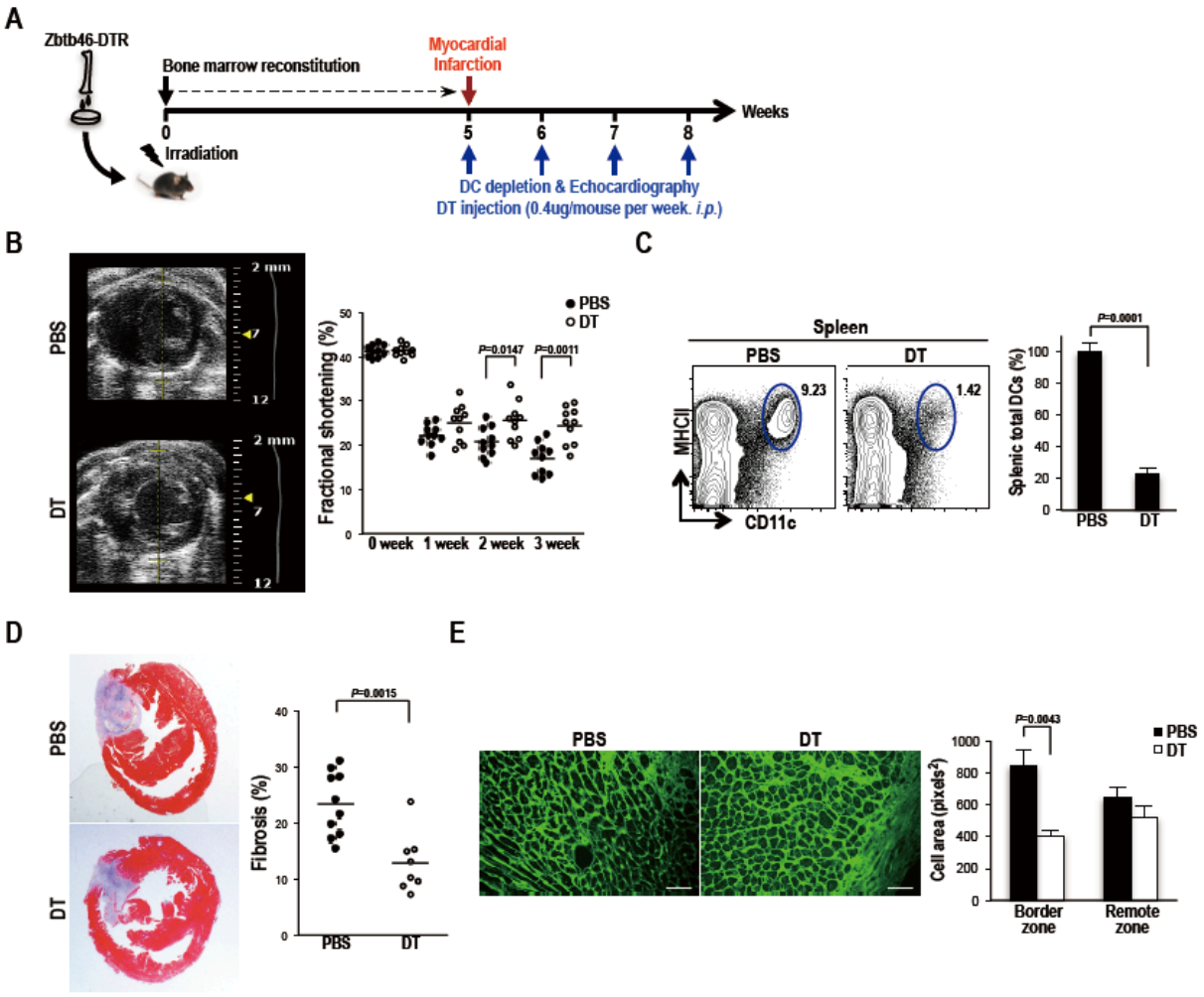

Figure 2.6. Depletion of cDCs improves LV remodeling after MI. (A) Schematic representation of the protocol used to assess heart damage following infarction. **(B-E)** Five weeks after the transplantation of Zbtb46-DTR BM into irradiated WT mice, MI surgery was performed and mice were injected with PBS or DT for 3 weeks. **(B)** Left ventricular fractional shortening was measured by echocardiography 3 weeks after MI. Graphs indicate mean ± SD; n = 10 mice. **(C)** Representative FACS plots (left panels) and percentage (right panels; graph indicates mean ± SD; n = 10) of total DCs from spleen of Zbtb46-DTR mice in **Figureure 2.6B**. **(D)** Histomorphological changes of the heart at 3 weeks after MI, as detected by Masson's trichrome staining. Graphs indicate mean ± SD; PBS n = 10, MI n = 8. **(E)** Wheat germ agglutinin staining at 3 weeks after MI. Quantitative analyses represent counting of

multiple fields from three independent samples per group (~50 cells per field assessed). Scale bar, 100 μm. Graphs indicate mean ± SD; PBS n = 23, MI n = 19.

Thus, our results indicate that the myocardium contains both pDC and cDCs and that after MI, only cDCs are functionally involved and play a key pathological role. By specifically depleting cDCs, we demonstrate that the immune response, as measured by infiltration of MΦs, neutrophils, and multiple T cells subsets is blunted, correlating with improved indices of cardiac structure and function. Indeed, we found that depletion of cDCs correlated with less IL-1β and IFN-γ proinflammatory cytokine mRNAs in the heart (**Figure. 2.7F–H**). Interestingly, TGF-β mRNA was increased following depletion of cDCs, suggesting that this cytokine may exert protective functions if inflammation is controlled.[45]

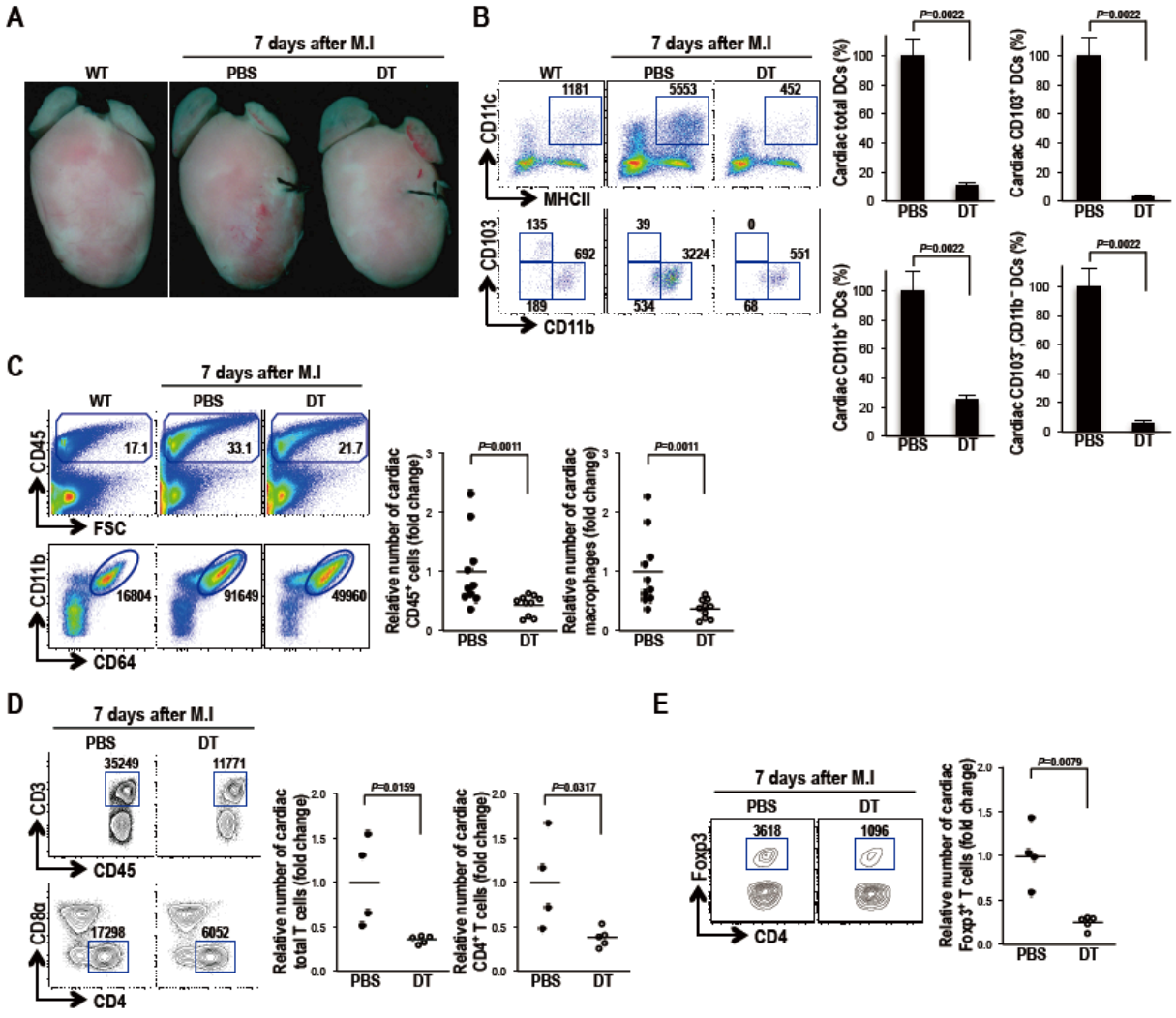

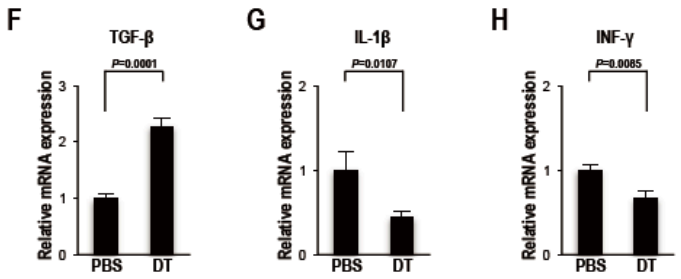

Figure 2.7. Depletion of cDCs correlates with reduced numbers of heart MΦs and Tregs 7 days after MI. (A) Hearts were isolated from myocardial infarcted-Zbtb46-DTR mice that received DT or control PBS for 7 days. **(B)** Left: selective elimination of cardiac total DCs (top) and DCs subsets (bottom) in Zbtb46-DTR mice injected with DT twice at a 72 h interval. Right: percentage (mean ± SD; n = 6 mice) of total DCs and cDC subsets. **(C)** Left: heart cells were analyzed by flow cytometry and the percentages of $CD45^+$ cells (top) and absolute numbers of MΦs (down) are shown. Right: Relative numbers (mean ± SD; n = 10) of cardiac $CD45^+$ cells and MΦs normalized to the control PBS group. **(D and E)** Representative FACS plots and absolute numbers of gated cells (left panels) and relative numbers (right panels; mean ± SD; PBS n = 4, MI n = 5) of cardiac total T cells, $CD4^+$ T cells **(D)** and Tregs **(E)** 7 days after MI. for mice reconstituted with Zbtb46-DTR BM and treated with PBS or DT. **(F-H)** mRNA expression levels of RGF-β **(F)**, IL-1β **(G)**, and INF-γ **(H)** from heart of myocardial infarcted-Zbtb46-DTR mice treated with DT or control PBS for 7 days, measured by qPCR. Relative mRNA expressions were normalized to β-actin. Graphs indicate mean ± SD; n = 10.

2. 4 Discussion

Cardiovascular diseases represent major global health issues that are expected to worsen in the coming decades. Although our understanding of the contribution of MΦs to this process has yielded many important insights, the role of DC subsets has remained elusive.[7] In a number of experimental settings, DCs were shown to have a major impact on adaptive immune responses but also on inflammation per se. To shed light on the role of cardiac DCs in the modulation of sterile inflammation, we examined the local and distal quantitative/qualitative changes occurring in hematopoietic cells in response to MI. These issues are particularly relevant given the recently demonstrated role of cDCs in priming autoreactive T cells following MI.[46]

In this study, we identified two types of cardiac classical DCs, known as cDC1s ($CD103^+CD24^+XCR1^+$) and cDC2s ($CD11b^+CD172\alpha^+$), which are poorly phagocytic as compared with MΦs.[47] Cardiac $CD103^+$ DCs express Clec9a, DEC205, CD24, and CD283 as well as IRF8 and Flt3/CD135, which are critical for their development but lack monocyte-specific markers such as CD14, CD172α, CX_3CR1, F4/80, Ly6C, CD11b, and CD115/M-CSFR. In contrast, $CD11b^+$ DCs express CX_3CR1, F4/80, Ly6C, and CD14 as well as IRF4 and CD115/M-CSFR. However, they do not express XCR1, CD24, CD103, Clec9a, DEC205, CD24, CD283, and Flt3/CD135. Importantly, both types of cDCs express *Zbtb46*. This transcription factor is not found in pDCs, monocytes, or MΦs, allowing for the identification and deletion of cDCs in vivo.[48] Moreover, we were able to detect $HLA\text{-}DR^+CD11c^+$ DCs, including both $BDCA1^+$ and $BDCA3^+$ subsets in the heart of hu-mice. Similar to mouse cardiac DC subsets, human $BDCA3^+$ DCs expressed IRF8, whereas $BDCA1^+$ DCs expressed IRF4. These human DCs were also dependent on Flt3/CD115, more so for the $IRF8^{hi}$ cells. The density of cDCs subsets and MΦs appears to culminate in the RA. Such specificity was not observed for monocytes or granulocytes. This finding is particularly interesting given the recently described role of MΦs in normal and aberrant atrioventricular conduction.[49] If DCs are involved directly or indirectly in cardiac conduction remains to be addressed. Altogether, our findings reveal the existence of bona fide cardiac cDCs with phenotypes that comply with the recent criteria proposed for the identification of these cells in various tissues and across species.[10]

In addition to cDCs, the heart contains a population of pDCs that increased in the infarcted heart. However, depletion of this DC subset did not affect fractional shortening. The function of cardiac pDCs may lie in their capacity to produce type I IFN and protect the tissue against viral infections. We have recently demonstrated the role of tolerogenic $CCR9^+$ pDCs in producing IDO and regulating Tregs in the aorta during atherosclerosis.[15] As shown in this paper, however, pDC functions do not appear critical in the pathophysiology of cardiac repair after MI.

As we focused on $CD64^-$ DCs, we cannot exclude the possibility that monocyte-derived DCs (moDCs) are somehow involved in cardiac inflammation. A great deal has been learned of these cells over the last decade, but their precise identification will require a better knowledge of their origin and phenotype.[50] Recent fate-mapping experiments using Zbtb46-DTR mice showed that monocytes generate GM-CSF–dependent moDCs and that these monocytes precursors are distal from the DC lineage.[51] Although *Zbtb46* expression appears to be restricted to cDCs[52], it was postulated that moDCs may lose Ly6c expression and start expressing *Zbtb46* upon differentiation from monocytes, as was seen for BM-derived DCs in vitro.[28, 53, 54] If this is the case, such cells would have been eliminated in experiments based on the use of the Zbtb46-DTR mice. Future studies should address the importance of the $CD11b^+$ population heterogeneity.

Besides the DC subsets described above, there was a prominent $CD103^-$ $CD11b^-$ DN DC population in the heart at steady state. Just like precursor DCs, these cardiac cells are $Zbtb46^+$, and their number, principally the IRF8hi subset, dramatically increased in response to Flt3L. So far, such DN DCs have been described in mouse dermis and intestinal lymph, but they remain poorly characterized.[20, 55, 56] Our data suggest that the heart harbors pre-cDCs showing lineage-imprinted programs based on their mutually exclusive IRF4 and IRF8 expression.[17, 57]

After MI, we found that the myocardium recruits large numbers of leukocytes, including MΦs and granulocytes, most likely with the objective of protecting the injured or infected tissue and initiating wound healing.[38, 58] Notably, $CD11b^+$ cDCs were massively increased in heart and mediastinal LN of infarcted mice, whereas the number of these cells decreased in spleen and skin-draining LNs. We speculate that the cardiac insult resulted in the

local production of GM-CSF by endothelial cells and MΦs, allowing the differentiation of cardiac precursors into cDC2s. Indeed, it was shown in rats that administration of GM-CSF following MI increased DC infiltration and exacerbated LV remodeling.[6] Such cDC2s may secrete IL-23 to the detriment of IL-10 and lead to the polarization of T cells toward Th17.[59] Of note, 3 days after MI, some DCs could be found in the ventricle and septum, whereas after 7 days, DCs also appeared in the left atrium (**Supplemental figure. 2.5**).

Recently, the role of DCs in various pathologies, including postinfarction healing, was studied using genetic models such as CD11c-DTR, CD11b-DTR, and LysM–Cre x iDTR.[60] Although these mice allow the depletion of cells expressing these markers, the specificity toward cDCs has been questioned.[25] To overcome these limitations, we used chimeric Zbtb46-DTR mice in which the DTR is only expressed in mouse DCs.[28] We confirmed that DT treatment successfully and selectively eliminated cardiac, LN, and splenic $CD11c^{+}MHC\ II^{+}$ DCs in chimeric mice reconstituted with BM from Zbtb46-DTR mice. Importantly, these DT-treated Zbtb46-DTR mice showed a dramatic reduction in postischemic injury size by preventing ventricular remodeling and improving cardiac function compared with the PBS-treated control group. We next checked that any cell populations in the heart of WT/Zbtb46-DTR mice with MI-treated DT were changed. Surprisingly, the selective depletion of heart DCs in Zbtb46-DTR mice caused a significant decrease of MΦs as well as $CD45^{+}$ cells at 7 days but not at 3 days after MI. This suggested that inflammatory responses after MI, which trigger accumulation of DCs in injured tissue, are involved in wound healing but can lead to detrimental effects, such as expansion of infarct size and interstitial fibrosis, wall thinning, and lower cardiac function. The exact mechanisms by which cDCs maintain inflammation and negatively impact cardiac function will require further investigation. In addition to their T cell stimulatory role in draining LNs, cDCs could act locally in the cardiac tissue. For example, cDCs could sustain the immune reaction by secreting some proinflammatory cytokines and chemokines in response to damage-associated molecular patterns.[61] These reactions, potentially of autoimmune nature, would contribute to cardiomyocyte death.[62] Also, as seen in the allergic eye, cDC2s with increased aldehyde dehydrogenase activity could directly activate fibroblasts through the retinoic acid receptor and increase fibrosis.[63] Secretion of IL-12 by

myeloid DCs has also been shown to inhibit angiogenesis.[64] This could be due, in part, to polarization of MΦs toward a less angiogenic M1 phenotype.[65, 66]

The role of $CD4^+CD25^+Foxp3^+$ Tregs in the initial development and progression of many cardiovascular diseases is pivotal.[39] It has previously been reported that the depletion of Treg cells before MI induction resulted in aggravated cardiac inflammation.[67] Although our data showed that Tregs in the heart and spleen of mice with MI were significantly increased, the depletion of cDCs correlated with a significant decrease in cardiac Treg numbers. These results demonstrate the importance of cDCs in shaping the immune landscape of the heart following MI. The fact that depletion of cDCs reduces infiltration of both proinflammatory cells and Tregs demonstrates that protection of the infarcted heart from further injury results from a delicate balance between various cell populations under the control of cDCs. This implies that interventions aimed at controlling cDCs numbers or functions have therapeutic potential.[68] Indeed, modulating proinflammatory signals transduction pathways or generating tolerogenic DCs in various mixtures, including cytokines such as IL-37 and TNF-α, were shown to have a beneficial role in post-MI remodeling.[69, 70, 71] Future experiments should address more in depth the spatio-temporal relationship between DCs and other immune cells in health and disease.

2. 5 Methods

2. 5. 1 Mice

C57BL/6, *Ldlr*$^{-/-}$[72], CX_3CR1-GFP, Zbtb46-GFP, Zbtb46-DTR, NSG (NOD/SCID/γc-null) mice were purchased from The Jackson Laboratory (Bar Harbor, Me). *Flt3*$^{-/-}$ mice[73] (I. Lemischka, Mount Sinai School of medicine) were a generous gift of M. Nussenzweig. BDCA2-DTR mice[26] were from M. Colonna (Washington University, St. Louis, MO). For humanized mice, NSG mice reconstituted with human $CD34^+$ cells (hu-mice) were used. To expand the number of DCs, mice were injected *i.p.* with 2μg of human FMS-Like tyrosine kinase 3 ligand (Flt3L) per day for 9 consecutive days.[15] All mice were bred under specific pathogen-free conditions. All mouse experiments were performed according to guidelines of the Canadian Council on Animal Care.

2. 5. 2 Heart Single-Cell Isolation and Flow Cytometry

Cardiac single cells were isolated according to a previously described method[25] with minor modifications. Mouse hearts were incubated for 40 min at 37 °C with gentle shaking in Hank's balanced salt solution containing 675 U/ml collagenase I, 18.75 U/mL collagenase XI, and 9U/mL hyaluronidase (Sigma-Aldrich). Cells were centrifuged on a discontinuous Percoll (Sigma-Aldrich) gradient (40% and 80%) and leukocytes were collected. Mouse spleen and LNs were digested in 400U/mL of collagenase D XI in RPMI-1640 for 30 min at 37 °C. Foxp3+ T cells were stained using a Foxp3 staining buffer set (eBioscience), according to a previously described method[74]; all other intracellular stainings were performed using a fixation/permeabilization solution kit (BD Biosciences). Stained cells were acquired or sorted using a LSRFortessa flow cytometer or FACSAriaIII (BD Biociences), respectively, and analyzed with FlowJo (Tree Star). Sorted cells were cytospined at 500 rpm for 5 min using Cytospin4 (Thermo Scientific) for phagocytosis analysis.

2. 5. 3 Immunohistochemistry and Confocal Microscopy

CD11c-YFP mice hearts were perfused with cold PBS and fixed in 4% formaldehyde for 1 hour. After careful removal of the pericardial fat and blood vessels, heart were processed using standard procedures, embedded in OCT and frozen, and sectioned (12-μm thick). Cryosections were singly immunostained with the indicated antibodies. Immunoreactive proteins were visualized using an ImmPRESS-AP anti-rabbit Ig polymer detection kit, an ImmPRESS HRP anti-mouse Ig polymer detection kit. All experiments were performed according to the manufacturer's instructions. Confocal images were acquired along the z axis using an LSM 710 laser-scanning confocal microscope (Carl Zeiss), and Z-stacked images were analyzed with Imaris software (Bitplane).

2. 5. 4 Antibodies and Reagents

Antibodies to mouse Foxp3 for FACS analysis was from eBioscience. All other antibodies were from BioLegend. Cells were incubated in culture supernatant from the 2.4G2 hybridoma (Fc Receptor Block, ATCC: HB-197) prior to staining with the indicated antibodies. Poly I:C (Sigma) was given i.v., at a dose of 25 μg to induce DC maturation.

2. 5. 5 BM Chimeras and Depletion of DCs

Although in the mouse hematopoietic cell compartment the expression of genes under the control of *Zbtb46* and the human *BDCA2* promoters is restricted to cDCs and pDCs, respectively, DT-driven depletion experiments were performed in BM chimeras in order to rule out any interference from the possible depletion of non-immune cells.[26, 28, 52] C57BL6/J male mice (8 weeks old) were lethally γ-irradiated (2 × 5 Gy, 4hr apart) and reconstituted for 5 weeks with BM of BDCA2-DTR or Zbtb46-DTR mice. For systemic DC depletion, mice were injected i.v. with DT (20ng/g weight; in PBS; Sigma Chemical Co., St. Louis, MO, USA).

2. 5. 6 Cell Culture

For phagocytosis assay, cardiac cells from Flt3L-injected C57BL/6 mice were incubated with Fluoresbrite YG Carboxylate Microspheres 1.0 μm (Polysciences) at 37°C for 1 hr. Then, cells were incubated in Fc Receptor Block and stained with antibodies at 4°C for cell sorting. All mouse cells were incubated in RPMI 1640 containing 5% FBS, 1x antibiotic-antimycotic, GlutaMAX, MEM nonessential amino acids and 2-mercaptoethanol (Gibco).

2. 5. 7 Myocardial Infarction Surgery

Cardiac surgery was performed by the Surgery Core of the Lady Davis Institute.[75] C57bl/6J reconstituted with Zbtb46-DTR or BDCA2-DTR mouse BM for 5 weeks were anesthetized with isoflurane and intubated. Analgesia for the next 3 days was provided by an injection of slow release buprenorphine. A permanent occlusion in blood flow downstream of the left anterior descending coronary artery approximately 2mm distal to the left atrial appendage was created using a 7-0 silk suture ligature. Using a similar surgery, it was estimated that this ligation places approximately 38% of the left ventricle at risk for infarction.[76]

2. 5. 8 Tissue Harvesting, Histology, and Morphometric Analyses

Mice were deeply euthanized, and the hearts were perfused with saline followed by catheter (Anatech Ltd, Battle Creek, M.I). To measure myocardial infarct size, hearts were sectioned transversely into 3 mm thick slices and incubated in 2% triphenyltetrazolium chloride (TTC) at 37°C for 30 min to identify the non-infarcted and infarcted areas. The infarcted area appeared as a yellow-white area that was unstained by TTC. The true infarct size on the TTC-stained slices was measured directly and was calculated as the ratio (%) of cumulative infarct area to the entire LV area using ImageJ software (National Institutes of Health).

2. 5. 9 Masson's Trichrome Staining

To measure myocardial fibrosis, Masson's trichrome stain was used for each paraffin-embedded trans-axial LV section. We stained two slides of each heart (PBS, n = 10 and DT, n = 8) with the Masson trichrome staining and quantified fibrous infarct regions (blue color in RGB mode, white color in black/white mode). The total levels of fibrosis in the areas of the fibrous infarct regions were measured with ImageJ software and expressed as percentages of the total LV surface. An independent investigator, who was blinded to the experimental groups, quantified all experiments.

2. 5. 10 Wheat Germ Agglutinin Staining

To quantify individual myocyte size, some sections were stained with fluorescein FITC-conjugated wheat germ agglutinin (5μg/ml, Invitrogen, Grand Island, NY). Myocyte area was assessed with ImageJ program (National Institutes of Health). The mean cardiomyocyte area was evaluated by measurement of 500 cells per heart (6–9 hearts per genotype).

2. 5. 11 Quantitative RT-PCR analysis

Total heart RNA was extracted from a single cell suspension using TRIzol Lysis Reagent (5 PRIME GmbH Hamburg, Germany), cDNA was prepared using the Revert Aid First Strand cDNA Synthesis Kit (Fermentas). Quantitative Real-time PCR was performed using StepOnePlus^{TM} Real-Time PCR systems (Applied Biosystems) instrument and SYBR green PCR Master Mix (KAPA bio systems) and was quantified on StepOne Software v2.3 (Applied Biosystems) using ΔCT method and β-actin as a control.

2. 5. 12 Echocardiography

Echocardiography was performed under anesthesia by inhalation of 1.5–2% isoflurane (Forene isoflurane, Abbott Scandinavia AB, Sweden). Images were acquired using the Vevo 2100 system (Visual Sonics) with a 30-MHz linear array transducer. The left ventricle was investigated in both long-axis and short-axis views during 3 weeks after MI. We selected the two-dimensional image slice, in which infarction-related regional wall motion abnormality was most significant then used the M-mode scan, which crossing site of the most significant regional wall motion abnormalities. To reduce measurement variability by observer, after image acquisition, automatic border detection software was used to measure left ventricular systolic and diastolic dimensions, and then fractional area change was calculated using those values. All the measurement variables such as left ventricular end-diastolic and systolic dimensions, stroke volume and cardiac output are in the **supplementary table 2.1** and TTC-stained data in the **supplementary figure 2.4F**.

2. 5. 13 Statistics

All statistical significance between two groups was tested using a Mann-Whitney test with two-tailed P-values unless indicated otherwise. R-value was obtained from linear regression analysis. Data are presented as mean ± SD.

2. 6 Author Contributions

Junseong Lee, **Gootaeg Oh**, **Jacques Thibodeau, and Cheolho Cheong** designed the experiments.

Junseong Lee executed the majority of experiments presented.

Lorraine Chalifour performed myocardial infarctions.

Se-Jin Jeong, Sinai Kim and Eui-Young Choi did Masson's trichrome staining and Wheat germ agglutinin staining, as well as echocardiography.

Tae Jin Yun performed phagocytosis assay and marker analysis for pDCs.

Mohammad Alam Miah and Bin Li prepared mouse and hu-mice heart for FACS.

Abdelilah Majdoubi and Antoine Sabourin helped analyze flow cytometry data for identification of DC subsets.

Tibor Keler provided human Flt3L.

Jean V Guimond, Elie Haddad provided hu-mice.

Junseong Lee, **Se-Jin Jeong , Gootaeg Oh**, **Jacques Thibodeau, and Cheolho Cheong** interpreted the data.

Junseong Lee, **Se-Jin Jeong , Gootaeg Oh and Jacques Thibodeau** wrote the manuscript.

2. 7 Acknowledgements

This work is dedicated to the memory of Dr. Cheolho Cheong. We thank Ms. Amanda Kasneci and Ms. Kathy Ann Forner for performing cardiac surgeries. We thank the excellent support provided by the IRCM animal facility.

2. 8 Sources of Funding

This work was supported by grants from the Canadian Foundation for Innovation (John R. Evans Leaders Fund to Cheolho Cheong) and the Canadian Institutes of Health Research (CIHR) (MOP 125933 to Cheolho Cheong and Jacques Thibodeau, MOP 136802 to Jacques Thibodeau, and MOP 133050 to Cheolho Cheong), by Canadian HIV Cure Enterprise Team Grant HIG-133050 (to Cheolho Cheong and Elie Haddad), and by a National Research Foundation of Korea grant funded by the Korean government (2012R1A3A2026454 to G.T.O.). Junseong Lee was supported by the Fonds de Recherche du Québec – Nature et Technologies. J.T. holds the Saputo Research Chair. Cheolho Cheong was a recipient of a CIHR New Investigator Award and held a Société Québécoise d'Hypertension Artérielle – Le Fonds de Recherche du Québec - Santé J1 scholarship.

2. 9 Additional Information

Supplemental movie 2.1. Related to Figure 2.6. M-Mode scan of left ventricle of PBS-injected Zbtb46-DTR BM chimera mice before M.I induction as detected by echocardiography (http://www.jimmunol.org/highwire/filestream/356330/field_highwire_adjunct_files/2/JI_1800322_Supplemental_Video_1.mov).

Supplemental movie 2.2. Related to Figure 2.6. M-Mode scan of left ventricle of DT-injected Zbtb46-DTR BM chimera mice before M.I induction as detected by echocardiography (http://www.jimmunol.org/highwire/filestream/356330/field_highwire_adjunct_files/3/JI_1800322_Supplemental_Video_2.mov).

Supplemental movie 2.3. Related to Figure 2.6. M-Mode scan of left ventricle of PBS-injected Zbtb46-DTR BM chimera mice 3 weeks after M.I as detected by echocardiography (http://www.jimmunol.org/highwire/filestream/356330/field_highwire_adjunct_files/4/JI_1800322_Supplemental_Video_3.mov).

Supplemental movie 2.4. Related to Figure 2.6. M-Mode scan of left ventricle of DT-injected Zbtb46-DTR BM chimera mice 3 weeks after M.I as detected by echocardiography (http://www.jimmunol.org/highwire/filestream/356330/field_highwire_adjunct_files/5/JI_1800322_Supplemental_Video_4.mov)

2. 10 References

1. Sanchis-Gomar, F., Perez-Quilis, C., Leischik, R. & Lucia, A. Epidemiology of coronary heart disease and acute coronary syndrome. *Ann Transl Med* **4**, 256 (2016).

2. Liu, J., Wang, H. & Li, J. Inflammation and Inflammatory Cells in Myocardial Infarction and Reperfusion Injury: A Double-Edged Sword. *Clin Med Insights Cardiol* **10**, 79-84 (2016).

3. Nian, M., Lee, P., Khaper, N. & Liu, P. Inflammatory cytokines and postmyocardial infarction remodeling. *Circ Res* **94**, 1543-1553 (2004).

4. Nahrendorf, M., Pittet, M.J. & Swirski, F.K. Monocytes: protagonists of infarct inflammation and repair after myocardial infarction. *Circulation* **121**, 2437-2445 (2010).

5. Korf-Klingebiel, M. *et al.* Myeloid-derived growth factor (C19orf10) mediates cardiac repair following myocardial infarction. *Nat Med* **21**, 140-149 (2015).

6. Naito, K. *et al.* Differential effects of GM-CSF and G-CSF on infiltration of dendritic cells during early left ventricular remodeling after myocardial infarction. *J Immunol* **181**, 5691-5701 (2008).

7. Epelman, S., Liu, P.P. & Mann, D.L. Role of innate and adaptive immune mechanisms in cardiac injury and repair. *Nat Rev Immunol* **15**, 117-129 (2015).

8. Frangogiannis, N.G. & Entman, M.L. Chemokines in myocardial ischemia. *Trends Cardiovasc Med* **15**, 163-169 (2005).

9. Epelman, S. *et al.* Embryonic and adult-derived resident cardiac macrophages are maintained through distinct mechanisms at steady state and during inflammation. *Immunity* **40**, 91-104 (2014).

10. Guilliams, M. *et al.* Unsupervised High-Dimensional Analysis Aligns Dendritic Cells across Tissues and Species. *Immunity* **45**, 669-684 (2016).

11. Steinman, R.M. Decisions about dendritic cells: past, present, and future. *Annu Rev Immunol* **30**, 1-22 (2012).

12. Murphy, T.L. *et al.* Transcriptional Control of Dendritic Cell Development. *Annu Rev Immunol* **34**, 93-119 (2016).

13. Merad, M., Sathe, P., Helft, J., Miller, J. & Mortha, A. The dendritic cell lineage: ontogeny and function of dendritic cells and their subsets in the steady state and the inflamed setting. *Annu Rev Immunol* **31**, 563-604 (2013).

14. Sage, A.P. *et al.* MHC Class II-restricted antigen presentation by plasmacytoid dendritic cells drives proatherogenic T cell immunity. *Circulation* **130**, 1363-1373 (2014).

15. Yun, T.J. *et al.* Indoleamine 2,3-Dioxygenase-Expressing Aortic Plasmacytoid Dendritic Cells Protect against Atherosclerosis by Induction of Regulatory T Cells. *Cell Metab* **24**, 886 (2016).

16. Lippens, C. *et al.* IDO-orchestrated crosstalk between pDCs and Tregs inhibits autoimmunity. *J Autoimmun* **75**, 39-49 (2016).

17. Schlitzer, A. *et al.* Identification of cDC1- and cDC2-committed DC progenitors reveals early lineage priming at the common DC progenitor stage in the bone marrow. *Nat Immunol* **16**, 718-728 (2015).

18. Worbs, T., Hammerschmidt, S.I. & Forster, R. Dendritic cell migration in health and disease. *Nat Rev Immunol* **17**, 30-48 (2017).

19. Hildner, K. *et al.* Batf3 deficiency reveals a critical role for CD8alpha+ dendritic cells in cytotoxic T cell immunity. *Science* **322**, 1097-1100 (2008).

20. Ginhoux, F. *et al.* The origin and development of nonlymphoid tissue CD103+ DCs. *J Exp Med* **206**, 3115-3130 (2009).

21. Geissmann, F. *et al.* Development of monocytes, macrophages, and dendritic cells. *Science* **327**, 656-661 (2010).

22. Hashimoto, D., Miller, J. & Merad, M. Dendritic cell and macrophage heterogeneity in vivo. *Immunity* **35**, 323-335 (2011).

23. Schlitzer, A. & Ginhoux, F. Organization of the mouse and human DC network. *Curr Opin Immunol* **26**, 90-99 (2014).

24. Liu, K. *et al.* In vivo analysis of dendritic cell development and homeostasis. *Science* **324**, 392-397 (2009).

25. Choi, J.H. *et al.* Flt3 signaling-dependent dendritic cells protect against atherosclerosis. *Immunity* **35**, 819-831 (2011).

26. Swiecki, M., Gilfillan, S., Vermi, W., Wang, Y. & Colonna, M. Plasmacytoid dendritic cell ablation impacts early interferon responses and antiviral NK and CD8(+) T cell accrual. *Immunity* **33**, 955-966 (2010).

27. Meredith, M.M. *et al.* Expression of the zinc finger transcription factor zDC (Zbtb46, Btbd4) defines the classical dendritic cell lineage. *J Exp Med* **209**, 1153-1165 (2012).

28. Satpathy, A.T. *et al.* Zbtb46 expression distinguishes classical dendritic cells and their committed progenitors from other immune lineages. *J Exp Med* **209**, 1135-1152 (2012).

29. Tsapogas, P., Mooney, C.J., Brown, G. & Rolink, A. The Cytokine Flt3-Ligand in Normal and Malignant Hematopoiesis. *Int J Mol Sci* **18** (2017).

30. Maraskovsky, E. *et al.* Dramatic increase in the numbers of functionally mature dendritic cells in Flt3 ligand-treated mice: multiple dendritic cell subpopulations identified. *J Exp Med* **184**, 1953-1962 (1996).

31. Waskow, C. *et al.* The receptor tyrosine kinase Flt3 is required for dendritic cell development in peripheral lymphoid tissues. *Nat Immunol* **9**, 676-683 (2008).

32. Belz, G.T. & Nutt, S.L. Transcriptional programming of the dendritic cell network. *Nat Rev Immunol* **12**, 101-113 (2012).

33. Guilliams, M. *et al.* Dendritic cells, monocytes and macrophages: a unified nomenclature based on ontogeny. *Nat Rev Immunol* **14**, 571-578 (2014).

34. Banchereau, J. & Steinman, R.M. Dendritic cells and the control of immunity. *Nature* **392**, 245-252 (1998).

35. Liu, P. *et al.* CX3CR1 deficiency impairs dendritic cell accumulation in arterial intima and reduces atherosclerotic burden. *Arterioscler Thromb Vasc Biol* **28**, 243-250 (2008).

36. Vigen, R., Maddox, T.M. & Allen, L.A. Aging of the United States population: impact on heart failure. *Curr Heart Fail Rep* **9**, 369-374 (2012).

37. Gao, E. *et al.* A novel and efficient model of coronary artery ligation and myocardial infarction in the mouse. *Circ Res* **107**, 1445-1453 (2010).

38. Luster, A.D., Alon, R. & von Andrian, U.H. Immune cell migration in inflammation: present and future therapeutic targets. *Nat Immunol* **6**, 1182-1190 (2005).

39. Meng, X. *et al.* Regulatory T cells in cardiovascular diseases. *Nat Rev Cardiol* **13**, 167-179 (2016).

40. Gautier, E.L. *et al.* Gene-expression profiles and transcriptional regulatory pathways that underlie the identity and diversity of mouse tissue macrophages. *Nat Immunol* **13**, 1118-1128 (2012).

41. Jakubzick, C. *et al.* Minimal differentiation of classical monocytes as they survey steady-state tissues and transport antigen to lymph nodes. *Immunity* **39**, 599-610 (2013).

42. Swiecki, M. & Colonna, M. The multifaceted biology of plasmacytoid dendritic cells. *Nat Rev Immunol* **15**, 471-485 (2015).

43. Bjorck, P. Isolation and characterization of plasmacytoid dendritic cells from Flt3 ligand and granulocyte-macrophage colony-stimulating factor-treated mice. *Blood* **98**, 3520-3526 (2001).

44. Defays, A. *et al.* BAD-LAMP is a novel biomarker of nonactivated human plasmacytoid dendritic cells. *Blood* **118**, 609-617 (2011).

45. Euler, G. Good and bad sides of TGFbeta-signaling in myocardial infarction. *Front Physiol* **6**, 66 (2015).

46. Van der Borght, K. *et al.* Myocardial Infarction Primes Autoreactive T Cells through Activation of Dendritic Cells. *Cell Rep* **18**, 3005-3017 (2017).

47. Steinman, R.M. & Cohn, Z.A. Identification of a novel cell type in peripheral lymphoid organs of mice. II. Functional properties in vitro. *J Exp Med* **139**, 380-397 (1974).

48. Cybulsky, M.I., Cheong, C. & Robbins, C.S. Macrophages and Dendritic Cells: Partners in Atherogenesis. *Circ Res* **118**, 637-652 (2016).

49. Hulsmans, M. *et al.* Macrophages Facilitate Electrical Conduction in the Heart. *Cell* **169**, 510-522 e520 (2017).

50. Mildner, A. & Jung, S. Development and function of dendritic cell subsets. *Immunity* **40**, 642-656 (2014).

51. Menezes, S. *et al.* The Heterogeneity of Ly6Chi Monocytes Controls Their Differentiation into iNOS+ Macrophages or Monocyte-Derived Dendritic Cells. *Immunity* **45**, 1205-1218 (2016).

52. Meredith, M.M. *et al.* Zinc finger transcription factor zDC is a negative regulator required to prevent activation of classical dendritic cells in the steady state. *J Exp Med* **209**, 1583-1593 (2012).

53. Briseno, C.G. *et al.* Distinct Transcriptional Programs Control Cross-Priming in Classical and Monocyte-Derived Dendritic Cells. *Cell Rep* **15**, 2462-2474 (2016).

54. Wu, X. *et al.* Mafb lineage tracing to distinguish macrophages from other immune lineages reveals dual identity of Langerhans cells. *J Exp Med* **213**, 2553-2565 (2016).

55. Shklovskaya, E., Roediger, B. & Fazekas de St Groth, B. Epidermal and dermal dendritic cells display differential activation and migratory behavior while sharing the ability to stimulate CD4+ T cell proliferation in vivo. *J Immunol* **181**, 418-430 (2008).

56. Cerovic, V. *et al.* Intestinal CD103(-) dendritic cells migrate in lymph and prime effector T cells. *Mucosal Immunol* **6**, 104-113 (2013).

57. Grajales-Reyes, G.E. *et al.* Batf3 maintains autoactivation of Irf8 for commitment of a CD8alpha(+) conventional DC clonogenic progenitor. *Nat Immunol* **16**, 708-717 (2015).

58. Swirski, F.K. *et al.* Identification of splenic reservoir monocytes and their deployment to inflammatory sites. *Science* **325**, 612-616 (2009).

59. Schlitzer, A. *et al.* IRF4 transcription factor-dependent CD11b+ dendritic cells in human and mouse control mucosal IL-17 cytokine responses. *Immunity* **38**, 970-983 (2013).

60. Anzai, A. *et al.* Regulatory role of dendritic cells in postinfarction healing and left ventricular remodeling. *Circulation* **125**, 1234-1245 (2012).

61. Piccinini, A.M. & Midwood, K.S. DAMPening inflammation by modulating TLR signalling. *Mediators Inflamm* **2010** (2010).

62. Eriksson, U. *et al.* Dendritic cell-induced autoimmune heart failure requires cooperation between adaptive and innate immunity. *Nat Med* **9**, 1484-1490 (2003).

63. Ahadome, S.D. *et al.* Classical dendritic cells mediate fibrosis directly via the retinoic acid pathway in severe eye allergy. *JCI Insight* **1** (2016).

64. Curiel, T.J. *et al.* Dendritic cell subsets differentially regulate angiogenesis in human ovarian cancer. *Cancer Res* **64**, 5535-5538 (2004).

65. Jetten, N. *et al.* Anti-inflammatory M2, but not pro-inflammatory M1 macrophages promote angiogenesis in vivo. *Angiogenesis* **17**, 109-118 (2014).

66. Yu, X.L. *et al.* Overexpression of IL-12 reverses the phenotype and function of M2 macrophages to M1 macrophages. *Int J Clin Exp Pathol* **9**, 8963-8972 (2016).

67. Weirather, J. *et al.* Foxp3+ CD4+ T cells improve healing after myocardial infarction by modulating monocyte/macrophage differentiation. *Circ Res* **115**, 55-67 (2014).

68. Takahashi, K. *et al.* Modulated inflammation by injection of high-mobility group box 1 recovers post-infarction chronically failing heart. *Circulation* **118**, S106-114 (2008).

69. Zhu, R. *et al.* Interleukin-37 and Dendritic Cells Treated With Interleukin-37 Plus Troponin I Ameliorate Cardiac Remodeling After Myocardial Infarction. *J Am Heart Assoc* **5** (2016).

70. Choo, E.H. *et al.* Infarcted Myocardium-Primed Dendritic Cells Improve Remodeling and Cardiac Function After Myocardial Infarction by Modulating the Treg and Macrophage Polarization. *Circulation* (2017).

71. Maekawa, Y. *et al.* Survival and cardiac remodeling after myocardial infarction are critically dependent on the host innate immune interleukin-1 receptor-associated kinase-4 signaling: a regulator of bone marrow-derived dendritic cells. *Circulation* **120**, 1401-1414 (2009).

72. Ishibashi, S. *et al.* Hypercholesterolemia in low density lipoprotein receptor knockout mice and its reversal by adenovirus-mediated gene delivery. *J Clin Invest* **92**, 883-893 (1993).

73. Matthews, W., Jordan, C.T., Wiegand, G.W., Pardoll, D. & Lemischka, I.R. A receptor tyrosine kinase specific to hematopoietic stem and progenitor cell-enriched populations. *Cell* **65**, 1143-1152 (1991).

74. Cheong, C. & Choi, J.H. Dendritic cells and regulatory T cells in atherosclerosis. *Mol Cells* **34**, 341-347 (2012).

75. Patel, B.B. *et al.* Chronic Exposure to Bisphenol A Reduces Successful Cardiac Remodeling After an Experimental Myocardial Infarction in Male C57bl/6n Mice. *Toxicol Sci* **146**, 101-115 (2015).

76. Thibault, H. *et al.* Acute myocardial infarction in mice: assessment of transmurality by strain rate imaging. *Am J Physiol Heart Circ Physiol* **293**, H496-502 (2007).

2. 11 Supplementary Information

2. 11. 1 Supplementary Figures

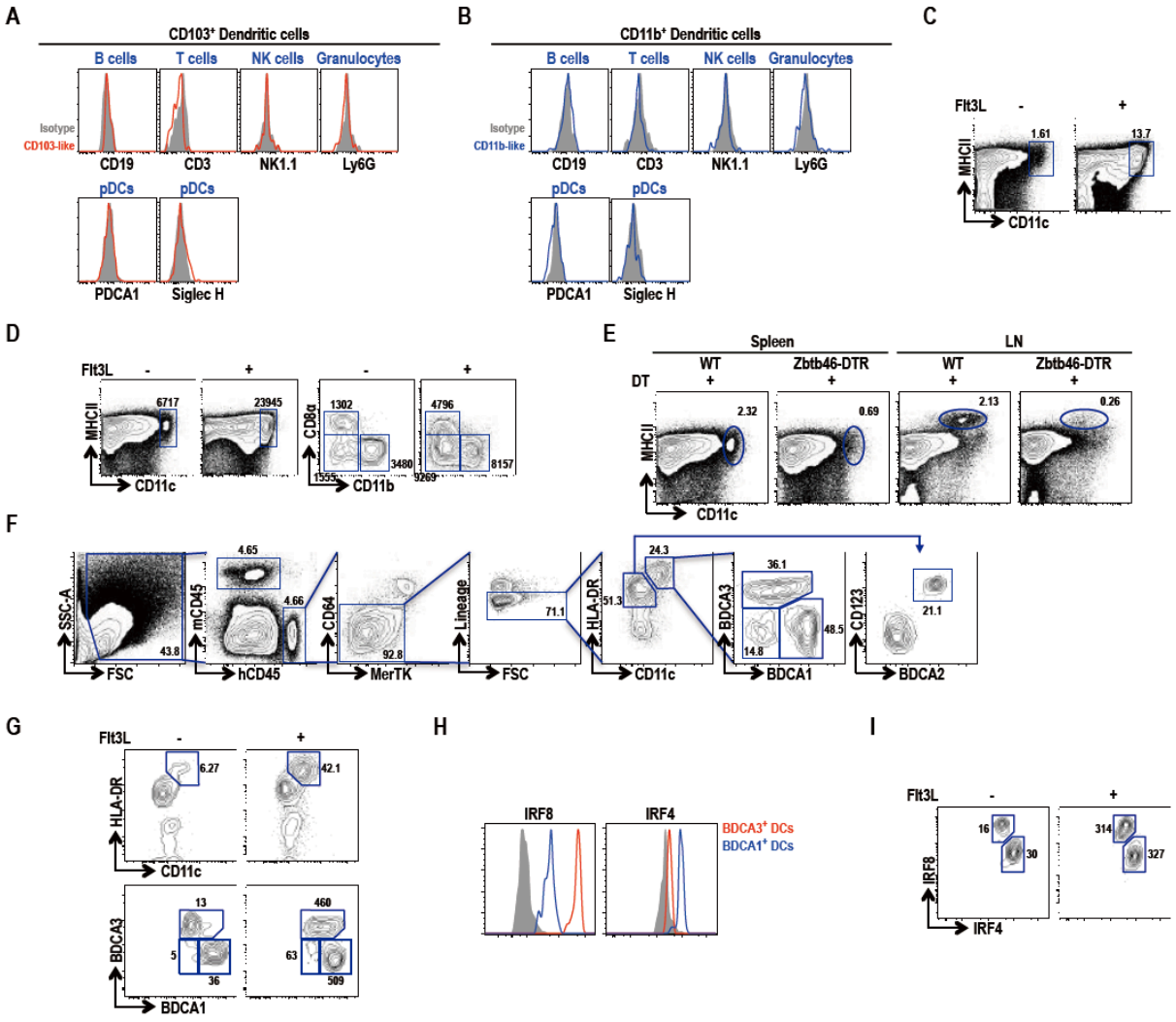

Supplemental figure 2.1. Characterization of heart DCs of mice and hu-mice. related to Figure 2.1 and Figure 2.2. (A-B) Cardiac CD103^{+} DCs (red lines) and CD11b^{+} DCs (blue lines) gated as in **figure 2.1A** were further characterized phenotypically using a series of mAbs and their specific isotype controls (gray filled lines). Expression of specific markers for B cells, T cells, NK cells, granulocytes and pDCs is shown. **(C-D)** WT and Flt3/Flk2/CD135-deficient mice were injected intraperitoneally with PBS (−) or with 2 µg of Flt3L (+) each day for nine consecutive days. **(C)** Percentages of total DCs in spleen of C57BL/6 mice. **(D)**

Representative FACS plots showing absolute numbers of total DCs (top), $CD8\alpha^+$ DCs, $CD11b^+$ DCs and double negative cells (bottom) from spleen of WT mice. **(E)** Selective depletion of DCs from the spleen and lymph nodes of WT and Zbtb46-DTR mice treated with DT in **Figure 2.2A**. **(F)** Gating strategy for total heart DCs in hu-mice. Cells were gated from the $hCD45^+$, $CD64^-$, $MerTK^-$, $Lineage^-$ (CD14, CD19, CD56), $HLA\text{-}DR^+$ and $CD11c^+$ population. **(G)** Hu-mice were injected intraperitoneally with PBS (−) or with 2 μg of Flt3L (+) each day for nine consecutive days. Representative FACS plots showing percentages of hu-cardiac total DCs (upper panels), including $BDCA1^+$ DCs and $BDCA3^+$ DCs gated from $HLA\text{-}DR^+$ $CD11c^+$ cells (lower panels). **(H)** Representative FACS plots of hu-mice cardiac showing expression of IRF4 and IRF8 in $BDCA1^+$ DCs (blue), $BDCA3^+$ DCs (red). Isotype control antibody staining is shown in grey. **(I)** Hu-mice were injected intraperitoneally with PBS (−) or with 2 μg of Flt3L (+) each day for nine consecutive days and $HLA\text{-}DR^{hi}$ $CD11c^{hi}$ cDCs were stained for IRF4 and IRF8. Absolute numbers are shown.

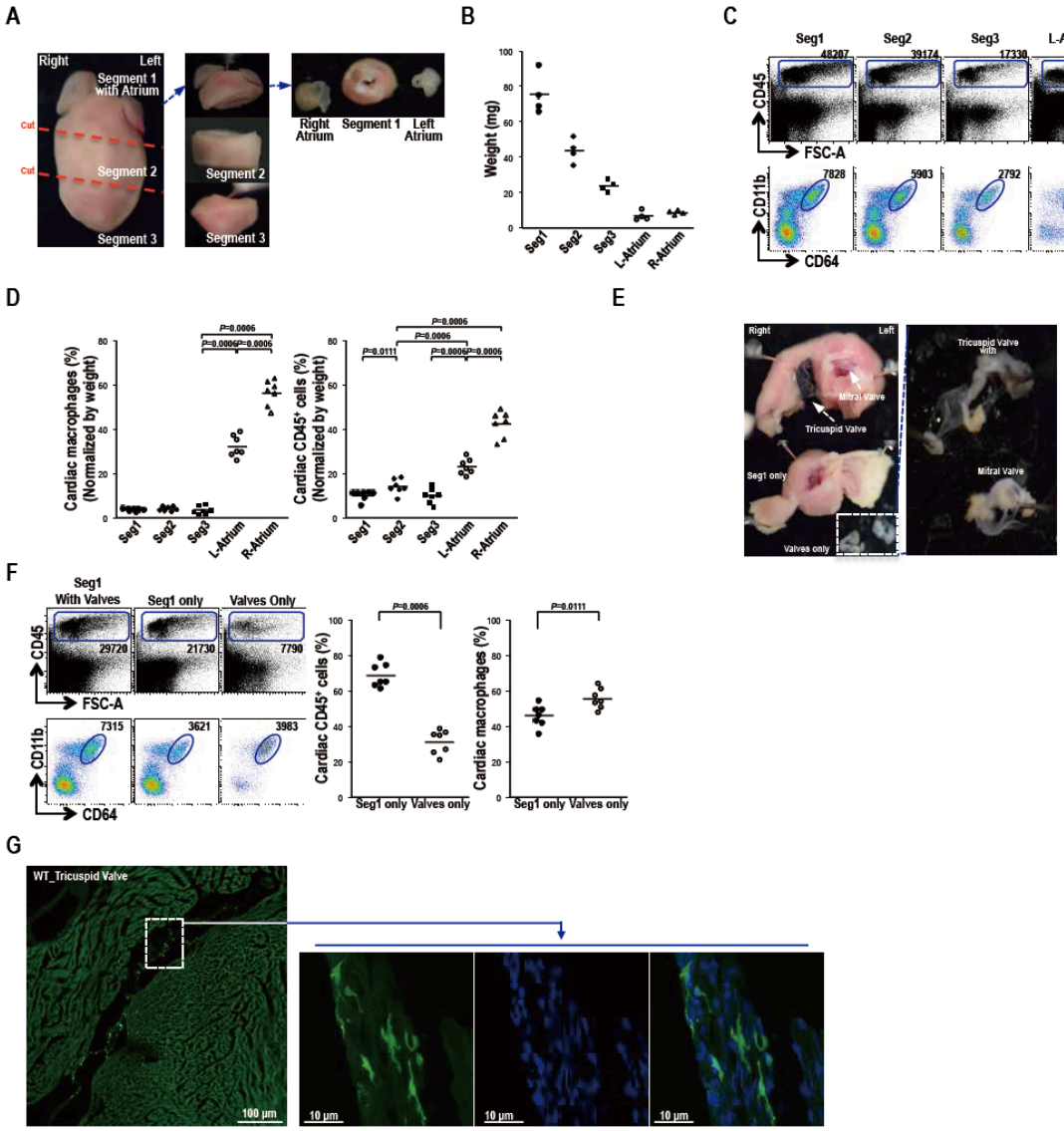

Supplemental figure 2.2. Anatomical location of MΦs under steady state conditions in the mouse heart. related to Figure 2.3. (A) Heart from a WT mouse (left panel) separated into Segment1 (Seg1) with Atrium, Segment2 (Seg2), and Segment3 (Seg3) (middle panels). On the right panel, Segment1 with atria was again separated into Segment1, Right Atrium (R-Atrium) and Left Atrium (L-Atrium). **(B)** The weight of each cardiac segment (mice age: 220 days) was plotted (n = 4). **(C)** Absolute numbers of cardiac $CD45^+$ cells and MΦs in different parts of the heart were quantified by flow cytometry. **(D)** Percentages (mean ± SD; n = 7 mice) were normalized by weight. **(E)** Tricuspid and mitral valves were surgically separated from Seg1. **(F)** Absolute numbers for Seg1 with valves, Seg1 only and combined valves only (left panels) and percentages (right panels; mean ± SD; n = 7 mice) of $CD45^+$ (top panels) and MΦs (lower panels) were determined by flow cytometry. **(G)** Representative immune-fluorescence sections (left, tile scan confocal image) of tricuspid valve in CD11c-$YFP^{+/+}$ mice

under steady state condition stained with anti-GFP antibody (green) and DAPI (blue). All experiments were performed on 12 µm frozen sections.

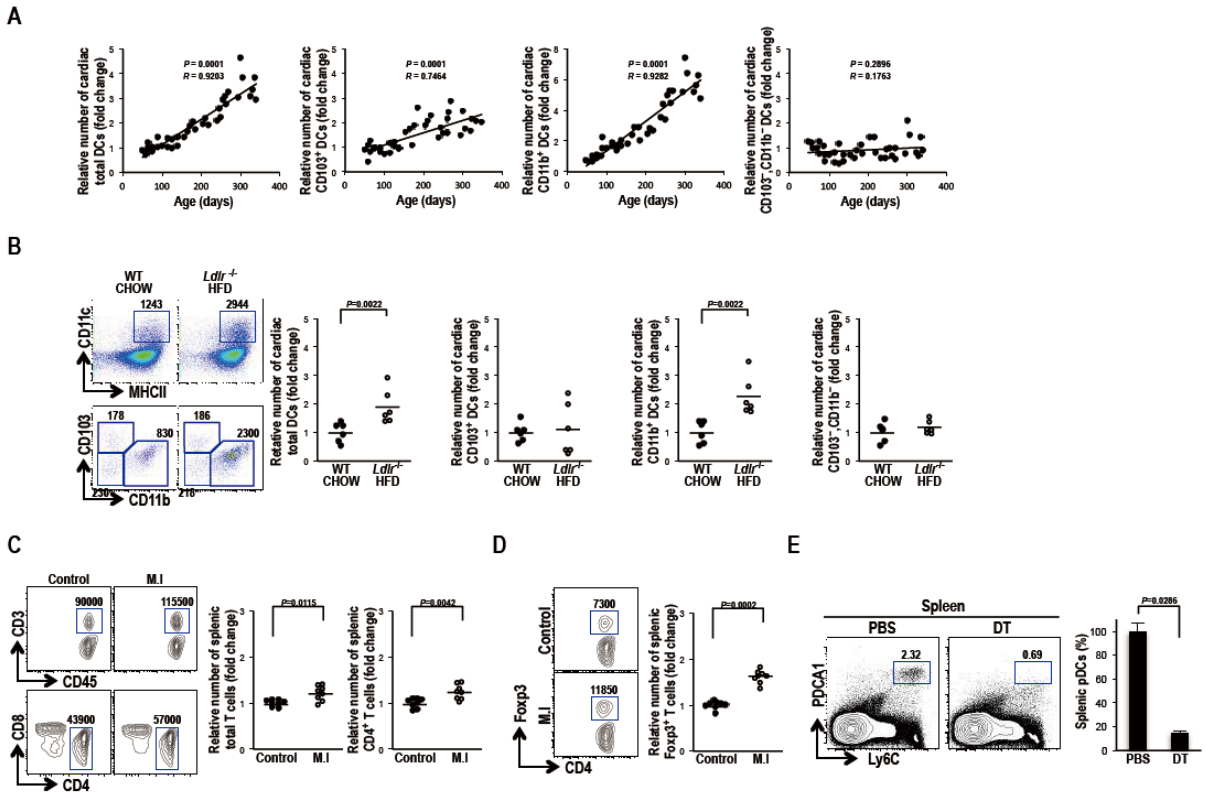

Supplemental figure 2.3. Aging and M.I affect the number of immune cell subsets. related to Figure 2.4 and Figure 2.5. (A) Relative numbers of cardiac total DCs and DC subsets in WT C57BL/6 mice at different time points were determined by flow cytometry (n = 38). **(B)** Absolute numbers and relative numbers of cardiac total DCs including $CD103^{+}$ DCs, $CD11b^{-}$ DCs and double negative cells from WT mice fed a normal diet (CHOW) and *Ldlr*$^{-/-}$ mice fed WD (HFD) for 10 wk. Left: representative FACS plots of cardiac total DCs (up), $CD103^{+}$ DCs, $CD11b^{+}$ DCs and double negative cells (down). Right: relative absolute numbers of cardiac total DCs, $DC103^{+}$ DCs, $CD11b^{+}$ DCs and double negative cells per heart (n = 6). **(C-D)** Cells from control mice or mice 3 days after M.I were analyzed by flow cytometry. Representative FACS plots and absolute numbers of gated cells (left panels) and relative numbers (right panels; mean ± SD; n = 8 mice) of splenic total T cells, $CD4^{+}$ T cells **(C)** and Tregs **(D). (E)** Representative FACS plots (left panels) and percentage (right panels; graph indicates mean ± SD; n = 4) of pDCs in spleen of BDCA2-DTR mice injected with PBS alone or DT alone for 3 weeks.

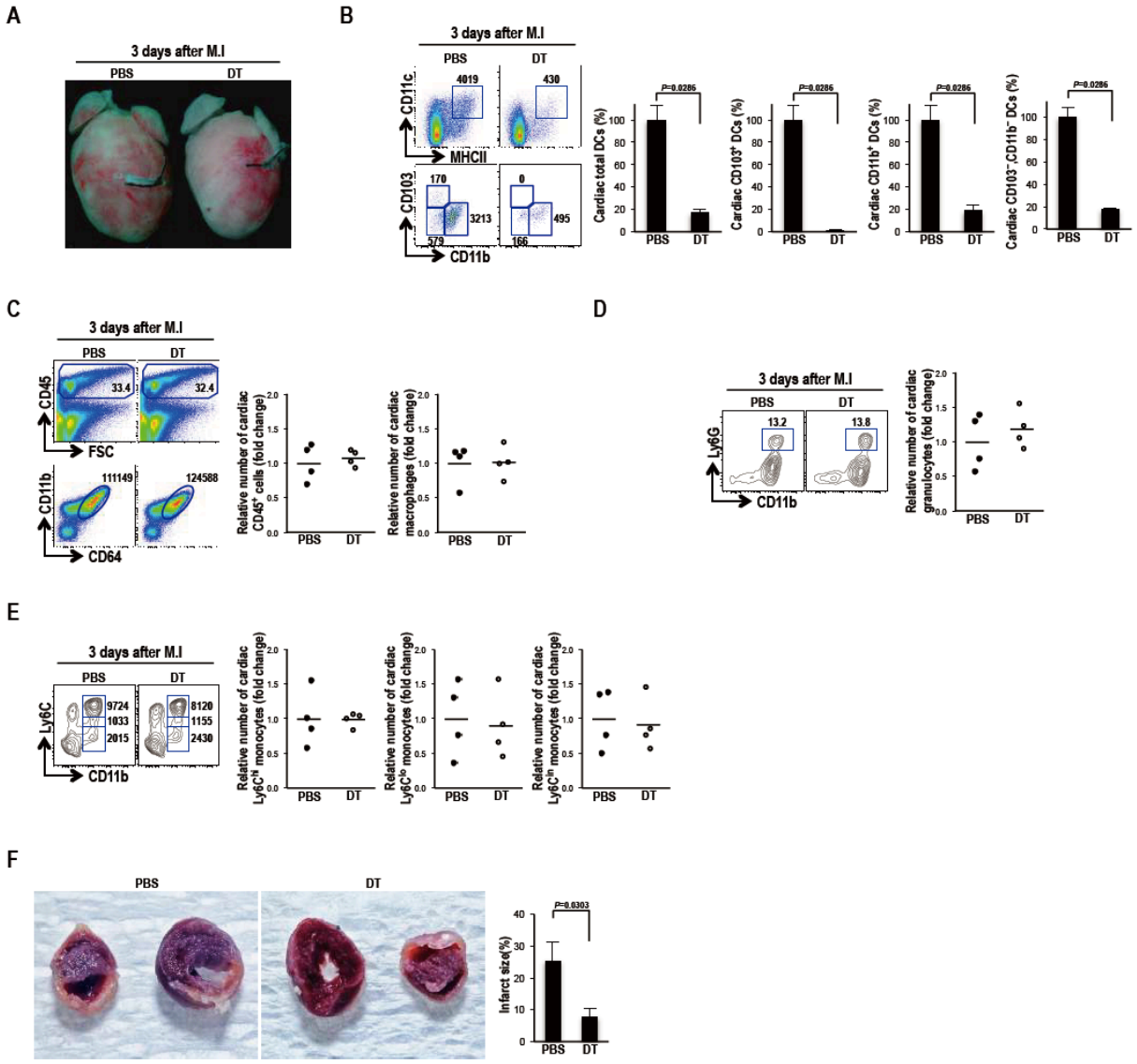

Supplemental figure 2.4. Selective depletion of zDCs for 3 days following M.I. does not affect the number of heart MΦs, granulocytes and monocytes. related to Figure 2.6 and 2.7. (A) Hearts were isolated from myocardial-infarcted Zbtb46-DTR mice injected with PBS or DT for 3 days. **(B)** Selective elimination of cardiac total DCs in Zbtb46-DTR mice injected with DT. Left: representative FACS plots of total DCs (top) and DC subsets (bottom). Right: percentages of total DCs and DC subsets. **(C-E)** Representative FACS plots (left panels) and relative numbers (right panels) of **(C)** $CD45^+$ cells (up) and MΦs (down), **(D)** granulocytes and **(E)** monocyte subsets in M.I-induced Zbtb46-DTR mice injected with PBS or DT. All graphs indicate mean ± SD; n ≥ 4. (F) Evans blue and TTC staining of heart from myocardial-infarcted Zbtb46-DTR mice injected with PBS or DT for 3 weeks. PBS n = 5, DT n = 6.

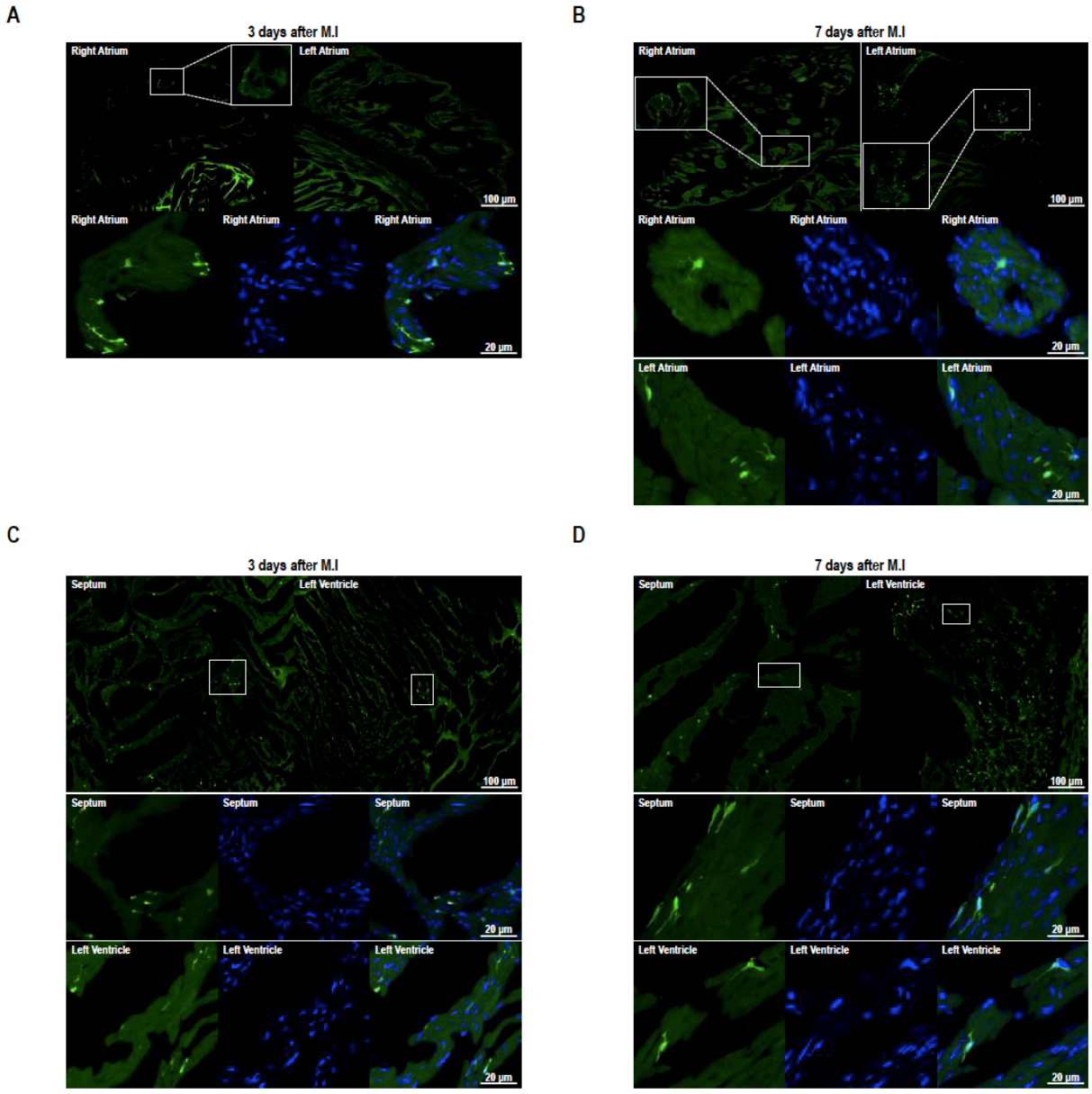

Supplemental figure 2.5. The location of cardiac DCs after M.I. related to Figure 2.4. Immunofluorescence sections from hearts of CD11c-YFP$^{+/+}$ mice 3 or 7 days after M.I stained with anti-GFP antibody (GFP) and DAPI (blue). All experiments were performed on 12µm frozen sections. Right and Left atrium (top, tile scan confocal images) 3 days **(A)** and 7 days **(B)** after M.I. Septum and Left ventricle (top, tile scan confocal images) 3 days **(C)** and 7 days **(D)** after M.I.

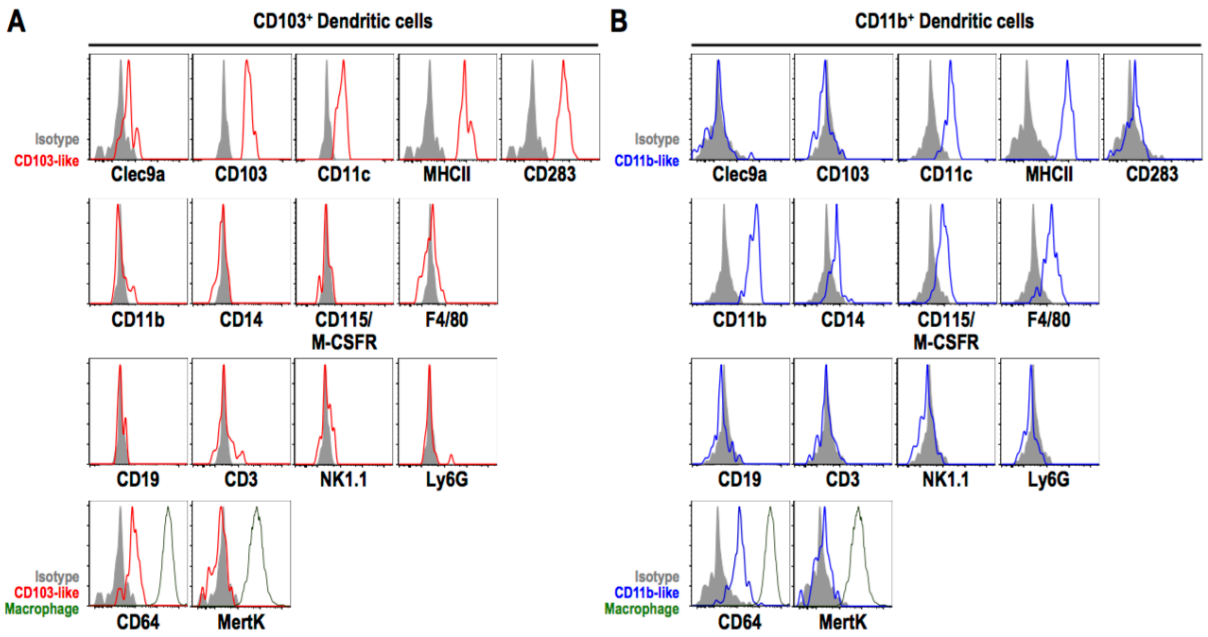

Supplemental figure 2.6. The phenotypes of cardiac DC subpopulations under myocardial infarcted mice heat. (A and B) Cardiac $CD103^+$ DCs (red line) and $CD11b^+$ DCs (blue line) were further characterized phenotypically using a series of mAbs and their specific isotype controls (gray filled lines). All markers were surface stained except Clec9a, which was stained following permeabilization. Cardiac macrophages were included as positive controls for the assessment of CD64, and MertK expression.

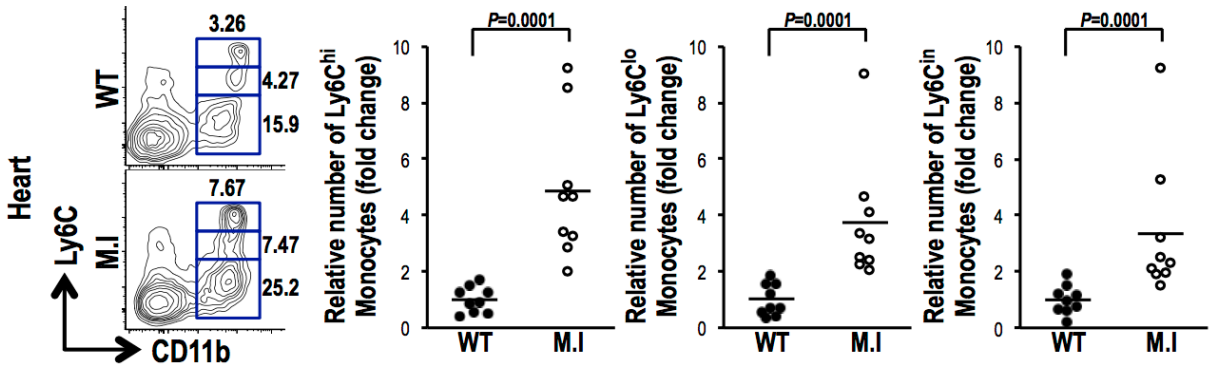

Supplemental figure 2.7. Increased monocyte-subpopulations in heart with MI. The proportions of monocytes were compared between control WT mice and mice 3 days after myocardial infarction (MI). Relative numbers cells were normalized to the group without MI. Graph indicates mean ± SD; n ≥ 8 mice. Representative FACS plots (left panels) and relative numbers (right panels) of monocytes.

2. 11. 2 Supplementary Tables

Supplemental table 2.1. the measurement variables.

Parameter	Units	PBS	DT	P value
Heart Rate	BPM	492.2±120.79	500.7±139.25	ns
Left ventricular internal diameter (LVID) at systole (LVIDs)	mm	3.5±0.38	3.2±0.44	*P*=0.018
Left ventricular internal diameter (LVID) at diastole (LVIDd)	mm	4.2±0.52	4.1±0.54	ns
Stroke Volume	µL	27.9±8.55	36.3±11.4	*P*=0.009
Cardiac Output	mL/min	14.2±5.98	19.8±10.05	*P*=0.035

CHAPTER 3

3 Transcriptome Analysis Reveals Non-foamy Rather Than Foamy Plaque Macrophages Are Proinflammatory in Atherosclerotic Murine Models

Kyeongdae Kim[1], Dahee Shim[1], Jun Seong Lee[2,3], Konstantin Zaitsev[4,5], Jesse W. Williams[4], Ki-Wook Kim[4], Man-Young Jang[1], Hyung Seok Jang[1], Tae Jin Yun[3,6], Seung Hyun Lee[1], Won Kee Yoon[7], Annik Prat[8], Nabil G. Seidah[8], Jungsoon Choi[9], Seung-Pyo Lee[10], Sang-Ho Yoon[1], Jin Wu Nam[1], Je Kyung Seong[11], Goo Taeg Oh[12], Gwendalyn J. Randolph[4], Maxim N. Artyomov[4], Cheolho Cheong[2,3,6,8], Jae-Hoon Choi[1]

[1]Department of Life Sciences, College of Natural Sciences, Research Institute for Natural Sciences, Hanyang University, Seoul, Republic of Korea

[2]Département de microbiologie, infectiologie et immunologie, Université de Montréal, Montreal, Quebec H3T 1J4, Canada

[3]Institut de Recherches Cliniques de Montréal (IRCM), Montréal, Quebec H2W 1R7, Canada

[4]Pathology and Immunology, Washington University School of Medicine, St. Louis, MO, USA

[5]Computer Technologies Department, ITMO University, St. Petersburg, Russia

[6]Division of Experimental Medicine, Medicine, McGill University, Montreal, Canada

[7]Biomedical Mouse Resource Center, KRIBB, Chungbuk

[8]Laboratory of Biochemical Neuroendocrinology, Institut de Recherches Cliniques de Montréal, Montréal, Canada

[9]Department of Mathematics, College of Natural Sciences, Research Institute for Natural Sciences, Hanyang University, Seoul, Republic of Korea

[10]Cardiovascular Center, and Internal Medicine, Seoul National University Hospital, Seoul

[11]the Laboratory of Developmental Biology and Genomics, Research Institute for Veterinary Science, College of Veterinary Medicine and Korea Mouse Phenotyping Center, Seoul National University, Seoul

[12]Immune and Vascular Cell Network Research Center, National Creative Initiatives, Department of Life Sciences, Ewha Womans University, Seoul,

Kyeongdae Kim, Dahee Shim, Jun Seong Lee, and Konstantin Zaitsev contributed equally to this article.

 # corresponding authors

Dr. Jae-Hoon Choi
Life Science College of natural Sciences
Hanyang University, 222 Wangsimniro, Seongdong Gu, Seoul, 04763, Korea
E-mail: jchoi75@hanyang.ac.kr

Dr. Gwendalyn J. Randolph
Department of Pathology and Immunology
Washington University School of Medicine, 425 S Euclid Ave, Box 8118
St. Louis, MO 63110
E-mail: gjrandolph@wustl.edu

Dr. Maxim N. Aryomov
Pathology and Immunology
Department of Pathology and Immunology
Washington University School of Medicine, 425 S Euclid Ave, Box 8118
St. Louis, MO 63110
E-mail: martyomov@email.wustl.edu

Circulation Research. (2018). 123:1127-1142

3. 1 Novelty and Significance

3. 1. 1 What is Known?

- Macrophages process excessive cholesterol and induce inflammatory responses via TLRs (Toll-like receptors) and inflammasome activation during atherogenesis.
- Macrophages are the major contributors of foam cells in atherosclerotic lesions.
- Generation of foamy macrophages suppresses the inflammatory status of cells via activation of the LXR (liver X receptor).

3. 1. 2 What New Information Dose This Article Contribute?

- We developed a straightforward method to readily differentiate foam cells in plaques from other macrophages in the aortic wall.
- The foamy macrophages in atherosclerotic lesions do not express RNAs that are primarily associated with inflammation; instead, they express genes related to lipid processing.
- Intimal non-foamy macrophages form the major population expressing IL (inter-leukin)-1β and other inflammatory transcripts in atherosclerotic aorta.

Macrophages in atherosclerotic plaques internalize excessive lipids, become foamy macrophages, and produce proinflammatory molecules. However, excessive uptake of exogenous lipids has been shown to suppress inflammatory responses in macrophages. Therefore, understanding the characteristics of foamy plaque macrophages is important for understanding their roles in atherosclerosis. In this study, we used single-cell RNA sequencing to unbiasedly classify aortic macrophages in atherosclerosis. We first developed a fluorescence-activated cell sorting–based method to distinguish foamy macrophages from other macrophages in atherosclerotic aorta. Then, using this newly developed method, we

sorted out the intimal non-foamy and foamy macrophages and performed transcriptomic analysis using RNA sequencing. These 2 RNA sequencing approaches revealed that whereas non-foamy macrophages predominantly expressed genes related to immune response, the foamy macrophages mainly expressed genes related to lipid processing instead of inflammation. Similarly, the foamy macrophages in human atheroma showed scant expression of IL-1β—an inflammatory cytokine. These results suggest that intimal non-foamy macrophages, rather than foamy plaque macrophages, perform proinflammatory roles in the atherosclerotic aorta.

3. 2 Abstract

Monocyte infiltration into the subintimal space and its intracellular lipid accumulation are the most prominent features of atherosclerosis. To understand the pathophysiology of atherosclerotic disease, we need to understand the characteristics of lipid-laden foamy macrophages in the subintimal space during atherosclerosis. We sought to examine the transcriptomic profiles of foamy and non-foamy macrophages isolated from atherosclerotic intima. Single-cell RNA sequencing analysis of $CD45^+$ leukocytes from murine atherosclerotic aorta revealed that there are macrophage subpopulations with distinct differentially expressed genes involved in various functional pathways. To specifically characterize the intimal foamy macrophages of plaque, we developed a lipid staining–based flow cytometric method for analyzing the lipid-laden foam cells of atherosclerotic aortas. We used the fluorescent lipid probe BODIPY493/503 and assessed side-scattered light as an indication of cellular granularity. $BODIPY^{hi}SSC^{hi}$ foamy macrophages were found residing in intima and expressing CD11c. Foamy macrophage accumulation determined by flow cytometry was positively correlated with the severity of atherosclerosis. Bulk RNA sequencing analysis showed that compared with non-foamy macrophages, foamy macrophages expressed few inflammatory genes but many lipid-processing genes. Intimal non-foamy macrophages formed the major population expressing IL (interleukin)-1β and many other inflammatory transcripts in atherosclerotic aorta. RNA sequencing analysis of intimal macrophages from atherosclerotic aorta revealed that lipid-loaded plaque macrophages are not likely the plaque macrophages that drive lesional inflammation.

3. 3 Introduction

Atherosclerosis is a chronic inflammatory disease and the leading cause of cardiovascular disease, which is a major contributor to mortality in Western countries.[1] Atherosclerosis can lead to myocardial infarction, ischemic stroke, renal impairment, and aneurysms with hypertension.[2] An especially prominent feature of atherosclerotic lesions is the accumulation of lipids within cells in the aortic wall. As atherosclerosis progresses, macrophages are recruited to the intima and take up modified LDL (low-density lipoprotein) particles via their scavenger receptors, leading to the progression of atherosclerotic lesions.[3, 4] Intracellular accumulation of lipid molecules results in the formation of lipid-laden cells called foam cells, which comprise the major cellular component of atherosclerotic lesions.[1]

The number of foam cells in a lesion increases as atherosclerosis develops and decreases as regression occurs.[5, 6, 7] Foam cells, especially macrophage foam cells, participate in all developmental phases of a lesion (ie, formation, maintenance, and rupture) and affect the status of a lesion through cellular responses, such as cytokine secretion, apoptosis, and necrosis.[8, 9] Therefore, an important part of atherosclerosis research is examining the quantitative and qualitative changes in foam cells. Macrophage foam cell formation has been shown to be initiated by bone marrow-derived macrophage infiltration that follows monocytosis or extramedullary hematopoiesis.[10] In steady-state mouse blood vessels, a small number of macrophages reside in the intimal area, whereas the majority of such cells reside in the adventitia.[11] Aortic macrophages arise from CX_3CR1^+ (CX3C chemokine receptor 1) embryonic precursors (yolk sac macrophages) and bone marrow-derived monocytes that were briefly introduced in the postnatal period.[12] Under steady state, there is no significant influx of macrophages from blood monocytes.[11] During lesion formation, however, the intima experiences infiltration/fixation of incoming monocytes and activation of monocyte proliferation[13] caused by hypercholesterolemia and its inflammatory response.[11, 14, 15, 16] Infiltration depends on the expression of CCR2 (C-C chemokine receptor type 2), CCR5, and CX_3CR1 on monocytes[14, 15] and various adhesion molecules on endothelial cells.[17] macrophages take up excess cholesterol, which is converted to cholesteryl ester that gathers into cytosolic lipid droplets to form foamy macrophages.[18] Cholesterol accumulation induces macrophages to undergo inflammatory responses.[19] Furthermore, decreased cellular

cholesterol efflux also causes inflammatory responses and inflammasome activation.[20] However, lipid accumulation in macrophages was associated with suppression, rather than activation, of inflammatory gene expression.[21] Therefore, considering the phenotypic plasticity of macrophages, further characterization of plaque macrophages according to their lipid content is required.

To investigate lipid-enriched atherosclerotic lesions, researchers have used various staining methods. For example, the combination of Oil Red O staining and immunofluorescence-based analysis is commonly used to examine aortic sections and entire aortas[22] and has come to be regarded as the standard approach for evaluating atherogenicity and characterizing foam cells in atherosclerotic lesions under different experimental conditions. However, it is difficult to define the cellular components of a lesion, as such characterization would require the analysis of numerous cellular biomarkers. For example, some markers (eg, CD11c, MHCII [major histocompatibility complex II], and CD11b) are shared by dendritic cells (DCs) and macrophages, making it difficult to distinguish these cell groups. Thus, technically advanced, simpler, and more sensitive methods that combine objective measurements of lipid-rich atherosclerotic lesions with multiple cellular analyses are required. To overcome the limitations inherent to immunohistochemistry, multiparametric flow cytometry has been used to analyze aortic immune cells from atherosclerotic mice.[23, 24, 25]

Previously, BODIPY493/503 [4,4-difluoro-1,3,5,7,8-pen- tamethyl-4-bora-3a,4a-diaza-s-indacene]—a fluorescent lipid probe—was shown to stain cytosolic neutral lipids of cultured foamy macrophages.[26] We used BODIPY493/503 and assessed side-scattered light (SSC) as an indication of cellular granularity to detect atherosclerotic foamy macrophages in flow cytometric analysis. Before analyzing the characteristics of foamy macrophages from atherosclerotic aortas, we first used single-cell RNA sequencing (scRNA-seq) to identify cell subtypes by their transcriptomic signatures and confirmed the heterogeneity of macrophages in atherosclerotic aorta. We then characterized and sorted intimal foamy and non-foamy macrophages from atherosclerotic aorta, using a newly established lipid staining–based flow cytometric protocol. Finally, we used bulk RNA sequencing (RNA-seq) to compare the transcriptomes of isolated foamy and non-foamy macrophages.

3. 4 Results

3. 4. 1 scRNA-seq Reveals Macrophage Subpopulations in Murine Atherosclerotic Aorta

To investigate the heterogeneity of leukocytes in whole atherosclerotic aorta, we first performed unbiased classification of leukocytes present in whole atherosclerotic aorta by scRNA-seq analysis. We extracted live propidium iodide^{-} CD45^{+} leukocytes from mouse (LDLR KO [LDL receptor knockout]) atherosclerotic vessels and used scRNA-seq to determine the leukocyte subpopulations according to gene expression patterns (GSE116240, *Ldlr*$^{-/-}$ aorta dataset). Unsupervised graph-based clustering algorithm was used to define 12 clusters according to their gene expression profiles (**Figure 3.1A**). Expression of some genes was common among the clusters, but heterogeneity was evident from differentially expressed genes (DEGs) of which separated the clusters on the t-distributed stochastic neighbor embedding plots (**Figure 3.1B; Supplemental figure 3.1; Supplemental table 3.1; Online data set 3.1**). Cluster 11 was excluded from further analysis because it was a nonleukocyte population (data not shown).

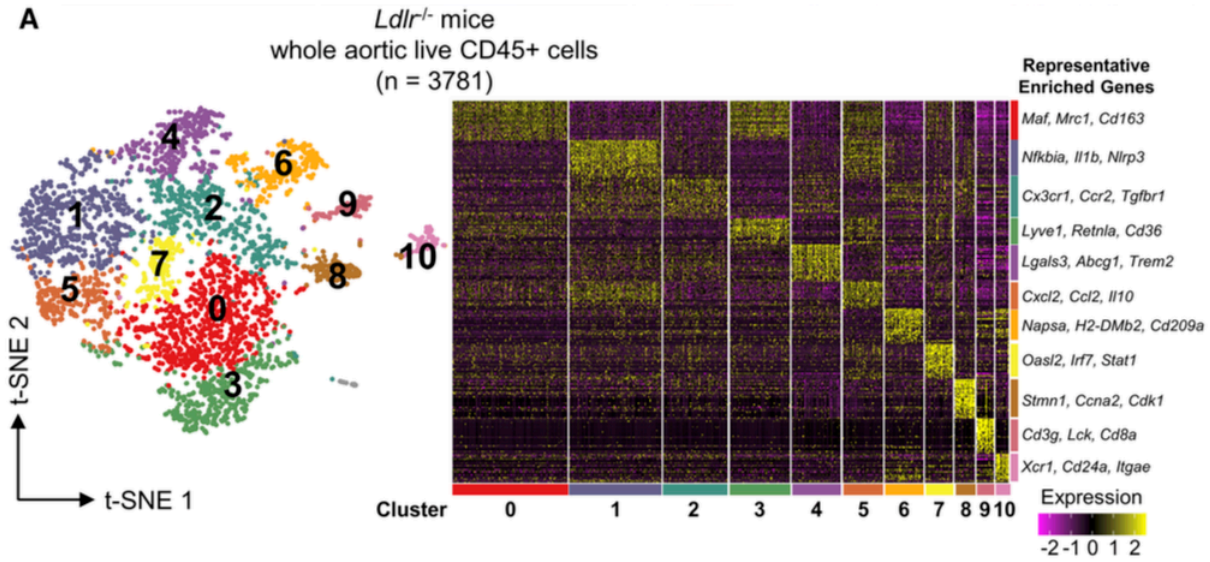

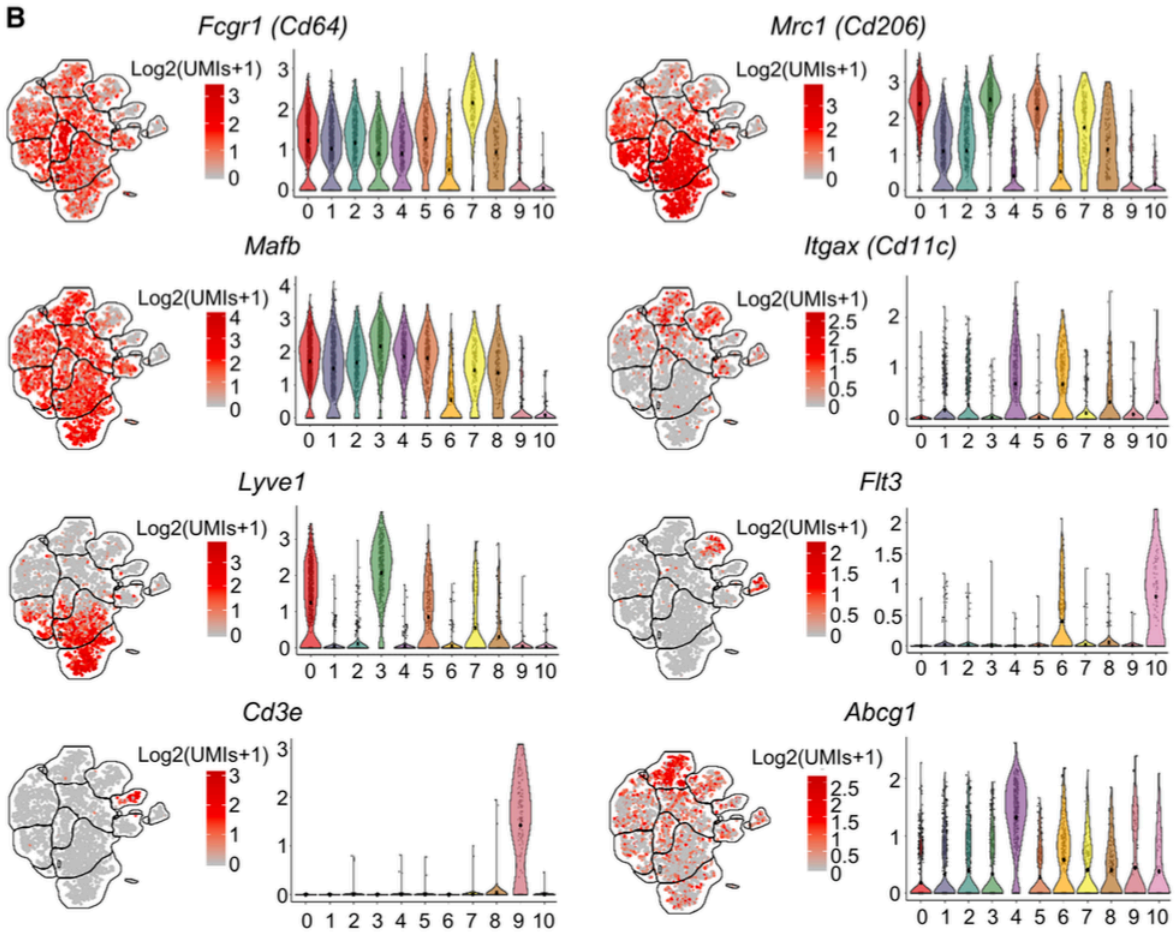

Figure 3.1. Single-cell RNA sequencing (scRNA-seq) reveals macrophage subpopulations in murine atherosclerotic aorta. (A) Left: scRNA-seq of CD45^{+} cells isolated from pooled whole aortas of LDLR KO mice (n=6) fed a WD for 12 wk. Dimensionality reduction and identification of clusters of transcriptionally similar cells were performed in an unsupervised manner using Seurat package. **Right**: Heatmap showing the top 30 differentially expressed genes for each leukocyte cluster. Normalized gene expression is shown. **(B)** Expression of principal hematopoietic markers in the 11 identified cell clusters shown as a t-distributed stochastic neighbor embedding (t-SNE) plot with colors corresponding to expression levels or shown as a distribution of gene expression levels in clusters. UMIs indicate unique molecular identifiers.

To identify cells in the 11 leukocyte clusters, we examined well-known immune cell markers. First, macrophages showed the largest cell numbers and had the most diverse subpopulations (**Figure 3.1B**) among CD45^{+} aortic leukocytes. Clusters 0 to 5, 7, and 8 exhibited high-level expression of macrophage marker genes, such as those encoding *Cd64*

(*Fcgr1*) and *Mafb* (**Figure 3.1B**). Four macrophage clusters (0, 3, 5, and 7) expressed high levels of *Cd206* (*Mrc1*), whereas *Lyve1* was highly expressed in clusters 0, 3, and 5 suggesting that these populations may be resident adventitial macrophages (**Figure 3.1B**). *Itgax* was highly expressed in cluster 4 (**Figure 3.1B**). Next, we performed gene set enrichment analysis to observe functional enrichment of DEGs (all enriched genes and pathways are listed in **Online data set 3.1 and 2, Supplemental figure 3.1, and Supplemental table 3.1**). Clusters 0 and 3 showed upregulated expression of genes related to endocytosis pathways. Cluster 1 showed increased expression of inflammatory genes related to NF-κB (nuclear factor κB), TNF (tumor necrosis factor), IL (interleukin)-17, cytokine, and TLR (Toll-like receptor) signaling pathways. Cluster 2 genes were involved in DNA replication and ribosome pathways. Cluster 4 contained highly expressed genes associated with metabolic pathways, including cholesterol metabolism, oxidative phosphorylation, and PPAR (peroxisome proliferator-activated receptor) signaling pathway. Cluster 5 contained inflammatory genes involved in cytokine/chemokine pathways similar to the gene expression pattern of cluster 1. Cluster 7 showed upregulated expression patterns in interferon-stimulated genes, including *Mx1*, *Oasl1*, and *Stat1/2*, suggesting interferon-responsive macrophages (**Supplemental table I**). Cells in cluster 8 showed highly enriched cell cycle-related genes, such as *Ccna2*, *Cdk1*, and *Cdk4*, suggesting proliferating macrophages.

Cluster 9 was enriched for T-cell receptors (*CD3e/d/g*) and T-cell subset markers (*CD8a* and *Foxp3*), indicating that this cluster represents T cells (**Figure 3.1B; Supplemental figure 3.1; and Supplemental table 3.1**). Clusters 6 and 10 showed high-level expression of genes required for DC differentiation, such as *Flt3* and *Zbtb46* (**Figure 3.1B; Supplemental table 3.1**). CD11c (*Itgax*) and some MHCII molecule (*H2-DM/-O*)-encoding genes (**Figure 3.1B**) were also expressed those clusters, and cluster 10 was the only group in which the gene for CD103 (*Itgae*) was expressed (**Supplemental figure 3.1; and Supplemental table 3.1**), indicating that clusters 6 and 10 are classical DC2 and DC1, respectively.

3. 4. 2 Lipid Staining-Based Flow Cytometric Method Identifies Lipid-Laden Foam Cells of Atherosclerosis

To confirm and characterize the cells of the scRNA-seq identified cluster that appeared to represent intimal foamy macrophages, we set out to develop a new flow cytometric method for detecting lipid-laden cells in aortic single-cell suspensions. To first examine the use of the neutral lipid stain BODIPY493/503 in atherosclerotic aortas, we performed en face costaining using Oil Red O and BODIPY493/503 (**Figure 3.2A**) and found that the atherosclerotic lesions formed at aortic intimal surfaces were specifically stained by both Oil Red O and BODIPY493/503.

To examine whether BODIPY493/503 can be used in flow cytometry to detect lipid-laden foam cells, we stained single-cell suspensions of mouse atherosclerotic aortas with BODIPY493/503 and Zombie Aqua viability dye (**Figure 3.2B and 3.2C**). After gating out the autofluorescent dead cells and debris, we found that aortic cells have higher granularity (SSC^{hi}) and positivity for BODIPY493/503 staining ($BODIPY^{hi}$; **Figure 3.2B**). These $SSC^{hi}BODIPY^{hi}$ cells were only found in atherosclerotic aortas from Western diet (WD)-fed LDLR KO and ApoE KO (apolipoprotein E knockout) mice (**Figure 3.2D**). To define the location of $SSC^{hi}BODIPY^{hi}$ cells in the atherosclerotic aorta, aortic adventitia was separated by partial enzyme digestion and peeling (**Supplemental figure 3.2**). $SSC^{hi}BODIPY^{hi}$ cells were not found in the adventitia of atherosclerotic aorta and normal aorta (**Figure 3.2E**). The number of $SSC^{hi}BODIPY^{hi}$ cells was positively correlated with the anatomic distribution of atherosclerotic lesions (**Supplemental figure 3.3**).

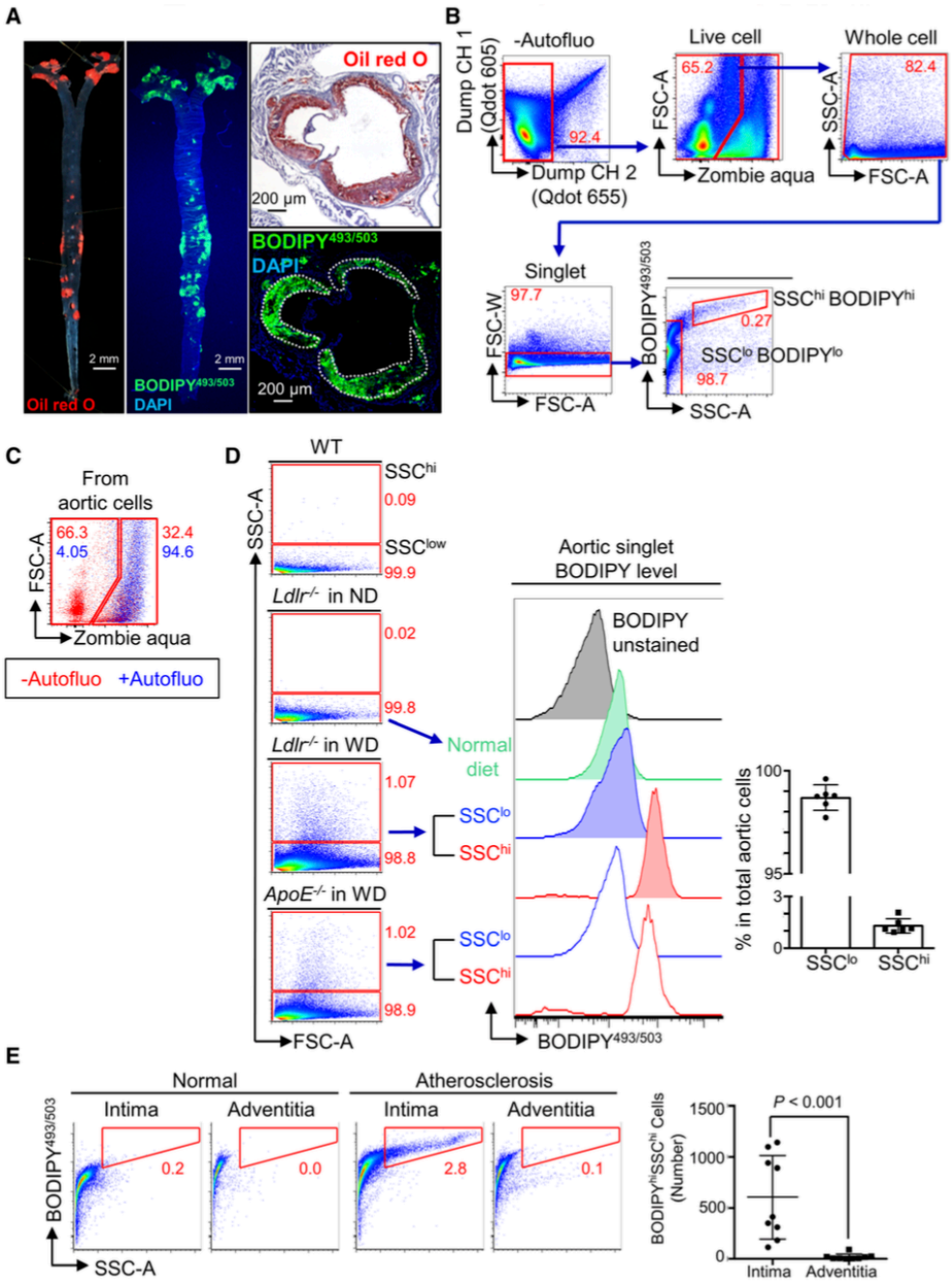

Figure 3.2. BODIPY493/503-based lipid staining and flow cytometry define lipid-laden cells from atherosclerotic aortas. (A) Lipid staining of atherosclerotic lesions. The lesions were first stained with BODIPY493/503 (green) and imaged and then subsequently stained with Oil Red O and imaged (red). **(B)** Gating strategy of lipid probe–based flow cytometry for detecting aortic foam cells. **(C)** Live/dead staining using Zombie Aqua showed that most autofluorescent cells were dead. **(D)** Cells with high granularity (SSC^{hi}) were strongly stained with BODIPY493/503. Aortic cells from B6, normal diet (ND)-fed LDLR KO, Western diet (WD)-fed LDLR KO, and ApoE KO mice were analyzed. This result is representative of at

least 3 independent experiments. **(E)** Aortic $SSC^{hi}BODIPY^{hi}$ cells were found in atherosclerotic intimal tissue but not in adventitia or normal aorta. The separation of adventitia from aorta was performed by partial enzyme digestion. $SSC^{hi}BODIPY^{hi}$ foam cells were counted by flow cytometry (n=9 per group). DAPI indicates 4',6-diamidino-2-phenylindole; FSC, forward side cytometer; SSC, side-scattered light; and WT, wild type.

3. 4. 3 Assessment of Atherosclerosis in Mouse Models, Using Lipid Probe-Based Flow Cytometry

We next examined whether atherosclerosis can be quantitatively assessed by our flow cytometric approach in LDLR KO and ApoE KO mice fed a WD for 4, 8, or 12 weeks. In WD-fed ApoE KO and LDLR KO mice, total cholesterol and LDL levels were dramatically increased (**Supplemental figure 3.4A**). As shown in **Supplemental figure 3.3B**, atherosclerotic lesions in the aorta were marginal at 4 weeks but markedly increased after 8 and 12 weeks. In flow cytometric analysis, the number of $SSC^{hi}BODIPY^{hi}$ foam cells in these mice gradually increased (**Figure 3.3A and 3.3B**). We compared atherosclerosis assessment using our flow cytometric method with the classic measurement of atherosclerotic lesions by Oil Red O staining and found that the 2 methods were comparable in assessing the severity of atherosclerosis (**Figure 3.3A and 3.3B**). The aortic foam cells were divided into $CD45^+$ and $CD45^-$ populations (**Supplemental figure 3.5A**). Of the total foam cells in ApoE KO and LDLR KO mice fed a WD for 12 weeks, 90.5±1.6% and 80.8±5.5% were $CD45^+$, respectively. A prolonged WD decreased $CD45^+$ cells to 67.2±6.2% of the total foam cells. In $CD45^+$ foam cells, 98.7±0.5% (ApoE KO; 12-week WD), 96.9±2.5% (LDLR KO; 12-week WD), and 93.9±2.5% of cells (LDLR KO; 33-week WD) were $CD11b^+CD64^+$ (**Supplemental figure 3.5B**). We then compared the time-dependent changes in abundance of $CD11b^+CD64^+SSC^{hi}BODIPY^{hi}$ foamy macro- phages and total aortic macrophages (**Figure 3.3C through 3.3E**). Whereas the number of foamy macrophages was markedly increased in WD-fed mice (≤100–1000-fold), the total number of aortic macrophages only showed a slight change (**Figure 3.3D and 3.3E, left**). We further assessed atherosclerotic lesions in a transgenic mouse model expressing a gain-of-function D374Y- hPCSK9 (D374Y mutant form of human proprotein convertase subtilisin/kexin type 9) with elevated plasma total cholesterol, triglyceride levels, and atherosclerotic lesions (**Supplemental figure 3.4A and 3.4C**).[27, 28, 29,

[30] The number of SSC^{hi}BODIPY^{hi} foam cells was significantly increased in D374Y-hPCSK9 transgenic mice (10574±3738 cells per aorta) compared with that in WT (wild type) controls (343±136 cells per aorta; **Supplemental figure 3.4C**). During foam cell formation, cellular granularity and size can increase through the accumulation of lipid droplets. Because flow cytometric analysis can be used to monitor the relative granularity and size of cells through analysis of forward side cytometer and SSC parameters, respectively, we compared the granularity and size of foam cells in mice fed a WD for 4, 8, and 12 weeks and divided the foam cells into 4 groups (**Supplemental figure 3.6A and 3.6B**). In ApoE KO mice, small foam cells with high granularity (P4) were markedly increased between 4 and 8 weeks (**Supplemental figure 3.6A**). Similarly, LDLR KO mice fed a WD showed increased levels of small foam cells with high granularity (**Supplemental figure 3.6B**). These results indicate that aortic phagocytic cells take up and accumulate more lipids in their cytosols during atherosclerosis progression.

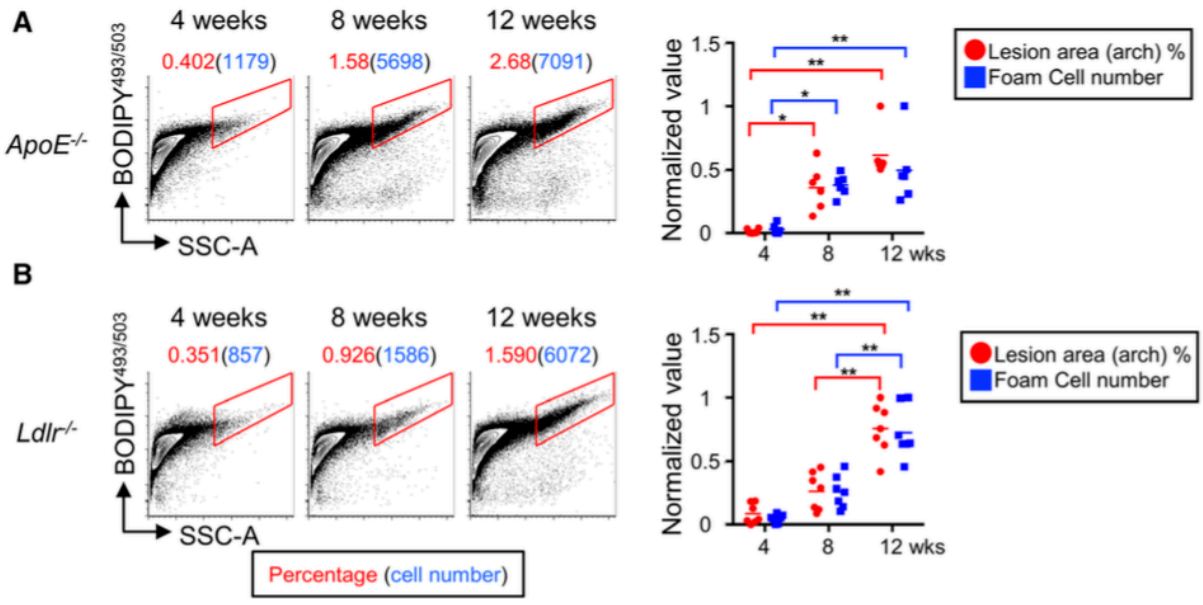

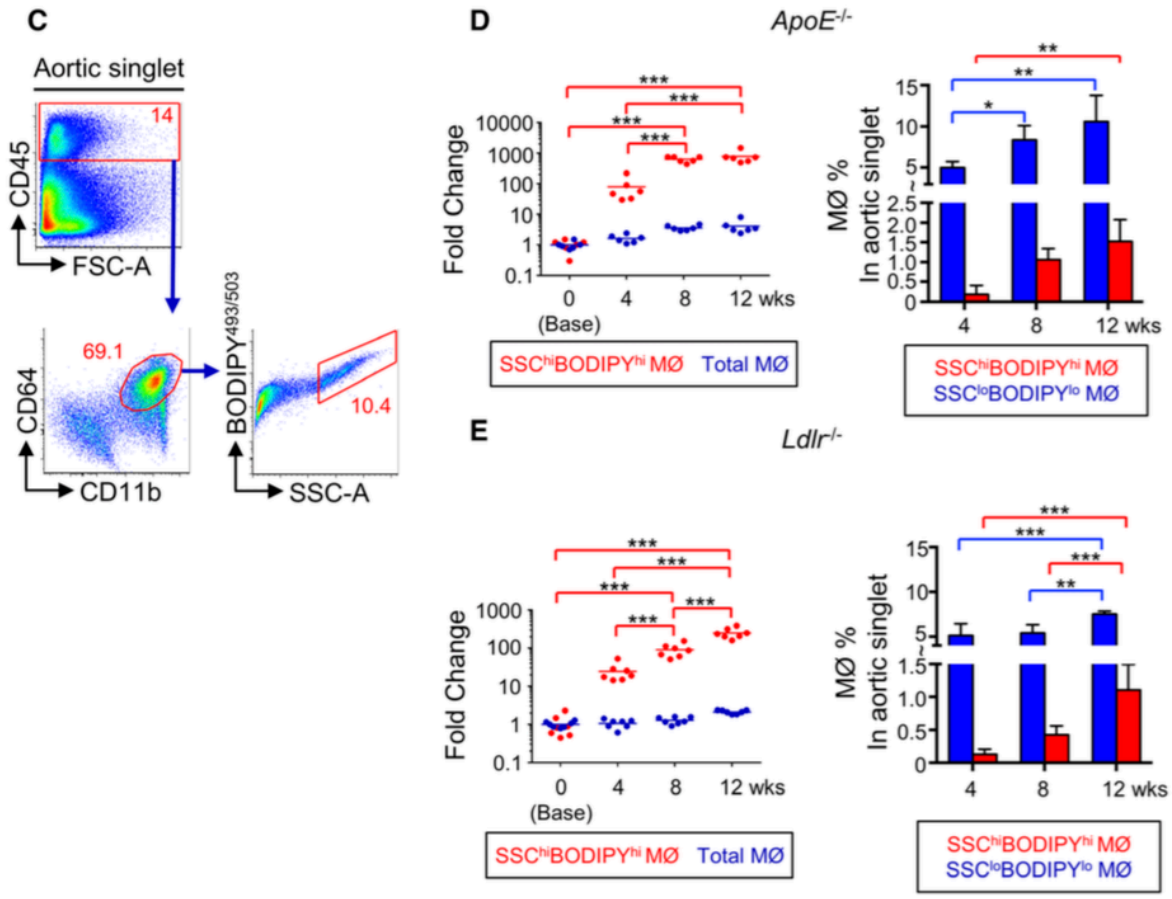

Figure 3.3. The frequency of SSC^{hi}BODIPY^{hi} cells is positively correlated with the severity of atherosclerosis. (A and B) Comparison of atherosclerosis assessment by en face Oil Red O staining and lipid probe–assisted flow cytometry in ApoE KO (n=6) and LDLR KO (n=7) mice. **Left**: Increase in SSC^{hi}BODIPY^{hi} foam cells (red, percentage of foam cells; blue, number of foam cells) during a Western diet (WD) for 4, 8, or 12 wk. **Right**: Similarity between atherosclerosis assessment by flow cytometry and en face Oil Red O staining. The size of the Oil Red O-stained area (red) and number of foam cells (blue) were normalized to between 0 and 1. **P*<0.01, ***P*<0.001. **(C)** Gating strategy to identify foamy macrophages (MØs) from whole atherosclerotic aorta. **(D and E)** Comparison of abundance changes in aortic foamy MØs and total aortic MØs in ApoE KO (n=6) and LDLR KO (n=7) mice. **Left** (dot graph): Fold changes compared with cells at the 0 time point (t_0=0 wk; base=1). The number of foamy MØs (red) dramatically increased during WD. **Right** (bar graph): Percentages of foamy (red) and non-foamy (blue) MØs in total aortic singlets at each time point (4, 8, and 12 wk). FSC indicates forward side cytometer; and SSC, side-scattered light. **P*<0.05, ***P*<0.01, ****P*<0.001.

3. 4. 4 Evaluating The Therapeutic Potential of Anti-atherosclerotic Treatments Using Lipid Probe-Based Flow Cytometry

We examined whether our method can be used to evaluate the therapeutic potential of antiatherogenic drugs. We treated LDLR KO mice for 10 weeks with atorvastatin or rosuvastatin, which are 2 representative HMG-CoA reductase inhibitors used to treat atherosclerosis.[31] The administration of statins effectively attenuated atherosclerosis (**Supplemental figure 3.7**), and the number of foam cells significantly decreased by atorvastatin (2454±1109 cells per aorta) and rosuvastatin (2172±704 cells per aorta) treatment compared with that of control PBS-injected mice (6356±1032 cells per aorta; **Supplemental figure 3.8A**). Foamy macrophage numbers also significantly decreased by atorvastatin (1908±982 cells per aorta) and rosuvastatin (1693±621 cells per aorta) treatment compared with that of PBS controls (4828±802 cells per aorta; **Supplemental figure 3.8A**). We next analyzed the foam cells of a plaque regression model by injecting ApoE KO mice with adeno-associated viral vectors encoding *apoE*6 (**Supplemental figure 3.8B and 3.8C**). The number of foam cells and foamy macrophages were markedly decreased in the adeno-associated viral vectors encoding *apoE* group compared with that in the control group (**Supplemental figure 3.8B**). 2-hydroxypropyl-β-cyclodextrin (CD) has been reported to induce the plaque regression by removing cholesterol crystals[32, 33, 34], lowering intracellular cholesterol levels in vivo[35] and inducing macrophage reprogramming and LXR (liver X receptor)-dependent atheroprotection.[36] LDLR KO mice with advanced atherosclerosis (WD for 25 weeks) were injected with CD (2 g/kg body weight) or PBS (vehicle control) for 8 weeks on a WD. CD treatment did not alter body weight (data not shown) but significantly decreased the number of aortic foam cells (1766±529 cells per aorta) compared with that in PBS controls (3138±1114 cells per aorta; **Supplemental figure 3.8D**). These results indicate that our flow cytometric method can be used to evaluate the antiatherogenic potential of drug candidates.

3. 4. 5 $CD45^{+}SSC^{hi}BODIPY^{hi}$ Foam Cells Mostly Originate From Macrophages

Although most $CD45^{+}$ foam cells were $CD11b^{+}CD64^{+}$ macrophages, we examined whether other immune cells can participate in foam cell formation. As we reported previously[37], aortic $CD45^{+}$ immune cells included macrophages ($CD11b^{+}CD64^{+}$), plasmacytoid DCs ($PDCA1^{+}B220^{int}Ly6c^{+}CD11b^{-}CD64^{-}$), DCs ($CD64^{-}CD11c^{+}MHCII^{+}$), monocytes ($CD64^{-}CD11c^{-}CD11b^{+}Ly6c^{lo\text{-}hi}$), neutrophils ($CD11b^{+}CD64^{-}Ly6G^{+}$), T cells ($CD11b^{-}CD64^{-}CD3^{+}$), and B cells ($CD11b^{-}CD64^{-}MHCII^{+}B220^{+}$; **Figure 3.4A**). Unlike macrophages, other immune cells were SSC^{lo} and $BODIPY^{lo}$ except very few DCs and monocytes (**Figure 3.4B**). In the t-distributed stochastic neighbor embedding plot produced by fluorescence-activated cell sorting data, most $CD45^{+}$ foam cells were found in the $CD11b^{+}CD64^{+}$ macrophage population (**Figure 3.4C; Supplemental figure 3.5B**). Collectively, these results support the notion that most atherosclerotic foamy leukocytes originate from macrophages. Furthermore, $SSC^{hi}BODIPY^{hi}$ foamy macrophages showed relatively higher levels of CD11c than did non-foamy macrophages (**Figure 3.5A**). T-distributed stochastic neighbor embedding analysis confirmed that foamy macrophages are $CD11c^{+}$ macrophages (**Figure 3.5B**). Importantly, the cytosol of aortic $SSC^{hi}BODIPY^{hi}$ macrophages sorted out from atherosclerotic aorta contained abundant lipid droplets, whereas cytosol lipid droplets in $SSC^{lo}BODIPY^{lo}$ macrophages were scant (**Figure 3.5C**). $CD11c^{+}$ foamy macrophages were in the atherosclerotic lesion area (**Figure 3.5D**), and immunostaining CD206 and CD11c showed that most $CD11c^{+}$ cells were found in the intimal lesion area, whereas $CD206^{+}$ cells were located in the adventitia (**Figure 3.5E and 3.5F; Online movie 3.1; Supplemental figure 3.2C**). When we analyzed macrophage populations in CD-treated mice, we found that CD treatment effectively decreased both foamy macrophages and non-foamy macrophage levels. $CD11c^{+}$ non-foamy macrophages were more susceptible than $CD206^{+}$ non-foamy macrophages to CD treatment (**Supplemental figure 3.8E**). We then separated aortic intimal tissue and adventitia and analyzed their macrophage populations using flow cytometry (**Figure 3.5G**). The adventitia of atherosclerotic aortas contained $CD206^{+}$ macrophages (**Figure 3.5E and 3.5G**), whereas $CD11c^{+}$ macrophages were mostly found in intimal tissue (**Figure 3.5G**).

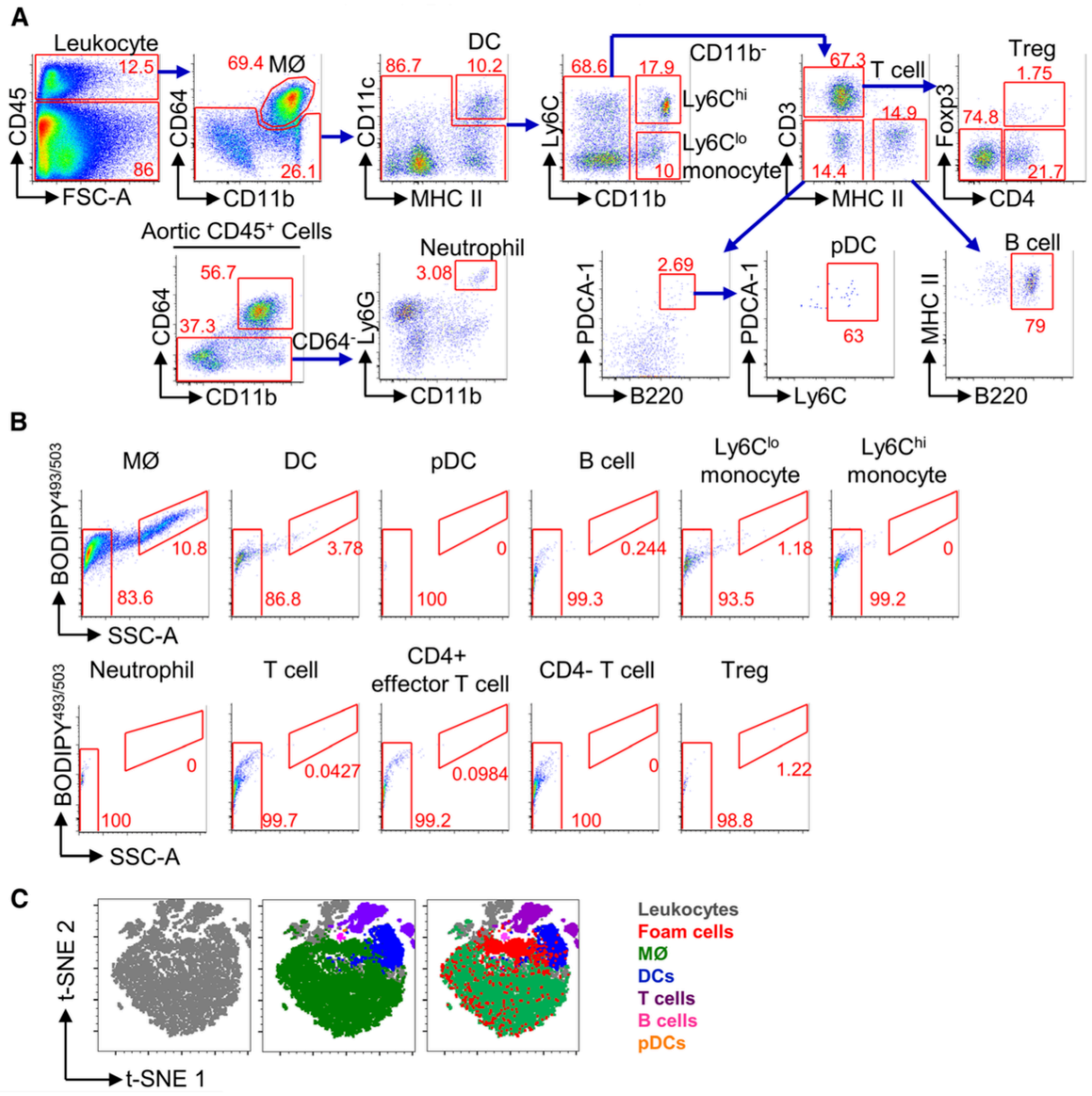

Figure 3.4. CD45^{+}SSC^{hi}BODIPY^{hi} leukocytes originate from macrophages (MØs). (A) Gating strategy to identify immune cell populations, including MØs, dendritic cells (DCs), plasmacytoid DCs (pDCs) monocytes, T cells, regulatory T cells (Tregs), B cells, and neutrophils from whole atherosclerotic aorta. **(B)** Representative plots of side-scattered light (SSC) and BODIPY levels from aortic immune cells in atherosclerosis. **(C)** t-distributed stochastic neighbor embedding (t-SNE) analysis of fluorescence-activated cell sorting (FACS) data. The colored clusters correspond to each leukocyte population. CD45^{+}SSC^{hi}BODIPY^{hi} foam cells (red) mostly overlapped with the MØ population. The results are representative of at least 3 independent experiments. FSC indicates forward side cytometer; Ly6C, lymphocyte antigen 6; MHC II, major histocompatibility complex II; and PDCA-1, plasmacytoid dendritic cell antigen 1.

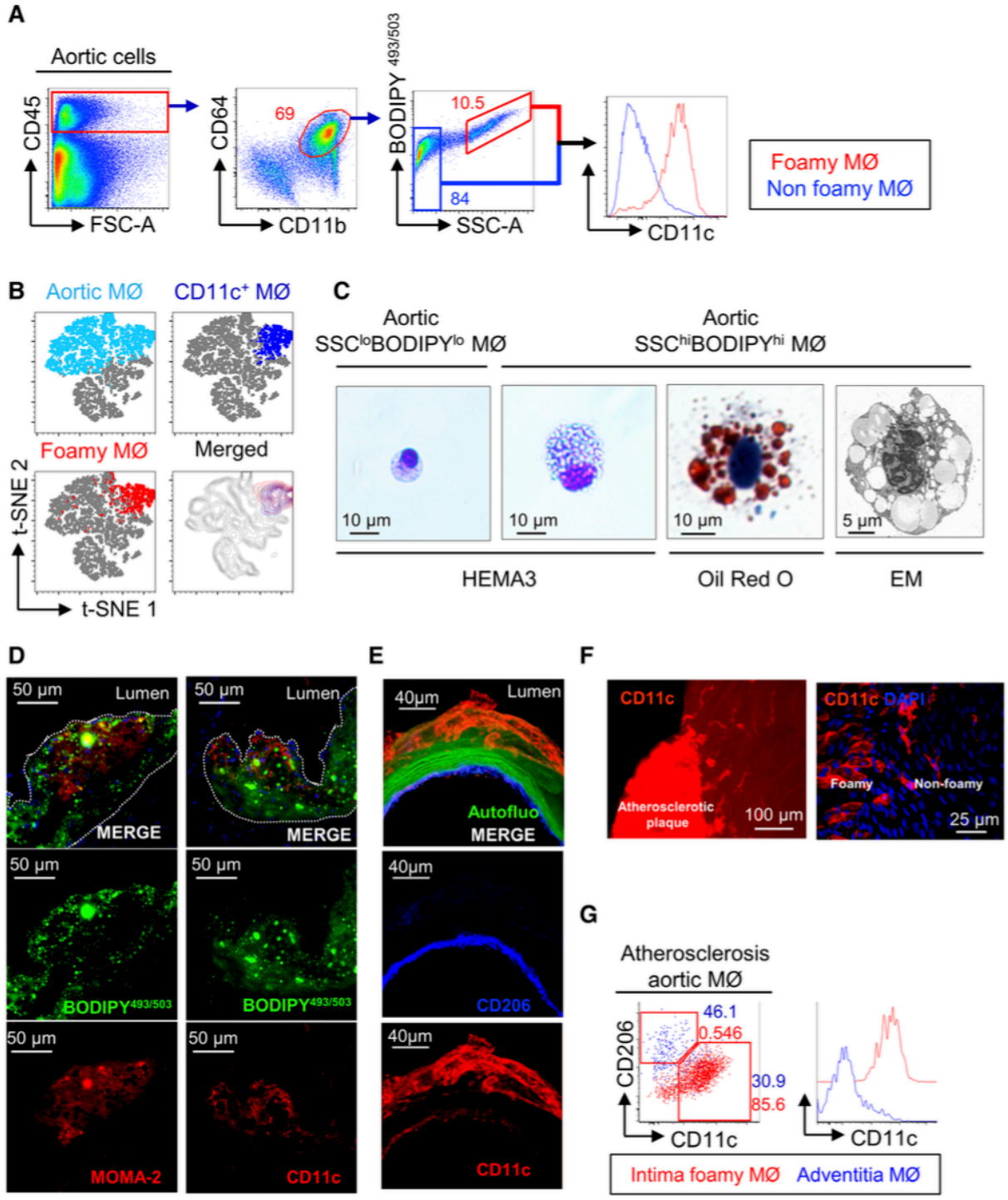

Figure 3.5. SSC^{hi}BODIPY^{hi}CD11c^{+} macrophages (MØs) contain cytosolic lipid droplets and reside in the atherosclerotic intima. (A) Flow cytometric detection of foamy MØs from LDLR KO mice fed a Western diet for 12 wk. Foamy MØ (red box) CD11c levels were higher than in non-foamy MØs (blue box). These plots represent of data from 6 atherosclerotic aortas.

(B) t-distributed stochastic neighbor embedding (t-SNE) analysis of fluorescence-activated cell sorting (FACS) data. The majority of foamy MØs (red) overlapped with $CD11c^+$ MØs (blue). These figures are representative of 3 experiments. **(C)** Morphology of aortic $SSC^{hi}BODIPY^{hi}$ and $SSC^{lo}BODIPY^{lo}$ MØs. $SSC^{hi}BODIPY^{hi}$ and $SSC^{lo}BODIPY^{lo}$ cells were sorted from atherosclerotic aortas (n=3), stained with Hema 3 (**left**) or Oil Red O (**middle**), and analyzed by optical or transmission electron microscopy (EM). **(D)** Immunofluorescence staining of CD11c and MOMA-2 (antimacrophage/monocyte antibody). Lesional $CD11c^+$ and $MOMA\text{-}2^+$ cells (red) were costained with BODIPY493/503 (green). **(E)** Immunofluorescence staining of CD11c (red) and CD206 (blue) in an atherosclerotic aortic arch. CD11c (red) staining was mostly detected in the aortic lesion and some adventitial areas. The green signal is autofluorescence. **(F)** Whole-mount immunostaining of CD11c in intimal lesions. **(G)** Comparison of CD206 and CD11c expression in adventitial MØ (blue) and intimal foamy MØs (red). FSC indicates forward side cytometer; and SSC, side-scattered light.

We next examined the proportional changes of intimal foamy ($CD64^+$ $CD11b^+$ SSC^{hi} $BODIPY^{hi}$) and non-foamy ($CD64^+$ $CD11b^+$ SSC^{lo} $BODIPY^{lo}$) macrophages during atherosclerosis progression (**Supplemental figure 3.9A**). Intimal macrophages were gradually increased in aortic intima of LDLR KO mice fed WD for 12 and 24 weeks (2001±936 versus 4817±550 cells per aorta, respectively; *P*=0.017; **Supplemental figure 3.9B**). The percentage of foamy macrophages in total intimal macrophages was not markedly increased at 24 weeks compared with 12 weeks (12 weeks, 18.5±11%; 24 weeks, 23.8±4.9%; *P*=0.26; **Supplemental figure 3.9B**).

3. 4. 6 RNA-seq Uncovers Distinct Gene Expression Between Intima Foamy and Non-foamy Macrophages in Atherosclerosis

To analyze the transcriptomic profile of intimal foamy and non-foamy macrophages, live (propidium $iodide^-$) SSC^{hi} $BODIPY^{hi}$ foamy macrophages and SSC^{lo} $BODIPY^{lo}$ non-foamy macrophages were simultaneously isolated from adventitia-removed atherosclerotic aortas (**Figure 3.6A**). We performed RNA-seq on the 2 populations (GSE116239) and found that non-foamy and foamy macrophages had different degrees of variation in their expressed genes (**Figure 3.6B and 3.6C; and Online data set 3.3**). Non-foamy and foamy macrophages had different numbers of DEGs, with 580 genes for foamy macrophages and 748 genes for the non-foamy macrophages (adjusted *P* value [*P* adj], <0.05; **Figure 3.6C and 3.6D**).

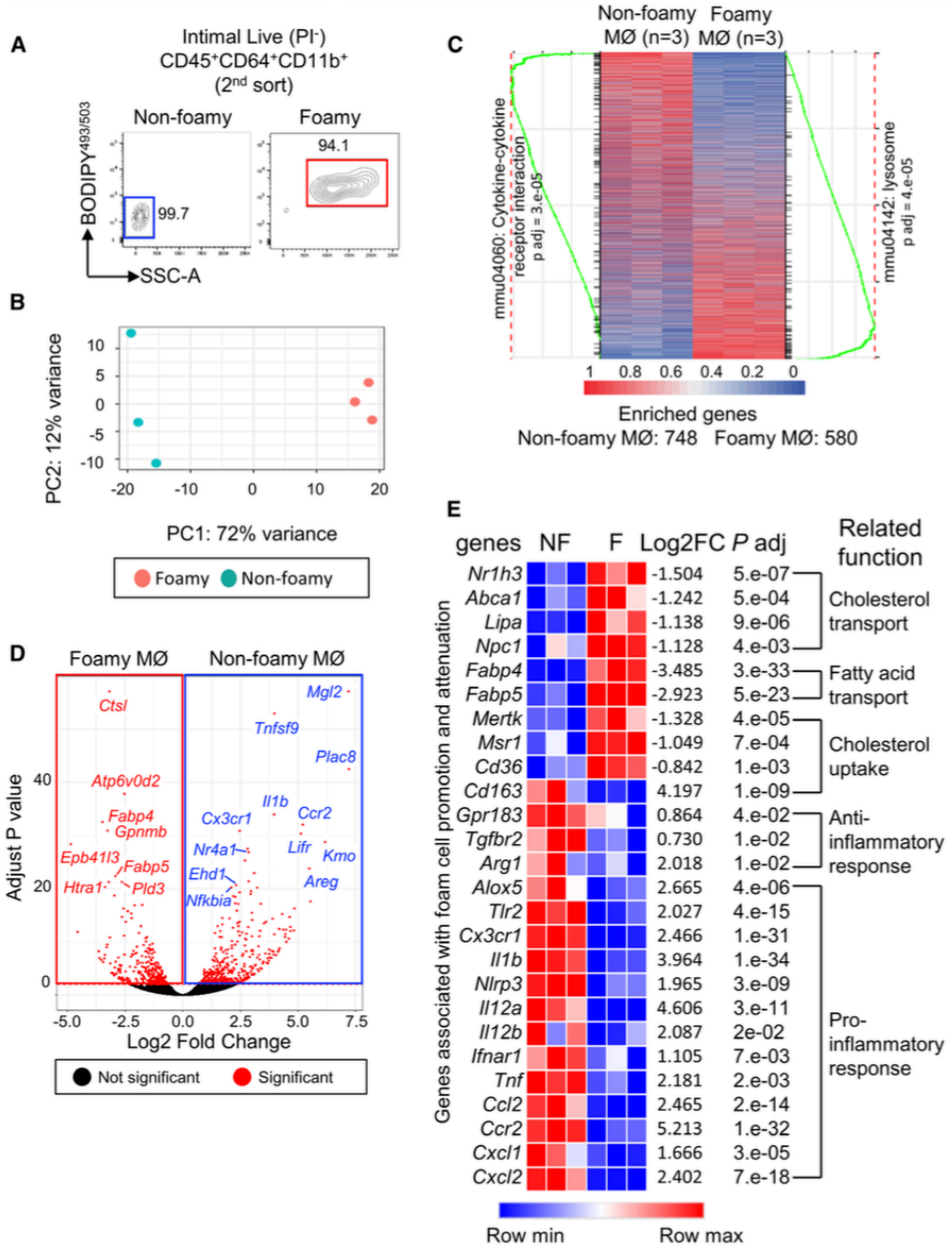

Figure 3.6. Transcriptome profiling reveals distinct gene expression between intimal foamy (F) and non-foamy (NF) macrophages (MØs) in atherosclerosis. (A) Fluorescence-activated cell sorting (FACS) of live (propidium iodide [PI-]) $SSC^{lo}BODIPY^{lo}$ and $SSC^{hi}BODIPY^{hi}$ MØs from the aortic tissues without adventitia of ApoE KO mice (n=6) fed a Western diet for 28 wk. **(B)** Principal component analysis (PCA) of variances in the bulk RNA-seq dataset of intima F and NF MØs. PCA plot was generated using the 500 most variable genes. **(C)** Differential expression between F and NF MØs represented as a heatmap

(genes are sorted by T statistic). Gene Set Enrichment Analysis (GSEA) plots for 2 representative Kyoto encyclopedia of genes and genomes (KEGG) pathways (cytokine-cytokine receptor interaction for NF MØs and lysosome for F MØs) are shown next to the heatmap. **(D)** Volcano plot of genes enriched in each cell group. Genes with adjusted *P* values <0.05 (red) are arranged by their *P* values and fold changes (log2). **(E)** Heatmap of representative genes involved in foam cell formation during atherosclerosis, as assessed by a comparison between intimal NF and F MØs. Genes were enriched in each NF or F MØ group with an adjusted *P* <0.05. The fold change of each gene (log2FC) and adjusted *P* value (*P* adj) were shown with the heatmap. PC1 and PC2 indicate principal component 1 and 2; and SSC, side-scattered light.

We then analyzed the expression of genes related to cholesterol and fatty acid transport, cholesterol uptake, and proinflammatory and anti-inflammatory responses and found that the 2 populations showed markedly different gene expression profiles (**Figure 3.6E; Online data set 3.3; Supplemental figure 3.10**).[38] Furthermore, the expression of some genes related to efferocytosis, such as *Cd36*, *Mertk*, and *Nr1h3*, was found elevated in foamy macrophages, whereas genes like *Ccl2*, *Ccr2*, and *Abca7* were downregulated. The inflammatory genes, such as *I1b*, *Nfkbia*, *Tlr2*, and *Tnf*, were mostly upregulated in non-foamy macrophages. In contrast, resolving/regression-related genes were upregulated in foamy macrophages compared with that in non-foamy macrophages (**Supplemental figure 3.10**). Next, we compared the gene expression signatures of foamy and non-foamy intimal macrophages with those of each scRNA-seq cluster. The top 100 DEGs enriched in foamy macrophages were mostly found in cluster 4, whereas many of those from non-foamy macrophages were specifically expressed in cluster 1 (**Figure 3.7A; Online data set 3.3**). This suggests that scRNA-seq cluster 4 represents the intima foamy macrophages, and cluster 1 corresponds to intima non-foamy macrophages.

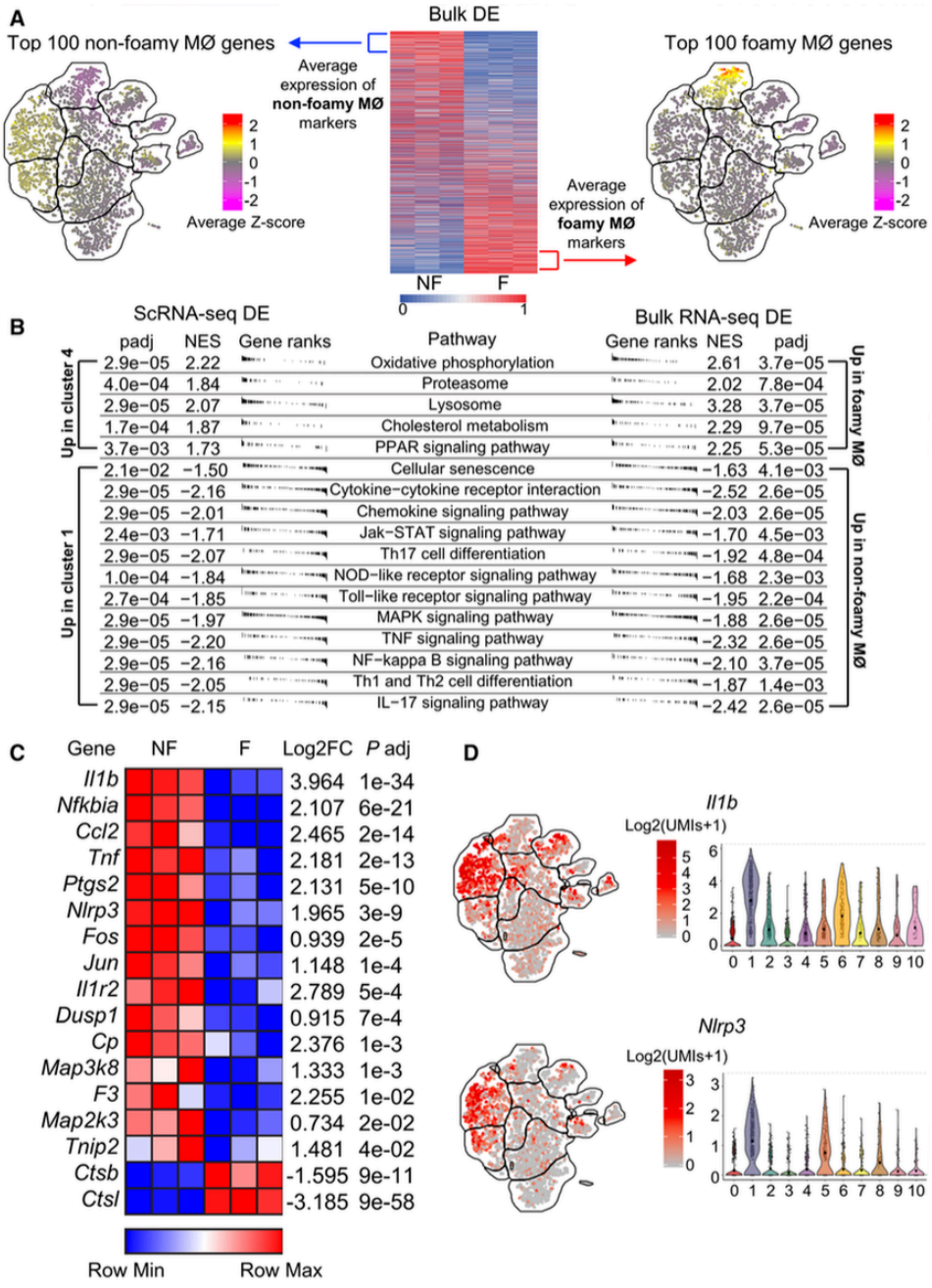

Figure 3.7. Intimal non-foamy (NF) macrophages (MØs), rather than foamy (F) MØs, are proinflammatory. (A) Top 100 (**left**) and bottom 100 (**right**) genes sorted by T statistics from bulk RNA-seq were used to identify clusters corresponding to F and NF MØs in the single-cell RNA sequencing (scRNA-seq) dataset. Averaged normalized expression of these gene is shown as a t-distributed stochastic neighbor embedding plot with colors corresponding to averaged normalized expression. **(B)** Enriched KEGG pathways comparing cluster 1 with cluster 4 in the scRNA-seq dataset (**left**) or comparing F MØs with NF MØs (**right**). All pathways listed are statistically significant in both comparisons (adjusted *P*, 0.01). **(C and D)**

Analysis of IL-1β signaling pathway genes in bulk RNA-seq **(C**; heatmap**)** and scRNA-seq **(D**; plots**)**. The genes were enriched in each NF or F MØ groups (adjusted *P*, <0.05) or each cluster (adjusted *P*, <0.01; logFC, >0). DE indicates different expression of genes; IL, interleukin; MAPK, mitogen-activated protein kinase; NES, normalized enrichment score; NF kappa B, nuclear factor κB; NOD, nucleotide-binding oligomerization domain; PPAR, peroxisome proliferator-activated receptor; RNA-seq, RNA sequencing; STAT, signal transducer and activator of transcription proteins; Th, type of helper T cell; and TNF, tumor necrosis factor.

3. 4. 7 Intimal Non-foamy Macrophages and Not Foamy Macrophages Are Proinflammatory

In gene set enrichment analysis of DEGs, foamy macrophages expressed fewer inflammation-related genes than intimal non-foamy macrophages, whereas genes related to lipid metabolism and transport pathways, including cholesterol metabolism (*P* adj, 9.7e-05), and PPAR signaling pathways (*P* adj, 5.3e-05), such as *Abca1*, *Fabp4*, *Lipa*, and *Mertk*, were highly expressed (**Figures 3.6E and 3.7B**). Moreover, foamy macrophages showed increased expression of genes related to oxidative phosphorylation (*P* adj, 3.7e-05), lysosome (*P* adj, 3.7e-05), and proteasome (*P* adj, 7.8e-04; **Figure 3.7B**). In contrast, intimal non-foamy macrophages were enriched in genes involved in inflammatory processes, including cytokine-cytokine receptor interaction (*P* adj, 2.6e-05), NF-κB signaling (*P* adj, 3.7e-05), IL-17 signaling (*P* adj, 2.6e-05), TLR signaling (*P* adj, 2.2e-04), and TNF signaling pathways (*P* adj, 2.6e-05; **Figures 3.6E and 3.7B, and Supplemental figure 3.11A**).

Recent successful clinical trials on IL-1β targeted therapy prompted us to compare the expression of inflammasome-related genes in foamy and non-foamy macrophages.(39) In bulk RNA-seq analysis, inflammasome-related genes were upregulated in non-foamy macrophages rather than in foamy macrophages (**Figure 3.7C**). Likewise, the expression of *IL1*β and *Nlrp3* was mostly enriched in scRNA-seq cluster 1 (**Figure 3.7D; Supplemental figure 3.11B**). Thus, we attempted to analyze IL-1β mRNA expression in human and mouse atherosclerotic lesions by in situ hybridization. We found that IL-1β mRNA expression was downregulated in foamy $CD68^+$ macrophages compared with that of non-foamy macrophages in human atheroma (**Figure 3.8A and 3.8B**). Likewise, foam cells poorly expressed IL-1β mRNA in mouse atherosclerotic plaque (**Figure 3.8C**). Moreover, quantitative polymerase chain

reaction analysis on sorted foamy and intimal non-foamy macrophages demonstrated that non-foamy macrophages expressed *IL1*β, whereas foamy macrophages did not (**Figure 3.8D**). These results suggest that intimal non-foamy macrophages, rather than foamy macrophages, are inflammatory in atherosclerotic lesions.

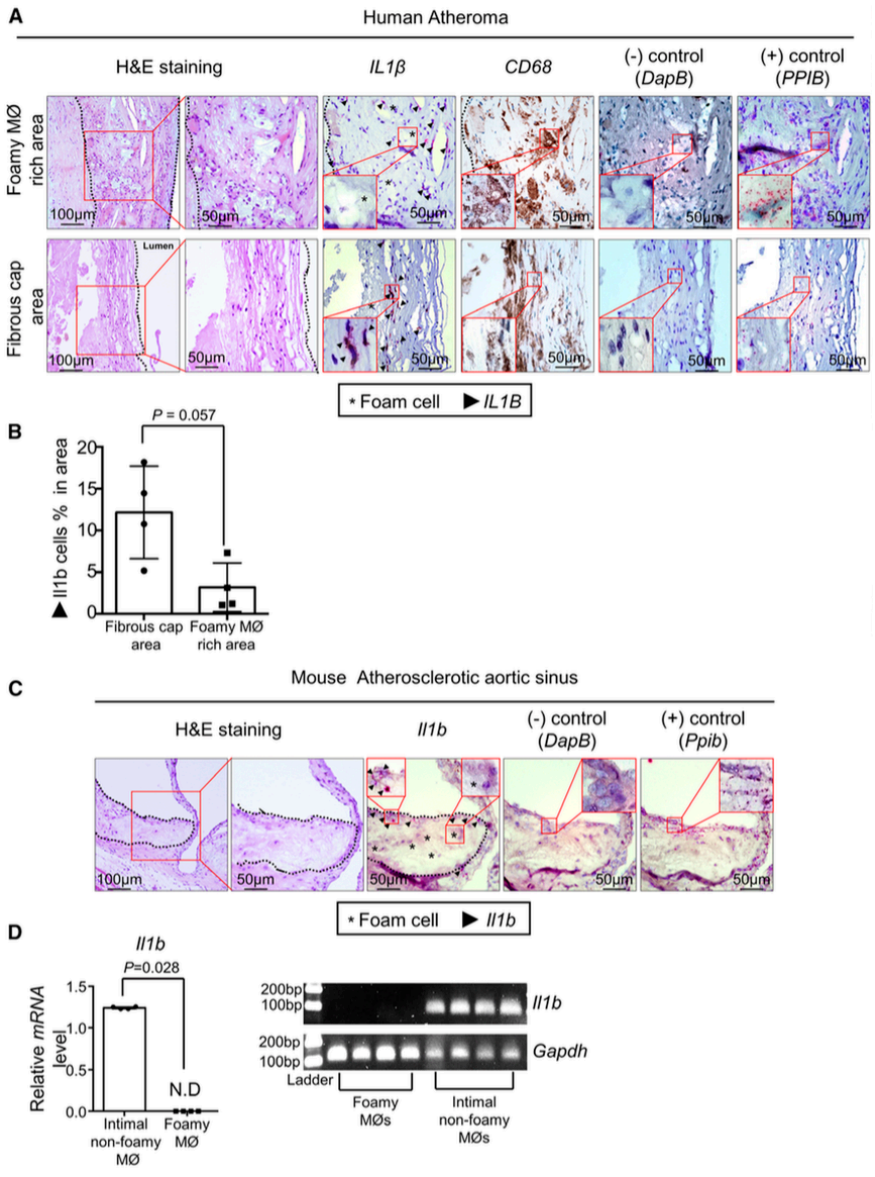

Figure 3.8. IL-1β mRNA expression in human and mouse atheroma. (A) Localization of IL-1β mRNA in human atheroma (n=4). CD68 (DAB staining) and H&E staining was performed to identify foamy macrophage (MØ)-rich and fibrous cap regions with MØs. In situ hybridization for *DapB* and human *PPIB* was performed as negative and positive controls,

respectively. Stars indicate foam cells, and arrow heads mark *IL1*β-stained cells. **(B)** The percentage of IL-1β mRNA-positive cells in CD68-positive areas of fibrous cap or foam cell-rich areas (5 different areas, 8.4×10^4 μm^2 each) in human atheroma (n=4). **(C)** IL-1β mRNA expression in mouse atheroma. The stars indicate foam cells, and the arrowhead indicates *IL1b*-stained cells. These figures are representative of 3 experiments. **(D)** Single-cell quantitative polymerase chain reaction (qPCR) analysis of IL-1β mRNA expression in foamy or intimal non-foamy MØs sorted from mouse atherosclerotic aorta. **Left**: mRNA expression was normalized to Gapdh mRNA levels (cells from 4 mice). **Right**: Gel analysis of qPCR end products; *IL1b* and *Gapdh*. DAB indicates 3,3'-diaminobenzidine; H&E, hematoxylin and eosin; IL, interleukin; N.D., not detected; and ND, normal diet.

3. 5 Discussion

The formation of foam cells and their role in atherosclerosis are important topics of discussion when we seek to understand atherosclerosis pathogenesis and in exploring new therapeutic targets. Immune cells that are recruited to the subintimal space appear to create an inflammatory environment that affects lesion formation and deterioration.[5, 8, 9] Therefore, the targeting of inflammatory cells is potentially an effective therapeutic regimen for attenuating atherosclerosis. Although statins are currently used to control blood lipid levels as a major treatment for atherosclerosis, a recent clinical trial of IL-1β–targeting antibody showed promising results in attenuating atherosclerosis.[39] This indicates that atherosclerosis can be treated by an inflammation-regulating drug without controlling blood lipid levels. Clearly, we need to better understand the role of inflammatory cells in atherosclerosis.

Recently, 2 intriguing studies using scRNA-seq demonstrated the heterogeneity of leukocyte populations in atherosclerotic aorta containing macrophages, DCs, T cells, B cells, NK cells, and granulocytes.[40, 41] However, in our scRNA-seq data, macrophages were found to compose the largest immune cell population in atherosclerotic aorta, whereas the identification of B cells, NK cells, and neutrophils was failed. In our fluorescence-activated cell sorting analysis, macrophage was also the largest cell population in aortic $CD45^+$ immune cells (**Figure 3.4A; Supplemental figure 3.12**). Actually, the composition of $CD45^+$ leukocyte populations sorted from tissue can vary depending on how the cells are isolated from the tissue, that is, type and concentration of digestive enzymes, digestion time, and pore size of strainer. Because the aim of this study was to examine the transcriptome of macrophage populations in aortic tissue, we used a higher concentration of the enzyme mixture and longer digestion time than previous studies (**Supplemental table 3.2**). This means that our cell extraction method is more optimized for isolating macrophages that are more firmly attached to the aortic tissue than other immune cells. Because relatively small population may not be recovered in scRNA-seq analysis owing to technical limitation, our isolation method seems to be responsible for the difference in immune cell composition between our scRNA data and 2 previous data.

Various cellular markers for macrophages overlap with those of DCs, even though the 2 cell types are completely different in their functions. For example, CD11c (Itgax)-positive DCs are involved in the formation of early atherosclerotic lesions[42], whereas proinflammatory macrophages and foamy macrophages also express *Itgax* on the protein and mRNA level. In the absence of a clear method for separating foamy and non-foamy macrophages from atherosclerotic aorta, most previous studies used in vitro cultures of macrophage cell lines. Although such cultures reasonably mimic the foam cells of atherosclerosis, they do not recapitulate various in vivo microenvironmental factors that affect the formation or pathophysiology of foam cells in atherosclerotic lesions, as cell phenotypes can vary depending on the culture conditions. Indeed, in vivo studies have shown the changes in gene and protein expressions of foam cells directly extracted from the peritoneum of atherosclerotic mice.[21] Laser capture microdissection was found to recapitulate the specific propensity of in situ foam cells in lesions.[43] However, because many marker genes overlap between cell types, this method did not enable researchers to distinguish among the myeloid cells. Moreover, recent reports have indicated that smooth muscle cells (SMCs) can generate lesional foam cells that express some macrophage markers.[44] Foamy peritoneal macrophages were previously shown to be enriched for molecules involved in physical interaction and vesicular transport rather than lipid metabolism or proinflammatory responses.[45] Lipid-laden peritoneal macrophages exhibited upregulation of genes related to angiogenesis, lipid metabolism, and extracellular matrix organization, as well as downregulation of genes involved in inflammatory sterol metabolism, genes through desmosterol-induced activation of the LXR pathway.[21] In animal experiments, foamy macrophages recruited to subcutaneously inserted sponges showed upregulation of genes related to connective tissue development and function, cell growth, cell proliferation, and cholesterol metabolism (eg, *Abca1*, *Pparγ*, *Rxra*, *Rxrb*, and *Srebp1*).[46] Laser capture microdissection followed by transcriptome analysis showed that lesional foam cells were enriched for CD68 and CD14, negative for the SMC markers, α-actin and MYH11, and exhibited increased expressions of TNF, IL-1β, SR-A, ABCA1, and ADFP.[47] In a laser capture microdissection experiment comparing mice fed a high-cholesterol diet for 2 or 14 weeks, lesional foam cells showed upregulation of CXCL13 (CXC motif ligand 13) in the 2-week group and upregulation of GBPs (guanylate-binding proteins) in the 14-week group with no overall change in inflammatory genes expression.[43] Notably, however,

these laser capture microdissection experiments failed to clearly separate lesional foamy macrophages from other cell types.

In this study, foamy macrophages showed a strikingly reduced expression of inflammatory genes and increased expression of genes related to cholesterol uptake, processing, and efflux, whereas intimal non-foamy macrophages expressed elevated levels of genes encoding cytokines that are related to the recruitment of leukocytes to lesions and exacerbation of inflammation (eg, *IL1*β and *Nlrp3*), indicating that the inflammasome is activated. These results suggest that newly recruited macrophages promote lesion development by producing proinflammatory molecules. Considering the success of a recent clinical trial of an anti–IL-1β antibody canakinumab[39], it appears that highly proinflammatory intimal non-foamy macrophages may critically contribute to the development and progression of plaque, whereas foamy macrophages may try to defuse plaque progression by exhibiting enhanced lipid uptake and efflux until they undergo apoptotic cell death. To confirm the transcriptomic profiles of lesional macrophages and further characterize total foam cell populations containing $CD45^+$ and $CD45^-$ foam cells, we performed another scRNA-seq analysis (GSE116240, $ApoE^{-/-}$ aorta dataset) on isolated live total foam cells from atherosclerotic aorta. The gene expression profiles of $SSC^{hi}BODIPY^{hi}$ foam cells (n=809) sorted from pooled atherosclerotic aortas of ApoE KO mice (n=6) were successfully analyzed, and the cells were divided into 2 large groups containing 8 clusters (**Supplemental figure 3.13A**).

Clusters 2, 3, 4, 5, and 6 expressed *Ptprc* (CD45) and *Mafb*, indicating these clusters are foamy macrophages (**Supplemental figure 3.13B**). In agreement with our previous data, the clusters of foamy macrophages (clusters 2–6) expressed low levels of inflammatory genes like *IL1b*, *Nlrp3*, *Tnfsf9*, and *Nfkb1* (**Supplemental figure 3.13C**) but showed increased expression levels of *Lgals3*, *Ctsb*, *Itgax*, and *Trem2* (**Supplemental figure 3.13D**). Furthermore, we confirmed the expressions of the top 100 enriched genes of non-foamy or foamy macrophages in scRNA-seq data of total foam cells (**Supplemental figure 3.14A**). Whereas foamy macrophage genes were enriched in clusters 2 to 6, non-foamy macrophage genes were poorly expressed in these clusters. In accordance with our previous data, the functional enrichment analysis on scRNA data of total foam cells demonstrated that foamy

macrophages had increased expression of genes related to oxidative phosphorylation, cholesterol metabolism, lysosome, and proteasome (**Supplemental figure 3.14B**). Previously, macrophages contributing to lesion formation have been known to be mostly derived from circulating precursors and increase during disease progression.[48] But recently, local proliferation of macrophages importantly contributes to lesion formation during the atherogenesis.[49, 50] Interestingly, there was a macrophage subpopulation having increased expression of gene-related cell cycle and proliferation in our scRNA-seq data of $CD45^+$ aortic cells (**Figure 3.1A, cluster 8; Supplemental table 3.1**). In addition, a small foam cell subpopulation expressing high level of cell cycle/proliferation-related genes was also identified in scRNA-seq analysis on total mouse foam cells (**Supplemental figure 3.15A and 3.15B**, cluster 6). 5.8±2.8% of total foamy macrophages expressed KI-67 in foam cell-rich area of human atheroma. In fibrous cap area, 9.54±0.54% non-foamy macrophages were Ki-67 positive, which was slightly higher than the percentage of foamy macrophages. (**Supplemental figure 3.15C**). Thus, although macrophages seem to proliferate constantly irrespective of lipid accumulation, proliferation was more during the non-foamy stage. Thus, the proliferation of macrophages seems to happen constantly, regardless of their lipid accumulation, but it seems to occur more during non-foamy stage. However, further studies are required to understand the exact origin and characteristics of plaque macrophages. For instance, additional scRNA-seq analysis on lesional macrophages isolated from early or advanced plaques would be useful to dissect macrophage subsets in lesions and understand the phenotypic changes of macrophages during disease progression. Furthermore, fate-mapping experiments may be useful for tracing lesional macrophages and examining the origin of foamy and non-foamy macrophages, that is, whether foamy macrophages are generated mostly from non-foamy macrophages or a specific subset of macrophages.

In our scRNA-seq data of total foam cells, clusters 0 and 1 expressed *Tagln* and *Acta2*, whereas cluster 7 had high expression levels of *Pecam1* (**Supplemental figure 3.13B**). This result suggests that $CD45^-$ foam cells would be derived from SMCs and endothelial cells. Because previous reports suggested that vascular SMCs can also generate foam cells in atherosclerotic plaque[51, 52], we stained foam cells with SMC markers to define SMC derived-foam cells. In flow cytometric analysis, we found that foam cells included $CD45^-$ cells

expressing αSMA (α-smooth muscle; **Supplemental figure 3.16A**). In atherosclerotic plaque, some $BODIPY^+$ cells also expressed SM22α (smooth muscle protein 22 alpha)—another SMC marker (**Supplemental figure 3.16B and 3.16C**). These results indicate that although a large proportion of foam cells is derived from macrophages, SMCs also contribute to foam cell formation.

Collectively, we first established a lipid probe–based flow cytometric method for analyzing foamy macrophages of the atherosclerotic intima to further enable transcriptomic profiling of intimal foamy and non-foamy macrophages. Our RNA-seq analysis revealed for the first time that macrophage subtypes of atherosclerotic aorta exhibit distinct transcriptomic profiles according to their lipid content. Although we showed attenuated *IL1*β expression in foamy macrophages in human atherosclerotic lesions, the transcriptomic profile of human lesional macrophages remains to be elucidated. Actually, the preparation of foamy and non-foamy macrophages for scRNA-seq or bulk RNA-seq analyses from human atherosclerotic aorta is still highly challenging. But it is very important to demonstrate whether the transcriptomic profiles of human foamy and non-foamy macrophages are comparable with those of murine counterparts, which will provide new immunologic insights on the innate immune responses that take place in atherosclerosis.

3. 6 Methods

3. 6. 1 Mice

ApoE$^{-/-}$, *Ldl*$^{-/-}$, CX3CR1-GFP, LysM-Cre and ROSA26tdTomato mice (C57BL6/J background) were obtained from Jackson Laboratory (Bar Harbor, ME). D374Y-hPCSK9 transgenic mice (C57BL6/J background) were obtained from Dr. Anne K. Soutar.[29] All mice were maintained under specific pathogen-free conditions. Mice were randomly assigned to either experimental or control group, using a single sequence of simple randomization assignments. Western diet (WD) (49.9% carbohydrates, 17.4% protein, 20% fat, and 0.15% cholesterol) was obtained from Test Diet (cat. AIN-76A; St. Louis, MO). D374-hPCSK9 mice were fed a WD for 19 weeks, whereas *ApoE*$^{-/-}$ and *Ldlr*$^{-/-}$ mice were fed a WD as indicated for each experiment. To assess the effects of drugs on atherosclerosis, *Ldlr*$^{-/-}$ mice were fed a WD for 10 or 12 weeks and intraperitoneally injected with atorvastatin or rosuvastatin (10 g/kg body weight) twice a week during WD feeding. The control mice were injected with phosphate-buffered saline (PBS; 200 μL). *Ldlr*$^{-/-}$ mice fed a WD for 25 weeks were injected subcutaneously with 2-hydroxypropyl-ß-cyclodextrin (CD; 2g/kg body weight, H-107; Sigma-Aldrich, St. Louis, MO) or PBS (200 μL) twice a week for an additional 8 weeks on a WD.[36] For the plaque-regression model, *ApoE*$^{-/-}$ mice were fed a WD for 22 weeks, intravenously injected with adeno-associated virus 8 (AAV8; 1×10^{12} genome copies) and sacrificed 3 weeks later. Male mice were used to minimize hormonal effects (e.g., of estrogen). All animal protocols were approved by the Institutional Animal Care and Use Committee of Hanyang University, Seoul, Korea; the Institut de Recherches Cliniques de Montréal, Montreal, Canada; the Washington University School of Medicine, St. Louis, MO.

3. 6. 2 Human Samples

Atherosclerotic aortic tissues were obtained from patients after receipt of written informed consent in accordance with the Declaration of Helsinki. The study protocol was

approved by the Institutional Review Board of Seoul National University hospital, Seoul, Korea.

3. 6. 3 Antibodies and Reagents

The biotinylated anti-CD11c antibody (clone HL3; cat. 553800) was obtained from BD Biosciences (Franklin Lakes, NJ). Antibodies against CD16/32 (clone 93; cat. 101320), CD45 (clone 30-F11; cat. 103113), CD11b (clone M1/70; cat. 101241), CD11c (clone N418; cat. 117335), CD64 (clone X54- 5/7.1; cat. 139307), MHCII (clone M5/114.15.2; cat. 107621), CD206 (clone C068C2; cat. 141712), CD3 (clone 17A2; cat. 100245), CD4 (clone GK1.5; cat. 100426), PDCA-1 (clone 927; cat. 127019), B220 (clone RA3-6B2; cat. 103244), Ly6G (clone 1A8; cat. 127612) and Ly6C (clone HK1.4; cat. 128031) were obtained from BioLegend (San Diego, CA). The anti-FoxP3 antibody (clone FJK-16s; cat. 17-5773-82) and FoxP3 transcription factor-staining buffer set (cat. 00-5523-00) were obtained from eBioscience (San Diego, CA). The anti-macrophage/monocyte antibody (clone MOMA-2; cat. MCA519GT) was obtained from Bio-Rad Laboratories (Hercules, CA). Alexa 780-conjugated streptavidin (cat. 47-4317-82) and Alexa 647-conjugated streptavidin (cat. S21374) were obtained from eBioscience and Invitrogen (Waltham, MA), respectively. Anti-SM22α (cat. ab10135) and anti-goat IgG(H+L) A594-conjugated antibody (ab150132) was obtained from Abcam (Boston, MA). Anti-KI- 67 (clone MIB-1; cat. M7240) was obtained from DAKO (Santa Clara, CA) and anti-human CD68 antibody (clone 514H12 cat. PA0273) was purchased from Leica. The Zombie Aqua fixable viability kit (cat. 423101), used to stain dead cells was purchased from BioLegend. Propidium iodide solution (cat. 130-093-233) was used to detect dead cells, purchased from Miltenyi Biotec (Bergisch Gladbach, Germany). BODIPY493/503 was obtained from Invitrogen (cat. D3922), and stock solutions were prepared by dissolving it in DMSO to a final concentration of 10 mmol/L. Before use, 10 mmol/L BODIPY493/503 was diluted with PBS to the appropriate concentration. DNase I (cat. DN25), collagenase I (cat. C0130), collagenase XI (cat. C7657) and hyaluronidase (cat. H1115000) were obtained from Sigma-Aldrich.

3. 6. 4 Aortic Singlet Preparation for Lipid Probe-Based Flow Cytometry

Single-cell suspensions of the aorta were prepared as previously reported[24] with minor modifications. In brief, mice were perfused with at least 10 mL of fresh cold PBS to eliminate blood contamination before isolating the aorta. The isolated aortas were further perfused with PBS and opened longitudinally and washed again with PBS. The whole aorta (including the aortic sinus, arch, thoracic aorta and abdominal aorta) was carefully dissected and the perivascular fat and cardiac muscle were removed. The aortic tissue was cut into 2–5 mm pieces and incubated at 37 °C for 70 min with gentle shaking in a PBS solution with calcium and magnesium containing DNase I (90 U/mL), collagenase I (675 U/mL), collagenase XI (187.5 U/mL), hyaluronidase (90 U/mL). To separate the intima-media tissue from the adventitia, the whole aorta was incubated in collagenase II (400 U/mL; cat. C6885; Sigma Aldrich) with hyaluronidase (90 U/mL) for 8 min and then the intima and adventitia were physically separated. For discriminating dead cells, the cells were pre-stained with Zombie Aqua, or stained with PI solution just before cell loading of the flow cytometer as recommended by the manufacturers. Non-specific binding to the Fc receptor was blocked, and the cells were incubated with the indicated antibodies at 4 °C for 30 min. The cells were permeabilized with the Foxp3 transcription factor-staining buffer set and then incubated with a biotinylated anti-α-SMA antibody and fluorochrome-conjugated streptavidin at 4 °C for 30 min and 20 min, respectively. The cells were gently washed with 2% fetal bovine serum (FBS) in PBS and incubated with 40 nmol/L BODIPY493/503 in PBS at 4 °C for 30 min. Flow cytometric analyses, including t-distributed stochastic neighbor Embedding (t-SNE), were performed using a fluorescence-associated cell sorter (FACS) Fortessa or LSRII (BD Biosciences) instrument and FlowJo software (version 10.3; Tree Star Inc, Ashland, OR).

3. 6. 5 RNA-seq

For single cellRNA sequencing (scRNA-seq) analysis of aortic $CD45^+$ cells, aortas from *Ldlr*$^{-/-}$ mice (n = 6) fed a high-fat diet for 12 weeks were pooled and digested with an enzyme mixture. Aortic single cells were stained with anti-CD45 antibody and PI. PI^-CD45^+ cells were sorted out using FACSAriaIII (BD Bioscicences). For scRNA-seq analysis of total

aortic foam cells including both $CD45^+$ and $CD45^-$ foam cells, the aortas from *ApoE*$^{-/-}$ mice (n=6) fed a high-fat diet for 27 weeks were used and the cells were stained with PI and $BODIPY^{493/503}$. $PI^-SSC^{hi}BODIPY^{hi}$ cells were sorted out for scRNA-seq analysis. The cells are prepared and resuspended in a final concentration of 10^3 cells/μL in 1X PBS containing 0.04% bovine serum albumin (BSA) to minimize cell loss and aggregation. Approximately ~17,400 cells were partitioned into nanoliter-scale Gel Bead-In-EMulsions (GEMs) to achieve single-cell resolution for a maximum recovery of 10,000 individual cells per sample. Utilizing the v2 ChromiumTM Single Cell 3′ Library Kit and Chromium instrument (10x Genomics, Pleasanton, CA), poly-adenylated mRNA from an individual cell was tagged with a unique 16-bp 10x barcode and a 10-bp Unique Molecular Identifier (UMI). Full-length cDNA was then amplified to generate sufficient mass for library construction. Enzymatic fragmentation and size selection were used to optimize cDNA amplicon size (~400 bp) for library construction. The final library is sequence ready and contains four unique sample indices. The concentration of the 10x single-cell library was accurately determined through qPCR (Kapa Biosystems, Wilmington, MA) to produce cluster counts appropriate for the HiSeq4000 platform (Illumina). Read lengths (26 x 98 nt) were generated targeting 50,000 reads per cell.

For bulk RNA-seq, the aortic intimal cells were prepared from *ApoE*$^{-/-}$ mice fed a high-fat diet for 28 weeks. Intimal foamy and non-foamy MØs were then sorted out. The libraries were prepared from cell lysates in 10X Single-Cell Lysis Buffer (Takara-Clontech, Kusatsu, Japan) containing 5% RNase inhibitor. Double stranded (ds)-cDNA was prepared using the SMARTer Ultra Low RNA Kit for Illumina Sequencing (Takara-Clontech) according to manufacturer's instructions. cDNA was fragmented using a Covaris E220 sonicator with the following parameter, duty cycle, 10; intensity, 5; cycles/burst, 200; time, 180 seconds. The cDNAs were blunt ended, supplemented with an A base at the 3′ end, and then ligated with Illumina sequencing adapters. The ligated fragments were amplified for 12 cycles using primers that incorporated unique index tags. The amplified fragments were sequenced on an Illumina HiSeq-3000 using single reads extending 50 bases.

3. 6. 6 Alignment, Barcode Assignment and UMI Counting

The Cell Ranger Single-Cell Software Suite (version 2.0.2; https://support.10xgenomics.com/single-cell-gene-expression/software/pipelines/latest/what-is-cell-ranger) was used to perform sample demultiplexing, barcode processing, and single-cell 3′ counting. "Cellranger mkfastq" was used to demultiplex raw base call files from the HiSeq4000 sequencer into sample-specific FASTQ files. Files were demultiplexed with 98%+ perfect barcode match, and 73%+ q30 reads. Subsequently, FASTQ files for each sample were processed with "cellranger count" to align reads to the mm10 mouse genome. The default estimated cell count value of 10,000 was used. For $CD45^+$ cells from $Ldlr^{-/-}$ mice fed a WD for 12 weeks barcodes with less than 2,341 UMIs were considered as background noise and low-quality cells and filtered out. After filtering we identified 3,781 cells with a mean of 201,659 reads per cell, a median of 8,687 UMIs per cell, and a median 2,365 genes detected within a cell. For total foam cells from $ApoE^{-/-}$ fed a WD for 27 weeks barcodes with less than 3,673 UMIs were considered as background noise and low-quality cells and filtered out. After filtering we identified 809 cells with a mean of 908,007 reads per cell, a median of 20,130 UMIs per cell, and a median of 4,151 genes detected within a cell.

3. 6. 7 Preprocessing Analysis with Seurat Package

For analysis, Seurat package (version 2.1) was used.[53] Cell Ranger filtered genes by barcode expression matrices were used as analysis inputs. The fraction of mitochondrial genes was calculated for every cell, and cells with a mitochondrial fraction > 5% were filtered out. UMI counts and fraction of mitochondrial reads were two sources of unwanted variation and were removed with the "RegressOut" function. Expression measurements for each cell were normalized to total expression and then scaled to 10,000, after which log normalization was performed.

3. 6. 8 Dimensionality Reduction and Clustering

The most variable genes were detected using the "FindVariableGenes" function and a principal component analysis (PCA) was run with these genes only. Cells were then represented with t-SNE plots. We applied the "RunTSNE" function to normalized data using the first 10 PCA components. A threshold of 10 principal components (PCs) was identified using the elbow method applied to explained variance by each component (**Supplemental figure 3.17**). For clustering, we used "FindClusters", which implements shared nearest neighbor (SNN) modularity optimization-based clustering algorithm on 10 PCA components with a resolution of 0.6 (**Supplemental figure 3.17**).

For the total foam cell scRNA-seq dataset, dimensionality reduction and clustering were performed in the same manner but only first 8 PCs were used (different elbow threshold).

3. 6. 9 Identification of Cluster-Specific Genes and Marker-Based Classification

To identify marker genes, the "FindAllMarkers" function was used with a likelihood-ratio test for single-cell gene expression. For each cluster, genes that were expressed in more than 25% of cells with at least 0.25-fold difference were considered.

3. 6. 10 Bulk RNA-seq Data Acquisition, Quality Control, and Processing

RNA-seq reads were aligned to the Ensembl 76 top-level assembly with STAR (version 2.0.4b). Gene counts were derived from the number of uniquely aligned unambiguous reads by Subread:featureCount (version 1.4.5). Transcript counts were produced by Sailfish (version 0.6.3). Sequencing performance was assessed for total number of aligned reads, total number of uniquely aligned reads, genes and transcripts detected, ribosomal fraction, known junction saturation, and read distribution over known gene models with RSeQC (version 2.3).

3. 6. 11 scRNA-seq Differential Expression

To obtain differentially expressed genes between cluster 1 and cluster 4, a MAST test was performed, and all *P* values were corrected for testing multiple genes (Bonferroni correction).

3. 6. 12 Bulk RNA-seq Differential Expression

We used Deseq2 R/Bioconductor package to perform PCA and to obtain differential expression between foamy and non-foamy intimal MØs.[54] PCA was performed in the space of the 500 most variable genes; variance stabilizing transformation was performed and then PCA was calculated. Differential expression for comparisons between foamy and non-foamy intimal MØs was obtained by Deseq2 guidelines; all *P* values were corrected for testing multiple genes (Bonferroni correction). Genes with adjusted *P* value < 0.05 were considered significantly differentially expressed.

3. 6. 13 Pathway Enrichment Analysis

For pathway enrichment, we used pathways from the KEGG database. We used fgsea R/Bioconductor package[55] to perform pre-ranked gene set enrichment analysis. For bulk RNA-seq we used t-statistic provided by Deseq2 as the gene score to rank the genes. For scRNA-seq we used the average log fold change detected between clusters 1 and 4 as the gene score to the rank the genes. Enrichment plots for specific pathways were obtained by the "plotEnrichment" function of fgsea package. All *P* values were corrected for testing multiple pathways (Benjamini–Hochberg correction).

3. 6. 14 Assessment of Atherosclerosis by Oil Red O Staining

Blood samples were taken from the retro-orbital plexus, and then mice were euthanized by CO_2 inhalation and perfused with cold PBS. Plasma samples were prepared from the collected blood by centrifugation at 14,500 rcf (Eppendorf) for 10 min at 4 °C. An automated

blood chemical analyzer (Hitachi) was used to analyze the levels of plasma total cholesterol, triglycerides, high-density lipoprotein (HDL), and low-density lipoprotein (LDL). For *en face* analyses, the aorta was opened longitudinally and pinned onto a silicone plate in a "Y" shape. The aorta was then fixed with 4% paraformaldehyde for 60 min, washed with PBS for 60 min, and stained overnight with 0.5% oil red O (Sigma-Aldrich) in propylene glycol. De-staining was performed with 85% propylene glycol in distilled water to reduce background staining. For analysis of lesions in the aortic sinus, 5-μm-thick cryosections were prepared as previously described[25], hydrated with distilled water, stained with oil red O and counterstained with hematoxylin. Lesion sizes in the sinus and the extent of atherosclerotic lesions throughout the aorta were measured using TSViewer (ver.7.1.1.5) or Photoshop CS6 software (Adobe, San Jose, CA). The quantification of atherosclerotic lesion was done by independent researcher blinded to sample identity.

3. 6. 15 Immunostaining

For fluorescence microscopy-based detection of atherosclerotic lesions, hydrated 5-μm-thick cryosections or whole-mount aortic preparations were stained at room temperature with 1 μM BODIPY493/503 for 60 min. Slide-mounted atherosclerotic sinus sections were immunostained with MOMA-2 or antibodies against SM22α and CD11c using an Alexa 594 TSA Kit (Invitrogen) according to the manufacturer's instructions. Stained sections and whole mounts were observed under a confocal laser-scanning microscope (LSM780; Carl Zeiss, Oberkochen, Germany or TCS SP8; Leica, Wetzlar, Germany) and an Axio Zoom V16 stereo microscope (Carl Zeiss). Three-dimensional (3D) reconstructions were created using the IMARIS software (Bitplane, Zurich, Switzerland).

For immunohistochemistry or in situ hybridization, 4% paraformaldehyde overnight-fixed, paraffin-embedded human or mouse samples were processed using standard procedures. Paraffin-embedded samples were serially sectioned into 4-μm-thick slices. After antigen retrieval by boiling with citric acid solution (autoclave), sections were immunostained with anti-SM22α or KI-67 antibody, then visualized by 3,'3-Diaminobenzidine (DAB) staining kit (cat. RE7230-K; Leica). For staining human MØs, anti-CD68 antibody was stained and

visualized with DAB (Leica) or ultraView Universal Alkaline Phosphatase (AP) Red Detection kit (cat. 760-501; Ventana Medical System, Tucson, AZ). Nuclei were counterstained with hematoxylin solution.

For hematoxylin and eosin (H&E) staining, deparaffinized slides were gradually hydrated in ethanol solution (100% to 80%), placed in hematoxylin (ClearView^{TM}; BBC biochemical, Mount Vernon, WA) for 5 minutes, and then rinsed in tap water and dipped in 80% ethanol for 30 seconds. The samples were stained with eosin solution for 6 minutes, dehydrated in graded ethanol (80% to 100%), and then incubated with xylene before mounting with Permount solution (SP15-500; Fisher Chemicals, Pittsburgh, PA). The measurement of KI-67 positive foamy MØs in atherosclerotic lesion was done by independent researcher blinded to sample identity. The average percentage of KI-67 positive foamy or non-foamy MØs was calculated at five different foamy MØ-rich or fibrous cap areas (8.4×10^4 μm^2 each) of human atherosclerotic lesion (n = 3).

3. 6. 16 In Situ Hybridization

To detect human/mouse IL-1β transcripts in atherosclerotic plaques, we used RNAscope® 2.5 HD Detection Kit (RED; cat.322370, Advanced Cell Diagnostics [ACD], Newark, CA) according to manufacturer's instructions. After deparaffinization and tissue pretreatment (antigen retrieval and proteinase treatment) of Formalin-fixed paraffin-embedded sections, the slides were incubated with hybridized probes in 40 °C oven. Human *IL1β* (RNAscope® Probe-Hs-IL1B; cat. 310361, ACD) or mouse *Il1b* target probes (RNAscope® Probe-Mm-Il1b; cat. 316891, ACD) were used for detection while human *PPIB* or mouse *Ppib* probes and the bacterial *dapB* probe were for positive and negative controls, respectively. The signal was then amplified and visualized for detection and was considered positive by observing red dots around the nucleus. The slides were counter-stained with hematoxylin for 5 minutes after in situ hybridization. The measurement of *IL1β*-expressing cells in atherosclerotic lesion was done by independent researcher blinded to sample identity.

3. 6. 17 t-SNE Plot for FACS Data

t-SNE plots representing flow cytometry data in **figure 3.4C and 3.5B** were produced by FlowJo software as described in the software manual. From $CD45^+$ singlet leukocytes, all stained leukocyte parameters were selected and then analyzed for separating populations. Analyzing options were iterations 1000, perplexity 20, eta (learning rate) 200, and theta 0.5.

3. 6. 18 Electron Microscopy and Cytological Analyses

Aortic single cells were stained as described above and sorted by flow cytometry using the FACS AriaIII system. For electron microscopic analyses, aortic $SSC^{lo}BODIPY493/503^{lo}$ cells and $SSC^{hi}BODIPY493/503^{hi}$ cells were sorted and subjected to cytospinning at 300 rcf for 4 min. The specimens were immersed in 2.5% glutaraldehyde (Ted pella, Redding, CA) in PBS for 2 h, fixed in 1% osmium tetroxide (Ted Pella) for 90 min, dehydrated in graded ethanol and propylene oxide (Acros Organics, Geel, Belgium), and then embedded in Embed812 epoxy resin containing DMP-30 (Electron Microscopy Sciences, Hatfield, PA). Serial ultrasections (70-nm thick) were cut using an Ultracut S 51 microtome (Leica) and double stained with uranyl acetate and lead citrate. Samples were imaged and photographed using an H-7600 transmission electron microscope (Hitachi, Tokyo, Japan). For cytological analyses, FACS-sorted cells were plated on slide and co-stained with Hema 3 (Thermo Fisher Scientific) and oil red O. Next, the cells were imaged using an Eclipse 50i (Nikon) microscope.

3. 6. 19 Single Cell Quantitative Real-Time PCR

ScRNA was extracted from sorted aortic foamy or non-foamy MØs (10 cells per each reaction), reverse transcribed and then amplified using Single Cell-to-CT qRT-PCR kit (PN4458237; Ambion) according to manufacturer's instructions. qPCR was performed using a thermal cycler (Applied Biosystems) using Taqman gene expression assay FAM-labeled *IL1b* (Mm00434228_m1) and *Gapdh* (Mm99999915_g1) probes. mRNA expression level of each gene was normalized to *Gapdh* expression.

3. 6. 20 Statistical Analysis

We conducted a Shapiro-Wilk normality test for the samples. The two-group independent t-test, one-way analysis of variance (ANOVA), and two-way ANOVA were used if the variables satisfied the normality assumption. Otherwise, the Mann-Whitney U test, Kruskal-Wallis one-way ANOVA test, and Friedman two-way ANOVA test were used. Bonferroni correction was used for post-hoc multiple comparison in ANOVA. Statistical analyses were performed with SAS (version 9.4, SAS Institute, Inc., Cary, NC), Prism 6 (GraphPad Software, La Jolla, CA), or InStat (GraphPad Software).

3. 7 Author Contributions

Dahee Shim, Junseong Lee, **Jae-Hoon Choi,** a**nd Cheolho Cheong** designed the experiments.

Kyeongdae Kim, Dahee Shim, Jun Seong Lee, and Konstantin Zaitsev executed the majority of experiments presented.

Kyeongdae Kim, Dahee Shim, Jun Seong Lee, Konstantin Zaitsev, Gwendalyn J. Randolph, Maxim N. Artyomov, Cheolho Cheong, and Jae-Hoon Choi interpreted the data and wrote the manuscript.

3. 8 Acknowledgments

This work is dedicated to the memory of Cheolho Cheong. We appreciate Erica Lantelme and Dorjan Brinja for fluorescence-activated cell sorting sorting and also thank Inhyuk Jung, Soo Young Cho, and Sung Ho Park for technical assistance and scientific comments, respectively. We thank McDonnell Genome Institute and Genome Technology Access Center in the Department of Genetics at Washington University School of Medicine for help with genomic analysis. We thank Dr Eunwoo Nam of Medical statistical office at the Hanyang University College of Medicine for statistical advice.

3. 9 Sources of Funding

This work was supported by grants from the Bio and Medical Technology Development Program of the National Research Foundation and funded by the Korean government (Ministry of Health and Welfare, Ministry of Science and ICT, No. 2016M3A9D5A01952413 and 2018R1A2B6003393 to J.-H. Choi and 2015M3A9B6029138 to G.T. Oh), the Korean Health Technology R&D Project (HI15C0399 to J.-H. Choi), Ministry of Health, Welfare, and Family Affairs, and Canadian Institutes of Health Research (CIHR; FRN 125933 to C. Cheong, CIHR Foundation 148363 and Canada Research Chair 950-231335 to N.G. Seidah), American Heart Association grant 17POST33410473 to J.W. Williams and Government of Russian Federation grant 074-U01 to K. Zaitsev. Genome Technology Access Center at Washington University School of Medicine is partially supported by National Cancer Institute Cancer Center Support grant No. P30 CA91842 to the Siteman Cancer Center and by ICTS/CTSA grant No. UL1TR002345 from the National Center for Research Resources (NCRR)—a component of the National Institutes of Health (NIH)—and NIH Roadmap for Medical Research. This publication is solely the responsibility of the authors and does not necessarily represent the official views of NCRR or NIH.

3. 10 Additional Information

The authors declare that all supporting data are available within the article and its Online Data Supplement. All sequencing data sets in this article are deposited in international public repository, Gene Expression Omnibus, under accession identification as GSE116239 for bulk RNA-seq and GSE116240 for scRNA-seq from mouse atherosclerotic aorta.

Online data set 3.1. All enriched genes and pathways.
(https://www.ahajournals.org/action/downloadSupplement?doi=10.1161%2FCIRCRESAHA.118.312804&file=312804_data_set_i.xlsx)

Online data set 3.2. All enriched genes and pathways.
(https://www.hajournals.org/action/downloadSupplement?doi=10.1161%2FCIRCRESAHA.118.312804&file=312804_data_set_ii.xlsx)

Online data set 3.3. Different gene expression profiles in non-foamy and foamy MΦs.
(https://www.ahajournals.org/action/downloadSupplement?doi=10.1161%2FCIRCRESAHA.118.312804&file=312804_data_set_iii.xlsx)

Online video 3.1. 3D reconstruction from confocal microscopic images of CD11c and CD206 double-immunofluorescence staining. Whole-mount atherosclerotic aorta from an *ApoE*$^{-/-}$ mouse fed a WD for 12 weeks was permeabilized with 1% Triton X-100 and immunostained with antibodies against CD11c (red; Cy3) and CD206 (blue; Alexa 647). The stained aorta was cleared with methyl salicylate (Sigma-Aldrich), images were acquired, and then 3D reconstructions were prepared as described in the Materials and Methods.
(https://www.ahajournals.org/action/downloadSupplement?doi=10.1161%2FCIRCRESAHA.118.312804&file=312804_video_i.avi)

3. 11 References

1. Hansson, G.K. & Hermansson, A. The immune system in atherosclerosis. *Nat Immunol* **12**, 204-212 (2011).

2. Hansson, G.K. & Libby, P. The immune response in atherosclerosis: a double-edged sword. *Nat Rev Immunol* **6**, 508-519 (2006).

3. Weber, C. & Noels, H. Atherosclerosis: current pathogenesis and therapeutic options. *Nat Med* **17**, 1410-1422 (2011).

4. Suzuki, H. *et al.* A role for macrophage scavenger receptors in atherosclerosis and susceptibility to infection. *Nature* **386**, 292-296 (1997).

5. Feig, J.E. *et al.* LXR promotes the maximal egress of monocyte-derived cells from mouse aortic plaques during atherosclerosis regression. *J Clin Invest* **120**, 4415-4424 (2010).

6. Potteaux, S. *et al.* Suppressed monocyte recruitment drives macrophage removal from atherosclerotic plaques of Apoe-/- mice during disease regression. *J Clin Invest* **121**, 2025-2036 (2011).

7. Luo, Y. *et al.* Macrophagic CD146 promotes foam cell formation and retention during atherosclerosis. *Cell Res* **27**, 352-372 (2017).

8. Moore, K.J. & Tabas, I. Macrophages in the pathogenesis of atherosclerosis. *Cell* **145**, 341-355 (2011).

9. Cochain, C. & Zernecke, A. Macrophages in vascular inflammation and atherosclerosis. *Pflugers Arch* **469**, 485-499 (2017).

10. Robbins, C.S. *et al.* Extramedullary hematopoiesis generates Ly-6C(high) monocytes that infiltrate atherosclerotic lesions. *Circulation* **125**, 364-374 (2012).

11. Swirski, F.K., Robbins, C.S. & Nahrendorf, M. Development and Function of Arterial and Cardiac Macrophages. *Trends Immunol* **37**, 32-40 (2016).

12. Ensan, S. *et al.* Self-renewing resident arterial macrophages arise from embryonic CX3CR1(+) precursors and circulating monocytes immediately after birth. *Nat Immunol* **17**, 159-168 (2016).

13. Llodra, J. *et al.* Emigration of monocyte-derived cells from atherosclerotic lesions characterizes regressive, but not progressive, plaques. *Proc Natl Acad Sci U S A* **101**, 11779-11784 (2004).

14. Swirski, F.K. *et al.* Ly-6Chi monocytes dominate hypercholesterolemia-associated monocytosis and give rise to macrophages in atheromata. *J Clin Invest* **117**, 195-205 (2007).

15. Tacke, F. *et al.* Monocyte subsets differentially employ CCR2, CCR5, and CX3CR1 to accumulate within atherosclerotic plaques. *J Clin Invest* **117**, 185-194 (2007).

16. Combadiere, C. *et al.* Combined inhibition of CCL2, CX3CR1, and CCR5 abrogates Ly6C(hi) and Ly6C(lo) monocytosis and almost abolishes atherosclerosis in hypercholesterolemic mice. *Circulation* **117**, 1649-1657 (2008).

17. Gerhardt, T. & Ley, K. Monocyte trafficking across the vessel wall. *Cardiovasc Res* **107**, 321-330 (2015).

18. Brown, M.S. & Goldstein, J.L. A receptor-mediated pathway for cholesterol homeostasis. *Science* **232**, 34-47 (1986).

19. Westerterp, M. *et al.* ATP-binding cassette transporters, atherosclerosis, and inflammation. *Circ Res* **114**, 157-170 (2014).

20. Duewell, P. *et al.* NLRP3 inflammasomes are required for atherogenesis and activated by cholesterol crystals. *Nature* **464**, 1357-1361 (2010).

21. Spann, N.J. *et al.* Regulated accumulation of desmosterol integrates macrophage lipid metabolism and inflammatory responses. *Cell* **151**, 138-152 (2012).

22. Paigen, B., Morrow, A., Holmes, P.A., Mitchell, D. & Williams, R.A. Quantitative assessment of atherosclerotic lesions in mice. *Atherosclerosis* **68**, 231-240 (1987).

23. Galkina, E. *et al.* Lymphocyte recruitment into the aortic wall before and during development of atherosclerosis is partially L-selectin dependent. *J Exp Med* **203**, 1273-1282 (2006).

24. Choi, J.H. *et al.* Identification of antigen-presenting dendritic cells in mouse aorta and cardiac valves. *J Exp Med* **206**, 497-505 (2009).

25. Choi, J.H. *et al.* Flt3 signaling-dependent dendritic cells protect against atherosclerosis. *Immunity* **35**, 819-831 (2011).

26. Gold, E.S. *et al.* ATF3 protects against atherosclerosis by suppressing 25-hydroxycholesterol-induced lipid body formation. *J Exp Med* **209**, 807-817 (2012).

27. Horton, H. *et al.* Optimization and validation of an 8-color intracellular cytokine staining (ICS) assay to quantify antigen-specific T cells induced by vaccination. *J Immunol Methods* **323**, 39-54 (2007).

28. Horton, J.D., Cohen, J.C. & Hobbs, H.H. PCSK9: a convertase that coordinates LDL catabolism. *J Lipid Res* **50 Suppl**, S172-177 (2009).

29. Herbert, B. *et al.* Increased secretion of lipoproteins in transgenic mice expressing human D374Y PCSK9 under physiological genetic control. *Arterioscler Thromb Vasc Biol* **30**, 1333-1339 (2010).

30. Seidah, N.G., Awan, Z., Chretien, M. & Mbikay, M. PCSK9: a key modulator of cardiovascular health. *Circ Res* **114**, 1022-1036 (2014).

31. Erez, G. & Leitersdorf, E. The rationale for using HMG-CoA reductase inhibitors ('statins') in peripheral arterial disease. *Eur J Vasc Endovasc Surg* **33**, 192-201 (2007).

32. Kritharides, L., Kus, M., Brown, A.J., Jessup, W. & Dean, R.T. Hydroxypropyl-beta-cyclodextrin-mediated efflux of 7-ketocholesterol from macrophage foam cells. *J Biol Chem* **271**, 27450-27455 (1996).

33. Wang, X. *et al.* Macrophage ABCA1 and ABCG1, but not SR-BI, promote macrophage reverse cholesterol transport in vivo. *J Clin Invest* **117**, 2216-2224 (2007).

34. Liu, S.M. *et al.* Cyclodextrins differentially mobilize free and esterified cholesterol from primary human foam cell macrophages. *J Lipid Res* **44**, 1156-1166 (2003).

35. Walenbergh, S.M. *et al.* Weekly Treatment of 2-Hydroxypropyl-beta-cyclodextrin Improves Intracellular Cholesterol Levels in LDL Receptor Knockout Mice. *Int J Mol Sci* **16**, 21056-21069 (2015).

36. Zimmer, S. *et al.* Cyclodextrin promotes atherosclerosis regression via macrophage reprogramming. *Sci Transl Med* **8**, 333ra350 (2016).

37. Yun, T.J. *et al.* Indoleamine 2,3-Dioxygenase-Expressing Aortic Plasmacytoid Dendritic Cells Protect against Atherosclerosis by Induction of Regulatory T Cells. *Cell Metab* **24**, 886 (2016).

38. Tabas, I. & Bornfeldt, K.E. Macrophage Phenotype and Function in Different Stages of Atherosclerosis. *Circ Res* **118**, 653-667 (2016).

39. Ridker, P.M. *et al.* Antiinflammatory Therapy with Canakinumab for Atherosclerotic Disease. *N Engl J Med* **377**, 1119-1131 (2017).

40. Cochain, C. *et al.* Single-Cell RNA-Seq Reveals the Transcriptional Landscape and Heterogeneity of Aortic Macrophages in Murine Atherosclerosis. *Circ Res* **122**, 1661-1674 (2018).

41. Winkels, H. *et al.* Atlas of the Immune Cell Repertoire in Mouse Atherosclerosis Defined by Single-Cell RNA-Sequencing and Mass Cytometry. *Circ Res* **122**, 1675-1688 (2018).

42. Paulson, K.E. *et al.* Resident intimal dendritic cells accumulate lipid and contribute to the initiation of atherosclerosis. *Circ Res* **106**, 383-390 (2010).

43. Goo, Y.H., Son, S.H., Yechoor, V.K. & Paul, A. Transcriptional Profiling of Foam Cells Reveals Induction of Guanylate-Binding Proteins Following Western Diet Acceleration of Atherosclerosis in the Absence of Global Changes in Inflammation. *J Am Heart Assoc* **5**, e002663 (2016).

44. Chappell, J. *et al.* Extensive Proliferation of a Subset of Differentiated, yet Plastic, Medial Vascular Smooth Muscle Cells Contributes to Neointimal Formation in Mouse Injury and Atherosclerosis Models. *Circ Res* **119**, 1313-1323 (2016).

45. Becker, L. *et al.* A macrophage sterol-responsive network linked to atherogenesis. *Cell Metab* **11**, 125-135 (2010).

46. Thomas, A.C., Eijgelaar, W.J., Daemen, M.J. & Newby, A.C. Foam Cell Formation In Vivo Converts Macrophages to a Pro-Fibrotic Phenotype. *PLoS One* **10**, e0128163 (2015).

47. Paul, A., Yechoor, V., Raja, R., Li, L. & Chan, L. Microarray gene profiling of laser-captured cells: a new tool to study atherosclerosis in mice. *Atherosclerosis* **200**, 257-263 (2008).

48. Swirski, F.K. *et al.* Monocyte accumulation in mouse atherogenesis is progressive and proportional to extent of disease. *Proc Natl Acad Sci U S A* **103**, 10340-10345 (2006).

49. Robbins, C.S. *et al.* Local proliferation dominates lesional macrophage accumulation in atherosclerosis. *Nat Med* **19**, 1166-1172 (2013).

50. Lhotak, S. *et al.* Characterization of Proliferating Lesion-Resident Cells During All Stages of Atherosclerotic Growth. *J Am Heart Assoc* **5** (2016).

51. Rong, J.X., Shapiro, M., Trogan, E. & Fisher, E.A. Transdifferentiation of mouse aortic smooth muscle cells to a macrophage-like state after cholesterol loading. *Proc Natl Acad Sci U S A* **100**, 13531-13536 (2003).

52. Allahverdian, S., Chehroudi, A.C., McManus, B.M., Abraham, T. & Francis, G.A. Contribution of intimal smooth muscle cells to cholesterol accumulation and macrophage-like cells in human atherosclerosis. *Circulation* **129**, 1551-1559 (2014).

53. Butler, A., Hoffman, P., Smibert, P., Papalexi, E. & Satija, R. Integrating single-cell transcriptomic data across different conditions, technologies, and species. *Nat Biotechnol* **36**, 411-420 (2018).

54. Love, M.I., Huber, W. & Anders, S. Moderated estimation of fold change and dispersion for RNA-seq data with DESeq2. *Genome Biol* **15**, 550 (2014).

55. Sergushichev, A.A. An algorithm for fast preranked gene set enrichment analysis using cumulative statistic calculation. *biorxiv*, https://doi.org/10.1101/060012 (2016).

3. 12 Supplementary Information

3. 12. 1 Supplementary Figures

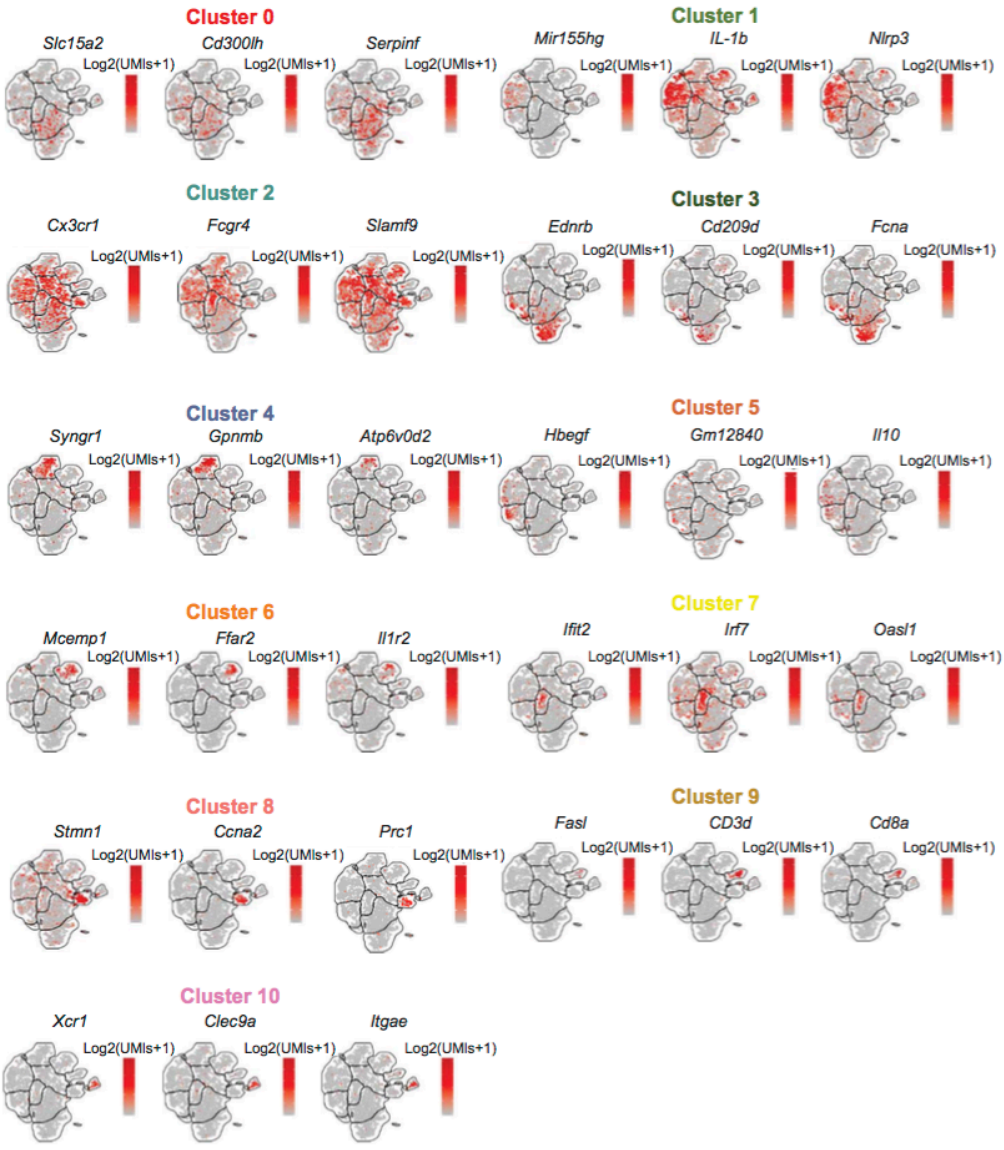

Supplemental figure 3.1. Representative enriched genes in each scRNA-seq cluster. t-SNE plots of the genes expressed in each cluster. Representative enriched genes in each cluster are shown. Adjusted *P* value < 0.01; logFC > 0.

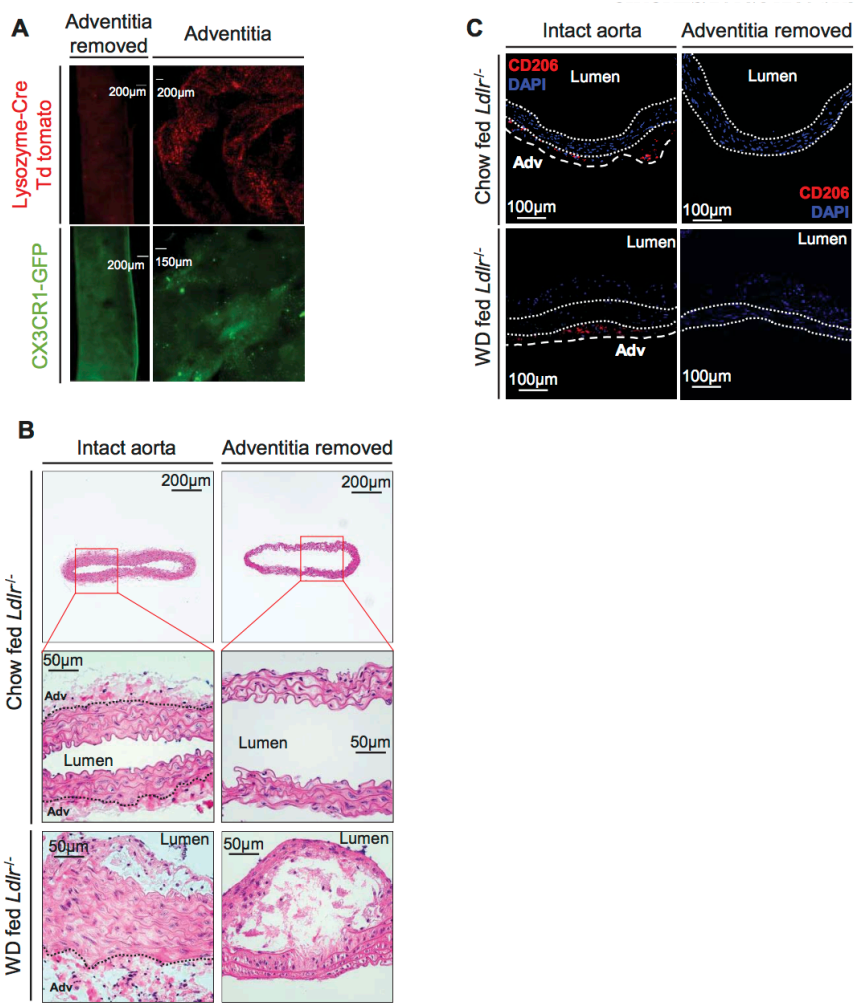

Supplemental figure 3.2. Separation of adventitia from aorta. (A) Resident MØs were mostly located at the aortic adventitia of LysM-Cre and ROSA26tdTomato mice (upper; red) as well as CX3CR1-GFP (lower; green) mice, but yet poorly detected in the intima-media portion. **(B)** H&E-stained cross-sections of aortas with or without adventitia from chow- or WD-fed *Ldlr*$^{-/-}$ mice. **(C)** Immunofluorescence staining of CD206 (red) on cross-sections of aortas with or without adventitia from chow- or WD-fed *Ldlr*$^{-/-}$ mice. DAPI (blue) staining for nuclei. Adventitial CD206^{+} MØs were clearly eliminated by the removal of adventitial tissue.

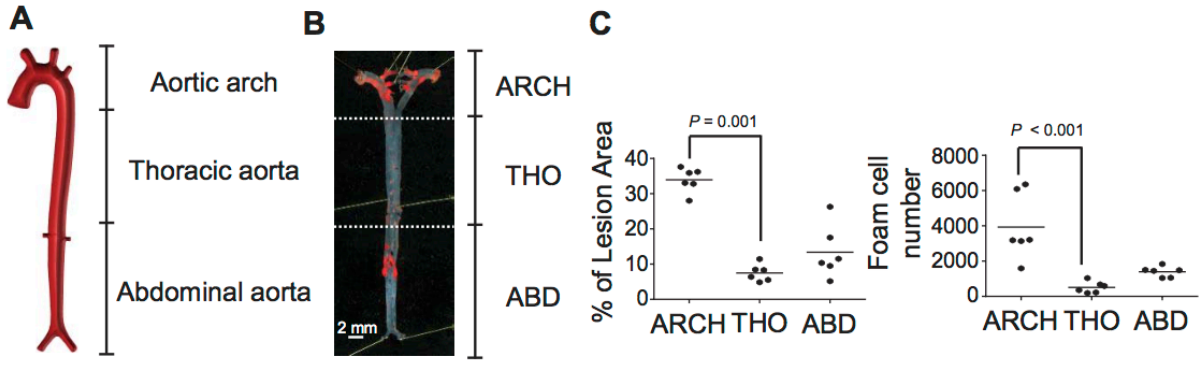

Supplemental figure 3.3. Flow cytometric detection of SSC^{hi}BODIPY^{hi} cells in different parts of the aorta. (A) Aortic arch, thoracic area, and abdominal area of the aorta. **(B)** *en face* oil red O staining of atherosclerotic lesions. **(C)** Comparison of the lesion area (*left*) and with foam cell counts (*right*; n = 6).

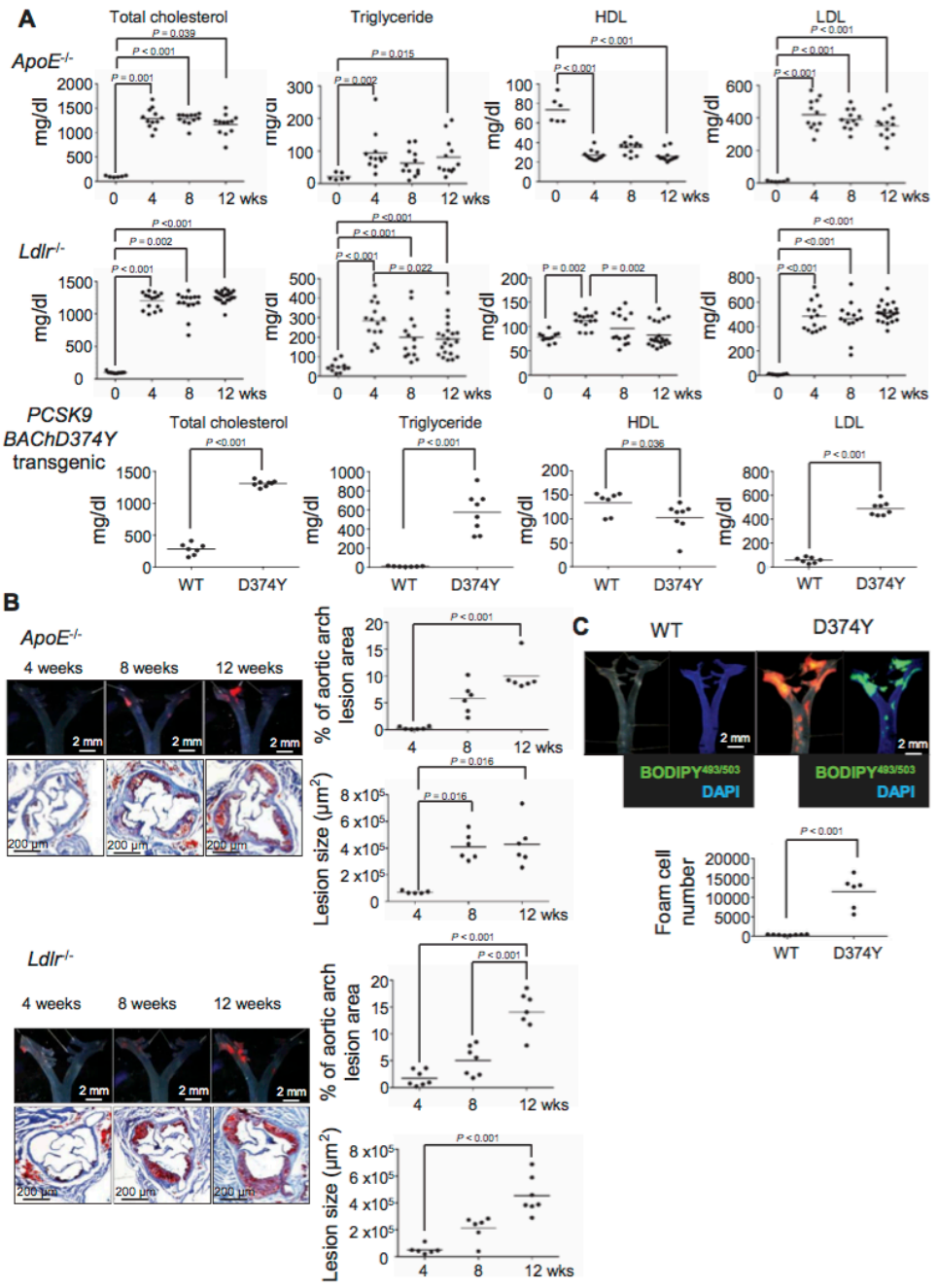

Supplemental figure 3.4. The change in lipid profiles and lesion size during atherosclerosis. (A) Plasma levels of total cholesterol, triglycerides, HDL, and LDL in *ApoE*$^{-/-}$ mice (*top*; n=6 for control and n=12 for experimental group), *Ldlr*$^{-/-}$ mice (*middle*; n=11 for control, n=15 for the 4-week group, and n=14 for the 8-week group, and n=21 for the 12-week group), and D374Y-hPCSK9 transgenic (Tg) mice (*bottom*; n=7 for control and n=8 for the Tg group). **(B)** Aortic lesion area in *ApoE*$^{-/-}$ (top; n=6) and *Ldlr*$^{-/-}$ mice (bottom; n=7) fed a WD for 4, 8, or 12 weeks. **(C)** Aortic lesion area and foam cell number of D374Y-hPCSK9 tg mice fed a WD (n=8 for control and n=6 for Tg group).

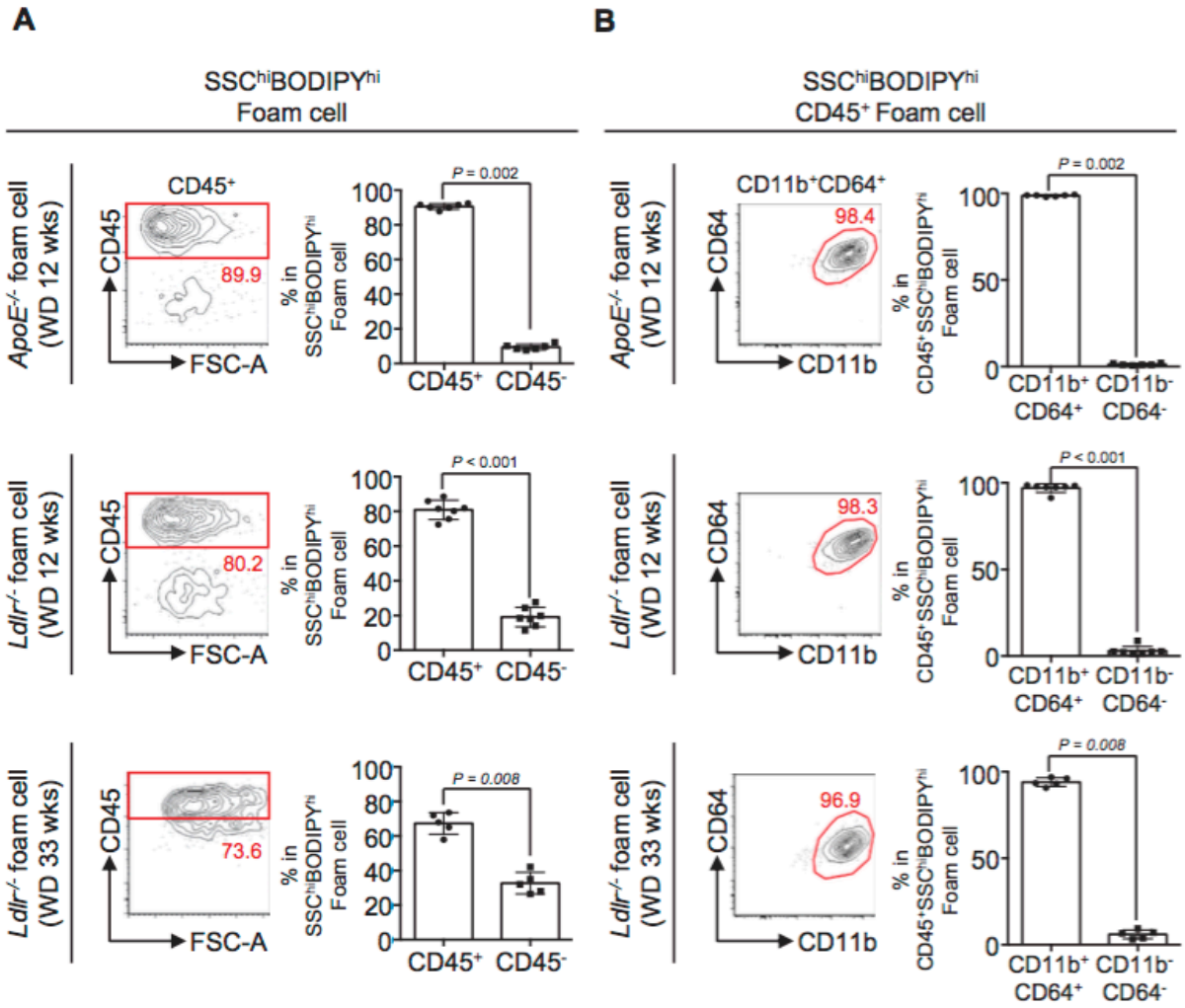

Supplemental figure 3.5. SSC^{hi} BODIPY^{hi} CD45^{+} foam cells are CD11b^{+}CD64^{+}. (A) Percentage of CD45^{+} foam cells in total foam cells from *ApoE*$^{-/-}$ mice fed a WD for 12 weeks (*top;* n=6), *Ldlr*$^{-/-}$ mice fed aWD for 12 weeks (*middle;* n=5), and *Ldlr*$^{-/-}$ mice fed a WD for 33 weeks (*Bottom;* n=5). **(B)** Percentage of CD11b^{+}CD64^{+} cells in CD45^{+} foam cells.

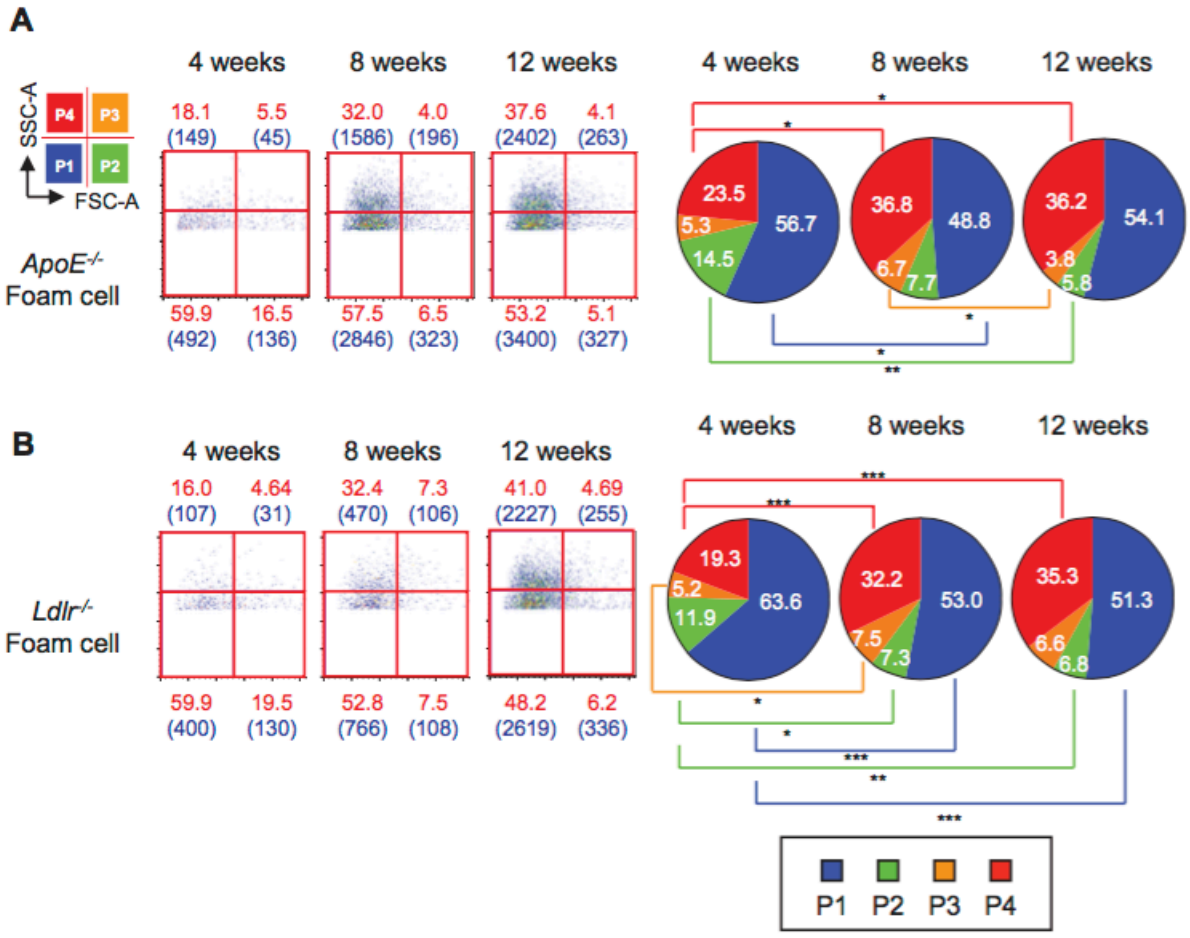

Supplemental figure 3.6. Changes in granularity and size of foam cells during atherosclerosis progression. (A, B) Aortic $SSC^{hi}BODIPY^{hi}$ foam cells were subdivided based on their size (FSC) and granularity (SSC). The size and granularity of mouse aortic cells changed during the progression of atherosclerosis in (A) *ApoE*$^{-/-}$ (4weeks, n=5; 8 or 12 weeks, n=6) and (B) *Ldlr*$^{-/-}$ mice (n=7). *P<0.05, ** $P < 0.01$, *** $P < 0.001$.

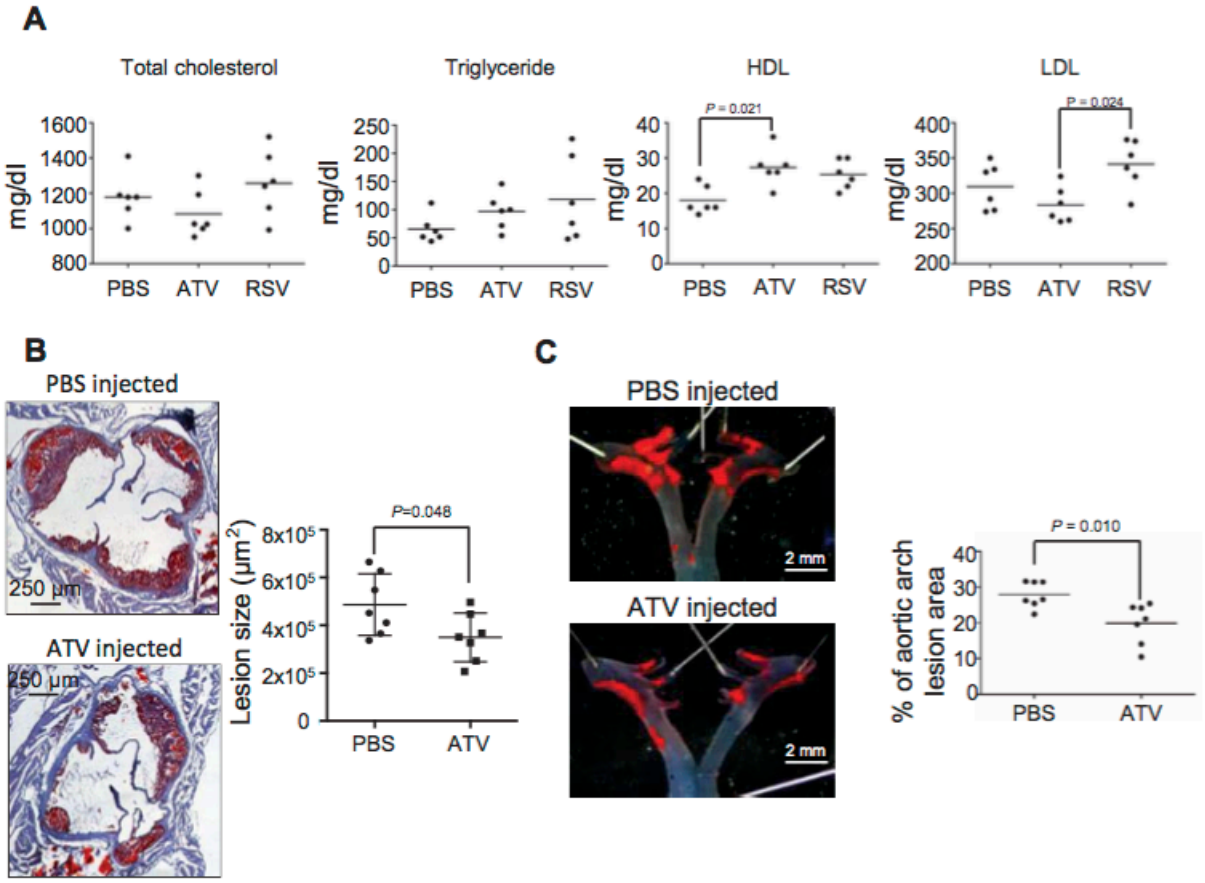

Supplemental figure 3.7. The effect of statins on plasma lipid profiles and atherosclerotic lesion formation. (A) Plasma levels of total cholesterol, triglycerides, HDL, and LDL in *ApoE*$^{-/-}$ mice fed a WD for 6 weeks with atorvastatin, rosuvastatin, or PBS treatment (n = 6 per group). **(B, C)** Measurement of lesions in **(B)** aortic sinus (µm2) and **(C)** arch (%) of PBS- or atorvastatin-treated mice (n = 7 per group).

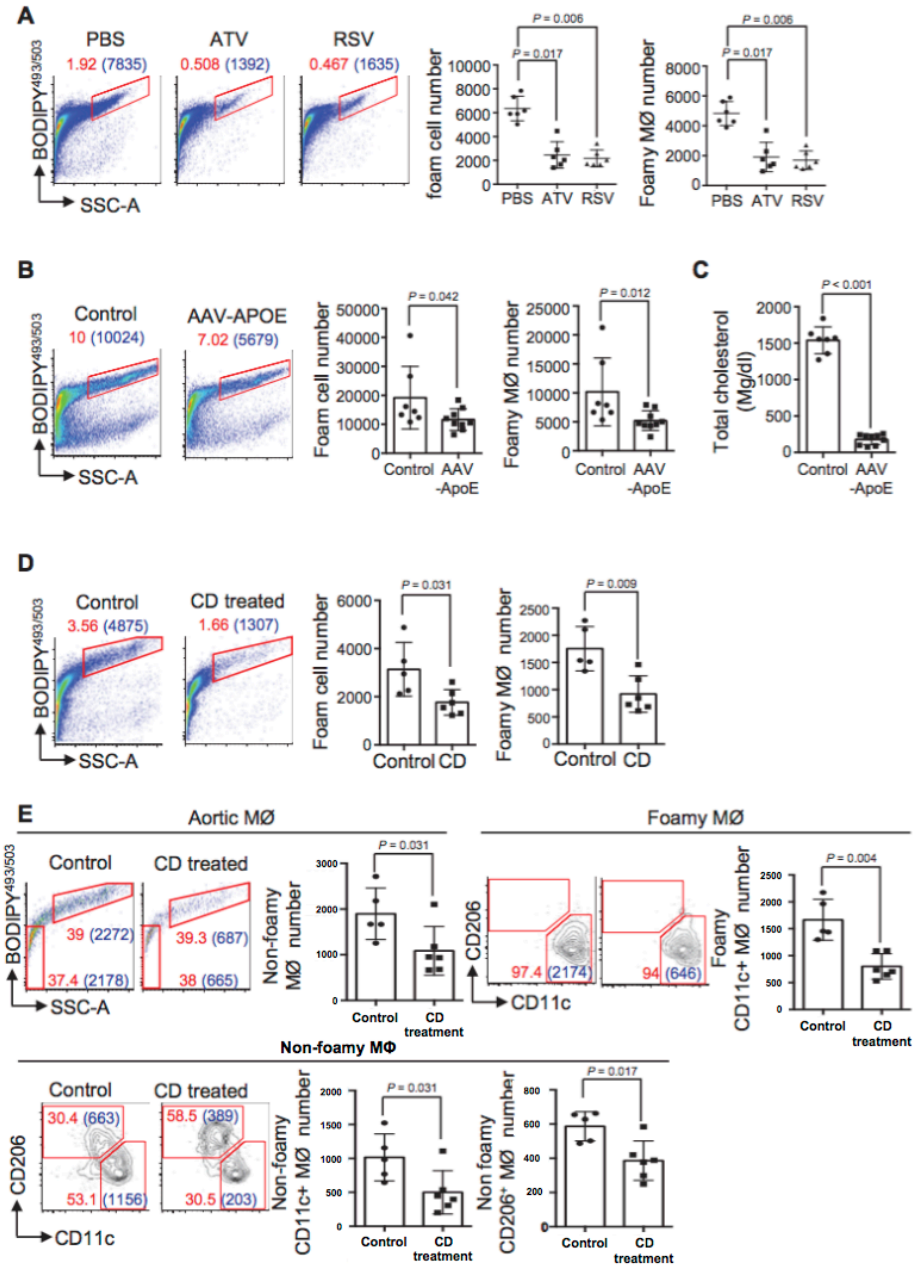

Supplemental figure 3.8. BODIPY493/503-based flow cytometry can be used to evaluate anti- atherogenic treatments. (A) Abundance changes in total foam cells and MØ foam cells after anti-atherosclerotic drug treatment (n=6 per group). **(B)** Abundance changes in foam cells during plaque regression in *ApoE*$^{-/-}$ mice induced by AAV8-mediated ApoE gene transfer. (n=7 for control and n=9 for the AAV8-injected group). **(C)** Plasma cholesterol levels of control (n=7) and AAV-ApoE-injected *ApoE*$^{-/-}$ mice (n=9). **(D)** The effect of CD treatment on the number of total aortic foam cells and foamy MØs in *Ldlr*$^{-/-}$ mice (n=5 for control and n=6 for the CD-treated group). **(E)** The number of foamy and non-foamy MØs decreased by CD treatment (n=5 for control and n=6 for CD-treated group; red, %; blue, cell number).

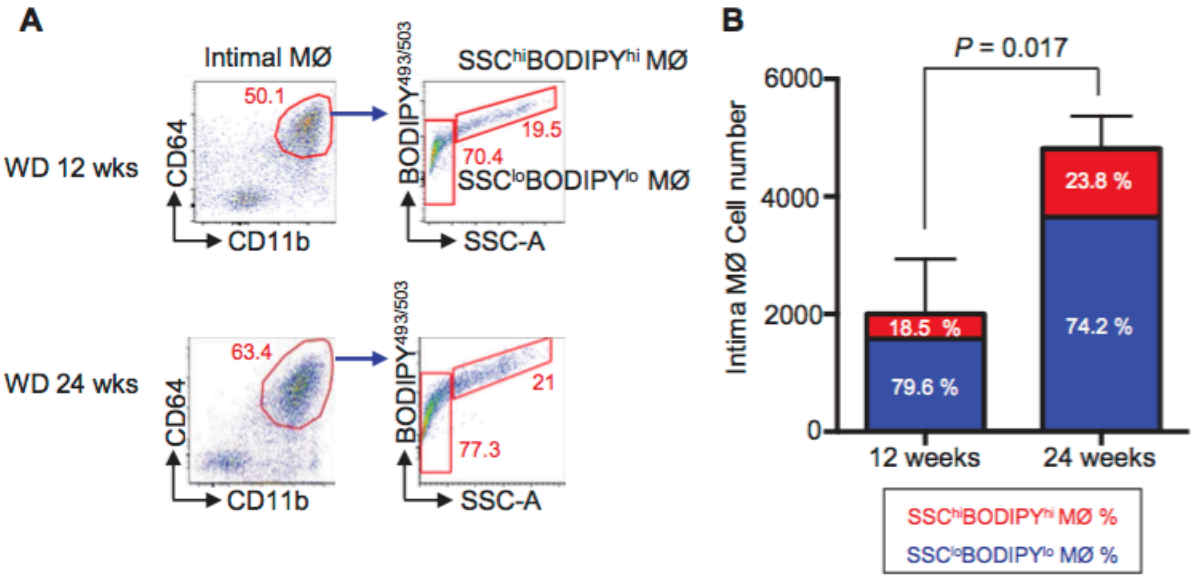

Supplemental figure 3.9. Increase of intimal foamy and non-foamy MØs and their relative abundance during atherosclerosis progression. (A) Representative FACS plots showing intimal foamy and non-foamy MØs from *Ldlr*$^{-/-}$ mice fed WD for 12 weeks (n=7) or 24 weeks (n=3). **(B)** Intimal MØ cell number (bar graph) and the percentage of foamy and non-foamy MØs (red = foamy [SSC^{hi}BODIPY^{hi}] MØ, blue = non-foamy [SSC^{lo}BODIPY^{lo}] MØ).

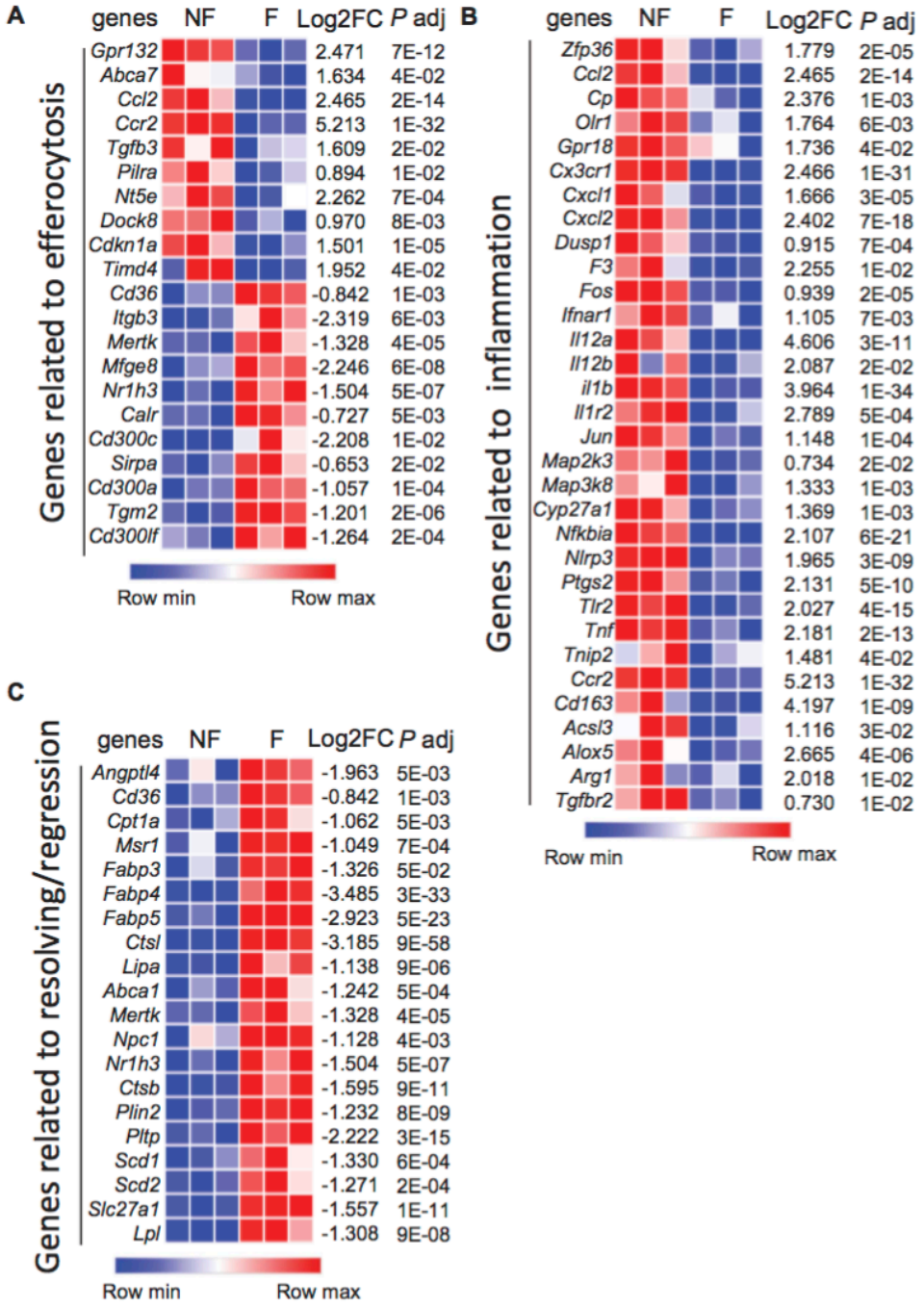

Supplemental figure 3.10. Comparison of atherosclerosis-related gene expression in intimal foamy and non-foamy MØs. (A-C) Representative expression of genes related to **(A)** efferocytosis, **(B)** inflammation, and **(C)** resolving/regression in non-foamy and foamy MØ in bulk RNA-seq. Adjusted *P* value of heatmap genes is less than 0.05.

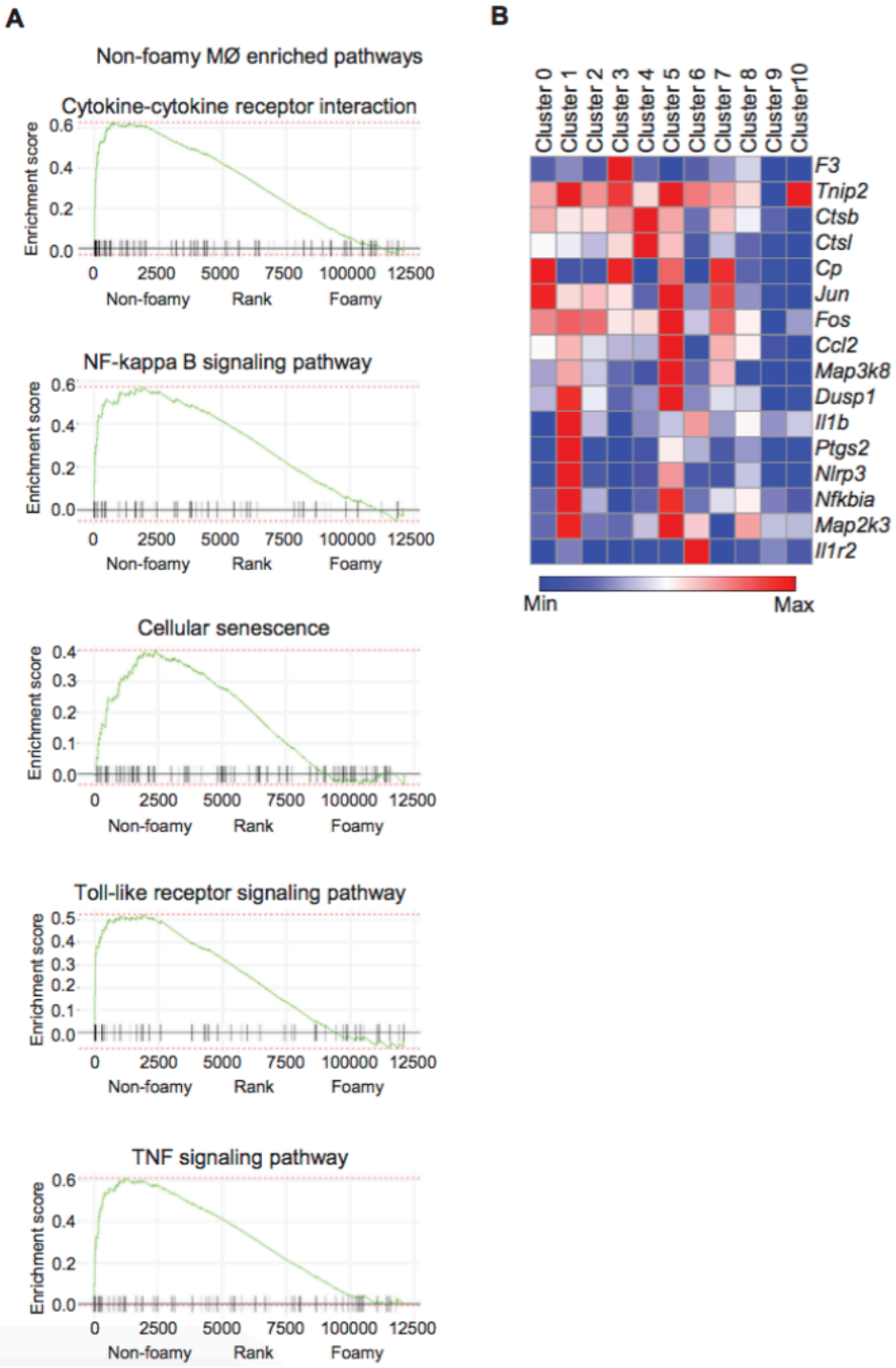

Supplemental figure 3.11. Expression of inflammatory genes in intimal non-foamy MØs. (A) Gene pathways related inflammation are enriched in non-foamy MØs (bulk RNA-seq; adjusted *P* value < 0.05). **(B)** Gene expression of the *Il-1* pathway in $CD45^{+}$ scRNA-seq clusters.

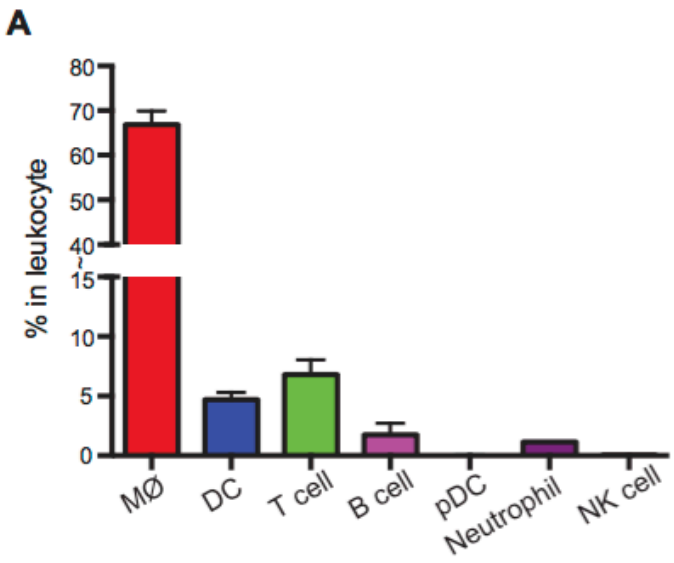

Supplemental figure 3.12. The composition of immune cells in atherosclerotic aorta. Gating strategy was shown in **Figure 3.4A**. In FACS analysis on aortic immune cells isolated by our method, MØ was a biggest aortic immune cell population in *Ldlr*$^{-/-}$ mice fed a WD for 12 weeks.

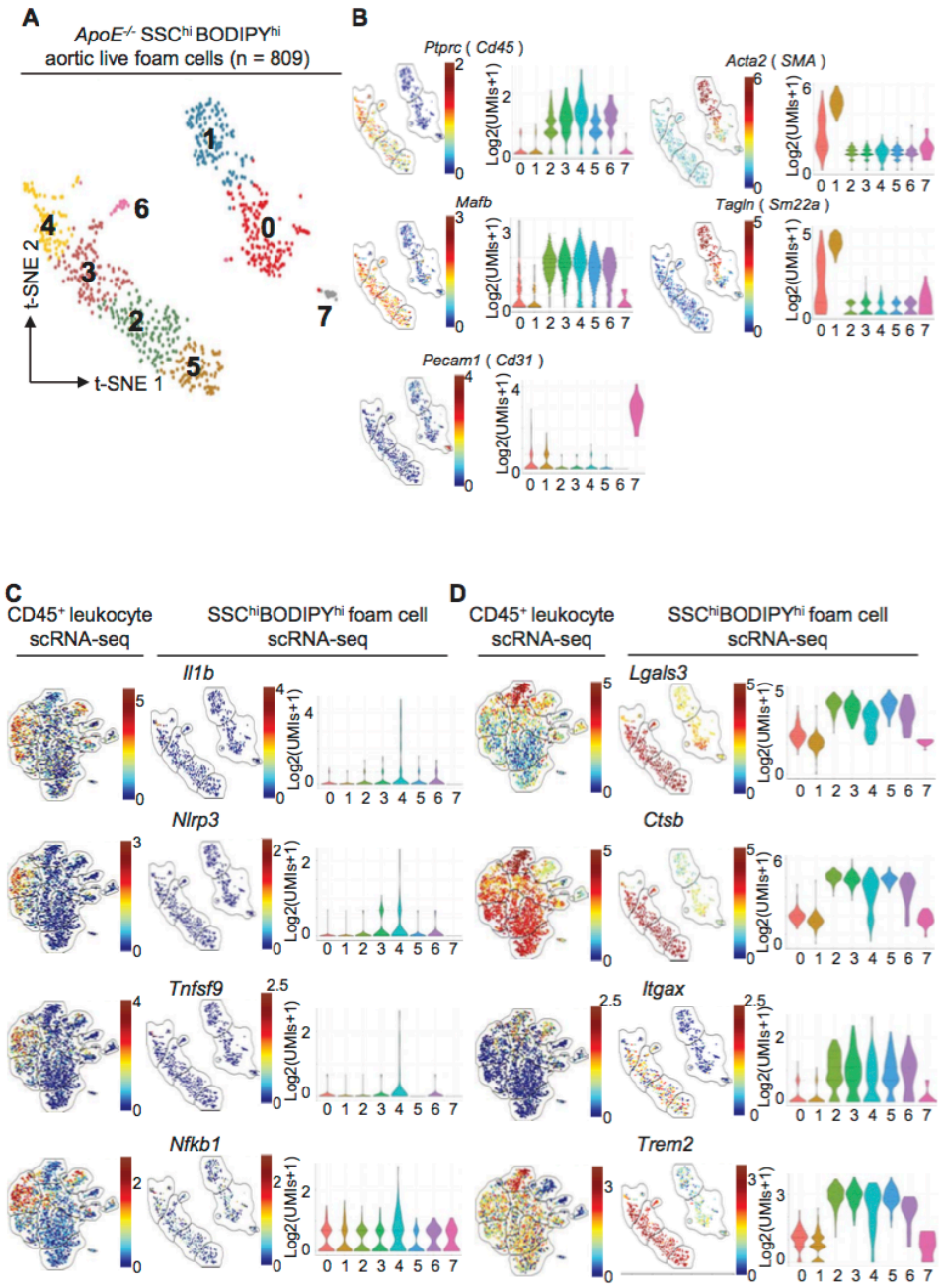

Supplemental figure 3.13. Clustering of total SSC^{hi}BODIPY^{hi} foam cells according to their gene expression profiles in scRNA-seq analysis. (A) Clusters of total aortic foam cells containing CD45^{+} and CD45^{-} cells. SSC^{hi}BODIPY^{hi} foam cells were isolated from the pooled aortas of *ApoE*$^{-/-}$ mice (n=6) fed a WD for 27 weeks. The cells (n=809) were grouped according to their mRNA expression patterns, analyzed similarly to the 10X single-cell sequencing results in **Figure 3.1**. **(B)** t-SNE and violin plots of *Ptprc*, *Mafb*, *Acta2*, *Tagln*, and *Pecam1* expression in each cluster. Gene expression is presented as log2 (UMIs+1). Clusters (2-6) are foamy MØs, while cluster 1 and 0 are smooth muscle foam cells. **(C and D)** Expression of previously defined representative enriched genes of foamy and non-foamy

MØs in the clusters of newly performed total foam cell scRNA-seq analysis. Representative genes of **(C)** non-foamy MØs and **(D)** foamy MØs are shown in t-SNE and violin plots of total foam cell scRNA-seq data. Gene expression is presented as log2 (UMIs+1).

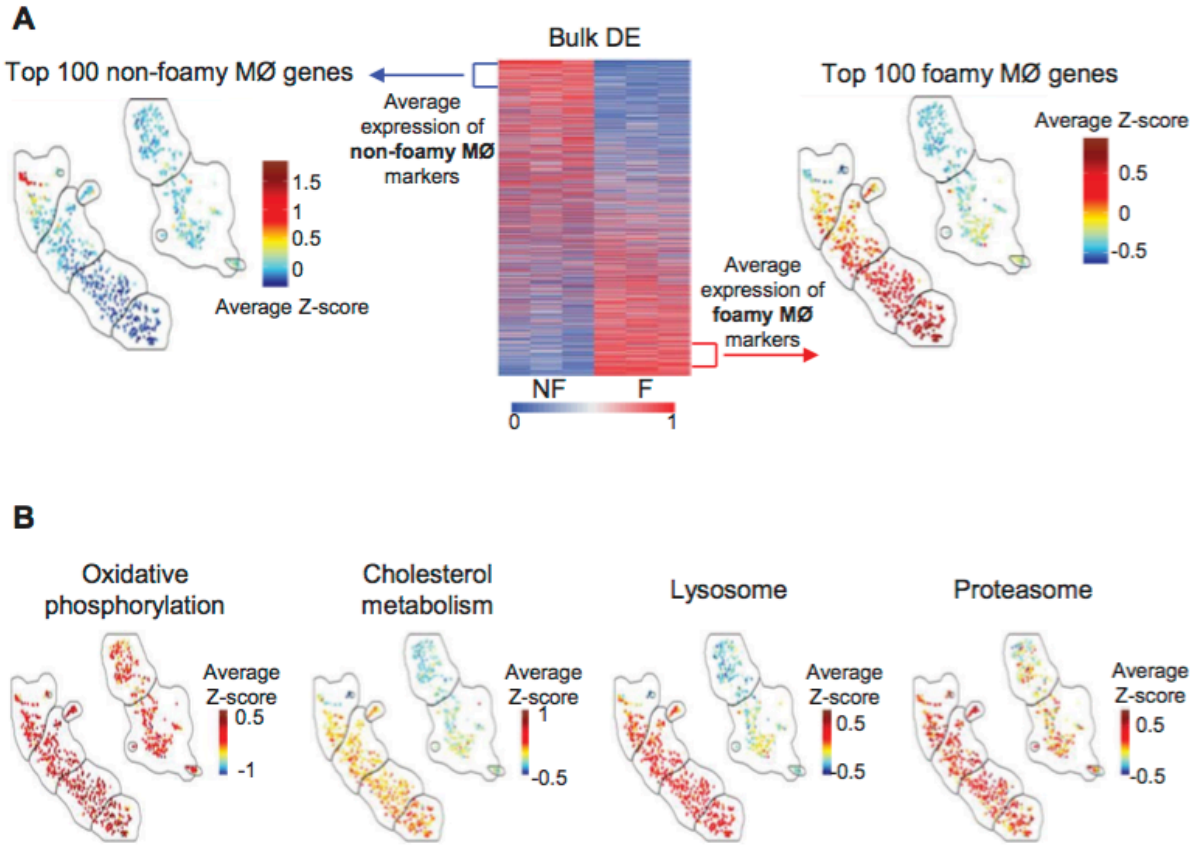

Supplemental figure 3.14. Enrichment of foamy MØ-related genes in *cd45*$^{+}$ foam cell cluster of scRNA-seq data. (A) The expressions of the top 100 enriched genes of non-foamy (left) or foamy (right) MØs in scRNA-seq data of total foam cells. Averaged normalized expression of these genes is shown as a t-SNE plot with colors corresponding to averaged normalized expression. **(B)** Average Z-score of genes in foamy MØ-related pathways. Gene enrichments from the KEGG pathways are shown as t-SNE plots.

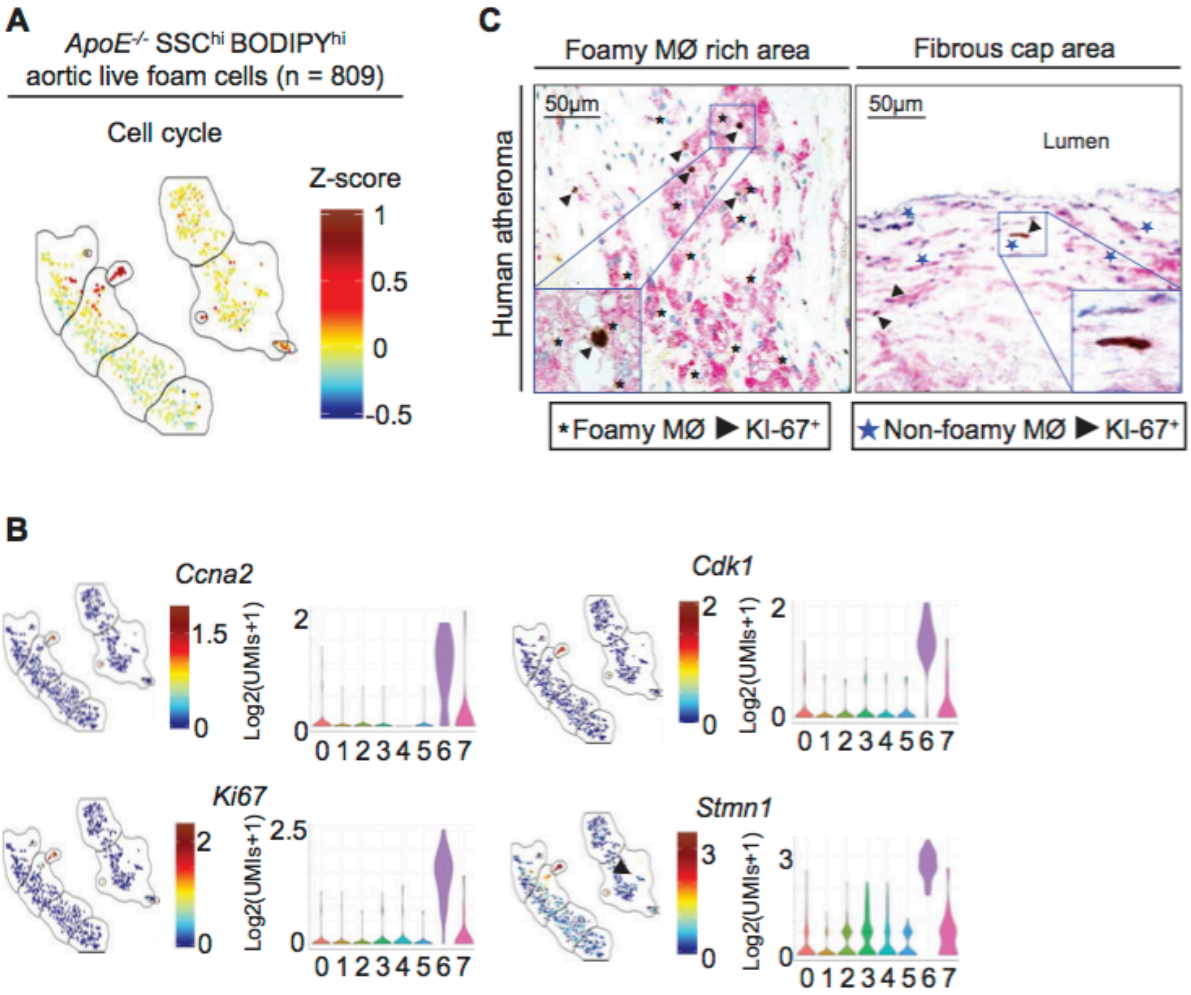

Supplemental figure 3.15. Identification of proliferative foamy MØs in atherosclerotic lesion. (A) Average gene enrichment score related to cell cycle and DNA replication pathways in scRNA-seq data of total foam cells. The average Z-score of genes are presented as t-SNE plots. **(B)** Representative gene expression related to cell proliferation. The expressions of *Ccna2*, *Cdk1*, *Ki67*, and *Stmn1* are presented as log2 (UMIs+1) in t-SNE and violin plots. **(C)** Double immunostaining with anti-KI-67 & CD68 antibodies on human atherosclerotic section. KI-67 (dark brown) and CD68 (red) were stained to identify proliferating foamy or non-foamy MØs in foamy MØ-rich or fibrous cap areas. Left, asterisks indicate foamy MØs, and arrow heads indicate KI-67 positive foamy MØs. Right, blue stars indicate non-foamy MØs, and arrow heads indicate KI-67 positive non-foamy MØs. This figure shows a representative immunostaining of three human samples.

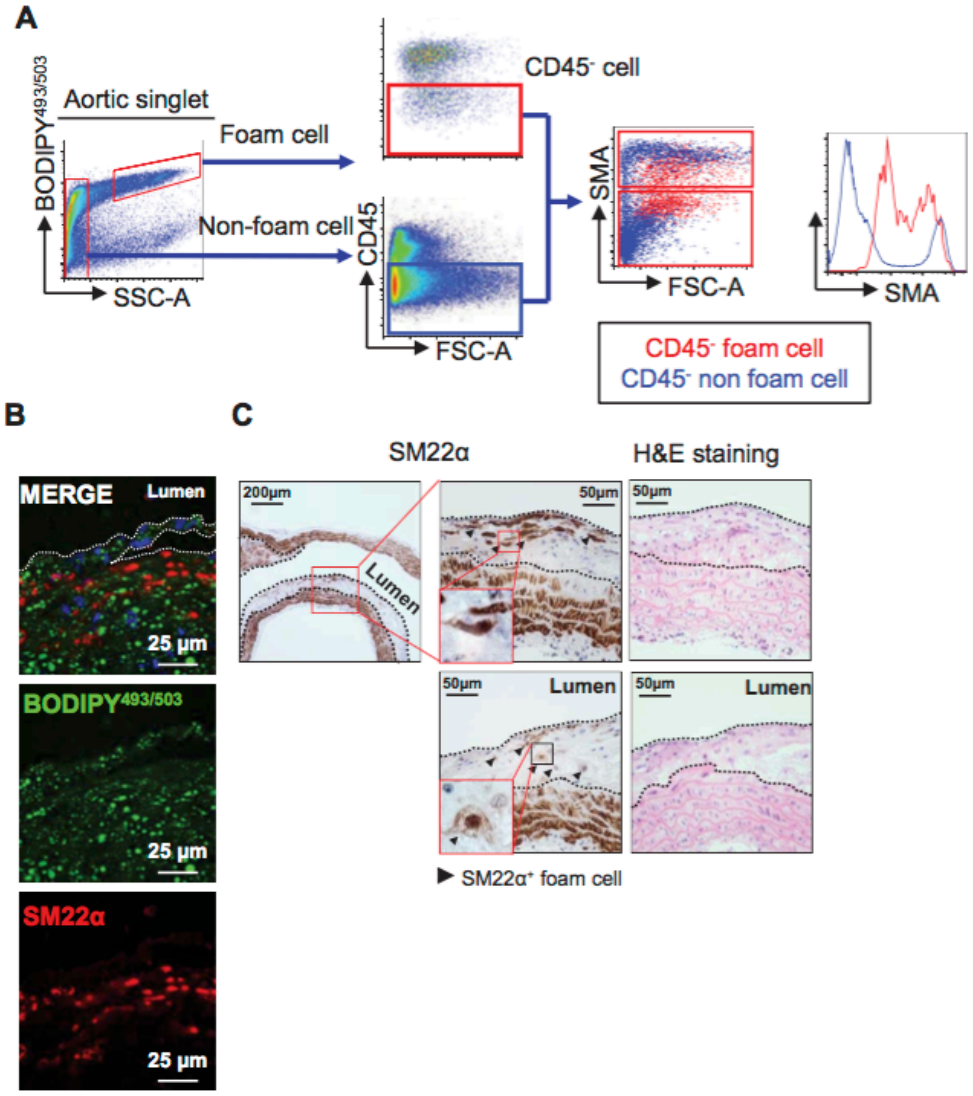

Supplemental figure 3.16. Identification of foam cells derived from SMC using flow cytometry and immunostaining. (A) Representative FACS gating strategy for detecting SMC-derived foam cells. Aortic CD45^{-} foam cells (red) expressed mid to high level of Smooth muscle alpha actin (SMA) compared with CD45^{-} non-foamy cells (blue). **(B and C)** Immunostaining of SM22α in mouse atherosclerotic lesions. SM22α-stained tissues **(B**, red; **C**, DAB**)** were **(B)** co-stained with BODIPY$^{493/503}$ or **(C)** serially stained with H&E. Dotted line indicates the lesion boundary.

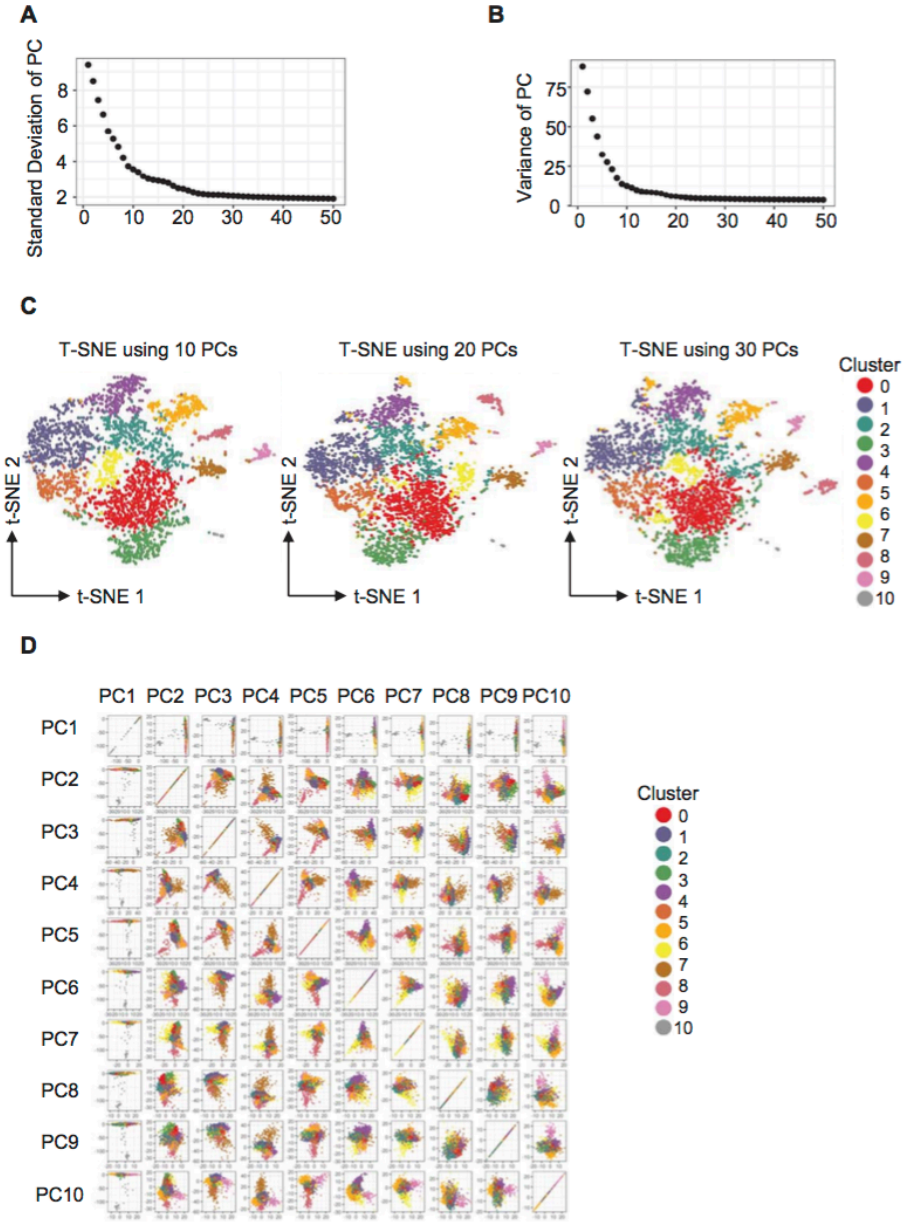

Supplemental figure 3.17. Standard deviation and explained variance for each principal component of scRNA-seq for CD45^{+} cells from whole aorta of *Ldlr*$^{-/-}$ mice. (A and B) Distribution of the **(A)** standard deviation and **(B)** variance of the first 50 PCs in CD45^{+} scRNA-seq. **(C)** t-SNE plot of the first 10, 20, and 30 PCs. The plots indicate that general leukocyte structure after dimensionality reduction remains the same. **(D)** PCA of the variances of the first 10 PCs (PC1 - PC10) of CD45^{+} scRNA-seq clusters. The clusters are not defined in t-SNE space and while the t-SNE algorithm does an excellent job of turning high-dimensional data into 2D space, t-SNE cannot guarantee accurate performance for each cell.

3. 12. 2 Supplementary Tables

Supplemental table 3.1. Representative DEGs and pathways enriched in each cluster of CD45^{+} scRNA-seq from whole atherosclerotic aortas.

Clusters	DEGs	Enriched pathways
Cluster 0	*Mrc1, F13a1, Gas6, CD163, Lyve1*	Endocytosis
Cluster 1	*Cd83, Nfkbia, Il1b, Tlr2, Nlrp3*	NF-kappa B, IL-17 signaling, TNF signaling, MAPK signaling, Apoptosis, TLR signaling, Cytokine-receptor interaction,
Cluster 2	*Cx3cr1, Ccr2, Mmp14, Tgfbr1*	Ribosome, DNA replication
Cluster 3	*Ccl6, F13a1, Lyve1, Retnla, Gas6*	Endocytosis
Cluster 4	*Lgals3, Ctsd, Abcg1, Trem2, Itgax*	Oxidative phosphorylation, Lysosome, PPAR signaling, Cholesterol metabolism
Cluster 5	*Cxcl2, Ccl7, Ccl2, Mrc1, Lyve1*	MAPK signaling, Cytokine-receptor interaction, IL-17 signaling, TNF signaling, Chemokine signaling, NK-kappa B signaling
Cluster 6	*Cd209a, Flt3, Itgax, Il1b, Zbtb46*	Ribosome, Cell adhesion molecule, proteasome
Cluster 7	*Oasl2, Irf7, Stat1, Mx1, Oasl1*	Antigen processing and presentation, interferon alpha/gamma response
Cluster 8	*Ccna2, Cdk1, Cdk4, Stmn1*	Cell cycle, DNA replication, cellular senescence, oxidative phosphorylation
Cluster 9	*Cd3e, Ccl5, Thy1, Lck, CD8a*	Ribosome, T cell receptor signaling, NK cell mediated cytotoxicity
Cluster 10	*Irf8, Xcr1, CD24a, Itgae, Flt3, Ccr7*	Ribosome, Cell adhesion molecules, proteasome

Representative DEGs (*left*) and pathways (*right*) in each cluster. *Left,* adjusted *P* value <0.01 and logFC > 0. Right, adjusted *P* value < 0.01 and NES > 0. Full data are available in Online data 3.1 [genes] and 3.1 [pathways].

Supplemental table 3.2. Comparison of aortic cell isolation protocols used for scRNA-seq analysis.

$CD45^+$ aortic cell isolation protocols for scRNA-seq			
	Cochain et al (Circ Res, 2018;122:1661-1674)	Winkels et al (Circ Res, 2018;122:1675-1688)	Kim et al
Mice	6-8wks male $Ldlr^{-/-}$ mice, Western diet: 11wks (n=8), 20wks (n=7); 8wks female $ApoE^{-/-}$ mice, WD: 12wks (n=10)	8wks male $Ldlr^{-/-}$ mice, High cholesterol diet: 12 wks; 8wks female $ApoE^{-/-}$ mice Western diet: 12 wks (n=10)	8wks male $Ldlr^{-/-}$ mice, WD: 12wks (n=6)
aorta Preparation	Intracardiac perfusion with ice-cold PBS perivascular adipose tissue was carefully removed	Intracardiac perfusion with ice -cold PBS+20U/ml of heparin perivascular adipose tissue was carefully removed	Intracardiac perfusion with ice-cold PBS perivascular adipose tissue was carefully removed
Enzyme mixture	RPMI + Col I (450 U/mL), + Col XI (125 U/mL), + Hyaluronidase (60 U/mL)	HBSS + Col I (450U/mL) + Col XI (250U/mL) + DNase I (120U/mL)	$Ca^{2+}Mg^{2+}$PBS + Col I (675 U/mL), + Col XI (187.5 U/mL), + DNase I (90 U/mL), + Hyaluronidase (90 U/mL)
Incubation time	37°C ,40 minutes	37°C ,60minutes	37°C ,70 minutes, with gentle shaking
Mesh size	40 µm	50 µm	100µm
Sorting machine	100 µm nozzle, BD FACSAria Fusion	100 µm nozzle, BD FACSAria Fusion	100 µm nozzle, BD FACSAriaIII

CHAPTER 4

4 Discussion

Cardiovascular diseases, including myocardial infarction (MI) and atherosclerosis, are a major global health problem that is expected to worsen in future. Many studies have previously confirmed that DCs and macrophages play an important role in lesion formation and its exacerbation by creating an inflammatory environment. Targeting these inflammatory cells could be an effective therapeutic approach to cure cardiovascular disease. Therefore, the purpose of this thesis is to clarify the functions of dendritic cells and macrophages in cardiovascular diseases, thereby contributing to the development of new conceptual therapies.

4. 1 cDCs Impair Recovery after MI

To better understand the functional properties of DCs and macrophages in cardiovascular diseases, such as atherosclerosis and MI, it would be desirable to analyze these cells in healthy and diseased organs. For example, immuno-histochemistry provides important information on their anatomic location and distribution in normal or inflammatory reactions, and multi-parameter flow cytometry strategies simultaneously allow analyses of various immune cell types. Recent advances in various methods have enabled immune cell analysis in the blood vessels (chapter 2) and the heart[241].

4. 1. 1 Cardiac DC Sub-Populations Similar to Non-Lymphoid Tissue DC Sub-Populations

In our study, aiming at the characterization of DCs, the cardiac macrophages that could affect flow cytometry analyses were first separated by the use of macrophage-specific markers, such as CD11b, F4/80, CD64 and MertK (**Figure 3.1**). $MHCII^{+}CD11c^{+}$ cardiac DCs expressed Zinc finger transcription factor Zbtb46 (Zbtb46), which was not found in other immune cells.[152, 153] These DCs had very low phagocytosis capacity compared to cardiac macrophages.[135] Interestingly, these cardiac DCs accumulate in the right atrium and valves, including tricuspid and mitral valves at steady state. The difference of CD103 expression in

cardiac DCs allowed us to clearly distinguish two DC subpopulations in healthy heart of mice.[155, 156] This feature is very similar to what is seen for non-lymphoid tissue DCs. Cardiac $CD103^+$ DCs (cDC1, conventional DC1) strongly expressed Clec9A, DEC205, CD24, XCR1, CD283 and CD180/RP105, whereas other markers, such as macrophages, T cells, B cells, NK cells, granulocytes and pDCs, were deficient (**Figure 3.1 and supplemental figure 3.1**). In particular, the growth of cDC1 was highly dependent on Flt3/Flt3L signaling[145, 146] and IRF8[160], but in Flt3 deficient mice their number was dramatically decreased. The expression pattern of these markers was very similar to that of the $CD8^+$ DCs in spleen.[157, 158] In contrast, cardiac $CD11b^+$ DCs (cDC2) strongly expressed some macrophage markers, such as CX3CR1, CD172α, CD115 and F4/80. The development of cDC2 was dependent on IRF4.[174] cDC2 are similar to those $CD8^-$ DCs found in lymphoid tissue. These results suggest that the origin and function of cardiac DC sub-populations are closely related to non-lymphoid tissue DCs.[148, 149, 150, 151]

Furthermore, we were able to detect HLA-DR^+CD11c^+ DCs containing two DC sub-populations in hu-mice, whose bone marrow was reconstituted from human stem cells. Similar to mouse cardiac DC subsets, human $BDCA3^+$ DCs expressed IRF8[167], whereas $BDCA1^+$ DCs were dependent on IRF4.[168, 169] In addition, $BDCA1^+$ DCs exhibited a slight proliferation following signaling through Flt3/Flt3L. Still, the response was low compared to $CD103^+$ DC.[145, 164] These observations in humanized mice can help us understand the features of DC sub-populations in normal human heart.

4. 1. 2 Are Cardiac DN cells Progenitors?

$MHCII^+CD11c^+$ DCs in normal mouse heart included cDC1 and cDC2 but also double negative cells (DNs) that did not express CD103 or CD11b. Similar to other DC subsets, these DN cells were found mostly in the right atrium and valves. Upon Flt3L treatment, these DN cells not only increased in numbers, but also increased DN cells by Flt3/Flt3L signaling were very positive for IRF8. Notably, they also expressed Zbtb46. Cells of similar phenotypes, such as cardiac DN cells, have previously been found in other tissues, such as mouse dermis and gut, but their characteristics are poorly understood.[150, 242, 243] DCs are derived from pre-cDCs

that circulate blood away from the bone marrow and consistently require the inflow of Pre-cDCs in order to maintain their numbers in tissues (**Figure 1.8**).[150, 151] The expression of Zbtb46 begins in Pre-cDCs.[153] Therefore, our observations suggest that Pre-cDCs may be present in the heart. Furthermore, to understand the precise properties and the origin of these cells in heart, the analyses of sc-RNA-seq and fate mapping will be required.

4. 1. 3 Cardiac pDCs under Normal and Inflammatory Conditions

pDCs are known to play an important role in the differentiation of Tregs.[244] Previously, we provided support for this statement.[193] Mouse aortic pDCs are distributed in specific blood vessel areas that develop atherosclerosis and they regulate the generation of Tregs in blood vessels by expressing indoleamine 2,3-dioxygenase 1 (IDO-1). In normal mouse heart, we found cardiac pDCs with a phenotype similar to aortic pDCs. These cardiac pDCs are predominantly distributed in the right and left atrium of the mouse heart and show high expression of Ly6C, Clec9A, PDCA-1, Flt3/CD135 and IRF8. Surprisingly, cardiac pDCs showed a 4-fold increase in the infarcted heart in mice. Nevertheless, our results demonstrated that their selective elimination using BDCA2-DTR mice did not improve left ventricle function of myocardial-infarcted heart (**Figure 3.5**). These results suggest that viral infections may induce the activity of cardiac pDCs through TLR7 and TLR9, and activated cardiac pDCs may secrete large amounts of type 1 IFN in order to protect the cardiac tissue.[245]

4. 1. 4 Cardiac DCs in The Infarcted Heart

The occurrence of MI leads to myocardial cell death, which accompanies local inflammation and activation of cardiac endothelial cells. Neutrophils recruited to the infarcted site initiate the elimination of damaged or dead cells and the secretion of IL-6 that attracts macrophages and neutrophils.[127, 128] We observed a significantly increased recruitment of leukocytes including macrophages ($\leq$ 9 fold) and neutrophils ($\leq$ 15 fold) in the hearts of mice 3 days after MI (**Figure 3.4**). In addition, DC numbers in the myocardial infarcted heart showed a four-fold increase compared to the non-infarcted heart. This result is similar to those

described from human patients.[237, 238] The phenotype of DC subpopulations recruited at the infarcted site was consistent with the one of cardiac DC subpopulations in non-infarcted mice (**Figure 3.1 and Supplemental figure 3.6**). These cells were found in ventricle and septum 3 days after MI and in the right atrium 7 days later (**Supplemental figure 3.5**).

In particular, DCs recruited at wound sites in patients with MI expressed high levels of CD209[239] and CD86[240], indicating their maturation status. Compared to other DC subpopulations, a massive recruitment of $CD11b^+$ DCs (≥ 9 folds) was observed in the infarcted heart, all of which expressed the co-stimulatory molecule CD40. These results indicate that cytokines, such as GM-CSF secreted by macrophages and activated myocardial endothelial cells after MI, may accelerate the differentiation of DC precursors into $CD11b^+$ DCs. In these cells, IRF4 enhances the expression of TGF-β and IL-6, which induce polarization to Th17 cells. This promotes tissue inflammatory responses and increases neutrophils recruitment at wound sites.[216, 246] Indeed, the administration of GM-CSF to myocardial infarcted mice increases DC infiltration and accelerates of LV remodeling.[124]

4. 1. 5 Heterogeneity of Cardiac $CD11b^+$ DCs

DCs derived from $Ly6C^{high}$ monocytes circulating in the blood are increased in the infarcted area and they can promote the inflammatory response.[185, 186] Their levels of Ly6C are reduced after migration to infarcted heart and they begin to express Zbtb46[153] together with macrophage markers, including CD209/DC-SIGN.[182, 247] One remarkable feature is that they are very similar phenotypically to $CD103^-CD11b^+$ DCs that differentiated from Pre-DCs. We observed the increased recruitment of monocyte subpopulations in the myocardial infarcted heart 3 days after MI **(Supplemental figure 3.7)**. In addition, a significant increase of $CD11b^+$ DC numbers in the heart under representative inflammatory conditions, including aging and atherosclerosis, supports the association of monocyte-derived DCs (**Supplemental figure 3.3**) These results strongly suggest that monocyte-derived DCs could be associated with cardiac inflammation, such as MI.

4. 1. 6 The Selective Depletion of Cardiac DCs

Various genetic models, such as CD11c-DTR, CD11b-DTR, and LysM-Cre x iDTR, have been used to investigate the role of DCs in various pathologies.[248] However, these mouse models also affect other cell populations, including monocytes and macrophages.[229] Because the expression of Zbtb46 is restricted to both Pre-cDCs and cDCs, the use of Zbtb46-DTR mice has made it possible to overcome these limitations.[153] DT administration in chimeric mice reconstituted with BM from Zbtb46-DTR mice led to the selective depletion of $CD11c^{+}MHCII^{+}$ DCs in the lymph node, spleen, and heart. The selective depletion of Zbtb46-expressing DCs in myocardial infarcted mice resulted in a dramatic reduction in heart infarcted-size preventing ventricular remodeling, improved cardiac function. It also caused a significant decrease of macrophages and $CD45^{+}$ cells at 7 days but not at 3 days after MI (**Figure 3.6 and 3.7, supplemental figure 3.4, and supplemental movie 1-4**). The accumulation of DCs in injured tissue may be necessary to heal wounds and protect myocardial tissue. Nevertheless, activated DCs not only prime naïve T cells in the nearby secondary lymphoid tissues, but also can participate directly in immune responses in the cardiac tissue. For example, DAMPs signals released from dead cardiomyocytes can activate cDCs[249] and the production of pro-inflammatory cytokines, such as TGF-β, IL-6 and IL-23, can sustain inflammatory responses.[133, 247] In particular, IL-12 secreted by DCs appears to inhibit angiogenesis.[250] Eventually, these reactions can be detrimental and lead to interstitial fibrosis, wall thinning, and lower cardiac function.

4. 1. 7 Immune Responses Modulated by Cardiac DCs

Treg cells expressing the Foxp3 transcription factor secrete IL-10 and TGF-β and play important roles in suppressing autoimmune disease and maintaining immune homeostasis.[251] It was previously reported that the depletion of Treg cells prior to MI induction accelerated cardiac inflammation.[252] Our results showed that Tregs were reduced about 2 fold in infarcted hearts. Their numbers were significantly increased upon infiltration of DCs. However, the selective depletion of DCs led to a significant decrease in Treg and IL-1β. Previous studies have shown that the down-regulation of the pro-inflammatory signaling pathway, such as IL-

1β, protects the infarcted heart by reducing the mobilization of white blood cells in the wound area.[253] Interestingly, the heart of myocardial infarcted mice with the selective depletion of cDCs showed reduced mobilization of $CD45^+$ cells, including macrophages, $CD3^+$ T cells and $CD4^+$ T cells. This suggests that cardiac DCs are closely involved in the formation of an immune-rich environment following MI.(Figure 4.1)

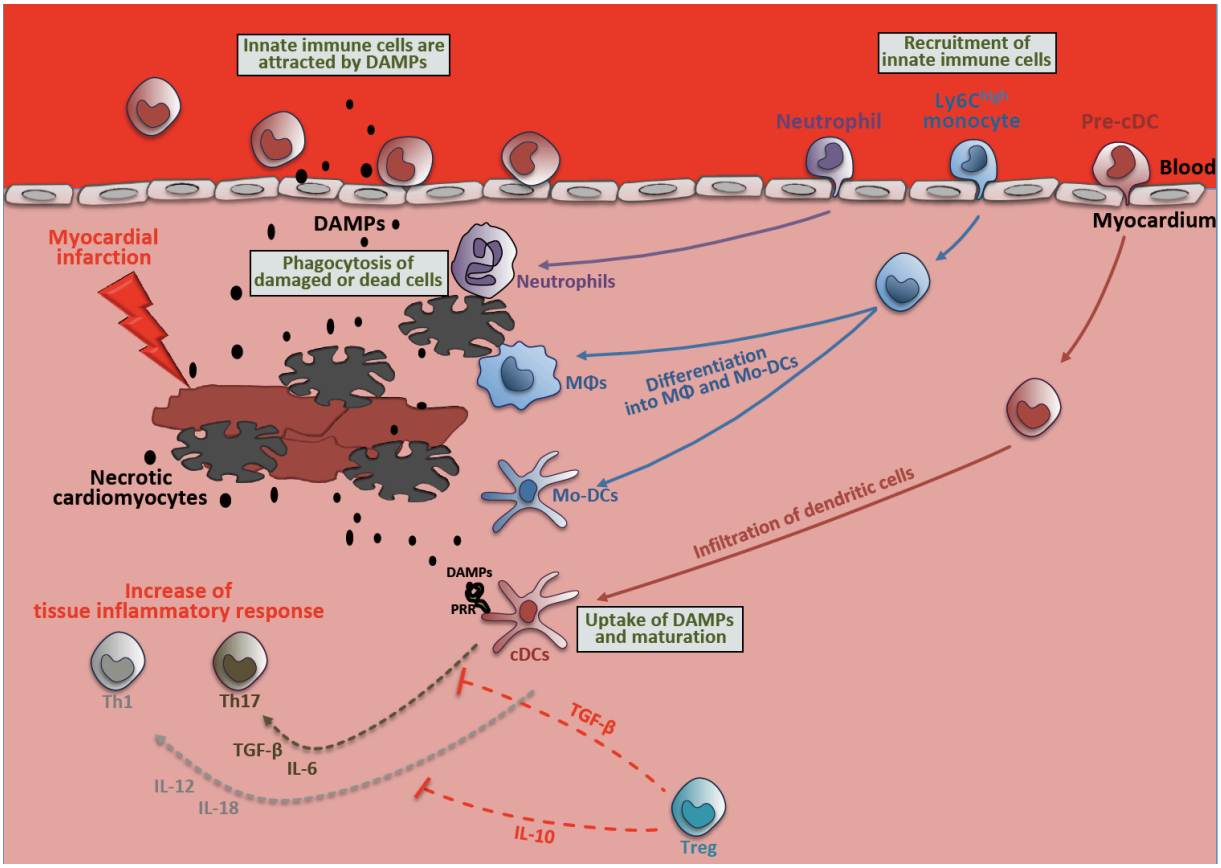

Figure 4.1. The role of dendritic cells in myocardial infarction. Myocardial infarction results in the death of cardiomyocytes, releasing intracellular contents that act as DAMP. To remove damaged or dead cells and protect myocardial tissue, innate immune cells, such as neutrophils, monocytes, and DCs are recruited at the damaged area by DAMP. Monocytes differentiate into macrophages and Mo-DCs, while pre-cDCs differentiate into cDCs. Neutrophils and macrophages phagocytize and cleanse dead cells and tissue debris. cDCs are also activated by DAMPs, and migrated to the draining lymph node where DCs activate naïve T cells. The differentiation of Th1 cells is induced by IL-12 and IL-18 secreted by cDCs and Th17 cells can be promoted by TGF-β and IL-6. These inflammatory cytokines, which are secreted by cDCs, have a detrimental effect on the heart and lead to persistent inflammatory response. On the other hand, Tregs play an important role in maintaining the homeostasis of cardiac immune by releasing TGF-β and IL-10. MΦ: macrophages, Mo-DCs: monocyte-

derived dendritic cells, Pre-cDC: Pre-classical dendritic cells, cDC: conventional DCs, Th1: Type 1 T helper cells, Th17 cells: Type 17 T helper cells.

Acute inflammatory responses, such as MI, specifically up-regulate IL-6 expression, which may induce the polarization into Th17 cells. Therefore, the cardiac immune response following MI may be regulated by the minute differences in cytokines, such as TGF-β and IL-6, secreted by cardiac DCs. Indeed, the generation of tolerogenic DCs using cytokines, including IL-37 and TNF-α, can improve ventricular remodeling and cardiac function.[254, 255] After myocardial infarction, the injection of HMGB1 (high-mobility group box 1) improved heart function via reducing the recruitment of dendritic cells.[256] HMGB1 acts as a cytokine to regulate inflammation its high affinity receptors on the surface of target cells, such as dendritic cells.[257] In addition, DT treatment to CCR2-DTR mice effectively depleted monocytes, macrophages and dendritic cells with the exception of neutrophils or lymphocytes.[258] After myocardial infarction, DT treated-CCR2-mice also did not show a significant impairment of heart function compared to control.[259] Combining our data with these results, it shows that interventions to control the number or function of cDCs have therapeutic potential. Furthermore, in the future, experiments should deal more deeply with the relationship between DCs and other immune cells in health and disease.

4. 2 Foamy Plaque Macrophage are Pro-inflammatory

Atherosclerosis is the result of complex inflammatory reactions implicating several immune cell populations, including vascular endothelial cells.[11] To better understand atherosclerosis as a whole, the definition of the central cellular components in the lesion is essential. However, the disadvantages of classical methods, such as Oil Red O and immunofluorescence, in studying atherosclerotic lesions did not make this possible.[85] Our new flow cytometry-based approach using BODIPY493/503 showed several advantages compared to pre-existing histological methods. First, the assessment of atherosclerosis using flow cytometry showed high accuracy and sensitivity. Second, this method enabled us to perform multiple simultaneous analyses for cellular proteins expression. Third, while pre-existing

measurements require several weeks to assess atherosclerosis gravity, this method can deliver successful assessment of atherosclerosis status within a day.

4. 2. 1 Advantages and Disadvantages of Our Cell Isolation method

Atherosclerotic aorta contains leukocytes, including macrophages, dendritic cells, T cells, B cells, NK cells and granulocytes, and each of these subsets is highly heterogeneous.[260, 261] Our RNA-seq data of leukocytes from atherosclerotic aorta (*Ldlr*$^{-/-}$ mice) revealed the composition of various immune cell populations, including T cells, DCs and macrophages. Among the CD45^{+} leukocytes of atherosclerotic aorta, macrophages were the largest cell population. However, the use of our method failed to identify aortic B cells, NK cells and neutrophils. The efficient separation of cells from tissues depends on the digestion time, pore size of strainer, and type and concentration of digestive enzymes. We used longer digestion times to isolate macrophages that are more tightly bound to aortic tissue than other immune cells. This indicates that our cell extraction method, slightly modified from chapter 2, is more optimized for isolation of macrophages and should be optimized for the characterization of each and every cellular subset.

4. 2. 2 Establishment of Multi-Parametric Flow Cytometry using BODIPY493/503

An exact measurement of lipid-rich lesions size is important to assess the severity of atherosclerosis in any mouse model. In this study, we assessed atherosclerosis via enumeration of foam cells using multi-parametric flow cytometry combined with BODIPY493/503 staining. We used two mouse knockout models: *ApoE*$^{-/-}$ and *Ldlr*$^{-/-}$ mice. Although these strains are widely utilized to study atherosclerosis, there are some differences in lipid profiles and in progression of lesions between these two models.[262, 263, 264] While Oil red O-stained atherosclerotic lesions increased rapidly after feeding WD for up to 8 weeks in *ApoE*$^{-/-}$ mice, the lesions were exacerbated gradually in *Ldlr*$^{-/-}$ mice and these results correlated with the data from our flow cytometry analyses. By performing flow cytometry on aortic tissue devoid

of the adventitia, we confirmed that a lipid probe-based flow cytometry approach was the method of choice for detecting intimal atherosclerotic foam cells.

Atherosclerotic lesions show site-specific features in their initiation and progression.[265] While aortic sinus and arch are the most susceptible areas, thoracic aorta is most resistant to atherosclerosis. The site-specific atherosclerosis comes from different oscillation, blood turbulence, and shear stress.[266, 267, 268] In our study, we divided aorta into 3 segments, including aortic sinus with arch, thoracic aorta, and abdominal aorta, and analyzed site susceptibility for atherosclerosis (**Supplemental figure 4.3**). Our flow cytometry analysis could efficiently assess the atherosclerosis and corroborated with the results from Oil red O staining (**Supplemental figure 4.4**). As previously reported, many treatments for atherosclerosis showed site-specific effects.[265] We suggest that our lipid-probe based flow cytometry for analysis site-specificity of atheroscelrosis lesions. In addition, this method could be adapted to design a diagnostic approach to assess the location, size and progression of atherosclerotic lesions using echography imaging.

4. 2. 3 Evaluation of The Therapeutic Potential of Anti-Atherosclerotic Drugs using Lipid Probe-Based Flow Cytometry

Atorvastatin is a member of statins, HMG-CoA reductase inhibitors, which are currently used to ameliorate hyperlipidemia, coronary artery disease, and atherosclerosis.[269] In our experiments, we examined whether our flow cytometry analysis could highlight the effect of atorvastatin on atherosclerotic lesion formation (**Supplemental figure 4.7**). Anti-atherogenic activity of atorvastatin was well-monitored by our assay.

In addition to the LDLR and ApoB loci, mutations on the PCSK9 gene have been linked to autosomal hypercholesterolemia.[270] Overexpression of PCSK9 results in degradation of the LDL receptor.[271] In mice, PCSK9 overexpression induces atherosclerosis and its knockout has protective effects.[272, 273, 274] The treatment with monoclonal antibodies targeting PCSK9 can lower LDL cholesterol[275] and attenuate atherosclerosis.[276] In human patients, monoclonal antibodies targeting PCSK9 could decrease atherosclerotic lesions, and ongoing phase III trials could provide evidence of safety and efficacy of these antibodies.[277, 278, 279, 280]

Thus, novel PCSK9 inhibitors have been developed and tested for their therapeutic efficacy on atherosclerosis. In this study, we successfully assessed atherosclerosis in D347Y-PCSK9 transgenic mice and the therapeutic potential of the PCSK9 blocking antibody, AMG 145, using our lipid probe-based flow cytometry (**Supplemental figure 4.4**). These results indicate that our method can be utilized for the screening of new drug candidates.

4. 2. 4 Characterization of Lipid-Laden Cells

Lesional accumulation of lipid-laden foam cells carrying many lipid droplets is a key feature of atherosclerosis and the death of some of these cells is a pivotal step to the formation of a necrotic core.[281, 282, 283] To understand the mechanism of foam cell formation, mostly *in vitro* studies have been performed using MΦ cell lines[284], peritoneal macrophages[283, 285], and bone marrow derived macrophages[286, 287]. However, these experiments cannot take into account various *in vivo* mircoenvironmental factors in atherosclerotic lesions, which may affect foam cell formation. In our study, we have compared the expression levels of CD11b, CD11c, CD64, MHCII, and Ly6C among three groups of macrophages including aortic macrophages of normal aorta, non-foamy and foamy macrophages of atherosclerotic aorta. In previous studies, macrophages treated with LDL particles increased their expression of CD11c and MHC II, adopting a DC like phenotype.[288] Consistently, foamy macrophages had higher CD11c and MHCII expression than normal macrophages. Still, the foamy macrophages showed comparable expression of CD64, a Fc receptor and a specific marker for macrophages.[289] In addition to lipid metabolism, cholesterol uptake and efflux are critical steps in the regulation of foam cells formation.[290] Recently, several scavenger receptors and cholesterol efflux regulatory proteins have been shown to play pivotal roles in formation of foam cells.[291] Here, we analyzed four different groups of $SSC^{hi}BODIPY^{hi}$ foam cells based on their size and granularity (**Supplemental figure 4.6**). Interestingly, the size and granularity increased as atherosclerosis progressed during WD. This increase was attenuated by anti-atherosclerotic drugs, including atorvastatin and rosuvastatin. Therefore, our method would apply to the investigation of the effects of activators or inhibitors of foam cell formation.

4. 2. 5 What is Different between $SSC^{hi}BODIPY^{hi}$ foamy macrophages and $SSC^{lo}BODIPY^{lo}$ non-foamy macrophages

RNA-seq data from $SSC^{hi}BODIPY^{hi}$ foamy macrophages and $SSC^{lo}BODIPY^{lo}$ non-foamy macrophages isolated from atherosclerotic aorta of $Ldlr^{-/-}$ mice showed different patterns of gene expression. Foamy macrophages increased expression of genes related to cholesterol transport, fatty acid transport, and cholesterol uptake, whereas non-foamy macrophages exhibited up-regulation of inflammatory cytokines, such as IL-1β, in atherosclerotic lesions. Inflammatory cytokines secreted by non-foamy macrophages promote the recruitment of white blood cells and the activation of vascular endothelial cells.[93] These results demonstrate that non-foamy cells promote lesions development and atherosclerosis, while foamy macrophages increase lipid uptake and outflow through their scavenger receptors, such as SR-A1 and SCARB3, which persist until apoptosis occurs.

Previous studies have shown that DCs[81] and SMC[82, 292] are also involved in foam cell formation. Therefore, we investigated the characteristics of total foamy macrophages, including $CD45^{+}$ and $CD45^{-}$. Gene expression patterns of $SSC^{hi}BODIPY^{hi}$ foamy macrophages (n=809) pooled from atherosclerotic aortas of $ApoE^{-/-}$ mice (n=6) were analyzed. A total of 8 clusters were identified, and these clusters were again divided into two large groups. Compared to clusters 2 to 6, clusters 0 and 1 expressed high levels of Tagln and Acta2, while cluster 7 exhibited the increased expression of Pecam1 (**Supplemental figure 4.13**). Surprisingly, we also identified foamy macrophages expressing smooth muscle cell alpha actin in atherosclerotic plaques using flow cytometry and immunostaining (**Supplemental figure 4.16**). These results demonstrated that foamy macrophages could be derived from SMC and endothelial cells, as well as macrophages.

Another group of cells, included in clusters 2 to 6, exhibited low levels of inflammatory genes expression, such as IL-1b, Nlrp3, Tnfsf9 and Nfkb1, while high levels of mRNAs for genes, such as Mafb and Ptprc (CD45), which represent foamy macrophages. This also indicates that cells forming clusters 2 to 6 are foamy macrophages. In animal experiments, the genes related to connective tissue development and function, cell growth, cell proliferation, and cholesterol metabolism (eg, Abca1, Pparγ, Rxra, Rxrb, and Srebp1) were all up-regulated in foamy macrophages.[293] Most of the human lesional foam cells are positive for CD68 and

CD14, but the genes associated with smooth muscle cells (αSMA and MYH11) were not expressed. In particular, lesional foamy macrophages expressing CD68 showed significantly lower expression of IL-1β than non-foamy macrophages (**Figure 4.8**). We could confirm by scRNA-seq that a small population of non-foamy macrophages or foamy macrophages exhibited high expression of genes related to cell cycle and proliferation. In the fibrous cap area, 9.54±0.54% of the non-foamy macrophages expressed KI-67 and 5.8±2.8% of total foamy macrophages in foam cell-rich area of human atheroma were KI-67 positive. Thus, it appears that macrophages are consistently proliferating regardless of lipid accumulation. Nonetheless, additional scRNA-seq analyses will be required to understand the full characteristics and origin of foamy and non-foamy macrophages in atherosclerotic lesions. For example, analysis of foamy or non-foamy macrophages separated from early or advanced lesions could help to understand the physiology of macrophage subpopulations and their phenotypic changes. Additionally, to understand whether foamy macrophages are generated mostly from non-foamy macrophages or a specific subset of macrophages, we could combine our scRNA-seq with genetic fate mapping of macrophage precursors, such as $CX3CR1^{+}$ precursors. It can also be very useful in examining their maturation and origin of foamy and non-foamy macrophages.

4. 3 Conclusion

In this thesis, we showed that DCs and macrophages in cardiovascular diseases, such as atherosclerosis and MI, have strong influence on lesion formation and exacerbation by creating a pro-inflammatory environment.

Mouse cardiac $MHCII^{+}CD11c^{+}$ DCs include $CD103^{+}$ DCs and $CD11b^{+}$ DCs as well as double negative cells (DNs) that do not express either CD103 or CD11b. cDC1 are dependent on Flt3/Flt3L signaling and IRF8, whereas cDC2 are dependent on IRF4. MI significantly recruited leukocytes, including macrophages, neutrophils and DCs at the wound site. cDC2 was the most significant increase among DC subpopulations. The selective depletion of Zbtb46-expressing DCs following MI resulted in a dramatic reduction in the heart infarct size and improved cardiac function. Moreover, cDC depletion showed a significant decrease of IL-1β and the recruitment of $CD45^{+}$ leukocytes, including macarophages, $CD3^{+}$ T cells, and $CD4^{+}$ T cells. These results demonstrate that cardiac DCs play an important role in immune cells infiltration after MI. Future studies should address the accurate and origins of DC sub-populations in healthy and infarcted heart.

We established for the first time a lipid probe-based flow cytometric method to investigate foam cells in atherosclerosis. The number of $SSC^{hi}BODIPY^{hi}$ foam cells detected by this method correlated with lesion size. Therefore, our flow cytometry analysis not only enables trancriptome analysis of foamy macrophages and non-foamy macrophages, it can also be used to assess the severity of atherosclerosis and the characteristics of foam cells. The lipid-laden macrophages, which accumulate lipids in their cytoplasm in atherosclerotic lesions, exhibited clearly different gene expressions compared to non-foamy macrophages. Notably, IL-1β expression in lesional foamy macrophages in mouse and human was significantly reduced. Furthermore, scRNA-seq or bulk RNA-seq analysis of foamy and non-foamy macrophages in the human atherosclerotic aorta is very important for our understanding of foam cell formation in atherosclerosis.

The purpose of this thesis was to contribute to the prospective development of therapeutic agents by clarifying the functions of dendritic cells and macrophages in the pathogenesis and the formation of cardiovascular diseases. Targeting of cells responsible for

the inflammatory response can be an effective therapeutic mean to that attenuate cardiovascular disease.

4. 4 References

1. Organization, W.H. Cardiovascular diseases (CVDs). *Available at:* https://www.who.int/en/news-room/fact-sheets/detail/cardiovascular-diseases-(cvds) (2017).

2. Roth, G.A. *et al.* Global, Regional, and National Burden of Cardiovascular Diseases for 10 Causes, 1990 to 2015. *J Am Coll Cardiol* **70**, 1-25 (2017).

3. Organization, W.H. Global atlas on cardiovascular disease prevention and control. https://www.who.int/cardiovascular_diseases/publications/atlas_cvd/en/ (2011).

4. Kessler, T., Erdmann, J. & Schunkert, H. Genetics of coronary artery disease and myocardial infarction--2013. *Curr Cardiol Rep* **15**, 368 (2013).

5. O'Donnell, C.J. & Elosua, R. [Cardiovascular risk factors. Insights from Framingham Heart Study]. *Rev Esp Cardiol* **61**, 299-310 (2008).

6. O'Donnell, C.J. & Nabel, E.G. Genomics of cardiovascular disease. *N Engl J Med* **365**, 2098-2109 (2011).

7. Organization, W.H. Causes of death. Geneva: World Health Organization *Abailable at:* https://www.who.int/healthinfo/global_burden_disease/cod_2008_sources_methods.pdf (2008).

8. Organization, W.H. The global burden of disease: 2004 update. Geneva: World Health Organization. (2008).

9. Organization, W.H. Global health risks : mortality and burden of disease attributable to selected major risks. Geneva: World Health Organization *Abailable at:* http://www.who.int/iris/handle/10665/44203 (2009).

10. Davis, N.E. Atherosclerosis--an inflammatory process. *J Insur Med* **37**, 72-75 (2005).

11. Ross, R. Atherosclerosis--an inflammatory disease. *N Engl J Med* **340**, 115-126 (1999).

12. Libby, P., Ridker, P.M. & Maseri, A. Inflammation and atherosclerosis. *Circulation* **105**, 1135-1143 (2002).

13. Mendis, S., Puska, Pekka, Norrving, B, World Health Organization, World Heart Federation. et al. Global Atlas on cardiovascular disease provention and control. (2011).

14. Randomised trial of cholesterol lowering in 4444 patients with coronary heart disease: the Scandinavian Simvastatin Survival Study (4S). *Lancet* **344**, 1383-1389 (1994).

15. Shepherd, J. *et al.* Prevention of coronary heart disease with pravastatin in men with hypercholesterolemia. West of Scotland Coronary Prevention Study Group. *N Engl J Med* **333**, 1301-1307 (1995).

16. Gotlieb, A. & Langille, B. The role of rheology in atherosclerotic coronary artery disease. In: Fuster V, Ross R, Topol EJ, eds. Atherosclerosis and coronary artery disease. *Philadelphia lippincott-raven* **Vol. 1**, 595-606 (1996).

17. Chatzizisis, Y.S. *et al.* Role of endothelial shear stress in the natural history of coronary atherosclerosis and vascular remodeling: molecular, cellular, and vascular behavior. *J Am Coll Cardiol* **49**, 2379-2393 (2007).

18. Steinberg, D. Low density lipoprotein oxidation and its pathobiological significance. *J Biol Chem* **272**, 20963-20966 (1997).

19. Khoo, J.C., Miller, E., McLoughlin, P. & Steinberg, D. Enhanced macrophage uptake of low density lipoprotein after self-aggregation. *Arteriosclerosis* **8**, 348-358 (1988).

20. Khoo, J.C., Miller, E., Pio, F., Steinberg, D. & Witztum, J.L. Monoclonal antibodies against LDL further enhance macrophage uptake of LDL aggregates. *Arterioscler Thromb* **12**, 1258-1266 (1992).

21. Griendling, K.K. & Alexander, R.W. Oxidative stress and cardiovascular disease. *Circulation* **96**, 3264-3265 (1997).

22. Morel, D.W., Hessler, J.R. & Chisolm, G.M. Low density lipoprotein cytotoxicity induced by free radical peroxidation of lipid. *J Lipid Res* **24**, 1070-1076 (1983).

23. Zinserling, W.D. Untersuchungen fiber Atherosklerose. 1. Über die Aortaverfettung bei Kindern. *Virchows Arch. path Anat.* **255**, 677-705 (1925).

24. Stary, H.C. Macrophages, macrophage foam cells, and eccentric intimal thickening in the coronary arteries of young children. *Atherosclerosis* **64**, 91-108 (1987).

25. Glagov, S., Weisenberg, E., Zarins, C.K., Stankunavicius, R. & Kolettis, G.J. Compensatory enlargement of human atherosclerotic coronary arteries. *N Engl J Med* **316**, 1371-1375 (1987).

26. Stary, H.C. *et al.* A definition of advanced types of atherosclerotic lesions and a histological classification of atherosclerosis. A report from the Committee on Vascular Lesions of the Council on Arteriosclerosis, American Heart Association. *Circulation* **92**, 1355-1374 (1995).

27. Rzucidlo, E.M., Martin, K.A. & Powell, R.J. Regulation of vascular smooth muscle cell differentiation. *J Vasc Surg* **45 Suppl A**, A25-32 (2007).

28. Rosenson, R.S. *et al.* HDL measures, particle heterogeneity, proposed nomenclature, and relation to atherosclerotic cardiovascular events. *Clin Chem* **57**, 392-410 (2011).

29. Shih, D.M. *et al.* Combined serum paraoxonase knockout/apolipoprotein E knockout mice exhibit increased lipoprotein oxidation and atherosclerosis. *J Biol Chem* **275**, 17527-17535 (2000).

30. Hansson, G.K. Inflammation, atherosclerosis, and coronary artery disease. *N Engl J Med* **352**, 1685-1695 (2005).

31. Williams, K.J. & Tabas, I. Lipoprotein retention--and clues for atheroma regression. *Arterioscler Thromb Vasc Biol* **25**, 1536-1540 (2005).

32. Cybulsky, M.I. & Gimbrone, M.A., Jr. Endothelial expression of a mononuclear leukocyte adhesion molecule during atherogenesis. *Science* **251**, 788-791 (1991).

33. Collins, R.G. *et al.* P-Selectin or intercellular adhesion molecule (ICAM)-1 deficiency substantially protects against atherosclerosis in apolipoprotein E-deficient mice. *J Exp Med* **191**, 189-194 (2000).

34. Lusis, A.J. Atherosclerosis. *Nature* **407**, 233-241 (2000).

35. Dong, Z.M. *et al.* The combined role of P- and E-selectins in atherosclerosis. *J Clin Invest* **102**, 145-152 (1998).

36. Cushing, S.D. *et al.* Minimally modified low density lipoprotein induces monocyte chemotactic protein 1 in human endothelial cells and smooth muscle cells. *Proc Natl Acad Sci U S A* **87**, 5134-5138 (1990).

37. Rajavashisth, T.B. *et al.* Induction of endothelial cell expression of granulocyte and macrophage colony-stimulating factors by modified low-density lipoproteins. *Nature* **344**, 254-257 (1990).

38. Gosling, J. *et al.* MCP-1 deficiency reduces susceptibility to atherosclerosis in mice that overexpress human apolipoprotein B. *J Clin Invest* **103**, 773-778 (1999).

39. Boring, L., Gosling, J., Cleary, M. & Charo, I.F. Decreased lesion formation in CCR2-/- mice reveals a role for chemokines in the initiation of atherosclerosis. *Nature* **394**, 894-897 (1998).

40. Qiao, J.H. *et al.* Role of macrophage colony-stimulating factor in atherosclerosis: studies of osteopetrotic mice. *Am J Pathol* **150**, 1687-1699 (1997).

41. Weber, C., Zernecke, A. & Libby, P. The multifaceted contributions of leukocyte subsets to atherosclerosis: lessons from mouse models. *Nat Rev Immunol* **8**, 802-815 (2008).

42. Napoli, C. *et al.* Fatty streak formation occurs in human fetal aortas and is greatly enhanced by maternal hypercholesterolemia. Intimal accumulation of low density lipoprotein and its oxidation precede monocyte recruitment into early atherosclerotic lesions. *J Clin Invest* **100**, 2680-2690 (1997).

43. Auffray, C., Sieweke, M.H. & Geissmann, F. Blood monocytes: development, heterogeneity, and relationship with dendritic cells. *Annu Rev Immunol* **27**, 669-692 (2009).

44. Geissmann, F. *et al.* Blood monocytes: distinct subsets, how they relate to dendritic cells, and their possible roles in the regulation of T-cell responses. *Immunol Cell Biol* **86**, 398-408 (2008).

45. Ley, K., Laudanna, C., Cybulsky, M.I. & Nourshargh, S. Getting to the site of inflammation: the leukocyte adhesion cascade updated. *Nat Rev Immunol* **7**, 678-689 (2007).

46. Woollard, K.J. & Chin-Dusting, J. Therapeutic targeting of p-selectin in atherosclerosis. *Inflamm Allergy Drug Targets* **6**, 69-74 (2007).

47. Katayama, Y. *et al.* PSGL-1 participates in E-selectin-mediated progenitor homing to bone marrow: evidence for cooperation between E-selectin ligands and alpha4 integrin. *Blood* **102**, 2060-2067 (2003).

48. Grage-Griebenow, E., Flad, H.D. & Ernst, M. Heterogeneity of human peripheral blood monocyte subsets. *J Leukoc Biol* **69**, 11-20 (2001).

49. Newman, P.J. & Newman, D.K. Signal transduction pathways mediated by PECAM-1: new roles for an old molecule in platelet and vascular cell biology. *Arterioscler Thromb Vasc Biol* **23**, 953-964 (2003).

50. Geissmann, F. *et al.* Development of monocytes, macrophages, and dendritic cells. *Science* **327**, 656-661 (2010).

51. Swirski, F.K. *et al.* Ly-6Chi monocytes dominate hypercholesterolemia-associated monocytosis and give rise to macrophages in atheromata. *J Clin Invest* **117**, 195-205 (2007).

52. Averill, L.E., Meagher, R.C. & Gerrity, R.G. Enhanced monocyte progenitor cell proliferation in bone marrow of hyperlipemic swine. *Am J Pathol* **135**, 369-377 (1989).

53. Zernecke, A., Shagdarsuren, E. & Weber, C. Chemokines in atherosclerosis: an update. *Arterioscler Thromb Vasc Biol* **28**, 1897-1908 (2008).

54. Tacke, F. *et al.* Monocyte subsets differentially employ CCR2, CCR5, and CX3CR1 to accumulate within atherosclerotic plaques. *J Clin Invest* **117**, 185-194 (2007).

55. Brocheriou, I. *et al.* Antagonistic regulation of macrophage phenotype by M-CSF and GM-CSF: implication in atherosclerosis. *Atherosclerosis* **214**, 316-324 (2011).

56. Martinez, F.O. & Gordon, S. The M1 and M2 paradigm of macrophage activation: time for reassessment. *F1000Prime Rep* **6**, 13 (2014).

57. Swirski, F.K., Weissleder, R. & Pittet, M.J. Heterogeneous in vivo behavior of monocyte subsets in atherosclerosis. *Arterioscler Thromb Vasc Biol* **29**, 1424-1432 (2009).

58. Woollard, K.J. & Geissmann, F. Monocytes in atherosclerosis: subsets and functions. *Nat Rev Cardiol* **7**, 77-86 (2010).

59. Audoy-Remus, J. *et al.* Rod-Shaped monocytes patrol the brain vasculature and give rise to perivascular macrophages under the influence of proinflammatory cytokines and angiopoietin-2. *J Neurosci* **28**, 10187-10199 (2008).

60. Moore, K.J., Sheedy, F.J. & Fisher, E.A. Macrophages in atherosclerosis: a dynamic balance. *Nat Rev Immunol* **13**, 709-721 (2013).

61. Braunersreuther, V. *et al.* Ccr5 but not Ccr1 deficiency reduces development of diet-induced atherosclerosis in mice. *Arterioscler Thromb Vasc Biol* **27**, 373-379 (2007).

62. Combadiere, C. *et al.* Combined inhibition of CCL2, CX3CR1, and CCR5 abrogates Ly6C(hi) and Ly6C(lo) monocytosis and almost abolishes atherosclerosis in hypercholesterolemic mice. *Circulation* **117**, 1649-1657 (2008).

63. Randolph, G.J. Mechanisms that regulate macrophage burden in atherosclerosis. *Circ Res* **114**, 1757-1771 (2014).

64. Xue, J. *et al.* Transcriptome-based network analysis reveals a spectrum model of human macrophage activation. *Immunity* **40**, 274-288 (2014).

65. Murray, P.J. *et al.* Macrophage activation and polarization: nomenclature and experimental guidelines. *Immunity* **41**, 14-20 (2014).

66. Mosser, D.M. & Edwards, J.P. Exploring the full spectrum of macrophage activation. *Nat Rev Immunol* **8**, 958-969 (2008).

67. Martinez, F.O., Gordon, S., Locati, M. & Mantovani, A. Transcriptional profiling of the human monocyte-to-macrophage differentiation and polarization: new molecules and patterns of gene expression. *J Immunol* **177**, 7303-7311 (2006).

68. Mantovani, A. *et al.* The chemokine system in diverse forms of macrophage activation and polarization. *Trends Immunol* **25**, 677-686 (2004).

69. Mills, C.D., Kincaid, K., Alt, J.M., Heilman, M.J. & Hill, A.M. M-1/M-2 macrophages and the Th1/Th2 paradigm. *J Immunol* **164**, 6166-6173 (2000).

70. Mantovani, A., Sozzani, S., Locati, M., Allavena, P. & Sica, A. Macrophage polarization: tumor-associated macrophages as a paradigm for polarized M2 mononuclear phagocytes. *Trends Immunol* **23**, 549-555 (2002).

71. Jenkins, S.J. *et al.* Local macrophage proliferation, rather than recruitment from the blood, is a signature of TH2 inflammation. *Science* **332**, 1284-1288 (2011).

72. Tabas, I. & Bornfeldt, K.E. Macrophage Phenotype and Function in Different Stages of Atherosclerosis. *Circ Res* **118**, 653-667 (2016).

73. Ley, K., Miller, Y.I. & Hedrick, C.C. Monocyte and macrophage dynamics during atherogenesis. *Arterioscler Thromb Vasc Biol* **31**, 1506-1516 (2011).

74. Wang, X. *et al.* Macrophage ABCA1 and ABCG1, but not SR-BI, promote macrophage reverse cholesterol transport in vivo. *J Clin Invest* **117**, 2216-2224 (2007).

75. Fazio, S. *et al.* Increased atherosclerosis in mice reconstituted with apolipoprotein E null macrophages. *Proc Natl Acad Sci U S A* **94**, 4647-4652 (1997).

76. Hazen, S.L. Oxidized phospholipids as endogenous pattern recognition ligands in innate immunity. *J Biol Chem* **283**, 15527-15531 (2008).

77. Suzuki, H. *et al.* A role for macrophage scavenger receptors in atherosclerosis and susceptibility to infection. *Nature* **386**, 292-296 (1997).

78. Febbraio, M. *et al.* Targeted disruption of the class B scavenger receptor CD36 protects against atherosclerotic lesion development in mice. *J Clin Invest* **105**, 1049-1056 (2000).

79. Landsman, L. *et al.* CX3CR1 is required for monocyte homeostasis and atherogenesis by promoting cell survival. *Blood* **113**, 963-972 (2009).

80. Zernecke, A. & Weber, C. Chemokines in atherosclerosis: proceedings resumed. *Arterioscler Thromb Vasc Biol* **34**, 742-750 (2014).

81. Paulson, K.E. *et al.* Resident intimal dendritic cells accumulate lipid and contribute to the initiation of atherosclerosis. *Circ Res* **106**, 383-390 (2010).

82. Rong, J.X., Shapiro, M., Trogan, E. & Fisher, E.A. Transdifferentiation of mouse aortic smooth muscle cells to a macrophage-like state after cholesterol loading. *Proc Natl Acad Sci U S A* **100**, 13531-13536 (2003).

83. Davies, M.J., Richardson, P.D., Woolf, N., Katz, D.R. & Mann, J. Risk of thrombosis in human atherosclerotic plaques: role of extracellular lipid, macrophage, and smooth muscle cell content. *Br Heart J* **69**, 377-381 (1993).

84. van der Wal, A.C., Becker, A.E., van der Loos, C.M., Tigges, A.J. & Das, P.K. Fibrous and lipid-rich atherosclerotic plaques are part of interchangeable morphologies related to inflammation: a concept. *Coron Artery Dis* **5**, 463-469 (1994).

85. Paigen, B., Morrow, A., Holmes, P.A., Mitchell, D. & Williams, R.A. Quantitative assessment of atherosclerotic lesions in mice. *Atherosclerosis* **68**, 231-240 (1987).

86. Adiguzel, E., Ahmad, P.J., Franco, C. & Bendeck, M.P. Collagens in the progression and complications of atherosclerosis. *Vasc Med* **14**, 73-89 (2009).

87. Raines, E.W. The extracellular matrix can regulate vascular cell migration, proliferation, and survival: relationships to vascular disease. *Int J Exp Pathol* **81**, 173-182 (2000).

88. Barnes, M.J. & Farndale, R.W. Collagens and atherosclerosis. *Exp Gerontol* **34**, 513-525 (1999).

89. Owens, G.K., Kumar, M.S. & Wamhoff, B.R. Molecular regulation of vascular smooth muscle cell differentiation in development and disease. *Physiol Rev* **84**, 767-801 (2004).

90. Jang, Y., Lincoff, A.M., Plow, E.F. & Topol, E.J. Cell adhesion molecules in coronary artery disease. *J Am Coll Cardiol* **24**, 1591-1601 (1994).

91. Martinez-Lemus, L.A. *et al.* Integrins as unique receptors for vascular control. *J Vasc Res* **40**, 211-233 (2003).

92. Amento, E.P., Ehsani, N., Palmer, H. & Libby, P. Cytokines and growth factors positively and negatively regulate interstitial collagen gene expression in human vascular smooth muscle cells. *Arterioscler Thromb* **11**, 1223-1230 (1991).

93. Foster, L.C. *et al.* Regulation of CD44 gene expression by the proinflammatory cytokine interleukin-1beta in vascular smooth muscle cells. *J Biol Chem* **273**, 20341-20346 (1998).

94. Krettek, A., Sukhova, G.K., Schonbeck, U. & Libby, P. Enhanced expression of CD44 variants in human atheroma and abdominal aortic aneurysm: possible role for a feedback loop in endothelial cells. *Am J Pathol* **165**, 1571-1581 (2004).

95. Falk, E. Pathogenesis of atherosclerosis. *J Am Coll Cardiol* **47**, C7-12 (2006).

96. Ruan, X.Z. *et al.* Mechanisms of dysregulation of low-density lipoprotein receptor expression in vascular smooth muscle cells by inflammatory cytokines. *Arterioscler Thromb Vasc Biol* **26**, 1150-1155 (2006).

97. Lighvani, A.A. *et al.* T-bet is rapidly induced by interferon-gamma in lymphoid and myeloid cells. *Proc Natl Acad Sci U S A* **98**, 15137-15142 (2001).

98. Zhu, J. & Paul, W.E. CD4 T cells: fates, functions, and faults. *Blood* **112**, 1557-1569 (2008).

99. Suzuki, Y., Orellana, M.A., Schreiber, R.D. & Remington, J.S. Interferon-gamma: the major mediator of resistance against Toxoplasma gondii. *Science* **240**, 516-518 (1988).

100. Snapper, C.M., Pecanha, L.M., Levine, A.D. & Mond, J.J. IgE class switching is critically dependent upon the nature of the B cell activator, in addition to the presence of IL-4. *J Immunol* **147**, 1163-1170 (1991).

101. Snapper, C.M., Peschel, C. & Paul, W.E. IFN-gamma stimulates IgG2a secretion by murine B cells stimulated with bacterial lipopolysaccharide. *J Immunol* **140**, 2121-2127 (1988).

102. Snapper, C.M. & Paul, W.E. Interferon-gamma and B cell stimulatory factor-1 reciprocally regulate Ig isotype production. *Science* **236**, 944-947 (1987).

103. Krummel, M.F. *et al.* Paracrine costimulation of IFN-gamma signaling by integrins modulates CD8 T cell differentiation. *Proc Natl Acad Sci U S A* **115**, 11585-11590 (2018).

104. Farrar, J.D., Asnagli, H. & Murphy, K.M. T helper subset development: roles of instruction, selection, and transcription. *J Clin Invest* **109**, 431-435 (2002).

105. Hansson, G.K. Immune mechanisms in atherosclerosis. *Arterioscler Thromb Vasc Biol* **21**, 1876-1890 (2001).

106. Roselaar, S.E., Kakkanathu, P.X. & Daugherty, A. Lymphocyte populations in atherosclerotic lesions of apoE -/- and LDL receptor -/- mice. Decreasing density with disease progression. *Arterioscler Thromb Vasc Biol* **16**, 1013-1018 (1996).

107. Huber, S.A., Sakkinen, P., David, C., Newell, M.K. & Tracy, R.P. T helper-cell phenotype regulates atherosclerosis in mice under conditions of mild hypercholesterolemia. *Circulation* **103**, 2610-2616 (2001).

108. Stemme, S. *et al.* T lymphocytes from human atherosclerotic plaques recognize oxidized low density lipoprotein. *Proc Natl Acad Sci U S A* **92**, 3893-3897 (1995).

109. Fatkhullina, A.R., Peshkova, I.O. & Koltsova, E.K. The Role of Cytokines in the Development of Atherosclerosis. *Biochemistry (Mosc)* **81**, 1358-1370 (2016).

110. Geng, Y.J. & Hansson, G.K. Interferon-gamma inhibits scavenger receptor expression and foam cell formation in human monocyte-derived macrophages. *J Clin Invest* **89**, 1322-1330 (1992).

111. Gupta, S. *et al.* IFN-gamma potentiates atherosclerosis in ApoE knock-out mice. *J Clin Invest* **99**, 2752-2761 (1997).

112. Whitman, S.C., Ravisankar, P. & Daugherty, A. IFN-gamma deficiency exerts gender-specific effects on atherogenesis in apolipoprotein E-/- mice. *J Interferon Cytokine Res* **22**, 661-670 (2002).

113. Lahoute, C., Herbin, O., Mallat, Z. & Tedgui, A. Adaptive immunity in atherosclerosis: mechanisms and future therapeutic targets. *Nat Rev Cardiol* **8**, 348-358 (2011).

114. Binder, C.J. *et al.* IL-5 links adaptive and natural immunity specific for epitopes of oxidized LDL and protects from atherosclerosis. *J Clin Invest* **114**, 427-437 (2004).

115. King, V.L., Cassis, L.A. & Daugherty, A. Interleukin-4 does not influence development of hypercholesterolemia or angiotensin II-induced atherosclerotic lesions in mice. *Am J Pathol* **171**, 2040-2047 (2007).

116. Ait-Oufella, H., Taleb, S., Mallat, Z. & Tedgui, A. Recent advances on the role of cytokines in atherosclerosis. *Arterioscler Thromb Vasc Biol* **31**, 969-979 (2011).

117. Moore, K.W., de Waal Malefyt, R., Coffman, R.L. & O'Garra, A. Interleukin-10 and the interleukin-10 receptor. *Annu Rev Immunol* **19**, 683-765 (2001).

118. Pinderski, L.J. *et al.* Overexpression of interleukin-10 by activated T lymphocytes inhibits atherosclerosis in LDL receptor-deficient Mice by altering lymphocyte and macrophage phenotypes. *Circ Res* **90**, 1064-1071 (2002).

119. Dollery, C.M. & Libby, P. Atherosclerosis and proteinase activation. *Cardiovasc Res* **69**, 625-635 (2006).

120. Nagase, H., Visse, R. & Murphy, G. Structure and function of matrix metalloproteinases and TIMPs. *Cardiovasc Res* **69**, 562-573 (2006).

121. Newby, A.C. Matrix metalloproteinases regulate migration, proliferation, and death of vascular smooth muscle cells by degrading matrix and non-matrix substrates. *Cardiovasc Res* **69**, 614-624 (2006).

122. Shipley, J.M., Wesselschmidt, R.L., Kobayashi, D.K., Ley, T.J. & Shapiro, S.D. Metalloelastase is required for macrophage-mediated proteolysis and matrix invasion in mice. *Proc Natl Acad Sci U S A* **93**, 3942-3946 (1996).

123. Shah, P.K. Pathophysiology of plaque rupture and the concept of plaque stabilization. *Cardiol Clin* **14**, 17-29 (1996).

124. Naito, K. *et al.* Differential effects of GM-CSF and G-CSF on infiltration of dendritic cells during early left ventricular remodeling after myocardial infarction. *J Immunol* **181**, 5691-5701 (2008).

125. Epelman, S., Liu, P.P. & Mann, D.L. Role of innate and adaptive immune mechanisms in cardiac injury and repair. *Nat Rev Immunol* **15**, 117-129 (2015).

126. Frangogiannis, N.G. *et al.* Resident cardiac mast cells degranulate and release preformed TNF-alpha, initiating the cytokine cascade in experimental canine myocardial ischemia/reperfusion. *Circulation* **98**, 699-710 (1998).

127. Gwechenberger, M. *et al.* Cardiac myocytes produce interleukin-6 in culture and in viable border zone of reperfused infarctions. *Circulation* **99**, 546-551 (1999).

128. Youker, K. *et al.* Neutrophil adherence to isolated adult cardiac myocytes. Induction by cardiac lymph collected during ischemia and reperfusion. *J Clin Invest* **89**, 602-609 (1992).

129. Zouggari, Y. *et al.* B lymphocytes trigger monocyte mobilization and impair heart function after acute myocardial infarction. *Nat Med* **19**, 1273-1280 (2013).

130. Auffray, C. *et al.* Monitoring of blood vessels and tissues by a population of monocytes with patrolling behavior. *Science* **317**, 666-670 (2007).

131. Carlin, L.M. *et al.* Nr4a1-dependent Ly6C(low) monocytes monitor endothelial cells and orchestrate their disposal. *Cell* **153**, 362-375 (2013).

132. Stark, M.A. *et al.* Phagocytosis of apoptotic neutrophils regulates granulopoiesis via IL-23 and IL-17. *Immunity* **22**, 285-294 (2005).

133. Oppmann, B. *et al.* Novel p19 protein engages IL-12p40 to form a cytokine, IL-23, with biological activities similar as well as distinct from IL-12. *Immunity* **13**, 715-725 (2000).

134. Steinman, R.M. & Cohn, Z.A. Identification of a novel cell type in peripheral lymphoid organs of mice. I. Morphology, quantitation, tissue distribution. *J Exp Med* **137**, 1142-1162 (1973).

135. Steinman, R.M. & Cohn, Z.A. Identification of a novel cell type in peripheral lymphoid organs of mice. II. Functional properties in vitro. *J Exp Med* **139**, 380-397 (1974).

136. Segura, E. & Villadangos, J.A. Antigen presentation by dendritic cells in vivo. *Curr Opin Immunol* **21**, 105-110 (2009).

137. Trombetta, E.S. & Mellman, I. Cell biology of antigen processing in vitro and in vivo. *Annu Rev Immunol* **23**, 975-1028 (2005).

138. Watts, C. Capture and processing of exogenous antigens for presentation on MHC molecules. *Annu Rev Immunol* **15**, 821-850 (1997).

139. Lanzavecchia, A. Receptor-mediated antigen uptake and its effect on antigen presentation to class II-restricted T lymphocytes. *Annu Rev Immunol* **8**, 773-793 (1990).

140. Banchereau, J. & Steinman, R.M. Dendritic cells and the control of immunity. *Nature* **392**, 245-252 (1998).

141. Crowley, M., Inaba, K. & Steinman, R.M. Dendritic cells are the principal cells in mouse spleen bearing immunogenic fragments of foreign proteins. *J Exp Med* **172**, 383-386 (1990).

142. Mellman, I., Turley, S.J. & Steinman, R.M. Antigen processing for amateurs and professionals. *Trends Cell Biol* **8**, 231-237 (1998).

143. Turley, S.J. *et al.* Transport of peptide-MHC class II complexes in developing dendritic cells. *Science* **288**, 522-527 (2000).

144. Fogg, D.K. *et al.* A clonogenic bone marrow progenitor specific for macrophages and dendritic cells. *Science* **311**, 83-87 (2006).

145. Waskow, C. *et al.* The receptor tyrosine kinase Flt3 is required for dendritic cell development in peripheral lymphoid tissues. *Nat Immunol* **9**, 676-683 (2008).

146. Onai, N., Obata-Onai, A., Schmid, M.A. & Manz, M.G. Flt3 in regulation of type I interferon-producing cell and dendritic cell development. *Ann N Y Acad Sci* **1106**, 253-261 (2007).

147. Schmid, M.A., Kingston, D., Boddupalli, S. & Manz, M.G. Instructive cytokine signals in dendritic cell lineage commitment. *Immunol Rev* **234**, 32-44 (2010).

148. Liu, K. *et al.* In vivo analysis of dendritic cell development and homeostasis. *Science* **324**, 392-397 (2009).

149. Bogunovic, M. *et al.* Origin of the lamina propria dendritic cell network. *Immunity* **31**, 513-525 (2009).

150. Ginhoux, F. *et al.* The origin and development of nonlymphoid tissue CD103+ DCs. *J Exp Med* **206**, 3115-3130 (2009).

151. Liu, K. *et al.* Origin of dendritic cells in peripheral lymphoid organs of mice. *Nat Immunol* **8**, 578-583 (2007).

152. Meredith, M.M. *et al.* Expression of the zinc finger transcription factor zDC (Zbtb46, Btbd4) defines the classical dendritic cell lineage. *J Exp Med* **209**, 1153-1165 (2012).

153. Satpathy, A.T. *et al.* Zbtb46 expression distinguishes classical dendritic cells and their committed progenitors from other immune lineages. *J Exp Med* **209**, 1135-1152 (2012).

154. Meredith, M.M. *et al.* Zinc finger transcription factor zDC is a negative regulator required to prevent activation of classical dendritic cells in the steady state. *J Exp Med* **209**, 1583-1593 (2012).

155. Zhan, Y. *et al.* GM-CSF increases cross-presentation and CD103 expression by mouse CD8(+) spleen dendritic cells. *Eur J Immunol* **41**, 2585-2595 (2011).

156. Greter, M. *et al.* GM-CSF controls nonlymphoid tissue dendritic cell homeostasis but is dispensable for the differentiation of inflammatory dendritic cells. *Immunity* **36**, 1031-1046 (2012).

157. Helft, J., Ginhoux, F., Bogunovic, M. & Merad, M. Origin and functional heterogeneity of non-lymphoid tissue dendritic cells in mice. *Immunol Rev* **234**, 55-75 (2010).

158. del Rio, M.L., Bernhardt, G., Rodriguez-Barbosa, J.I. & Forster, R. Development and functional specialization of CD103+ dendritic cells. *Immunol Rev* **234**, 268-281 (2010).

159. Kusunoki, T. *et al.* TH2 dominance and defective development of a CD8+ dendritic cell subset in Id2-deficient mice. *J Allergy Clin Immunol* **111**, 136-142 (2003).

160. Tamura, T. *et al.* IFN regulatory factor-4 and -8 govern dendritic cell subset development and their functional diversity. *J Immunol* **174**, 2573-2581 (2005).

161. Hildner, K. *et al.* Batf3 deficiency reveals a critical role for CD8alpha+ dendritic cells in cytotoxic T cell immunity. *Science* **322**, 1097-1100 (2008).

162. Schulz, O. *et al.* Intestinal CD103+, but not CX3CR1+, antigen sampling cells migrate in lymph and serve classical dendritic cell functions. *J Exp Med* **206**, 3101-3114 (2009).

163. Lee, J.S. *et al.* Conventional Dendritic Cells Impair Recovery after Myocardial Infarction. *J Immunol* **201**, 1784-1798 (2018).

164. Forster, R., Braun, A. & Worbs, T. Lymph node homing of T cells and dendritic cells via afferent lymphatics. *Trends Immunol* **33**, 271-280 (2012).

165. Caminschi, I. *et al.* The dendritic cell subtype-restricted C-type lectin Clec9A is a target for vaccine enhancement. *Blood* **112**, 3264-3273 (2008).

166. Bachem, A. *et al.* Superior antigen cross-presentation and XCR1 expression define human CD11c+CD141+ cells as homologues of mouse CD8+ dendritic cells. *J Exp Med* **207**, 1273-1281 (2010).

167. Jongbloed, S.L. *et al.* Human CD141+ (BDCA-3)+ dendritic cells (DCs) represent a unique myeloid DC subset that cross-presents necrotic cell antigens. *J Exp Med* **207**, 1247-1260 (2010).

168. Dzionek, A. *et al.* BDCA-2, BDCA-3, and BDCA-4: three markers for distinct subsets of dendritic cells in human peripheral blood. *J Immunol* **165**, 6037-6046 (2000).

169. MacDonald, K.P. *et al.* Characterization of human blood dendritic cell subsets. *Blood* **100**, 4512-4520 (2002).

170. Ginhoux, F. *et al.* Langerhans cells arise from monocytes in vivo. *Nat Immunol* **7**, 265-273 (2006).

171. Hoeffel, G. *et al.* Adult Langerhans cells derive predominantly from embryonic fetal liver monocytes with a minor contribution of yolk sac-derived macrophages. *J Exp Med* **209**, 1167-1181 (2012).

172. Chorro, L. *et al.* Langerhans cell (LC) proliferation mediates neonatal development, homeostasis, and inflammation-associated expansion of the epidermal LC network. *J Exp Med* **206**, 3089-3100 (2009).

173. Shortman, K. & Heath, W.R. The CD8+ dendritic cell subset. *Immunol Rev* **234**, 18-31 (2010).

174. Ichikawa, E. *et al.* Defective development of splenic and epidermal CD4+ dendritic cells in mice deficient for IFN regulatory factor-2. *Proc Natl Acad Sci U S A* **101**, 3909-3914 (2004).

175. Suzuki, S. *et al.* Critical roles of interferon regulatory factor 4 in CD11bhighCD8alpha- dendritic cell development. *Proc Natl Acad Sci U S A* **101**, 8981-8986 (2004).

176. Caton, M.L., Smith-Raska, M.R. & Reizis, B. Notch-RBP-J signaling controls the homeostasis of CD8- dendritic cells in the spleen. *J Exp Med* **204**, 1653-1664 (2007).

177. Lewis, K.L. *et al.* Notch2 receptor signaling controls functional differentiation of dendritic cells in the spleen and intestine. *Immunity* **35**, 780-791 (2011).

178. Randolph, G.J., Angeli, V. & Swartz, M.A. Dendritic-cell trafficking to lymph nodes through lymphatic vessels. *Nat Rev Immunol* **5**, 617-628 (2005).

179. Worbs, T., Hammerschmidt, S.I. & Forster, R. Dendritic cell migration in health and disease. *Nat Rev Immunol* **17**, 30-48 (2017).

180. Lutz, M.B., Strobl, H., Schuler, G. & Romani, N. GM-CSF Monocyte-Derived Cells and Langerhans Cells As Part of the Dendritic Cell Family. *Front Immunol* **8**, 1388 (2017).

181. Varol, C. *et al.* Monocytes give rise to mucosal, but not splenic, conventional dendritic cells. *J Exp Med* **204**, 171-180 (2007).

182. Cheong, C. *et al.* Microbial stimulation fully differentiates monocytes to DC-SIGN/CD209(+) dendritic cells for immune T cell areas. *Cell* **143**, 416-429 (2010).

183. Tamoutounour, S. *et al.* Origins and functional specialization of macrophages and of conventional and monocyte-derived dendritic cells in mouse skin. *Immunity* **39**, 925-938 (2013).

184. Jakubzick, C. *et al.* Minimal differentiation of classical monocytes as they survey steady-state tissues and transport antigen to lymph nodes. *Immunity* **39**, 599-610 (2013).

185. Dominguez, P.M. & Ardavin, C. Differentiation and function of mouse monocyte-derived dendritic cells in steady state and inflammation. *Immunol Rev* **234**, 90-104 (2010).

186. Randolph, G.J., Inaba, K., Robbiani, D.F., Steinman, R.M. & Muller, W.A. Differentiation of phagocytic monocytes into lymph node dendritic cells in vivo. *Immunity* **11**, 753-761 (1999).

187. Serbina, N.V., Salazar-Mather, T.P., Biron, C.A., Kuziel, W.A. & Pamer, E.G. TNF/iNOS-producing dendritic cells mediate innate immune defense against bacterial infection. *Immunity* **19**, 59-70 (2003).

188. Diao, J. *et al.* In situ replication of immediate dendritic cell (DC) precursors contributes to conventional DC homeostasis in lymphoid tissue. *J Immunol* **176**, 7196-7206 (2006).

189. Naik, S.H. *et al.* Intrasplenic steady-state dendritic cell precursors that are distinct from monocytes. *Nat Immunol* **7**, 663-671 (2006).

190. Ghosh, H.S., Cisse, B., Bunin, A., Lewis, K.L. & Reizis, B. Continuous expression of the transcription factor e2-2 maintains the cell fate of mature plasmacytoid dendritic cells. *Immunity* **33**, 905-916 (2010).

191. Cisse, B. *et al.* Transcription factor E2-2 is an essential and specific regulator of plasmacytoid dendritic cell development. *Cell* **135**, 37-48 (2008).

192. Tsujimura, H., Tamura, T. & Ozato, K. Cutting edge: IFN consensus sequence binding protein/IFN regulatory factor 8 drives the development of type I IFN-producing plasmacytoid dendritic cells. *J Immunol* **170**, 1131-1135 (2003).

193. Yun, T.J. *et al.* Indoleamine 2,3-Dioxygenase-Expressing Aortic Plasmacytoid Dendritic Cells Protect against Atherosclerosis by Induction of Regulatory T Cells. *Cell Metab* **24**, 886 (2016).

194. Heil, F. *et al.* Species-specific recognition of single-stranded RNA via toll-like receptor 7 and 8. *Science* **303**, 1526-1529 (2004).

195. Lund, J., Sato, A., Akira, S., Medzhitov, R. & Iwasaki, A. Toll-like receptor 9-mediated recognition of Herpes simplex virus-2 by plasmacytoid dendritic cells. *J Exp Med* **198**, 513-520 (2003).

196. Reizis, B., Colonna, M., Trinchieri, G., Barrat, F. & Gilliet, M. Plasmacytoid dendritic cells: one-trick ponies or workhorses of the immune system? *Nat Rev Immunol* **11**, 558-565 (2011).

197. Mellman, I. & Steinman, R.M. Dendritic cells: specialized and regulated antigen processing machines. *Cell* **106**, 255-258 (2001).

198. Mosmann, T.R. & Coffman, R.L. TH1 and TH2 cells: different patterns of lymphokine secretion lead to different functional properties. *Annu Rev Immunol* **7**, 145-173 (1989).

199. Kalinski, P., Hilkens, C.M., Wierenga, E.A. & Kapsenberg, M.L. T-cell priming by type-1 and type-2 polarized dendritic cells: the concept of a third signal. *Immunol Today* **20**, 561-567 (1999).

200. Biron, C.A. Activation and function of natural killer cell responses during viral infections. *Curr Opin Immunol* **9**, 24-34 (1997).

201. Afkarian, M. *et al.* T-bet is a STAT1-induced regulator of IL-12R expression in naive CD4+ T cells. *Nat Immunol* **3**, 549-557 (2002).

202. Mullen, A.C. *et al.* Role of T-bet in commitment of TH1 cells before IL-12-dependent selection. *Science* **292**, 1907-1910 (2001).

203. Kidd, P. Th1/Th2 balance: the hypothesis, its limitations, and implications for health and disease. *Altern Med Rev* **8**, 223-246 (2003).

204. Kaplan, M.H., Schindler, U., Smiley, S.T. & Grusby, M.J. Stat6 is required for mediating responses to IL-4 and for development of Th2 cells. *Immunity* **4**, 313-319 (1996).

205. Ouyang, W. *et al.* Inhibition of Th1 development mediated by GATA-3 through an IL-4-independent mechanism. *Immunity* **9**, 745-755 (1998).

206. Zhang, D.H. *et al.* Inhibition of allergic inflammation in a murine model of asthma by expression of a dominant-negative mutant of GATA-3. *Immunity* **11**, 473-482 (1999).

207. Zhang, D.H., Yang, L. & Ray, A. Differential responsiveness of the IL-5 and IL-4 genes to transcription factor GATA-3. *J Immunol* **161**, 3817-3821 (1998).

208. Zheng, W. & Flavell, R.A. The transcription factor GATA-3 is necessary and sufficient for Th2 cytokine gene expression in CD4 T cells. *Cell* **89**, 587-596 (1997).

209. Zhang, D.H., Cohn, L., Ray, P., Bottomly, K. & Ray, A. Transcription factor GATA-3 is differentially expressed in murine Th1 and Th2 cells and controls Th2-specific expression of the interleukin-5 gene. *J Biol Chem* **272**, 21597-21603 (1997).

210. Lafaille, J.J. The role of helper T cell subsets in autoimmune diseases. *Cytokine Growth Factor Rev* **9**, 139-151 (1998).

211. Wang, Z.Y. *et al.* Regulation of Th2 cytokine expression in NKT cells: unconventional use of Stat6, GATA-3, and NFAT2. *J Immunol* **176**, 880-888 (2006).

212. Kopf, M. *et al.* Disruption of the murine IL-4 gene blocks Th2 cytokine responses. *Nature* **362**, 245-248 (1993).

213. Zheng, Y. & Rudensky, A.Y. Foxp3 in control of the regulatory T cell lineage. *Nat Immunol* **8**, 457-462 (2007).

214. Pulendran, B., Tang, H. & Manicassamy, S. Programming dendritic cells to induce T(H)2 and tolerogenic responses. *Nat Immunol* **11**, 647-655 (2010).

215. Mangan, P.R. *et al.* Transforming growth factor-beta induces development of the T(H)17 lineage. *Nature* **441**, 231-234 (2006).

216. Ouyang, W., Kolls, J.K. & Zheng, Y. The biological functions of T helper 17 cell effector cytokines in inflammation. *Immunity* **28**, 454-467 (2008).

217. Bevan, M.J. Helping the CD8(+) T-cell response. *Nat Rev Immunol* **4**, 595-602 (2004).

218. Wearsch, P.A. & Cresswell, P. The quality control of MHC class I peptide loading. *Curr Opin Cell Biol* **20**, 624-631 (2008).

219. Gil-Torregrosa, B.C. *et al.* Control of cross-presentation during dendritic cell maturation. *Eur J Immunol* **34**, 398-407 (2004).

220. Alloatti, A. *et al.* Toll-like Receptor 4 Engagement on Dendritic Cells Restrains Phago-Lysosome Fusion and Promotes Cross-Presentation of Antigens. *Immunity* **43**, 1087-1100 (2015).

221. den Haan, J.M., Lehar, S.M. & Bevan, M.J. CD8(+) but not CD8(-) dendritic cells cross-prime cytotoxic T cells in vivo. *J Exp Med* **192**, 1685-1696 (2000).

222. Millonig, G. *et al.* Network of vascular-associated dendritic cells in intima of healthy young individuals. *Arterioscler Thromb Vasc Biol* **21**, 503-508 (2001).

223. Millonig, G., Malcom, G.T. & Wick, G. Early inflammatory-immunological lesions in juvenile atherosclerosis from the Pathobiological Determinants of Atherosclerosis in Youth (PDAY)-study. *Atherosclerosis* **160**, 441-448 (2002).

224. Inder, S.J. *et al.* Accumulation of lymphocytes, dendritic cells, and granulocytes in the aortic wall affected by Takayasu's disease. *Angiology* **51**, 565-579 (2000).

225. Galkina, E. *et al.* Lymphocyte recruitment into the aortic wall before and during development of atherosclerosis is partially L-selectin dependent. *J Exp Med* **203**, 1273-1282 (2006).

226. Choi, J.H. *et al.* Identification of antigen-presenting dendritic cells in mouse aorta and cardiac valves. *J Exp Med* **206**, 497-505 (2009).

227. Liu, P. *et al.* CX3CR1 deficiency impairs dendritic cell accumulation in arterial intima and reduces atherosclerotic burden. *Arterioscler Thromb Vasc Biol* **28**, 243-250 (2008).

228. Zhu, S.N., Chen, M., Jongstra-Bilen, J. & Cybulsky, M.I. GM-CSF regulates intimal cell proliferation in nascent atherosclerotic lesions. *J Exp Med* **206**, 2141-2149 (2009).

229. Choi, J.H. *et al.* Flt3 signaling-dependent dendritic cells protect against atherosclerosis. *Immunity* **35**, 819-831 (2011).

230. Ait-Oufella, H. *et al.* Natural regulatory T cells control the development of atherosclerosis in mice. *Nat Med* **12**, 178-180 (2006).

231. Akkaya, B. *et al.* Regulatory T cells mediate specific suppression by depleting peptide-MHC class II from dendritic cells. *Nat Immunol* **20**, 218-231 (2019).

232. Niessner, A. *et al.* Pathogen-sensing plasmacytoid dendritic cells stimulate cytotoxic T-cell function in the atherosclerotic plaque through interferon-alpha. *Circulation* **114**, 2482-2489 (2006).

233. Daissormont, I.T. *et al.* Plasmacytoid dendritic cells protect against atherosclerosis by tuning T-cell proliferation and activity. *Circ Res* **109**, 1387-1395 (2011).

234. Colonna, M., Trinchieri, G. & Liu, Y.J. Plasmacytoid dendritic cells in immunity. *Nat Immunol* **5**, 1219-1226 (2004).

235. Hadeiba, H. *et al.* Plasmacytoid dendritic cells transport peripheral antigens to the thymus to promote central tolerance. *Immunity* **36**, 438-450 (2012).

236. Klingenberg, R. *et al.* Depletion of FOXP3+ regulatory T cells promotes hypercholesterolemia and atherosclerosis. *J Clin Invest* **123**, 1323-1334 (2013).

237. Yokoyama, H. *et al.* Cardiac dendritic cells and acute myocarditis in the human heart. *Jpn Circ J* **64**, 57-64 (2000).

238. Kretzschmar, D. *et al.* Recruitment of circulating dendritic cell precursors into the infarcted myocardium and pro-inflammatory response in acute myocardial infarction. *Clin Sci (Lond)* **123**, 387-398 (2012).

239. Nagai, T. *et al.* Decreased myocardial dendritic cells is associated with impaired reparative fibrosis and development of cardiac rupture after myocardial infarction in humans. *J Am Heart Assoc* **3**, e000839 (2014).

240. Kofler, S., Sisic, Z., Shvets, N., Lohse, P. & Weis, M. Expression of circulatory dendritic cells and regulatory T-cells in patients with different subsets of coronary artery disease. *J Cardiovasc Pharmacol* **57**, 542-549 (2011).

241. Aronoff, L., Epelman, S. & Clemente-Casares, X. Isolation and Identification of Extravascular Immune Cells of the Heart. *J. Vis. Exp.* **138**, e58114 (2018).

242. Shklovskaya, E., Roediger, B. & Fazekas de St Groth, B. Epidermal and dermal dendritic cells display differential activation and migratory behavior while sharing the ability to stimulate CD4+ T cell proliferation in vivo. *J Immunol* **181**, 418-430 (2008).

243. Cerovic, V. *et al.* Intestinal CD103(-) dendritic cells migrate in lymph and prime effector T cells. *Mucosal Immunol* **6**, 104-113 (2013).

244. Puccetti, P. & Grohmann, U. IDO and regulatory T cells: a role for reverse signalling and non-canonical NF-kappaB activation. *Nat Rev Immunol* **7**, 817-823 (2007).

245. Clemente-Casares, X. *et al.* A CD103(+) Conventional Dendritic Cell Surveillance System Prevents Development of Overt Heart Failure during Subclinical Viral Myocarditis. *Immunity* **47**, 974-989 e978 (2017).

246. Swirski, F.K. *et al.* Identification of splenic reservoir monocytes and their deployment to inflammatory sites. *Science* **325**, 612-616 (2009).

247. Schlitzer, A. *et al.* IRF4 transcription factor-dependent CD11b+ dendritic cells in human and mouse control mucosal IL-17 cytokine responses. *Immunity* **38**, 970-983 (2013).

248. Anzai, A. *et al.* Regulatory role of dendritic cells in postinfarction healing and left ventricular remodeling. *Circulation* **125**, 1234-1245 (2012).

249. Piccinini, A.M. & Midwood, K.S. DAMPening inflammation by modulating TLR signalling. *Mediators Inflamm* **2010** (2010).

250. Curiel, T.J. *et al.* Dendritic cell subsets differentially regulate angiogenesis in human ovarian cancer. *Cancer Res* **64**, 5535-5538 (2004).

251. Vignali, D.A., Collison, L.W. & Workman, C.J. How regulatory T cells work. *Nat Rev Immunol* **8**, 523-532 (2008).

252. Weirather, J. *et al.* Foxp3+ CD4+ T cells improve healing after myocardial infarction by modulating monocyte/macrophage differentiation. *Circ Res* **115**, 55-67 (2014).

253. Maekawa, Y. *et al.* Survival and cardiac remodeling after myocardial infarction are critically dependent on the host innate immune interleukin-1 receptor-associated kinase-4 signaling: a regulator of bone marrow-derived dendritic cells. *Circulation* **120**, 1401-1414 (2009).

254. Zhu, R. *et al.* Interleukin-37 and Dendritic Cells Treated With Interleukin-37 Plus Troponin I Ameliorate Cardiac Remodeling After Myocardial Infarction. *J Am Heart Assoc* **5** (2016).

255. Choo, E.H. *et al.* Infarcted Myocardium-Primed Dendritic Cells Improve Remodeling and Cardiac Function After Myocardial Infarction by Modulating the Treg and Macrophage Polarization. *Circulation* (2017).

256. Takahashi, K. *et al.* Modulated inflammation by injection of high-mobility group box 1 recovers post-infarction chronically failing heart. *Circulation* **118**, S106-114 (2008).

257. Lotze, M.T. & Tracey, K.J. High-mobility group box 1 protein (HMGB1): nuclear weapon in the immune arsenal. *Nat Rev Immunol* **5**, 331-342 (2005).

258. Hohl, T.M. *et al.* Inflammatory monocytes facilitate adaptive CD4 T cell responses during respiratory fungal infection. *Cell Host Microbe* **6**, 470-481 (2009).

259. Bajpai, G. *et al.* Tissue Resident CCR2- and CCR2+ Cardiac Macrophages Differentially Orchestrate Monocyte Recruitment and Fate Specification Following Myocardial Injury. *Circ Res* **124**, 263-278 (2019).

260. Cochain, C. *et al.* Single-Cell RNA-Seq Reveals the Transcriptional Landscape and Heterogeneity of Aortic Macrophages in Murine Atherosclerosis. *Circ Res* **122**, 1661-1674 (2018).

261. Winkels, H. *et al.* Atlas of the Immune Cell Repertoire in Mouse Atherosclerosis Defined by Single-Cell RNA-Sequencing and Mass Cytometry. *Circ Res* **122**, 1675-1688 (2018).

262. Priyadharsini, R.P. Animal models to evaluate anti-atherosclerotic drugs. *Fundam Clin Pharmacol* **29**, 329-340 (2015).

263. Mukhopadhyay, R. Mouse models of atherosclerosis: explaining critical roles of lipid metabolism and inflammation. *J Appl Genet* **54**, 185-192 (2013).

264. Getz, G.S. & Reardon, C.A. Animal models of atherosclerosis. *Arterioscler Thromb Vasc Biol* **32**, 1104-1115 (2012).

265. VanderLaan, P.A., Reardon, C.A. & Getz, G.S. Site specificity of atherosclerosis: site-selective responses to atherosclerotic modulators. *Arterioscler Thromb Vasc Biol* **24**, 12-22 (2004).

266. Nigro, P., Abe, J. & Berk, B.C. Flow shear stress and atherosclerosis: a matter of site specificity. *Antioxid Redox Signal* **15**, 1405-1414 (2011).

267. Takabe, W., Warabi, E. & Noguchi, N. Anti-atherogenic effect of laminar shear stress via Nrf2 activation. *Antioxid Redox Signal* **15**, 1415-1426 (2011).

268. Harrison, M. *et al.* The role of platelet-endothelial cell adhesion molecule-1 in atheroma formation varies depending on the site-specific hemodynamic environment. *Arterioscler Thromb Vasc Biol* **33**, 694-701 (2013).

269. Cilla, D.D., Jr., Whitfield, L.R., Gibson, D.M., Sedman, A.J. & Posvar, E.L. Multiple-dose pharmacokinetics, pharmacodynamics, and safety of atorvastatin, an inhibitor of HMG-CoA reductase, in healthy subjects. *Clin Pharmacol Ther* **60**, 687-695 (1996).

270. Abifadel, M. *et al.* Mutations in PCSK9 cause autosomal dominant hypercholesterolemia. *Nat Genet* **34**, 154-156 (2003).

271. Maxwell, K.N., Fisher, E.A. & Breslow, J.L. Overexpression of PCSK9 accelerates the degradation of the LDLR in a post-endoplasmic reticulum compartment. *Proc Natl Acad Sci U S A* **102**, 2069-2074 (2005).

272. Denis, M. *et al.* Gene inactivation of proprotein convertase subtilisin/kexin type 9 reduces atherosclerosis in mice. *Circulation* **125**, 894-901 (2012).

273. Herbert, B. *et al.* Increased secretion of lipoproteins in transgenic mice expressing human D374Y PCSK9 under physiological genetic control. *Arterioscler Thromb Vasc Biol* **30**, 1333-1339 (2010).

274. Roche-Molina, M. *et al.* Induction of sustained hypercholesterolemia by single adeno-associated virus-mediated gene transfer of mutant hPCSK9. *Arterioscler Thromb Vasc Biol* **35**, 50-59 (2015).

275. Yang, R. *et al.* A genome-wide linkage scan identifies multiple quantitative trait loci for HDL-cholesterol levels in families with premature CAD and MI. *J Lipid Res* **51**, 1442-1451 (2010).

276. Kuhnast, S. *et al.* Alirocumab inhibits atherosclerosis, improves the plaque morphology, and enhances the effects of a statin. *J Lipid Res* **55**, 2103-2112 (2014).

277. Li, A.C. & Glass, C.K. The macrophage foam cell as a target for therapeutic intervention. *Nat Med* **8**, 1235-1242 (2002).

278. Dadu, R.T. & Ballantyne, C.M. Lipid lowering with PCSK9 inhibitors. *Nat Rev Cardiol* **11**, 563-575 (2014).

279. Desai, N.R. *et al.* AMG 145, a monoclonal antibody against PCSK9, facilitates achievement of national cholesterol education program-adult treatment panel III low-density lipoprotein cholesterol goals among high-risk patients: an analysis from the LAPLACE-TIMI 57 trial (LDL-C assessment with PCSK9 monoclonal antibody inhibition combined with statin thErapy-thrombolysis in myocardial infarction 57). *J Am Coll Cardiol* **63**, 430-433 (2014).

280. Robinson, J.G. & Kastelein, J.J. PCSK9 Inhibitors and Cardiovascular Events. *N Engl J Med* **373**, 774 (2015).

281. Weber, C. & Noels, H. Atherosclerosis: current pathogenesis and therapeutic options. *Nat Med* **17**, 1410-1422 (2011).

282. Hansson, G.K. & Hermansson, A. The immune system in atherosclerosis. *Nat Immunol* **12**, 204-212 (2011).

283. Saeed, O. *et al.* Pharmacological suppression of hepcidin increases macrophage cholesterol efflux and reduces foam cell formation and atherosclerosis. *Arterioscler Thromb Vasc Biol* **32**, 299-307 (2012).

284. Ringseis, R., Wen, G., Saal, D. & Eder, K. Conjugated linoleic acid isomers reduce cholesterol accumulation in acetylated LDL-induced mouse RAW264.7 macrophage-derived foam cells. *Lipids* **43**, 913-923 (2008).

285. Rousselle, A. *et al.* CXCL5 limits macrophage foam cell formation in atherosclerosis. *J Clin Invest* **123**, 1343-1347 (2013).

286. Anzinger, J.J. *et al.* Murine bone marrow-derived macrophages differentiated with GM-CSF become foam cells by PI3Kgamma-dependent fluid-phase pinocytosis of native LDL. *J Lipid Res* **53**, 34-42 (2012).

287. Zhou, Q. *et al.* Rho-associated coiled-coil-containing kinase 2 deficiency in bone marrow-derived cells leads to increased cholesterol efflux and decreased atherosclerosis. *Circulation* **126**, 2236-2247 (2012).

288. Cho, H.J. *et al.* Induction of dendritic cell-like phenotype in macrophages during foam cell formation. *Physiol Genomics* **29**, 149-160 (2007).

289. Gautier, E.L. *et al.* Gene-expression profiles and transcriptional regulatory pathways that underlie the identity and diversity of mouse tissue macrophages. *Nat Immunol* **13**, 1118-1128 (2012).

290. Bobryshev, Y.V. Monocyte recruitment and foam cell formation in atherosclerosis. *Micron* **37**, 208-222 (2006).

291. Yu, X.H., Fu, Y.C., Zhang, D.W., Yin, K. & Tang, C.K. Foam cells in atherosclerosis. *Clin Chim Acta* **424**, 245-252 (2013).

292. Allahverdian, S., Chehroudi, A.C., McManus, B.M., Abraham, T. & Francis, G.A. Contribution of intimal smooth muscle cells to cholesterol accumulation and macrophage-like cells in human atherosclerosis. *Circulation* **129**, 1551-1559 (2014).

293. Thomas, A.C., Eijgelaar, W.J., Daemen, M.J. & Newby, A.C. Foam Cell Formation In Vivo Converts Macrophages to a Pro-Fibrotic Phenotype. *PLoS One* **10**, e0128163 (2015).

CHAPTER 5
(APPENDIX I)

5 Isolation and Characterization of Aortic Dendritic Cells and Lymphocytes in Atherosclerosis

Tae Jin Yun[1,2], Jun Seong Lee[1,3], Dahee Shim[4], Jae-Hoon Choi[4], and Cheolhog Cheong[1,2,3]

[1]Laboratory of Cellular Physiology and Immunology, Institut de Recherches Cliniques de Montre´ al, Montre´ al, QC H2W 1R7, Canada

[2]Division of Experimental Medicine, Department of Medicine, McGill University, Montre´ al, QC H3A 1A3, Canada

[3]Department of Microbiology, Infectiology, and Immunology, Universite´ de Montre´ al, Montre´ al, QC H3C 3J7, Canada

[4]Department of Life Science, College of Natural Sciences, Research Institute for Natural Sciences, Hanyang University, Seoul 133-791, South Korea

[*]Contributed Equally.

Methods in Molecular Biology. (2017). 1559:419-437. doi: 10.1007/978-1-4939-6786-5_29.

5. 1 Abstract

Dendritic cells (DCs) are central to initiate antigen-specific immunity and tolerance. The in vivo development and distribution of DCs are now better understood even in nonlymphoid tissues.[1] Atherosclerosis is a chronic inflammatory disease of blood vessels and DCs are highly enriched in the intimal area of the aorta, which is predisposed to develop atherosclerosis. Previously, we were the first to show antigen presenting DCs and their subsets in the aorta.[2, 3] Here, we discuss several useful methods to characterize not only DCs but also other immune cells in steady state and atherosclerotic aorta. These comprise multiparameter flow cytometry strategies including intracellular staining and cell sorting, en face immunohistochemistry of DCs and regulatory T cells (Tregs), and Oil Red O staining of atherosclerotic lesions in the aorta.

5. 2 Introduction

In addition to their role in lipid uptake and systemic lipid metabolism[4, 5], DCs have been shown to be important in modulating immune responses in atherosclerosis in mouse models. For example, these studies have demonstrated an atherosclerosis-promoting role of T cell costimulatory and antigen-presenting molecules expressed on the surface of DCs (e.g., CD80, CD86, MHCI/II)[6, 7], an atheroprotective role of the DC maturation-signaling pathway through DC-specific elimination of Myd88[8], and regulation of regulatory T cell (Treg) homeostasis by subsets of DCs, such as $CCL17^+$ DCs and Flt3-dependent DCs.[3, 9] These observations suggest a critical role for DCs in the regulation of T cells and possibly atheroprotective Tregs.[10]

However, it is very demanding to obtain enough aortic DCs to functionally address their characteristics. In this regard, many studies in the field of atherosclerosis have used preferentially bone marrow-derived or lymphoid DCs to uncover the mechanism behind observed atherosclerotic phenotypes. Of note, it is prudent to analyze the interplay of immune cells in healthy and diseased aorta to understand the initiation and progression of atherosclerosis. Here we summarize useful methods to analyze DCs and immune cells in healthy and diseased aorta.

The advent of genetically modified mouse models such as low-density lipoprotein receptor (Ldlr) or Apolipoprotein E (ApoE)-deficient mice has facilitated atherosclerosis studies in mice that closely recapitulate human disease.[11, 12] While cell type analysis in atherosclerotic lesions by immunohistochemistry has been informative, recent advances in flow cytometric analysis of aortic cell suspensions allowed monitoring various immune cell types simultaneously in the aorta.[13] However, autofluorescent macrophages affect flow cytometric analysis of aortic cell suspensions especially in multiparameter flow cytometry. Therefore, it is critical to remove macrophages from the beginning to faithfully analyze other immune cells such as DCs and Tregs. To this end, the use of macrophage specific markers such as CD64 and MerTK in combination with CD11b or F4/80 is very helpful.[14, 15] In our protocol, FACS staining is optimized for 96 well formats to save antibody-related reagents and minimize cell loss. Of note, several cell surface markers are easily degraded via collagenase

treatment. To overcome this issue, intracellular staining of CD4 is employed in our protocol.[16] To measure regulatory T cells in the aorta, CD4 and Foxp3 are simultaneously stained. Notably, the Foxp3 staining method (eBioscience) has been modified and optimized for aortic Treg measurement.

Traditionally, staining aortic immune cells en face has provided valuable information on their anatomical location and distribution. We previously reported that DCs are enriched in the intimal space of aortas while macrophages are enriched in adventitia.[2, 3] En face staining allows one to image both the intimal and adventitia sides of the aorta. Here, we describe a method to stain whole mount en face of aortic DCs and macrophages. To this aim, the basic protocol (TSA Protocol, Life Technologies) has been modified and optimized for the aorta. In atherosclerotic lesions, Oil Red O staining is a classical method to measure lesions and assess the severity of atherosclerosis in mouse models.[17] For a sound assessment of atherosclerotic lesions, it is critical to embed the aorta in the correct orientation for frozen section preparation. We illustrate this procedure in detail and show representative stainings of Oil Red O and $CD11c^+$ cells in the aorta. Finally, we also provide one example of functional analysis to differentiate DCs from macrophages. The classical feature of DCs is their lower phagocytic activity compared with macrophages.[3] In this protocol, aortic cell suspensions are incubated with fluorescent beads to assess phagocytic activity and then purified by fluorescence-activated cell sorting to observe the morphological characteristics of DCs and macrophages.

5. 3 Materials

5. 3. 1 Mouse Aorta Isolation

5. 3. 1. 1 Mouse Handling

1. C57BL/6 mouse.
2. 70% ethanol.
3. Surgical scissors (**Figure. 5.1a**).
4. Surgical forceps.
5. 10ml syringe.
6. 24-gauge needle.
7. 1x PBS.
8. Surgical tray.

5. 3. 1. 2 Aorta Isolation

1. Dissecting microscope.
2. Dissecting dish: heat-resistant glass dishes, black wax(Nasco, SA04451MH), hotplate stirrer (**Figure. 5.1b and c**, see **Note** 1).
3. Micro-dissection scissors.
4. Micro-dissection forceps.
5. Pin.

5. 3. 2 Flow Cytometry Analysis

5. 3. 2. 1 Preparation of Single Cell Suspension

1. 1ml collagenase cocktail: 880µl 1x HBSS, 100µl collagenase type I (Sigma-Aldrich, C0130, 10x stock: 675 U/ml), 10µl collagenase type XI (Sigma-Aldrich, C7657, 10x stock: 187.5U/ml), 10µl hyaluronidase type I-s (Sigma-Aldrich, H1115000, 10x stock: 9 U/ml) (see **Note** 2).
2. Rotator.

3. Collagenase digestion tube with cap (Falcon, 352063) (see **Note** 3).
4. Parafilm M.
5. 70-μm strainers.
6. 15ml tube.
7. 500ml wash media: 25ml heat-inactivated FBS, 475ml 1x RPMI-1640, 5ml 100x antibiotic–antimycotic.
8. Swinging rotor.

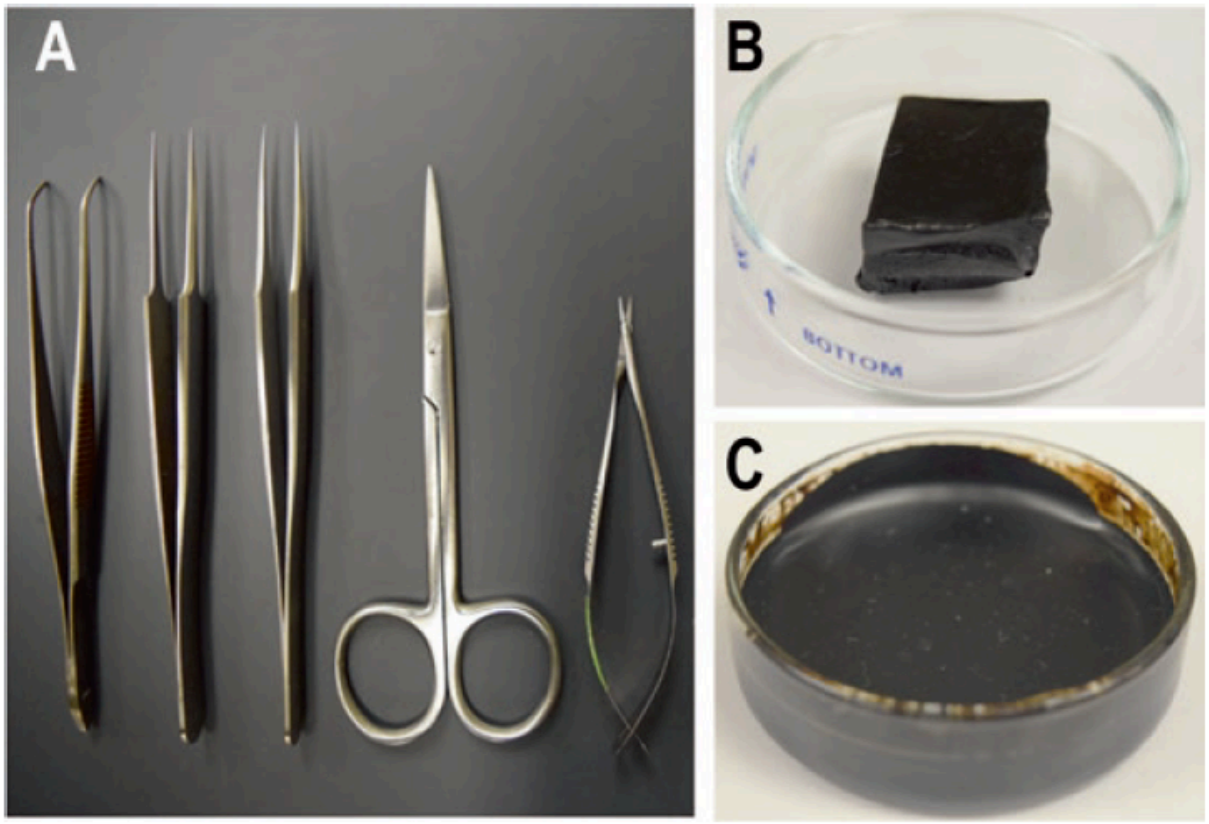

Figure 5.1. Materials for mouse aorta isolation. (A) From left to right; angled surgical forceps with serrated tips, sharp-nose surgical forceps, microdissection forceps, surgical scissors, and microdissection scissors. **(B,C)** Dissecting dish preparation. Heat-resistant glass dish before **(B)** and after **(C)** black wax was applied.

5. 3. 2. 2 Surface Staining

1. Fluorochrome-conjugated monoclonal antibodies (all from BioLegend): PE-CD45 (clone 30-F11), PerCP/Cy5.5-CD64 (clone X54-5/7.1), BV711-CD11b (clone M1/70), PeCy7-CD11c (clone N418) and A700-MHCII (clone M5/114.15.2).
2. FcBlock: culture supernatant from 2.4G2 hybridoma (ATCC, HB-197).
3. 500ml FACS buffer: 10ml heat-inactivated FBS, 490ml 1x PBS withcalcium/ magnesium, 5ml 100x antibiotic–antimycotic.
4. 96-well v-bottom plates.
5. Microtiter tubes.
6. 5ml tubes.
7. Flow cytometry analyzer.

5. 3. 2. 3 Intracellular Foxp3 Staining

1. Fluorochrome-conjugated monoclonal antibodies (all from BioLegend, unless noted otherwise): APC-CD45 (BD Biosciences, clone 30-F11), PerCP/Cy5.5-CD64 (clone X54-5/7.1), BV711-CD11b (clone M1/70), APC-e780-CD3 (eBioscience, clone 17A2), BV785-CD4 (clone RM4-5), and PE-Foxp3 (eBioscience, clone FJK-16s).
2. Foxp3/Transcription Factor Staining Buffer Set (eBioscience, 00-5523-00).
3. Materials as described in Subheading **5.3.2.2**, from **item 2 to 7**.

5. 3. 3 Visualization in Aorta

5. 3. 3. 1 Dendritic Cell Staining

1. 6-well plate.
2. 0.25% Triton X-100: 125µl Triton X-100, 50ml 1x PBS (see **Note** 4).
3. 1.5ml tube.
4. 0.3% H2O2: 100µl 30% H2O2, 10ml 1x PBS (see **Note** 5).
5. Monoclonal antibody: Biotin-CD11c mAb (BioLegend, clone N418).
6. TSA kit, HRP-Streptavidin with Alexa Flour 555 (Invitrogen, T-30955).
7. Shaker.

8. DAPI.
9. Glass slides for cryosection.
10. 4% formaldehyde: 4ml 10% formaldehyde, 6ml 1x PBS.
11. 1x PBS.
12. Mounting solution.
13. Coverslip.
14. Transparent nail polish.
15. Scotch tape.

5. 3. 3. 2 Oil Red O Staining (*en face*)

1. $Ldlr^{-/-}$ mouse or $ApoE^{-/-}$ mouse.
2. CHOW diet (TestDiet, 5015) or Western diet (TestDiet, AIN-76A).
3. Dissecting dish.
4. Distilled water.
5. Glass slides.
6. Pin.
7. 0.5% Oil Red O solution I: 0.5g Oil Red O, 100ml 100% propylene glycol (see **Note** 6).
8. 85% propylene glycol: 85ml 100% propylene glycol, 15ml distilled water.
9. Materials from Subheading **5.3.3.1**, **items 10-15**.

5. 3. 3. 3 Oil Red O Staining (Cryosection)

1. Razor blade.
2. Embedding mold.
3. OCT compound.
4. Cryostats.
5. Glass slides for cryosection.
6. Harris' hematoxylin (National Diagnostics, HS-400).
7. 0.5% Oil Red O solution II: 1g Oil Red O, 100ml 70% ethanol, 100ml acetone (see **Note** 7).

8. 70% ethanol.
9. Materials from the Subheading **5.3.3.1**, from **items 10 to 15**.
10. Mice and materials from Subheading **5.3.3.2**, **items 1-4**.

5. 3. 3. 4 Immunostaining (Cryosection)

1. TSA kit, HRP-Streptavidin with Alexa Flour 594 (Invitrogen, T-20935).
2. 0.3% H2O2: 100µl 30% H2O2, 10ml 1x PBS (see **Note** 5).
3. Monoclonal antibody: Biotin-CD11c mAb (BD Pharmigen, clone HL3).
4. DAPI.
5. Materials from the Subheading **5.3.3.1**, from **items 10 to 15**.
6. Mouse and materials from the Subheading **5.3.3.2**, from **items1 to 4**.
7. Materials from the Subheading **5.3.3.3**, from **items 2 to 5**.

5. 3. 4 Bead Phagocytosis Assay

5. 3. 4. 1 Bead Phagocytosis and Sorting

1. Fluoresbrite 1µm bead (Polysciences, 15702).
2. Collagenase digestion tube with cap (Falcon, 352063).
3. 500ml culture media: 25ml sterile heat-inactivated FBS, 475ml sterile 1x RPMI-1640, 5ml sterile 100x antibiotic-antimycotic, 5ml sterile 100x GlutaMAX, 5ml sterile 100x MEM nonessential amino acids.
   Add sterile 0.5ml 1000x 2 mercaptoethanol right before using culture media.
4. Fluorochrome-conjugated monoclonal antibodies (all from BioLegend, unless noted otherwise): APC-CD45 (BD Biosciences, clone 30-F11), PerCP/Cy5.5-CD64 (clone X54-5/7.1), BV711-CD11b (clone M1/70), PeCy7-CD11c (clone N418), and A700-MHCII (clone M5/114.15.2).
5. 15ml tube.
6. Cell sorter.
7. 500ml FACS buffer: 10ml heat-inactivated FBS, 490ml 1x PBS with calcium/ magnesium, 5ml 100x antibiotic–antimycotic.

5. 3. 4. 2 Cytospin and Fixation

1. Glass slides for cryosection.
2. Shanon filter card.
3. Cytospin cytocentrifuge.
4. 4% formaldehyde: 4ml 10% formaldehyde, 6ml 1x PBS.
5. 1x PBS.
6. DAPI.
7. Mounting solution.
8. Coverslip.
9. Transparent nail polish.

5. 4 Methods

5. 4. 1 Mouse Aorta Isolation

5. 4. 1. 1 Mouse Handling

1. Prepare a 10ml syringe filled with 10ml of ice cold 1x PBS (per mouse).
   Attach a 24-gauge needle to the syringe.
2. Euthanize mouse with CO2. As soon as the mouse stops breathing, bring it out of the CO2 chamber.
3. Spray 70% ethanol onto the mouse and place it on a surgical tray under a light source.
4. Place mouse abdomen up and stretched with 24-gauge needles onto its four paws.
5. Locate and lift abdominal skin, insert scissors and make incisions from thoracic cavity to peritoneum. Avoid cutting blood vessels, which can cause bleeding.
6. Open the abdominal wall below the ribcage.
7. Lift the sternum with forceps and cut the diaphragm. The heart should be visible.
8. Locate right and left iliac blood vessels between peritoneum and hind legs and make incisions for blood drainage.
9. Insert the 10 ml syringe needle into the apex of the right ventricle and flush the blood out of the mouse for 2 min.
10. Cut away the entire ribcage to expose the heart and lungs.
11. Remove lungs, esophagus, and intestine with scissors.

5. 4. 1. 2 Aorta Isolation

1. You should be able to see connective tissues along the spine.
   The aorta is located along the spine and surrounded by connective tissues.
2. Lift the heart and detach connective tissues all the way down to the bladder.
3. Flush the heart again through the right and left ventricles using a 10ml syringe containing10ml of cold 1x PBS to clean out residual blood.
4. Place the aorta on the dissecting dish (see **Figure. 5.1** for the preparation of

dissection dish) with 1x cold PBS under a dissecting microscope.

5. Using microdissection scissors cut the heart horizontally and pin the heart with a needle (**Figure. 5.2a**).
6. Remove the fat and connective tissues surrounding aorta carefully, leaving intact the sinus, aortic arch and three arteries (Brachiocephalic, Left common carotid and Left subclavian artery) on aortic arch (**Figure. 5.2b, c**).
7. Cut along the lesser curvature side of aorta from aortic sinus to the end of descending aorta (**Figure. 5.2d, e**).
8. Cut distal ascending side of aorta where three arteries are located, from aortic sinus to the end of left subclavian artery (**Figure. 5.2f, g**).

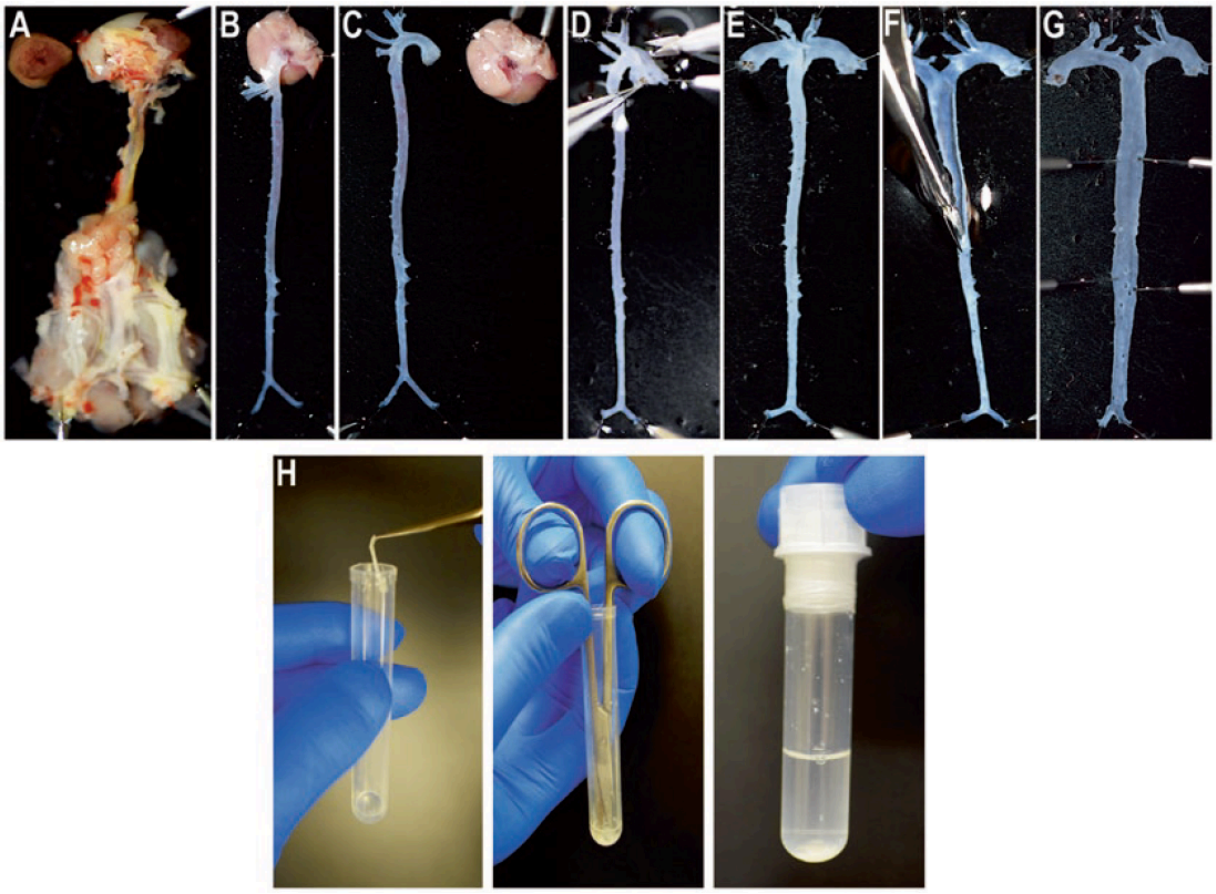

Figure 5.2. Mouse aorta isolation under dissecting microscope. (A) Isolated tissues containing aorta and heart on dissecting dish with cold 1x PBS. Heart was cut in half horizontally and pinned on the dissection dish to facilitate locating aortic arch and three

arteries. **(B, C)** Aorta was trimmed but aortic sinus is still inside the heart **(B)** and aortic sinus was separated intact from the heart **(C)**. **(D-G)** Trimmed aorta was opened in Y shape. Distal ascending side of aorta where three arteries are located was cut **(D and E)** and lesser curvature side of aorta from aortic sinus to the end of descending aorta was cut **(F and G)**. **(H)** Isolated aorta in a collagenase digestion tube was cut into small pieces with surgical scissors and filled with 1 ml of collagenase cocktail. The tube was closed with cap and tightly sealed with Parafilm.

5. 4. 2 Facs Analysis

5. 4. 2. 1 Preparation of Single Cell Suspension

1. Prepare 1ml collagenase cocktail.
2. Add 100µl of collagenase cocktail into a collagenase digestion tube per one isolated aorta (**Figure. 5.2h**).
3. Cut the aorta into small pieces with surgical scissors to facilitate collagenase digestion and add additional 900µl of collagenase cocktail to make 1ml in total (**Figure. 5.2h**).
4. Close the tube with a cap and seal the cap tightly with Parafilm.
   Then, incubate at 37 °C for 40 min with rotation (**Figure. 5.2h**).
5. Remove the tube from incubator after 40 min and centrifuge the tubes briefly at 800x**g**.
6. Pipette the digested aorta up and down about 100 times and pass through 70-µm strainers into a 15ml tube.
7. Wash the collagenase digestion tube with 1 ml of wash media to minimize cell loss and transfer the 1 ml into the 15 ml tube.
8. Centrifuge the 15ml tube at 800x**g** for 5 min at 4 °C and aspirate supernatant (Use swinging rotor to maximize cell pellet).
9. Repeat **step**s 7 and 8.

5. 4. 2. 2 Surface Staining

1. Resuspend and incubate cells in 150µl FcBlock at 4 °C for at least 20 min.
2. Prepare antibody cocktail in FACS buffer (anti-CD45, anti-CD64, anti-CD11b, anti-CD11c, and anti-MHCII mAb).

3. Transfer cells into one well of a 96-well v-bottom plate.
4. Centrifuge the plate at 800x**g**, 4 °C for 2 min and flick the plate in a quick single motion with sufficient force to discard supernatant (Do not aspirate).
5. Wash the cells in 100µl of FACS buffer and repeat **step** 4.
6. Resuspend the cells in 30µl of antibody cocktail at 4 °C in the dark for 30 min.
7. Add 100µl of FACS buffer, resuspend the stained cells and repeat **step** 4.
8. Repeat **step** 7, twice.
9. Suspend the stained cells in 100µl of FACS buffer and pass through 70-µm strainers into a microliter tube.
10. Place the microliter tube into a 5 ml tube used for flow cytometry analysis and read the cells on a flow cytometer (**Figure. 5.3a**).

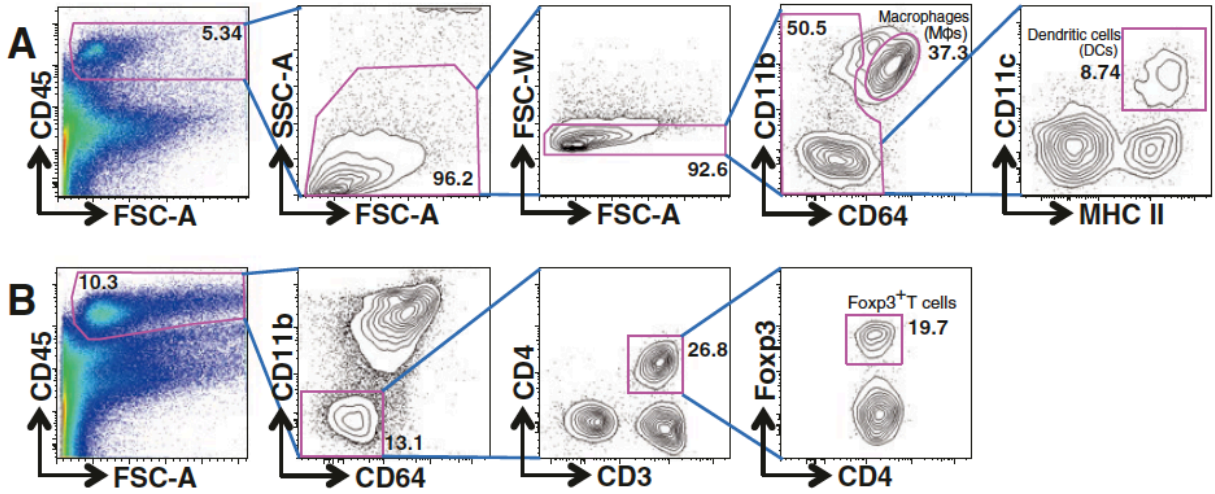

Figure 5.3. Aortic lymphocytes gating strategy. (A) Aortic cells from C57BL/6 mouse were stained for CD45, CD64, CD11b, CD11c, and MHCII. Entire cells from one aorta were acquired. First $CD45^+$ lymphocytes were gated and plotted onto forward scatter (FSC) and side scatter (SSC). Cell doublets were excluded using FCS-A and FSC-W, and $CD64^+$ macrophage and $CD64^-$ non-macrophage cells were separated. Finally, $CD64^-$ non-macrophage cells were plotted onto CD11c and MHCII and $CD11c^+$ $MHCII^+$ aortic dendritic cells can be identified. **(B)** Aortic cells from $Ldlr^{-/-}$ mouse fed with western diet for 8 weeks were stained for CD45, CD64, CD11b, CD3, CD4, and Foxp3. Entire cells from one aorta were acquired. First, $CD45^+$ lymphocytes were gated and plotted onto forward scatter (FSC, not shown) and side scatter (SSC, not shown). Cell duplets were excluded using FCS-A and FSC-W (not shown). Second, $CD64^-$ $CD11b^-$ cells were gated. Third, $CD3^+$ $CD4^+$ cells were

isolated and, finally, $CD4^+$ $Foxp3^+$ cells can be identified. Data was analyzed using FlowJo software (TriStar).

5. 4. 2. 3 Intracellular Foxp3 Staining

1. Resuspend and incubate cells in FcBlock at 4 °C for at least 20 min.
2. Prepare antibody cocktail in FACS buffer (anti-CD45, anti-CD64, anti-CD11b, and anti-CD3 mAb).
3. Transfer cells into one well of a 96-well v-bottom plate.
4. Centrifuge the plate at 800x**g**, 4 °C for 2 min and flick the plate in a quick single motion with sufficient force to discard supernatant (Do not aspirate).
5. Wash the cells in 100µl of FACS buffer and repeat **step** 4.
6. Resuspend the cells in 30µl of antibody cocktail for surface markers at 4 °C in the dark for 30 min.
7. Add 100µl of FACS buffer, resuspend the stained cells, and repeat **step** 4.
8. Repeat **step** 7, twice.
9. Prepare fresh 1x Fixation/Permeabilization buffer (50µl per sample/well, **see Note** 8).
10. Resuspend and fix the surface stained cells in 50µl of 1x Fixation/Permeabilization buffer at 4 °C at least 7 h or overnight (Cover the plate if fixed overnight).
11. Centrifuge the plate at 800x**g** for 3 min and flick the plate in a quick single motion with sufficient force to discard buffer (Do not aspirate, **see Note** 9).
12. Prepare fresh 1x Permeabilization buffer (Total 340µl per sample/well).
13. Prepare antibody cocktail in 1x Permeabilization buffer (anti-CD4 and anti-Foxp3 mAb).
14. Resuspend and wash the fixed cells in 100µl of 1x Permeabilization buffer.
15. Centrifuge the plate at 800x**g** for 3 min and flick the plate in a quick single motion with sufficient force to discard buffer (Do not aspirate).
16. Repeat **step**s 14 and 15.
17. Resuspend and incubate the fixed cells in 40µl of antibody cocktail for intracellular staining at 4 °C for 7 h.
18. Resuspend the stained cells in 100µl of 1x Permeabilization buffer and repeat **step** 15.

19. Resuspend the stained cells in 100µl of FACS buffer and repeat **step** 15.
20. Repeat **step** 19.
21. Resuspend the surface and intracellular stained cells in 100µl of FACS buffer and pass through 70-µm strainers into a microliter tube.
22. Place the microliter tube into a 5ml tube used for flow cytometry and analyze the cells on a flow cytometer (**Figure. 5.3b**).

5. 4. 3 Visualization in Aorta

5. 4. 3. 1 Dendritic Cell Staining (*en face*)

1. Fix the isolated aorta (prepared from Subheading **5.4.1.2**) in 4 % formaldehyde in a 6-well plate at 4 °C, 40 min.
2. Wash the fixed aorta in 1x PBS in a 6-well plate on shaker for 10 min, three times.
3. Permeabilize the aorta in 0.25% Triton X-100 in 1.5ml tube for 20 min with rotation at room temperature.
4. Repeat **step** 2.
5. Inactivate endogenous peroxidase by incubating the permeabilized aorta in 0.3% H2O2 in a 6-well plate at room temperature for 1 h.
6. Repeat **step** 2.
7. Block the aorta with 2% TSA blocking solution for 1 h with rotation at room temperature (see **Note** 10).
8. Repeat **step** 2.
9. Incubate the aorta with biotin-CD11c mAb (0.75µg in 300µl of 1% TSA blocking solution) in a 48-well plate at room temperature for 2 h on shaker.
10. Repeat **step** 2.
11. Incubate the aorta with streptavidin-HRP Ab (0.325µg in 300µl of 1% TSA blocking solution) at room temperature for 1 h on shaker.
12. Repeat **step** 2.
13. Label the aorta in 300µl of TSA reaction mix (1µl Alexa fluorochrome in 300µl reaction buffer) in 48 well plates on shaker for 20 min.

14. Wash the fixed aorta in 1x PBS in a 6-well plate on shaker for 10 min.
15. Incubate the stained aorta with DAPI (1µl in 5ml 1x PBS) for 1 min.
16. Repeat **step** 2 (see **Note** 11).
17. Place the aorta in a Y shape onto a coverslip under a dissecting microscope and close the coverslip with mounting solution and another coverslip. (CAUTION: DO NOT fold aorta, this will result in autofluorescence, poor images, and difficulty in Distinguishing intima and adventitia).
18. Dry the slide in the dark and seal the coverslip with nail polish.
    Tape the sample onto a glass slide.
19. Examine intima and adventitia by fluorescence microscope (**Figure. 5.4a–c**).

5. 4. 3. 2 Oil Red O Staining (*en face*)

1. Prepare $Ldlr^{-/-}$ mouse or $ApoE^{-/-}$ mouse fed with western diet for at least 6 weeks, or at least 200 days old $ApoE^{-/-}$ mouse fed with CHOW diet.
2. Place the aorta (prepared from Subheading **5.4.1.2**) on the dissecting dish with ice cold 1x PBS under a dissecting microscope.
3. Pin the aorta in a Y shape so that the atherosclerosis lesions of intima are exposed.
4. Replace PBS with 4% formaldehyde and incubate at room temperature for 1 h.
5. Replace 4% formaldehyde with 1x PBS and wash for 1 h.
6. Replace PBS with 100% propylene glycol and incubate for 5 min.
7. Replace 100 % propylene glycol with 0.5% Oil Red O solution I and incubate the aorta for 9 h at room temperature.
8. Replace 0.5% Oil Red O solution with 85% propylene glycol and wash the aorta for 10 min.
9. Replace 85% propylene glycol with 1x PBS and wash the aorta in 1x PBS at room temperature for 1 h.
10. Place the aorta in a Y shape onto a coverslip under a dissecting microscope and close the coverslip with mounting solution and another coverslip.
11. Dry the slide and seal the coverslip with nail polish.
    Tape the sample onto a glass slide.

12. Examine intima by microscope (**Figure. 5.4d and e**).

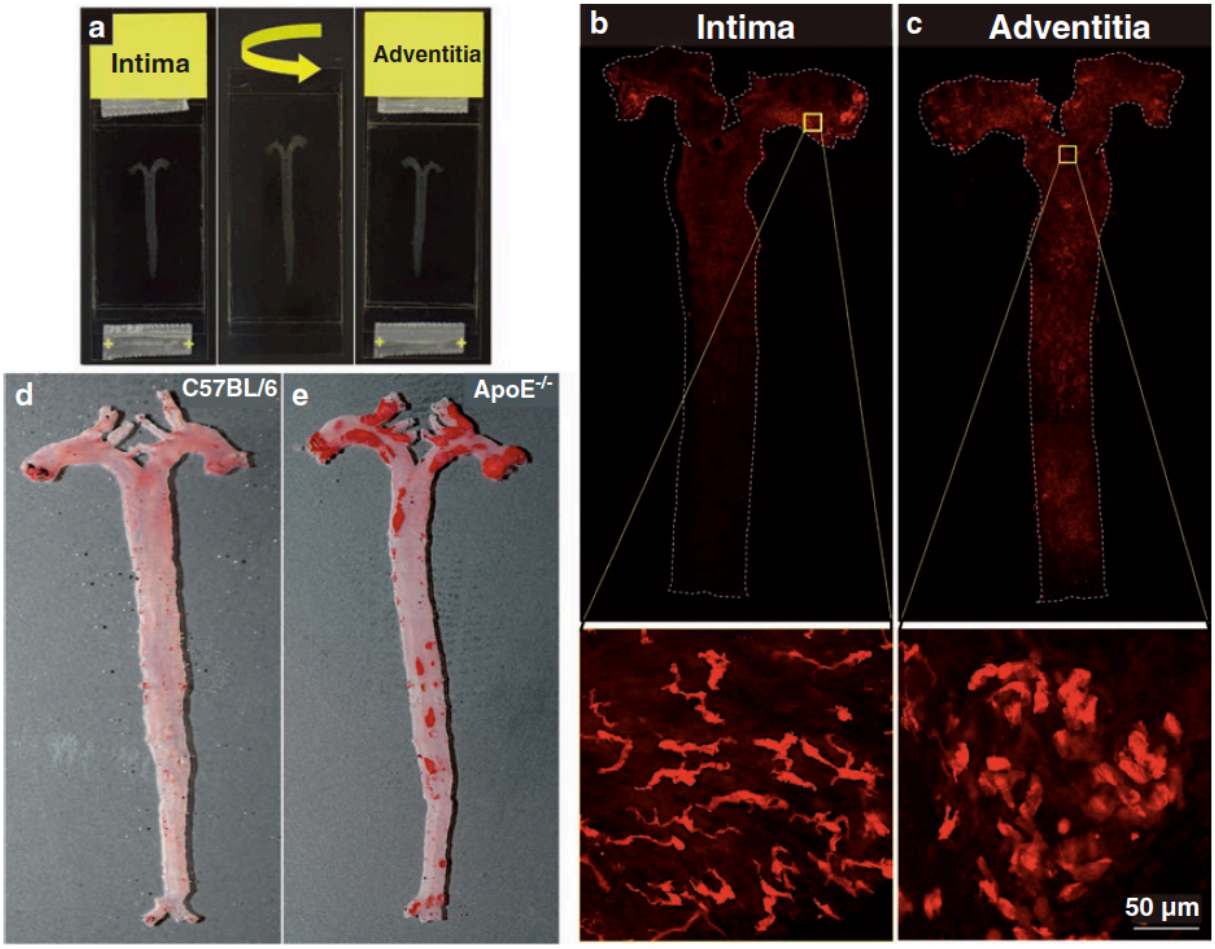

Figure 5.4. Visualization of aortic CD11c^{+} cells and atherosclerotic lesions. (A) Fixed and stained aorta was mounted on coverslips. Intima can be examined by placing it on a glass slide with tape, and adventitia can be examined by flipping only the cotverslips. **(B and C)** Aorta from C57BL/6 mouse was isolated, fixed and stained for CD11c and labeled with TSA Alexa 555 kit. White dotted line indicates boundary of aorta and entire aorta image was taken by tile scanning. Alexa 555 positive cells can be observed in lesser curvature in intima **(B)** and throughout in adventitia **(C)**. Inset image shows dendritic cell morphology in intima and non-dendritic cell morphology with no dendrites in adventitia. Images were examined using LSM 710 confocal microscope (Zeiss). **(D and E)** Aortas from C57BL/6 mouse and ApoE$^{-/-}$ mouse, both fed with CHOW diet and 300 days old, were fixed and stained for Oil Red O. Aorta from ApoE$^{-/-}$ mouse **(E)** shows atherosclerotic lesions which are not observed in aorta of C57BL/6 **(D)**. Most of atherosclerotic lesions in ApoE$^{-/-}$ mouse are located in aortic sinus and aortic arch. Both images show the intima.

5. 4. 3. 3 Oil Red O Staining (Cryosection)

1. Prepare Ldlr$^{-/-}$ mouse or ApoE$^{-/-}$ mouse fed with Western diet for at least 6 weeks, or at least 200-day-old ApoE$^{-/-}$ mouse fed with CHOW diet.
2. Follow the **step**s in Subheading **5.4.1.1** until **step** 5 in Subheading **5.4.1.2**.
3. Using a sharp razor blade cut along Line-a in the middle between the bottom of the heart and a plane of both bottom of right and left atria (Line-b). Line-a is also parallel with Line-c (**Figure. 5.5a**, see **Note** 12).

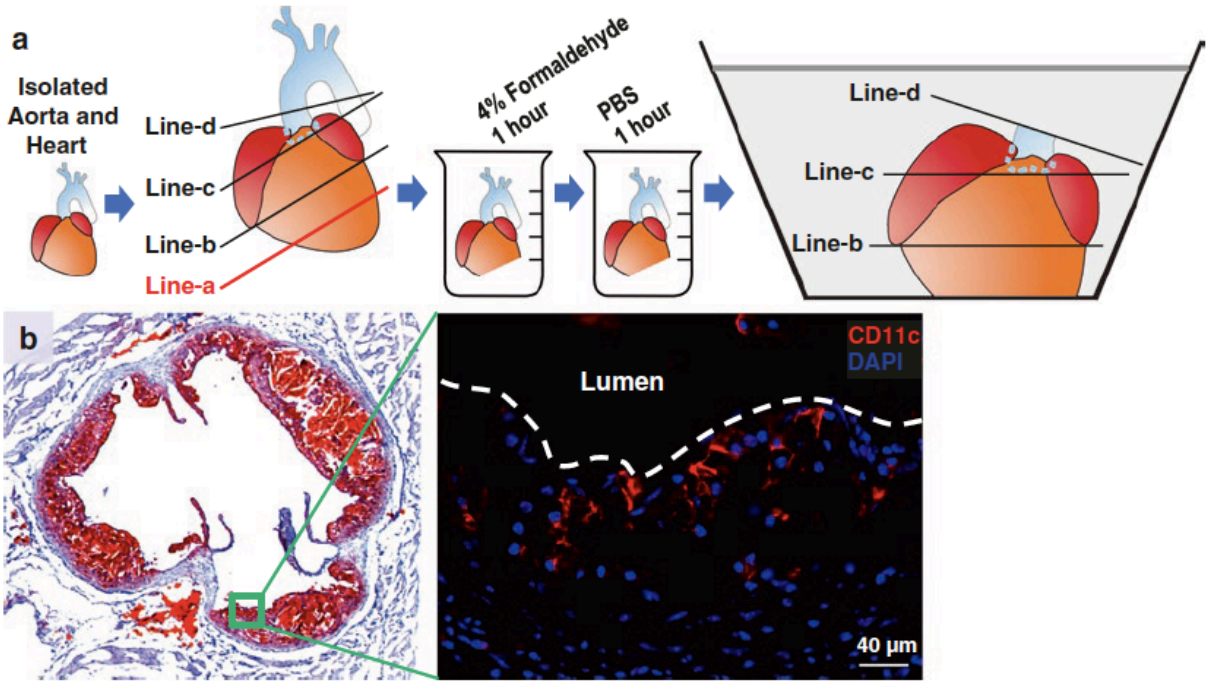

Figure 5.5. Oil Red O staining and CD11c^{+} cell staining with frozen sections from atherosclerotic lesions in aortic sinus. (A) Isolated heart was cut along Line-a, which is located halfway between the bottom of the heart and a plane of both lower right and left atria (Line-b). Line-a must be parallel with Line-b, which results in also being parallel with Line-c. The trimmed heart was fixed and washed in 4% formaldehyde and PBS, respectively. The fixed heart was cut along Line-d, which is parallel to both apex of right and left atria, and placed frozen in an embedding mold filled with OCT compound. **(B)** The cross section of aortic sinus with three sinus valves was stained with Oil Red O and Harris' hematoxylin. Atherosclerotic lesions are shown in red in sinus valves [left]. Image in inset shows cells stained for CD11c by TSA staining kit [right] using Eclipse 50i microscope (Nikon).

4. Pin the heart with a needle and remove the fat and connective tissues surrounding aorta carefully, leaving intact the aortic arch and three arteries (Brachiocephalic, Left common carotid and Left subclavian artery) on aortic arch. Please do not separate the heart and aorta.
5. Fix the heart and aorta in 4% formaldehyde at room temperature for 1 h (**Figure. 5.5a**).
6. Wash the fixed heart and aorta in 1x PBS at room temperature for 1 h (**Figure. 5.5a**).
7. Cut along Line-d to remove aorta but only leaving the aortic sinus (**Figure. 5.5a**).
8. Place the heart and aortic sinus in an embedding mold and fill with OCT compound at room temperature. Wait for 10 min (**Figure. 5.5a**).
9. If the sample floats to the surface, squeeze the tissue with forceps slightly to remove air bubbles.
10. Bring the embedding cassette to −80 °C for at least 4 h.
11. Start cryosection in 5μm thickness.
12. Cut the frozen block until the heart is exposed and place it on a glass slide.
13. Examine the slide under the microscope if aortic sinus and valves are visible.
14. Prepare several slides with intact aortic sinus with all three leaflets of the valve.
15. Wash the slides with distilled water for 3 min.
16. Stain in Harris' hematoxylin for 30s.
17. Aspirate hematoxylin and repeat **step** 15.
18. Apply 70% ethanol for 2s.
19. Aspirate 70% ethanol and add 0.5% Oil Red O solution II for 2 min.
20. Aspirate Oil Red O solution and wash with 70% ethanol for 30s.
21. Aspirate and wash with 70% ethanol for 30s again.
22. Aspirate 70% ethanol and stain in hematoxylin for 30s.
23. Wash the slides with distilled water for 3 min.
24. Close the slides with mounting solution and coverslips.
25. Dry the slide and seal the coverslip with nail polish.
26. Examine by light microscopy (**Figure. 5.5b Left**).

5. 4. 3. 4 Immunostaining (Cryosection)

1. Prepare aortic sinus slides according to the description in Subheading **5.4.3.3** up to **step** 14.
2. Dry the slides at 60 °C for 1 h.
3. Hydrate sections with PBS at room temperature for 5 min.
4. Block endogenous peroxidase activity with 0.3% H2O2 for 1 h.
5. Wash the slides twice with PBS for 5 min.
6. Block sections with 1% TSA blocking solution for 1 h.
7. Repeat **step** 5.
8. Stain sections with biotin-CD11c mAb (0.5µg in 100µl of 1% TSA blocking solution) at room temperature for 1 h.
9. Repeat **step** 5.
10. Incubate sections with streptavidin-HRP Ab (0.125µg in 100µl of 1% TSA blocking solution) at room temperature for 1 h.
11. Repeat **step** 5.
12. Label sections in 100µl of TSA reaction mix (0.25µl Alexa fluorochrome in 100µl reaction buffer) for 20 min at room temperature. Avoid light.
13. Repeat **step** 5.
14. Incubate sections with DAPI (1µl in 5ml 1x PBS) for 1 min.
15. Repeat **step** 5.
16. Close the slides with mounting solution and coverslips.
17. Dry the slides in the dark and seal the coverslip with nail polish.
18. Examine by fluorescence microscopy (**Figure. 5.5b Right**).

5. 4. 4 Bead Phagocytosis Assay

5. 4. 4. 1 Bead Phagocytosis and Sorting

1. Perform Subheadings **5.4.1** and **5.4.2.1** under sterile conditions in a cell culture hood (Centrifuge samples at 450x**g** in Subheading **5.4.2.1**, instead of 800x**g**).
2. All procedures in this Subheading (**5.4.4.1**) should be carried out

in sterile conditions in a culture hood.

3. Incubate the cells with beads (1µl of beads/ml) in 1 ml of sterile culture media in a collagenase digestion tube at 37 °C in an incubator for 1 h (see **Note** 13).
4. Transfer the cells into a sterile 15 ml tube.
5. Add 1 ml of sterile culture media into the collagenase digestion tube to collect leftover cells, and transfer into the 15 ml tube.
6. Wash the cells with an additional 2 ml of sterile culture media by centrifuge at 450x**g**, 4 °C for 5 min.
7. Aspirate supernatant and repeat **step** 6.
8. Resuspend and incubate cells in 300µl of sterile FcBlock at 4 °C for at least 20 min.
9. Prepare antibody cocktail in culture media (anti-CD45, anti-CD64, anti-CD11b, anti-CD11c, and anti-MHCII mAb).
10. Repeat **step** 6.
11. Aspirate supernatant and stain the cells with 300µl antibody cocktail at 4 °C for 30 min.
12. Repeat **step** 6.
13. Aspirate supernatant and repeat **step** 6.
14. Resuspend the stained cells in 500µl culture media and pass through 70-µm strainers into an appropriate tube used for cell sorting.
15. Sort the aortic cells into two groups; $CD64^{+}CD11b^{+}$ macrophages and $CD11c^{+}$ $MHCII^{+}$ dendritic cells.
16. Wash the sorted cells with 5 ml of sterile FACS buffer at 4 °C at 450x**g** for 15 min.
17. Aspirate supernatant and repeat **step** 16.
18. Aspirate supernatant and resuspend cells in 100µl of FACS buffer in the dark at 4 °C (**see Note** 14).

5. 4. 4. 2 Cytospin and Fixation

1. Assemble a pre-coated slide and a filter card into one of the slots of a cytospin centrifuge.
2. Transfer 100µl of FACS sorted sample into the assembled slot, and spin at 32xg

for 5 min.

3. Carefully separate the slide from the filter card not to damage the sample on the slide.
4. Dry the slide for 10 min in the dark at room temperature.
5. Prepare 4% formaldehyde and apply it carefully onto the sample on the slide to fix the cells in the dark at room temperature for 20 min.
6. Wash the slide with PBS for 5 min in the dark at room temperature.
7. Prepare diluted DAPI solution (1µl in 5ml of 1x PBS).
8. Aspirate 1x PBS from the slide and gently apply 100µl diluted DAPI solution for 1 min.
9. Aspirate and repeat **step** 6, twice.

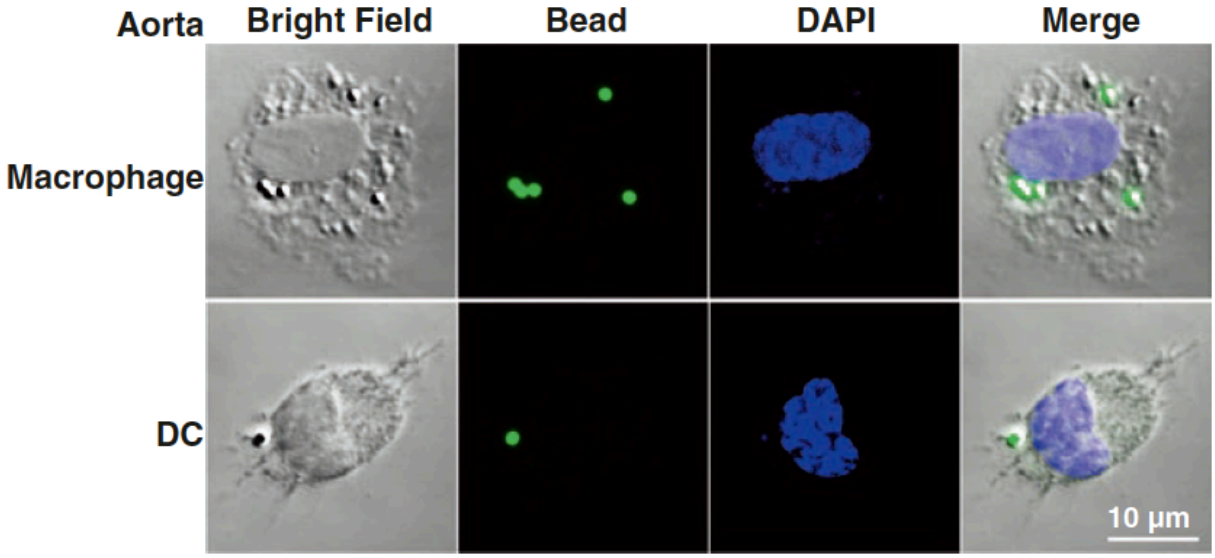

Figure 5.6. Visualization of Bead phagocytosis in sorted and cytospin centrifuged aortic cells. Total aortic cells from a C57BL/6 mouse were incubated with Fluoresbrite 1-µm beads for phagocytosis, stained with antibodies (CD45, CD64, CD11b, CD11c and MHCII) for cell sorting and cytospin centrifugation (32x**g**, 5 min). Aortic macrophages were gated from $CD45^+$ $CD64^+$ $CD11b^+$ cells and aortic dendritic cells (DC) were gated from $CD45^+$ $CD64^-$ $CD11c^+$ $MHCII^+$ cells. Cytospin slides were fixed and stained with DAPI. The images were examined using a LSM 710 confocal microscope (Zeiss).

10. Close the slide with mounting solution and coverslip.
11. Dry the slide in the dark and seal the coverslip with nail polish and examine by fluorescence microscopy (**Figure. 5.6**).

5. 5 Notes

1. Put glass dishes on a hotplate stirrer. Cut black wax into small chunks and place into the glass dishes. Increase temperature of hotplate stirrer until the black wax starts melting. Once the black wax melts and spreads evenly, leave the glass dishes at room temperature to solidify. Be careful since the plates are very hot. Prepare dissecting dishes in fume hood as black wax produces an unpleasant odor when melted (see **Figure. 5.1**).
2. All 10x stock enzymes are sterilely reconstituted in 1x HBSS and aliquots are stored at −20 °C. Carefully check the original units of each enzyme from the company website.
3. All plastic tubes should be made of polypropylene to prevent the scarce number of aortic lymphocytes from adhering to the plasticware.
4. Always prepare and use fresh 0.25% Triton X-100. Prepare the solution at least 1 h earlier since it takes time to dissolve Triton X-100 in PBS. Triton X-100 is viscous. Slowly release pipette plunger to allow the pipette tip to fill up with the correct volume. Discharge Triton X-100 and the pipette tip in PBS to recover full amount of Triton X-100.
5. Always prepare and use fresh 0.3% H2O2.
6. Gently heat Oil Red O mixed propylene glycol in boiled water. Avoid overheating above 110 °C, which causes high background staining of Oil Red O. Filter the Oil Red O solution with 25μm filter paper and store in the dark at room temperature.
7. Filter the Oil Red O solution with 25μm filter paper right before use.
8. Fixation and permeabilization buffers should be diluted according to the manufacturer's instructions.
9. Fixed cells become slippery and pellets may seem less condensed even after centrifugation. Please make sure not to flick the 96-well plate more than once after centrifugation. If insufficient force was applied, please re-centrifuge the plate and flick again to minimize cell loss. If cell loss is still a concern, centrifuge the plate for 4–5

min at 800x**g**. Aspiration of supernatant on a 96-well plate has a high risk of touching cell pellets, and is not recommended.

10. Buffers of the TSA kit should be prepared according to the manufacturer's instructtions.
11. If the aorta still has high background fluorescent staining in TSA protocol, wash in PBS for longer until background decreases. Thus, it is critical to examine background fluorescence under a fluorescent microscope or confocal microscope before mounting.
12. Line-a and Line-b should be parallel, so that the three aortic valves can be visualizeed on the same cross section as Line-c.
13. During incubation, leave the cap loosely attached to the tube to allow gas exchange.
14. 1% BSA containing PBS can replace FACS Buffer.

5. 6 Author Contributions

Tae Jin Yun, Junseong Lee, Jae-Hoon Choi, and Cheolho Cheong designed the experiments, interpreted data, and wrote the manuscript.

Tae Jin Yun and **Junseong Lee** executed the majority of experiments presented.

5. 7 Acknowledgements

This work was supported by grants from National Research Foundation of Korea (GRN-2013S1A2A2035348) (JHC and CC) and Canadian Institutes of Health Research (CIHR, MOP-125933 and HIG-133050) (CC). CC holds a Chercheur-Boursier Junior of Fonds de recherche du Québec-Santé (FRQS)—Société québécoise d'hypertension artérielle (SQHA) and CIHR New Investigator Salary Award.

5. 8 References

1. Steinman, R.M. Decisions about dendritic cells: past, present, and future. *Annu Rev Immunol* **30**, 1-22 (2012).

2. Choi, J.H. *et al.* Identification of antigen-presenting dendritic cells in mouse aorta and cardiac valves. *J Exp Med* **206**, 497-505 (2009).

3. Choi, J.H. *et al.* Flt3 signaling-dependent dendritic cells protect against atherosclerosis. *Immunity* **35**, 819-831 (2011).

4. Paulson, K.E. *et al.* Resident intimal dendritic cells accumulate lipid and contribute to the initiation of atherosclerosis. *Circ Res* **106**, 383-390 (2010).

5. Gautier, E.L. *et al.* Conventional dendritic cells at the crossroads between immunity and cholesterol homeostasis in atherosclerosis. *Circulation* **119**, 2367-2375 (2009).

6. Buono, C. *et al.* B7-1/B7-2 costimulation regulates plaque antigen-specific T-cell responses and atherogenesis in low-density lipoprotein receptor-deficient mice. *Circulation* **109**, 2009-2015 (2004).

7. Sun, J. *et al.* Deficiency of antigen-presenting cell invariant chain reduces atherosclerosis in mice. *Circulation* **122**, 808-820 (2010).

8. Subramanian, M., Thorp, E., Hansson, G.K. & Tabas, I. Treg-mediated suppression of atherosclerosis requires MYD88 signaling in DCs. *J Clin Invest* **123**, 179-188 (2013).

9. Weber, C. *et al.* CCL17-expressing dendritic cells drive atherosclerosis by restraining regulatory T cell homeostasis in mice. *J Clin Invest* **121**, 2898-2910 (2011).

10. Ait-Oufella, H. *et al.* Natural regulatory T cells control the development of atherosclerosis in mice. *Nat Med* **12**, 178-180 (2006).

11. Ishibashi, S. *et al.* Hypercholesterolemia in low density lipoprotein receptor knockout mice and its reversal by adenovirus-mediated gene delivery. *J Clin Invest* **92**, 883-893 (1993).

12. Zhang, S.H., Reddick, R.L., Piedrahita, J.A. & Maeda, N. Spontaneous hypercholesterolemia and arterial lesions in mice lacking apolipoprotein E. *Science* **258**, 468-471 (1992).

13. Butcher, M.J., Herre, M., Ley, K. & Galkina, E. Flow cytometry analysis of immune cells within murine aortas. *J Vis Exp* (2011).

14. Gautier, E.L. *et al.* Gene-expression profiles and transcriptional regulatory pathways that underlie the identity and diversity of mouse tissue macrophages. *Nat Immunol* **13**, 1118-1128 (2012).

15. Jakubzick, C. *et al.* Minimal differentiation of classical monocytes as they survey steady-state tissues and transport antigen to lymph nodes. *Immunity* **39**, 599-610 (2013).

16. Cheong, C. & Choi, J.H. Dendritic cells and regulatory T cells in atherosclerosis. *Mol Cells* **34**, 341-347 (2012).

17. Paigen, B., Morrow, A., Holmes, P.A., Mitchell, D. & Williams, R.A. Quantitative assessment of atherosclerotic lesions in mice. *Atherosclerosis* **68**, 231-240 (1987).

CHAPTER 6
(APPENDIX II)

6 Indoleamine 2,3-Dioxygenase-Expressing Aortic Plasmacytoid Dendritic Cells Protect against Atherosclerosis by Induction of Regulatory T Cells

Tae Jin Yun,[1,2] Jun Seong Lee,[1,3] Kawthar Machmach,[1,3] Dahee Shim,[4] Junhee Choi,[4] Young Jin Wi,[4] Hyung Seok Jang,[4] In-Hyuk Jung,[5] Kyeongdae Kim,[4] Won Kee Yoon,[6] Mohammad Alam Miah,[1,3] Bin Li,[1,7] Jinsam Chang,[1,7] Mariana G. Bego,[8] Tram N.Q. Pham,[8] Jakob Loschko,[9] Jörg Hermann Fritz,[10] Anne B. Krug,[9] Seung-Pyo Lee,[11] Tibor Keler,[12] Jean V. Guimond,[13] Elie Haddad,[3,14] Eric A. Cohen,[3,8] Martin G. Sirois,[15,16] Ismail El-Hamamsy,[17] Marco Colonna,[18] Goo Taeg Oh,[5,*] Jae-Hoon Choi,[4,*] and Cheolho Cheong[1,2,3,*]

[1]Laboratory of Cellular Physiology and Immunology, Institut de Recherches Cliniques de Montréal, Montréal, QC H2W 1R7, Canada

[2]Division of Experimental Medicine, Department of Medicine, McGill University, Montréal, QC H3A 1A3, Canada

[3]Department of Microbiology, Infectiology, and Immunology, Université de Montréal, Montréal, QC H3C 3J7, Canada

[4]Department of Life Science, College of Natural Sciences, Research Institute for Natural Sciences, Hanyang University, Seoul 133-791, South Korea

[5]Department of Life Sciences, Ewha Womans University, Seoul 120-750, South Korea

[6]Laboratory Animal Resource Center, KRIBB, Chungbuk 363-883, South Korea

[7]Department of Molecular Biology, Université de Montréal, Montréal, QC H3C 3J7, Canada

[8]Laboratory of Human Retrovirology, Institut de Recherches Cliniques de Montréal, Montréal, QC H2W 1R7, Canada

[9]Institute for Immunology, Ludwig-Maximilians-Universität München, München 80336, Germany

[10]Department of Microbiology and Immunology, McGill University, Montréal, QC H3A 2B4, Canada

[11]Cardiovascular Center, and Department of Internal Medicine, Seoul National University Hospital, Seoul 110-744, South Korea
[12]Celldex Therapeutics, Hampton, NJ 08827, USA
[13]Centre de Santéet de Services Sociaux Jeanne-Mance, Montréal, QC H2H 2B4, Canada
[14]CHU Sainte-Justine Research Center, Montréal, QC H3T 1C5, Canada
[15]Research Center, Montréal Heart Institute, Montréal, QC H1T 1C8, Canada
[16]Department of Pharmacology, Université de Montréal, Montréal, QC H3C 3J7, Canada
[17]Department of Cardiac Surgery, Montréal Heart Institute, Montréal, QC H1T 1C8, Canada
[18]Department of Pathology and Immunology, Washington University School of Medicine, St. Louis, MO 63110, USA

*Correspondence:

gootaeg@ewha.ac.kr (G.T.O.)
jchoi75@hanyang.ac.kr (J.-H.C.)
cheolho.cheong@ircm.qc.ca (C.C.)

Cell Metabolism. (2016). 23(5):852-866

6. 1 Abstract

Plasmacytoid dendritic cells (pDCs) are unique bone marrow-derived cells that produce large amounts of type I interferon in response to microbial stimulation. Furthermore, pDCs also promote T cell tolerance in sterile-inflammation conditions. However, the immune-modulatory role of aortic pDCs in atherosclerosis has been poorly understood. Here, we identified functional mouse and human pDCs in the aortic intima and showed that selective, inducible pDC depletion in mice exacerbates atherosclerosis. Aortic pDCs expressed CCR9 and indoleamine 2,3-dioxygenase 1 (IDO-1), an enzyme involved in driving the generation of regulatory T cells (Tregs). As a consequence, loss of pDCs resulted in decreased numbers of Tregs and reduced IL-10 levels in the aorta. Moreover, antigen presentation by pDCs expanded antigen-specific Tregs in the atherosclerotic aorta. Notably, Tregs ablation affected pDC homeostasis in diseased aorta. Accordingly, pDCs in human atherosclerotic aortas colocalized with Tregs. Collectively, we identified a mechanism of atheroprotection mediated by tolerogenic aortic pDCs.

6. 1. 1 Highlights

- Mouse and human aorta contain type I interferon-producing pDCs
- Selective depletion of aortic pDCs with BDCA2-DTR mice aggravates atherosclerosis
- pDCs and Tregs are concomitantly induced and colocalized in atherosclerotic intima
- Local induction of Tregs by aortic IDO-1^{+} pDCs prevents atherosclerosis

6. 2 Introduction

Dendritic cells (DCs) are the principal cell type responsible for bridging innate and adaptive immunity and are central for the initiation of antigen-specific immunity and tolerance.[1] DCs have been shown to reside in both lymphoid and non-lymphoid tissues.[2] Recent studies on DC development and differentiation have defined subsets of DCs not only in lymphoid tissues but also in non-lymphoid tissues, including the aorta.[3] The presence of DCs in the blood vessels of mice and humans suggests that these cells may be involved in atherosclerosis, a representative chronic vascular inflammatory disease.[2, 4] Interestingly, in healthy mice, DCs are mainly found in aortic roots, the lesser curvature of the aortic arch, and openings of arterial branches, regions with hemodynamic disturbance that promotes atherosclerosis in humans and experimental animals[3] and that are also involved in lipid uptake and systemic lipid metabolism.[2]

Plasmacytoid DCs (pDCs), although a rare bone-marrow (BM)-derived DC subset, serve an essential function by producing copious amounts of type I interferons (IFNs) upon microbial stimulation.[5] Consequently, the potential function of pDCs in both innate and adaptive immune responses to most viruses has been the subject of intensive investigation.

pDCs are also reported to have a role in peripheral and central tolerance, e.g., tolerance to vascularized cardiac allografts[6], tolerance against graft-versus-host disease[7], and chemokine (C-C motif) receptor 9 (CCR9)-dependent central tolerance.[8] These tolerogenic properties of pDCs are mostly associated with the induction of regulatory T cells (Tregs).[9] Importantly, systemic deletion of Tregs by anti-CD25 antibody (Ab) or selective depletion of Tregs by transgenic mice expressing diphtheria toxin receptor (DTR) under the control of Treg-specific *Foxp3* promoter aggravated atherosclerosis.[10, 11]

Several reports have begun to provide evidence, albeit conflicting, for pDCs' role in mouse models of atherosclerosis.[12, 13, 14, 15] Although these previous studies are informative, they did not assess many classical functional features of pDCs in the aorta, including involvement in hematopoietic development, production of type I IFNs, localization in athero-prone areas of healthy and diseased aorta, and expression of known cell-surface markers specific for pDCs. Therefore, the identification of authentic pDCs in mouse and human aortas

and the establishment of their contribution to the initiation, progression, or regression of atherosclerosis remain unmet challenges.

Addressing these gaps in our knowledge requires new approaches for identifying pDCs and assessing their role in atherosclerosis. To this end, we first sought to identify cells expressing pDC markers in healthy and atherosclerotic aortas of mouse and human. Here, we show that these aortic cells are bona fide pDCs with the capacity to produce IFN-α. They also reside mainly in athero-prone areas of the healthy aorta but are distributed throughout lesions that develop in diseased aortas. Of note, aortic pDCs expressed indoleamine 2,3-dioxygenase (IDO-1), an enzyme critical to induce Tregs and *Ido1* deficiency in athero-prone *Ldlr*$^{-/-}$ mice had significantly decreased aortic Tregs. In line with this, when pDCs are selectively removed, mice developed more severe atherosclerosis, concomitant with a decrease in aortic Tregs. Finally, we also identified authentic tolerogenic pDCs in human atherosclerotic aortas and established their colocalization with Tregs.

6. 3 Results

6. 3. 1 Identification of pDCs in Normal Mouse Aorta

Despite constituting a very low proportion of splenocytes (<0.4%; **Figure S1A**), pDCs are central to mounting innate immune responses against most viruses through their production of type I IFNs. We had previously sought to identify pDCs as $CD11c^{+}B220^{+}CD19^{-}$ cells in the normal aorta but found that these cells were very scarce.[4] To overcome this and better identify pDCs, we further optimized our multicolor flow cytometry procedure and applied it to cell suspensions obtained from at least 10–15 pooled healthy mouse aortas, including the aortic root (with valves), ascending aorta, aortic arch, and descending aorta (**Figure 6.1A**). $CD45^{+}$ leukocytes were first separated from macrophages (MΦs, $CD11b^{+}CD64^{+}$), which are a major source of autofluorescence among aortic $CD45^{+}$ cells (**Figure S1B**), and these cells were further separated from DCs ($CD11c^{+}MHCII^{+}$), monocytes ($CD11b^{hi}Ly6C^{hi}$), granulocytes ($CD11b^{+}Ly6C^{int}Ly6G^{+}$), T cells ($CD3^{+}$), B cells ($CD19^{+}$), and natural killer (NK) cells ($CD49b^{+}$).[16, 17] After all of these non-pDC populations had been removed, the remaining cells (~0.05% of total $CD45^{+}$ cells) were found to represent a distinct population of cells bearing a pDC phenotype (**Figure 6.1A**). Similar to splenic pDCs, these aortic pDCs expressed high levels of plasmacytoid dendritic cell antigen-1 (PDCA-1)/BST2/CD317, lymphocyte antigen 6 complex (Ly6C), FMS-related tyrosine kinase 3 (Flt3)/CD135, B220/CD45R, Siglec-H (**Figure S1C**), and Clec9a, compared with aortic B cells (**Figure 6.1B**), but lesser amounts of other leukocyte markers specific for granulocytes, B cells, T cells, and NK cells (**Figure 6.1C**). In addition, pDCs did not express monocyte or MΦ-specific markers, such as CD11b, CX3CR1, F4/80, CD115/MCSF-R, CD14, CD64, CD206, and MerTK (**Figures 6.1D and 6.1E**). Notably, these pDCs also lacked expression of the DC-specific markers, such as Zbtb46, XCR1, and CD103, and expressed low levels of CD11c and major histocompatibility complex class II (MHC II), compared with DCs (**Figure 6.1F**).[4, 18]

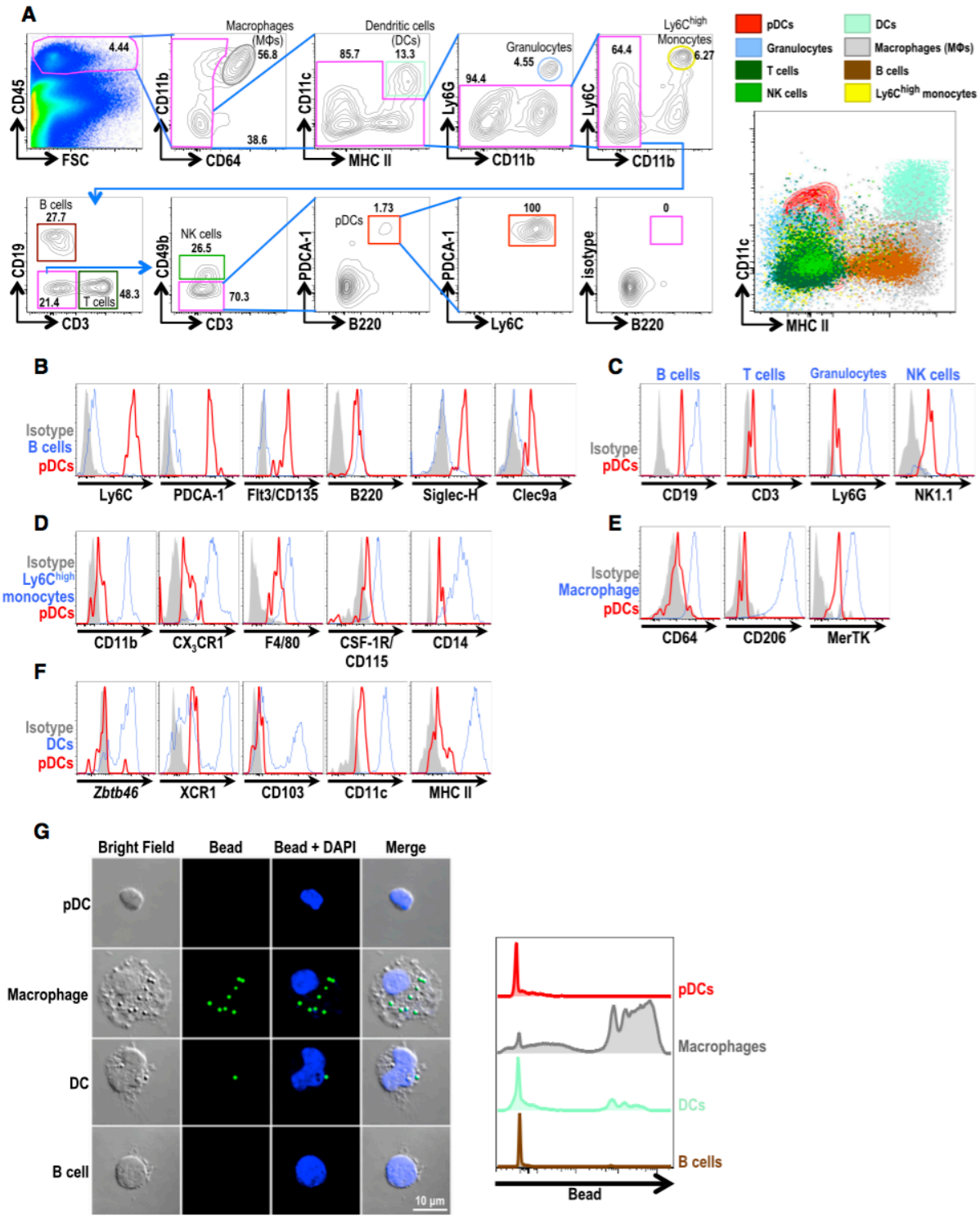

Figure 6.1. Identification of pDCs under Steady State in Mouse Aortas. (A) Gating strategy used in this study. SSC^{low} and FSC^{low} dead cells and doublet cells were gated out. The subpopulations of aortic leukocytes are visualized on the dot blot (right) according to the

expression of CD11c and MHCII. A representative FACS plot of 10–15 pooled aortas of C57BL/6 (WT). **(B–F)** Aortic pDCs (red lines) were analyzed for surface markers and compared with other aortic cell populations (blue lines) and isotypes (gray filled lines). Expression of specific markers for pDCs **(B)**; B, T, and NK cells and granouocytes **(C)**; Ly6C^{high} monocytes **(D)**; MΦs **(E)**; and DCs **(F)**. All markers were surface stained except CD206 and Clec9a (ICS); *Zbtb46* (*Zbtb46*$^{+/+}$ [WT] and *Zbtb46*$^{gfp/+}$) and *Cx₃cr1* (*Cx₃cr1*$^{+/+}$ [WT] and *Cx₃cr1*$^{gfp/+}$) reporter mice were used for evaluating the expression of these molecules in aortic pDCs. Representative marker histograms from at least three experiments are shown, and each histogram is from six to ten pooled WT aortas. **(G)** Morphology and phagocytic activity of aortic pDCs. Aortic cells from 40 pooled WT aortas were incubated with 1 μm beads (green) and stained with markers as in **(A)**. Cells were sorted out, cytospined to assess morphology (left), and counterstained for DAPI (blue), and phagocytic activity was assessed by FACS (right).

To further distinguish pDCs from other immune cells by functional criteria, we bathed aortic cell suspensions in serum-containing RPMI medium with 1 mm fluorescent yellow green (YG) microspheres for 1 hr to test whether pDCs had the phagocytic activity of MΦs. pDCs, DCs, and B cells were poorly phagocytic (took up zero to one bead), whereas MΦs were highly phagocytic (took up more than three to five beads) (**Figure 6.1G**). When sorted out, pDCs were round or spherical shapes separable from MΦs and the dendritic morphology of DCs.

6. 3. 2 Flt3L Treatment Increases pDC Numbers in the Aorta

Given the higher expression of Flt3/CD135 in aortic pDCs (**Figure 6.1B**), we next asked whether Flt3 ligand (Flt3L), a cytokine crucial for DC development, could expand this population. We previously reported that Flt3L treatment selectively increased CD11c^{+}MHCII^{+} DCs.[4] Similarly, Flt3L treatment increased DCs and pDCs in the spleen (**Figures S2A and S2B**). In these mice, the absolute number and percentage of aortic pDCs were increased (**Figure 6.2A**). However, MΦs, which are dependent on CD115, did not show any significant expansion (**Figure 6.2A, bottom**). To rule out nonspecific effects, we next tested Flt3L on *Flt3*$^{-/-}$ mice. Whereas Flt3L treatment increased the number of aortic pDCs in wild-type (WT) mice, this effect was completely absent in *Flt3*$^{-/-}$ mice (**Figure 6.2B; Figure S2C**).

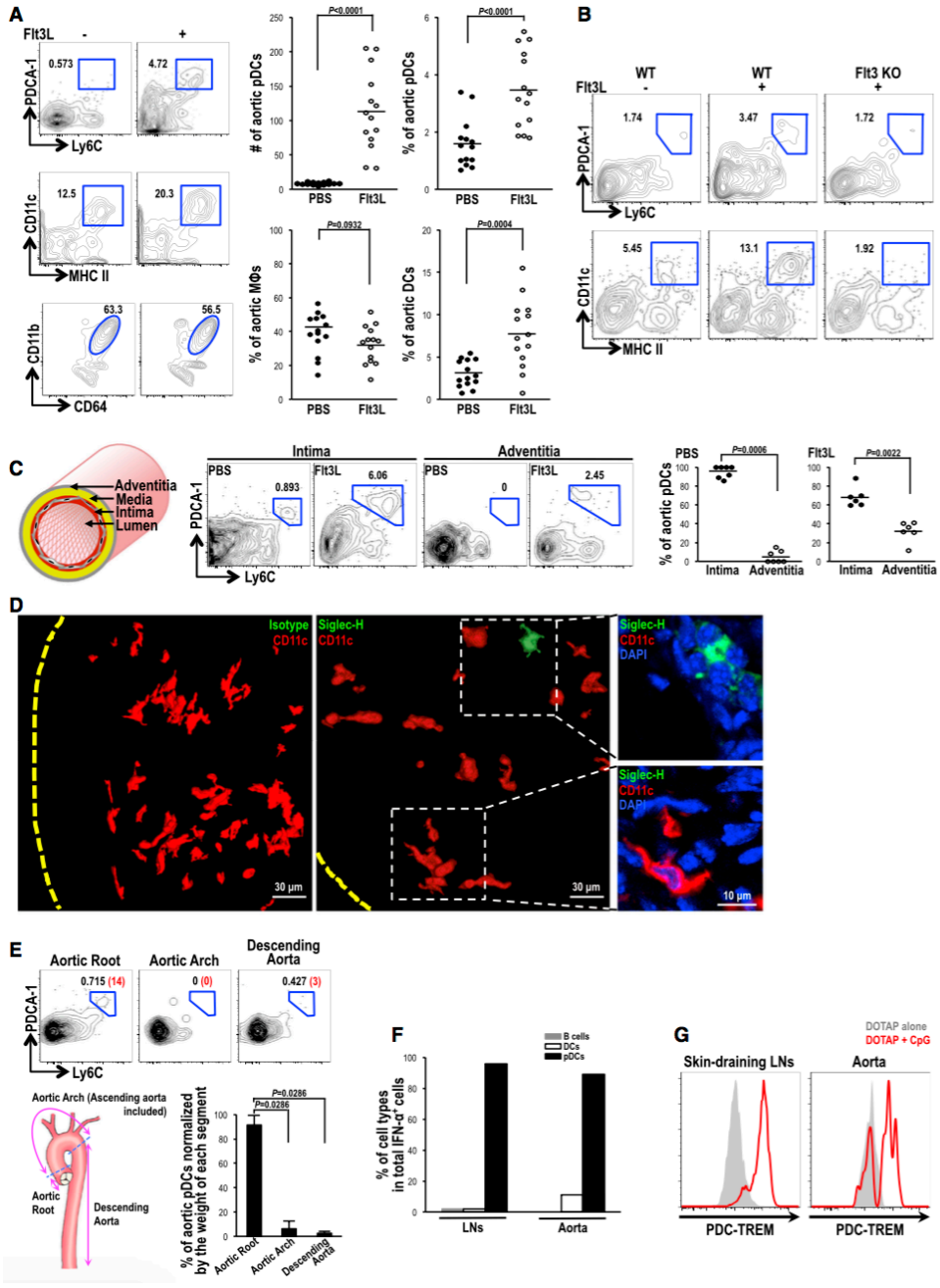

Figure 6.2. Flt3/Flt3L-Dependent Aortic pDCs Localize to Athero-prone Areas and Secrete Type I IFN upon TLR9 Ligation. (A–D) In (A)–(C), WT and *Flt3*$^{-/-}$ mice were injected with PBS or Flt3L. **(A)** Absolute numbers and percentages of aortic pDCs, DCs, and MΦs by FACS. Left: representative FACS plot of pDCs (top), DCs (middle), and MΦs (bottom). Right: absolute numbers of pDCs per aorta and percentages of pDCs, DCs, and MΦs per aortic CD45^{+} cells. Bars indicate mean; n=14. **(B)** Aortic pDCs and DCs from WT and *Flt3*$^{-/-}$ mice. Representative FACS plots from at least three experiments. **(C and D)** Localization and distribution of aortic pDCs. **(C)** Aortas from WT mice were surgically

separated into intima and adventitia. Representative FACS plots (middle) and quantitation (right). Each value is from five to seven pooled aortas (PBS) or two to three pooled aortas (Flt3L). Bar indicates mean. **(D)** *Z*-stacked en face IF with Siglec-H (pDC, green), CD11c (DC, red), and DAPI (nuclei, blue) in the aortic intima. Yellow dashed lines for borders of aortic valves. **(E)** Distribution of pDCs in each aortic segment from WT mice. Top: representative FACS plot of pDCs in each segment (percentages are in black; cell numbers are in red); Bottom: percentage of aortic pDCs normalized by the weight of each aortic segments. Graph indicates mean ± SD; n=10 mice per experiment; four experiments. **(F)** IFN-α^+ cells measured by incubating cells with media alone per BFA or with CpG per BFA. Total IFN-α^+ cells, defined as $CD45^+CD64^-$IFN-α^+ cells, were enumerated. Graph is representative of two independent experiments. **(G)** PDC-TREM expression in skin-draining LN pDCs and native aortic pDCs. Six to seven mice were injected i.v. with CpG or DOTAP alone, and LNs and aortas were harvested and pooled. Representative histogram of two independent experiments.

To further identify the anatomical location of pDCs in the aortic wall, we surgically separated adventitia from aorta. In the normal aorta, pDCs were not detected in the adventitia but were present in the intima (**Figure 6.2C**). Treatment with Flt3L slightly increased the number of pDCs in the adventitia, but most increases were restricted to the intima. To further confirm the anatomical location of pDCs, an en face preparation of the aorta was stained for immunofluorescence (IF) with the pDC marker Siglec-H and co-stained for CD11c. We had previously reported that DCs are enriched in the intimal space, based on staining with CD11c only (**Figure S2D**).[3, 4] Notably, Siglec-H^+ cells were only detected in the intima, and their morphology was spherical—clearly distinguishable from the dendritic morphology of DCs (**Figure 6.2D; Movie S1**). To further define the exact location of these cells, we separated aortas into aortic root, aortic arch including the ascending aorta, and descending aorta. This analysis revealed that most pDCs were localized in the sinus area of the normal aorta (**Figure 6.2E; Figure S2D**), an area known to be athero-prone.

6. 3. 3 Aortic pDCs Are Bona Fide pDCs that Secrete IFN-α

It is well established that pDCs secrete type I IFN upon Toll-like receptor (TLR)-7 or -9 ligation.[5] Previous studies had failed to measure IFN-α in the mouse aorta.[12, 13, 14, 15] Given the scarcity of pDCs, we reasoned that a method for obtaining more aortic pDCs was needed to successfully assay for secreted IFN-α. First, we expanded pDCs by treating them with Flt3L. Then, we compared the capacity of splenocytes, which typically contain ~0.4% pDCs in

WT mice (**Figure S1A**), with single-cell suspensions prepared from hearts and aortas of ten WT mice, treated with Flt3L. Notably, cells obtained from hearts and aortas secreted detectable IFN-α when challenged with TLR9 agonist, synthetic oligodinucleotides containing CpG motifs (CpG ODNs, hereinafter termed CpG) (**Figures S2E and S2F**). To further identify the types of aortic cells that secreted IFN-α, we performed intracellular staining (ICS) for IFN-α and analyzed cells by fluorescence-activated cell sorting (FACS). Of the total aortic IFN-α^+ cell population, more than 80% were pDCs, similar to lymph node pDCs (**Figure 6.2F**). Within each cell type (aortic pDCs and LNs pDCs), 5%~7% of cells produced IFN-α^+ (**Figure S2G**). To further confirm these in vitro results, we next questioned whether aortic pDCs upregulate the expression of PDC-TREM, a pDC-specific receptor responsible for increased production of type I IFNs.[19] When CpG was injected intravenously (i.v.) for 9–12 hr, LNs pDCs did preferentially upregulate PDC-TREM (**Figure 6.2G**). Of note, we observed inducible expression of PDC-TREM in native aortic pDCs (**Figure 6.2G**). Therefore, pDCs identified in the normal mouse aorta are functional pDCs with a morphology clearly distinguishable from that of other DCs and possess the unique capacity to produce IFN-α in vivo.

6. 3. 4 pDCs Are Present in Human and Humanized Mouse Aortas

Our ability to analyze human aortas was constrained by the paucity of pDCs as well as the limited availability of human tissues. Therefore, we next assessed whether human pDCs could be identified in the steady-state mouse aorta reconstituted with human stem cells (HSCs). To this end, we used humanized mice (hu-mice) whose BM is reconstituted from purified human cord blood HSCs. pDCs in these mice can be easily detected in peripheral blood as cells that are negative for monocyte/MΦ markers (CD14, CD64, and CD16) and the B cell marker CD19 but positive for HLA-DR, CD123, and blood dendritic cell antigen 2 (BDCA2) (**Figure 6.3A**).[5, 20] pDCs were detectable in aortas isolated from these mice and were further increased in number by Flt3L treatment (**Figure 6.3B; Figure S3A**). To test systemic IFN-α secretion in hu-mice, we injected CpG i.v. and measured serum IFN-α levels over a 12-hr period. Functional human IFN-α was detected in the blood of hu-mice as early as 4 hr after CpG ligation (**Figure 6.3C**).

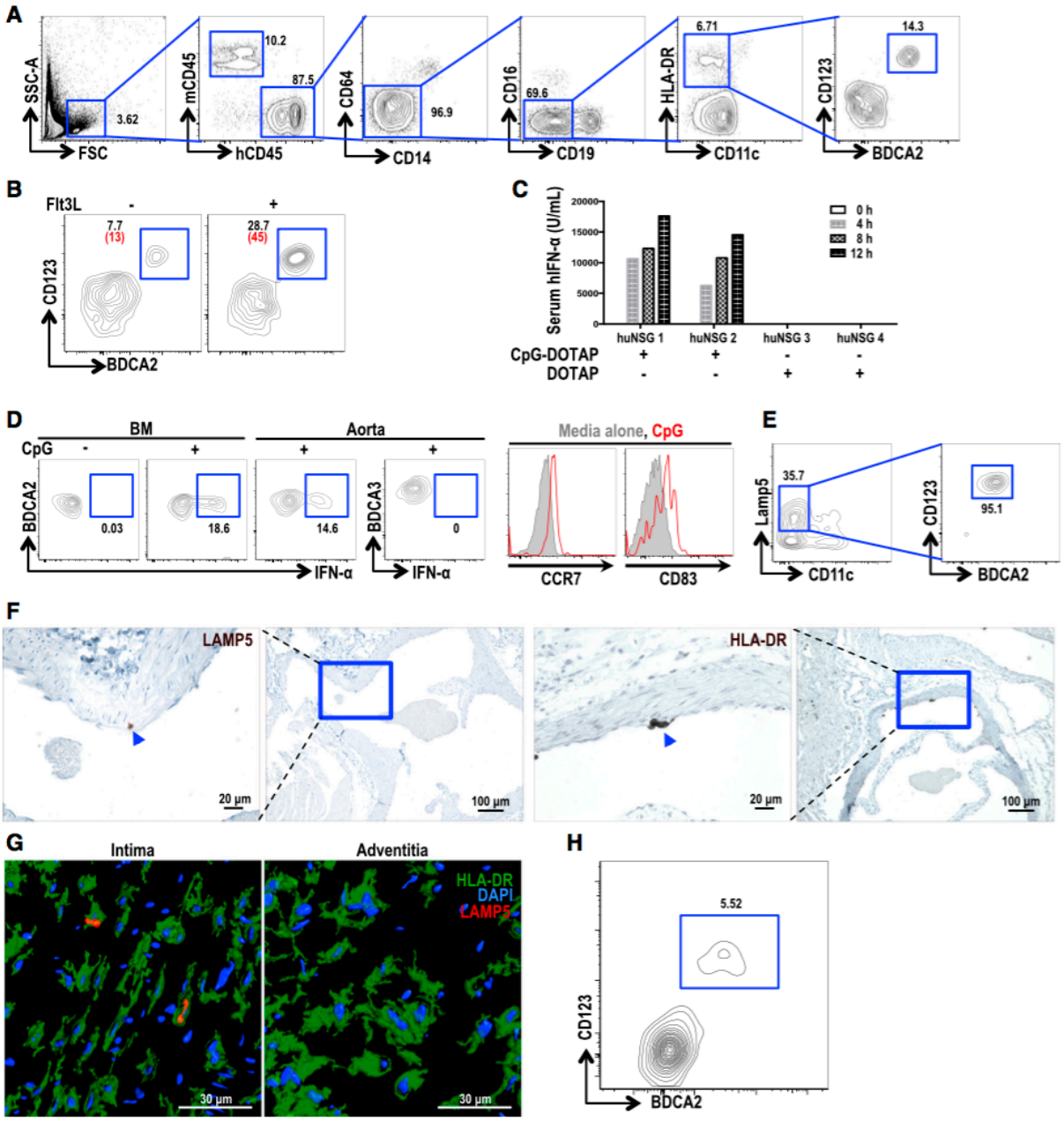

Figure 6.3. Identification and Localization of Human Aortic pDCs in hu-Mice and Human Patient. (A–G) Hu-mice were injected with Flt3L. **(A)** Gating strategy for blood pDCs. **(B)** Representative FACS plots of aortic pDCs with or without Flt3L treatment (percentages are in black; cell numbers are in red). **(C)** Secretion of functional IFN-α. Hu-mice were injected i.v. with CpG or DOTAP alone. Serum was collected at 0, 4, 8, and 12 hr after injection. **(D)** Expression of IFN-α (ICS), CCR7, and CD83 in aortic pDCs from hu-mice (six pooled). Cells were incubated with media alone/BFA or with CpG/BFA. $BDCA2^{+}$ aortic pDCs and $BDCA3^{+}$ aortic DCs were from the same sample. **(E)** BM cells were immunostained with the indicated Abs. **(F)** Paraffin-embedded sections of aorta. IHC for LAMP5 and HLA-

DR (brown) and counterstained with hematoxylin. Arrowheads indicate LAMP5$^+$ (left) and HLA-DR$^+$ (right) cells. **(G)** *Z*-stacked confocal microscopy images of Flt3L-injected hu-mouse aortas, stained for LAMP5 (red), HLA-DR (green), and DAPI (blue). **(H)** CD123$^+$BDCA2$^+$ aortic cells from a human patient. Cells were gated from the CD45$^+$ lineage (CD14, CD19, CD56)$^-$ HLA-DR$^+$ population.

We next asked whether pDCs in the hu-mice aorta could produce functional IFN-α. To this end, we incubated aortic cell suspensions from hu-mice with CpG (10 mg/mL) for 9 hr. For the last 6 hr, Brefeldin A (BFA) was added to block secretion of IFN-α. Notably, pDCs produced IFN-α and also showed upregulated surface expression of CCR7 and CD83 upon TLR9 ligation, whereas other BDCA3$^+$ DCs in the same culture well did not (**Figure 6.3D**). These results suggest that pDCs in the hu-mice aorta are authentic pDCs with the capacity to produce copious amounts of IFN-α (**Figure 6.3D**). pDCs were also detected in the aortas of hu-BLT mice, another hu-mice model transplanted with HSCs isolated from fetal liver, and donor-matched thymus (**Figure S3B**). To localize these pDCs in the hu-mice aorta, we needed an additional reliable, single marker to stain tissue samples. To this end, we chose lysosome-associated membrane protein 5 (LAMP5), a newly discovered marker for pDCs.[21] We found that LAMP5 expression was restricted to human pDCs (**Figure S3C**).[22] Moreover, LAMP5 staining was sufficient to mark CD123$^+$BDCA2$^+$BDCA4$^+$ pDCs in human peripheral blood (**Figure S3D**); this was further confirmed using pDCs from hu-mice BM (**Figure 6.3E; Figure S3E**). Using an anti-LAMP5 Ab, we found that pDCs were localized in the aortic root (sinus) of hu-mice (**Figure 6.3F, left**), where numerous HLA-DR$^+$ cells were also found (**Figure 6.3F, right**). Notably, pDCs were only detected in the intimal space of the normal hu-mice aorta (**Figure 6.3G**). These pDCs were also easily detected in non-atherosclerotic human aortas (**Figure 6.3H; Figure S3F**).

6. 3. 5 pDCs Specifically Expand in the Intimal Layer of Atherosclerotic Aorta in Mice

It was previously reported that aging increases the accumulation of intimal DCs (**Figure S4A**).[23] However, we found no correlation between pDC number and mouse age (**Figure 6.4A**). We and others have observed that Western-type diet (WD)-induced

atherosclerosis increases the number of DCs in the aorta.[4, 23] Indeed, the total number of DCs increased in WD-fed *Ldlr*$^{-/-}$ mice (**Figure 6.4B, bottom**). Notably, we observed an increase in pDCs in the aortas of these mice, but not in other organs such as the spleens, para-aortic LNs, and mediastinal LNs (**Figures 6.4B and 6.4C; Figure S4B**). Importantly, similar to the distribution of DCs, pDCs were mostly enriched in the intimal layer where atherosclerosis develops (**Figure 6.4D; Figures S4C–S4E**), and their distribution was further expanded into the descending aorta region, where lesions develop in the later stage of atherosclerosis (**Figure 6.4E**). When tested for type I IFN response by TLR9 ligation, these aortic pDCs in atherosclerotic lesions were functional in terms of PDC-TREM upregulation (**Figure 6.4F**). To further confirm type I IFN production, we sorted cells from atherosclerotic aorta for qPCR, and only aortic pDCs expressed IFN-β1 at single-cell level (**Figure 6.4G**).

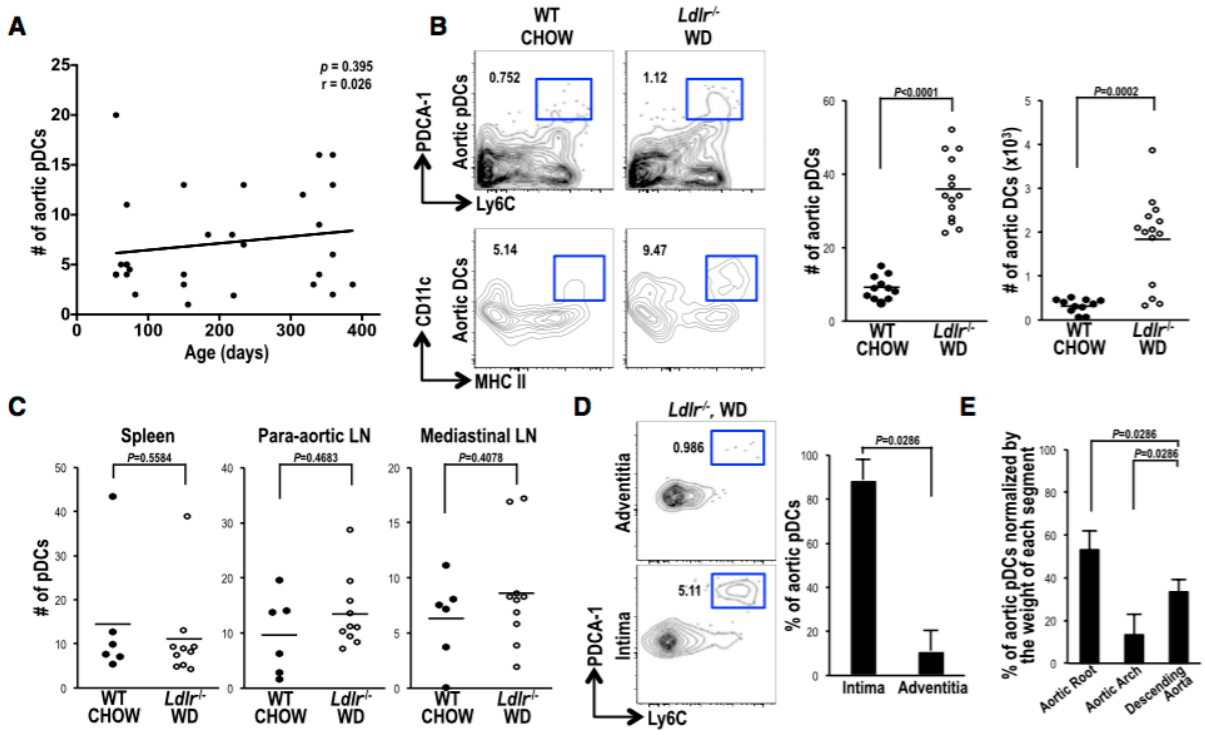

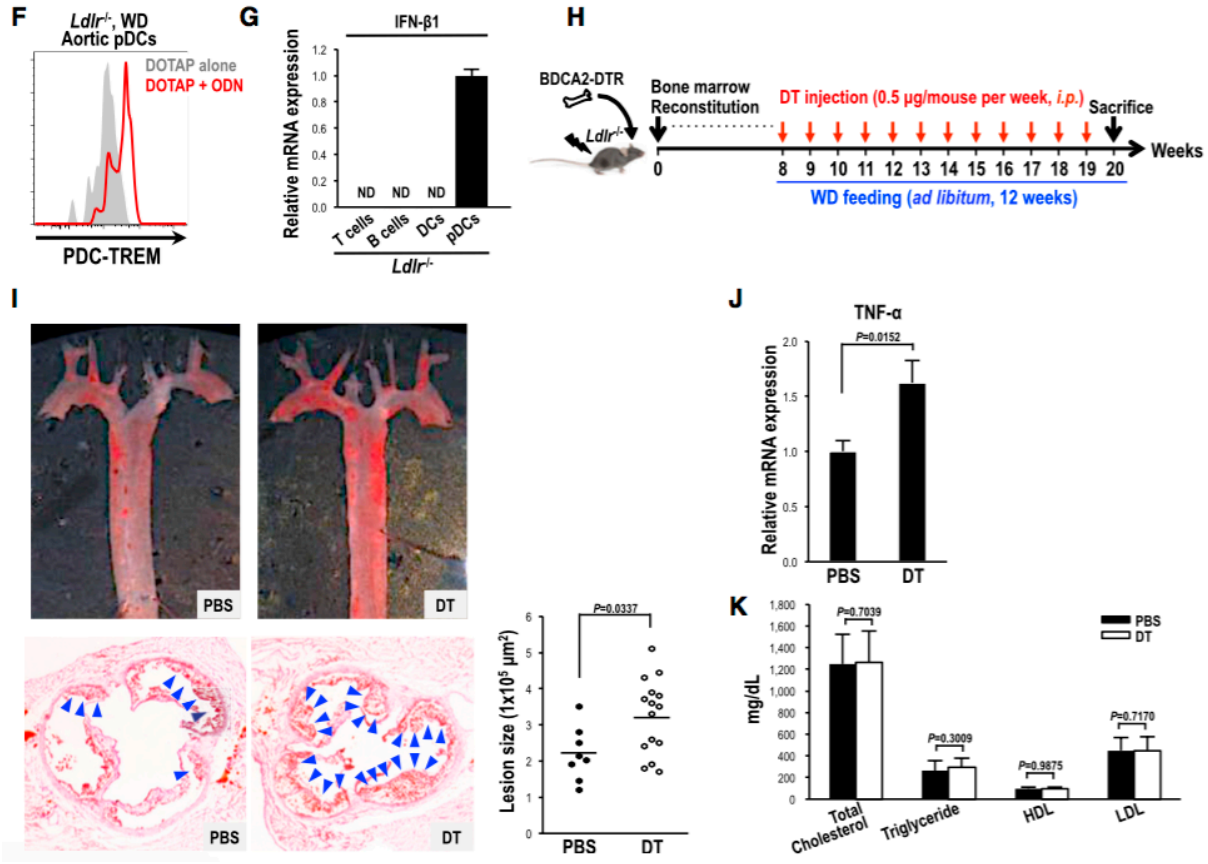

Figure 6.4. pDCs Expand Exclusively in the Atherosclerotic Aorta and Protect against Atherosclerosis. (A) Absolute numbers of pDCs in WT mice at different ages quantified by FACS. n=27. **(B)** Absolute numbers of pDCs and DCs from WT mice fed a normal diet (CHOW) and *Ldlr*$^{-/-}$ mice fed WD for 10 weeks. Left: representative FACS plots of aortic pDCs and DCs (numbers in the plot are percentages); Right: absolute numbers of pDCs and DCs per aorta (bars indicate mean; n ≥ 11). **(C)** Absolute numbers of pDCs/1 × 10^4 CD45$^+$ cells from indicated organs from the mice in (B). Bar indicates mean; n ≥ 6. **(D and E)** FACS analysis of aortic pDC localization and distribution in *Ldlr*$^{-/-}$ mice fed WD for 12 weeks. Bars indicate mean ± SD. **(D)** Aortic pDCs in intima and adventitia. Left: representative plots. Right: percentage of pDCs in each layer of the aorta. n=4. **(E)** Distribution of pDCs in each aortic segments. Percentage of pDCs normalized by the weight of each segment. n=4. **(F)** PDC-TREM expression in pDCs. *Ldlr*$^{-/-}$ mice fed WD for 6 months were injected i.v. with CpG or DOTAP alone. **(G)** Relative mRNA expression of IFN-β1 in FACS-sorted aortic immune cells from WD-fed *Ldlr*$^{-/-}$ mice (9 weeks). Data were normalized to TATA box-binding protein (TBP). Bar indicates mean ± SD. Representative of two independent experiments. **(H–K)** Lethally irradiated *Ldlr*$^{-/-}$ mice were reconstituted with BM from BDCA2-DTR mice. **(H)** After 8 weeks, reconstituted *Ldlr*$^{-/-}$ mice were fed WD and injected with PBS alone (n = 8) or with DT (n = 15) for 12 weeks. **(I)** Left: representative images of oil red O staining of atherosclerotic lesions in en face aorta (top), with atherosclerotic lesions in the sinus indicated by blue arrowheads (bottom). Bottom right: quantification of athero-

sclerotic lesion size. Bars indicate mean. **(J)** TNF-α mRNA expression levels in the aorta, measured by qPCR. Data were normalized to β-actin. Bars indicate mean ± SD; n=6. **(K)** Lipid profile in serum measured from the samples in (H). Bars indicate mean ± SD.

6. 3. 6 pDCs Depletion in Ldlr$^{-/-}$ Mice Reconstituted with BDCA2-DTR BM Aggravates Atherosclerosis

To explore the role of pDCs in disease, we generated atherosclerotic mice lacking pDCs by reconstituting *Ldlr*$^{-/-}$ mice with BM from BDCA2-DTR mice. It was previously reported that pDCs can be inducibly and selectively depleted by injecting BDCA2-DTR mice with diphtheria toxin (DT).[20] These mice were fed WD for 12 weeks, with or without DT treatment, to deplete pDCs (**Figure 6.4H**). To understand the role of pDCs in the development of atherosclerosis, we measured lesion size in the aortic sinuses of these mice. The average lesion size in pDC-depleted mice was significantly increased by 47% (**Figure 6.4I**). In line with this, levels of the inflammatory cytokine tumor necrosis factor alpha (TNF-α) were increased in pDC-depleted mice aorta (**Figure 6.4J**), whereas there was no significant change in IFN-α levels (**Figure S4F**). We also found that lipid profiles were not significantly changed in these mice (**Figure 6.4K**). These results suggest that pDCs function to reduce inflammation and immunity but do not play a role in systemic lipid metabolism.

6. 3. 7 Treatment with a pDC-Targeting Ab Depletes MΦs

An Ab-mediated cell-ablation approach using pDC-depleting Abs was widely used to study in vivo function of pDCs.[24] In this regard, a monoclonal Ab against BST2 (bone marrow stromal cell antigen 2) had previously been used to investigate the role of pDCs in atherosclerosis.[12, 13, 14] However, none of these previous reports clearly demonstrated specific ablation of pDCs in the mouse aorta. Thus, given our demonstration of a specific increase in pDC numbers in athero-prone areas of the mouse aorta and the atheroprotective role of pDCs, we were interested in revisiting this previously applied approach. As expected, based on previous studies, treatment with anti-PDCA-1 resulted in specific depletion of pDCs in spleen and LNs, assessed by monitoring the pDC markers Siglec-H and Ly6C (**Figure 6.5A; Figure S5A**).

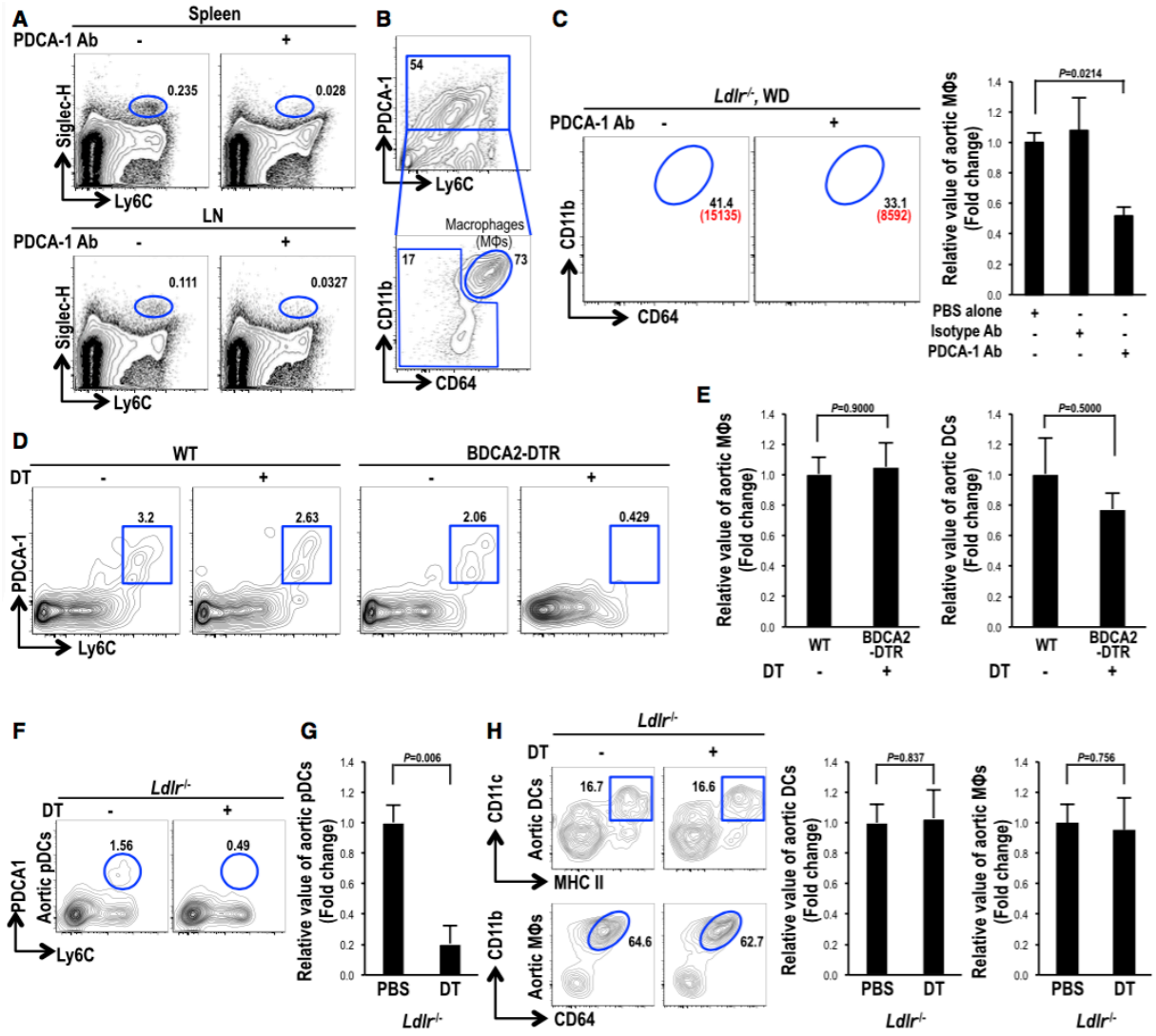

Figure 6.5. Selective and Inducible pDC Ablation in BDCA2-DTR Transgenic Mice Strain. (A–C) Ab-mediated depletion of pDCs. *Ldlr*$^{-/-}$ mice fed WD for 12–14 weeks were injected i.v. with PBS or 250 mg of PDCA-1 Ab or isotype control twice at 36-hr intervals. **(A)** Selective depletion of pDCs of spleen and skin-draining LNs. **(B)** CD45^{+} aortic cells were analyzed for indicated markers. **(C)** Aortic MΦs from the mice in (A). Left: representative FACS plot of aortic cells (percentages are in black; cell numbers are in red). Right: relative number of aortic MΦs normalized to the PBS group. Graph indicates mean ± SD; n ≥ 3. **(D)** Selective and inducible depletion of aortic pDCs in indicated mice. Cells were gated from the CD45^{+}CD64^{-}CD11b^{-}CD11c^{low} population. Mice were injected with PBS or with DT twice at 24-hr intervals. **(E)** Relative number of aortic MΦs (left) and DCs (right) from (D). Graph indicates mean ± SD; n=4. **(F–H)** Selective depletion of pDCs from *Ldlr*$^{-/-}$ mice reconstituted with BM cells of BDCA2-DTR mice. Reconstituted *Ldlr*$^{-/-}$ mice were fed WD for 12 weeks and injected with PBS or DT as described in **Figure 4H** (graph indicates mean ± SD; n ≥ 5). pDCs are indicated in **(F and G)**, and DCs and MΦs are indicated in **(H)**.

Surprisingly, validation of this depletion strategy, in conjunction with a FACS analysis, to cells prepared from atherosclerotic aortas revealed that more than 50% of cells in the atherosclerotic aorta were positive for PDCA-1 (**Figure S1B**). Most of these cells were found to be $CD11b^{+}CD64^{+}$ MΦs (**Figure 6.5B**). This finding is consistent with the fact that, although PDCA-1 is known to be restricted to pDCs under steady-state conditions, it is expressed promiscuously upon stimulation with type I IFN or IFN-γ.[25] Because the concentration of inflammatory cytokines is elevated in the atherosclerotic lesion, it is likely that PDCA-1 is expressed on multiple cell types. Therefore, we next questioned whether treatment with an anti-PDCA-1 Ab also affects the MΦs population. We found that PDCA-1 Ab treatment depleted more than 50% of MΦs (**Figure 6.5C**).

6. 3. 8 Selective Depletion of Aortic pDCs in Steady State and Atherosclerotic *Ldlr*$^{-/-}$ Mice Reconstituted with BDCA2-DTR BM

The off-target effects of the Ab-based depletion strategies, noted earlier, highlight the need for a more selective and inducible pDC-depletion model to precisely address the impact of pDCs in atherogenesis. Accordingly, we next sought to determine whether BDCA2-DTR mice could be used to ablate aortic pDCs. Treatment of these mice with DT specifically eliminated splenic and LN pDCs (**Figure S5B**), as reported. Importantly, this treatment also selectively eliminated aortic pDCs in steady state (**Figure 6.5D**), without significantly affecting MΦs or DCs (**Figure 6.5E**). To explore the specificity of the BDCA2-DTR strain in atherosclerosis, we generated atherosclerotic mice lacking pDCs by reconstituting *Ldlr*$^{-/-}$ mice with BM from BDCA2-DTR mice and fed WD as described in **Figure 6.4H**. DT treatment successfully depleted splenic and LNs pDCs in these mice (**Figure S5C**). Of note, aortic pDCs were selectively depleted (**Figures 6.5F and 6.5G**), not affecting MΦs and DCs (**Figure 6.5H**).

6. 3. 9 Spatio-temporal Correlation of Tregs and pDCs Expansion during Atherosclerosis

It has previously been shown that atherosclerosis is exacerbated in *Flt3*$^{-/-}$ mice, presumably because of a reduction in Treg frequency in these mice.[4] However, measuring Treg frequency in the mouse aorta is very demanding, and only a few papers have tried to demonstrate the presence of Tregs in this tissue.[26, 27] By further optimizing our method, which importantly includes the essential step of MΦ elimination (**Figure 6.6A; Figures S6A and S6B**), we were able to reliably and precisely quantify Tregs in the aorta. We found that Treg numbers were increased in the atherosclerotic mouse aorta (**Figure 6.6B**), but not in other tissues such as spleen and LNs (data not shown). These Tregs were mainly localized in the intimal area of the atherosclerotic aorta (**Figure 6.6C**). To further dissect the kinetics of Treg and pDC expansion, we measured the number of pDCs and Tregs during WD intake in *Ldlr*$^{-/-}$ mice (0, 4, 8, and 12 weeks). As we previously reported, DCs numbers rose according to disease development (data not shown). Notably, both pDCs and Treg numbers showed similar pattern of increase (**Figure 6.6D**). In steady state, Tregs were largely restricted to the sinus area of the aorta, a distribution similar to that of pDCs (**Figure 6.6E, left**). However, following WD, Tregs had expanded and were distributed throughout atherosclerotic aorta with similar distribution to that of pDCs (**Figure 6.6E, right**). This spatio-temporal correlation suggests a possible link between pDCs and Tregs in atherosclerosis. In line with this, pDCs were essential to mediate tolerance to vascularized allograft and acute graft-versus-host disease.[6, 7]

6. 3. 10 Aortic pDCs Express IDO-1 and Induce Antigen-Specific Tregs

Given the close relationship between Treg and pDC numbers during atherogenesis, we next investigated the tolerogenic capacity of aortic pDCs.[28] Of note, local expression of IDO-1, an enzyme critical for the induction of Tregs, was elevated in atherosclerotic aorta (**Figure 6.6**F). To identify IDO-1^{+} cells, we sorted out cells from atherosclerotic aorta for single- cell gene expression analysis. Importantly, we found a higher expression of IDO-1 in pDCs (**Figure 6.6G**). In line with this, aortic pDCs expressed CCR9 and IDO-1 (**Figure 6.6H**). To

further test that IDO-1 expression by pDCs causes local Treg generation in atherosclerotic aorta, we reconstituted *Ldlr*$^{-/-}$ mice with BMs from WT and *Ido1*$^{-/-}$ mice. We did not detect a statistically significant difference of Treg number in the spleen of either WT or *Ido1*$^{-/-}$ *mice*. However, atherosclerotic aortas from *Ido1*$^{-/-}$ mice possessed reduced Treg numbers compared with WT (40% reduction) (**Figure 6.6I**). In keeping with this, depletion of pDCs in atherosclerotic mice resulted in a reduction in Treg numbers only in affected aortas, not in lymphoid organs such as spleen and LNs (**Figure 6.6J**). In addition, the level of interleukin-10 (IL-10), a cytokine that is a hallmark of Tregs, was decreased in pDC-depleted aortas (**Figure 6.6K**). Previously, antigen presentation by pDCs was reported to promote proatherogenic T cell immunity.[13, 15] However, these conclusions were largely based on in vitro experimentations with splenic or BM-derived pDCs. To assess the antigen-specific T cell response in atherosclerotic aorta, we established *Ldlr*$^{-/-}$ mice reconstituted with OT-II transgenic mouse BM. To selectively deliver an antigen to pDCs, we genetically cloned and engineered anti-SiglecH Ab fused with ovalbumin (OVA) (**Figure S6C**). In these mice, we injected anti-SiglecH-OVA i.v. to target aortic pDCs. Of note, antigen presentation by aortic pDCs in an atherosclerotic environment induced OVA-specific Tregs (**Figure 6.6L**). Together, these results demonstrate a direct functional link between the presence of IDO-1^{+} pDCs and the regulation of Treg generation in atherosclerotic aorta.

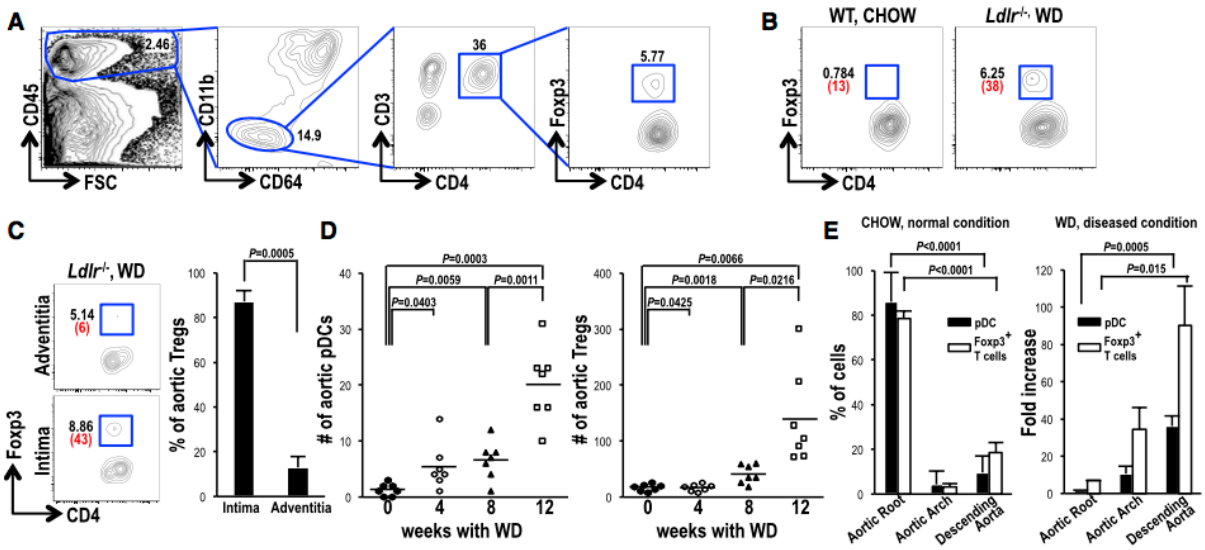

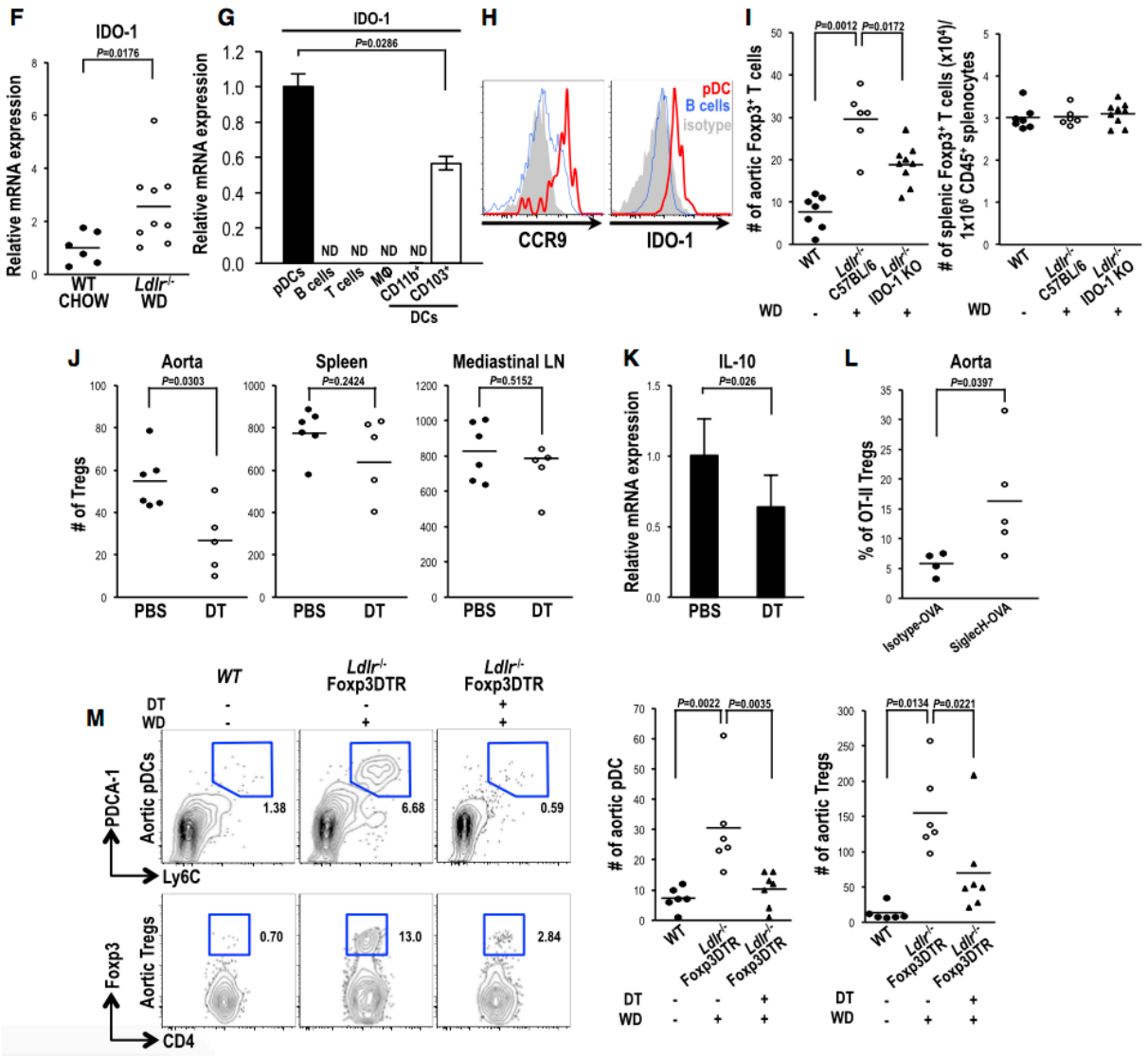

Figure 6.6. Tregs and CCR9^{+}IDO-1^{+} pDCs Accumulate Concomitantly in the Atherosclerotic Aorta and Their Interaction Is Essential for Their Homeostatic Maintenance. (A) Gating strategy for aortic Tregs. Cells were surface stained with indicated Abs except ICS for CD4 and Foxp3 (numbers in the plots indicates percentages). **(B)** Aortic Tregs from WT mice fed CHOW and *Ldlr*$^{-/-}$ mice fed WD for 14 weeks (percentages are in black; cell numbers are in red). **(C)** Distribution of Tregs in intima and adventitia of aortas of *Ldlr*$^{-/-}$ mice fed WD for 12 weeks. Left: representative FACS plots (percentages are in black; cell numbers are in red). Right: quantitation of the percentage of Tregs. Graph indicates mean ± SD; n=4. **(D)** Absolute numbers of pDCs and Tregs from *Ldlr*$^{-/-}$ mice fed WD for 0, 4, 8, and 12 weeks. Bar indicates mean; n=7 per group. **(E)** Distribution of pDCs and Tregs in each aortic segments of CHOW-fed WT and WD-fed *Ldlr*$^{-/-}$ mice after 12 weeks. Left: percentage of each aortic population in WT mice. Right: fold increase in each population in WD-fed *Ldlr*$^{-/-}$ mice normalized by WT value. Graph indicates mean ± SD; n ≥ 3. **(F)** IDO-1 mRNA

expression levels in the aorta from CHOW-fed WT mice and WD-fed *Ldlr*$^{-/-}$ mice for 7 weeks, measured by qPCR. Data were normalized to β-actin. Bar indicates mean ± SD; n=9. **(G)** Relative IDO-1 mRNA expression from FACS-sorted aortic immune cells from WD-fed *Ldlr*$^{-/-}$ mice for 9 weeks by qPCR. Data were normalized to TBP. Bar indicates mean ± SD. **(H)** Comparison of CCR9 and IDO-1 expression in pDCs and B cells in aortas from WD-fed *Ldlr*$^{-/-}$ mice for 12 weeks. **(I–M)** Lethally irradiated *Ldlr*$^{-/-}$ mice were reconstituted with BM from WT mice or *Ido1*$^{-/-}$ mice **(I)**, BDCA2-DTR mice **(J and K)**, OT-II mice **(L)**, and Foxp3-DTR mice **(M)**. **(I)** Absolute numbers of Tregs in aortas and splenic Tregs per 1×10^6 CD45$^+$ splenocytes from indicated mice. *Ldlr*$^{-/-}$ mice were fed WD for 3 weeks. Bars indicate mean; n ≥ 6. **(J and K)** *Ldlr*$^{-/-}$ mice were fed WD and injected with PBS or DT weekly for 12 weeks. **(J)** Enumeration of Tregs in aorta (absolute number) and spleen and mediastinal LNs (per 1×10^4 CD45$^+$ cells). Bars indicate mean; n ≥ 5. **(K)** Relative IL-10 mRNA expression levels in the aorta, measured by qPCR. Data were normalized to b-actin. Bars indicate mean ± SD; n=6. **(L)** Enumeration of OT-II Tregs. WD-fed *Ldlr*$^{-/-}$ mice (4 weeks) were injected with 10 mg of isotype-OVA (n=4) or SiglecH-OVA (n = 5) i.v. and sacrificed 3 days post-injection. Bars indicate mean. **(M)** Aortic pDCs and Tregs from *Ldlr*$^{-/-}$ mice fed WD and injected with PBS or DT weekly for 4 weeks. Left: representative FACS plots of pDCs and Tregs. Right: absolute numbers of pDCs and Tregs per aorta. Bars indicate mean; n ≥ 6.

6. 3. 11 Tregs regulate the Homeostasis of pDCs in Atherosclerotic Aortas

While Tregs are important for atheroprotection[4, 10, 29], there is no report on the impact of Treg depletion in regulating the homeostasis of pDCs in diseased aorta. To this end, we established selective Treg depletion model with *Ldlr*$^{-/-}$ mice reconstituted with Foxp3-DTR mouse BM.[30] As expected, WD expanded pDCs and Tregs in the aorta (**Figure 6.6M**). Of note, constitutive in vivo ablation of Treg during the course of WD decreased aortic pDCs (**Figure 6.6M**), demonstrating an important role of Tregs to maintain the homeostasis of pDCs in diseased aorta.

6. 3. 12 Aortas from Human Atherosclerotic Patients Contain Authentic pDCs that Colocalize with Tregs

Next, we sought to extend these findings to humans, investigating whether aortas from human atherosclerotic patients also contain pDCs. Indeed, human atherosclerotic aortas contained pDCs (CD123$^+$BDCA2$^+$BDCA4$^+$) (**Figure 6.7A**). Upon CpG challenge, these human pDCs secreted IFN-α (**Figure 6.7B**) and exhibited CCR7 and CD86 upregulation (**Figure 6.7C**), further suggesting that these cells are authentic pDCs. In the diseased aorta, we

could easily detect these pDCs by virtue of their positive staining for both BDCA2 and LAMP5 (**Figure 6.7D; Figure S7A**).

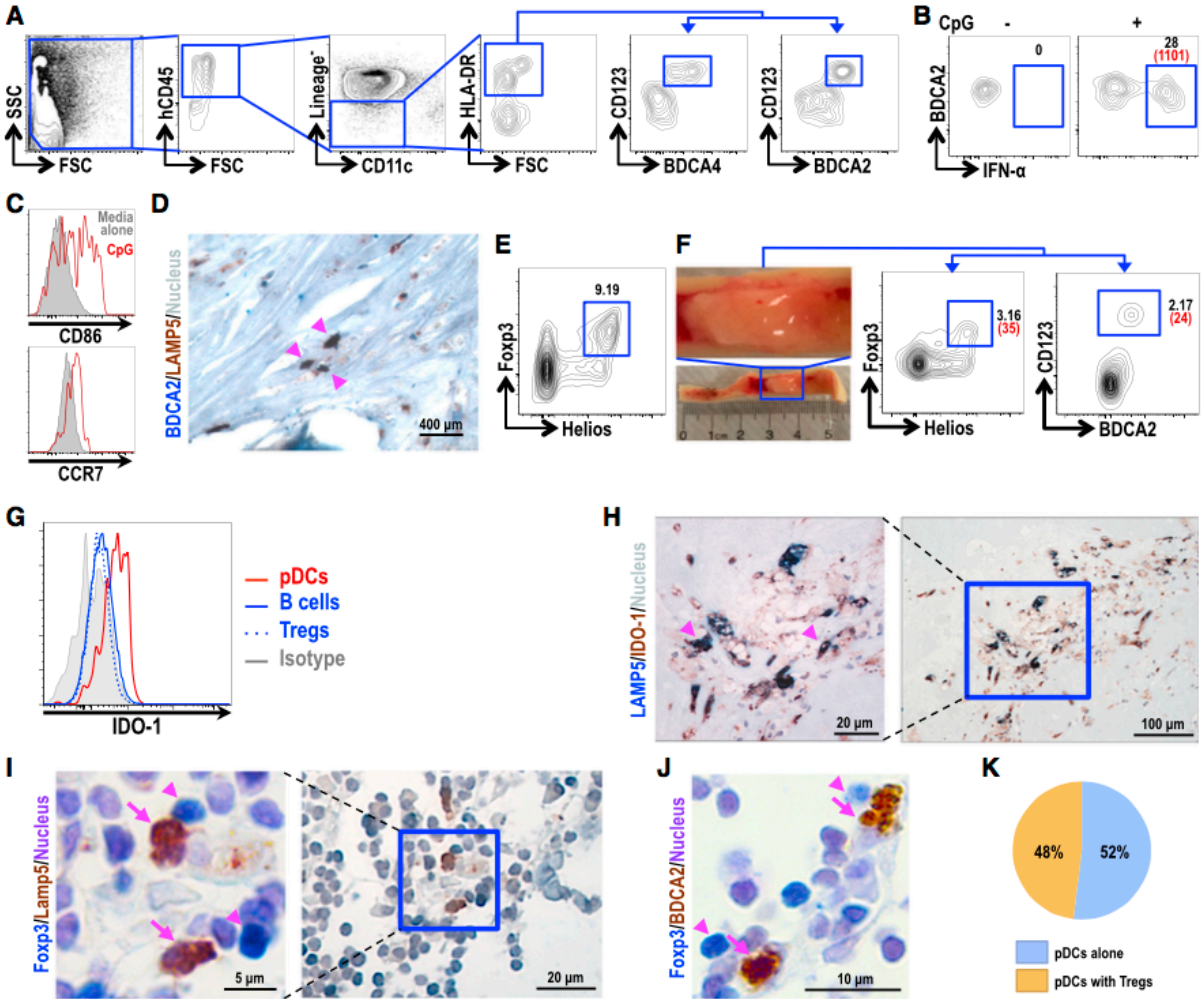

Figure 6.7. Functional pDCs and Tregs in Human Atherosclerotic Aorta. (A) Gating strategy for pDCs from patient's aorta. Lineage: CD3, CD14, CD16, CD19. **(B)** IFN-α production by pDCs from human atherosclerotic patients. Aortic cells were incubated with media alone/BFA or with CpG/BFA (percentages are in black; cell numbers are in red). **(C)** Expression of CCR7 and CD86 in cells from media-treated pDCs and CpG-treated IFN-α^+ pDCs in (B). **(D)** Paraffin-embedded sections from human atherosclerotic aorta stained for IHC with LAMP5 (brown) and BDCA2 (blue) and counterstained with hematoxylin. LAMP5$^+$ cells (pDCs) are indicated by arrowheads. **(E)** Aortic Tregs from a human patient with atherosclerosis. **(F)** Fatty plaques from atherosclerotic human tissue were isolated and subjected for analysis of pDCs and Tregs (percentages are in black; cell numbers are in red). **(G)** IDO-1 expression in pDCs, B cells, and Tregs from human patients with

atherosclerosis. **(H)** Localization of LAMP5$^+$IDO-1$^+$ pDCs in human atherosclerotic aorta. **(I and J)** Colocalization of LAMP5$^+$ pDCs (I, arrows) or BDCA2$^+$ pDCs (J, arrows) with Foxp3$^+$ Tregs (arrowheads). (K) IHC analysis of cell-to-cell contact between pDCs and Tregs in human atherosclerotic aortas (n=7). Double IHC for BDCA2 and FoxP3 was performed to visualize pDCs and Tregs in human atherosclerosis. The BDCA2$^+$ pDCs contacting Foxp3$^+$ Tregs have been counted by microscopy and shown as the percentage of pDCs with or without contacting Tregs.

Interestingly, there was a positive correlation between pDC numbers and the severity of atherosclerosis (**Figure S7B**), comparable to that observed in the mouse model (**Figure 6.6D**). Given the close relationship between Tregs and pDCs observed in the diseased mouse aorta, we further investigated patient aortas for the presence of Tregs. As was the case in the mouse model, Tregs were detected in the aortas of atherosclerosis patients, labeled by Foxp3 and Helios (**Figure 6.7E; Figure S7C**)[26], where they were colocalized with pDCs in plaques (**Figure 6.7F; Figure S7D**). In addition, pDCs in plaque areas also expressed the Treg-inducing enzyme, IDO-1, as determined by FACS (**Figure 6.7G; Figures S7E and S7F**) and immunohistochemistry (IHC) of sections (**Figure 6.7H**). Furthermore, these pDCs were colocalized with Foxp3$^+$ Tregs in the diseased aortas, as determined by monitoring for LAMP5 (**Figure 6.7I; Figure S7G**) and BDCA2 (**Figure 6.7J**) expression. Notably, ~48% of pDCs were observed together with Tregs, reinforcing their direct functional link (**Figure 6.7K**).

6. 4 Discussion

To understand the role of pDCs in atherosclerosis, sequential monitoring of the quantitative and qualitative changes in the localization, phenotype, and function of aortic pDCs during initiation, progression, or regression of atherosclerosis is a prerequisite.

6. 4. 1 Mouse and Human pDCs in Steady-State Aortas

In this study, we provide the first comprehensive IHC, flow cytometry, and functional analyses of both human and mice pDCs in the aorta at both steady state and at the inflammatory stage during atherosclerosis. pDCs in the aorta have plasma cell morphology and are distinguishable from typical classical DCs, which contain numerous dendrites. As previously described, pDCs, alongside with most DCs and T cells, are mainly located in the intimal areas of the aortic roots, a location that is prone to atherosclerosis development. The phenotype of aortic pDCs is very similar to that of pDCs in spleen, including the expression of PDCA-1/BST2/CD317, Siglec-H, Ly6C, B220 and Clec9a, as well as the Flt3/CD135 dependence of their generation. In contrast, aortic pDCs lack or express lower levels of classical DCs and monocyte/MΦ markers and markers of other lymphocyte lineages, such as B cells, T cells, NK cells, and granulocytes. Importantly, pDCs isolated from aorta have the capacity to produce large quantities of type I IFN upon stimulation through TLR9. As a result, IFN-α-secreting native aortic pDCs upregulate surface expression of PDC-TREM in vivo. Thus, aortic pDCs are equivalent, in many functional respects, to pDCs identified in other tissues. Notably, none of these functional features of aortic pDCs has been previously described under steady-state conditions. To further identify mouse equivalents of human aortic pDCs under normal conditions, we harnessed hu-mice reconstituted with human hematopoietic stem cells, thereby possessing human immune cells in their aortas. With two widely used hu-mice models (hu-NSG and BLT), we were able to identify $CD123^+BDCA2^+BDCA4^+$ authentic human pDCs in the mouse aorta. Similar to mouse aortic pDCs, human aortic pDCs produced IFN-α upon TLR9 ligation and were mainly found in the intima, where HLA-DR^+ DCs also reside. Our observation in hu-mice further indicates the

usefulness of these models to recapitulate normal human aorta. In addition, pDCs were also found in samples of healthy human aorta.

6. 4. 2 Mouse pDCs in Atherosclerosis Aortas

These steady-state findings allowed us to explore aortic pDCs under inflammatory conditions. One mildly inflammatory condition is aging, and it has previously been reported that the number of aortic DCs increases with increasing age.[23] We did not detect any significant change in the number of pDCs with age (up to 400 days). We did, however, find a remarkable increase in aortic pDC numbers upon feeding WD to athero-prone *Ldlr*$^{-/-}$ mice. Notably, this increase was only observed in the aorta, and not in other lymphoid organs, such as the spleen and even aorta-draining LNs (para-aortic and mediastinal). Anatomically, the increase in pDC number was mainly restricted to the intimal space, further corroborating the possible role of pDCs in atherosclerosis.

6. 4. 3 Comparison of pDC-Depleting Strategies : AB-Mediated Depletion and BDCA2-DTR

On the basis of results obtained using pDC-depleting Abs or constitutive depletion of pDCs, previous studies had suggested a contradictory role for pDCs in atherosclerosis. However, there are potential issues that cloud interpretation of these studies. First, it is reported that two Abs, anti-BST2 and anti-mPDCA-1, that are pDC specific in steady state might cross-react with other cell types under inflammatory conditions.[25] This promiscuous binding of anti-pDC Abs could conceivably cause these Abs to affect additional cell types critical for atherogenesis, yielding ambiguous phenotypes in atherosclerosis. Indeed, we found that these Abs target not only pDCs but also MΦs, resulting in more than 50% depletion of MΦs, even when administered i.v. twice. Second, the constitutive removal of E2-2 transcription factors in a DC-restricted fashion does deplete pDCs. However, in this mutant mouse, there is a compensatory increase in DC-like cells[31] which could also reflect a conversion of E2-2$^{-/-}$ pDCs into DCs. Given this, further analysis of the atherosclerosis

phenotype in a DC-specific E2-2$^{-/-}$ mice background will be required to allow any solid conclusions to be drawn. Given these caveats, it is reasonable to conclude that the specific contribution of pDCs to atherosclerosis in vivo has not yet been investigated in detail. To address these limitations, we used BDCA2-DTR mice, in which the DTR is only expressed in mouse pDCs, enabling us to achieve selective and inducible pDC depletion upon DT administration. Using this strain, we confirmed that DT administration depletes only pDCs in the aorta, sparing MΦs and DCs. This model afforded us an unequivocal opportunity to answer questions regarding the potential role of pDCs in atherosclerosis. Notably, mice without pDCs developed severe atherosclerosis (47% more than non-DT-treated group). However, there was no change in serum lipid profile. Furthermore, there was no significant change in IFN-α mRNA levels in pDC-depleted aortas compared with non-depleted aortas. This led us to seek an immune-modulatory function of aortic pDCs.

6. 4. 4 Mechanistic Link of Aortic pDCs and Tregs for the Prevention of Atherosclerosis

One such possible function is induction of Tregs. For example, depletion of Tregs has been shown to aggravate atherosclerosis.[10, 11] It was also reported that Treg numbers reach a peak at 4 weeks after WD-induced atherogenesis but remain decreased at later stages of atherosclerosis.[27] However, none of these previous studies have reported the enumeration of Tregs in the aorta using an unbiased approach, such as FACS. In addition, most studies in the field have relied on measuring Tregs in spleen and LNs of atherosclerotic mice or mRNA expression and IHC for Foxp3 in the aorta.[26] To fill this gap, we devised a new approach for precisely enumerating aortic Tregs, both in steady state and during atherosclerosis development, without using *Foxp*3-reporter strain.[32] Of importance, removal of autofluorescent MΦs was an essential step. Using this approach, we found a positive correlation between pDC and Treg numbers during atherosclerosis development. Anatomically, both pDCs and Tregs were found in the intima of aortic roots under normal conditions but were distributed throughout lesions that developed in atherosclerosis. Again, this phenomenon was restricted only to the atherosclerotic aorta and did not manifest in the

other lymphoid tissues tested such as spleen and draining LNs. Notably, aortic pDCs expressed two markers of tolerogenic pDCs: CCR9 and IDO-1. In line with this, depletion of pDCs during atherosclerosis resulted in decreased Treg numbers only in the aorta, with a concomitant reduction in IL-10 levels. To further investigate the local role of aortic pDCs in Treg generation, we made *Ido1*$^{-/-}$ athero-prone mice. Indeed, *Ido1*$^{-/-}$ atherosclerotic aorta possessed 40% fewer Treg numbers, compared with WT. However, there was no statistically significant difference in Treg number in the spleen of WT and *Ido1*$^{-/-}$ mice. To further pursue the outcome of pDCs-targeted antigen delivery, we used pDC-targeting Abs fused with OVA. Of importance, antigen presentation by pDCs resulted in the induction of OT-II Tregs in atherosclerotic aorta. In addition, selective ablation of Tregs by Foxp3-DTR mice decreased pDC numbers in atherosclerotic aorta, suggesting essential interaction of IDO-1^{+} pDCs and Tregs for the homeostasis of these cell populations in diseased aorta.

6. 4. 5 Relevance for Human Atherosclerosis

Although mechanistic studies in the mouse are informative, the identification of aortic pDCs in humans equivalent to those in mice would facilitate translational applications. To this end, we examined the aortas of human patients. Remarkably, human patient aortas contained functional pDCs similar to their mouse counterparts. First, these pDCs underwent maturation and pro-duced IFN-α following stimulation with TLR9 agonist. Second, there was a positive correlation between pDC number and the severity of atherosclerosis closely recapitulating our mouse studies. Finally, these human aortic pDCs also expressed IDO-1 and colocalized with Tregs in plaque tissues.

On the basis of our findings, we propose that aortic pDCs described herein have two roles. First, they are part of the innate response initiated upon microbial stimulation (e.g., TLR7 and TLR9 ligation), a response concomitant with the rapid production of type I IFN. Confirming this role will require additional studies in vivo in the future. The second is that of an immune modulator. Accordingly, during atherogenesis, aortic pDCs increase in number and become one of the dominant cell types, thereby inducing Tregs and balancing the adverse effects of cytopathic T cells. Therefore, future therapeutic strategies harnessing tolerogenic

pDC-based atheroprotective vaccines will be promising and beneficial for atherosclerosis in humans.

6. 5 Author Contributions

Tae Jin Yun, Goo Taeg Oh, Jae-Hoon Choi, and Cheolho Cheong designed the experiments, interpreted data, and wrote the manuscript.

Tae Jin Yun and **Junseong Lee** executed the majority of experiments presented.

Kawthar Machmach acquired and analyzed human and hu-mice samples for FACS.

Dahee Shim, Junhee Choi, Young Jin Wi, Hyung Seok Jang, In-Hyuk Jung, and Kyeongdae Kim did the histopathological assessment of atherosclerosis, as well as mouse and human IHC, IF, and qPCR.

Won Kee Yoon profiled serum lipid.

Mohammad Alam Miah, Bin Li, and Jinsam Chang prepared mouse and hu-mice aortas for FACS.

Mariana G. Bego, Tram N.Q. Pham , Jörg Hermann Fritz, and Eric A. Cohen designed and helped mouse and human type I IFN measurement.

Jakob Loschko and Anne B. Krug provided OVA-linked anti-Siglec-H Ab.

Tibor Keler provided human Flt3L. **Jean V. Guimond and Elie Haddad** provided hu-mice.

Eric A. Cohen, Seung-Pyo Lee, Martin G. Sirois, and Ismail El-Hamamsy provided human patient samples.

Marco Colonna provided BDCA2-DTR mouse, anti-BST2, and anti-SiglecH monoclonal Abs. All authors actively reviewed and edited the manuscript.

6. 6 Acknowledgements

This work is dedicated to the memory of Dr. Cheolho Cheong. We thank the excellent support provided by the IRCM animal facility. This work was supported by grants from the Canadian Foundation for Innovation (John R. Evans Leaders Fund) and the Canadian Institutes of Health Research (CIHR) (MOP 125933 and 133050 to C.C.; MOP 111226 to E.A.C.; and MOP 97943 to M.G.S); by Canadian HIV Cure Enterprise Team Grant HIG-133050 (to C.C., E.A.C., and E.H.); and by National Research Foundation of Korea (NRF) grants funded by the Korean government (the Ministry of Science, ICT and Future Planning [NRF-2013S1A2A2035348 and 2013M3A9D5072550 to J.-H.C.; and 2012R1A3A2026454, 2015M3A9B6029138, 2010-0020878, and 2010-0019866 to G.T.O.]). E.A.C. holds a Canada Research Chair in Human Retrovirology. C.C. is a recipient of a CIHR New Investigator Award and holds an SQHA-FRQS J1 Scholarship. T.K. is an employee and shareholder of Celldex Therapeutics. Except T.K., none of the authors have a financial interest related to this work.

6. 7 Additional Information

Supplemental Information includes Supplemental Experimental Procedures, seven figures, and one movie and can be found with this article online at (http://dx.doi.org/10.1016/j.cmet.2016.04.010.)

6. 8 References

1. Steinman, R.M. Decisions about dendritic cells: past, present, and future. *Annu Rev Immunol* **30**, 1-22 (2012).

2. Cybulsky, M.I., Cheong, C. & Robbins, C.S. Macrophages and Dendritic Cells: Partners in Atherogenesis. *Circ Res* **118**, 637-652 (2016).

3. Choi, J.H. *et al.* Identification of antigen-presenting dendritic cells in mouse aorta and cardiac valves. *J Exp Med* **206**, 497-505 (2009).

4. Choi, J.H. *et al.* Flt3 signaling-dependent dendritic cells protect against atherosclerosis. *Immunity* **35**, 819-831 (2011).

5. Colonna, M., Trinchieri, G. & Liu, Y.J. Plasmacytoid dendritic cells in immunity. *Nat Immunol* **5**, 1219-1226 (2004).

6. Ochando, J.C. *et al.* Alloantigen-presenting plasmacytoid dendritic cells mediate tolerance to vascularized grafts. *Nat Immunol* **7**, 652-662 (2006).

7. Hadeiba, H. *et al.* CCR9 expression defines tolerogenic plasmacytoid dendritic cells able to suppress acute graft-versus-host disease. *Nat Immunol* **9**, 1253-1260 (2008).

8. Hadeiba, H. *et al.* Plasmacytoid dendritic cells transport peripheral antigens to the thymus to promote central tolerance. *Immunity* **36**, 438-450 (2012).

9. Puccetti, P. & Grohmann, U. IDO and regulatory T cells: a role for reverse signalling and non-canonical NF-kappaB activation. *Nat Rev Immunol* **7**, 817-823 (2007).

10. Ait-Oufella, H. *et al.* Natural regulatory T cells control the development of atherosclerosis in mice. *Nat Med* **12**, 178-180 (2006).

11. Klingenberg, R. *et al.* Depletion of FOXP3+ regulatory T cells promotes hypercholesterolemia and atherosclerosis. *J Clin Invest* **123**, 1323-1334 (2013).

12. Daissormont, I.T. *et al.* Plasmacytoid dendritic cells protect against atherosclerosis by tuning T-cell proliferation and activity. *Circ Res* **109**, 1387-1395 (2011).

13. Doring, Y. *et al.* Auto-antigenic protein-DNA complexes stimulate plasmacytoid dendritic cells to promote atherosclerosis. *Circulation* **125**, 1673-1683 (2012).

14. Macritchie, N. *et al.* Plasmacytoid dendritic cells play a key role in promoting atherosclerosis in apolipoprotein E-deficient mice. *Arterioscler Thromb Vasc Biol* **32**, 2569-2579 (2012).

15. Sage, A.P. *et al.* MHC Class II-restricted antigen presentation by plasmacytoid dendritic cells drives proatherogenic T cell immunity. *Circulation* **130**, 1363-1373 (2014).

16. Gautier, E.L. *et al.* Gene-expression profiles and transcriptional regulatory pathways that underlie the identity and diversity of mouse tissue macrophages. *Nat Immunol* **13**, 1118-1128 (2012).

17. Jakubzick, C. *et al.* Minimal differentiation of classical monocytes as they survey steady-state tissues and transport antigen to lymph nodes. *Immunity* **39**, 599-610 (2013).

18. Satpathy, A.T., Wu, X., Albring, J.C. & Murphy, K.M. Re(de)fining the dendritic cell lineage. *Nat Immunol* **13**, 1145-1154 (2012).

19. Watarai, H. *et al.* PDC-TREM, a plasmacytoid dendritic cell-specific receptor, is responsible for augmented production of type I interferon. *Proc Natl Acad Sci U S A* **105**, 2993-2998 (2008).

20. Swiecki, M., Gilfillan, S., Vermi, W., Wang, Y. & Colonna, M. Plasmacytoid dendritic cell ablation impacts early interferon responses and antiviral NK and CD8(+) T cell accrual. *Immunity* **33**, 955-966 (2010).

21. Defays, A. *et al.* BAD-LAMP is a novel biomarker of nonactivated human plasmacytoid dendritic cells. *Blood* **118**, 609-617 (2011).

22. Heng, T.S., Painter, M.W. & Immunological Genome Project, C. The Immunological Genome Project: networks of gene expression in immune cells. *Nat Immunol* **9**, 1091-1094 (2008).

23. Liu, P. *et al.* CX3CR1 deficiency impairs dendritic cell accumulation in arterial intima and reduces atherosclerotic burden. *Arterioscler Thromb Vasc Biol* **28**, 243-250 (2008).

24. Reizis, B., Colonna, M., Trinchieri, G., Barrat, F. & Gilliet, M. Plasmacytoid dendritic cells: one-trick ponies or workhorses of the immune system? *Nat Rev Immunol* **11**, 558-565 (2011).

25. Blasius, A.L. *et al.* Bone marrow stromal cell antigen 2 is a specific marker of type I IFN-producing cells in the naive mouse, but a promiscuous cell surface antigen following IFN stimulation. *J Immunol* **177**, 3260-3265 (2006).

26. Foks, A.C., Lichtman, A.H. & Kuiper, J. Treating atherosclerosis with regulatory T cells. *Arterioscler Thromb Vasc Biol* **35**, 280-287 (2015).

27. Maganto-Garcia, E., Tarrio, M.L., Grabie, N., Bu, D.X. & Lichtman, A.H. Dynamic changes in regulatory T cells are linked to levels of diet-induced hypercholesterolemia. *Circulation* **124**, 185-195 (2011).

28. Pallotta, M.T. *et al.* Indoleamine 2,3-dioxygenase is a signaling protein in long-term tolerance by dendritic cells. *Nat Immunol* **12**, 870-878 (2011).

29. Subramanian, M., Thorp, E., Hansson, G.K. & Tabas, I. Treg-mediated suppression of atherosclerosis requires MYD88 signaling in DCs. *J Clin Invest* **123**, 179-188 (2013).

30. Kim, J.M., Rasmussen, J.P. & Rudensky, A.Y. Regulatory T cells prevent catastrophic autoimmunity throughout the lifespan of mice. *Nat Immunol* **8**, 191-197 (2007).

31. Ghosh, H.S., Cisse, B., Bunin, A., Lewis, K.L. & Reizis, B. Continuous expression of the transcription factor e2-2 maintains the cell fate of mature plasmacytoid dendritic cells. *Immunity* **33**, 905-916 (2010).

32. Bettelli, E. *et al.* Reciprocal developmental pathways for the generation of pathogenic effector TH17 and regulatory T cells. *Nature* **441**, 235-238 (2006).

CHAPTER 7
(APPENDIX III)

7 Lifelong Exposure of C57bl/6n Male Mice to Bisphenol A or Bisphenol S Reduces Recovery From a Myocardial Infarction

Amanda Kasneci,[1] Jun Seong Lee,[2] Tae Jin Yun,[2] Jijun Shang,[1] Shaun Lampen,[1] Tamar Gomolin,[1] Cheolho C. Cheong,[2,3,*] and Lorraine E. Chalifour[1,3,†]

[1]Lady Davis Institute for Medical Research, Montréal, Québec H3T 1E2, Canada;
[2]Institut de Recherches Cliniques de Montréal, Montréal, Québec H2W 1R7, Canada;
[3]Division of Experimental Medicine, Department of Medicine, McGill University, Montréal, Québec H3A 1A2, Canada

*Deceased.

[†]Correspondence:
lorraine.chalifour@mcgill.ca. (L.E.C)

Toxicological Sciences. (2017). 159(1):189-202

7. 1 Abstract

Bisphenol A (BPA) leaches from plastics to contaminate foodstuffs. Analogs, such as bisphenol S (BPS), are now used increasingly in manufacturing. Greater BPA exposure has been correlated with exacerbation of cardiovascular disease, including myocardial infarction (MI). To test the hypothesis that bisphenol exposure impairs cardiac healing, we exposed C57bl/6n mice to water containing 25ng/ml BPA or BPS from conception and surgically induced an MI in adult male progeny. Increased early death and cardiac dilation, and reduced cardiac function were found post-MI in BPA- and BPS-exposed mice. Flow cytometry revealed increased monocyte and macrophage infiltration that correlated with increased chemokine C-C motif ligand-2 expression in the infarct. In vitro BPA and BPS addition increased matrix metalloproteinase-9 (MMP) protein and secreted activity in RAW264.7 macrophage cells suggesting that in vivo increases in MMP2 and MMP9 in exposed infarcts were myeloid-derived. Bone marrow-derived monocytes isolated from exposed mice had greater expression of pro-inflammatory polarization markers when chemokine stimulated indicating an enhanced susceptibility to develop a pro-inflammatory monocyte population. Chronic BPA exposure of estrogen receptor beta (ERβ) deficient mice did not worsen early death, cardiac structure/function, or expression of myeloid markers after an MI. In contrast, BPS exposure of ERβ-deficient mice resulted in greater death and expression of myeloid markers. We conclude that lifelong exposure to BPA or BPS augmented the monocyte/ macrophage inflammatory response and adverse remodeling from an MI thereby reducing the ability to survive and successfully recover, and that the adverse effect of BPA, but not BPS, is downstream of ERβ signaling.

7. 2 Introduction

The possibility that the estrogenic chemicals which leach from plastics may adversely affect human health is a growing concern. Bisphenol A (BPA) is a high-volume chemical with millions of tons consumed each year in the manufacture of polycarbonate plastics and epoxies used in everyday life as well as a dye developer in thermal paper products such as register receipts.[1] People of all ages, including pregnant women, have detectable BPA or its metabolized products in their body fluids.[2] This persistent exposure is likely due to continual exposure from packaging in contaminated food and beverages and not because of BPA bioaccumulation.[2] Although a Tolerable Daily Intake for BPA of 50 μg/kg/d was proposed, a reduction to 4 μg/kg/d was recently suggested by the European Food Science Authority.[3]

Most epidemiological analyses investigating BPA exposure and cardiovascular diagnoses, as well as rodent exposure studies, support the idea that increased exposure to BPA may worsen cardiovascular disease morbidity and mortality, including diseases such as atherosclerosis and its major adverse outcome myocardial infarction (MI).[4, 5] Exposure of BPA in the context of a high fat diet to atherosclerosis-prone mouse and rabbit models lead to increased atherosclerotic plaques.[6, 7] Other epidemiological studies have linked greater BPA exposure with increased frequency of diagnosis of diseases associated with chronic inflammation, such as metabolic syndrome and diabetes.[8, 9, 10] More recently, plastic manufacturers are replacing BPA with analogs such as bisphenol S (BPS)[1] although the limited toxicological data available suggest that BPS has adverse effects similar to those of BPA.[11, 12, 13, 14] Network analyses in TOX21 high throughput screens comparing estradiol derivative, BPA and BPA analogs demonstrates some clustering of their estrogenizing activity suggesting some overlap in action.[15] Together, these data suggest that exposure to BPA, and perhaps BPS may influence and promote multiple facets of cardiovascular disease and that the mechanism may lie in estrogen agonist activity.

Cardiac wall rupture, loss of adequate left ventricle (LV) function or arrhythmia can be adverse outcomes after an MI.[16] Selection of the Watanabe heritable hyperlipidemic rabbits produced a strain more prone to MI, the WHHL-MI rabbit.[17] Hearts of these susceptible rabbits showed greater numbers of disarrayed cardiomyocytes, increased inflammatory cell

infiltration and calcium deposition after exposure to high dose BPA for 8weeks than control treated rabbits.[18] These data suggest that BPA may exacerbate and promote cardiac damage. Previously, we used a chronic exposure model and found reduced early survival, increased cardiac dilation as well as increased monocyte infiltration after an MI in male mice exposed to BPA versus unexposed mice.[19] Others have found acute exposure to BPA of isolated rat heart preparations induced arrhythmia that was ablated by estrogen receptor β (ERβ) antagonists.[20, 21, 22] These data suggest that BPA directly alters cardiac structure/function and reduces the ability to remodel successfully and repair a cardiac injury and that this is a consequence of ERβ agonism. To our knowledge, there are no reports assessing the consequences of in vivo exposure to BPS on cardiac structure/function or in response to injury.

In the present study, we directly compare how lifelong exposure to BPA and BPS influences cardiac structure/function at baseline and during recovery after an MI. Because of the similarity in structure of BPA and BPS, similar impact on reproductive tissues in mice[13], and arrhythmia promotion by BPA and BPS in ex vivo rat heart preparations[12], we hypothesized that BPA and BPS would be equally cardiotoxic and would reduce successful cardiac remodeling and repair postMI. We observed significantly reduced survival early after an MI in BPA and BPS exposed mice and found that those which did survive presented with greater inflammation, greater early cardiac dilation and worse remodeling than control mice. Similar effects were not found in ERβ deficient mice. These data suggest that exposure to BPA, and its leading replacement chemical BPS, reduces successful wound healing and recovery postMI via ERβ signaling.

7. 3 Results

7. 3. 1 Physiological Impact of Chronic Exposure to BPA and BPS

The chemical structures of BPA and BPS are similar, **Figure 7.1A**. To mimic the oral mode and directly compare the impact of BPA and BPS, we treated mice with drinking water containing Vehicle (VEH, 0.01% ethanol), BPA (25 ng BPA/ml), or BPS (25 ng BPS/ml), **Figure 7.1B**. To address the impact of lifelong exposure from conception to euthanasia, we initiated treatment at mating and maintained treatment of the progeny until euthanasia. Based on an average daily consumption of 5ml drinking water in adult C57bl/6n mice[23], we estimate that mice were exposed to approximately 5 µg BPA or BPS/kg BW/day. Using the formula (human equivalent dose 1⁄4 mouse dose in mg/kg x [animal Km/human Km] where the Km for mice is 3 and the Km for humans is 37,[24] we calculate that the mice were exposed to a human equivalent dose of approximately 0.41µg BPA or BPS/kg BW/day. This amount is below the current tolerable daily intake dose and can be considered to be "low dose".[25, 26]

To determine whether lifelong exposure to BPA or BPS altered body size or reproductive tissue weights, we measured BW, AGD, combined testes and combined seminal weights and calculated the BSA of adult progeny at euthanasia (**Table 7.1**). There were no differences in these gross measures of body size and neither compound altered AGD indexed to BL, testes or seminal vesicle weights. Further, HW, HW indexed to BW and HW indexed to the calculated BSA were similar regardless of treatment regimen. Lung weight and lung weight indexed to BW did not vary suggesting no overt heart failure by this gross measure. Spleen weight in BPS-treated mice was greater than in VEH- or BPA-exposed mice, but this difference was lost when indexed to BW. Thus, exposure to BPA or BPS from the time of conception did not alter adult male reproductive tissue weights, lead to increased BW, BSA, or induce cardiac or spleen hypertrophy at approximately 4 months of age.

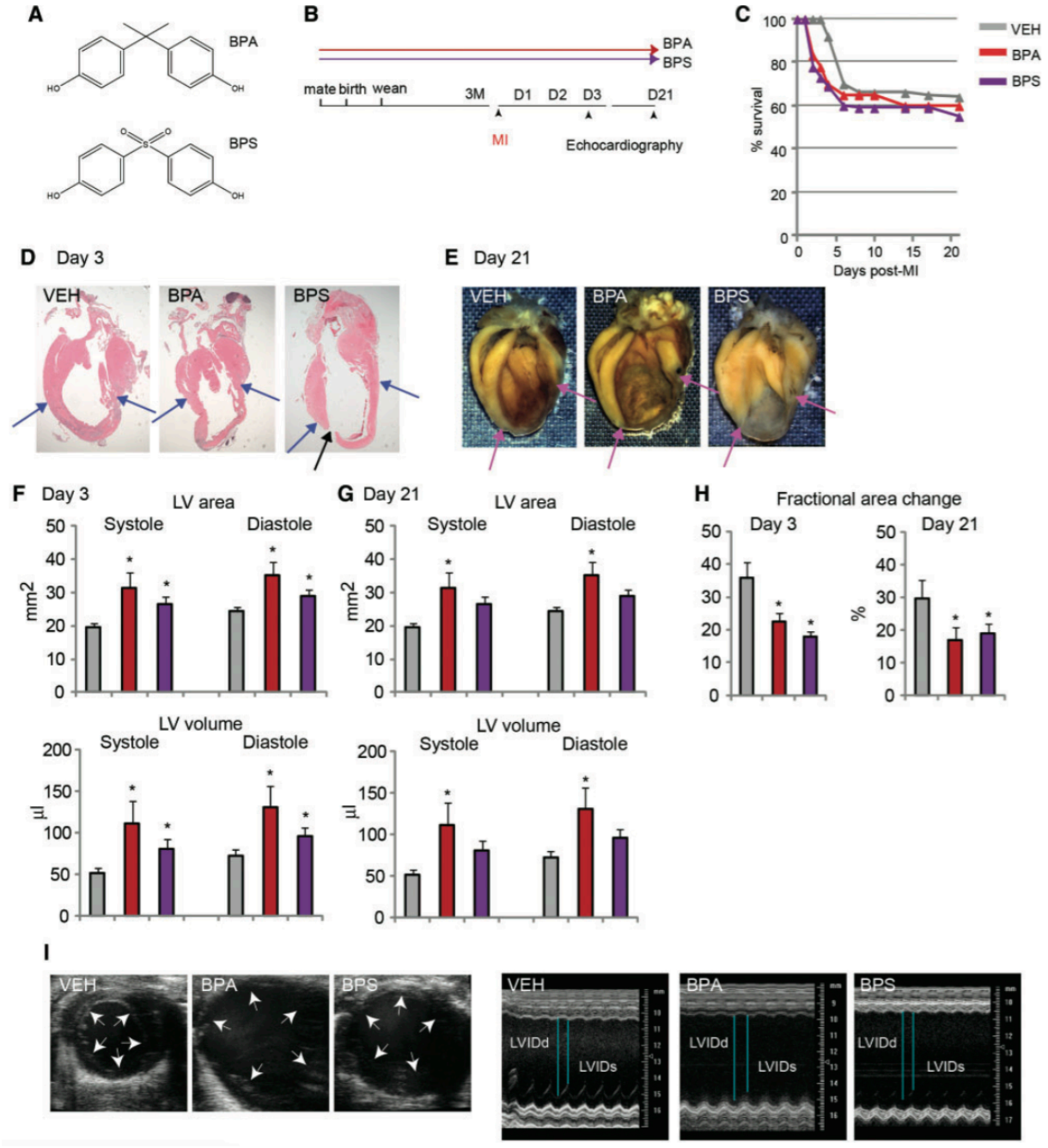

Figure 7.1. Influence of lifelong exposure on cardiac structure/function remodeling after an MI. (A) Schematic of BPA and BPS chemical structures. **(B)** Time frame. Male and female C57bl/6n mice were paired and immediately treated with drinking water containing either VEH (0.01% ethanol), BPA (25 ng/ml), or BPS (25 ng/ml). Male progeny were maintained on the same regimen until euthanasia. An MI was performed and echocardiography acquisitions were obtained on the indicated days. **(C)** Survival. Surgery was performed to create a permanent blockage in the coronary artery. Survival postMI was monitored with time. **(D)**

H&E stain. Representative coronal sections of hearts (n=6 per exposure group) obtained on day 3 postMI were stained with H&E. Arrows indicate the interface between uninfarcted and infracted regions. The inside arrow indicated a rupture site. Photographs were taken using a Leica Dissecting microscope at 1.25-fold magnification and Image Capture software. **(E)** Fixed hearts. Fixed hearts (n=3 per exposure group) obtained from mice 21 days after MI were sliced coronally and photographs taken using a Leica Dissecting microscope at 1.25-fold magnification and Image Capture software. **(F and G)** LV area and volume on days 3 and 21, respectively. The LV internal area and volume in systole and diastole were calculated using the long axis view and EKV-gated acquisitions. Data are the mean ± SEM. A p-value of $< .05$ was considered significant and is indicated by an * in comparison with VEH. **(H)** Fractional area change on days 3 and 21, respectively. The LV internal area in systole and diastole were measured and FAC calculated using the short axis view and EKV-gated acquisitions. Data are the mean ± SEM. A p-value of $< .05$ was considered significant and is indicated by an * in comparison with VEH. **(I)** Short axis acquisitions. Left. Representative EKV-gated short axis view acquisitions. Arrows indicate the outline of the LV wall in diastole to indicate the greater dilation of the LV in BPA and BPS exposed versus VEH-exposed mice. Right. Representative M-mode acquisitions. The lines indicate the LVIDd and LVIDs.

To assess baseline cardiac structure/function, we measured ECG parameters and performed echocardiography in the adult progeny (**Table 7.2**). There were no differences in any ECG parameter suggesting no difference in cardiac electrical conduction was induced by BPA or BPS exposure. Confirming the physiological data, we found echocardiography-derived LVmass and indexed LVmass were similar in all treatment groups. Although there was a trend toward reduced FS and Vcf in BPA- and BPS-exposed mice, these differences did not reach significance Also, FAC, AoVTI, SV, or CO measures of LV systolic function were not different. LV internal diameters in systole or diastole were analogous indicating no change in LV structure. The equivalent PA VTI in all groups implies no change in RV systolic function. Hence, we conclude that lifelong exposure to BPA or BPS did not influence these measures of cardiac structure/function.

Table 7.1. Physiological Parameters at Baseline

	VEH	BPA	BPS
BW	24.7 ± 1.6	25.2 ± 1.2	27.1 ± 1.4
BSA	29.8 ± 1.5	31.4 ± 0.9	33.0 ± 1.4
AGD/BL	16.6 ± 1.8	15.2 ± 1.6	14.3 ± 1.5
Testes	213 ± 4	204 ± 5	212 ± 7
Sem. Ves.	213 ± 28	220 ± 25	263 ± 19
HW	133.6 ± 5.0	128.0 ± 5.9	148.0 ± 9.7
HW/BW	5.55 ± 0.36	5.17 ± 0.3	5.45 ± 0.21
HW/BSA	4.47 ± 0.28	4.10 ± 0.22	4.52 ± 0.29
Lung	159 ± 11	160 ± 9	197 ± 14
Lung/BW	6.5 ± 0.4	6.5 ± 0.5	7.3 ± 0.3
Spleen	65.4 ± 2.4	63.0 ± 2.1	81.7 ± 6.6
Spleen/BW	2.71 ± 0.17	2.60 ± 0.18	2.99 ± 0.14

Mice (VEH, n=9; BPA, n=10; BPS, n=9) were euthanized at approximately 4 months of age and BW, BL, AGD, and the wet weight of solid organs measured. BW is in g; BSA is in cm^2; AGD indexed to BL is in mm/cm; Testes is the combined weight of both testis in g; Sem. Ves. is the combined weight of both seminal vesicle lobes including contents in g; HW is in mg; HW/BW is in mg/g; HW/ BSA is in mg/cm^2; lung is the weight of all lobes in mg; lung weight/BW is in mg/g; spleen weight is in mg; spleen/BW is in mg/g. Data are the mean ± SEM. A p-value of $< .05$ was considered significant and is indicated by an * in comparison with VEH and $^{\&}$ in comparison with BPA-treated mice.

Table 7.2. Electrocardiograph and Cardiac Structure/Function Parameters at Baseline

	VEH	BPA	BPS
PR	38.20 ± 0.71	37.30 ± 0.57	36.97 ± 0.86
Pdur	16.37 ± 0.72	17.14 ± 0.41	16.58 ± 0.80
QRS	13.25 ± 0.17	13.02 ± 0.35	12.85 ± 0.28
QTc	39.08 ± 0.77	40.11 ± 0.85	41.18 ± 0.49
HR	587 ± 6	588 ± 15	574 ± 12
LVIDd	3.73 ± 0.10	4.01 ± 0.17	4.02 ± 0.17
LVIDs	2.24 ± 0.07	2.43 ± 0.14	2.59 ± 0.18
AoVTI	4.74 ± 0.47	4.34 ± 0.29	5.3 ± 0.70
FS	40.1 ± 0.8	39.3 ± 1.9	36.0 ± 2.1
FAC	53.0 ± 2.8	55.5 ± 3.4	50.0 ± 3.1
Vcf	45.1 ± 2.7	42.7 ± 1.1	40.1 ± 0.8
SV	41.8 ± 2.1	48.9 ± 4.1	45.8 ± 4.0
CO	23.9 ± 1.4	27.6 ± 2.1	26.4 ± 2.2
PAVTI	2.8 ± 0.1	3.0 ± 0.1	3.2 ± 0.2
LVmass/BW	3.5 ± 0.2	3.3 ± 0.1	4.0 ± 0.4
LVmass/BSA	2.11 ± 0.1	2.0 ± 0.1	2.4 ± 0.2
HR	555 ± 14	556 ± 12	580 ± 14

Surface ECG or echocardiography was performed on approximately 4-month-old adult mice (VEH, n=10; BPA, n=9; BPS, n=9). Mice were anesthetized with isoflurane. Electrocardiography quantified PR, P-dur, QRS, and QTc which are expressed in msec. HR at the time of ECG data collection is in beats/min. Echocardiography quantified LVIDd and LVIDs (mm), AoVTI (cm^2), FS (%), FAC (%), Vcf (cm/s), SV (ml), CO (ml), and PAVTI (cm^2). LVmass indexed to BW (LVmass/ BW) or BSA (LVM/BSA) was calculated. HR at the time of echocardiograph data collection is in beats/min. Data are the mean ± SEM.

7. 3. 2 Survival and Cardiac Function Are Reduced PostMI in Mice Chronically Exposed to BPA and BPS

We used permanent ligation of the left anterior descending coronary artery to create an area of cardiac injury on approximately 50 mice per treatment. Necropsy of mice which died suddenly revealed the presence of blood in the thoracic cavity suggesting that death was due to cardiac rupture. We found survival in the immediate postMI period was reduced in BPA- and BPS-exposed mice (**Figure 7.1C**). Interestingly, survival at 3 weeks was approximately 55%–60% in all treatment groups. These data suggest that recovery in the immediate postMI period was reduced by exposure to BPA and BPS. H&E staining of coronal heart sections revealed thinning of the LV indicating an infarct was evident on day 3 (**Figure 7.1D**). Coronal sections of hears collected on day 21 showed extensive loss of the myocardium in all treatment groups (**Figure 7.1E**).

To quantify cardiac dilation and function, we performed echocardiography on the surviving mice (**Figure 7.1F–I**). Analyses of the heart using long axis views postMI found greater dilation in systole and diastole in BPA- and BPS-exposed versus VEH mice (**Figure 7.1F and 7.1G**). On Day 3 postMI LV area and LV volume in systole and diastole were greater in BPA and BPS-exposed mice than VEH mice (**Figure 7.1F**). On Day 21 postMI, the dilation of BPA-, but not BPS-exposed mice was significantly greater than VEH mice (**Figure 1G**). Further, analyses found reduced FAC in BPA- and BPS-exposed mice on days 3 and 21 (**Figure 7.1H**). B-mode images collected using the short axis view show representative acquisitions indicating greater LV dilation in BPA- and BPS-treated mice (**Figure 7.1I**). Further, representative M-mode images show LV walls with greater reductions in wall movement evident in BPA and BPS-treated mice suggesting reduced cardiac contraction (**Figure 7.1I**). Thus, although cardiac structure/function was similar in all mice at baseline, we observed greater cardiac dilation and greater reductions in LV function in BPA- and BPS- versus VEH-exposed mice that survived an MI. Further, the greater reductions in cardiac function evident 21 days postMI in BPA- and BPS-treated mice suggest the possibility for reduced long-term survival of exposed mice.

7. 3. 3 PostMI Myeloid Cell Accumulation Is Increased by Chronic Exposure to BPA and BPS

H&E staining of formaldehyde fixed sections of hearts, showed increased cellular infiltration into the infarct area in BPA- and BPS-exposed mice (**Figure 7.2A**). Monocytes and MΦ infiltrate into a wounded area and are important in the initial inflammatory response after an MI to remove dead cells and remodel the extracellular matrix.[27, 28] Circulating $F4/80^{+}Ly6C^{hi}$ expressing monocytes are actively recruited to the injury. Within the wound they develop into $F4/80^{+}Ly6C^{lo}MerTK^{-}$ monocytes and then into $F4/80^{+}Ly6C^{lo}MerTK^{+}$ MΦ. Staining of sections prepared from the infarct area using an antiF4/80 antibody revealed the presence of $F4/80^{+}$ cells within the infarct region (**Figure 7.2B**). To further characterize the infiltrating cells, we probed protein homogenates prepared from the infarct area with antiF4/80 (**Figure 7.2C**). We found increased F4/80-specific protein in homogenates from BPA- and BPS-treated mice. Tissue-resident MΦ track to organs such as the heart during fetal life where they self-renew.[29] To determine whether exposure to BPA or BPS during fetal life increased their presence postMI, we probed infarct homogenates with the tissue-resident MΦ marker Lyve-1[30] (**Figure 7.2G**). Lyve-1 expression was similar in infarct homogenates from exposed versus unexposed mice making it unlikely that this cell population increased postMI.

To establish whether myeloid cell infiltration was increased in BPA- and BPS-exposed mice postMI on a cell-by-cell basis, we performed flow cytometry of single cells isolated from whole hearts collected on day 4 postMI (**Figure 7.2D–F**). We found increased CD45 positive cells in the BPS-exposed mice suggesting increased infiltration of myeloid cells (**Figure 7.2D**). $CD45^{+}$ cells were further characterized as monocytes ($CD11b^{+}Ly6C^{+}$) which were then subclassified into $CD11b^{+}Ly6C^{hi+}$, and $CD11b^{+}Ly6C^{-/lo}$. Macrophages were identified as $CD64^{+}MerTK^{+}$, and dendritic cells (DC) as $MHCII^{+}CD11c^{+}$ (**Figure 7.2D**). We observed increased numbers of DCs, $Ly6c^{hi}$ and $Ly6c^{lo}$ monocytes infiltrated into the hearts of BPA- and BPS-exposed hearts versus those present in VEH-exposed mice. Also, increased numbers of MerTK+ MΦ were found in BPS-exposed hearts than in hearts from the other treatment groups (**Figure 7.2E and 7.2F**). BPS-exposed, but not BPA-exposed mice had increased accumulation of $CD4^{+}$-T-cells and $CD8^{+}$-T-cells in the heart (**Supplementary figure 1A and B**). No differences were detected in myeloid or T-cell numbers in the mediastinal lymph node

that drains the heart (**Supplementary figure 2**). These data suggest increased infiltration of proinflammatory myeloid cells in bisphenol-treated mice after an MI.

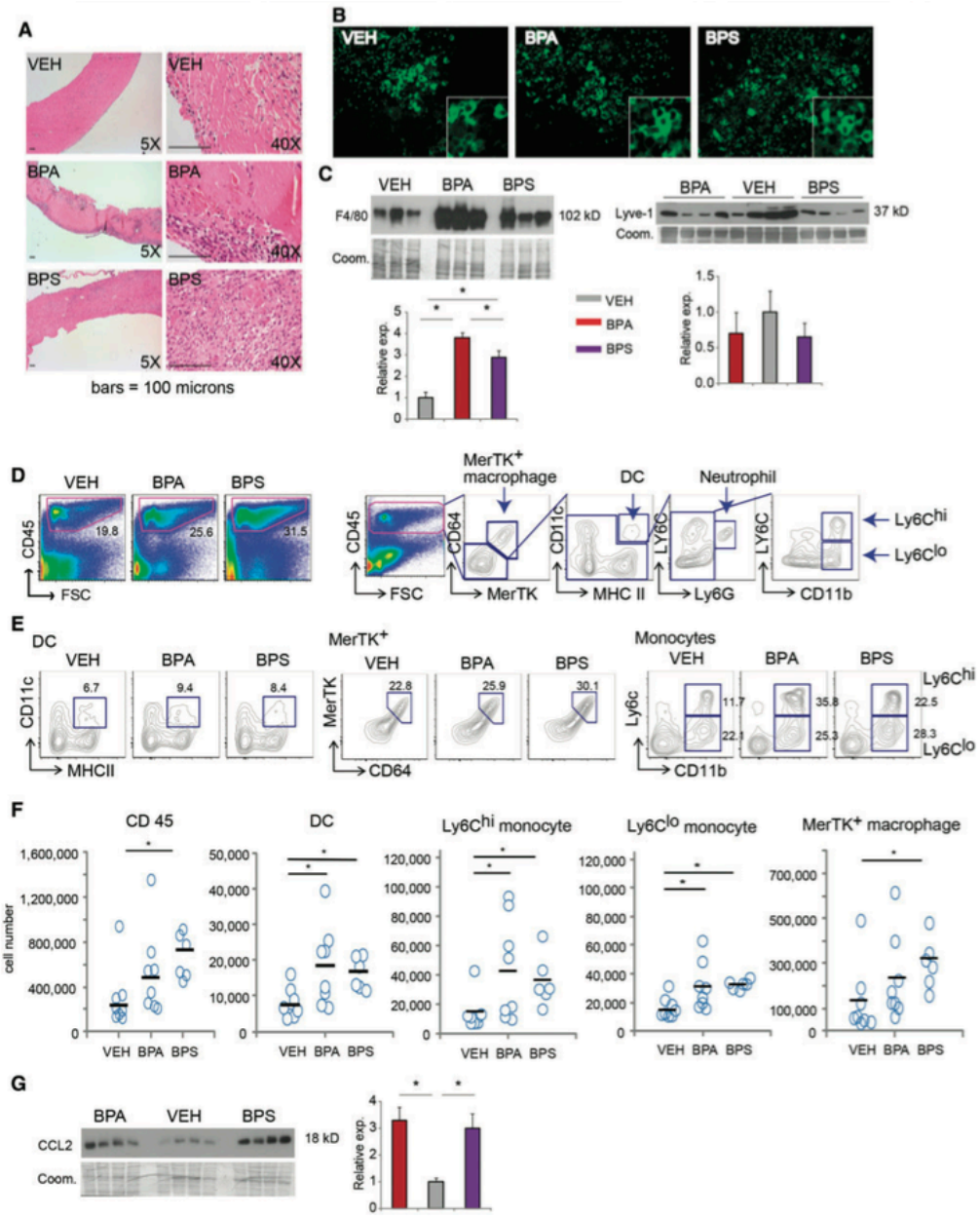

Figure 7.2. Characterization of the myeloid infiltration into the infarct. (A) Histology. Hearts n=6 mice/treatment were collected on day 3 postMI, fixed in formaldehyde, coronal sections prepared and stained with H&E. Photographs were acquired using Image Capture software. Representative sections of the infarct region are shown. The bar is equal to 100 microns. **(B)** F4/80 immunofluorescence. Heart sections from panel A underwent antigen

retrieval and then incubation with anti-F4/80 antibody with specific staining revealed using fluorescently tagged secondary antibody. Images were collected as described in panel A. Cropped images were obtained using Adobe Photoshop. **(C)** F4/80 and Lyve-1 expression. Protein was isolated from the infarct region of mice (VEH, n=8; BPA n=8; BPS n=8) on day 4 postMI. Representative blots for expression of F4/80 (left), and Lyve-1 (right) are shown. The size of each protein is indicated to the right of the immunoblot. Expression of F4/80 and Lyve-1 was calculated relative to the stained and scanned Coomassie (Coom.) membrane which was used as a loading control. The bar graphs show the combined results. Expression in the VEH samples was artificially designated as 1.0. A p-value of $< .05$ was considered significant and is indicated by an * in comparison with VEH. **(D)** Left: Flow cytometry of $CD45^+$ single cell preparation isolated whole hearts postMI. Single cell preparations were prepared from the hearts of mice (VEH n=8; BPA n=8; and BPS n=7) on day 4 postMI. A representative result with the percentage of cells expressing CD45 detected is indicated. Right, Gating strategy to characterize myeloid cells from mice postMI. $CD45^+$ cells were sequentially separated using flow cytometry. Reactivity to CD64, MerTk, CD11c, MHCII, Ly6G, CD11b, and the amount of Ly6C staining allowed identification of specific myeloid cell populations. The myeloid cell types identified are indicated by boxes. **(E)** Subclassification of myeloid cells. Shown are representative flow cytometry results indicating the percentage of DCs (left, $CD45^+$, $MHCII^+$, and $CD11c^+$), MΦs (middle, $CD45^+$, $CD64^+$, and $MerTK^+$), and monocytes (right, $CD45^+$, $CD11b^+$, and $Ly6c^+$) cells isolated from the hearts of VEH-, BPA-, or BPS-treated mice, Mice were euthanized on day 4 postMI. **(F)** Flow cytometry. The number of the indicated cell types present in the heart of each mouse is indicated. Each circle represents an individual mouse. Data are the mean ± SEM. A p-value of $< .05$ was considered significant and is indicated by an * in comparison with VEH. **(G)** CCL2 expression. Protein homogenates described in panel C were probed for CCL2 expression. CCL2 expression was calculated relative to the stained and scanned Coom. membrane which was used as a loading control. The bar graphs show the combined results. Expression in the VEH samples was artificially designated as 1.0. A p-value of $< .05$ was considered significant and is indicated by an * in comparison with VEH.

The release of cell contents from oxygen-deprived cardiomyocytes as well as the secretion of chemokines by surviving cells stimulates monocyte migration into the infarct.[31] Circulating monocytes are actively recruited to an injury in response to chemokines such as chemokine (C-C motif) ligand 2 (CCL2).[32] IB revealed increased CCL2 protein in homogenates from the ischemic area of BPA- and BPS-exposed versus VEH mice (**Figure 7.2G**). Hence, our data show increased infiltration by bone marrow-derived monocytes and MΦ in BPA- and BPS-exposed hearts postMI that may be a consequence of local increases in the monocyte chemoattractant CCL2.

To identify whether a monocytosis contributed to the increase in myeloid cell infiltration, we enumerated the circulating myeloid cells (**Table 7.3**). At baseline, we found no

difference in any white blood cell or red blood cell parameter as a consequence of BPA or BPS exposure. To determine whether any differences were revealed after an MI, we analyzed blood samples collected on day 3 postMI. When baseline versus postMI sampling was compared, all groups had an approximately 60% increase in circulating granulocyte and a 9%–15% reduction in hemoglobin after the MI. Here, BPA-treated mice had increased and BPS-treated mice had reduced circulating monocytes postMI. We did not detect large increases in circulating monocytes at baseline or after MI in exposed mice indicating that increased inflammatory cell infiltration after the MI was not secondary to a monocytosis.

Table 7.3. Circulating Myeloid Cells

	Baseline			D3 postMI		
	VEH	BPA	BPS	VEH	BPA	BPS
Total WBC	12.56 ± 0.84	13.54 ± 1.53	13.88 ± 1.48	14.26 ± 1.04	16.16 ± 1.46	12.8 ± 0.75
Lymphocytes	7.82 ± 0.82	8.16 ± 0.92	8.96 ± 0.84	7.23 ± 0.39	7.46 ± 0.58	5.84 ± 0.68$^{\#}$
Monocytes	1.08 ± 0.07	1.26 ± 0.15	1.22 ± 0.15	1.1 ± 0.05	1.60 ± 0.11$^{*\#}$	0.93 ± 0.09$^{\#\&}$
Granulocytes	3.66 ± 0.20	4.14 ± 0.51	3.7 ± 0.51	5.93 ± 0.72$^{\#}$	7.10 ± 1.11$^{\#}$	6.04 ± 0.33$^{\#}$
RBC	11.4 ± 0.1	11.2 ± 0.4	11.8 ± 0.1	10.2 ± 0.6$^{\#}$	11.1 ± 0.1	10.6 ± 0.2$^{\#}$
Hemoglobin	17.1 ± 0.1	16.7 ± 0.5	17.1 ± 0.1	14.7 ± 0.7$^{\#}$	15.9 ± 0.1$^{\#}$	15.6 ± 0.4$^{\#}$
Hematocrit	53.8 ± 0.8	53.4 ± 1.7	54.7 ± 0.4	46.8 ± 3.0$^{\#}$	52.0 ± 0.4	48.8 ± 0.9$^{\#}$

Blood was collected from the saphenous vein of adult mice, n=5 per treatment at baseline and n=7 mice per treatment on day 3 postMI. Total WBC (10^3 cells/mm^3), lymphocytes (10^3 cells/mm^3), monocytes (10^3 cells/mm^3), granulocytes (10^3 cells/mm^3), RBC (10^6 cells/mm^3), hemoglobin (g/100ml), and hematocrit (%) were measured. Data are the mean ± SEM. A p-value of < .05 was considered significant and is indicated by an * in comparison with VEH, # in comparison with MI, and $^{\&}$ in comparison with BPA-treated mice.

To determine whether BPA or BPS might increase infarct monocyte numbers by promoting proliferation, we treated the male MΦ cell line RAW264.7 with graded amounts of BPA or BPS. We found no change in sulforhodamine B dye binding with BPA or BPS treatment (**Figure 7.3A**). To discover whether BPA or BPS might increase migration and thereby increase myeloid cell movement into the infarct, we cultured RAW264.7 macrophage cell line and quantified migration in a scratch assay. We observed no increase in RAW264.7 cell migration into the monolayer wound in BPA- or BPS-treated cells (**Figure 7.3B**). Collectively, these data demonstrate no increase in monocyte proliferation or monocyte

migration with BPA or BPS treatments in vitro suggesting no impact of BPA or BPS on monocyte/MΦ proliferation or migration within the infarct.

The spleen can contribute infiltrating monocytes and MΦ cells to the injured area postMI.[33] Spleen wet weights on post MI day 3 (VEH 87 ± 4; BPA 97 ± 8; BPS 96 ± 12) and day 21(VEH 88 ± 8; BPA 74 ± 10; BPS 86 ± 4) were similar indicating no gross differences in spleen size. Further, flow cytometry analyses of the myeloid and T-cell compartments of the spleen on day 4 postMI did not identify significant differences with exposure (**Supplementary figure 3**). These data suggest no significant increase in myeloid or T-cells originated from the spleen in BPA or BPS exposed mice.

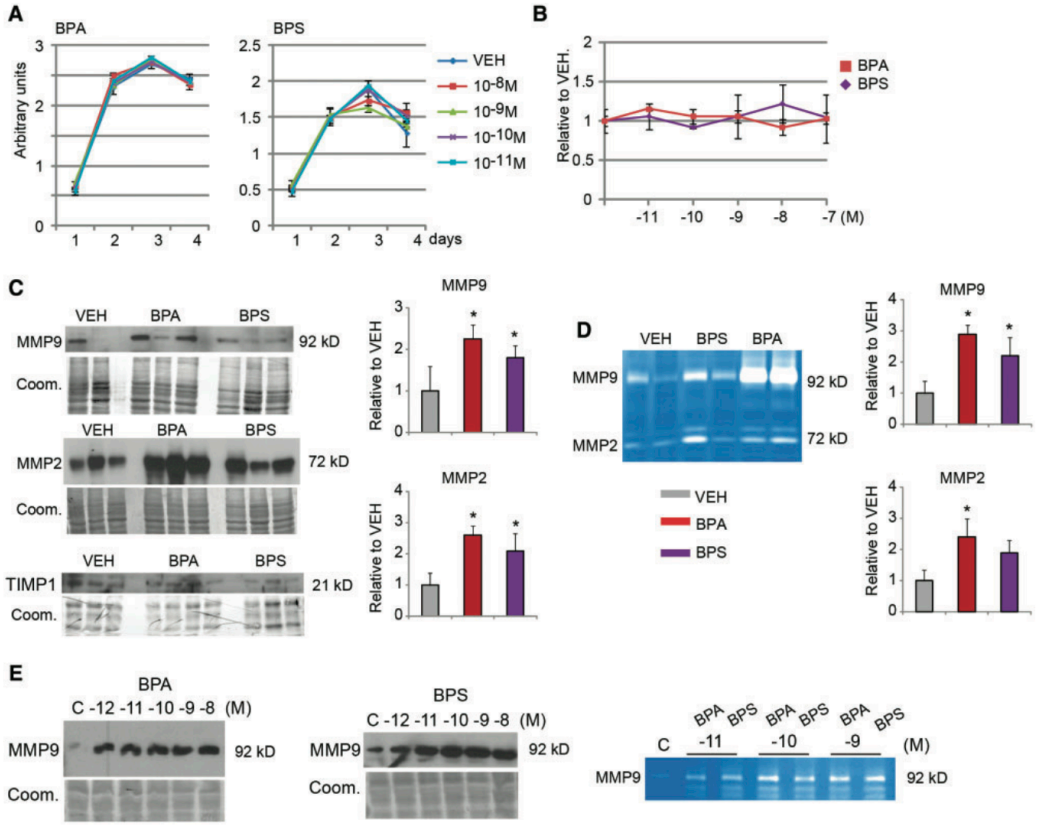

Figure 7.3. Impact of BPA and BPS on proliferation, migration and MMP expression and activity. (A) Proliferation. Raw 264.7 cells were cultured on 24-well plates. Once adhered, the cells were treated with VEH or the indicated amounts of BPA or BPS in triplicate. The SRB assay was performed on the indicated days. Data are the mean ± SEM. **(B)** Migration. Raw 264.7 cells were cultured on 24-well plates. Once approximately 70% confluent, a

scratch was made and the media replaced with VEH or the indicated amounts of BPA or BPS in triplicate. The monolayer was stained with SRB 24 h later. Photographs were taken using Image Capture software and the cell-free area quantified using Image J software. The cell-free area in VEH-treated cells was considered to be 100% migration. Shown are the results of 2 independent experiments. **(C)** MMP9, MMP2 and TIMP1 expression in infarct heart. Protein homogenates, n=6/treatment, were prepared from the ischemic area and immunoblotted for expression of MMP9, MMP2, or TIMP1. Expression of individual proteins is relative to the stained and scanned Coom. membrane which was used as a loading control. Representative blots are shown. The size of each protein is indicated to the right of the immunoblot. The bar graph shows the results of MMP9 and MMP2 expression. Expression in the VEH samples was artificially designated as 1.0. A p-value of $< .05$ was considered significant and is indicated by an * in comparison with VEH. **(D)** MMP9 and MMP2 in gel zymography in infarct heart. Protein homogenates, n=6/treatment, of the ischemic area were prepared and in gel zymography was performed. The size of the clear bands is indicated to the right of the gel. A representative gel is shown. The bar graph shows the combined results of MMP9 and MMP2 activity. Gelatinolytic activity (unstained area) in the VEH samples was artificially designated as 1.0. A p-value of $< .05$ was considered significant and is indicated by an * in comparison with VEH. **(E)** MMP expression and activity in vitro. RAW 264.7 cells were cultured on 6-well plates until approximately 60% confluent and then cultured in media containing the indicated amounts of BPA or BPS for 24 h. Cell lysates were immunoblotted for expression of MMP9 and MMP2 as above. The size of each protein is indicated to the right of the immunoblot. Expression of individual proteins is relative to the stained and scanned Coom. membrane which was used as a loading control. The media was collected for in gel zymography as above. The size of the clear bands is indicated to the right of the gel. Representative gels from 3 independent experiments are shown.

7. 3. 4 Monocyte-Associated MMP Expression and Activity Is Increased by Exposure to BPA and BPS

Increased cardiac dilation postMI can be due to excessive degradation of the supporting extracellular matrix by MMPs secreted by myeloid cells.[16, 34] To determine whether the increased monocyte/MΦ infiltration increased MMP protein and activity in the infarct area, we isolated protein homogenates from the infarct of VEH-, BPA-, and BPS-exposed mice and performed IB and in gel zymography. IB revealed increased expression of MMP9 and MMP2 with no change in the Tissue Inhibitor of Metalloproteinase-1 protein in samples from BPA and BPS versus VEH exposed mice (**Figure 7.3C**). In gel zymography revealed increased MMP9 activity in homogenates from BPA- and BPS-exposed and an increase in MMP2 activity in BPA-exposed versus VEH mice (**Figure 7.3D**). To ascribe these increases to monocyte/MΦ, we treated RAW264.7 cells with BPA or BPA for 24h. Increased MMP9

protein in cell lysates and increased secreted MMP9 activity in the culture media was induced by BPA and BPS (**Figure 7.3E**). These data suggest the increased MMP protein and MMP activity in the infarct area of bisphenol exposed compared with VEH mice postMI was the result of BPA- and BPS-mediated activation of infiltrating monocyte/MΦ.

7. 3. 5 BPA and BPS Exposure Promotes a Pro-Inflammatory Cell Population

Chemokine addition in vitro has been used to delineate two major monocyte phenotypes. Culture with IFNγ and/or LPS induces monocyte polarization to a "classically activated" and pro-inflammatory MΦ phenotype sometimes called M1 MΦ characterized by increased expression of proteins such as NOS2 and COX2, ARG1. Culture with IL-4 induces polarization to an "alternatively activated" and anti-inflammatory MΦ phenotype sometimes called M2 MΦ characterized by increased expression of ARG1. To determine whether BPA or BPS influence monocyte polarization in vitro, we exposed RAW264.7 cells to IFNγ or IL-4 along with BPA or BPS (**Figure 7.4A**). IFNγ-stimulated expression of NOS2 was increased and IL-4-stimulated expression of ARG1 was reduced by nanomolar BPA and BPS. These data suggest that acute in vitro exposure to BPA or BPS enhances polarization to proinflammatory MΦ and reduces polarization to anti-inflammatory MΦ phenotype.

Circulating monocytes that enter the infarct arise from the bone marrow. Monocyte progenitor cells in the bone marrow can be induced to polarize into activated monocytes in vitro.

To test whether lifelong in vivo exposure to BPA or BPS influences polarization to the proinflammatory MΦ phenotype, bone marrow cells from VEH, BPA, and BPS exposed mice were isolated, cultured to induce monocyte development and then differentiated in vitro by exposure to increasing amounts of IFNγ or LPS (**Figure 7.4B**). Both treatments induced increased NOS2 and COX2 expression. However, greater inductions were detected in bone marrow-derived cultures isolated from BPA or BPS exposed mice. Thus, lifelong in vivo exposure to BPA or BPS increased the susceptibility of bone marrow-derived monocytes to respond to proinflammatory MΦ polarization inducers in vitro.

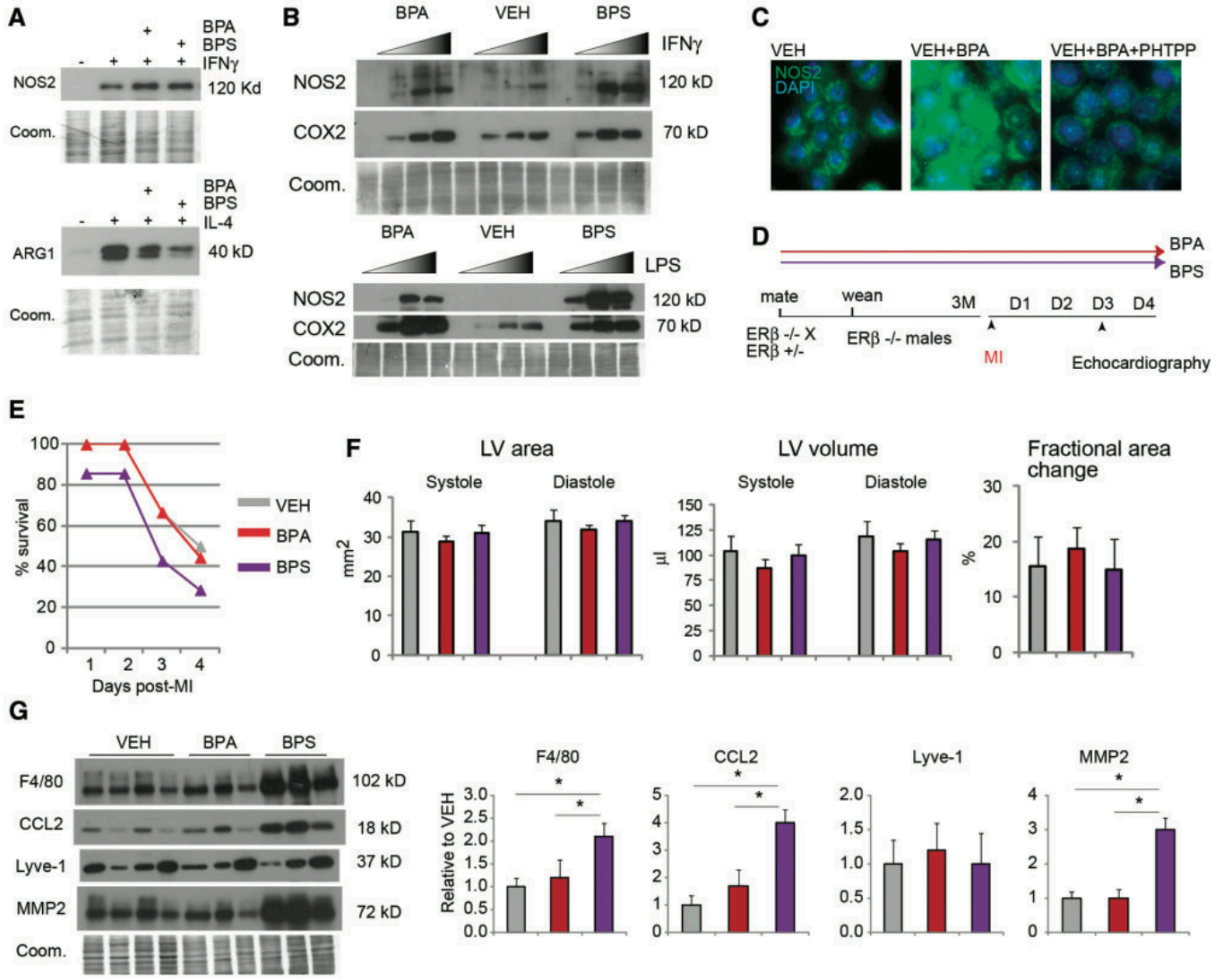

Figure 7.4. Role of ERβ signaling in mediating the consequences of BPA and BPS exposure. (A) Chemokine stimulation of RAW 264.7 cells. Top: RAW 264.7 cells were cultured on 6-well plates until approximately 60% confluent and then in media containing VEH, IFNγ^{-} alone (50 ng/ml), IFNβ + BPA (10^{-9} M) or IFNβ + BPS (10^{-9} M) for 24 h. Protein lysates were prepared and probed for NOS2 expression. The size of NOS2 protein is indicated to the right of the immunoblot. A representative immunoblot is shown. Expression of individual proteins is relative to the stained and scanned Coom. membrane which was used as a loading control. Representative gels from 3 independent experiments are shown. Bottom, RAW 264.7 cells were cultured on 6-well plates until approximately 60% confluent and then cultured in media containing VEH, IL-4-alone (10 ng/ml), IL-4 + BPA (10^{-9} M) or IL-4 + BPS (10^{-9} M) for 24 h. Protein lysates were prepared and probed for ARG1 expression. The size of ARG1 is indicated to the right of the immunoblot. A representative immunoblot is shown. Expression of individual proteins is relative to the stained and scanned Coom. membrane which was used as a loading control. Representative gels from 3 independent experiments are shown. **(B)** Chemokine addition to BMDM isolated from exposed mice.

BMDM were isolated from mice exposed to VEH, BPA, or BPS. When approximately 70% confluent, the media was changed to contain VEH, or increasing concentrations of IFNγ (5, 25, and 50 ng/ml) or LPS (10, 50, and 100 ng/ml). Twenty-four hours later cell lysates were collected as above and immunoblotted for NOS2 and COX2. The size of each protein is indicated to the right of the immunoblot. Expression of individual proteins is relative to the stained and scanned Coom. membrane which was used as a loading control. Representative gels from 6 independent experiments are shown. **(C)** Impact of ERβ antagonist PHTPP. RAW 264.7 cells were cultured on glass cover slips in 6-well plates. When approximately 60% confluent they were treated with VEH or PHTPP (10^{-8} M) for 2 h and then VEH or BPA (10^{-9} M) was added and culture continued for 24 h. After 24 h, the cells were washed, fixed and stained with antibody to NOS2 (green). Nuclei were stained with DAPI (blue). Images were acquired at 400x magnification and merged using Adobe Photoshop. Representative images from 3 independent experiments are shown. **(D)** Chronic treatment of $ERβ^{-/-}$ mice. $ERβ^{-/-}$ male and $ERβ^{+/-}$ female mice were paired and immediately treated with either VEH, BPA, or BPS treated water. Male progeny were genotyped at weaning. $ERβ^{-/-}$ male progeny were maintained on the same regimen until euthanasia. An MI was performed and echocardiography acquisitions were obtained on day 3. **(E)** Survival. Surgery was performed and a permanent coronary ligation created to induce an MI. $ERβ^{-/-}$ mice, n=15/treatment were used. Survival postMI was monitored with time. **(F)** LV area and FAC on day 3. Echocardiography was performed on n=6 mice/treatment. The LV internal area in systole and diastole were calculated using the long axis view and EKV gated acquisitions. The LV internal area in systole and diastole were measured and FAC calculated using the short axis view and EKV gated acquisitions. Data are the mean ± SEM. A p-value of $< .05$ was considered significant and is indicated by an * in comparison with VEH. **(G)** Protein expression. Protein was isolated from the infarct region of n=5 mice/treatment on day 4 postMI. Representative blots for expression of F4/80, CCL2, Lyve-1, and MMP2 are shown. The size of each protein is indicated to the right of the immunoblot. Expression of individual proteins was calculated and is expressed relative to the stained and scanned Coom. membrane which was used as a loading control. The bar graph shows the combined results. Expression in the VEH samples was artificially designated as 1.0. A p-value of $< .05$ was considered significant and is indicated by an * in comparison with VEH.

7. 3. 6 ERβ Signaling Is Involved

To explore the mechanism, we treated RAW264.7 cells with BPA in the absence or presence of a 10-fold excess of the ERβ-antagonist PHTPP. Immunofluorescence staining detected reduced NOS2 expression in cells treated with BPA + PHTPP (**Figure 7.4C**). These data suggest that the mechanism for BPA-mediated increases was downstream of ERβ-signaling.

To determine whether ablation of ERβ signaling in vivo would reduce the impact of lifelong exposure to BPA or BPS, we exposed ERβ mating pairs to BPA or BPS at the time of

mating as described above and performed an MI on the adult male progeny (**Figure 7.4D–G**). Survival to 4 days was similar for VEH and BPA-exposed mice, but was reduced in BPS-exposed mice (**Figure 7.4E**). Echocardiography performed on day 3 postMI revealed no significant differences in the LV area or LV volume in ERβ$^{-/-}$ mice regardless of treatment (**Figure 7.4F**). Moreover, FAC was similar regardless of exposure. However, IB of infarct homogenates revealed greater expression of the monocyte/MΦ marker F4/80 and MMP2 in BPS-exposed ERβ$^{-/-}$ mice than in samples from BPA-exposed and VEH treated ERβ$^{-/-}$ mice and greater expression of the chemoattractant CCL2 than VEH treated ERβ$^{-/-}$ mice (**Figure 7.4G**). In contrast, expression of F4/ 80, CCL2 or MMP2 in VEH and BPA exposed ERβ$^{-/-}$ mice was comparable. There were no differences in expression the tissue macrophage marker Lyve-1 marker expression (**Figure 7.5G**). Thus, the absence of ERβ ablated the adverse impact of chronic BPA and BPS exposure on cardiac structure/function measures. However, although BPA-mediated increases in expression of inflammatory markers were reduced to control levels by ERβ ablation, their continued high level of expression in BPS-exposed ERβ$^{-/-}$ mice suggests that the adverse effects of BPS exposure do not solely depend on ERβ signaling.

7. 4 Discussion

Data directly comparing the safety of BPS are scant yet, temporal analyses show that BPA exposure is reducing[35] while exposure to BPS is increasing.[36] Our study is significant because it directly compares and explores the consequences of lifelong oral exposure to BPA and BPS on the ability to heal from a clinically relevant cardiovascular insult, MI. Overall, our data are consistent with a model where BPA and BPS are equally toxic to the injured heart and where their adverse impact on cardiac healing postMI is centered on increasing inflammation in the infarct. Moreover, we equate this increase in myeloid infiltration to local increases in monocyte chemoattractant, an increased susceptibility to proinflammatory chemokines in the bone-marrow-derived cells that infiltrate the ischemic heart and further show that BPA-mediated, but not BPS-mediated, effects are downstream of ERβ signaling.

7. 4. 1 BPA and BPS Exposure Induces Synonymous Reductions in Survival and Cardiac Function PostMI

Our data suggest that continual exposure to BPA and BPS promotes cardiac rupture and LV dysfunction after an MI. We found early death from cardiac rupture was greater in BPA- and BPS-exposed mice than in VEH mice. Moreover, surviving mice had greater dilation suggesting more adverse LV geometric remodeling, and had reduced FAC indicating sustained LV dysfunction. Other studies have showed that acute BPA treatment of ex vivo isolated rat heart preparations increased arrhythmia following an ischemic-reperfusion injury.[22] Similarly, optical mapping of ex vivo heart preparations found that acute BPA treatment prolonged the PR segment and the atrium failed to propagate impulses to the ventricle.[21] Further, using an ex vivo rat heart preparation, exposure to low doses of BPA and BPS exposure induced arrhythmia.[12] Together, these data imply that BPA and BPS are equally cardiotoxic, that exposure can promote the three major complications of MI, rupture, LV dysfunction and arrhythmia and that this adverse impact is species-independent.

7. 4. 2 Lifelong BPA and BPS Exposure Led to Greater Inflammation PostMI

In all mammals, monocytes and MΦ are key innate immune cells that participate in infection control and wound healing.[27, 37, 38] Wound healing is equivalent in all mammals, follows the same pathway in all solid organs and depends absolutely on the orchestrated infiltration of monocytes and MΦ. Greater expression of CCL2 and numbers of DC and monocyte/MΦ cells infiltrated the postMI ischemic area of BPA- and BPS-exposed versus VEH hearts. Hence, we conclude that local increases in chemoattractant are a primary factor inducing a greater accumulation of inflammatory cells in the exposed mice. Using models of inflammatory bowel disease, allergic lung inflammation, or challenge by influenza virus no differences in outcome, CCL2 level, or leukocyte infiltration were found when mice developmentally exposed to BPA were compared with unexposed mice.[39, 40, 41] Thus, although developmental BPA exposure did not influence the capacity to respond appropriately to inflammation, we found lifelong exposure to BPA and BPS resulted in an exaggerated and proinflammatory response linked to increased CCL2 chemokine.

The greater influx of DC and monocyte/MΦ cells is likely detrimental and we suspect that the increase in MMP activity in infarct homogenates may be a composite of increased myeloid cell infiltration, and increased expression and secretion of MMPs. MMP9 secretion is primarily attributed to proinflammatory MΦ suggesting a link between the increased accumulation of monocyte/MΦ and the increased MMP9 activity in the BPA- and BPS-exposed mice. Increased MMP activity is linked to greater dilatation and death postMI[16, 34] and reductions in MMP protein or activity have improved survival[42] and dilation as well as cardiac function postMI.[19] In support of the idea that the increased MMP activity in the infarcts was monocyte derived, acute exposure of RAW 264.7 MΦ cells to BPA and BPS in vitro increased MMP9 protein and activity. In other work using human ovarian and lung cancer cell lines, estrogen-, and BPA-mediated increases in cell migration were linked to increased MMP2 activity.[43, 44] Thus, increased MMP activity is a consistent feature of in vivo and in vitro BPA exposure. Here, we extend these results and demonstrate that BPA- and BPS-mediated increases in MMP activity result from continued exposure in vivo and link this increased

MMP activity to acute exposure in monocyte/MΦ in vitro, greater cardiac dilation and an unstable ventricle wall postMI.

Monocyte/MΦ cells entering the infarcts of BPA- or BPS-exposed mice are likely highly inflammatory. The transition from inflammatory to repair phenotypes in vivo resembles the polarization of monocytes to pro-inflammatory or antiinflammatory phenotypes in vitro. BPA and BPS enhanced the expression of the proinflammatory MΦ polarization marker NOS2 and reduced expression of the anti-inflammatory MΦ marker ARG1 in RAW 264.7 cells suggesting that exposure promotes polarization to a proinflammatory cell population. The circulating monocyte/MΦ that infiltrate wounds, such as after an MI, arise from the bone marrow. Bone marrow-derived monocytes isolated from mice chronically exposed to BPA or BPS had enhanced expression of the proinflammatory MΦ polarization markers when IFNγ, LPS, or IFNγ+LPS were added. This suggests that the cells entering the infarct from exposed mice were highly susceptible to polarization to a proinflammatory phenotype and at lower concentrations of inflammatory chemokines than nonexposed mice. In other studies, nanomolar BPA increased the release of pro-inflammatory cytokines in THP-1 MΦ and human monocytes[45] and estradiol treatment of NR8383 macrophages increased polarization to the pro-inflammatory M1-type MΦ phenotype.[46] In contrast, other in vitro studies found that BPA reduced MΦ function.[47, 48, 49] High (micromolar) amounts of BPA and only short term exposure to mg/kg/d doses of BPA in these studies complicate integration with the data here. However, the combined data suggest that BPA- and BPS-exposure induces increased pro-inflammatory MΦ polarization and increased secreted MMP activity from activated MΦ infiltrating the infarct zone.

7. 4. 3 Mechanism for BPA, but Not BPS Mediated Effects, Depends on ERβ Signaling

The mechanism of BPA-mediated, but not BPS-mediated, increases in inflammation and ablation of cardiac repair activities postMI likely depends on activation of ERβ. ERβ$^{-/-}$ mice treated with VEH, BPA, or BPS shared similar cardiac structural and functional deficits after an MI. In ex vivo isolated rat heart preparations, ERβ antagonists ablated BPA- and BPS-

mediated changes in arrhythmia promotion and calcium homeostasis.[4, 12] Thus, the mechanism and negative influence of BPA and BPS on cardiac structure/ function is dependent on ERβ signaling ex vivo and in vivo with ablation resulting in reduced effects demonstrable in rats and mice. However, differences in survival and on myeloid cell marker expression reveal mechanistic insights. ERβ$^{-/-}$ mice exposed to VEH and BPA had similar survival and myeloid cell marker expression implying that BPA's adverse effects were strongly mediated by BPA:ERβ signaling. Yet, ERβ$^{-/-}$ mice exposed to BPS had reduced survival and greater expression of myeloid markers and MMP2. These data indicate that the adverse impact of BPS on myeloid cell infiltration was not relieved by ablation of ERβ signaling. These data imply that the mechanism of harm of BPA and BPS on myeloid cells are distinct. They also suggest that excessive myeloid cell infiltration was a greater driver of reduced survival than reduced cardiac function. Transcriptome analyses in disparate systems such as nematodes treated with BPA or BPS has identified low numbers of shared transcripts.[50] Further supporting the idea that BPA and BPS may have some shared but also disparate interactions, the result of studies included in the ToxCast data, suggest differences in the response to BPA versus BPS. Overall, these data indicate that bisphenols as a class may show substantial and important differences with bisphenol analogs demonstrating distinct impacts and unique signatures.

7. 4. 4 Relevance

The disease burden and relative economic loss to the USA and European communities of exposure to endocrine disruptors, including BPA, is enormous.[51, 52] Up to approximately $7.9 billion USD was attributed to endocrine disruptor-induced early cardiovascular mortality. Beyond cardiovascular disease, recent studies link increased BPA exposure with increased asthma[53, 54] and increased food intolerance[55] supporting the idea that chronic bisphenol exposure promotes a hyperimmune response.[56] The known association of female gender with greater incidence of chronic immune diseases such as systemic lupus or multiple sclerosis, and correlation of "flare-ups" or symptoms with the menstrual cycle[57] argues that modifications in ER signaling influences these and perhaps other chronic diseases that have a immune component. Extending the reduced cardiac wound healing found here, bisphenol exposure has the potential to adversely influence healing of other solid tissue injuries. Based on our results

and the results of other who also compared BPA with BPS, the use of BPS in replacement of BPA in manufacturing is unlikely to reduce human and economic costs.

7. 4. 5 Limitations

Endocrine disruptor responses are nonmonotonic therefore our study cannot predict the impact of BPA or BPS at other doses. Importantly, our studies cannot predict the response in other inbred lines or in female mice. Also, these studies were performed using mice and mouse cells and these results have not yet been identified in human tissues, monocytes or MΦs.

7. 5 Author Contributions

Junseong Lee performed experiments and helped interpret the data.

7. 6 Acknowledgements

We gratefully acknowledge the helpful comments of Dr Stephanie Lehoux and Dr Koren K. Mann. Further, we appreciate the outstanding technical aid of Kathy Ann Forner of the Surgery Core and the dedicated animal health care technicians of the Animal Quarters for their exemplary animal care. This work was supported by operating grants from the Canadian Institute for Health Research to L.E.C. and C.C.C. and the Heart and Stroke Foundation of Quebec to L.E.C.

7. 7 Additional Information

Supplementary data are available at Toxicological Sciences online.
(https://academic.oup.com/toxsci/article/159/1/189/3894576#supplementary-data)

7. 8 References

1. Geens, T. *et al.* A review of dietary and non-dietary exposure to bisphenol-A. *Food Chem Toxicol* **50**, 3725-3740 (2012).

2. Birnbaum, L.S. State of the science of endocrine disruptors. *Environ Health Perspect* **121**, A107 (2013).

3. Safety, E.F. Report on the two-phase public consultation on the draft EFSA scientific opinion on bisphenol A (BPA). *EFSA supporting publication* **12**, 740E (2015).

4. Gao, X. & Wang, H.S. Impact of bisphenol a on the cardiovascular system - epidemiological and experimental evidence and molecular mechanisms. *Int J Environ Res Public Health* **11**, 8399-8413 (2014).

5. Posnack, N.G. The adverse cardiac effects of Di(2-ethylhexyl)phthalate and Bisphenol A. *Cardiovasc Toxicol* **14**, 339-357 (2014).

6. Fang, C. *et al.* Bisphenol A exposure enhances atherosclerosis in WHHL rabbits. *PLoS One* **9**, e110977 (2014).

7. Sui, Y. *et al.* Bisphenol A increases atherosclerosis in pregnane X receptor-humanized ApoE deficient mice. *J Am Heart Assoc* **3**, e000492 (2014).

8. Han, C. & Hong, Y.C. Bisphenol A, Hypertension, and Cardiovascular Diseases: Epidemiological, Laboratory, and Clinical Trial Evidence. *Curr Hypertens Rep* **18**, 11 (2016).

9. Melzer, D. *et al.* Urinary bisphenol A concentration and risk of future coronary artery disease in apparently healthy men and women. *Circulation* **125**, 1482-1490 (2012).

10. Rochester, J.R. Bisphenol A and human health: a review of the literature. *Reprod Toxicol* **42**, 132-155 (2013).

11. Eladak, S. *et al.* A new chapter in the bisphenol A story: bisphenol S and bisphenol F are not safe alternatives to this compound. *Fertil Steril* **103**, 11-21 (2015).

12. Gao, X., Ma, J., Chen, Y. & Wang, H.S. Rapid responses and mechanism of action for low-dose bisphenol S on ex vivo rat hearts and isolated myocytes: evidence of female-specific proarrhythmic effects. *Environ Health Perspect* **123**, 571-578 (2015).

13. Rochester, J.R. & Bolden, A.L. Bisphenol S and F: A Systematic Review and Comparison of the Hormonal Activity of Bisphenol A Substitutes. *Environ Health Perspect* **123**, 643-650 (2015).

14. Vinas, R. & Watson, C.S. Bisphenol S disrupts estradiol-induced nongenomic signaling in a rat pituitary cell line: effects on cell functions. *Environ Health Perspect* **121**, 352-358 (2013).

15. Thayer, K.A., Pelch, K.E., Birnbaum, L.S. & and Bucher, J.R. Bisphenols: More unnecessary surprises. *Endocrine Disruptors* **4**, e1131032 (2016).

16. Myerburg, R.J. & Junttila, M.J. Sudden cardiac death caused by coronary heart disease. *Circulation* **125**, 1043-1052 (2012).

17. Shiomi, M., Ito, T., Yamada, S., Kawashima, S. & Fan, J. Development of an animal model for spontaneous myocardial infarction (WHHLMI rabbit). *Arterioscler Thromb Vasc Biol* **23**, 1239-1244 (2003).

18. Fang, C. *et al.* Bisphenol A exposure induces metabolic disorders and enhances atherosclerosis in hyperlipidemic rabbits. *J Appl Toxicol* **35**, 1058-1070 (2015).

19. Patel, B.B. *et al.* Chronic Exposure to Bisphenol A Reduces Successful Cardiac Remodeling After an Experimental Myocardial Infarction in Male C57bl/6n Mice. *Toxicol Sci* **146**, 101-115 (2015).

20. Gao, X., Liang, Q., Chen, Y. & Wang, H.S. Molecular mechanisms underlying the rapid arrhythmogenic action of bisphenol A in female rat hearts. *Endocrinology* **154**, 4607-4617 (2013).

21. Posnack, N.G. *et al.* Bisphenol A exposure and cardiac electrical conduction in excised rat hearts. *Environ Health Perspect* **122**, 384-390 (2014).

22. Yan, S. *et al.* Bisphenol A and 17beta-estradiol promote arrhythmia in the female heart via alteration of calcium handling. *PLoS One* **6**, e25455 (2011).

23. Bachmanov, A.A., Reed, D.R., Beauchamp, G.K. & Tordoff, M.G. Food intake, water intake, and drinking spout side preference of 28 mouse strains. *Behav Genet* **32**, 435-443 (2002).

24. Reagan-Shaw, S., Nihal, M. & Ahmad, N. Dose translation from animal to human studies revisited. *FASEB J* **22**, 659-661 (2008).

25. Teeguarden, J.G. & Hanson-Drury, S. A systematic review of Bisphenol A "low dose" studies in the context of human exposure: a case for establishing standards for reporting "low-dose" effects of chemicals. *Food Chem Toxicol* **62**, 935-948 (2013).

26. Vandenberg, L.N. *et al.* Low dose effects of bisphenol A: An integrated review of in vitro, laboratory animal, and epidemiology studies. *Endocrine Disruptors* **1**, endo.26490 (2013).

27. Crane, M.J. *et al.* The monocyte to macrophage transition in the murine sterile wound. *PLoS One* **9**, e86660 (2014).

28. Hulsmans, M., Sam, F. & Nahrendorf, M. Monocyte and macrophage contributions to cardiac remodeling. *J Mol Cell Cardiol* **93**, 149-155 (2016).

29. Ensan, S. *et al.* Self-renewing resident arterial macrophages arise from embryonic CX3CR1(+) precursors and circulating monocytes immediately after birth. *Nat Immunol* **17**, 159-168 (2016).

30. Pinto, A.R. *et al.* An abundant tissue macrophage population in the adult murine heart with a distinct alternatively-activated macrophage profile. *PLoS One* **7**, e36814 (2012).

31. Yan, X. *et al.* Temporal dynamics of cardiac immune cell accumulation following acute myocardial infarction. *J Mol Cell Cardiol* **62**, 24-35 (2013).

32. Nahrendorf, M., Pittet, M.J. & Swirski, F.K. Monocytes: protagonists of infarct inflammation and repair after myocardial infarction. *Circulation* **121**, 2437-2445 (2010).

33. Swirski, F.K. *et al.* Identification of splenic reservoir monocytes and their deployment to inflammatory sites. *Science* **325**, 612-616 (2009).

34. Gao, X.M., White, D.A., Dart, A.M. & Du, X.J. Post-infarct cardiac rupture: recent insights on pathogenesis and therapeutic interventions. *Pharmacol Ther* **134**, 156-179 (2012).

35. LaKind, J.S. & Naiman, D.Q. Temporal trends in bisphenol A exposure in the United States from 2003-2012 and factors associated with BPA exposure: Spot samples and urine dilution complicate data interpretation. *Environ Res* **142**, 84-95 (2015).

36. Ye, X. *et al.* Urinary Concentrations of Bisphenol A and Three Other Bisphenols in Convenience Samples of U.S. Adults during 2000-2014. *Environ Sci Technol* **49**, 11834-11839 (2015).

37. Brancato, S.K. & Albina, J.E. Wound macrophages as key regulators of repair: origin, phenotype, and function. *Am J Pathol* **178**, 19-25 (2011).

38. MacLeod, A.S. & Mansbridge, J.N. The Innate Immune System in Acute and Chronic Wounds. *Adv Wound Care (New Rochelle)* **5**, 65-78 (2016).

39. Bauer, S.M. *et al.* The effects of maternal exposure to bisphenol A on allergic lung inflammation into adulthood. *Toxicol Sci* **130**, 82-93 (2012).

40. Roy, A., Bauer, S.M. & Lawrence, B.P. Developmental exposure to bisphenol A modulates innate but not adaptive immune responses to influenza A virus infection. *PLoS One* **7**, e38448 (2012).

41. Roy, A., Gaylo, A., Cao, W., Saubermann, L.J. & Lawrence, B.P. Neither direct nor developmental exposure to bisphenol A alters the severity of experimental inflammatory colitis in mice. *J Immunotoxicol* **10**, 334-340 (2013).

42. Castro, M.M., Kandasamy, A.D., Youssef, N. & Schulz, R. Matrix metalloproteinase inhibitor properties of tetracyclines: therapeutic potential in cardiovascular diseases. *Pharmacol Res* **64**, 551-560 (2011).

43. Ptak, A., Hoffmann, M., Gruca, I. & Barc, J. Bisphenol A induce ovarian cancer cell migration via the MAPK and PI3K/Akt signalling pathways. *Toxicol Lett* **229**, 357-365 (2014).

44. Zhang, K.S. *et al.* Bisphenol A stimulates human lung cancer cell migration via upregulation of matrix metalloproteinases by GPER/EGFR/ERK1/2 signal pathway. *Biomed Pharmacother* **68**, 1037-1043 (2014).

45. Liu, Y. *et al.* Modulation of cytokine expression in human macrophages by endocrine-disrupting chemical Bisphenol-A. *Biochem Biophys Res Commun* **451**, 592-598 (2014).

46. Kou, X.X. *et al.* Estradiol promotes M1-like macrophage activation through cadherin-11 to aggravate temporomandibular joint inflammation in rats. *J Immunol* **194**, 2810-2818 (2015).

47. Byun, J.A., Heo, Y., Kim, Y.O. & Pyo, M.Y. Bisphenol A-induced downregulation of murine macrophage activities in vitro and ex vivo. *Environ Toxicol Pharmacol* **19**, 19-24 (2005).

48. Pyo, M.Y., Kim, H.J., Back, S.K. & Yang, M. Downregulation of peritoneal macrophage activity in mice exposed to bisphenol A during pregnancy and lactation. *Arch Pharm Res* **30**, 1476-1481 (2007).

49. Segura, J.J. *et al.* In vitro effect of the resin component bisphenol A on substrate adherence capacity of macrophages. *J Endod* **25**, 341-344 (1999).

50. Chen, Y. *et al.* Exposure to the BPA-Substitute Bisphenol S Causes Unique Alterations of Germline Function. *PLoS Genet* **12**, e1006223 (2016).

51. Attina, T.M. *et al.* Exposure to endocrine-disrupting chemicals in the USA: a population-based disease burden and cost analysis. *Lancet Diabetes Endocrinol* **4**, 996-1003 (2016).

52. Trasande, L. *et al.* Estimating burden and disease costs of exposure to endocrine-disrupting chemicals in the European union. *J Clin Endocrinol Metab* **100**, 1245-1255 (2015).

53. Kim, K.N. *et al.* Bisphenol A exposure and asthma development in school-age children: a longitudinal study. *PLoS One* **9**, e111383 (2014).

54. Petzold, S., Averbeck, M., Simon, J.C., Lehmann, I. & Polte, T. Lifetime-dependent effects of bisphenol A on asthma development in an experimental mouse model. *PLoS One* **9**, e100468 (2014).

55. Menard, S. *et al.* Food intolerance at adulthood after perinatal exposure to the endocrine disruptor bisphenol A. *FASEB J* **28**, 4893-4900 (2014).

56. Robinson, L. & Miller, R. The Impact of Bisphenol A and Phthalates on Allergy, Asthma, and Immune Function: a Review of Latest Findings. *Curr Environ Health Rep* **2**, 379-387 (2015).

57. Giefing-Kroll, C., Berger, P., Lepperdinger, G. & Grubeck-Loebenstein, B. How sex and age affect immune responses, susceptibility to infections, and response to vaccination. *Aging Cell* **14**, 309-321 (2015).

CHAPTER 8
(APPENDIX IV)

8 Self-renewing resident arterial macrophages arise from embryonic CX3CR1^{+} precursors and circulating monocytes immediately after birth

Sherine Ensan[1,*], Angela Li[1,*], Rickvinder Besla[3,*], Norbert Degousee[2], Jake Cosme[2], Mark Roufaiel[2], Eric A. Shikatani[3], Mahmoud El-Maklizi[1], Jesse W. Williams[4], Lauren Robins[2], Cedric Li[2], Bonnie Lewis[2], Tae Jin Yun[5], Jun Seong Lee[5], Peter Wieghofer[6], Ramzi Khattar[2], Kaveh Farrokhi[1], John Byrne[2,13], Maral Ouzounian[2,13], Caleb C.J. Zavitz[2], Gary A. Levy[1,2], Carla M.T. Bauer[7], Peter Libby[8], Mansoor Husain[2,3,13], Filip K. Swirski[9], Cheolho Cheong[5], Marco Prinz[10], Ingo Hilgendorf[11], Gwendalyn J. Randolph[4], Slava Epelman[1,2,13], Anthony O. Gramolini[2,12,13], Myron I. Cybulsky[2,3,13], Barry B. Rubin[2,13] and Clinton S. Robbins[1,2,3,13]

[1]Department of Immunology, University of Toronto, Toronto, ON, Canada.

[2]Toronto Ge neral Research Institute, University Health Network, Toronto, ON, Canada.

[3]Department of Laboratory Medicine and Pathobiology, University of Toronto, Toronto, ON, Canada.

[4]Department of Pathology and Immunology, Washington University School of Medicine, St. Louis, MO, USA.

[5]Laboratory of Cellular Physiology and Immunology, Institut de Recherches Cliniques de Montréal, Montréal, QC, Canada.

[6]Institute of Neuropathology and Faculty of Biology, University of Freiburg, Freiburg, Germany.

[7]Novartis Institutes for BioMedical Research, Cambridge, MA, USA.

[8]Department of Medicine, Brigham and Women's Hospital, Harvard Medical School, Boston, MA, USA.

[9]Center for Systems Biology, Massachusetts General Hospital, Harvard Medical School, Boston, MA, USA.

[10]Institute of Neuropathology & BIOSS Centre for Biological Signaling Studies, University of Freiburg, Germany.
[11]Department of Cardiology and Angiology I, Heart Center, University of Freiburg, Freiburg, Germany.
[12]Department of Physiology, University of Toronto, Toronto, ON, Canada.
[13]Peter Munk Cardiac Centre, University Health Network, Toronto, ON, Canada.
*authors contributed equally

Correspondence:

C.S.R. (clint.robbins@utoronto.ca)
Peter Munk Cardiac Centre and Toronto General Research Institute
University Health Network, Toronto Medical Discovery Tower, 101 College St., Toronto, ON

Nature Immunology. (2016). 17(2):59-168

8. 1 Abstract

Resident macrophages densely populate the normal arterial wall, yet their origins and the mechanisms that sustain them are poorly understood. Here we use gene-expression profiling to show that arterial macrophages constitute a distinct population among macrophages. Using multiple fate-mapping approaches, we show that arterial macrophages arise embryonically from $CX3CR1^{+}$ precursors and postnatally from bone marrow–derived monocytes that colonize the tissue immediately after birth. In adulthood, proliferation (rather than monocyte recruitment) sustains arterial macrophages in the steady state and after severe depletion following sepsis. After infection, arterial macrophages return rapidly to functional homeostasis. Finally, survival of resident arterial macrophages depends on a CX3CR1-CX3CL1 axis within the vascular niche.

8. 2 Introduction

Most tissues of the body harbor resident macrophages. Yet macrophages are phenotypically and functionally heterogeneous, a reflection of the diversity of tissue environments in which they reside. In addition to maintaining tissue homeostasis and responding to invading pathogens, macrophages contribute to numerous pathological processes, making them an attractive potential target for therapeutic intervention. This, however, will require a detailed understanding of macrophage origins, the mechanisms that maintain them and their functional attributes in different tissues and disease contexts.

Macrophage ontology has long engendered controversy.[1, 2] Nevertheless, the idea that tissue macrophages develop exclusively from circulating bone marrow-derived monocytes has prevailed for nearly a half-century.[3] But accumulating evidence, including studies using sophisticated fate-mapping approaches, has determined that some tissue macrophages and their precursors are established embryonically in the yolk sac (YS) and fetal liver before the onset of definitive hematopoiesis.[4, 5, 6, 7, 8, 9, 10, 11] Regardless of their origin, tissue macrophages can maintain themselves in adulthood by self-renewal independently of blood monocytes1.[12, 13]

Gene-expression profiling of macrophage populations from several tissues has established that all macrophages express only a small number of transcripts[14], indicating the importance of the context provided by the tissue in studies of macrophage function in homeostasis and disease. The normal arterial wall contains many tissue-resident macrophages that contribute crucially to immunity, tissue homeostasis and wound healing after injury.[15] However, the regulatory networks, ancestry and mechanisms that maintain arterial macrophages remain unknown.

Using gene-expression analysis, we have found that arterial macrophages constitute a distinct population among tissue macrophages. Multiple fate-mapping approaches demonstrated that arterial macrophages arise embryonically from CX3CR1^{+} precursors and postnatally from bone marrow–derived monocytes that colonize the tissue during a brief period immediately after birth. In adulthood, arterial macrophages were maintained by CX3CR1-CX3CL1 interactions and local proliferation without further substantial contribution

from blood monocytes. Self-renewal also sustained arterial macrophages after severe depletion during polymicrobial sepsis, rapidly restoring them to functional homeostasis.

8. 3 Results

8. 3. 1 Phenotype and Gene-Expression Profile of Arterial Macrophages

Flow cytometry–based analysis of single cell suspensions from healthy aortas of 6- to 8-week-old mice revealed that 38 ± 4% (mean ± s.e.m.) of all $CD45^+$ leukocytes were macrophages ($F4/80^+CD11b^+$ cells) (**Figure 8.1a**). Other myeloid cell populations observed included $F4/80^{lo}CD11c^+MHCII^+$dendritic cells (**Figure 8.1a**) and $F4/80^{lo}CD64^+Ly6C^{hi\text{-}lo}$ monocytes (**Figure 8.1a**). Principal component analysis revealed a distinct transcriptome in arterial macrophages, which clustered near other macrophage populations including microglia, alveolar macrophages and splenic red pulp macrophages, as characterized by the Immunological Genome Consortium (**Figure 8.1b and Supplementary figure 1a**).[14] Stringent comparison of gene-expression profiles among arterial, brain, alveolar and splenic red pulp macrophages revealed 212 transcripts that were at least five-fold higher or lower in arterial macrophages relative to expression in the three other macrophage populations (**Figure 8.1c,d and Supplementary figure 1b,c**). To gain insight into biological processes, we grouped transcripts encoding molecules with annotated functions according to Gene Ontology (GO) terms. Transcripts that were more abundant in arterial macrophages were enriched for molecular terms including translation and regulation of cell proliferation. The less abundant transcripts yielded GO enrichment of terms including homeostatic process, cell proliferation and macromolecular complex subunit organization (**Supplementary Table 1**). Flow cytometry analysis of specific cell surface markers confirmed that arterial macrophages share features with macrophage populations from other organs and express a unique signature. In addition to the core macrophage markers CD64 and the tyrosine kinase receptor MerTK[16], arterial macrophages expressed Lyve1, CD68, major histocompatibility complex class II (MHCII), CD86, the class A scavenger receptor Msr1, Toll-like receptor 4 (TLR4) and T cell immunoglobulin mucin 4 (Tim-4) (**Figure 8.1a,e**).

Zbtb46, encoding a BTB-ZF transcription factor, is selectively expressed in classical dendritic cells (cDCs).[17, 18] Analysis of mice in which a GFP reporter cassette replaces exon 2 of the *Zbtb46* BTB domain ($Zbtb46^{+/gfp}$mice) revealed high expression of Zbtb46 in

$CD11c^{+}MHCII^{+}CD11b^{-}$ cDCs of the aorta, liver, lung and brain (**Figure 8.1f**). GFP was undetected in alveolar macrophages and Kupffer cells but was expressed in microglia and aortic macrophages, albeit at lower levels than in cDCs (**Figure 8.1f**). These data extend published observations that resident macrophages in some tissues express Zbtb46[19] and show that the level of Zbtb46 expression, as inferred from the GFP reporter, differs between macrophages and cDCs in the arterial wall. cDCs were also distinguished from macrophages by expression of the DC marker CD11c (**Figure 8.1g**).

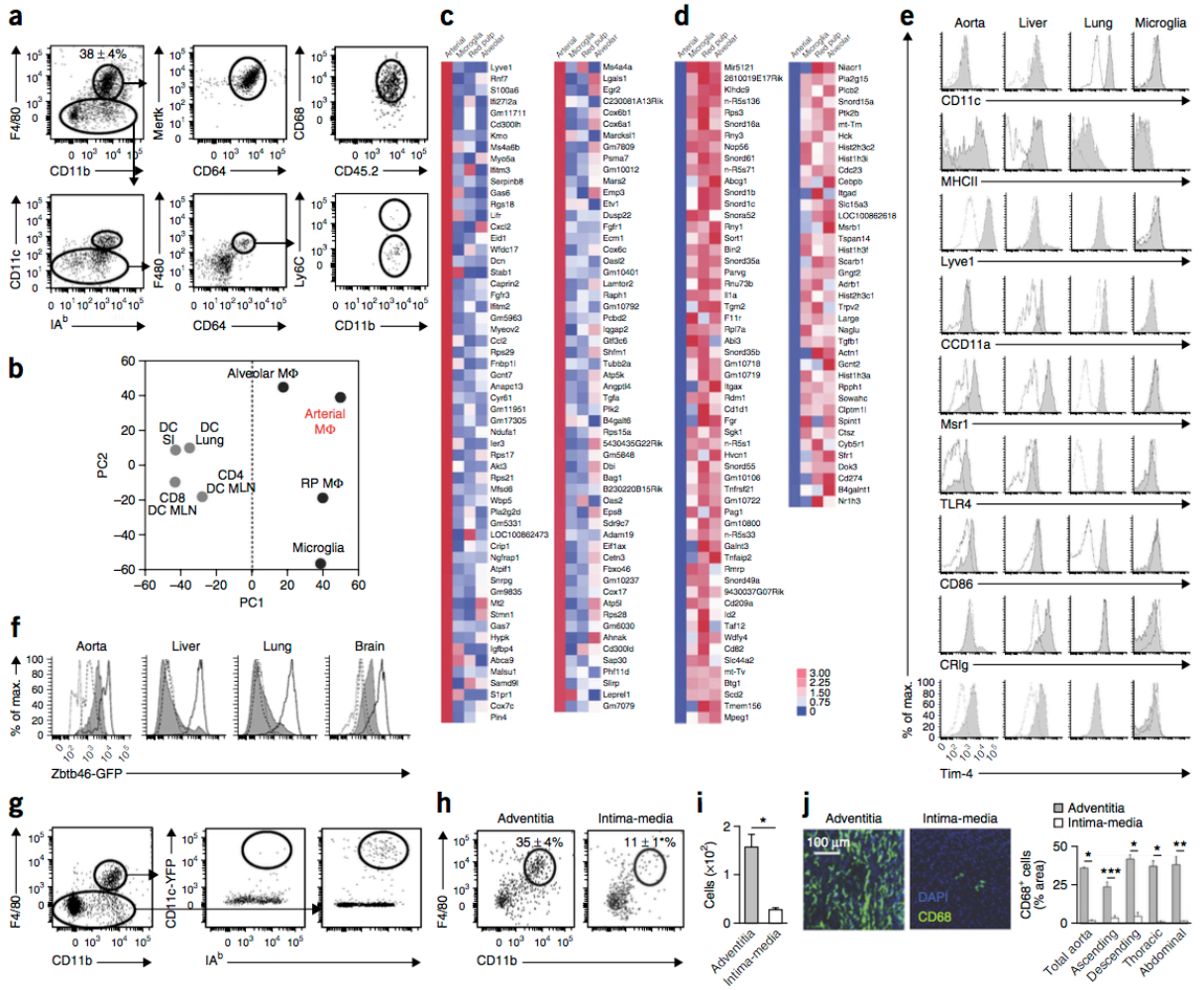

Figure 8.1. Phenotype and gene-expression profiling of arterial macrophages. (a) Identification of aortic macrophages. Dot plots show gating scheme for $F4/80^{+}CD11b^{+}$aortic macrophages, $F4/80^{lo}CD11c^{+}MHCII^{+}$ dendritic cells (DCs) and $Ly6C^{hi\text{-}lo}F4/80^{lo}CD64^{+}$ monocytes in 6- to 8-week-old C57BL6/J mice (mean ± s.e.m.; n = 15). Numbers adjacent to

outlined area indicate percentage of F4/80$^+$CD11b$^+$ aortic macrophages. **(b)** Principal component (PC) analysis of whole genome microarray data from isolated arterial macrophages compared to macrophages and DC populations collected by the Immunological Genome Project (GSE15907). For arterial macrophages, expression data are pooled from three independent experiments. **(c)** Heat map of mRNA transcripts increased in arterial macrophages by fivefold or more relative to their expression in microglia, splenic red pulp macrophages and alveolar macrophages. **(d)** Heat map of mRNA transcripts decreased in arterial macrophages by fivefold or more relative to their expression in the remaining 3 macrophage populations. **(e)** Flow cytometry analysis of cell surface markers expressed by arterial macrophages, Kupffer cells, alveolar macrophages and microglia (shaded curves). Open curves represent isotype controls. **(f)** Zbtb46-GFP expression in macrophages (shaded curves) and DC (open curves) from aorta, liver, lung and brain of *Zbtb46*$^{gfp/+}$ mice. One experiment of two is shown. Dashed lines, wild-type macrophages (GFP$^-$); dotted lines, wild-type DCs (GFP$^-$). **(g)** CD11c-eYPF expression in arterial macrophages and DCs from *CD11c*$^{eYFP/+}$ mice. Data are from one of three animals examined. **(h)** Flow cytometry analysis of arterial macrophages in adventitial and intima-media compartments (mean ± s.e.m.; adventitia $n = 27$, intima-media $n = 22$). Data are pooled from four independent experiments. *$P < 0.0001$ (unpaired *t*-test). Numbers adjacent to outlined areas indicate percentages of F4/80$^+$CD11b$^+$ macrophages. **(i)** Quantification of arterial macrophages from **h** (mean ± s.e.m.; adventitia $n = 27$, intima-media $n = 22$). Data are pooled from four independent experiments. *$P < 0.0001$ (unpaired Student's *t*-test). **(j)** CD68 staining of adventitia and intima-media from ascending, descending, thoracic and abdominal aortic segments (mean ± s.d.; $n = 3$). *$P <$ 0.0001 (total aorta, descending arch, thoracic arch), **$P < 0.0003$ (abdominal aorta), ***$P <$ 0.0006 (ascending arch) (unpaired *t*-test).

Intravenous administration of clodronate liposomes to mice depleted blood monocytes but not aortic macrophages (**Supplementary figure 1d**), indicating that arterial macrophages reside within the vessel wall. To examine the spatial distribution of arterial macrophages in more detail, we dissected the inner intimal and medial layers from the outer adventitia[20] and assessed the number of macrophages by flow cytometry. The adventitia contained significantly ($P < 0.05$) more CD45$^+$leukocytes than the intimal or medial layers of the vessel wall (**Supplementary figure 1e**). Consistent with this observation, macrophage number and percentage among CD45$^+$ cells (**Figure 8.1h,i**) were markedly higher in the adventitia than in the intima and media layers. We next used confocal microscopy to visualize CD68$^+$ cells in the intima, media and adventitia compartments of the aorta. On average, 29 ± 1% of the tissue area within the adventitia stained positive for CD68 (**Figure 8.1j**). In contrast, only 2.0 ± 0.2% of tissue area in the intima and media stained positive for CD68 (**Figure 8.1j**). Analysis at various locations in the aorta demonstrated comparable differences in macrophage content

within the adventitia and intima and media (**Figure 8.1j**). Consistent with published studies[21, 22], $CD11c^+$ DCs were most abundant in the intima of the aortic valves and arch (**Supplementary figure 1f**). We also detected macrophages in the carotid as well as femoral arteries (**Supplementary figure 1g**), indicating that resident macrophages occupy multiple arterial sites.

8. 3. 2 Arterial Macrophages Have Embryonic and Postnatal Origins

In many tissues, resident macrophages arise from embryonic precursors before birth.[5, 6, 7, 10, 11, 23] Similarly, arterial macrophages were observed in the aorta of mice at embryonic day 16.5 (E16.5) (**Figure 8.2a**). Flow cytometry revealed two phenotypically distinct cell populations expressing the macrophage marker F4/80 in the developing embryo: $F4/80^{hi}CD11b^{lo}$ cells that resembled YS-derived macrophages[6] and $F4/80^{int}CD11b^{hi}$ cells that appeared similar in phenotype to c-Myb–dependent fetal liver monocytes.[7, 23] At birth, arterial macrophages were predominately $F4/80^{hi}CD11b^{lo}$, although this phenotype was transient, and by 2 weeks of age the $F4/80^+$ cells in the aortic wall were mainly $F4/80^{int}CD11b^{hi}$ (**Figure 8.2a**). The proportion of arterial macrophages among $CD45^+$ cells increased with age (**Figure 8.2b**) and was associated with progressively increased expression of MHCII (**Figure 8.2c**), indicating a postnatal period of maturation.

The extra-embryonic YS is the main hematopoietic site in mice before E10.[4, 24] YS hematopoiesis supplies erythroid as well as myeloid precursors to the embryo after the onset of blood circulation at ~E9. Because arteries contained macrophages before birth, we investigated whether YS progenitors contributed to the arterial macrophage pool using pulse labeling of $CX3CR1^+$ progenitor cells in the YS.[15] Female *Cx3cr1*^{CreER} mice[25], which express Cre recombinase under the control of the *Cx3cr1* promoter upon exposure to tamoxifen (TAM), were crossed to male mice bearing the tdTomato red fluorescent reporter (*Rosa26*^{Tomato} mice) and injected with a single intraperitoneal dose of TAM at E8.5. This approach induces the 'preferential' and irreversible expression of the tdTomato reporter in YS-derived $CX3CR1^+$ cells and their progeny. In *Cx3cr1*^{CreER}; *Rosa26*^{Tomato} mice, 68 ± 8% of brain microglia showed tdTomato expression (Td^{tom+}) at E16.5, indicating robust labeling

efficiency of YS progenitors and their progeny (data not shown). Consistent with the hypothesis that YS progenitors give rise to arterial macrophages during embryogenesis, >40% of F4/80^{hi}CD11b^{lo}cells in aortas of mice at E16.5 and on the day of birth were Td^{tom+} (**Figure 8.2d–f**). Importantly, TAM injection labeled macrophages but not monocytes in fetal liver (**Supplementary figure 2a**) and did not label F4/80^{hi}CD11b^{lo} macrophages in the arterial wall (**Figure 8.2d**). Therefore, Td^{tom+} macrophages probably derive from early YS erythromyeloid progenitors [25] independently of a monocyte intermediate. Normalization of arterial macrophage labeling to labeling of microglia (% Td^{tom+} macrophages in the aorta / % Td^{tom+} microglia), which are entirely of YS origin[5, 26], indicated that ~60% of arterial macrophages at birth arise separate from fetal liver hematopoiesis (**Figure 8.2f**).

To address the possibility that fetal monocytes also contribute to the generation of arterial macrophages, we analyzed aortas in *Flt3*^{Cre} × *Rosa*$^{mT/mG}$ reporter mice. Definitive hematopoietic stem and progenitor cells (HSPC) transiently augment the receptor tyrosine kinase FLT3 during differentiation to all hematopoietic lineages.[27] The approach, therefore, allowed us to identify HSPC-dependent GFP^{+} macrophages (FLT3-Cre^{+}) and HSPC-independent GFP^{-} macrophages (FLT3-Cre^{-}). At birth, approximately 10 ± 1% and 28 ± 3% of F4/80^{hi}CD11b^{lo} and F4/80^{int}CD11b^{hi} arterial macrophages, respectively, were GFP^{+} and derived entirely from fetal monocytes (**Figure 8.2g**). Fetal monocytes are generated through both FLT3-dependent and FLT3-independent pathways.[10] The contribution of fetal liver hematopoiesis to development of the arterial macrophage pool, therefore, is likely to be underestimated. The data indicate that arterial macrophages are established through differentiation of early as well as late YS-derived EMPs.

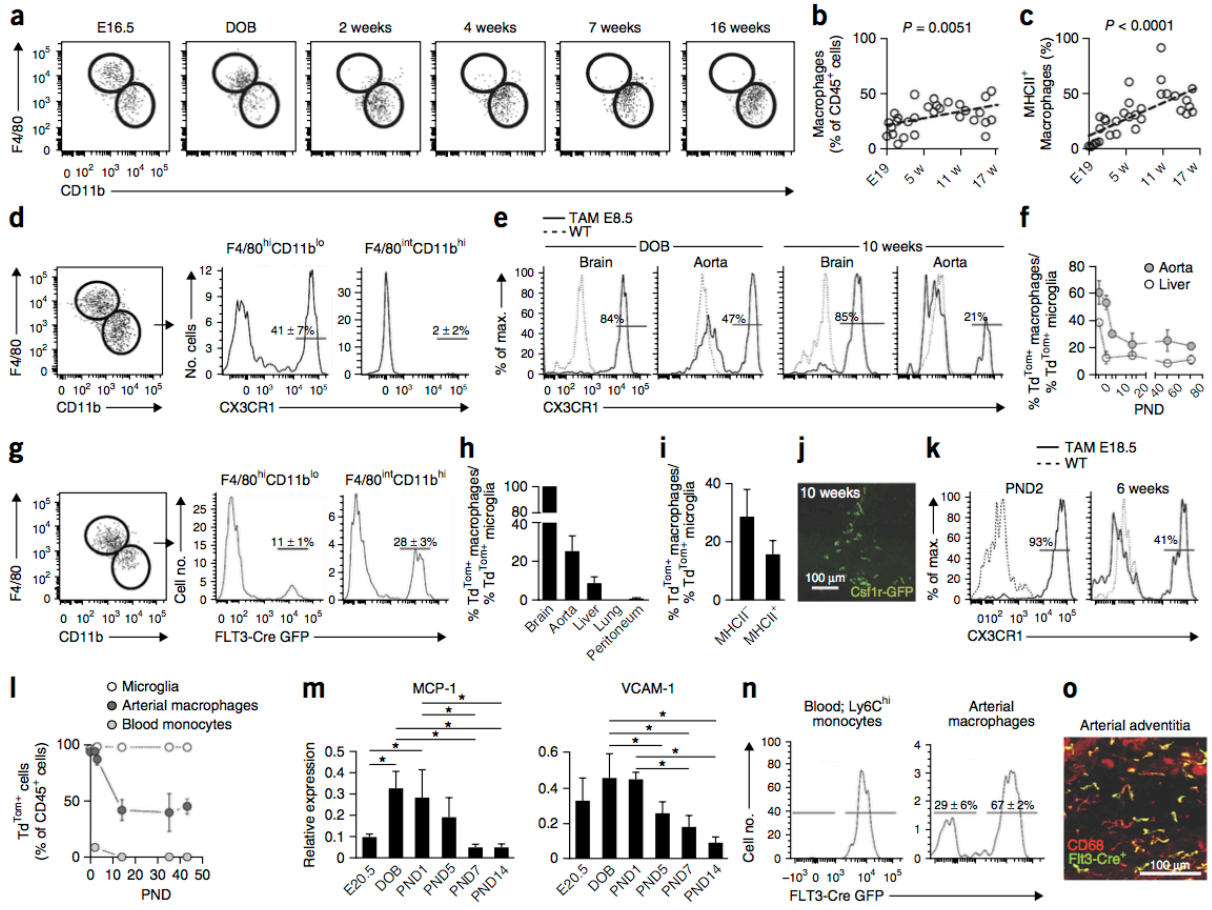

Figure 8.2. Arterial macrophages have embryonic and postnatal origins. (a) Phenotypic analysis of arterial macrophages before and after birth. Dot plots show F4/80 and CD11b staining at multiple ages. Outlined areas show F4/80^{hi}CD11b^{lo} and F4/80^{int}CD11b^{hi} macrophage populations. Representative data from one of three experiments. **(b)** Macrophage accumulation over time expressed as a percentage of total CD45^{+} leukocytes (n = 31 mice). Data points represent individual mice. P = 0.0051 (linear regression analysis). **(c)** Major histocompatibility (MHC) II expression on arterial macrophages over time (n = 34 mice). Data points represent individual mice. P < 0.0001 (linear regression analysis). **(d)** E8.5-induced CX3CR1-tdTomato expression in F4/80^{hi}CD11b^{lo}and F4/80^{int}CD11b^{hi} arterial macrophages at E16.5 (mean ± s.d.; n = 6). Representative data from 6 mice analyzed. Outlined areas on dot plots show F4/80^{hi}CD11b^{lo} and F4/80^{int}CD11b^{hi}macrophage populations. Gates indicate positive staining for CX3CR1. **(e)** E8.5-induced CX3CR1-tdTomato expression in arterial macrophages on day of birth [DOB] and 10 weeks of age. Gates indicate positive staining for CX3CR1. **(f)** Time course of E8.5-induced CX3CR1-tdTomato expression in arterial macrophages and Kupffer cells, normalized to CX3CR1-tdTomato expression in brain microglia (mean ± s.d.; E16.5 n = 6, DOB n = 7, postnatal day 3 (PND3) n = 1, PND13 n = 3, PND50 n = 3, PND70 n = 2). **(g)** Identification of FLT3-Cre^{+} (GFP^{+}) macrophages (aorta) in newborn [DOB] *Flt3*^{Cre} × *Rosa*$^{mT/mG}$ reporter mice (mean ± s.e.m.; n = 9). Data are representtative of one of nine mice examined. Gates indicate positive staining for FLT3-Cre GFP. **(h)**

CX3CR1-tdTomato expression in macrophages isolated from aorta, liver (Kupffer cells), lung (alveolar macrophages) and peritoneum normalized to CX3CR1-tdTomato expression in brain microglia. Macrophages isolated from mice at PND50 (mean ± s.d.; $n = 3$ mice per tissue). **(i)** CX3CR1-tdTomato expression in $MHCII^-$ and $MHCII^+$ arterial macrophages from mice at PND50 (mean ± s.d.; $n = 3$). **(j)** Immunofluorescence showing GFP^+ YS-derived arterial macrophages in aortic adventitia of adult *Csf1r*^{MeriCreMer} × *Rosa*^{mTmG} mice administered TAM at E8.5. Representative data from 3 mice examined. **(k)** CX3CR1-tdTomato expression in arterial macrophages of neonatal (PND2) and adult mice administered TAM at E18.5. Gates indicate positive staining for CX3CR1. **(l)** E18.5-induced CX3CR1-tdTomato expression in arterial macrophages, circulating $Ly6C^{hi}$ monocytes and microglia over time (mean ± s.d.; DOB $n = 1$, PND2 $n = 3$, PND3 $n = 2$, PND14 $n = 4$, PND35 $n = 2$, PND43 $n = 2$). **(m)** MCP-1 and VCAM-1 expression detected by RT-PCR in aortic tissue taken from mice at different time points (mean ± s.d.; $n = 4$ mice per time point except PND1, where $n = 3$). $^*P < 0.05$ (unpaired *t*-test). **(n)** Identification of FLT3-Cre^+ (GFP^+) monocytes (blood) and macrophages (aorta) in adult *Flt3*^{Cre} × *Rosa*$^{mT/mG}$ reporter mice (mean ± s.d.; $n = 3$). Representative data from 3 mice examined. **(o)** Immunofluorescence imaging from mice in **o** showing colocalization of FLT3-Cre recombination (GFP) and CD68 (Texas Red) in aortic adventitia of adult *Flt3*^{Cre} × *Rosa*$^{mT/mG}$ reporter mice.

In adult mice, E8.5-labeled Td^{tom+} YS progenitors contributed to the macrophage pool in the aorta to a greater extent than in the liver, lung and peritoneum (**Figure 8.2f,h**). Moreover, the appearance of $Td^{tom+}MHCII^+$arterial macrophages in adulthood (**Figure 8.2i**) indicated that $MHCII^-$ cells gave rise to $MHCII^+$ macrophages some time after birth, because arterial macrophages in newborn mice were $MHCII^-$ (**Figure 8.2c**). The persistence of YS-derived macrophages in the adult aorta was independently verified using *Csf1r*^{MeriCreMer} × *Rosa*^{mTmG} mice administered TAM at E8.5. These mice express the TAM-inducible MerCreMer fusion protein under control of the macrophage specific mouse *Csf1r* promoter. YS-derived macrophages appear as GFP^+ (**Figure 8.2j**). The decline in YS labeling of arterial macrophages from ~60% at birth to ~20% in adulthood (**Figure 8.2e,f**) could result from replacement of embryonic arterial macrophages by circulating monocytes.[9, 28]

To address this possibility, pregnant *Cx3cr1*^{CreER} mice were injected with TAM at E18.5. The approach labeled most arterial macrophages (and microglia) in *Cx3cr1*^{CreER}; *Rosa26*^{Tomato} mice at birth, but few blood monocytes (**Figure 8.2k,l**). tdTomato labeling in arterial macrophages, but not microglia, decreased during the first 2 weeks of life (**Figure 8.2k,l**), suggesting substantial turnover and replacement of arterial macrophages with unlabeled circulating monocytes. Consistent with these observations, monocyte influx was

associated with increased perinatal expression in the aorta of the chemokine CCL2 and the cellular adhesion molecules VCAM-1, E-selectin and ICAM-1 (**Figure 8.2m and Supplementary figure 2b**). We investigated the postnatal contribution of definitive hematopoiesis to the adult arterial macrophage pool further using *Flt3*^{Cre} × *Rosa*$^{mT/mG}$ reporter mice. *Flt3*^{Cre} × *Rosa*$^{mT/mG}$ Ly6C^{hi} blood monocytes were GFP^{+} and derived entirely from HSPC precursors (**Figure 8.2n**). In agreement with our earlier observations, arterial macrophages in mice comprised both GFP^{+} and GFP^{-} subsets, confirming the dual YS and HSPC origin of these cells (**Figure 8.2n,o**). These observations suggest successive waves of arterial macrophage colonization, initially by an embryonic wave derived from early YS EMP and fetal liver monocytes[9, 10, 11, 23]followed by a brief influx of bone marrow–derived monocytes immediately after birth.

8. 3. 3 CX3CL1-CX3CR1 Axis Determines Arterial Macrophage Survival

Described differences in tissue-specific macrophage requirements for the growth factors macrophage-colony stimulating factor (M-CSF) and granulocyte macrophage–colony stimulating factor (GM-CSF)[29, 30] led us to assess arterial macrophages in *Csf1*$^{-/-}$ and *Csf2*$^{-/-}$ mice, which lack the genes encoding M-CSF and GM-CSF, respectively. We found significantly ($P < 0.05$) fewer arterial macrophages in the arteries of *Csf1*$^{-/-}$, but not *Csf2*$^{-/-}$ mice than in wild-type mice (**Supplementary figure 3a,b**), consistent with other studies demonstrating profound macrophage deficiencies in M-CSF–deficient mice.[29]

Although many tissue macrophages lose expression of CX3CR1 as they mature[13], a large proportion of arterial macrophages in adult mice retain its expression (**Figure 8.3a–c and Supplementary figure 3c**). Therefore, we investigated whether CX3CR1 contributed directly to the maintenance of arterial macrophages. *Cx3cr1*$^{-/-}$ mice had fewer arterial macrophages than wild-type controls, as assessed by confocal microscopy (**Figure 8.3d**) and flow cytometry (**Figure 8.3e**). Neutralizing antibodies directed against the CX3CR1 ligand CX3CL1 also decreased arterial macrophage numbers in wild-type mice (**Figure 8.3f**). Arterial macrophage proliferation was unchanged in *Cx3Cr1*$^{-/-}$ mice compared to wild-type control mice (**Figure 8.3g**), but the percentage of Fas^{+} macrophages (**Figure 8.3h**) and the

number of TUNEL^{+}CD68^{+} cells (**Figure 8.3i**) was increased in the vessel adventitia, suggesting that CX3CR1-CX3CL1 controls the survival of arterial macrophages. We next used *Cx3cl1*^{cherry}mice[31], which have been modified to replace exon 1 of *Cx3cl1* with mCherry, to investigate the cellular source of CX3CL1. Confocal microscopy analysis of the arterial adventitia in *Cx3cl1*^{cherry} mice showed close proximity of CX3CL1^{+} (Cherry^{+}) cells and CD68^{+} resident macrophages (**Figure 8.3j**). Flow cytometry and immunofluorescence staining revealed two main populations of CX3CL1^{+} cells in the aorta of *Cx3cl1*^{cherry} mice, namely CD31^{+} endothelial cells and PDGFRα^{+}mesenchymal cells (**Figure 8.3k,l**). Therefore, arterial macrophage maintenance depends partially on a local CX3CR1-CX3CL1 axis.

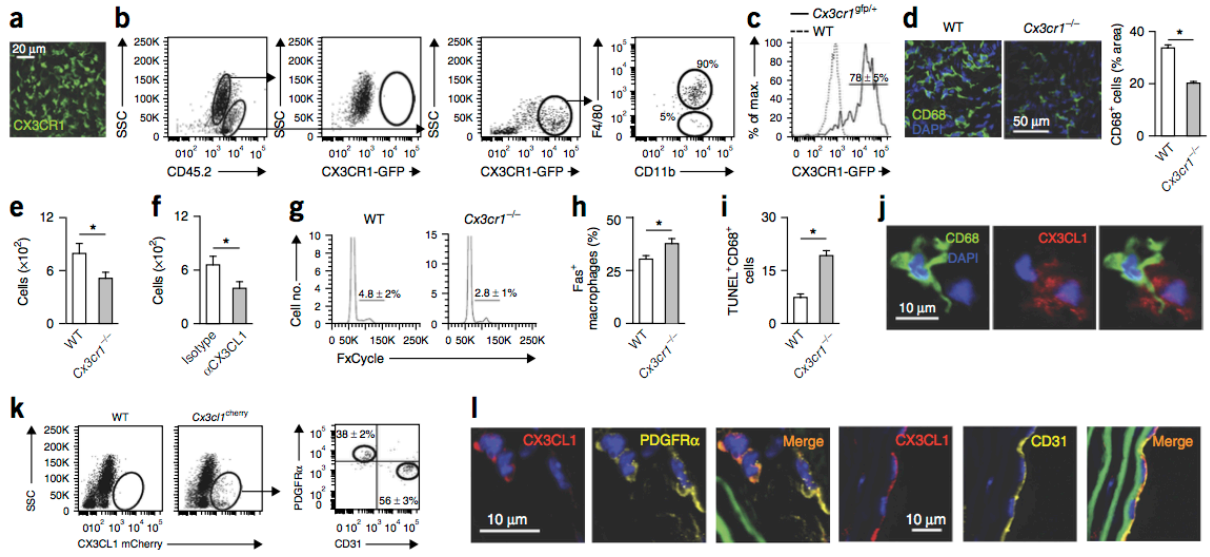

Figure 8.3. CX3CL1-CX3CR1 interactions determine survival of arterial macrophages. **(a)** Immunofluorescence showing GFP staining in aortic adventitia of *Cx3cr1*$^{gfp/+}$ mice. Representative image from 3 animals examined. **(b)** GFP staining of CD45^{+} arterial macrophages in aortas of *Cx3cr1*$^{gfp/+}$ mice. **(c)** CX3CR1 expression in F4/80^{+}CD11b^{+} arterial macrophages (mean ± s.d.; n = 3 mice; representative data from 2 experiments). Dot plots show CX3CR1 expression in CD45.2^{-} and CD45.2^{+} cells. Data show most CX3CR1 positive cells are F4/80^{+}CD11b^{+} macrophages. **(d)** CD68 staining of aortic adventitia and quantification of CD68^{+} cells in wild-type (WT) and *Cx3cr1*$^{-/-}$ mice. Data are means ± s.e.m.; n = 7 mice analyzed in one experiment. *P < 0.0001 (unpaired t-test). **(e)** Quantification of arterial macrophages in WT and *Cx3cr1*$^{-/-}$ mice, analyzed by flow cytometry. Data are pooled from three independent experiments (mean ± s.e.m.; WT n = 15, *Cx3cr1*$^{-/-}$ n = 14 mice). *P = 0.045 (unpaired t-test). **(f)** Arterial macrophage abundance in mice after antibody-mediated neutralization of CX3CL1. Data are pooled from two independent experiments (mean ± s.e.m.,

isotype $n = 11$, anti-CX3CL1 $n = 12$). $^*P = 0.042$ (unpaired t-test). **(g)** Per-centage of aortic macrophages from WT and *Cx3cr1*$^{-/-}$ mice in S and G2/M phases of the cell cycle (mean ± s.d.; WT $n = 4$, *Cx3cr1*$^{-/-}$ $n = 5$ mice). Data are from one experiment. $P = 0.09$ (unpaired t-test). **(h)** Percentage of aortic macrophages expressing Fas in WT and *Cx3cr1*$^{-/-}$ mice (mean ± s.e.m., $n = 7$). Data are from one experiment. $^*P = 0.0083$ (unpaired t-test). **(i)** Quantification of TUNEL$^+$CD68$^+$ cells in aortic adventitia of WT and *Cx3cr1*$^{-/-}$ mice (mean ± s.e.m., $n = 7$). $^*P < 0.0001$ (unpaired t-test). **(j)** Immuno-fluorescence showing association of adventitial aortic macrophages (CD68$^+$) with CX3CL1$^+$ cells in *Cx3cl1*^{cherry} mice. Representative image from one of five mice examined. **(k)** Arterial expression of CX3CL1 in CD45$^-$PDGFRα$^+$ and CD45$^-$CD31$^+$ cells. Data are from 3 mice (mean ± s.d.). Outlined areas show CX3CL1-expressing cells (left and middle) and PDGFRα and CD31 expression in CX3CL1$^+$ cells (right). **(l)** Localization of CX3CL1 and CD31$^+$ or PDGFRα$^+$ cells. Representative images from two experiments using 3 mice per group.

8. 3. 4 Arterial Macrophages Self-renew in Adulthood

To examine the mechanism of arterial macrophage renewal in adult mice, we examined the presence of arterial macrophages in mice deficient for the chemokine receptor CCR2 (*Ccr2*$^{-/-}$ mice), which have reduced numbers of circulating Ly6C^{hi} monocytes.[32] The arteries of wild-type and *Ccr2*$^{-/-}$ mice contained similar numbers of arterial macrophages (**Figure 8.4a**), which suggests that macrophage turnover at steady state occurs largely independently of circulating monocytes. To assess the rate of macrophage replacement in the arterial tissue, 8-week-old C57BL/6J and UBC-GFP mice, which express GFP under control of the human ubiquitin C promoter in all tissues, were joined by parabiosis for 8 months. Ly6C^{hi} and Ly6C^{lo} monocyte chimerism in the blood at equilibrium was high (~32% and ~41%, respectively; **Figure 8.4b**), as expected, but macrophage chimerism in the aorta of parabiotic mice was low (~6%), suggesting that monocyte contribution to the arterial macrophage pool was limited. Macrophage chimerism was similarly low in the heart, lung and liver of parabiotic mice[12] (**Figure 8.4b**). As shown in published studies[33], macrophage chimerism in the aorta alone in parabiotic mice underestimates the overall contribution of circulating monocytes to the arterial macrophage pool because Ly6C^{hi} monocyte chimerism in the blood, even at equilibrium, is only ~32% (**Figure 8.4b**). Assuming that individual GFP$^+$ and C57BL/6J monocytes can infiltrate the arterial wall equally well, for every C57BL/6J, partner-derived monocyte that entered the aorta of UBC-GFP mice, we also detected two endogenous

(GFP$^+$) infiltrating monocyte-derived macrophages. Hence, the total contribution of circulating monocytes (UBC-GFP and C57BL/6J) to macrophage accumulation was at most ~17% (**Figure 8.4c**). Local expansion, which accounts for the remaining ~83% of F4/80^{hi}CD11b$^+$ macrophages, dominated arterial macrophage renewal during steady-state conditions (**Figure 8.4c**). When we parabiotically linked *Ccr2*$^{-/-}$ and UBC-GFP (*Ccr2*$^{+/+}$) mice for 5 weeks, monocyte chimerism (GFP$^+$ cells) in the blood (CD115^{hi}) and aortas (F4/80^{int}CD11b$^+$Ly6G$^-$) of CCR2$^{-/-}$ partners was ~82% and ~73%, respectively (**Figure 8.4d**). Despite high chimerism of partner-derived wild-type monocytes in *Ccr2*$^{-/-}$ mice, chimerism of partner-derived F4/80^{hi}CD11b$^+$ arterial macrophages in *Ccr2*$^{-/-}$ mice remained low (~9%; **Figure 8.4d**). We also independently assessed the monocyte contribution to the arterial macrophage pool by pulse labeling adult *Cx3cr1*^{CreER} *Rosa26*^{Tomato} mice. TAM treatment induced CX3CR1-tdTomato expression in ~19% of blood Ly6C^{hi} monocytes and ~59% of arterial macrophages (**Figure 8.4e**). tdTomato expression remained high (~50%) among arterial macrophages at 9 and 11 months after labeling (**Figure 8.4e**) but was absent in blood monocytes[34] (**Supplementary figure 4a**), suggesting that maintenance of arterial macrophages depends little on blood monocytes.

Persistence of pulse-labeled CX3CR1$^+$ macrophages could also result from slow cell turnover. Therefore, arterial macrophage turnover was assessed in B6;129S4-*GtROSA26Sor*$^{tm1(rtTA*M2)Jae}$*Col1a1*$^{tm7(tetO-HIST1H2BJ/GFP)Jae}$/J(H2B-GFP) mice, in which doxycycline treatment induces H2B-GFP fluorescence labeling of cells ubiquitously.[35] Cellular expression of H2B-GFP was induced in adult mice by doxycycline treatment for 4 weeks, and the loss of GFP fluorescence per cell, which is indicative of cell division, was monitored during a 2-month chase period. As expected, H2B-GFP expression in blood monocytes and arterial macrophages exceeded background by orders of magnitude after 4 weeks of doxycycline (**Figure 8.4f and Supplementary figure 4b**). Consistent with observations that myeloid precursors turnover rapidly[35], expression of H2B-GFP in blood Ly6C^{hi} monocytes declined below the limit of detection after 2 months (**Supplementary figure 4b**). H2B-GFP expression was also completely lost in some arterial macrophages (~25%), and mean fluorescence intensity of the GFP signal was greatly reduced in others (**Figure 8.4f**),

indicating substantial turnover of arterial macrophages within 2 months. To estimate further the turnover and loss rate of arterial macrophages, we generated a mathematical model using a three-state absorbing continuous time Markov chain (CTMC). The approach assumed two transient states of GFP^{+}macrophages with different rates of GFP loss and one absorbing state, representing cells that have lost GFP expression (i.e., GFP^{-}macrophages) (Online Methods). Fitting the mathematical model to the observed dilution of the H2B-GFP signal in arterial macrophages suggested a turnover rate of ~84% every 12 months for these cells (**Figure 8.4g**). Independently, 5-bromodeoxyuridine (BrdU) injections into wild-type mice every other day for 9 d labeled 25% of aortic macrophages (**Figure 8.4h and Supplementary figure 4c**). Hence, arterial macrophage turnover is dynamic.

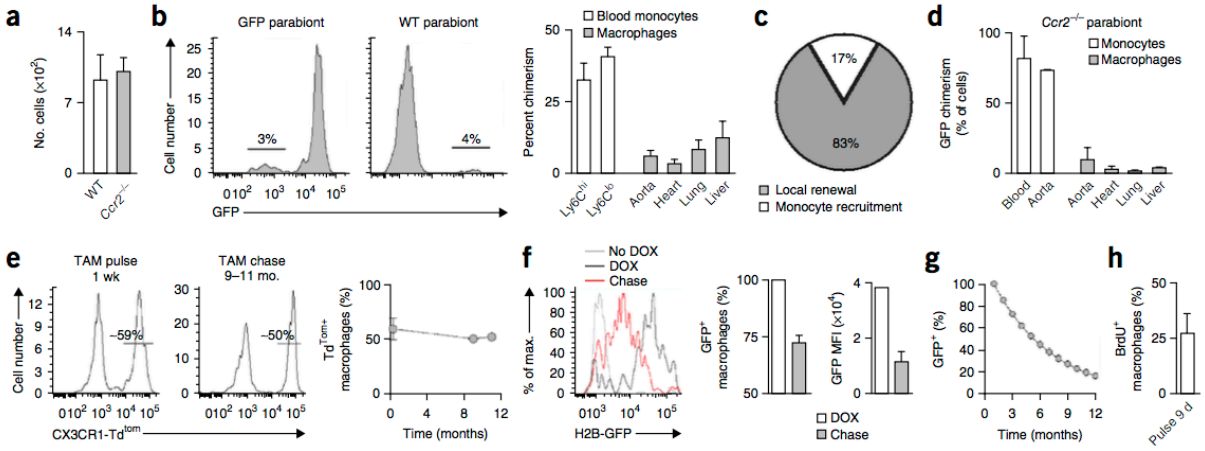

Figure 8.4. Arterial macrophages are maintained independently of monocytes in adulthood. (a) Quantification of aortic macrophages in wild-type (WT) and *Ccr2*$^{-/-}$ mice (mean ± s.e.m.; WT n = 6, *Ccr2*$^{-/-}$ n = 5). Data are pooled from two independent experiments. P = 0.79 (unpaired t-test). **(b)** WT and UBC-GFP mice were joined in parabiosis for 8 months. Ly6C^{hi}and Ly6C^{lo} monocyte chimerism in blood and macrophage chimerism in aorta, heart, lung and liver. Data are pooled from 6 (monocytes) or 2 (macrophages) pairs of parabionts (mean ± s.e.m.). **(c)** Relative contribution of local renewal and monocyte recruitment to macrophage accumulation over 8 months. **(d)** GFP and *Ccr2*$^{-/-}$ mice were joined in parabiosis for 6 weeks. Data show monocyte chimerism in the blood and macrophage chimerism in the aorta, heart, lung and liver. Data are from one pair of parabionts (mean ± s.d.). **(e)** CX3CR1-tdTomato expression in arterial macrophages 1 week and 9–11 months after TAM exposure (mean ± s.d.; 1 week n = 3, 9 months n = 2, 11 months n = 1). Gates indicate positive staining for CX3CR1. **(f)** Loss of fluorescence in aortic macrophages of adult H2B-GFP mice after induction of H2B-GFP expression by doxycycline [DOX] and

after a 2-month 'chase' period (mean ± s.d.; $n = 4$). Left, GFP expression in aortic macrophages from H2B-GFP mice. Middle, percentage of aortic macrophages that are GFP^+. Right, mean fluorescence intensity (MFI) of GFP expression in aortic macrophages. **(g)** Mathematical model predicting rate of loss of GFP^+ macrophages over time (Online Methods). **(h)** 5-bromodeoxyuridine (BrdU) incorporation by aortic macrophages (mean ± s.d.; $n = 5$). Data are from one experiment.

8. 3. 5 Arterial Macrophages Self-renew after Exposure to Bacteria

To address how arterial macrophages are replenished during inflammation, we assessed macrophage repopulation in irradiated $CD45.2^+$ mice transplanted with whole bone marrow from $CD45.1^+$ mice. Recipient mice showed near complete donor chimerism among blood leukocytes 6 months after transplantation (**Figure 8.5a**). Brain microglia excepted[36, 37], donor chimerism of resident macrophages in the liver, heart, lung and aorta exceeded 70% (**Figure 8.5a**), consistent with reports that lethal radiation impairs the local repopulation capacity of tissue-resident macrophages.[38]

To assess macrophage turnover after infection, we exposed mice to the Gram-negative bacterial cell wall component lipopolysaccharide (LPS) or subjected them to surgical puncture of the cecum. The number of $F4/80^{hi}CD11b^+CD115^+Lyve1^+$ resident arterial macrophages contracted immediately after LPS exposure or cecal puncture[39] (**Figure 8.5b and Supplementary figure 5a**). Depletion of resident macrophages was associated with accumulation of neutrophils (**Supplementary figure 5b**), $Ly6C^{hi}$ monocytes (**Figure 8.5b**) and a distinct macrophage population identified as $F4/80^{hi}CD11b^+CD115^-Lyve1^-$ (**Figure 8.5b,c and Supplementary figure 5c**). By 1 week after LPS exposure, resident $CD115^+Lyve1^+$ macrophage numbers rebounded to levels observed during steady-state conditions (**Figure 8.5b,c,e**), whereas neutrophils, monocytes and $CD115^-Lyve1^-$ macrophages were nearly absent (**Figure 8.5b,c and Supplementary figure 5b**). Arterial macrophage numbers rebounded in LPS-exposed *Ccr2*$^{-/-}$ mice as well (**Figure 8.5b**), indicating that local expansion rather than monocyte recruitment was the dominant mechanism of recovery. In agreement with this observation, LPS exposure in wild-type mice increased the number of aortic macrophages in S, G2 and M phases of the cell cycle compared to wild-type control mice (**Figure 8.5f**). In addition, we exposed parabiotic mice to LPS or subjected them

to cecal puncture. Partner chimerism was low among arterial resident $CD115^{+}Lyve1^{+}$ macrophages, yet chimerism of newly infiltrating $CD115^{-}Lyve1^{-}$ macrophages was high, suggesting that monocytes were the immediate precursors of these cells (**Figure 8.5c,d**). Intravenous transfer of $Ly6C^{hi}$ monocytes into LPS-treated mice showed that $Ly6C^{hi}$ monocytes gave rise to $CD115^{-}Lyve1^{-}$ macrophages but not $CD115^{+}Lyve1^{+}$ macrophages in the aorta (**Figure 8.5g**). Moreover, $CD115^{-}Lyve1^{-}$ arterial macrophages showed a greater *in vivo* capacity to phagocytose bacteria than $CD115^{+}Lyve1^{+}$ arterial macrophages (**Figure 8.5h**), indicating that functional differences exist between the two subsets of macrophages.

To determine whether YS-derived arterial macrophages respond differently than bone marrow–derived arterial macrophages, adult E8.5-labeled *Cx3cr1*^{CreER}; *Rosa26*^{Tomato} mice were exposed to LPS or subjected to cecal puncture and assessed the proportions of E8.5-labeled and unlabeled arterial macrophages during the macrophage recovery phase to determine whether one population was 'preferentially' expanded over the other. Neither LPS administration nor polymicrobial sepsis (cecal puncture) affected the percentage of $F4/80^{hi}CD11b^{+}$ macrophages that were $tdTom^{+}$ (**Figure 8.5i**), suggesting equal self-renewal capabilities of the two subsets of arterial macrophages during infection. Microarray analysis of aortic macrophages during homeostasis and after recovery from sepsis showed that bacterial exposure had little effect on the transcriptional program of self-renewing macrophages (**Figure 8.5j and Supplementary figure 5d**). Of 10,391 genes analyzed, only 12 were differentially expressed (10 at higher and 2 at lower levels) in arterial macrophages from mice subjected to cecal puncture and steady-state control mice. In addition, i*n vitro*, arterial macrophages could phagocytose bacteria before and after sepsis to the same extent (**Supplementary figure 5e**). Therefore, arterial macrophages return to functional homeostasis rapidly after infection.

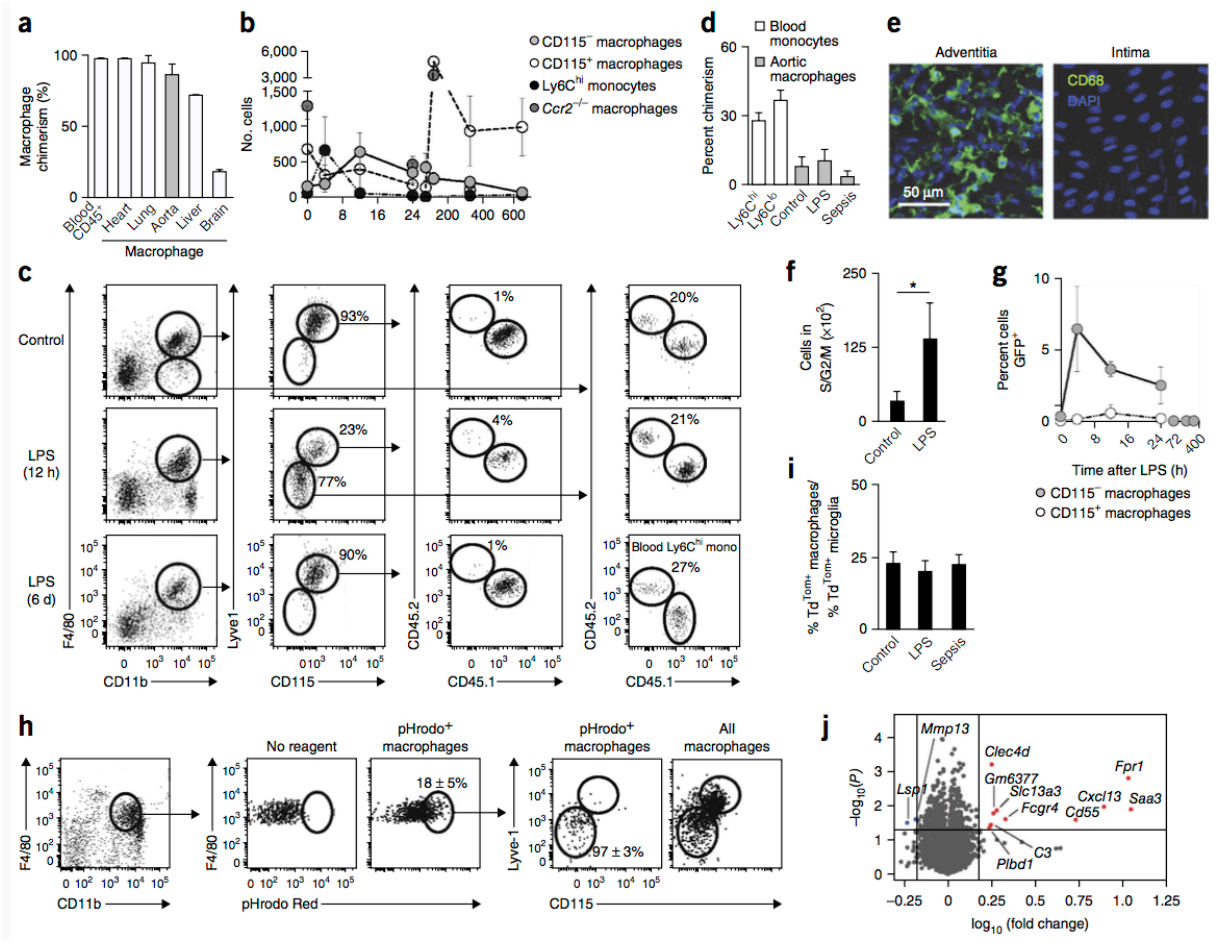

Figure 8.5. Arterial macrophages self-renew after exposure to bacteria. (a) Chimerism in blood CD45$^+$ leukocytes and macrophages in the heart, lung (alveolar), aorta, liver (Kupffer cells) and brain (microglia) of bone marrow chimeras generated by reconstituting lethally irradiated CD45.2$^+$ mice with CD45.1$^+$ bone marrow cells (mean ± s.d. from one experiment with n = 3 mice). **(b)** Quantification of Ly6C^{hi} monocytes, CD115$^+$macrophages (resident), CD115$^-$ macrophages (bone marrow monocyte–derived) and resident macrophages in *Ccr2*$^{-/-}$ mice after exposure to LPS. Data were collected at multiple time points (mean ± s.d.; day 0 n=8; 4h n=3; 12h n=3; 24h n=3; 72h n=4; 120h n=4; 336h n=3; 648h n=3). **(c)** Dot plots from CD45.1$^+$ parabiont showing chimerism in CD115$^+$Lyve1$^+$ and CD115$^-$Lyve1$^-$ macrophages. Gating in (left) shows CD115$^+$Lyve1$^+$ and CD115$^-$Lyve1$^-$ subsets gated through F4/80$^+$ CD11b$^+$ macrophages. Percentages (right) indicate partner chimerism. Data show a representtative CD45.1 partner. **(d)** Chimerism in blood monocytes and aortic macrophages 7 d after bacterial exposure in wild-type and UBC-GFP mice joined in parabiosis for 6 weeks and injected with lipopolysaccharide (LPS) or subjected to cecal puncture (mean ± s.d.; n = 4). Data are pooled from 2 pairs of parabionts. **(e)** CD68 staining in adventitia and intima of aorta 7 d after exposure to LPS. Representative image from 1 of 4 mice examined. **(f)** Number of aortic macrophages in S and G2/M phases of the cell cycle 5 d after LPS administration. Data are from one experiment (mean ± s.d., n = 6). *P = 0.0026 (unpaired t-test). **(g)** Percentage of

GFP^+ cells in $CD115^+$ (resident) and $CD115^-$(bone marrow monocyte–derived) macrophages in mice exposed to LPS and injected with flow-sorted $Ly6C^{hi}$ bone marrow monocytes at the indicated time points (mean ± s.d.; day 0 $n = 8$; 4 h $n = 3$; 12 h $n = 3$; 24 h $n = 3$; 72 h $n = 4$; 240 h $n = 4$; 336 h $n = 3$). **(h)** *In vivo* capacity of $CD115^-$ and $CD115^+$ macrophages to phagocytose pHrodo *Escherichia coli* BioParticles 12 h after exposure to LPS (mean ± s.e.m.; $n = 5$). Representative images from 1 of 5 mice analyzed in two independent experiments. **(i)** E8.5-induced CX3CR1-tdTomato expression in arterial macrophages 7 d after LPS administration or induction of sepsis by cecal puncture. Data are pooled from two independent experiments (mean ± s.e.m., control $n = 5$, LPS $n = 5$, sepsis $n = 4$ mice). **(j)** Gene-expression changes in aortic macrophages before and after sepsis. Of 10,391 genes analyzed, only 10 genes were upregulated (red) and 2 genes downregulated (blue) in macrophages from mice subjected to cecal puncture ($n = 3$ independently collected samples per experimental group).

8. 4 Discusstion

Here we identified the molecular signature of arterial macrophages, their developmental pathways and key mechanisms that ensure their homeostasis. We have shown that arterial macrophages are distinct among tissue-resident macrophages. Multiple fate-mapping approaches demonstrated that arterial macrophages originate embryonically from $CX3CR1^{+}$ precursors and postnatally from circulating monocytes immediately after birth. In adulthood, arterial macrophages were maintained by CX3CR1-CX3CL1 interactions and local proliferation rather than recruitment of circulating monocytes. Self-renewal also restored arterial macrophages to functional homeostasis after severe depletion induced by polymicrobial sepsis.

The microarray database generated by the Immunological Genome Consortium provides a valuable resource for comparing gene-expression profiles of macrophages from different organs.[14] Consistent with evidence demonstrating diversity among macrophage populations, our gene-expression and protein analyses revealed distinct patterns for arterial macrophages relative to other tissue macrophages. The data identified GO enrichment of transcripts with annotated functions that equip arterial macrophages for specialized local functions, supporting the concept that meaningful assessment of macrophage function requires careful consideration of the tissue context in which they reside.

Tissue macrophages arise from two distinct developmental programs: early YS-derived EMPs that give rise to macrophages without monocyte intermediates and fetal monocytes that derive from late c-Myb^{+} EMPs generated in the YS.[10, 11] These pathways contribute to macrophage development in several tissues, including the brain, skin, heart, liver and lung.[5, 8, 13, 23, 40, 41] Consistent with these findings, $F4/80^{hi}CD11b^{lo}$ arterial macrophages and $F4/80^{lo}CD11b^{hi}$ fetal monocytes were readily identified in aortas of embryonic (E16.5) mice. *Cx3cr1*-, *Csf1r*- and *Flt3*-driven fate-mapping approaches indicated that arterial macrophages were derived from early YS EMPs as well as fetal monocytes. Our data also indicated that arterial macrophage colonization associates with a period bone marrow–derived monocyte recruitment shortly after birth. Development of the arterial macrophage pool, therefore, is unique. The maintenance of intestinal macrophages also depends on circulating

monocytes, but renewal is constant and continues throughout adult life.[28] In arteries, the period of postnatal monocyte influx was brief, corresponding with transient expression of chemokines and cell adhesion molecules implicated in monocyte recruitment. Although adult arteries contained sizeable populations of both YS and bone marrow–derived macrophages, the relative contribution of the two subsets of macrophages to vessel homeostasis remains unknown.

In many tissues, resident macrophages lose expression of CX3CR1 during development.[13] In addition to retaining macrophage expression of the chemokine receptor in adulthood, CX3CL1 blockade and examination of *Cx3cr1*$^{-/-}$ mice indicated that CX3CR1-CX3CL1 interactions determine the survival of arterial macrophages, possibly through Fas-Fas ligand interactions. CX3CR1-CX3CL1 similarly promotes survival of macrophages in the brain[42], kidney[43], solid tumors[44] and circulating Ly6C^{lo} blood monocytes[45]. Visualization of the arterial macrophage niche using *Cx3cl1*^{cherry} reporter mice further showed that CD31^{+} endothelial cells and PDGFRα^{+} mesenchymal cells produced CX3CL1 locally in the artery; however, the relative contribution of these CX3CL1 producers to macrophage survival is not known. The data also suggested the dependence of macrophage survival in the arterial wall on signaling pathways other than CX3CR1, as not all arterial macrophages express the receptor and *Cx3cr1*$^{-/-}$ mice contain a moderate population of aortic macrophages. M-CSF deficiency was similarly associated with fewer arterial macrophages, although it remains to be determined whether M-CSF regulates macrophage differentiation, survival and/or proliferation.

Mathematical modeling of loss of arterial macrophages in H2B-GFP mice predicted near complete replacement of the macrophage population within ~1 year. Arterial macrophage turnover, therefore, is dynamic. Analysis of parabionts, *CCR2*$^{-/-}$ mice and pulse-labeled adult *Cx3cr1*^{CreER}; *Rosa26*^{Tomato} mice indicated that local proliferation rather than monocyte recruitment drives arterial macrophage renewal in the steady state and during polymicrobial sepsis. This result contrasts with a report on macrophage maintenance in the heart, where bone marrow–derived cells replace macrophages progressively with age.[9] The data further showed that the arterial macrophage response to bacteria is many-sided. Infection led first to the recruitment of Ly6C^{hi}monocytes and their differentiation into CD115^{-}Lyve1^{-} macrophages

that functioned to phagocytose bacteria. This was followed by the self-renewal and re-establishment of functional homeostasis of $CD115^{+}Lyve1^{+}$ resident macrophages. The diversity of origins (successive contributions of YS, fetal liver and conventional hematopoiesis) of arterial macrophages highlights the importance of tissue-specific extrinsic factors, including CX3CR1-CX3CL1 interactions, in maintaining their abundance. Of note, macrophage proliferation also amplifies arterial pathology, as has been observed in atherosclerosis.[33] Therefore, future design of therapeutic strategies that target arterial macrophages will require not only elucidation of the mechanisms that maintain them, but their activities in specific disease contexts.

8. 5 Author Contributions

S.E., A.L. and R.B. conceived the project, designed and performed experiments and analyzed and interpreted data.

N.D., J.C., M.R., M.E.M., J.W., E.S., C.L., B.L., L.R., T.J.Y., J.S.L., P.W., I.H., S.E., R.K. and K.F. performed experiments and helped interpret the data.

M.O., J.B., C.C.J.Z., G.A.L., C.M.T.B., P.L., M.H., F.K.S., C.C., M.P., I.H., G.J.R., S.E., A.O.G., M.C. and B.B.R. provided materials and intellectual input and edited the manuscript.

C.S.R. conceived the project, designed and performed experiments, supervised the study and wrote the manuscript.

8. 6 Acknowledgements

We acknowledge the administrative assistance of B. Bali. Supported by a Canadian Institutes of Health Research (CIHR) New Investigator Award (MSH136670), a CIHR operating grant (MOP133390), an Ontario Lung Association/Pfizer Award and the Peter Munk Chair in Aortic Disease Research (C.S.R.) and an Ontario Graduate Scholarship (S.E.).

8. 7 Additional Information

Any Supplementary Information and Source Data files are available in the online version of the paper. (https://www.nature.com/articles/ni.3343#supplementary-information)

8. 8 References

1. Akazaki, K. A concept of reticuloendothelial system. *Tohoku J Exp Med* **76**, 107-118 (1962).

2. Naito, M., Yamamura, F., Nishikawa, S. & Takahashi, K. Development, differentiation, and maturation of fetal mouse yolk sac macrophages in cultures. *J Leukoc Biol* **46**, 1-10 (1989).

3. van Furth, R. & Cohn, Z.A. The origin and kinetics of mononuclear phagocytes. *J Exp Med* **128**, 415-435 (1968).

4. Samokhvalov, I.M., Samokhvalova, N.I. & Nishikawa, S. Cell tracing shows the contribution of the yolk sac to adult haematopoiesis. *Nature* **446**, 1056-1061 (2007).

5. Ginhoux, F. *et al.* Fate mapping analysis reveals that adult microglia derive from primitive macrophages. *Science* **330**, 841-845 (2010).

6. Schulz, C. *et al.* A lineage of myeloid cells independent of Myb and hematopoietic stem cells. *Science* **336**, 86-90 (2012).

7. Hoeffel, G. *et al.* Adult Langerhans cells derive predominantly from embryonic fetal liver monocytes with a minor contribution of yolk sac-derived macrophages. *J Exp Med* **209**, 1167-1181 (2012).

8. Epelman, S. *et al.* Embryonic and adult-derived resident cardiac macrophages are maintained through distinct mechanisms at steady state and during inflammation. *Immunity* **40**, 91-104 (2014).

9. Molawi, K. *et al.* Progressive replacement of embryo-derived cardiac macrophages with age. *J Exp Med* **211**, 2151-2158 (2014).

10. Hoeffel, G. *et al.* C-Myb(+) erythro-myeloid progenitor-derived fetal monocytes give rise to adult tissue-resident macrophages. *Immunity* **42**, 665-678 (2015).

11. Gomez Perdiguero, E. *et al.* Tissue-resident macrophages originate from yolk-sac-derived erythro-myeloid progenitors. *Nature* **518**, 547-551 (2015).

12. Hashimoto, D. *et al.* Tissue-resident macrophages self-maintain locally throughout adult life with minimal contribution from circulating monocytes. *Immunity* **38**, 792-804 (2013).

13. Yona, S. *et al.* Fate mapping reveals origins and dynamics of monocytes and tissue macrophages under homeostasis. *Immunity* **38**, 79-91 (2013).

14. Gautier, E.L. *et al.* Gene-expression profiles and transcriptional regulatory pathways that underlie the identity and diversity of mouse tissue macrophages. *Nat Immunol* **13**, 1118-1128 (2012).

15. Majesky, M.W., Dong, X.R., Hoglund, V., Mahoney, W.M., Jr. & Daum, G. The adventitia: a dynamic interface containing resident progenitor cells. *Arterioscler Thromb Vasc Biol* **31**, 1530-1539 (2011).

16. Jakubzick, C. *et al.* Minimal differentiation of classical monocytes as they survey steady-state tissues and transport antigen to lymph nodes. *Immunity* **39**, 599-610 (2013).

17. Meredith, M.M. *et al.* Expression of the zinc finger transcription factor zDC (Zbtb46, Btbd4) defines the classical dendritic cell lineage. *J Exp Med* **209**, 1153-1165 (2012).

18. Satpathy, A.T. *et al.* Zbtb46 expression distinguishes classical dendritic cells and their committed progenitors from other immune lineages. *J Exp Med* **209**, 1135-1152 (2012).

19. McGovern, N. *et al.* Human dermal CD14(+) cells are a transient population of monocyte-derived macrophages. *Immunity* **41**, 465-477 (2014).

20. Galkina, E. *et al.* Lymphocyte recruitment into the aortic wall before and during development of atherosclerosis is partially L-selectin dependent. *J Exp Med* **203**, 1273-1282 (2006).

21. Choi, J.H. *et al.* Identification of antigen-presenting dendritic cells in mouse aorta and cardiac valves. *J Exp Med* **206**, 497-505 (2009).

22. Choi, J.H. *et al.* Flt3 signaling-dependent dendritic cells protect against atherosclerosis. *Immunity* **35**, 819-831 (2011).

23. Guilliams, M. *et al.* Alveolar macrophages develop from fetal monocytes that differentiate into long-lived cells in the first week of life via GM-CSF. *J Exp Med* **210**, 1977-1992 (2013).

24. Medvinsky, A. & Dzierzak, E. Definitive hematopoiesis is autonomously initiated by the AGM region. *Cell* **86**, 897-906 (1996).

25. Parkhurst, C.N. *et al.* Microglia promote learning-dependent synapse formation through brain-derived neurotrophic factor. *Cell* **155**, 1596-1609 (2013).

26. Prinz, M. & Priller, J. Microglia and brain macrophages in the molecular age: from origin to neuropsychiatric disease. *Nat Rev Neurosci* **15**, 300-312 (2014).

27. Karsunky, H., Merad, M., Cozzio, A., Weissman, I.L. & Manz, M.G. Flt3 ligand regulates dendritic cell development from Flt3+ lymphoid and myeloid-committed progenitors to Flt3+ dendritic cells in vivo. *J Exp Med* **198**, 305-313 (2003).

28. Bain, C.C. *et al.* Constant replenishment from circulating monocytes maintains the macrophage pool in the intestine of adult mice. *Nat Immunol* **15**, 929-937 (2014).

29. Davies, L.C., Jenkins, S.J., Allen, J.E. & Taylor, P.R. Tissue-resident macrophages. *Nat Immunol* **14**, 986-995 (2013).

30. Ginhoux, F. & Jung, S. Monocytes and macrophages: developmental pathways and tissue homeostasis. *Nat Rev Immunol* **14**, 392-404 (2014).

31. Kim, K.W. *et al.* In vivo structure/function and expression analysis of the CX3C chemokine fractalkine. *Blood* **118**, e156-167 (2011).

32. Serbina, N.V. & Pamer, E.G. Monocyte emigration from bone marrow during bacterial infection requires signals mediated by chemokine receptor CCR2. *Nat Immunol* **7**, 311-317 (2006).

33. Robbins, C.S. *et al.* Local proliferation dominates lesional macrophage accumulation in atherosclerosis. *Nat Med* **19**, 1166-1172 (2013).

34. Goldmann, T. *et al.* A new type of microglia gene targeting shows TAK1 to be pivotal in CNS autoimmune inflammation. *Nat Neurosci* **16**, 1618-1626 (2013).

35. Foudi, A. *et al.* Analysis of histone 2B-GFP retention reveals slowly cycling hematopoietic stem cells. *Nat Biotechnol* **27**, 84-90 (2009).

36. Mildner, A. *et al.* Microglia in the adult brain arise from Ly-6ChiCCR2+ monocytes only under defined host conditions. *Nat Neurosci* **10**, 1544-1553 (2007).

37. Ajami, B., Bennett, J.L., Krieger, C., Tetzlaff, W. & Rossi, F.M. Local self-renewal can sustain CNS microglia maintenance and function throughout adult life. *Nat Neurosci* **10**, 1538-1543 (2007).

38. Sieweke, M.H. & Allen, J.E. Beyond stem cells: self-renewal of differentiated macrophages. *Science* **342**, 1242974 (2013).

39. Barth, M.W., Hendrzak, J.A., Melnicoff, M.J. & Morahan, P.S. Review of the macrophage disappearance reaction. *J Leukoc Biol* **57**, 361-367 (1995).

40. Kierdorf, K. *et al.* Microglia emerge from erythromyeloid precursors via Pu.1- and Irf8-dependent pathways. *Nat Neurosci* **16**, 273-280 (2013).

41. Chorro, L. *et al.* Langerhans cell (LC) proliferation mediates neonatal development, homeostasis, and inflammation-associated expansion of the epidermal LC network. *J Exp Med* **206**, 3089-3100 (2009).

42. Boehme, S.A., Lio, F.M., Maciejewski-Lenoir, D., Bacon, K.B. & Conlon, P.J. The chemokine fractalkine inhibits Fas-mediated cell death of brain microglia. *J Immunol* **165**, 397-403 (2000).

43. Lionakis, M.S. *et al.* CX3CR1-dependent renal macrophage survival promotes Candida control and host survival. *J Clin Invest* **123**, 5035-5051 (2013).

44. Zheng, J. *et al.* Chemokine receptor CX3CR1 contributes to macrophage survival in tumor metastasis. *Mol Cancer* **12**, 141 (2013).

45. Landsman, L. *et al.* CX3CR1 is required for monocyte homeostasis and atherogenesis by promoting cell survival. *Blood* **113**, 963-972 (2009).

CHAPTER 9
(APPENDIX V)

9 Identification of a Novel Heart–Liver Axis: Matrix Metalloproteinase-2 Negatively Regulates Cardiac Secreted Phospholipase A_2 to Modulate Lipid Metabolism and Inflammation in the Liver

Samuel Hernandez-Anzaldo[1], Evan Berry[1], Vesna Brglez[2], Dickson Leung[1], Tae Jin Yun[3,4], Jun Seong Lee[3,5], Janos G. Filep[6], Zamaneh Kassiri[7,8,9], Cheolho Cheong[3,4,5], G_erard Lambeau[2], Richard Lehner[10,11], Carlos Fernandez-Patron[1,8,9]

[1]Departments of Biochemistry, Faculty of Medicine and Dentistry, University of Alberta, Edmonton, Alberta, Canada

[2]Institut de Pharmacologie Moléculaire et Cellulaire, Centre National de la Recherche Scientifique, Université de Nice-Sophia Antipolis, Valbonne, France

[3]Laboratory of Cellular Physiology and Immunology, Institut de Recherches Cliniques de Montréal, Montréal, Canada

[4]Division of Experimental Medicine, Department of Medicine, McGill University, Montréal, Canada

[5]Department of Microbiology, Infectiology, and Immunology, Université de Montréal, Montréal, Canada

[6]Innate Immunity System (Inflammation) and Vascular Immunology, The Maisonneuve-Rosemont Hospital Research Centre, University of Montreal, Quebec, Canada.

[7]Departments of Physiology, Faculty of Medicine and Dentistry, University of Alberta, Edmonton, Alberta, Canada

[8]Cardiovascular Research Group, Faculty of Medicine and Dentistry, University of Alberta, Edmonton, Alberta, Canada

[9]Mazankowski Alberta Heart Institute, Faculty of Medicine and Dentistry, University of Alberta, Edmonton, Alberta, Canada

[10]Departments of Pediatrics, Faculty of Medicine and Dentistry, University of Alberta, Edmonton, Alberta, Canada

[11]Group on Molecular and Cell Biology of Lipids, Faculty of Medicine and Dentistry, University of Alberta, Edmonton, Alberta, Canada

Correspondence to:

Carlos Fernandez-Patron (cf2@ualberta.ca)
Medical Sciences Building, Edmonton, Alberta, Canada

Journal of the American Heart Association. (2015). 13;4(11):
doi: 10.1161/JAHA.115.002553.

9. 1 Abstract

Endocrine functions of the heart have been well established. We investigated the hypothesis that cardiac secretion of a unique phospholipase A_2 recently identified by our laboratory (cardiac secreted phospholipase A_2 [$sPLA_2$]) establishes a heart–liver endocrine axis that is negatively regulated by matrix metalloproteinase−2 (MMP−2). In *Mmp2*$^{-/-}$ mice, cardiac (but not hepatic) $sPLA_2$ was elevated, leading to hepatic inflammation, immune cell infiltration, dysregulation of the sterol regulatory element binding protein−2 and liver X receptor−α pathways, abnormal transcriptional responses to dietary cholesterol, and elevated triglycerides in very low−density lipoprotein and in the liver. Expression of monocyte chemoattractant protein−3, a known MMP−2 substrate, was elevated at both mRNA and protein levels in the heart. Functional studies including in vivo antibody neutralization identified cardiac monocyte chemoattractant protein 3 as a possible agonist of cardiac $sPLA_2$ secretion. Conversely, systemic $sPLA_2$ inhibition almost fully normalized the cardiohepatic phenotype without affecting monocyte chemoattractant protein−3. Finally, wild−type mice that received high−performance liquid chromatography–isolated cardiac $sPLA_2$from *Mmp2*$^{-/-}$ donors developed a cardiohepatic gene expression profile similar to that of *Mmp2*$^{-/-}$ mice. These findings identified the novel MMP−2/cardiac $sPLA_2$pathway that endows the heart with important endocrine functions, including regulation of inflammation and lipid metabolism in the liver. Our findings could also help explain how *MMP2* deficiency leads to cardiac problems, inflammation, and metabolic dysregulation in patients.

9. 2 Introduction

Matrix metalloproteinase−2 (MMP−2), sometimes referred to as gelatinase A or 72 kDa collagenase, is a member of a family comprising 25 different Zn−dependent endo-proteases. A spectrum of cellular processes covering cellular proliferation, angiogenesis, and inflammation is modulated through MMP−2–dependent cleavage and regulation of extra-cellular matrix components, cell membrane receptors, latent growth factors, and cytokines.[1]

Among the cytokines targeted by MMP−2 is monocyte chemoattractant protein−3 (MCP−3 encoded by *Ccl7*).[2, 3] MCP−3 is a CC−motif (N−terminus has 2 consecutive conserved cysteine residues) chemokine that is 76 amino acids long. Binding of the hemopexin domain of MMP−2 to MCP−3 facilitates cleavage of MCP−3 at a glycine/isoleucine bond. The resultant MCP−3 peptide serves as a general antagonist of CC−chemokine receptors that inhibits inflammation signaling by intact MCP−3 and other chemokine receptor ligands.[2]

MCP−3 is also reported to be a physiological substrate of MMP−2 in arthritis.[2] Interestingly, humans with genetic loss of MMP−2 activity suffer from crippling arthritis[4, 5, 6] and a spectrum of cardiovascular problems including congenital cardiac malformations, transposition of the great arteries, mitral valve prolapse, bicuspid aortic valve, and atrial and ventricular septal defects.[4, 7] The molecular mechanisms underlying these pathologies are unknown, leaving clinicians without effective treatments.[4] In addition to inflammatory diseases, obesity has been linked to single−nucleotide polymorphisms in the human *MMP2* gene[8] and *MMP2* gene promoter.[9] Genetic loss of MMP−2 ($Mmp2^{-/-}$) in mice results in an arthritis−like phenotype associated with skeletal, bone, and craniofacial defects.[5] In addition, $Mmp2^{-/-}$ mice resist diet−induced obesity during development[10, 11], exhibit cardiac inflammation at baseline[12], and are predisposed to hypertensive heart disease due to abnormal regulation of the sterol regulatory binding protein 2 (SREBP−2) pathway in the heart.[13]

The evident coexistence of inflammation and metabolic dysregulation with MMP−2 deficiency is of potential clinical significance but is very poorly understood. In this study, we report that the hepatic metabolic phenotype in $Mmp2^{-/-}$ mice can be largely explained by a novel heart–liver axis involving myocardial secretion of a unique phospholipase A_2 (PLA_2),

which we coined *cardiac secreted PLA_2* ($sPLA_2$).[12] Our findings identify a novel functional link between cardiac inflammation and hepatic metabolism.

9. 3 Results

9. 3. 1 Loss of MMP−2 Affects Systemic Metabolism

Compared with age−matched WT mice, male *Mmp2*$^{-/-}$ mice aged 10 to 14 weeks exhibited normal food intake and reduced locomotor activity that were associated with decreased body weight and increased energy expenditure (**Figure 9.1**).

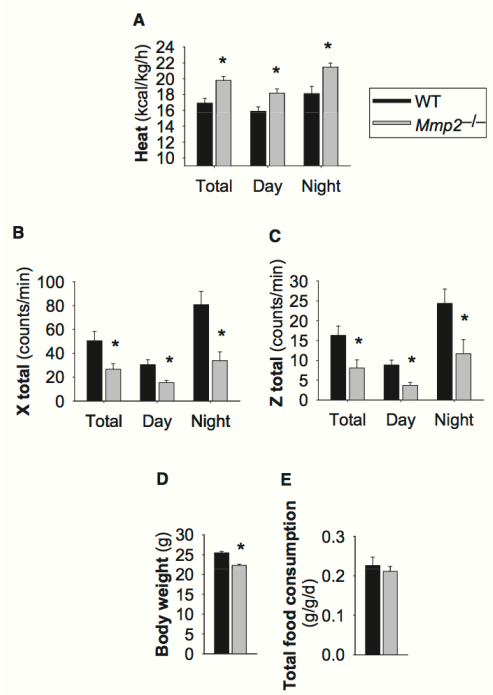

Figure 9.1. Systemic metabolic abnormalities of matrix metalloproteinase 2–deficient mice. (A) Heat/energy expenditure (normalized to body weight). **(B and C)** Locomotor activity. **(D)** Body weight. E, Total food consumption. n=11 *Mmp2*$^{-/-}$ mice, n=5 WT mice. **P*≤0.05 vs WT. The studies were conducted in metabolic cages. WT indicates wild type.

Loss of MMP−2 was associated with changes in hepatic and plasma lipids: Fasted *Mmp2*$^{-/-}$ mice had elevated triglycerides in the liver (**Figure 9.2A and 9.2B**) and very low−density lipoprotein (**Figure 9.2C, top**) and decreased cholesterol in high−density lipoprotein (**Figure 9.2C, bottom**). Nonfasted *Mmp2*$^{-/-}$ mice also had elevated hepatic triglycerides (**Figure 9.2D**).

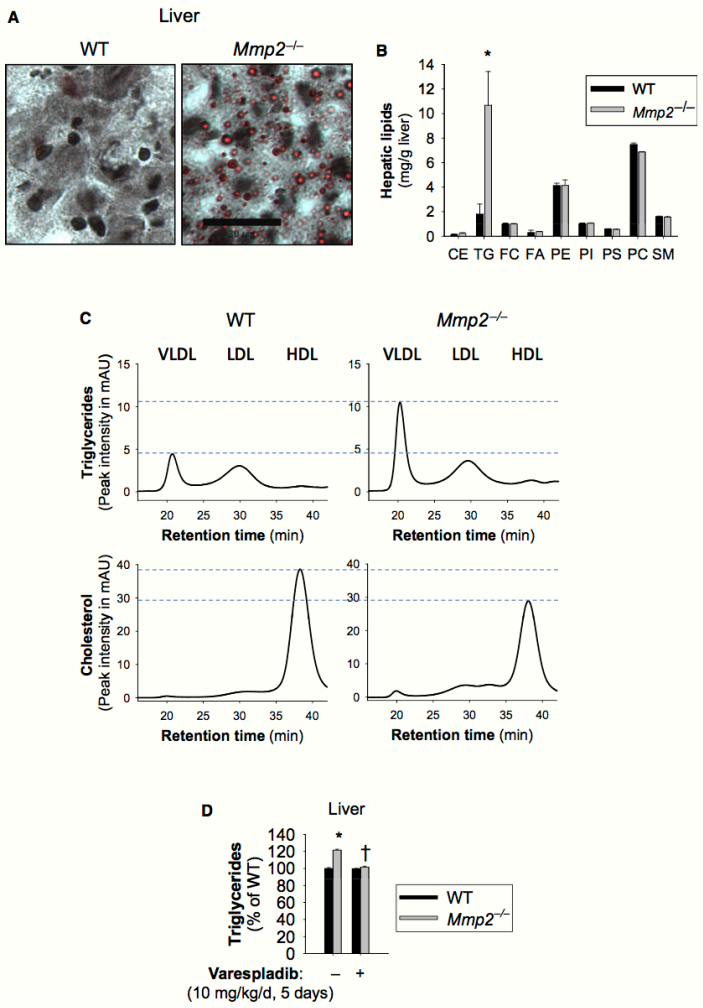

Figure 9.2. Matrix metalloproteinase 2 deficiency is associated with ab-normalities in lipid storage and transport. (A) Oil Red O stain of neutral lipid species from frozen liver sections of fasted mice. Scale bar=30 μm. **(B)** Fasting levels of hepatic lipids in *Mmp2*$^{-/-}$ vs WT mice as assessed by high performance liquid chromatography with in−line evaporative light scattering detection. n=3 per genotype. **P*<0.05 vs WT. **(C)** Fasted TG and cholesterol levels in lipoparticle fractions of plasma separated by fast−performance liquid chromatography (left). Traces correspond to pools of plasma from *Mmp2*$^{-/-}$ and WT. **(D)** Hepatic TGs were elevated in nonfasting mice. Gavage treatment with vehicle or pan–secreted phospholipase A_2 inhibitor varespladib; normalized hepatic TG levels in nonfasting *Mmp2*$^{-/-}$ mice. n=4 individual mice per genotype per group (or treatment). **P*≤0.05 vs WT. †*P*≤0.05 vs *Mmp2*$^{-/-}$ administered vehicle. CE indicates cholesteryl esters; FA, free fatty acids; FC, free cholesterol; HDL, high−density lipoprotein; mAU, milliabsorbance units; LDL, low−density lipoprotein; PC, phosphatidyl choline; PE, phosphatidyl ethanolamine; PI, phosphatidyl inositol; PS, phosphatidyl serine; SM, sphingomyelin; TG, triglyceride; VLDL, very low−density lipoprotein; WT, wild type.

The qRT−PCR analysis revealed *Nr1h3* (encoding LXR−α) to be the most down-regulated gene in the liver of *Mmp2*$^{-/-}$ mice (**Figure 9.3A**). Reduced LXR−α protein was confirmed by western blotting (**Figure 9.3B**). Consistent with LXR−α promotion of the transcription of genes involved in fatty acid synthesis[14], mRNA expression of hepatic *Fasn* (encoding fatty acid synthase) was repressed in *Mmp2*$^{-/-}$ mice (**Figure 9.3A**). Likewise, expression of another LXR−α target, lysophosphatidylcholine acyltransferase 3 (LPCAT3, encoded by *Lpcat3*), was downregulated (**Figure 9.3A**). LPCAT3 catalyzes the attachment of polyunsaturated fatty acids to membrane phospholipids.[15, 16] Downregulation of LXR−α

and *Lpcat3* (one of its target genes) suggested a potential link between the metabolic phenotype of MMP−2 deficiency and hepatic membrane phospholipid remodeling, a process potentially associated with inflammation signaling in MMP−2–deficient mice[12] and that was investigated in the experiments described below.

The hepatic gene expression phenotype in *Mmp2*$^{-/-}$ mice was complex, with some LXR−α target genes being significantly upregulated, for example, cholesterol 7α−hydroxylase (the rate−limiting enzyme in the classical bile acid biosynthesis pathway, encoded by *Cyp7a1*) and ATP−binding cassette G5 and G8 (2 cholesterol transporters, encoded by *Abcg5* and *Abcg8*) (**Figure 9.3C**).

Moreover, we detected increased hepatic expression of the transcription factor SREBP−2 (encoded by *Srebf2*) and many of its target genes including *Hmgcr*, *Ldlr*, and *Pcsk9* in *Mmp2*$^{-/-}$mice (**Figure 9.3C**). *Hmgcr* encodes 3−hydroxy−3−methylglutaryl−coenzyme A reductase, the rate−limiting enzyme in the cholesterol and isoprenoid synthesis pathways. *Ldlr* encodes the low−density lipoprotein receptor, which is involved in clearance of low−density lipoprotein from circulation. *Pcsk9* encodes proprotein convertase subtilisin/kexin type 9, a protein that binds and negatively regulates hepatic low−density lipoprotein receptor protein levels.[17] The upregulation of SREBP−2 protein and its proteolytically processed transcriptionally active form (nuclear SREBP−2) was confirmed by western blotting (**Figure 9.3D**) and was restricted to cardiac and hepatic tissues (**Figure S1**). LXR−α and SREBP−2 expression profiles were similar in *Mmp2*$^{-/-}$ and haploinsufficient (*Mmp2*$^{+/-}$) mice (**Figure 9.3E, left panel**). Furthermore, male and female *Mmp2*$^{-/-}$ mice exhibited similar gene expression profiles, demonstrating lack of sexual dimorphism in the regulation of LXR−α or SREBP−2 by MMP−2 (**Figure 9.3E, right panel**). Loss of MMP−2 (or MMP−7 or MMP−9, as determined in studies with *Mmp7*$^{-/-}$ and *Mmp9*$^{-/-}$ mice) (**Figure S2**) had only a limited impact on carbohydrate and nitrogen metabolism and bile acid production. Of note, insulin resistance was evident in the stress phase of the insulin−tolerance test, which is driven by adrenocorticotropic hormone–mediated signals such as cortisol release from the adrenals.[18] These data revealed MMP−2 as a modulator of the hepatic LXR and SREBP pathways.

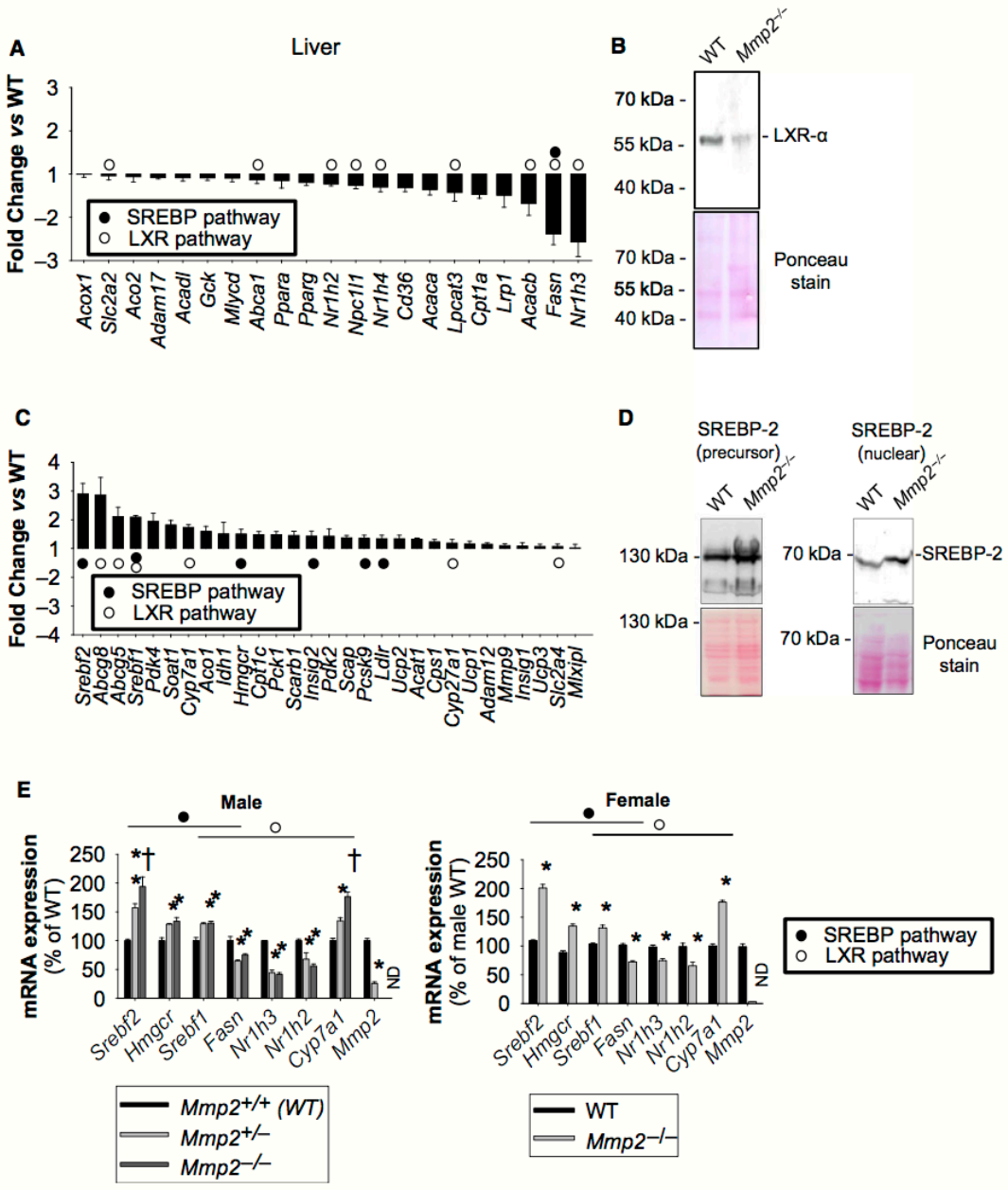

Figure 9.3. Lipid metabolic gene expression profile analysis of the hepatic phenotype of MMP−2–deficient mice. (A) qRT−PCR analysis identified several downregulated metabolic genes in *Mmp2*$^{-/-}$ mice. These results are representative of 4 mice per genotype. The data for the LXR−α (encoded by *Nr1h3*) pathway genes were confirmed in multiple studies and different batches of WT and *Mmp2*$^{-/-}$ mice. **(B)** Western blot confirming reduced hepatic LXR−α protein in *Mmp2*$^{-/-}$mice. Pool of 4 per genotype. **(C)** qRT−PCR analysis identified several upregulated metabolic genes in *Mmp2*$^{-/-}$mice. These results are representative of 4 mice per genotype. The data for the SREBP−2 (encoded by *Srebf2*) pathway genes were confirmed in multiple studies and different batches of WT and *Mmp2*$^{-/-}$ mice. **(D)** Western blot confirming elevated hepatic SREBP−2 protein in *Mmp2*$^{-/-}$mice. Pool

of 4 per genotype. **(E)** The major lipid metabolic gene expression abnormalities of MMP−2 deficiency are present in both sexes and in haploinsufficient mice. (Left) Male mice with both copies (*Mmp2*$^{+/+}$), lacking 1 copy (*Mmp2*$^{+/-}$), or lacking both copies (*Mmp2*$^{-/-}$) of *Mmp2*. n=4 for *Mmp2*$^{+/+}$ and n=4 for *Mmp2*$^{-/-}$, n=3 for *Mmp2*$^{+/-}$. *$P \leq 0.05$ vs WT. †$P \leq 0.05$ vs *Mmp2*$^{+/-}$. (Right) Female mice. n=5. *$P \leq 0.05$ vs WT. LXR−α indicates liver X receptor α; MMP−2, matrix metalloproteinase 2; ND, not detected; qRT−PCR, quantitative reverse transcription–polymerase chain reaction; SREBP−2, sterol regulatory binding protein 2; WT, wild type.

9. 3. 2 MMP−2 Modulates Transcriptional Responses to Dietary Cholesterol

To investigate the contribution of MMP−2 to hepatic transcriptional responses to metabolic cues, we subjected mice to dietary cholesterol supplementation. Dietary cholesterol inhibits the SREBP−2 pathway to decrease hepatic synthesis and uptake of cholesterol; at the same time, oxysterols activate LXR−α signaling to increase the clearance of hepatic cholesterol.[19, 20] Consistently, WT mice fed chow supplemented with 0.15% cholesterol exhibited decreased hepatic expression of *Srebf2*and *Hmgcr* along with a powerful induction of *Cyp7a1* and *Cyp27a*, 2 rate−limiting enzymes in the bile acid synthesis pathways. In contrast, in *Mmp2*$^{-/-}$ mice, the same genes (ie, *Srebf2, Hmgcr, Cyp7a1*, and *Cyp27a*) showed blunted transcriptional responses reminiscent of a hepatic insensitivity to dietary cholesterol, whereas other genes such as *Srebf1* and *Fasn*, were clearly uncoupled in their responses (**Figure 9.4**). These data identified MMP−2 as a modulator of hepatic transcriptional responses to dietary cholesterol.

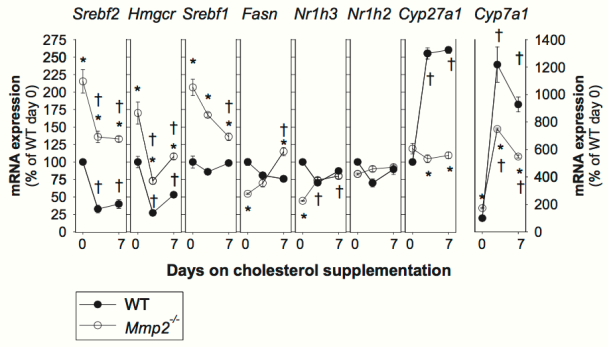

Figure 9.4. Time course of hepatic transcriptional responses to dietary cholesterol supplementation. Mice were fed either chow or chow supplemented with 0.15% cholesterol for up to 1 week. Gene expression analysis was conducted at 0, 2.5, and 7 days. Analysis involved a total of 12 *Mmp2*$^{-/-}$ mice and 12 WT mice (n=4 mice per time point). *$P<0.05$ vs WT. †$P<0.05$ vs 0 days on cholesterol. WT, wild type.

9. 3. 3 A Heart–Liver Axis Mediated by Cardiac $sPLA_2$ and Negatively Regulated by MMP−2

9. 3. 3. 1 Cardiac $sPLA_2$ localizes to cardiomyocytes

Recently, we reported an MMP−2/cardiac $sPLA_2$ mechanism that modulates blood pressure homeostasis, cardiac inflammation, and lipopolysaccharide−induced fever.[12] We confirmed the heart as a major source of systemic $sPLA_2$ activity in *Mmp2*$^{-/-}$ mice (**Figure 9.5A**). We also detected elevated $sPLA_2$ activity in the aorta but not in skeletal muscle or the liver (**Figure 9.5A**). Ex vivo release of $sPLA_2$ activity was evident from the heart but not from the liver (**Figure 9.5A and inset**). Cardiac $sPLA_2$ activity was significantly elevated in *Mmp2*$^{-/-}$ mice (versus WT) whether the substrate was diheptanoyl thio−phosphatidyl choline or [^{3}H]−oleic acid–radiolabeled *E coli* membranes. Analysis of plasma $sPLA_2$ activity with the highly sensitive *E coli* membrane assay indicated a 1000−fold elevation in *Mmp2*$^{-/-}$ mice (**Figure 9.5A inset, Figure S3**). Cardiac $sPLA_2$ activity was evenly distributed across left and right cardiac atria and ventricles (**Figure 9.5B**). Cardiomyocytes isolated from *Mmp2*$^{-/-}$ whole hearts displayed significantly elevated intracellular $sPLA_2$ activity (**Figure 9.5C**). Culture of *Mmp2*$^{-/-}$ cardiomyocytes with recombinant human MMP−2 at 40 nmol/L, a concentration that approximates that of plasma MMP−2, reduced $sPLA_2$ activity (**Figure 9.5C, left panel**). Brefeldin A (1 μmol/L), an inhibitor of the classical secretory pathway at the level of the endoplasmic reticulum to Golgi transition, blunted $sPLA_2$ activity in *Mmp2*$^{-/-}$ cardiomyocytes (**Figure 9.5C, right panel**).

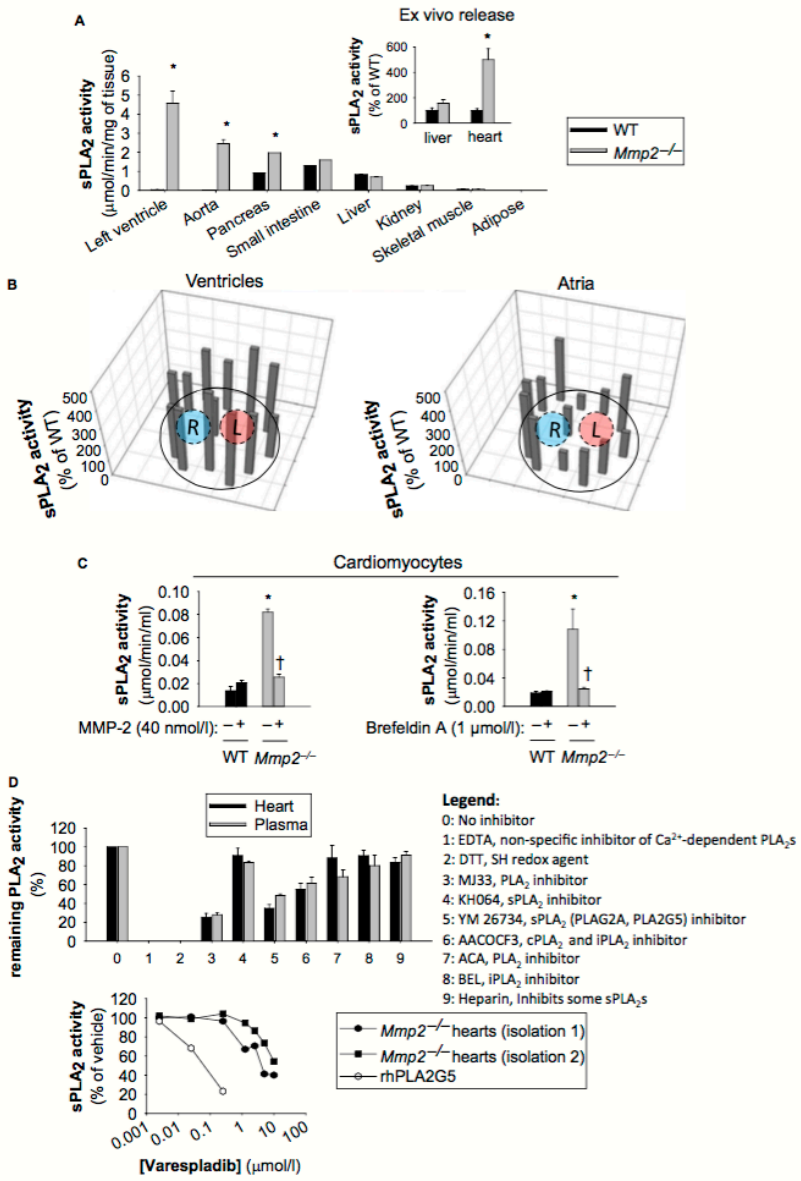

Figure 9.5. Tissue profiling and intracardiac localization of sPLA$_2$. (A) The heart is the predominant source of sPLA$_2$activity in *Mmp2*$^{-/-}$ mice. The sPLA$_2$ activity (pools of 4 mice per genotype) was analyzed in duplicate. **P*≤0.05 vs WT (statistical unit was the duplicate). (Inset) Ex vivo release of sPLA$_2$ activity was elevated for specimens of left ventricle, but not liver, from *Mmp2*$^{-/-}$ mice. Ex vivo release results are representative of 3 determinations conducted on different days with different mice.**P*≤0.05 vs WT. **(B)** Intracardiac distribution of sPLA$_2$ activity in *Mmp2*$^{-/-}$ mice. Frozen heart sections (≈1 mm thick) were divided into pieces with approximately equal surface area (≈1 mm^2), homogenized, and individually assessed for sPLA$_2$ activity. Diagrams present mean values of sPLA$_2$ activity normalized to protein content in each piece of tissue. n=3 mice per genotype. **(C)** Cardiac sPLA$_2$ localizes to cardiomyocytes. Isolated *Mmp2*$^{-/-}$ cardiomyocytes grown on 6−well plates in MMP−free media had significantly elevated intracellular sPLA$_2$ activity that was blunted by

extracellular MMP−2 and brefeldin A. Intracellular $sPLA_2$ activity pooled from 3 individual wells (≈10^5 cells per well) and analyzed in duplicate per genotype. *P≤0.05 vs WT untreated (−). †P≤0.05 vs *Mmp2*$^{-/-}$ untreated (−). No activity was detected in conditioned media. Results are representative of 3 independent preparations of cardiomyocytes. **(D)** (Top) PLA_2 activity inhibitor profiling indicates that cardiac $sPLA_2$is present in plasma. Pools of 4 WT and 5 *Mmp2*$^{-/-}$ were analyzed in duplicate. (Bottom) Varespladib inhibition clearly differentiated between $sPLA_2$ from *Mmp2*$^{-/-}$ heart homogenates and human (rh)PLA2G5. Comparison of the enzyme obtained in 2 independent heart homogenizations corresponding to 8 different *Mmp2*$^{-/-}$ mice. AACOCF3 indicates Arachidonyl trifluoromethyl ketone; ACA, *N*−(*p*−amylcinnamoyl) anthranilic acid; BEL, bromoenol lactone; $cPLA_2$, cytosolic phospholipase A_2; DTT, dithiothreitol; $iPLA_2$, calcium−independent phospholipase A_2; L, left; MMP−2, matrix metalloproteinase−2; R, right; rh, recombinant human; SH, sulfhydryl; $sPLA_2$, secreted phospholipase A_2; WT, wild type; YM 26734, 1,1′−[5−[3,4−Dihydro−7−hydroxy−2−(4−hydroxyphenyl)−2H−1−benzopyran−4−yl]−2,4,6−trihydroxy−1,3−phenylene]bis−1−dodecanone.

9. 3. 3. 2 Cardiac $sPLA_2$, an elusive unique enzyme, circulates in plasma

We reported previously that cardiac and plasma $sPLA_2$ had similar molecular weights (≈18–20 kDa), had similar apparent Michaelis–Menten constants for diheptanoyl thio-phosphatidyl choline of ≈235 μmol/L, required calcium for activity, and were not cleaved or inactivated by incubation with MMP−2.[12] Cardiac and plasma $sPLA_2$ had strikingly similar activity profiles against a panel of inhibitors indicative that the cardiac enzyme is present in the circulation (**Figure 9.5D, top panel**). The pan−$sPLA_2$ blocker varespladib[21] decreased cardiac $sPLA_2$ activity with a half maximal inhibitory concentration of 10 μmol/L, similar to what we reported for indoxam (≈2 μmol/L)[12] and different from PLA2G5 (**Figure 9.5D, bottom panel**). Using a time−resolved fluorescence immunoassay with highly specific antibodies against various mouse $sPLA_2$ isoforms, we excluded PLA2G1B, PLA2G2A/2D /2E/2F, PLA2G5, and PLA2G10 as major components of either cardiac or plasma $sPLA_2$ in *Mmp2*$^{-/-}$ mice (**Figure S4**).

9. 3. 3. 3 Systemic $sPLA_2$ activity contributes to the hepatic inflammatory and lipid metabolic phenotype of MMP−2 deficiency.

Treatment of *Mmp2*$^{-/-}$ mice with the pan−$sPLA_2$ inhibitor varespladib (10 mg/kg per day) reduced $sPLA_2$ activity time dependently to baseline (ie, WT) levels in the heart (**Figure**

9.6A, left) and in plasma (**Figure 9.6A, right**). Furthermore, varespladib normalized numerous lipid metabolic genes (in particular, *Nr1h3*[encodes LXR−α] and *Srebf2* [encodes SREBP−2]) and proinflammatory markers in the liver (**Figure 9.6B**) and the heart (**Figure 9.6C**) as well as immune cell infiltration in the liver of *Mmp2*$^{-/-}$ mice (**Figure 9.7**). Similarly, varespladib lowered prostaglandin E_2 levels in the heart and liver (Figure S5) and normalized the levels of hepatic triglycerides in *Mmp2*$^{-/-}$ mice (**Figure 9.2D**).

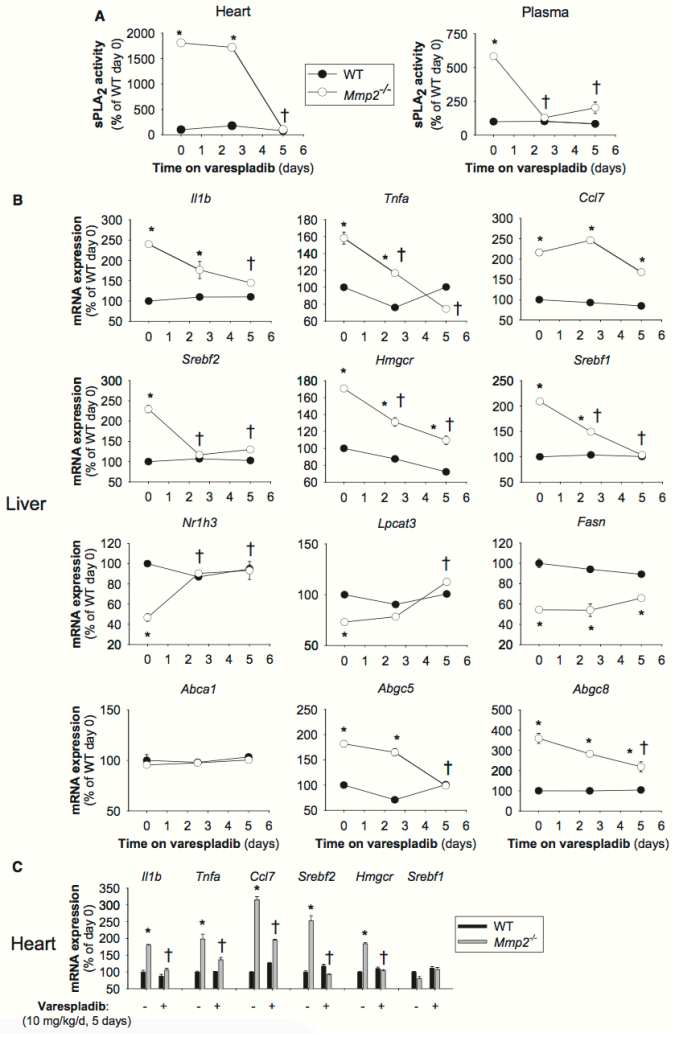

Figure 9.6. High systemic sPLA$_2$ activity sustains the inflammatory and lipid metabolic gene expression phenotype of matrix metallo-proteinase 2–deficient mice. (A) Cardiac and plasma sPLA$_2$ activity in *Mmp2*$^{-/-}$ mice administered the pan−sPLA$_2$ inhibitor varespladib (10 mg/kg per day). **(B)** Hepatic expression of inflammatory and lipid metabolic genes in mice administered varespladib (10 mg/kg per day). **(C)** Cardiac expression of inflammatory and lipid metabolic genes in administered varespladib (10 mg/kg per day). Analysis of 12 mice per genotype (n=4 per time point). *P≤0.05 vs WT (time 0 days). †P≤0.05 vs *Mmp2*$^{-/-}$ (time 0 days). sPLA$_2$ indicates secreted phospholipase A$_2$; WT, wild type.

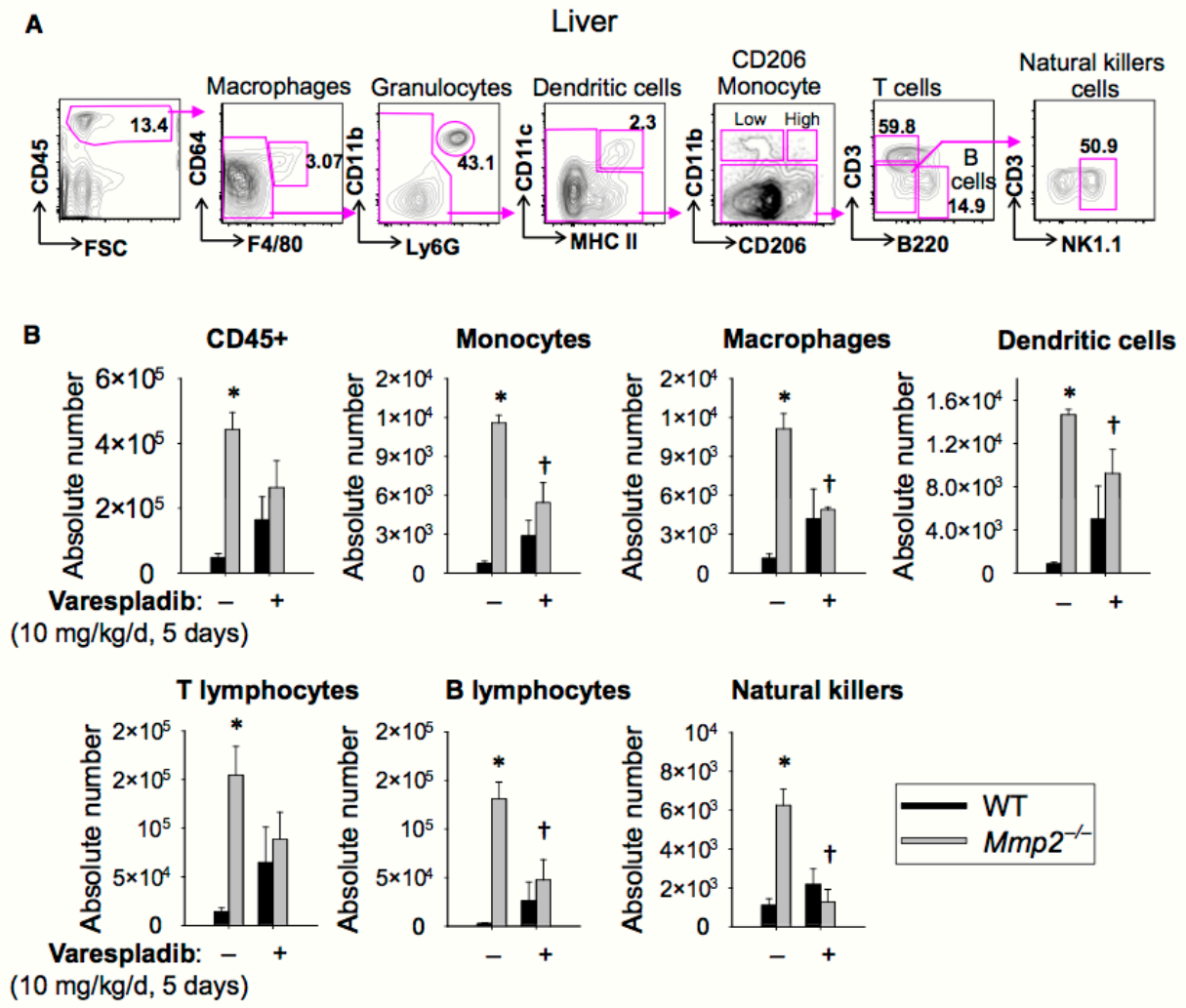

Figure 9.7. Hepatic immune cell infiltration in matrix metalloproteinase 2–deficient mice depends on high systemic sPLA$_2$ activity. (A) Gating strategy for infiltrating immune cells (CD45$^+$), hepatic macrophages (CD64$^+$F4/80$^+$), dendritic cells (CD11c$^+$MHC II$^+$), monocytes (CD206^{Low}CD11b$^+$), T cells (CD3$^+$), B cells (B220$^+$), and natural killer cells (NK1.1$^+$). **(B)** Hepatic immune cell infiltration in *Mmp2*$^{-/-}$ mice administered the pan−sPLA$_2$inhibitor varespladib (10 mg/kg per day, gavage, for 5 days). Collagenase−treated and liberated cells were surface−stained for indicated markers (A) and quantitated. n=3 WT and n=5 *Mmp2*$^{-/-}$. **P*≤0.05 vs WT untreated. †*P*≤0.05 vs *Mmp2*$^{-/-}$ untreated. MHC II, major histocompatibility complex II; sPLA$_2$, secreted phospholipase A$_2$; SSC, Side−scattered light (a magnitude proportional to cell granularity or internal complexity); WT, wild type.

9. 3. 3. 4 Adaptive transfer of cardiac $sPLA_2$ evokes the cardiohepatic phenotype of MMP−2–deficient mice.

When HPLC−isolated cardiac $sPLA_2$ from *Mmp2*$^{-/-}$ donors was injected into WT mice (fractions F6 and F7), the recipient WT mice displayed highly elevated plasma and cardiac $sPLA_2$activity (**Figure 9.8**). Moreover, the cardiohepatic gene expression profile of WT mice that received HPLC−isolated cardiac $sPLA_2$from *Mmp2*$^{-/-}$ donors was strikingly similar to that of *Mmp2*$^{-/-}$mice. The phenotypic changes evoked by cardiac $sPLA_2$ from *Mmp2*$^{-/-}$ donors were blunted in mice that also received the pan−$sPLA_2$ inhibitor varespladib (**Figure 9.9**).

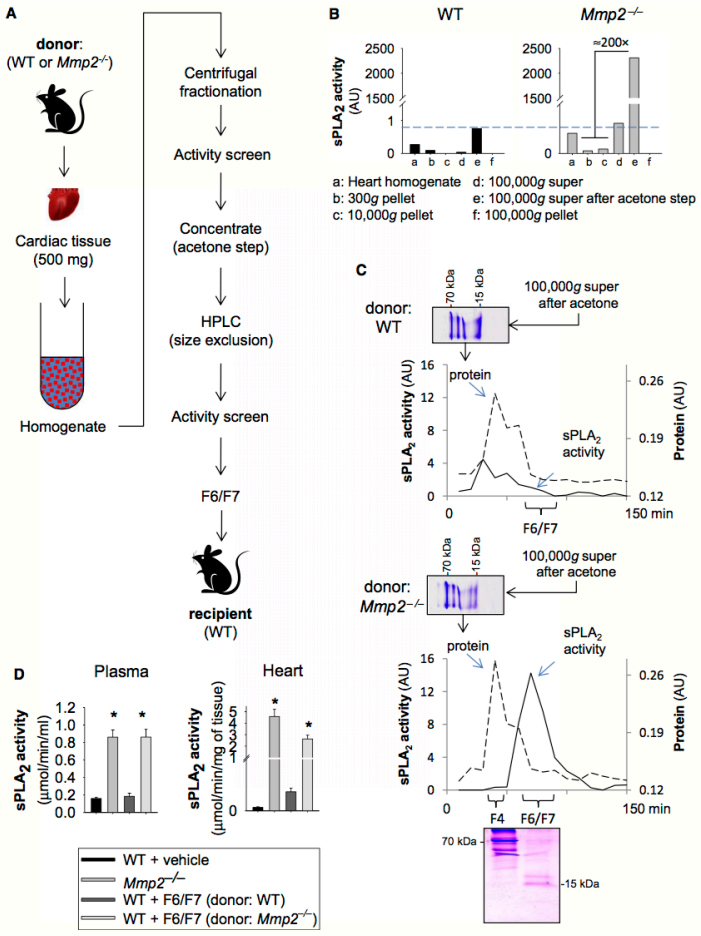

Figure 9.8. HPLC isolation of biologically active cardiac $sPLA_2$. (A) Strategy for isolation of biologically active cardiac $sPLA_2$ for in vivo studies. Hearts from 5 *Mmp2*$^{-/-}$ or WTmice were pooled to obtain sufficient cardiac $sPLA_2$ for in vivo characterization. **(B)** Representative centrifugal fractionation. Note that the 100 000*g* supernatant fraction is rich in active cardiac

$sPLA_2$, and WT hearts express negligible cardiac $sPLA_2$ activity, as opposed to *Mmp2*$^{-/-}$hearts. **(C)** Representative HPLC isolation of active cardiac $sPLA_2$ and Coomassie blue–stained 16% T, 3% C Tricine–SDS−PAGE gels of 100 000*g* supernatant before and after size−exclusion fractionation. **(D)** Phenotypes induced by HPLC fractions F6 and F7 from *Mmp2*$^{-/-}$ donors vs WTdonors in recipient WT mice. Injection of HPLC fractions F6 and F7 from *Mmp2*$^{-/-}$ donors (but not from WT donors) evoked high $sPLA_2$ activity in both plasma and the heart of WT recipient mice after 5 consecutive injection−days. For comparison, we show the levels of activity in intact *Mmp2*$^{-/-}$ mice. WT plus vehicle: Mice received 100 μL of HPLCmobile phase (vehicle) consistent with sterile PBS, 10 mmol/L $CaCl_2$. WT plus fractions F6 and F7: Mice received HPLC fractions F6 and F7 from WT donors and from *Mmp2*$^{-/-}$ donors. **P*≤0.05 vs WT. n=4 mice per treatment. AU indicates arbitrary units; HPLC, high−performance liquid chromatography; $sPLA_2$, secreted phospholipase A_2; WT, wild type.

No phenotypic transformation was evident in mice that received the HPLC fractions F6 and F7 from WT donors, which, despite originating from the same amount (500 mg) of cardiac tissue, contained negligible $sPLA_2$ activity (**Figure S6**).

These results clearly show that circulating cardiac $sPLA_2$ is a biological mediator and determinant of the cardiohepatic phenotype of MMP−2–deficient mice. Taken together with the potent in vivo effects of varespladib on $sPLA_2$ activity (**Figure 9.6**), the upregulation of both plasma and cardiac $sPLA_2$ in WT mice administered HPLC−isolated cardiac $sPLA_2$ from *Mmp2*$^{-/-}$donors is consistent with the autocrine feed−forward loop proposed previously for $sPLA_2$.[12, 22]

9. 3. 3. 5 Evidence in support of MCP−3 as an agonist of cardiac $sPLA_2$.

The data to date indicate that cardiac $sPLA_2$ is a unique enzyme produced and released by cardiomyocytes into plasma, where it circulates and affects liver function. Furthermore, cardiac $sPLA_2$intracellular activation is inhibited by extracellular MMP−2, likely by blocking an agonist.

To identify possible triggers of cardiac $sPLA_2$ activity, we first examined the impact of feeding and fasting. Neither fasting nor fasting and refeeding with a high−carbohydrate diet (**Figure S7**) or dietary supplementation with polyunsaturated fatty acids (data not shown) or cholesterol[12] affected cardiac $sPLA_2$ activity.

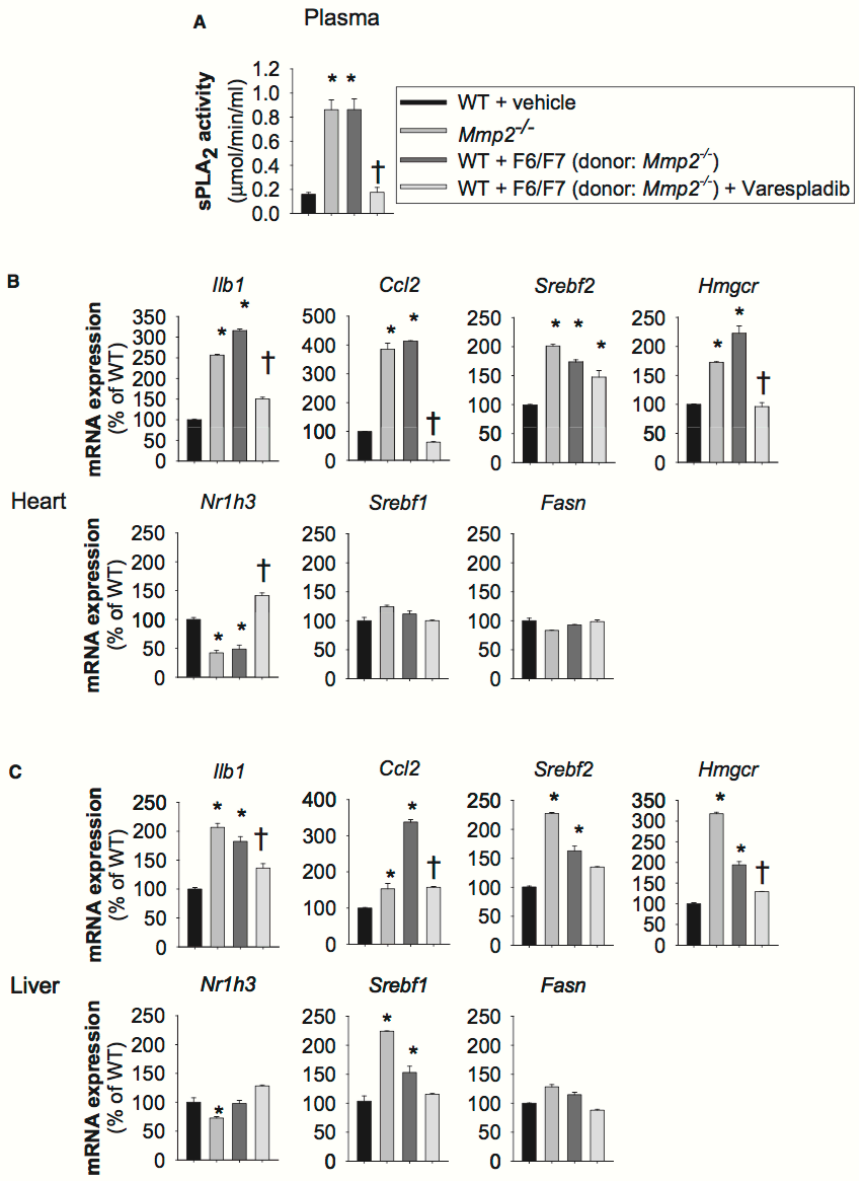

Figure 9.9. Cardiac $sPLA_2$ is a biological mediator and determinant of the cardiohepatic phenotype of matrix metalloproteinase 2–deficient mice. (A) The increase in plasma $sPLA_2$ evoked by high−performance liquid chromatography–isolated cardiac $sPLA_2$ from *Mmp2*$^{-/-}$ donors was prevented by coadministering varespladib (10 mg/kg per day). **(B and C)** Increased plasma $sPLA_2$ was associated with a cardiohepatic gene expression profile very similar to that of *Mmp2*$^{-/-}$ mice. These changes were prevented by coadministering varespladib. n=4 mice per group. **P*≤0.05 vs WT. †*P*≤0.05 vs WT+F6/F7 (donor: *Mmp2*$^{-/-}$). $sPLA_2$ indicates secreted phospholipase A_2; WT, wild type.

Second, we examined the influence of circadian rhythm on cardiac $sPLA_2$ activity. We observed small increases in the mRNA levels for conventional $sPLA_2$ isoforms in *Mmp2*$^{-/-}$ mice euthanized at night but no differences in cardiac $sPLA_2$ activity at night (9:30 pm±0.5 hour) versus day (11:30 am±0.5 hour) (**Figure S8**).

Third, we examined whether MCP−3 (a proinflammatory CC−chemokine bound, cleaved, and inactivated by MMP−2[2]) had the potential to induce cardiac $sPLA_2$ activation or secretion.

Although *Ccl7* mRNA (encodes MCP−3) was elevated at baseline in both *Mmp2*$^{-/-}$ liver and heart (**Figure 9.6B and 9.6C**), MCP−3 protein levels were significantly elevated only in the heart, not in the liver or plasma, of *Mmp2*$^{-/-}$ mice (**Figure 9.10**). The reason for the cardiac−specific overexpression of MCP−3 was not investigated further.

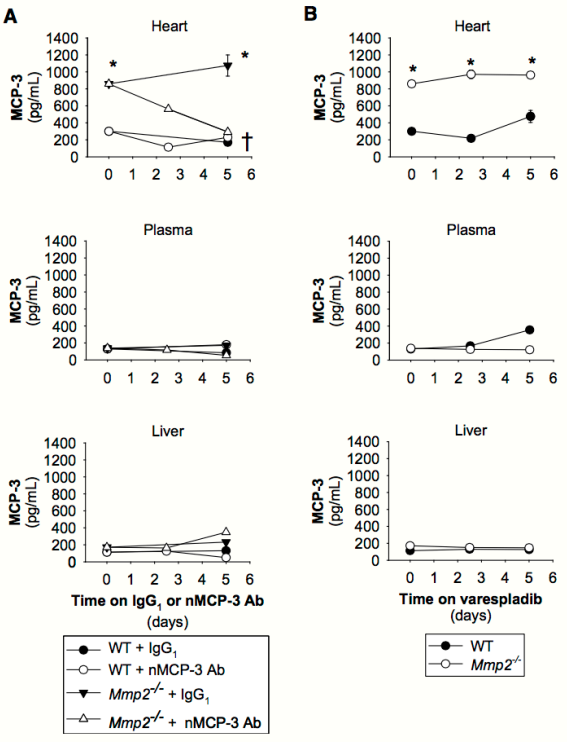

Figure 9.10. Cardiac MCP−3 expression is upregulated in *Mmp2*$^{-/-}$ mice and unrelated to systemic secreted phospholipase A_2 activity. (A) MCP−3 protein levels in the heart, plasma, and liver of mice administered nMCP−3 Ab or isotype−matched IgG_1 (0.6 mg/kg per day). Results are representative of 19 to 20 mice per genotype (n=3 to 4 mice per time point). **P*≤0.05 vs WT at day 0. †*P*≤0.05 vs *Mmp2*$^{-/-}$ plus IgG_1 at day 5. Note that the data presented for day 2.5 refer to pools of 3 to 4 mice for which MCP−3 levels were measured in duplicate; for simplicity, no statistical analysis is indicated at day 2.5. **(B)** MCP−3 protein levels in the heart, plasma, and liver of mice administered varespladib (10 mg/kg per day). Results are representative of 12 to 13 mice per genotype (3 to 5 mice per time point were pooled and MCP−3 levels were measured in duplicate). **P*≤0.05 vs WT at day 0. †*P*≤0.05 vs *Mmp2*$^{-/-}$ at day 5. MCP−3 indicates monocyte chemoattractant protein 3; nMCP−3 Ab, neutralizing MCP−3 monoclonal antibody; WT, wild type.

To assess the in vivo significance of MCP−3 for cardiac $sPLA_2$activity, we injected mice with either neutralizing MCP−3 monoclonal antibody or isotype−matched IgG_1 at a dose (0.6 mg/kg per day, intraperitoneally) validated in a previous study.[3] Neutralizing MCP−3 antibody (but not control IgG_1) treatment normalized cardiac MCP−3 protein levels in *Mmp2*$^{-/-}$mice (**Figure 9.10**). Ex vivo incubation during 3 hours with MCP−3 (200 nmol/L) enhanced the release of $sPLA_2$ activity by 87% from WT heart and 39% from *Mmp2*$^{-/-}$ heart; however, $sPLA_2$ release from liver was unchanged regardless of genotype (**Figure 9.11**). Most important, neutralizing MCP−3 antibody (but not IgG_1) fully normalized cardiac and plasma $sPLA_2$ activity in *Mmp2*$^{-/-}$ mice (**Figure 9.12A**). Neutralizing MCP−3 antibody partially restored gene expression of *Mmp2*$^{-/-}$ mice including LXR−α, SREBP−2, and inflammatory markers in the heart (**Figure 9.12B**) and liver (**Figure 9.12C**). In contrast to neutralizing MCP−3 antibody, systemic $sPLA_2$ inhibition with varespladib did not normalize MCP−3 protein expression in the heart of *Mmp2*$^{-/-}$ mice (**Figure 9.10**). These results identified cardiac MCP−3 as a possible agonist acting upstream of cardiac $sPLA_2$; however, the possibility that other cytokines or mechanisms contribute to cardiac $sPLA_2$ activation or release warrants further research.

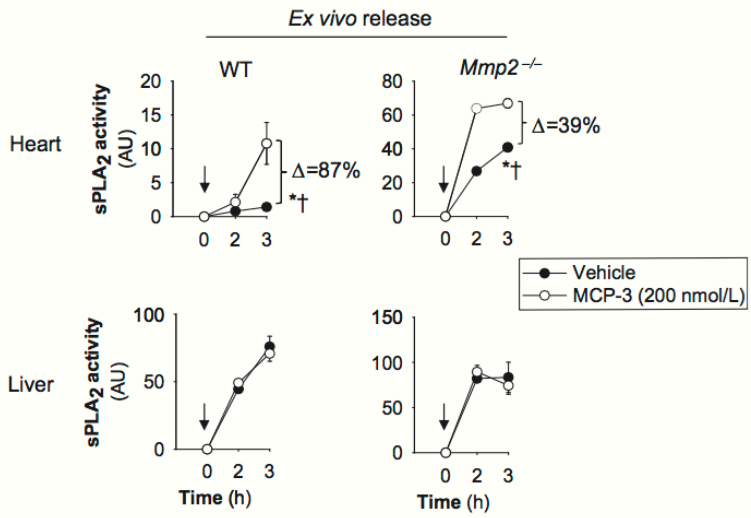

Figure 9.11. MCP−3 enhances $sPLA_2$ activity release from myocardium. MCP−3 enhanced the ex vivo release of $sPLA_2$ activity from heart but not liver. Freshly dissected specimens of the indicated organs (≈2 mm^3) were subjected to the ex vivo release bioassay described previously[12] in the presence or absence of MCP−3 (200 nmol/L). n=3 mice. Arrows indicate when MCP−3 or PBS (vehicle) was added. *$P\leq0.05$ vs time 0 hours. †$P\leq0.05$ vs vehicle (passive ex vivo release). MCP−3 indicates monocyte chemoattractant protein 3; $sPLA_2$, secreted phospholipase A_2; WT, wild type.

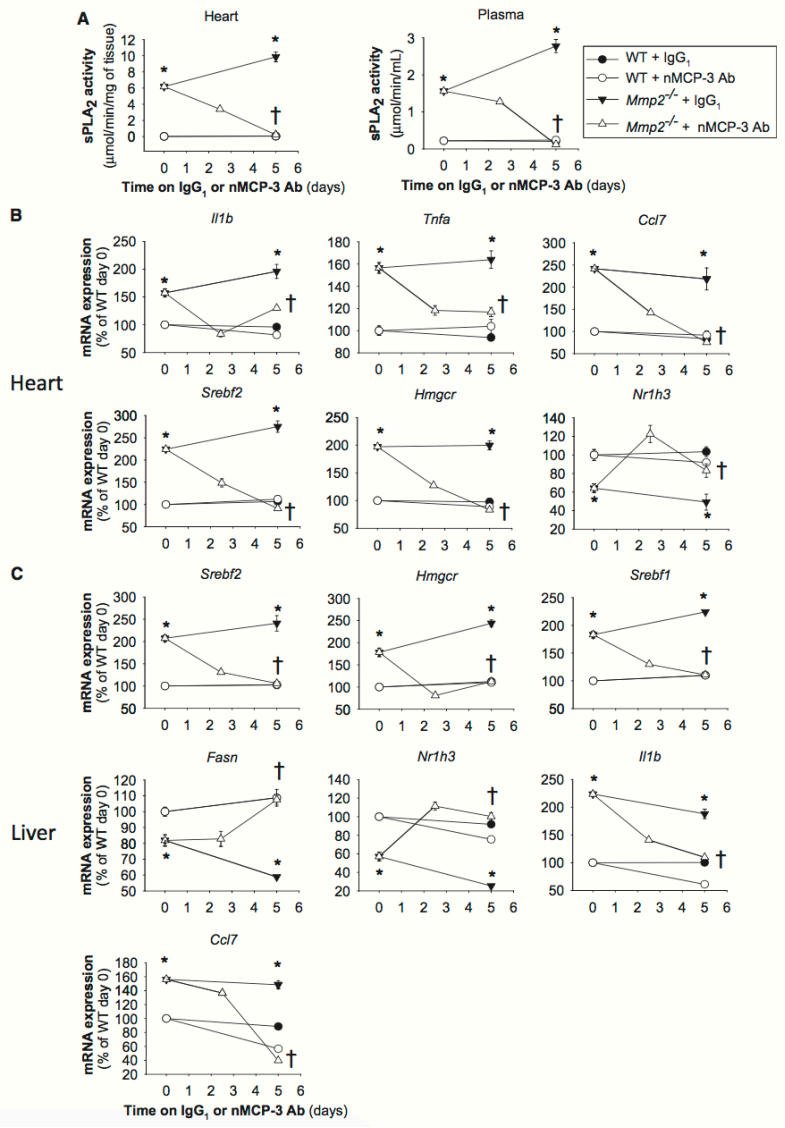

Figure 9.12. MCP−3 affects the cardiohepatic phenotype of *Mmp2*$^{-/-}$ mice mimicking effects of sPLA$_2$. (A) Cardiac and plasma sPLA$_2$ activity levels in mice administered nMCP−3 Ab or isotype−matched IgG$_1$ (0.6 mg/kg per day). **(B)** Cardiac gene expression in mice administered nMCP−3 Ab or IgG$_1$ (0.6 mg/kg per day). **(C)** Hepatic gene expression in mice administered nMCP−3 Ab or IgG$_1$ (0.6 mg/kg per day). Analysis of 9 to 12 mice per genotype (n=3 to 4 per time point). **P*≤0.05 vs WT (time 0 days). †*P*≤0.05 vs *Mmp2*$^{-/-}$(time 0 days). AU indicates arbitrary units; MCP−3, monocyte chemoattractant protein 3; nMCP−3 Ab, neutralizing MCP−3 monoclonal antibody; sPLA$_2$, secreted phospholipase A$_2$; WT, wild type.

9. 4 Discussion

Our study identified a novel endocrine function of the heart: the production and secretion of a unique PLA_2 by cardiomyocytes. Secretion of cardiac $sPLA_2$ into the plasma enables a previously unknown heart–liver axis that is activated, at least in part, by the proinflammatory CC−chemokine MCP−3 and negatively regulated by extracellular MMP−2, which cleaves MCP−3.[2] This heart–liver endocrine axis profoundly influences the inflammatory and lipid metabolic gene expression characteristics of the liver, effectively increasing the levels of hepatic and very low−density lipoprotein triglycerides. Because the heart is a major user of very low−density lipoprotein triglycerides, the MMP−2/cardiac $sPLA_2$system may enable the heart to signal the liver to satisfy the energy needs (**Figure 9.13**). Our findings identify cardiac $sPLA_2$ as a key biological mediator of the cardiohepatic phenotype associated with MMP−2 deficiency in mice. These findings could also help explain how *MMP2* deficiency leads to cardiac problems and delayed growth in patients.[4, 5, 6, 23]

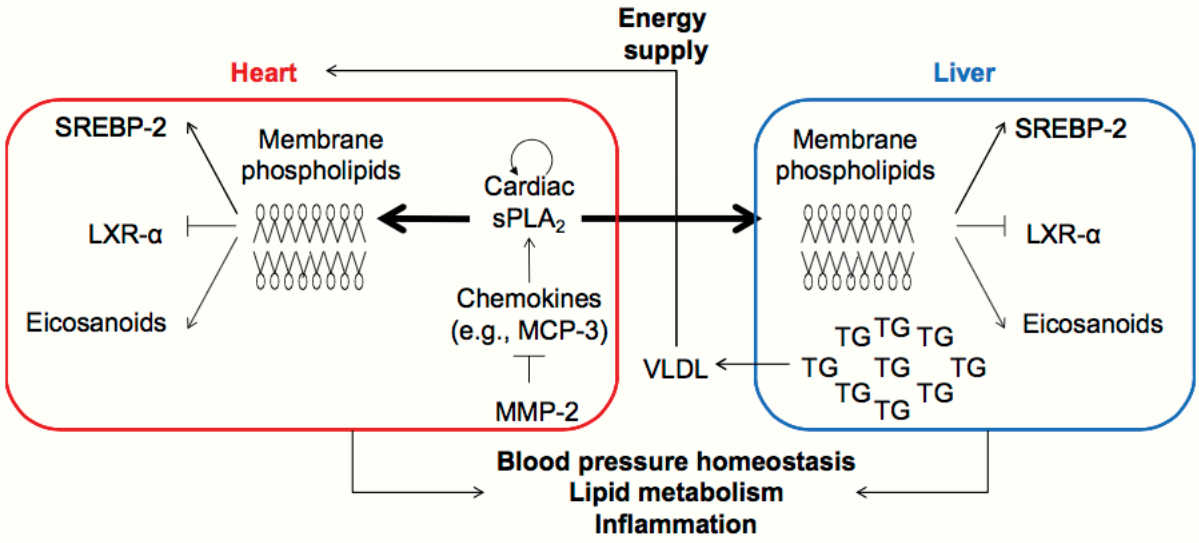

Figure 9.13. Proposed model for a novel heart–liver axis mediated by cardiac $sPLA_2$. Key elements of the proposed model are the heart (source and autocrine/paracrine target of cardiac $sPLA_2$), MCP−3 (agonist of cardiac $sPLA_2$), MMP−2 (endogenous inhibitor), cardiac $sPLA_2$ (signaling molecule), and liver (a noncardiac target of cardiac $sPLA_2$). We propose that, under physiological conditions, MMP−2 activity maintains low levels of certain chemokines, such as MCP−3, by proteolysis.[2, 3] MMP−2 deficiency (due to functional blockade or genetic

deletion) and MCP−3 may trigger cardiac $sPLA_2$ release from the heart. Cardiac $sPLA_2$ circulates in the plasma, reaching distant target organs (eg, liver) and affecting the inflammatory and lipid metabolic phenotype of these organs. The MMP−2/cardiac $sPLA_2$ system may serve multiple purposes including signaling to the liver to provide the heart with TGs and maintaining systemic blood pressure homeostasis. LXR−α indicates liver X receptor−α; MCP−3 indicates monocyte chemoattractant protein 3; MMP−2, matrix metalloproteinase 2; $sPLA_2$, secreted phospholipase A_2; SREBP−2, sterol regulatory binding protein 2; TG, triglyceride; VLDL, very low−density lipoprotein.

The endocrine function of the heart was first suggested in the days of the discovery of the circulatory system by William Harvey in the 17th century.[24] The concept has since evolved through the work of many. In 1921, Loewi discovered the release of acetylcholine from cardiac sympathetic nerves. Investigations conducted between 1971 and 1983 by de Bold's team revealed the secretion of cardiac natriuretic peptides from granules present in the atria (but absent in ventricles).[25] In addition to natriuresis, cardiac natriuretic peptides mediate vasodilation in the failing heart,[25] increase glucogenesis in the liver[26], regulate lipolysis in adipocytes[27], and promote thermogenesis and energy expenditure.[28] The heart is also source, albeit not exclusively, of other polypeptide hormones, including adrenomedullin and endothelins, which—acting in autocrine, paracrine, and endocrine fashion—provide additional cardiovascular and metabolic regulatory mechanisms.[25] Likewise, the heart may regulate white adipose tissue and liver function through as−yet−unidentified factors produced and released downstream of mediator complex subunit 13, a protein with transcription that is negatively regulated by the heart−specific microRNA−208a. This latter mechanism may promote resistance to obesity induced by a high−fat diet and improve insulin sensitivity.[29, 30] Bidirectional interactions between the heart and the liver have been demonstrated in mice bearing a hypertrophic cardiomyopathy−causing mutation in myosin (R403Q).[31] This mutation is associated with decreased cardiac lipid uptake and increased plasma and hepatic lipid content together with increased gluconeogenesis and blood glucose that may ultimately exacerbate cardiac disease.[31]

Our previous studies revealed autocrine/paracrine actions of cardiac $sPLA_2$ involving the modulation of inflammatory and lipid metabolic gene expression in the heart.[12] Furthermore, we documented the systemic effects of cardiac $sPLA_2$ on systolic blood pressure

and fever.[12] Extending these observations, our current research identifies the liver as the first target organ of cardiac $sPLA_2$.

Pioneering work on MMP−2–deficient mice revealed lipodystrophy as an important trait.[11] In this study, we identified new metabolic traits of MMP−2 deficiency. These include (1) hepatic lipid deposition; (2) altered expression of transcription factors and enzymes involved in sensing, biosynthesis, and catabolism of lipids in the liver; (3) altered transcriptional responses to dietary cholesterol; and (4) abnormal oxygen consumption and locomotor activity patterns.

Our study provides several lines of evidence indicating that this complex phenotype is caused, at least in part, by activation of a heart–liver axis mediated by cardiac $sPLA_2$. This axis is broken down as follows. First, systemic absence of MMP−2 increases the bioavailability of MCP−3; this was shown by the cardiac−specific excess of MCP−3 protein observed in this study. Second, MCP−3 enhances cardiac $sPLA_2$ release. Once secreted, cardiac $sPLA_2$ reaches distant target organs (eg, liver) where hydrolysis of the outer leaflet of membrane phospholipids releases *sn*−2 esterified fatty acids.[32, 33] Such fatty acids include precursors of eicosanoids and ligands of nuclear metabolic transcription factors such as LXR−α.[16, 33, 34] Downstream changes in the transcription of multiple inflammatory and lipid metabolic genes would profoundly affect cardiac, hepatic, and systemic metabolism.[35, 36, 37, 38, 39] Indeed, we detected abnormally high prostaglandin E_2 levels and significant dysregulation of the LXR−α and SREBP−2 pathways in the liver of MMP−2–deficient mice. Moreover, these mice exhibited hepatic immune cell infiltration, specifically, monocytes and macrophages, which are key cells for inflammation. We also detected elevated numbers of dendritic cells, T cells, B cells, and natural killer cells; however, the contribution of these cell types to the observed phenotype requires further investigations.

Importantly, treatment of mice with the pan−$sPLA_2$ inhibitor varespladib almost fully normalized the altered expression of the lipid metabolic pathways and inflammation in *Mmp2*$^{-/-}$ mice. The beneficial effects of varespladib were not attributed to reduction in MCP−3 levels but rather to inhibition of $sPLA_2$ activity.

MMP−2 serves as a metabolism modulatory signal and may exert multipronged anti−inflammatory actions.[2, 11, 40, 41] Consequently, one may expect that pharmacological MMP−2 inhibition could affect metabolic and inflammatory pathways, perhaps by elevating cardiac $sPLA_2$, as we demonstrated recently for doxycycline.[12] Currently, doxycycline is the only MMP inhibitor approved by the US Food and Drug Administration for clinical use. The therapeutic efficacy of doxycycline−based formulations are currently being explored in pathologies associated with extracellular matrix destruction and inflammation such as periodontitis, arthritis, Marfan syndrome, atherosclerosis, and arterial aneurysm.[42, 43] Our findings may support better understanding of the therapeutic principles of MMP inhibitors.

Our results indicate that cardiac $sPLA_2$ is a unique enzyme predominantly expressed in the heart and secreted to plasma in MMP−2 deficiency, a condition that can be genetic or pharmacologically induced.[12] The chemical identity of this $sPLA_2$with myocardial secretion that defines a novel heart–liver axis, remains elusive. Our data, however, excluded PLA2G1B, PLA2G2A/2D/2E/2F, PLA2G5, and PLA2G10 as major components of either cardiac or plasma $sPLA_2$ in *Mmp2*$^{-/-}$ mice. Our qRT−PCR, immunological, and chemical inhibitor data gathered to date would suggest that cardiac $sPLA_2$ may not be a classical $sPLA_2$ or may belong to an atypical or even unknown PLA_2 class.[32, 44, 45] Proteomic studies are ongoing in our laboratories to address this still open question.

In summary, our data identify a novel endocrine function of the heart to modulate lipid metabolic pathways and inflammation in the liver. The key component of this heart–liver axis is secretion of cardiac $sPLA_2$, a unique enzyme the release of which from cardiomyocytes is enhanced by chemokines that are substrates of MMP−2–mediated proteolysis, such as MCP−3. We propose that the MMP−2/cardiac $sPLA_2$ system enables the heart to signal the liver to satisfy the energy needs. Our findings may support understanding of the development of metabolic, inflammatory, and cardiac disturbances associated with MMP−2 deficiency in patients[4, 6, 8, 9] and may provide a rationale for the development of future therapies.

9. 5 Author Contributions

Junseong Lee performed experiments and helped interpret the data.

9. 6 Acknowledgements

Author Contributions: Hernandez−Anzaldo: Conducted vast majority of experiments, conducted statistical analysis. Berry: Conducted phospholipase A_2 (PLA_2) and hepatic gene determinations and contributed to data analysis. Brglez, Lambeau: Characterized cardiac and plasma PLA_2 inhibition profiles, time−resolved fluoroimmunoassay measurements and contributed to data analysis. Leung: Measured cardiac secreted PLA_2 distribution in ventricles and atria. Yun, Lee, Cheong: Determined and analyzed immune cell infiltration. Kassiri: Provided the MMP−2 deficient mice and contributed to data analysis. Filep, Cheong, Kassiri, Lambeau and Lehner: Provided critical conceptual input and proof−read the manuscript. Fernandez−Patron: Directed the research, provided most of the funding and wrote the manuscript.

This study was supported by operating grants from the Canadian Institutes of Health Research (CIHR) and Natural Sciences and Engineering Research Council of Canada (to Fernandez-Patron). Cheong is supported by CIHR operating grants and Global Research Network grant (GRN- 2013S1A2A2035348). HPLC analysis of lipids was performed at the Faculty of Medicine and Dentistry Lipid Analysis Core that receives partial funding from the Women and Children Health Research Institute.

9. 7 Additional Information

Any supplementary data are available at Journal of the American Heart Association online. (https://doi.org/10.1161/JAHA.115.002553)

9. 8 References

1. Berry, E., Bosonea, A.M., Wang, X. & Fernandez-Patron, C. Insights into the activity, differential expression, mutual regulation, and functions of matrix metalloproteinases and a disintegrin and metalloproteinases in hypertension and cardiac disease. *J Vasc Res* **50**, 52-68 (2013).

2. McQuibban, G.A. *et al.* Inflammation dampened by gelatinase A cleavage of monocyte chemoattractant protein-3. *Science* **289**, 1202-1206 (2000).

3. Westermann, D. *et al.* Reduced degradation of the chemokine MCP-3 by matrix metalloproteinase-2 exacerbates myocardial inflammation in experimental viral cardiomyopathy. *Circulation* **124**, 2082-2093 (2011).

4. Tuysuz, B. *et al.* A novel matrix metalloproteinase 2 (MMP2) terminal hemopexin domain mutation in a family with multicentric osteolysis with nodulosis and arthritis with cardiac defects. *Eur J Hum Genet* **17**, 565-572 (2009).

5. Mosig, R.A. *et al.* Loss of MMP-2 disrupts skeletal and craniofacial development and results in decreased bone mineralization, joint erosion and defects in osteoblast and osteoclast growth. *Hum Mol Genet* **16**, 1113-1123 (2007).

6. Martignetti, J.A. *et al.* Mutation of the matrix metalloproteinase 2 gene (MMP2) causes a multicentric osteolysis and arthritis syndrome. *Nat Genet* **28**, 261-265 (2001).

7. Castberg, F.C. *et al.* Multicentric osteolysis with nodulosis and arthropathy (MONA) with cardiac malformation, mimicking polyarticular juvenile idiopathic arthritis: case report and literature review. *Eur J Pediatr* **172**, 1657-1663 (2013).

8. Han, D.H. *et al.* Matrix Metallopeptidase 2 Gene Polymorphism is Associated with Obesity in Korean Population. *Korean J Physiol Pharmacol* **12**, 125-129 (2008).

9. Morgan, A.R., Han, D.Y., Thompson, J.M., Mitchell, E.A. & Ferguson, L.R. Analysis of MMP2 promoter polymorphisms in childhood obesity. *BMC Res Notes* **4**, 253 (2011).

10. Van Hul, M. *et al.* Effect of gelatinase inhibition on adipogenesis and adipose tissue development. *Clin Exp Pharmacol Physiol* **39**, 49-56 (2012).

11. Van Hul, M. & Lijnen, H.R. A functional role of gelatinase A in the development of nutritionally induced obesity in mice. *J Thromb Haemost* **6**, 1198-1206 (2008).

12. Berry, E. *et al.* Matrix metalloproteinase-2 negatively regulates cardiac secreted phospholipase A2 to modulate inflammation and fever. *J Am Heart Assoc* **4** (2015).

13. Wang, X. *et al.* Matrix metalloproteinase-2 mediates a mechanism of metabolic cardioprotection consisting of negative regulation of the sterol regulatory element-binding protein-2/3-hydroxy-3-methylglutaryl-CoA reductase pathway in the heart. *Hypertension* **65**, 882-888 (2015).

14. Kalaany, N.Y. *et al.* LXRs regulate the balance between fat storage and oxidation. *Cell Metab* **1**, 231-244 (2005).

15. Hishikawa, D. *et al.* Discovery of a lysophospholipid acyltransferase family essential for membrane asymmetry and diversity. *Proc Natl Acad Sci U S A* **105**, 2830-2835 (2008).

16. Rong, X. *et al.* LXRs regulate ER stress and inflammation through dynamic modulation of membrane phospholipid composition. *Cell Metab* **18**, 685-697 (2013).

17. Horton, J.D., Cohen, J.C. & Hobbs, H.H. PCSK9: a convertase that coordinates LDL catabolism. *J Lipid Res* **50 Suppl**, S172-177 (2009).

18. Kjaer, A. *et al.* Insulin/hypoglycemia-induced adrenocorticotropin and beta-endorphin release: involvement of hypothalamic histaminergic neurons. *Endocrinology* **132**, 2213-2220 (1993).

19. Peet, D.J. *et al.* Cholesterol and bile acid metabolism are impaired in mice lacking the nuclear oxysterol receptor LXR alpha. *Cell* **93**, 693-704 (1998).

20. Brown, M.S. & Goldstein, J.L. Cholesterol feedback: from Schoenheimer's bottle to Scap's MELADL. *J Lipid Res* **50 Suppl**, S15-27 (2009).

21. Oslund, R.C., Cermak, N. & Gelb, M.H. Highly specific and broadly potent inhibitors of mammalian secreted phospholipases A2. *J Med Chem* **51**, 4708-4714 (2008).

22. Beck, S. *et al.* Potentiation of tumor necrosis factor alpha-induced secreted phospholipase A2 (sPLA2)-IIA expression in mesangial cells by an autocrine loop involving sPLA2 and peroxisome proliferator-activated receptor alpha activation. *J Biol Chem* **278**, 29799-29812 (2003).

23. Ekbote, A.V. *et al.* Patient with mutation in the matrix metalloproteinase 2 (MMP2) gene - a case report and review of the literature. *J Clin Res Pediatr Endocrinol* **6**, 40-46 (2014).

24. Braunwald, E., Harrison, D.C. & Chidsey, C.A. The Heart as an Endocrine Organ. *Am J Med* **36**, 1-4 (1964).

25. Ogawa, T. & de Bold, A.J. The heart as an endocrine organ. *Endocr Connect* **3**, R31-44 (2014).

26. Rashed, H.M., Nair, B.G. & Patel, T.B. Regulation of hepatic glycolysis and gluconeogenesis by atrial natriuretic peptide. *Arch Biochem Biophys* **298**, 640-645 (1992).

27. Sengenes, C., Berlan, M., De Glisezinski, I., Lafontan, M. & Galitzky, J. Natriuretic peptides: a new lipolytic pathway in human adipocytes. *FASEB J* **14**, 1345-1351 (2000).

28. Bordicchia, M. *et al.* Cardiac natriuretic peptides act via p38 MAPK to induce the brown fat thermogenic program in mouse and human adipocytes. *J Clin Invest* **122**, 1022-1036 (2012).

29. Baskin, K.K. *et al.* MED13-dependent signaling from the heart confers leanness by enhancing metabolism in adipose tissue and liver. *EMBO Mol Med* **6**, 1610-1621 (2014).

30. Grueter, C.E. *et al.* A cardiac microRNA governs systemic energy homeostasis by regulation of MED13. *Cell* **149**, 671-683 (2012).

31. Magida, J.A. & Leinwand, L.A. Metabolic crosstalk between the heart and liver impacts familial hypertrophic cardiomyopathy. *EMBO Mol Med* **6**, 482-495 (2014).

32. Lambeau, G. & Gelb, M.H. Biochemistry and physiology of mammalian secreted phospholipases A2. *Annu Rev Biochem* **77**, 495-520 (2008).

33. Murakami, M., Sato, H., Miki, Y., Yamamoto, K. & Taketomi, Y. A new era of secreted phospholipase A(2). *J Lipid Res* **56**, 1248-1261 (2015).

34. Sato, H. *et al.* The adipocyte-inducible secreted phospholipases PLA2G5 and PLA2G2E play distinct roles in obesity. *Cell Metab* **20**, 119-132 (2014).

35. Ou, J. *et al.* Unsaturated fatty acids inhibit transcription of the sterol regulatory element-binding protein-1c (SREBP-1c) gene by antagonizing ligand-dependent activation of the LXR. *Proc Natl Acad Sci U S A* **98**, 6027-6032 (2001).

36. Jump, D.B., Tripathy, S. & Depner, C.M. Fatty acid-regulated transcription factors in the liver. *Annu Rev Nutr* **33**, 249-269 (2013).

37. Liu, S. *et al.* A diurnal serum lipid integrates hepatic lipogenesis and peripheral fatty acid use. *Nature* **502**, 550-554 (2013).

38. Semenkovich, C.F. Fatty acid metabolism and vascular disease. *Trends Cardiovasc Med* **14**, 72-76 (2004).

39. Leone, T.C., Weinheimer, C.J. & Kelly, D.P. A critical role for the peroxisome proliferator-activated receptor alpha (PPARalpha) in the cellular fasting response: the

PPARalpha-null mouse as a model of fatty acid oxidation disorders. *Proc Natl Acad Sci U S A* **96**, 7473-7478 (1999).

40. Greenlee, K.J., Werb, Z. & Kheradmand, F. Matrix metalloproteinases in lung: multiple, multifarious, and multifaceted. *Physiol Rev* **87**, 69-98 (2007).

41. Corry, D.B. *et al.* Decreased allergic lung inflammatory cell egression and increased susceptibility to asphyxiation in MMP2-deficiency. *Nat Immunol* **3**, 347-353 (2002).

42. Chung, A.W., Yang, H.H., Radomski, M.W. & van Breemen, C. Long-term doxycycline is more effective than atenolol to prevent thoracic aortic aneurysm in marfan syndrome through the inhibition of matrix metalloproteinase-2 and -9. *Circ Res* **102**, e73-85 (2008).

43. Gu, Y. *et al.* Non-antibacterial tetracyclines modulate mediators of periodontitis and atherosclerotic cardiovascular disease: a mechanistic link between local and systemic inflammation. *Pharmacol Res* **64**, 573-579 (2011).

44. Murakami, M. *et al.* Recent progress in phospholipase A(2) research: from cells to animals to humans. *Prog Lipid Res* **50**, 152-192 (2011).

45. Dennis, E.A., Cao, J., Hsu, Y.H., Magrioti, V. & Kokotos, G. Phospholipase A2 enzymes: physical structure, biological function, disease implication, chemical inhibition, and therapeutic intervention. *Chem Rev* **111**, 6130-6185 (2011).